Advanced Camera for Surveys Instrument Handbook for Cycle 29

(With Historical Information for the Inoperative HRC Channel)

STScI | SPACE TELESCOPE SCIENCE INSTITUTE

3700 San Martin Drive
Baltimore, Maryland 21218
http://hsthelp.stsci.edu/

Operated by the Association of Universities for Research in Astronomy, Inc., for the National Aeronautics and Space Administration

ACS Instrument Handbook

Version 20.0 – January 2021
[PDF version](#)

Advanced Camera for Surveys Instrument Handbook for Cycle 29

(With Historical Information for the Inoperative HRC Channel)

User Support

Please contact the HST Help Desk for assistance. We encourage users to access the new web portal where you can submit your questions directly to the appropriate team of experts.

- Web: http://hsthelp.stsci.edu
- E-mail: help@stsci.edu

Additional Resources

Information and other resources are available from the STScI website:

- http://www.stsci.edu/hst/instrumentation/acs

Revision History

Version	Date	Editors
20.0	January 2021	Ryon, J. E., et al.
19.0	December 2019	Ryon, J. E., et al.
18.0	January 2019	Ryon, J. E., et al.
17.0	May 2018	Ryon, J. E., et al.
16.0	January 2017	Avila, R., et al.
15.0	January 2016	Avila, R., et al.
14.0	January 2015	Avila, R., et al.
13.0	January 2014	Ubeda, L., et al.
12.0	December 2012	Ubeda, L., et al.
11.0	December 2011	Ubeda, L., et al.
10.0	December 2010	Maybhate, A. and Armstrong, A., et al.
9.0	January 2010	Maybhate, A., et al.
8.0	December 2007	Boffi, F.R., et al.
7.1	December 2006	Pavlovsky, C. et al.
7.0	October 2006	Pavlovsky, C., et al.
6.0	October 2005	Gonzaga, S., et al.
5.0	October 2004	Pavlovsky, C., et al.
4.0	October 2003	Pavlovsky, C., et al.
3.0	October 2002	Pavlovsky, C., et al.
2.1	July 2001	Pavlovsky, C., et al.
2.0	June 2001	Suchkov, A., et al.
1.0	June 2000	Jedrzejewski, R., et al.

Citation

In publications, refer to this document as:

- Ryon, J. E., et al. 2021, "ACS Instrument Handbook," Version 20.0 (Baltimore: STScI)

Acknowledgments

Acknowledgements

The technical and operational information contained in this Handbook is the summary of the experience gained by members of the STScI ACS Team, the ACS group at the former Space Telescope European Coordinating Facility (ST-ECF), and by the ACS Instrument Definition Team (IDT).

Members of the STScI ACS Team are:

Norman Grogin (Lead), Jay Anderson, Roberto Avila (Deputy Lead), Ralph Bohlin, Marco Chiaberge[1], Yotam Cohen, Tyler Desjardins, Nimish Hathi, Dean Hines, Samantha Hoffmann, Ray Lucas, Meaghan McDonald, Melanie Olaes, Vera Platais, and Jenna Ryon.

The ST-ECF ACS group comprised Martin Kuemmel, Harald Kuntschner, and Jeremy Walsh. The ST-ECF ceased operations on December 31, 2010.

The ACS IDT comprised Holland Ford (PI), Garth Illingworth (Deputy PI), George Hartig, Mark Rafal, Frank Bartko, Tom Broadhurst, Bob Brown, Chris Burrows, Ed Cheng, Mark Clampin, Jim Crocker, Paul Feldman, Marijn Franx, David Golimowski, Randy Kimble, John Krist, Tom La Jeunesse, Mike Lesser, Doug Leviton, George Miley, Marc Postman, Piero Rosati, Bill Sparks, Pam Sullivan, Zlatan Tsvetanov, Paul Volmer, Rick White, Bob Woodruff, Terence Allen, Kenneth Anderson, David Ardila, Narciso Benitez, John Blakeslee, Rychard Bouwens, Larry Bradley, Nicholas J.G. Cross, Ricardo Demarco, Tomotsugu Goto, Caryl Gronwall, Brad Holden, Nicole Homeier, Daniel Magee, André Martel, W. Jon McCann, Simona Mei, Felipe Menanteau, Gerhardt Meurer, Veronica Motta, Alessandro Rettura, Marco Sirianni, Hien Tran, and Andrew Zirm.

The contributions of Dan Coe, Michele de la Peña, Warren Hack, Pey-Lian Lim, Alan Welty, Tom Wheeler, and Susan Rose (Sr. Technical Editor) are greatly appreciated.

[1] European Space Agency (ESA)

Chapter 1: Introduction

The Advanced Camera for Surveys (ACS), a third-generation instrument, was installed in the *Hubble Space Telescope* during Servicing Mission 3B, on March 7, 2002. Its primary purpose was to increase *HST* imaging discovery efficiency by about a factor of 10, with a combination of detector area and quantum efficiency that surpassed previous instruments.

ACS has three independent channels that have provided wide field, high resolution, and ultraviolet imaging capabilities respectively, using a broad assortment of filters designed to address a large range of scientific goals. In addition, coronagraphic, polarimetric, and grism capabilities have made the ACS a versatile and powerful instrument.

The *ACS Instrument Handbook*, which is maintained by the ACS Team at STScI, describes the instrument properties, performance, operations, and calibration. It is the basic technical reference manual for the instrument, and should be used with other documents (listed in Table 1.1) for writing Phase I proposals, detailed Phase II programs, and for data analysis. (See Figure 1.1).

In May 2009, Servicing Mission 4 (SM4) successfully restored the ACS Wide Field Channel (WFC) to regular service after its failure in January 2007. Unfortunately, the ACS High Resolution Channel (HRC) was not restored to operation during SM4, so it cannot be proposed for new observations. Nevertheless, this handbook retains description of the HRC to support analysis of archived observations. The ACS Solar Blind Channel (SBC) was unaffected by the January 2007 failure of WFC and HRC. The SBC has remained in steady operation, and was not serviced during SM4. It remains available for new observations.

Table 1.1: Useful documents

Purpose	Document or Resource
General information and Phase I proposals	HST Proposal Opportunities and Science Policies, including the *HST Call for Proposals* and the *HST Primer*: https://hst-docs.stsci.edu/display/HSP/HST+Proposal+Opportunities+and+Science+Policies
Phase II programs	*Phase II Proposal Instructions* https://hst-docs.stsci.edu/hpiom Astronomer's Proposal Tool (APT) for Phase I and II preparations http://apt.stsci.edu/ ACS Dither Pointing Patterns http://www.stsci.edu/hst/instrumentation/acs/proposing/dither-strategies
Data analysis	*ACS Data Handbook* https://hst-docs.stsci.edu/display/ACSDHB *Drizzlepac Handbook* http://www.stsci.edu/scientific-community/software/drizzlepac.html Space Telescope Analysis Newsletter http://www.stsci.edu/hst/instrumentation/acs/documentation/stsci-analysis-newsletter-stan Instrument Science Reports http://www.stsci.edu/hst/instrumentation/acs/documentation/instrument-science-reports-isrs Post-observation Overview http://www.stsci.edu/hst/observing/post-observation ACS Data Calibration and Analysis http://www.stsci.edu/hst/instrumentation/acs/data-analysis
Instrument specific	ACS webpage http://www.stsci.edu/hst/instrumentation/acs

Figure 1.1: Handbook roadmap for proposal preparation.
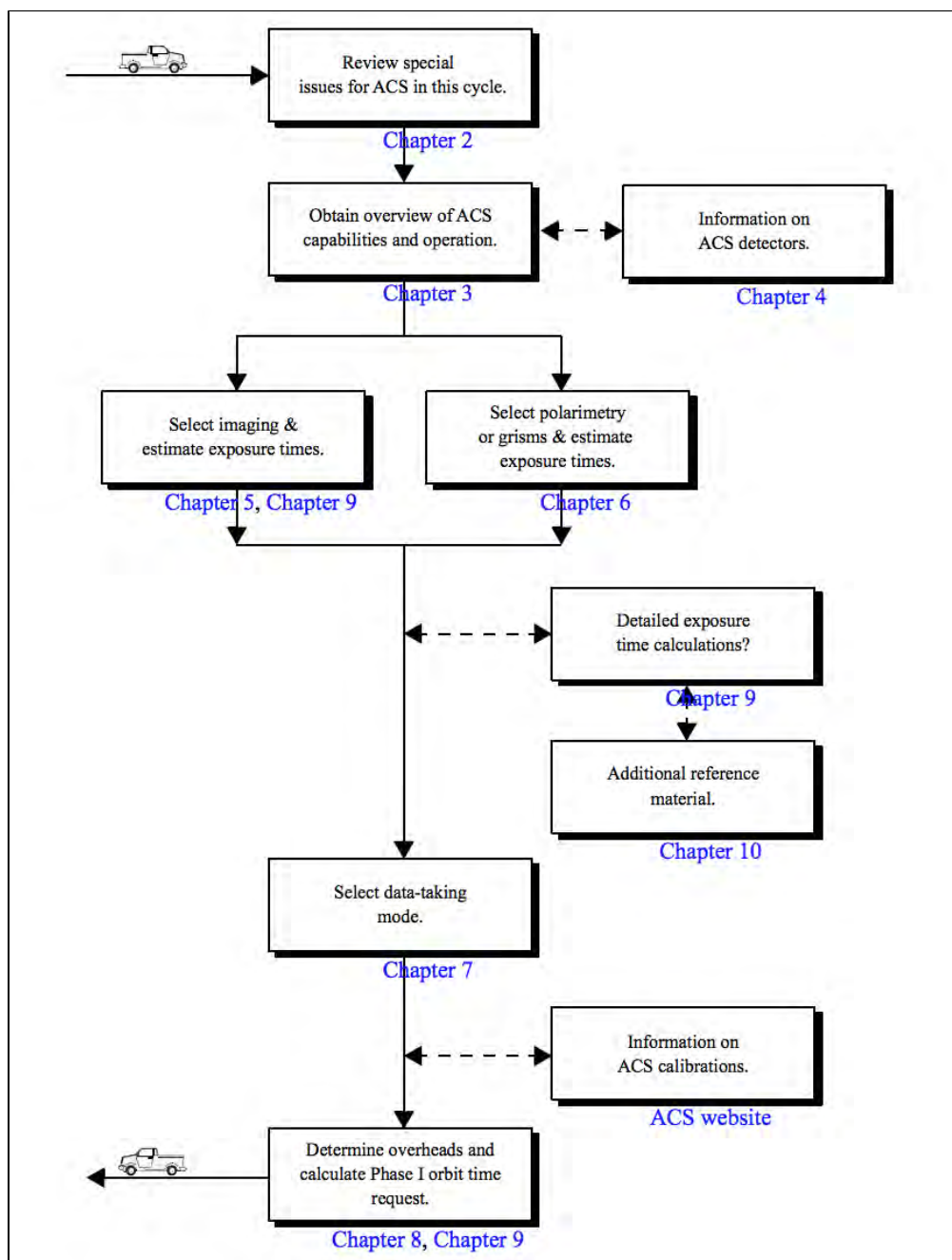
Chapter 2: Considerations and Changes After SM4

Chapter Contents

2.1 SM4 Repair of ACS

The ACS CCD Electronics Box (CEB) and Low Voltage Power Supply (LVPS) incrementally failed in June 2006 and January 2007, causing the loss of the ACS Wide Field Channel (WFC) and High Resolution Channel (HRC). The replacement components (CEB-R and LVPS-R) installed on 16 May 2009 during *HST* Servicing Mission 4 (SM4) successfully restored the function of the WFC but not that of the HRC. Unfortunately, the damage in 2006 to the circuitry that controlled the HRC occurred upstream of the location repaired by the CEB-R. This situation was not unexpected, as the post-failure analysis of the nature and location of the short in the HRC circuitry was ambiguous. Consequently, only the WFC and the Solar Blind Channel (SBC) are available to observers from 2009 onwards.

The CEB-R features new CCD controller and signal processing electronics based upon a programmable SIDECAR (system image, digitizing, enhancing, controlling, and retrieving) ASIC (Application-Specific Integrated Circuit) manufactured by Teledyne Scientific & Imaging. The dual-slope integrator within the CEB-R delivers nearly 1 e$^-$ lower read noise than was obtained with the old CEB. The CEB-R does, however, induce some low-level (0.9 e$^-$ RMS) correlated noise and a spatially variable bias level in the WFC images. The bias level of each pixel also shifts by 0.02–0.3% of the signal. These artifacts are removed in CALACS pipeline processing and have little to no effect on most WFC science programs. Because the bias gradient depends on the timing pattern of the CCD readout, the original WFC subarray modes were replaced at the end of Cycle 23 with new modes that match the full-frame readout timing. See Section 7.3.1 for details.

Table 2.1 lists the basic characteristics of the WFC CCDs. The second column lists the values before the failure of ACS in January 2007. The third column lists the values as of August 2020, well after the installation of the CEB-R during SM4 in May 2009. The fourth column in the table lists the section in this Handbook where detailed information about each characteristic can be found. Further details on improvements after SM4 can be found in ACS ISR 2011-04.

Table 2.1: WFC Performance Summary

Characteristic	January 2007 (pre-SM4)	August 2020 (post-SM4)	Handbook Section
Read noise (e$^-$; gain = 2)	5.5	3.75–5.65	Section 4.3.3
Dark current (e$^-$ /pix/hr)	10.7	40-50	Section 4.3.4
Hot pixels (%)	0.53	1.94	Section 4.3.5
Unstable Hot Pixels (%)	0.06	~0.2	Section 4.3.5
Full well depth (e$^-$)	84,000	>80,000	Section 4.3.1
Non-linearity (%)	<0.1	<0.2	Section 4.3.1
CTE (1620 e$^-$; EPER)	<0.999949	0.99973	Section 4.3.8
Bias shift (%)	0.02	0.02–0.30 [a]	Section 2.1

[a] <u>Before</u> application of bias-shift correction algorithm.

2.2 Comparison of WFC and UVIS

The UVIS channel of the Wide Field Camera 3 complements ACS/WFC over wavelengths ~3700 Å to 10,000 Å. Observers must determine which instrument is more appropriate for their science from the perspectives of field of view, pixel size, throughput, and filter availability. Table 2.2, Figure 2.1 and Figure 2.2 show these characteristics for each instrument. See also Figures 5.8 (limiting magnitude for point sources) and 5.9 (limiting magnitude for extended sources). ACS/WFC has a larger pixel scale (0.05 arcsec/pixel) than WFC3/UVIS (0.04 arcsec/pixel), so the field of view of ACS/WFC (202 × 202 arcsec^2) is considerably larger than that of WFC3/UVIS (162 × 162 arcsec^2). WFC3/UVIS may therefore be preferred if angular resolution is more important than field of view. On the other hand, ACS/WFC is more sensitive than WFC3/UVIS at wavelengths longward of ~4000 Å, so ACS/WFC is recommended if greater sensitivity at red wavelengths is important. However, users should also consider ACS's generally lower charge-transfer efficiency (CTE) compared to WFC3/UVIS caused by its lengthier exposure to *HST*'s trapped radiation environment. See Section 4.3.8 for details. It is also possible to use both ACS/WFC and WFC3/UVIS in parallel. The separation of the two cameras is ~360" (see Figure 3.1).

Table 2.2: Comparison of wavelength coverage, pixel scales, and fields of view of ACS and WFC3/UVIS. HRC is no longer available. More information can be found at the SIAF website.

Instrument	Wavelength coverage (nm)	Average Pixel size (arcsec)	Field of View (arcsec^2)
WFC3 UVIS	200–1000	0.04	162 × 162
ACS WFC	370–1100	0.05	202 × 202
ACS HRC	200–1100	0.028 × 0.025	29 × 25
ACS SBC	115–170	0.034 × 0.030	35 × 31

Figure 2.1: *HST* total system throughputs as a function of wavelength.
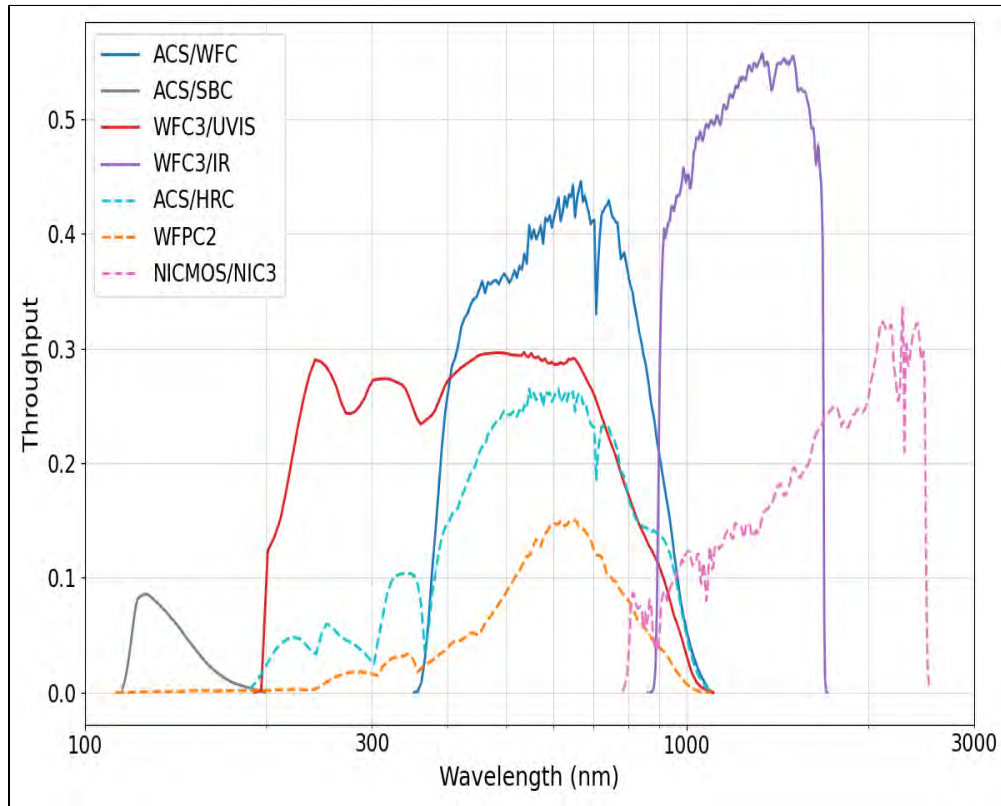
The plotted quantities are the maximum end-to-end throughputs, including filter transmissions, available for a given instrument at each wavelength. Full lines represent instruments currently active on board *HST*. Dashed lines represent instruments that are no longer offered (HRC, NICMOS) and a previously flown instrument (WFPC2).

Figure 2.2: *HST* survey discovery efficiencies.
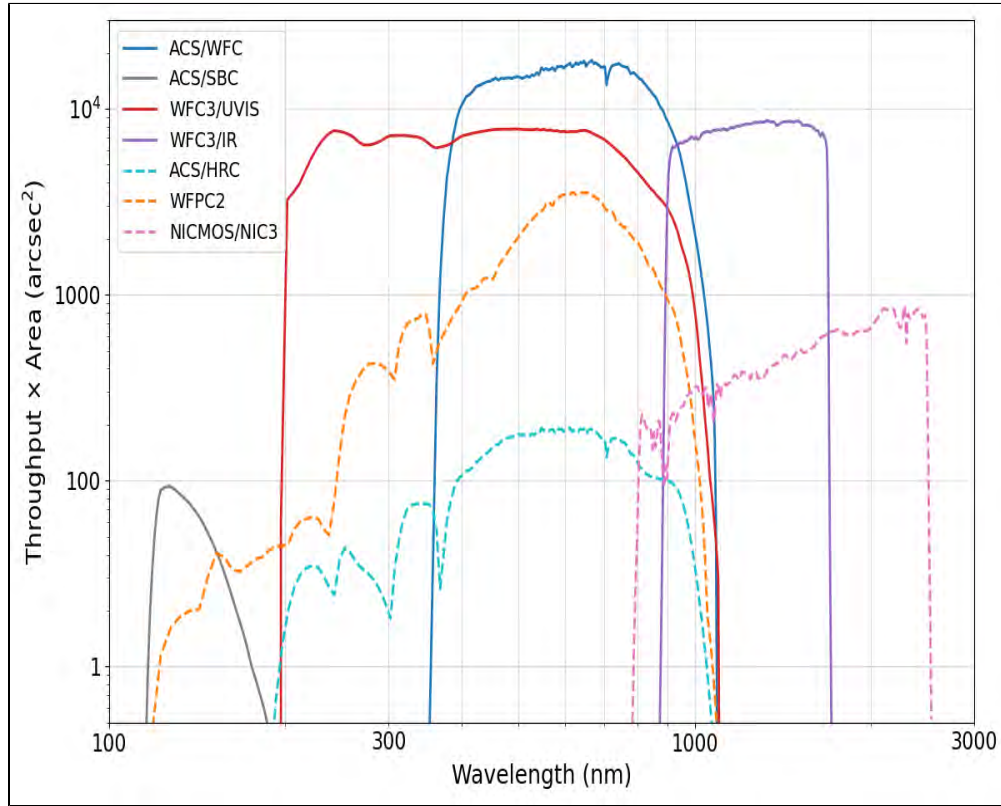
HST survey discovery efficiencies of the cameras, defined as the system throughput multiplied by the area of the field-of-view. Full lines represent instruments currently active on board HST. Dashed lines represent instruments that are no longer offered (HRC, NICMOS) and a previously flown instrument (WFPC2).

2.3 Comparison of HRC and UVIS

Because ACS/HRC is no longer available, WFC3/UVIS is the preferred camera for the 2000 Å to 3700 Å wavelength range. The Space Telescope Imaging Spectrograph (STIS) NUV-MAMA has imaging capabilities over some of this bandpass, but it has a much smaller field of view and lower sensitivity. Table 2.2, Figure 2.1 and Figure 2.2 compare the imaging characteristics of ACS/HRC and WFC3/UVIS. WFC3/UVIS has twice the U-band throughput of ACS/HRC (Figure 2.2), a field of view that is 35 times larger than that of ACS/HRC, and a pixel scale that is 60% coarser than that of ACS/HRC. WFC3/UVIS is insensitive below 2000 Å. Far-UV imaging on *HST* is provided by the ACS/SBC and the STIS/FUV-MAMA.

2.4 Dithering Considerations

The ACS Team recommends that observers dither (or offset) their observations to mitigate the effects of hot pixels, cosmic defects, and cosmic rays in their combined images. Dithering allows improved sampling of the point spread function and yields better images than are possible with the CR-SPLIT option, which does not remove hot pixels, permanent cosmetic defects (e.g., bad columns), or the gap between the WFC CCDs. It is noteworthy that hot pixels now contaminate nearly 2% of the WFC detector, though >90% of these are stable and can be reliably dark-subtracted (ACS ISR 2017-05).

Dithering can be performed in two ways:

1. explicit positional offsets between exposures via POS TARG instructions; or
2. flexible pre-defined dither patterns that can be nested to implement different pixel subsampling strategies.

Both methods yield associations of images for pipeline data processing. Currently available pre-defined dither patterns and their recommended uses are described on the ACS Dither webpage.

The ACS Team at STScI is available to help observers select dither patterns that best suit their science goals. Because STScI wishes to maximize the legacy value of *HST* observations, observers who choose not to dither their ACS/WFC exposures must provide a justification in the Description of Observations section of their Phase I proposal.

2.5 CTE Considerations

Observers should consider the effect of charge transfer efficiency (CTE) losses on their data. These issues and recommendations are discussed in some detail for ACS/WFC and WFC3/UVIS in the CTE White Paper and on the ACS CTE Information webpage. CTE losses can be mitigated using two different approaches: (1) post-processing using either a pixel-based correction algorithm to restore the values of the pixels or correcting photometry to account for the losses, and/or (2) adjusting the observing strategy to increase the CTE during the CCD readout process.

For option (1), the CALACS pipeline now employs a second generation pixel-based CTE correction algorithm described in ACS ISR 2018-04. This routine works well when CTE losses are not severe. Extensive testing has shown that for typical ACS backgrounds, the correction algorithm has a 75% reconstruction accuracy. For very low backgrounds, 90% of the charge can be lost as the CCD is read out, and these large losses cannot be reconstructed. An alternative technique for point sources is to apply the formula provided in ACS ISR 2012-05 to correct the measured photometry for CTE losses as a function of CCD position, background level, source flux, and observation date. This formula is similarly unable to estimate accurate fluxes for objects that have been CTE-trailed beyond detectability. A calculator is available to apply this CTE correction formula to measured photometry.

For option (2), there are several strategies that can be employed. The simplest is to place the source near the WFC serial registers (located furthest from the gap between the WFC CCDs) to reduce the number of CCD parallel transfers. This can be accomplished by using the aperture `WFC1-CTE` (Table 7.7). If this is not possible (e.g., if the source subtends >5 arcsec), then the observer should estimate the sky background using the information given in ACS ISR 2012-04. Here empirical sky backgrounds are provided for all of the ACS filters as a function of exposure time and compared to Exposure Time Calculator (ETC) estimates. Observers should check that the sky background is above 20 e$^-$ for a given exposure time. If the background is lower than this value, observers should consider increasing their exposure times or using a LED post-flash to increase the background. For the latest details and recommendations on ACS/WFC post-flash capabilities, please refer to ACS ISRs 2018-02 and 2014-01.

2.6 SBC Considerations

It is essential that observers proposing to use the SBC review and abide by the procedures and rules described in Section 4.6 and Section 7.2. Designing safe observing programs will protect the MAMA detectors in the SBC from being permanently damaged by over-illumination. We therefore ask all users to share the responsibility of STScI to ensure the safety of the MAMA detectors. All proposed SBC targets and fields must be discussed in the Phase I proposal, so that their feasibility can be assessed by the TAC and STScI.

> ⚠️ *In 2019, the zeropoints for the SBC were updated to correct a long-standing ~30% discrepancy in the absolute flux calibration of the imaging modes. The error was found to be caused by inaccuracies in the filter and detector throughput tables used to derive the SBC zeropoints. The discrepancy is such that the SBC is actually ~30% more sensitive than previously estimated: a source of a given astronomical flux produces a ~30% larger SBC count-rate. Conversely, prior conversions of observed SBC count-rate to flux have overestimated the astronomical flux by ~30%. The throughput tables have now been corrected, and new zeropoints have been derived for the relevant imaging modes. Details are provided in ACS ISR 2019-05.*

Chapter 3: ACS Capabilities, Design and Operations

Chapter Contents

3.1 ACS Location in the HST Focal Plane

ACS is mounted in one of the axial instrument bays behind the *HST* primary mirror. The relative locations of the science instruments (SI) in the focal plane and their fields of view are shown schematically in Figure 3.1. When referring to the *HST* and its focal plane, we use a coordinate system that is fixed to the telescope and consists of three orthogonal axes: U1, U2 and U3. U1 lies along the optical axis, U2 is parallel to the solar-array rotation axis, and U3 is perpendicular to the solar-array axis. (Note: Some HST documentation uses the alternative V1, V2, V3 coordinate system for which V1 = U1, V2 = –U2 and V3 = –U3.)

Figure 3.1: The *HST* field of view with the locations of the SI and the Fine Guidance Sensor (FGS) apertures in the (U2,U3) focal plane. The layout of the instrument entrance apertures in the telescope focal plane as projected onto the sky are shown. The scale in arcseconds is indicated.
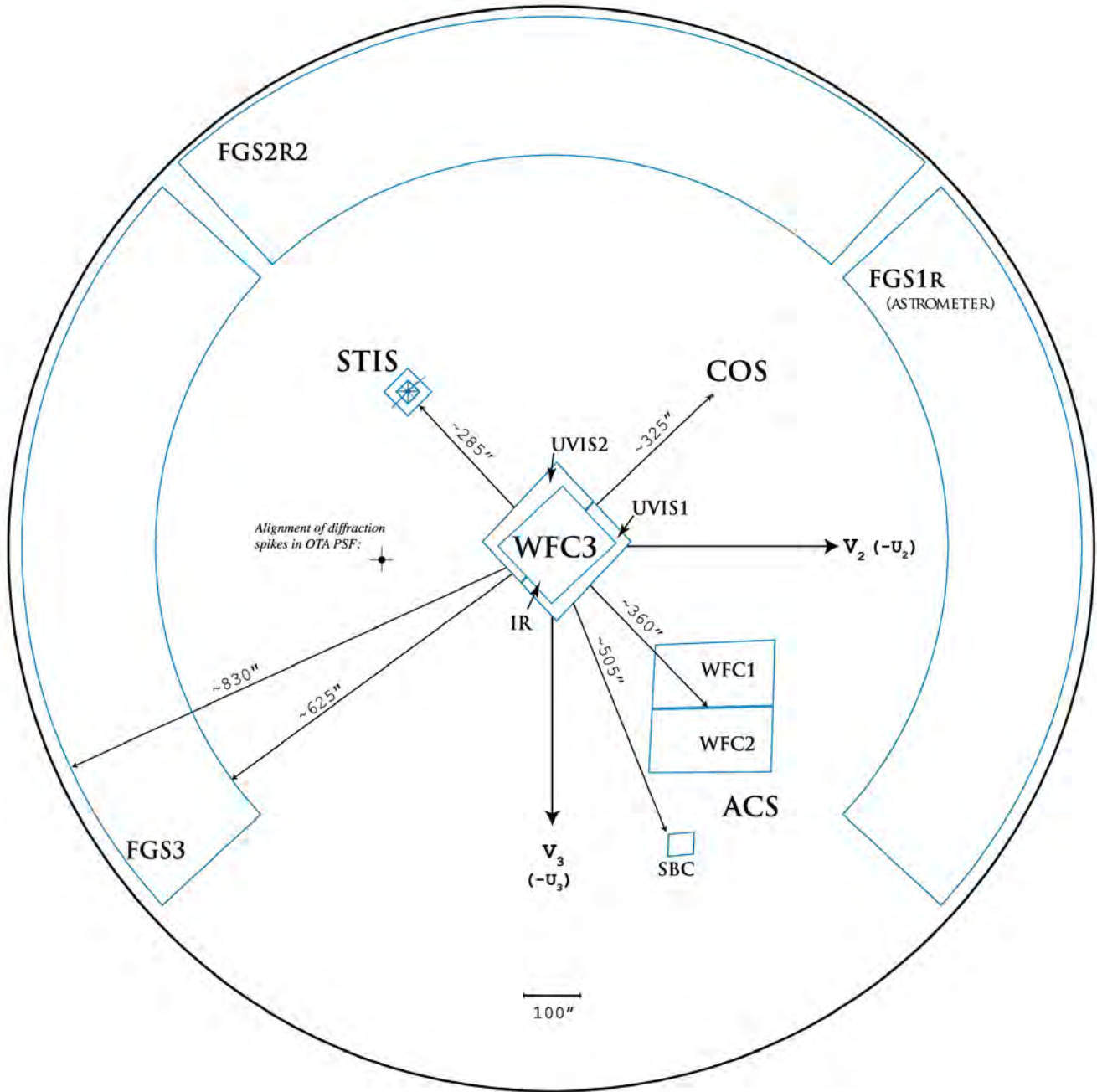
3.2 Instrument Capabilities

> ⊘ *Please check for updates on the [ACS website](#).*

ACS is a versatile instrument with a broad range of scientific capabilities: It was built with three channels, each optimized for a specific goal:

- deep, wide-field imaging from visible to near-IR wavelengths with the Wide Field Channel (WFC) (in service March 2002 to present).
- high spatial resolution imaging from near-UV to near-IR wavelengths with the High Resolution Channel (HRC) (in service March 2002 to January 2007).
- solar-blind UV imaging with the Solar Blind Channel (SBC) (in service March 2002 to present).

In addition to its primary capabilities listed above, ACS also provides:

- Grism spectroscopy: low resolution (R ~100 @ 8000 Å) wide field spectroscopy from 5500 Å to 10,500 Å with WFC (and HRC before January 2007).
- Prism spectroscopy: low resolution (R ~100 @ 1500 Å) far-UV spectroscopy from 1250 Å to 1800 Å with SBC (and low resolution, R = 59 @ 2500 Å, near-UV spectroscopy from 1700 Å to 3900 Å with HRC before January 2007).
- Imaging Polarimetry: polarimetric imaging with WFC (and HRC before January 2007) with relative polarization angles of 0°, 60°, and 120°.
- Coronagraphy (before January 2007): aberrated beam coronagraphy with HRC from 2000 Å to 11,000 Å with 1.8 arcsecond and 3.0 arcsecond diameter occulting spots.

3.3 Instrument Design

3.3.1 Detectors

The ACS channels feature the following detectors:

- The WFC employs a mosaic of two 4096 x 2048 Scientific Imaging Technologies (SITe) CCDs. The 15 × 15 μm^2 pixels provide ~0.05 arcsec/pixel spatial resolution, with critical (Nyquist) sampling at 11,600 Å, resulting in a nominal 202 × 202 arcsec^2 Field of View (FOV). The spectral sensitivity of the WFC ranges from ~3500 Å to ~11,000 Å, with a peak efficiency of 47% at ~6700 Å including the Optical Telescope Assembly (OTA).
- The nonfunctioning HRC has a 1024 × 1024 SITe CCD, with 21 × 21 μm^2 pixels that provided ~0.028 × 0.025 arcsec^2/pixel spatial resolution with critical sampling at 6300 Å. This gave the HRC a nominal 29 × 26 arcsec^2 field of view. The spectral response of the HRC ranged from ~1700 Å to ~11,000 Å, and it had a peak efficiency of 27% at ~6300 Å including OTA.
- The SBC detector is a solar-blind CsI microchannel plate (MCP) with Multi-Anode Microchannel Array (MAMA) readout. It has 1024 × 1024 pixels, each 25 × 25 μm^2 in size. This provides a spatial resolution of ~0.034 × 0.030 arcsec^2/pixels, producing a nominal FOV of 34.6 × 30.5 arcsec^2. The SBC UV spectral response ranges from ~1150 Å to ~1700 Å with a peak efficiency of 8.6% at 1260 Å.

The WFC & HRC CCDs

The ACS CCDs are thinned, backside-illuminated, full-frame devices. They are cooled by thermo-electric cooler (TEC) stacks housed in sealed, evacuated dewars with fused silica windows. The spectral response of the WFC CCDs is optimized for imaging at visible to near-IR wavelengths, while the HRC CCD spectral response was optimized specifically for near-UV wavelengths. The WFC CCD camera produces a time-integrated image in the ACCUM data-taking mode as did the HRC CCD before January 2007. As with all CCD detectors, there is noise and overhead associated with reading out the detector following an exposure.

The minimum WFC exposure time is 0.5 seconds. The minimum time between successive identical full-frame WFC exposures is 135 seconds. The dynamic range for a single exposure is ultimately limited by the depth of the CCD full well (~85,000 e⁻ for the WFC and 155,000 e⁻ for the HRC), which determines the total amount of charge that can accumulate in any one pixel during an exposure without physical saturation.

Cosmic rays will affect all CCD exposures. CCD observations should be broken into multiple exposures whenever possible to allow removal of cosmic rays in post-observation data processing (see Section 4.3.7).

The SBC MAMA

The SBC MAMA is a photon-counting detector that provides a two-dimensional ultraviolet imaging and spectroscopic capability. It is operated only in ACCUM mode. To protect the MAMA against permanent damage from over-illumination, local and global brightness limits of 50 counts/second/pixel and 200,000 counts/second, respectively, are imposed on all SBC targets. Note that the linearity of the MAMA deviates by 1% at a local (pixel) count rate of ~22 counts/second/pixel, which is about half the bright object screening limit. The global count rate becomes similarly nonlinear at the screening limit of 200,000 counts/second. More information on the SBC's nonlinearity and bright object limits is given in Section 4.5, Section 4.6, and Section 7.2, and in ACS ISRs 1998-03, 1999-07, and 2019-10.

3.3.2 ACS Optical Design

The ACS design incorporates two main optical channels: one for the WFC, and one which is shared by the HRC and SBC. Each channel has independent corrective optics to compensate for spherical aberration in the *HST* primary mirror. The WFC has silver-coated optics to optimize instrument throughput in the visible and near-IR. The silver coatings cut off wavelengths shortward of 3500 Å. The WFC has two filter wheels that it shared with the HRC, offering the possibility of internal WFC/HRC parallel observing for some filter combinations (Section 7.9). The optical design of the WFC is shown schematically in Figure 3.2. The HRC/SBC optical chain comprises three aluminized mirrors overcoated with MgF_2, shown schematically in Figure 3.3. The HRC or SBC channels are selected by means of a plane fold mirror (M3 in Figure 3.3). The HRC was selected by inserting the fold mirror into the optical chain so that the beam was imaged onto the HRC detector through the WFC/HRC filter wheels. The SBC channel is selected by moving the fold mirror out of the beam to yield a two mirror optical chain that focuses light through the SBC filter wheel onto the SBC detector. The aberrated beam coronagraph was accessed by inserting a mechanism into the HRC optical chain. This mechanism positioned a substrate with two occulting spots at the aberrated telescope focal plane and an apodizer at the re-imaged exit pupil. While there is no mechanical reason why the coronagraph could not be used with the SBC, for health and safety reasons, use of the coronagraph is forbidden with the SBC.

Figure 3.2: ACS optical design: Wide Field Channel (ACS/WFC).
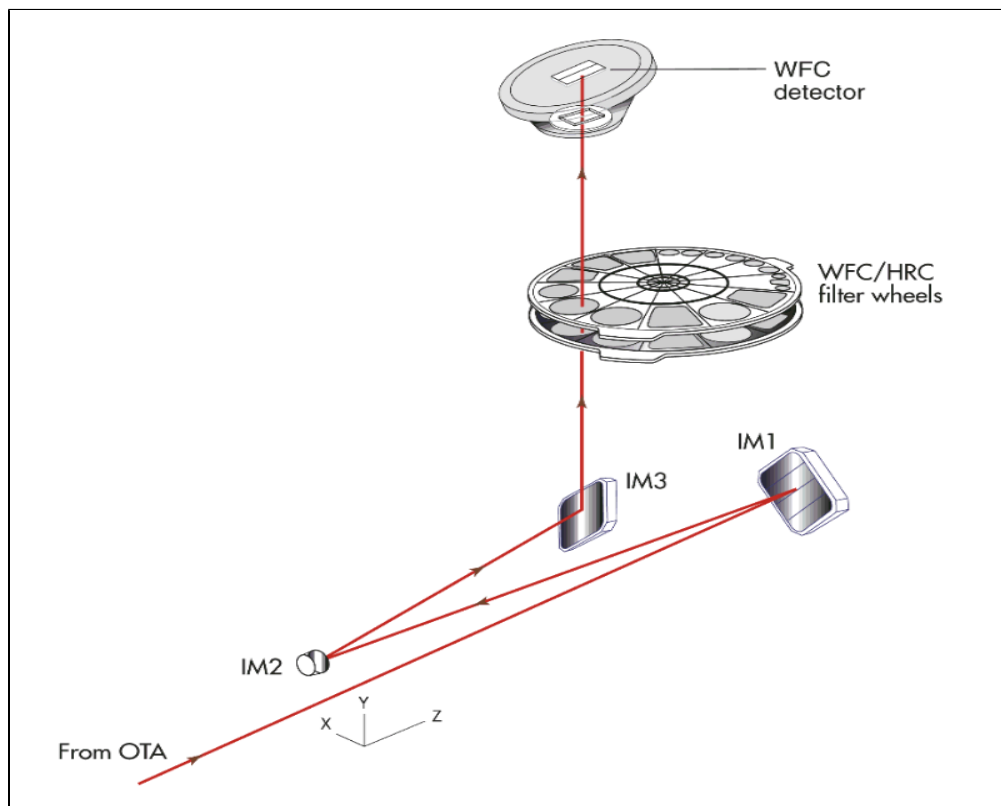
Figure 3.3: ACS optical design: High Resolution/Solar Blind Channels (ACS/HRC and ACS/SBC).
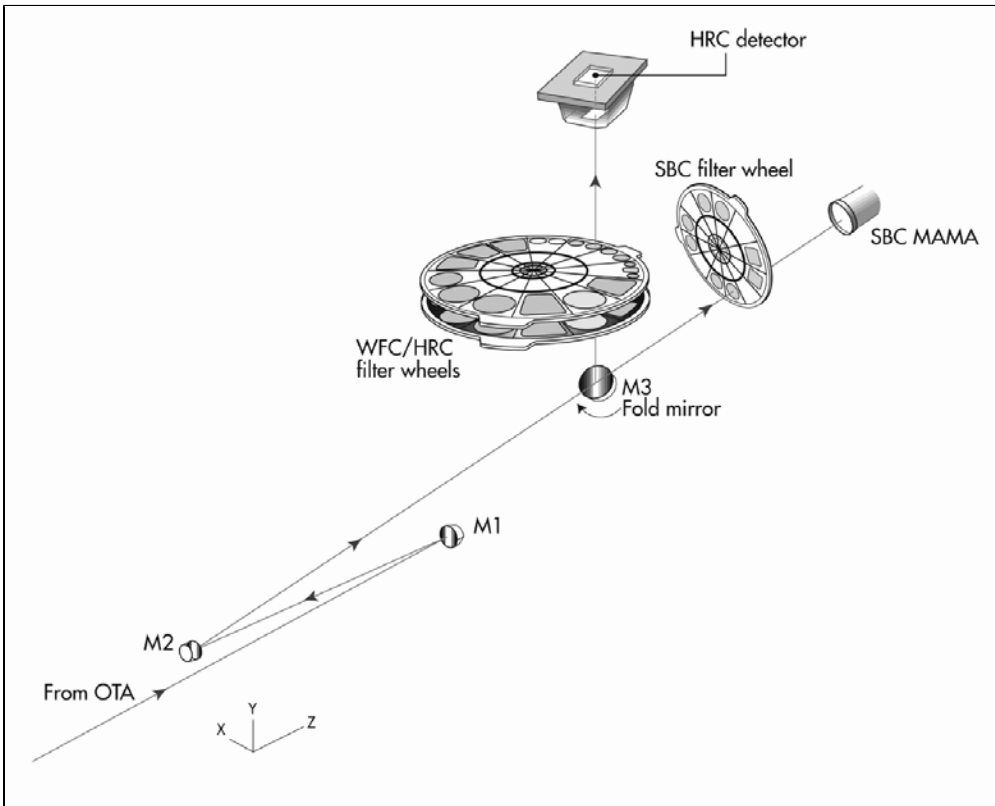
Filter Wheels

ACS has three filter wheels: two shared by the WFC and HRC, and a separate wheel dedicated to the SBC. The WFC/HRC filter wheels contain the major filter sets. Each wheel also contains one clear WFC aperture and one clear HRC aperture (see Chapter 5 for more on filters). Before January 2007, parallel WFC and HRC observations were possible for some filter combinations (auto-parallels). Because the filter wheels were shared, it was not possible to independently select the filter for WFC and HRC parallel observations.

Calibration Lamp Systems

ACS has a calibration subsystem consisting of tungsten lamps and a deuterium lamp for internally flat-fielding each of the optical channels. The calibration lamps illuminate a diffuser on the rear surface of the ACS aperture door, which must be closed for calibration exposures. Under normal circumstances, users are not allowed to use the internal calibration lamps.

Post-Flash LED

An Opto Diode OD-800W light emitting diode (LED) is attached to the ACS/WFC instrument housing. It is used to post-flash the detector after an exposure has completed and the shutter has closed. The post-flash raises the background level of an image by illuminating the LED at a specified current level (LOW, MEDIUM, HIGH) and for a specified duration. Post-flash is typically employed to mitigate the effects of poor charge transfer efficiency (CTE), especially at low background levels. For more details on the LED and post-flash calibration, see Sections 2.5 and 9.6, and ACS ISRs 2019-08, 2018-02, 2014-01, and 2006-07.

3.4 Basic Instrument Operations

3.4.1 Target Acquisitions

For the majority of ACS observations, target acquisition is simply a matter of defining the appropriate aperture for the observation. Once the telescope acquires its guide stars, the target will be positioned within 0.5 arcseconds of the specified aperture. For observations with the ramp filters, the desired central wavelength for the observation must be specified.

3.4.2 Typical ACS Observing Sequence

ACS is used primarily for deep, wide-field survey imaging. Important issues for observers to consider are the "packaging" of their observations, how observations can be CR-SPLIT to mitigate the impact of cosmic rays, how sub-stepping or "dithering" of images for removal of hot pixels is implemented, and how, if necessary, a mosaic pattern is constructed to map the target. It is also very important to consider the effects of charge transfer efficiency losses. See ACS ISR 2019-07 for more discussion of these issues in planning ACS observations.

Narrowband observations with the WFC are more likely to be readnoise-limited, requiring consideration of optimum number of readouts. Observations with the MAMA detectors are not affected by cosmic rays or readnoise, but long integration times will often be needed to obtain sufficient signal-to-noise.

A typical ACS observing sequence consists of a series of 10 to 20 minute dithered exposures for each desired filter. Observers will generally not take their own calibration exposures. See Chapter 7 for more details about observing strategies.

3.4.3 Data Storage and Transfer

At the conclusion of each exposure, the science data are read out from the detector and placed in ACS's internal buffer memory, where they are stored until they can be transferred to the *HST* solid state data recorder (and thereafter to the ground). The internal buffer memory is large enough to hold one full-frame WFC image, or sixteen SBC images, and so the buffer typically must be dumped before or during the following WFC exposure. If the following exposure is longer than ~337 seconds, then the buffer dump from the preceding exposure will be performed during integration (see Section 8.2 for a more complete discussion).

ACS's internal buffer stores the data in a 16 bit-per-pixel format. This structure imposes a maximum of 65,535 counts per pixel. For the MAMA detectors, this maximum is equivalent to a limit on the total number of detected photons per pixel which can be accumulated in a single exposure. For the WFC, the 16 bit buffer format is not an issue when the default GAIN = 2.0 is used. The full well will be reached before the buffer is overflowed. See Chapter 4 and Chapter 7 for a detailed description of ACS instrument operations.

3.5 ACS Quick Reference Guide

> ✅ *Please check for updates on the ACS website. Information regarding the HRC is provided for archival purposes only.*

Table 3.1: Instrument characteristics.

	WFC	HRC (inoperable)	SBC
Field of View	202 × 202 arcsec^2	29 × 26 arcsec^2	34.6 × 30.5 arcsec^2
Plate Scale	~0.05 × 0.05 arcsec^2/pixel	~0.028 × 0.025 arcsec^2/pixel	~0.034 × 0.030 arcsec^2/pixel
Pixel Size	15 × 15 μm^2	21 × 21 μm^2	25 × 25 μm^2
Image Format	2 × 2048 × 4096 pixels	1024 × 1024 pixels	1024 × 1024 pixels
Spectral Response	~3500 Å to 11,000 Å	~1700 Å to 11,000 Å	~1150 Å to 1700 Å
Detector	SITe CCDs thinned backside illuminated, anti-reflection coated, multiphased pinned	SITe CCD thinned backside illuminated, anti-reflection coated, multiphased pinned	CsI MCP with MAMA readout
Detector Efficiency [a]	~75% at 4000 Å ~81% at 6000 Å ~66% at 8000 Å	~32% at 2500 Å ~69% at 6000 Å ~53% at 8000 Å	~35% @ 1216 Å
Peak Efficiency [a]	47% at ~6700 Å [c]	27% at ~6400 Å	8.6% at ~1260 Å
Read Noise	3.75 e– to 5.65 e$^-$	4.7 e$^-$	0 counts
Dark Current [a]	0.0137 e$^-$/s/pixel [c]	0.0058 e$^-$/s/pixel	8.28 × 10^{-6} counts/s/pixel when instrument temperature < 25°C [d]
Saturation Level [b]	~77,400 ± 5000 e$^-$ [c]	155,000 e$^-$	Detector count rate linearity limit: 200,000 counts/sec Pixel count-rate linearity limit: ~22 counts/sec/pixel [e]
Gain	0.5, 1.0, 1.4, and 2.0 e$^-$/DN (Max 65,535 DN)	1,2,4 and 8 e$^-$/DN (Max 65,535 DN)	n/a
Operating Temperature	−81°C [c]	−80°C	n/a

a WFC and SBC values extrapolated to April 01, 2022, the middle of Cycle 29, based on recent monitoring trends.

b Saturation level varies over the detector area. See Section 4.3.1 for more information.

c Average value for WFC1 and WFC2.

d ACS ISR 2017-04

e Loss of linearity occurs at count rates larger than these values. For more information, please see Section 4.5.7.

Table 3.2: Calibration accuracies.

Attribute	WFC	HRC	SBC	Limiting factor
Distortion Solution Accuracy	0.1 pixel	0.1 pixel	0.13 pixel	Calibration & stability of geometric distortion [a]
Absolute Astrometry	0.2" to 0.5"	0.2" to 0.5"	0.2" to 0.5"	Guide Star Catalog uncertainties [b]
Absolute Photometry	2%	3%	5% [c]	Absolute flux of standard stars
Relative Photometry within an Image	1%	1%	2%	Flat-field characterization or characterization of geometric distortion.
Repeated Photometry of Same Star	0.3%	0.3%	1%	Stability of flat field
Transformation to Standard Magnitude Systems	0.02 mag SDSS 0.025 mag WFPC2 0.03 mag BVRI	0.02 mag SDSS 0.025 mag WFPC2 0.03 mag BVRI	n/a	DQE curve determination Color terms
Polarimetry	1%	1%	n/a	
Wavelength Calibration	20 Å grism	12 Å grism	1 pixel prisms	Accuracy of dispersion solution
Spectrophotometry	6% (Grism)	10% (Grism)	20% (Prism)	

a ACS ISR 2015-06; ACS ISR 2008-02; ACS ISR 2004-15

b ACS ISR 2005-06

c ACS ISR 2019-05

Table 3.3: ACS filters.

Filter type	Filter description	Camera
Broadband	Sloan Digital Sky Survey (SDSS): F475W, F625W, F775W, F850LP	WFC/HRC
	B, V, Medium V, Wide V, I: F435W, F555W, F550M, F606W, F814W	WFC/HRC
	Near-UV: F220W, F250W, F330W	HRC
	No Filter: CLEAR	WFC/HRC
Narrowband	Hα (2%), [OIII] (1%), [NII] (1%): F658N, F502N, F660N	WFC/HRC
	NeV (3440 Å): F344N	HRC
	Methane (8920 Å): F892N	HRC/[WFC[a]]
Ramp filters	2% bandpass (3700–10,700 Å): FR388N, FR505N, FR656N	WFC/HRC
	2% bandpass (3700–10,700 Å): FR423N, FR462N, FR716N, FR782N, FR853N, FR931N, FR1016N, FR551N, FR601N	WFC
	9% bandpass (3700–10,700 Å): FR459M, FR914M	WFC/HRC
	9% bandpass (3700–10,700 Å): FR647M	WFC
Spectroscopic	Grism: G800L	WFC/HRC
	Prism: PR200L	HRC
Polarizers	Visible (0°, 60°,120°): POL0V, POL60V, POL120V	HRC/[WFC[a]]
	Near-UV (0°, 60°, 120°): POL0UV, POL60UV, POL120UV	HRC/[WFC[a]]
Medium Band	Lyman-Alpha: F122M	SBC
Long Pass	MgF_2, CaF_2, BaF_2, Quartz, Fused Silica: F115LP, F125LP, F140LP, F150LP, F165LP	SBC

Prisms	LiF, CaF$_2$: PR110L, PR130L	SBC

[a] Limited field of view (72 × 72 arcsec^2) for these filters using WFC.

Table 3.4: ACS polarizers.

Polarizer set	Filters	Availability	Filter comments
POL0UV POL60UV POL120UV	F220W F250W F330W F435W F660N [a] F814W	unavailable unavailable unavailable available available available	HRC NUV short HRC NUV long HRC U Johnson B Broad I
POL0V POL60V POL120V	F475W [a] F502N F550M F555W F606W [a] F625W F658N [a] F775W [a] G800L	supported available available available supported available available supported supported	SDSS g Johnson V Johnson V Wide SDSS r Hα SDSS i

[a] These filters are part of an ACS program to calibrate the polarizer/filter combination to 1% or better

Table 3.5: ACS dispersers.

Disperser	Channel	Wavelength range (Å)	Resolving power
G800L	WFC	1st order: 5500 to 10,500	100 @ 8000 Å
G800L	WFC	2nd order: 5000 to 8500	200 @ 8000 Å
G800L	HRC	1st order: 5500 to 10,500	140 @ 8000 Å
G800L	HRC	2nd order: 5500 to 8500	280 @ 8000 Å
PR200L	HRC	1700 to 3900	59 @ 2500 Å
PR110L	SBC	1150 to 1800	79 @ 1500 Å
PR130L	SBC	1250 to 1800	96 @ 1500 Å

Table 3.6: Useful tables and figures list.

Topics	Tables/Figures
Proposal Preparation Tips	Table 7.1: Science decision guide. Table 7.2: Science feasibility guide. Table 9.1: Useful quantities for the ACS WFC, at -81C (since July 2006). Table 9.2: Useful quantities for the ACS SBC. Figure 7.1: Defining an ACS observation.
Overheads	Table 8.1: Science Exposure Overheads: General. Table 8.2: ACS Science Exposure Overhead Times (Minutes).
Aperture Parameters	Table 7.7: WFC aperture parameters. Table 7.8: Ramp filter apertures. Table 7.9: HRC aperture parameters. Table 7.10: SBC aperture parameters Figure 3.1: The HST field of view with the locations of the SI and the FGS apertures in the (U2,U3) focal plane. Figure 5.10: WFC and HRC filter wheels layout. Figure 5.11: SBC Filter wheel layout. Figure 7.8: Aperture and image feature orientation. Figure 7.9: ACS apertures in the V2/V3 reference frame.
Detector Characteristics	Table 2.1: WFC Performance Summary. Table 3.1: Instrument characteristics. Table 4.1: WFC amplifier gain and read noise after installation of the CEB-R (valid after May 2009). Table 4.7: SBC detector performance characteristics.
SBC Bright Object Protection Limits	Table 7.3: Absolute SBC count rate screening limits for nonvariable and variable objects. Table 7.4: Bright limit V-band magnitudes for observations with the SBC filters and prisms (no reddening). Table 7.5: Bright object protection policy for SBC observations.
Hot, Warm, and Unstable Pixels	Table 2.1: WFC Performance Summary. Table 4.4: Creation rate of new hot, warm, and unstable pixels (% of detector per year). Table 4.5: Hot and Warm Pixel Flags Over the History of ACS. Figure 4.7: Hot Pixel Growth Rate for HRC. Figure 4.8: Pixel Stability and Hot Pixel Growth in WFC.
Charge Transfer Efficiency	Table 4.6: Charge transfer efficiency measurements of the ACS CCDs prior to installation from Fe55 experiments (Sirianni et al. 2000, Proc. SPIE 4008)

Geometric Distortion	Figure 10.111: The geometric distortion map for the ACS/WFC, which shows only the non-linear component to the solution. Figure 10.113: The geometric distortion map for the HRC. Figure 10.115: The geometric distortion map for the ACS/SBC. Figure 10.116: The map of the effective pixel areas of the ACS/SBC. The areas are normalized to 0.025 arcsecond square pixels.
Encircled Energy	Table 9.3: Encircled energy comparison for WFC/F850LP. Figure 4.15: MAMA point spread function. Solid lines are from observations, dashed lines are from Tiny Tim models. Figure 5.12: Encircled energy for the CCD channels. Figure 5.13: Encircled energy for the SBC. Solid lines correspond to observations, dashed lines correspond to Tiny Tim models.
PSF	Table 5.9: ACS Model PSFs in central 5 × 5 pixel region (SBC). Figure 4.15: MAMA point spread function. Solid lines are from observations, dashed lines are from Tiny Tim models. Figure 5.12: Encircled energy for the CCD channels. Figure 5.13: Encircled energy for the SBC. Solid lines correspond to observations, dashed lines correspond to Tiny Tim models.
Filters	Table 3.3: ACS filters. Table 3.5: ACS dispersers. Table 5.1: ACS WFC/HRC filters in Filter Wheel #1. Table 5.2: ACS WFC/HRC filters in Filter Wheel #2. Table 5.3: ACS SBC filter complement. Table 5.5: In-band flux as a percentage of the total flux. Table 5.6: Visible-light rejection of the SBC F115LP imaging mode.
Polarizers:	Table 3.4: ACS polarizers. Table 6.1: Filters that can be used in conjunction ion with the ACS polarizers. Table 6.2: Examples of polarizer and non-polarizer exposures in a Phase II proposal. HRC apertures are no longer available but are shown for archival purposes.
Photometry	Table 5.4: V detection limits for ACS, HRC, and SBC direct imaging. Table 9.1: Useful quantities for the ACS WFC, at -81C (since July 2006). Table 9.2: Useful quantities for the ACS SBC. Table 10.1 Color corrections ABv to go from Johnson V magnitude to AB magnitude for the WFC. Table 10.2: Color corrections ABv to go from Johnson V magnitude to AB magnitude for the HRC. Table 10.3: Color corrections ABv to go from Johnson V magnitude to AB magnitude for the SBC. Table 10.4: Color corrections to go from GALEX NUV AB magnitude to AB magnitude for the SBC. Table 10.5: Color corrections to go from GALEX FUV AB magnitude to AB magnitude for the SBC.
Limiting Magnitudes for Direct Imaging	Table 5.4: V detection limits for ACS, HRC, and SBC direct imaging. Figure 5.8: HST Limiting Magnitude for point sources in 10 hours, as a function of wavelength. Figure 5.9: HST total integration time needed to attain ABMAG=26 for extended sources.

Spectroscopy	Table 6.3: Optical parameters of ACS dispersers. Table 6.4: V detection limits for the ACS grism/prism modes. Figure 6.16: Sensitivity versus pixel position for WFC G800L. Figure 6.18: Sensitivity versus wavelength for HRC G800L. Figure 6.19: Sensitivity versus pixel position for HRC G800L. Figure 6.21: Sensitivity versus wavelength for HRC/PR200L. Figure 6.22: Sensitivity versus wavelength for SBC PR110L. Figure 6.24: Sensitivity versus wavelength for SBC/PR130L.
Sky Backgrounds	Table 9.4: Approximate zodiacal sky background as a function of ecliptic latitude and ecliptic longitude. (In V magnitudes per square arcseconds.) Table 9.5: Geocoronal emission lines. Table 9.6: High sky backgrounds. Figure 9.1: High sky background intensity as a function of wavelength. Figure 9.2: Background contributions in V magnitude per arcseconds^2. Figure 9.3: Extinction versus wavelength.
Calibration Accuracies	Table 3.2: Calibration accuracies. Figure 4.7: Hot Pixel Growth Rate for HRC. Figure 4.8: Pixel Stability and Hot Pixel Growth in WFC. Figure 4.9: ACS/WFC Dark Current Histograms.

Chapter 4: Detector Performance

Chapter Contents

4.1 Overview

ACS employs two fundamentally different types of detectors: CCDs for use from the near-UV to the near-IR, and a Multi-Anode Microchannel Array (MAMA) detector for use in the far-UV. The CCD and the MAMA detectors impose unique limitations on the feasibility of observations. This chapter covers the properties of the ACS detectors and descriptions of how to optimize scientific programs and ensure the feasibility of observations. **It is essential that observers proposing to use the SBC read and abide by the procedures and rules described in Sections 4.6 and 7.2 to ensure the safety of the MAMA detectors.**

4.2 The CCDs

✓ *Information regarding the HRC is provided for archival purposes only. Please check for updates regarding WFC on the ACS website.*

4.2.1 Detector Properties

WFC Properties

The WFC detector consists of two 4096 × 2048 charge-coupled devices that are sensitive from the blue edge of the visual spectrum to the near-IR, called WFC1 and WFC2. These CCDs are thinned, backside-illuminated devices manufactured by Scientific Imaging Technologies (SITe), and are butted together to create an effective 4096 × 4096 pixel^2 (202 × 202 arcsec^2) array with a gap corresponding to approximately 50 pixels (2.5 arcsec) between the chips. The CCD camera design incorporates a warm dewar window, designed to prevent buildup of contaminants on the window that cause a loss of UV throughput. A summary of the ACS CCD performance is given in Table 3.1.

HRC

The HRC detector is a 1024 × 1024 pixel^2 (29 × 26 arcsec^2) CCD. It is a thinned, backside-illuminated device, manufactured by SITe. The coating uses a process developed by SITe to provide good quantum efficiency in the near-ultraviolet. The performance characteristics and specifications are given in Table 3.1.

4.2.2 CCD Spectral Response

The responsive quantum efficiency (RQE) of the WFC and HRC CCDs is shown in Figure 4.1; the RQE includes corrections needed to reproduce the instrument sensitivity measured on orbit (Bohlin 2016, AJ, 152, 60, ACS ISR 2020-08). The total spectral response of the camera (see Figure 5.7) is given by the product of the RQEs shown here and the throughput of optical elements of the camera and telescope. For example, the WFC silver coated mirrors enhance the reflectivity in the near-IR but impose a cutoff below 370 nm.

Figure 4.1: Responsive quantum efficiency of the HRC CCD (solid line) and WFC CCDs (dashed line).
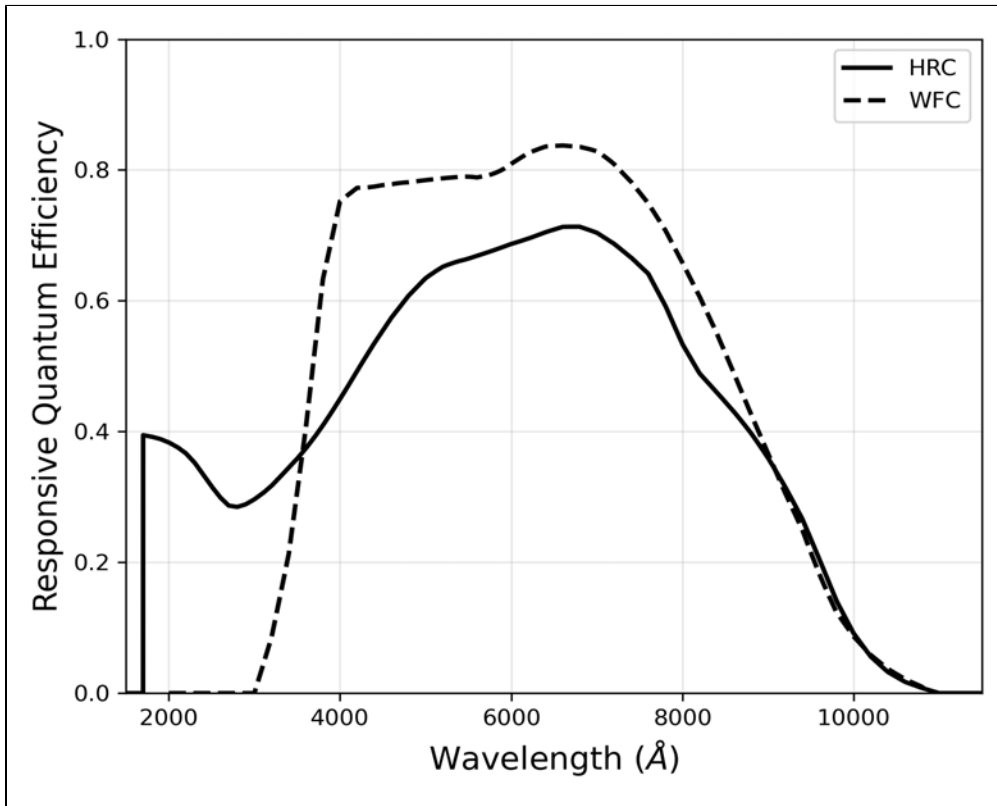
4.2.3 Quantum Efficiency Hysteresis

Based on current data, the ACS CCDs do not suffer from quantum efficiency hysteresis (QEH). The CCDs respond in the same way to light levels over their whole dynamic range, irrespective of the previous illumination level.

4.2.4 CCD Long-Wavelength Fringing

Like most thinned CCDs, the ACS CCDs exhibit fringing longward of ~7500 Å. The fringing is caused by interference of incident light reflected between the front and back surfaces of the CCD. The amplitude of the fringes is a strong function of wavelength and spectral bandpass. Only the F892N filter shows a fringe pattern for white light illumination. The fringe pattern is stable and can be removed to first order for continuum sources by the F892N flat field.

4.2.5 CCD Readout Format

WFC

Each WFC CCD is read out as a 4144 × 2068 pixel^2 array, including physical prescans and virtual overscans. Two amplifiers are used to read out each CCD. The final images of each CCD consist of 24 columns of physical prescan, 4096 columns of pixel data, and another 24 columns of physical prescan. Each column consists of 2048 rows of pixel data followed by 20 rows of virtual overscan. The orientation of the CCD is such that for the grism spectra, the dispersed images have wavelength increasing from left to right in the positive x-direction. A schematic of the WFC CCDs, including readout directions, prescans, and overscans, is provided in Figure 4.2.

Figure 4.2: The layout of WFC full-frame images, including parallel and serial readout directions, physical prescans, and virtual overscans.
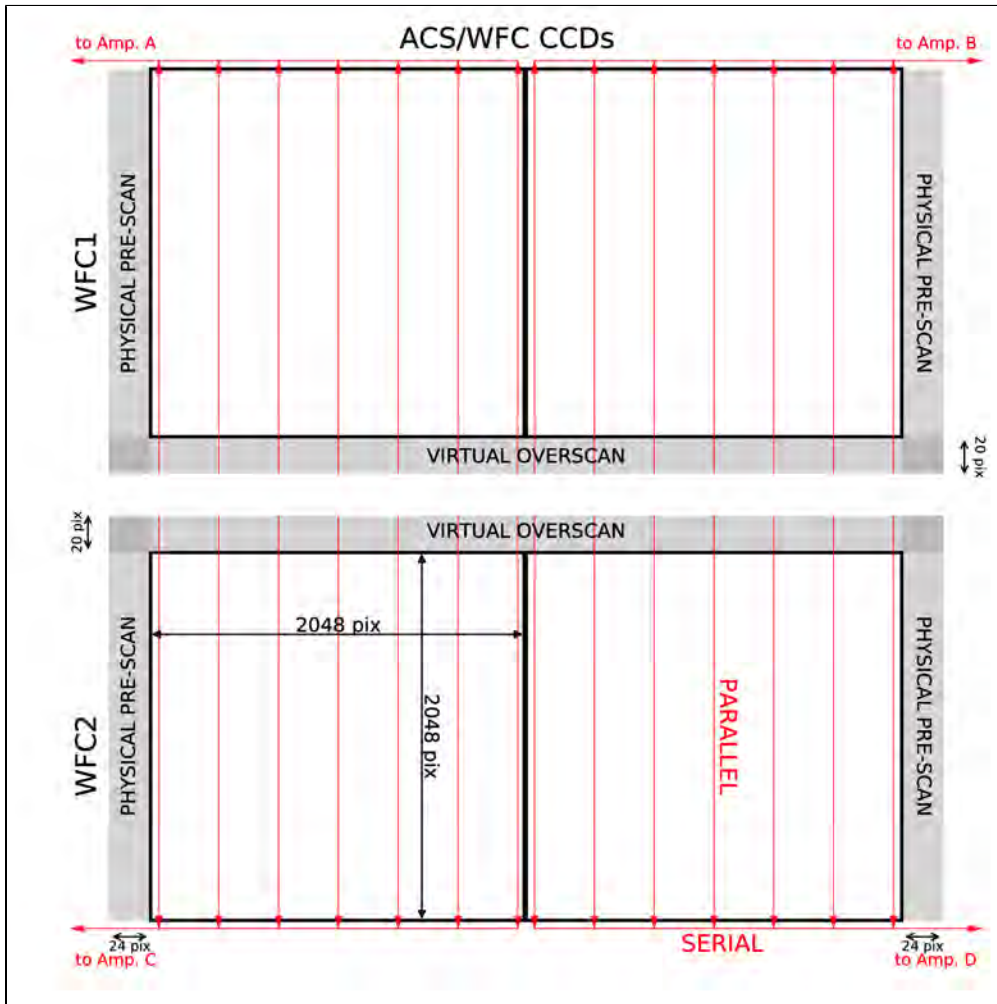
During readout, charge is transferred in the parallel direction to the serial register, and then shifted horizontally to the amplifiers, named A, B, C, and D.

HRC

The HRC CCD was read out as a 1062 × 1044 pixel^2 array, including physical and virtual overscans. There are 19 columns of physical prescan, followed by 1024 columns of pixel data, and then 19 more columns of physical prescan. Each column consists of 1024 rows of pixel data followed by 20 rows of virtual overscan. As with the WFC, the orientation of the HRC CCD was chosen so that grism images have wavelength increasing from left to right. A schematic of the HRC CCD, including prescans and overscans, is provided in Figure 4.3.

Figure 4.3: The layout of HRC images, including the prescans and overscans designated by dashed lines.
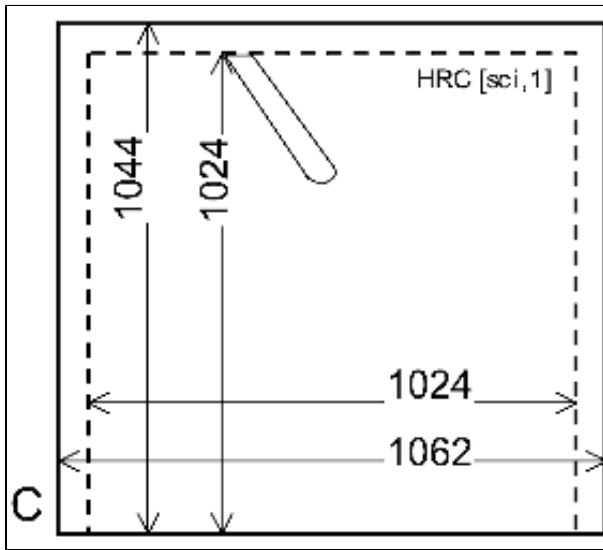
During readout, charge is transferred from top to bottom (parallel direction), then along the serial register to the amplifier (serial direction), labeled C here. The outline of the occulting finger shadow is also shown. This figure is reproduced from Sirianni et al. 2005, PASP, 117, 1049.

4.2.6 Analog-To-Digital Conversion

Electrons that accumulate in the CCD pixels are read out and converted to data numbers (DN) by the analog-to-digital converter (ADC). The ADC output is a 16 bit number, producing a maximum of 65,535 DN in one pixel. Before the failure of ACS in January 2007, the WFC and HRC CCDs could be operated at ADC gains of 1, 2, 4, or 8 electrons/DN. The current CCD Electronics Box (CEB-R) installed during SM4 changed the WFC's ADC operational gains to 0.5, 1.0, 1.4, and 2.0 electrons/DN. In addition, the post-SM4 A-to-D saturation limit appears to be somewhat less than 65,535 DN per pixel (ACS ISR 2020-03). Almost all gain 2.0 observations will not approach this limit, therefore the impact to most observers is negligible. Furthermore, reference files have been updated to reflect a new lower limit of 64,000 DN for A-to-D saturation, and data quality flags are appropriately marked by CALACS.

All four new gains are available to the observer but only the GAIN = 2.0 option is fully supported by the ACS Team since May 2010. Although lower ADC gains can in principle increase the dynamic range of faint source observations by reducing quantization noise, the improvement is not significant for the WFC. To mitigate undesirable features in ACS data (e.g., cross-talk), the ACS Team strongly recommends observers use only the GAIN = 2.0 setting.

Table 4.1 shows the gain and read noise values of the four WFC amplifiers measured during the orbital verification period after SM4 for each commanded gain available with the dual-slope integrator pixel sampling mode of the CEB-R. The read noise values apply to the imaging (light-sensitive) regions of the CCD quadrants and are about 0.1 electrons higher than the measured values in the corresponding prescan regions.

For archival purposes, Table 4.2 and Table 4.3 show the gain and read noise values of the four WFC amplifiers and the default HRC amplifier C when operated with Side 1 (March 2002 to June 2006) and Side 2 (June 2006 to January 2007) of the original CEB.

Table 4.1: WFC amplifier gain and read noise after installation of the CEB-R (valid after May 2009). Values apply to dual-slope integrator mode of pixel sampling.

CCD	Amp	Gain (e⁻/DN)				Read Noise (e⁻)			
		0.5	1.0	1.4	2.0[a]	0.5	1.0	1.4	2.0 [a], [b]
WFC1	A	0.53	1.03	1.45	2.020	3.92	4.05	4.28	4.35
WFC1	B	0.50	0.96	1.36	1.886	3.24	3.36	3.61	3.75
WFC2	C	0.53	1.03	1.45	2.017	3.54	3.69	3.95	4.05
WFC2	D	0.53	1.02	1.45	2.011	3.31 [c]	3.43 [c]	3.71 [c]	5.65 [d]

[a]Default gain.
[b]The 1σ scatter in the read noise is 0.01–0.02 electrons.
[c] May not be valid after July 24, 2020.
[d] Valid after July 24, 2020.

Table 4.2: CCD gain and read noise operated under Side 1 of original CEB (March 2002 to June 2006).

CCD	Amp	Gain (e⁻/DN)			Read noise (e⁻)		
		1	2 [a]	4	1	2 [a]	4
WFC1	A	1.000	2.002	4.01	5.57	5.84	--
WFC1	B	0.972	1.945	3.90	4.70	4.98	--
WFC2	C	1.011	2.028	4.07	5.18	5.35	--
WFC2	D	1.018	1.994	4.00	4.80	5.27	--
HRC	C	1.163	2.216	4.235	4.46	4.80	5.86

[a]Default gain.

Table 4.3: CCD gain and read noise operated under Side 2 of original CEB (June 2006 to January 2007).

CCD	Amp	Gain (e⁻/DN)			Read noise (e⁻)		
		1	2 [a]	4	1	2 [a]	4
WFC1	A	1.000	2.002	4.01	5.29	5.62	--
WFC1	B	0.972	1.945	3.90	4.45	4.74	--
WFC2	C	1.011	2.028	4.07	5.03	5.34	--
WFC2	D	1.018	1.994	4.00	4.55	4.89	--
HRC	C	1.163	2.216	4.235	4.36	4.82	5.44

[a]Default gain.

4.2.7 Flat Fields

WFC

The WFC flat-field reference images are constructed from both ground-based and on-orbit data. Ground-based flats with signal-to-noise ratios of ~300 per pixel were obtained for all filters. Low-frequency refinements of the ground-based flats were made using in-flight dithered observations of a rich star field (see ACS ISRs 2002-08 and 2003-10).

These low-frequency flats (L-flats) initially showed a corner-to-corner sensitivity gradient across the CCDs of 10–18%, depending on wavelength. The L-flats were updated in July 2006 after the operating temperature of the WFC was lowered to -81 °C (see ACS ISR 2006-06). The resulting flat fields are accurate to 1% over the WFC field of view for most broad-band filters and to 2% for F850LP and the narrow-band filters. Observations of a rich star field were obtained shortly after the ACS repair in May 2009 and have been used to verify that the L-flats remain stable. Internal observations made during SMOV SM4 show that the P-flats (high frequency pixel-to-pixel flats) are also stable (ACS ISR 2011-04).

Figure 4.4 shows the corrected WFC ground flats for several broadband filters. The 50 pixel gap between the top and bottom CCDs is not shown. Because the two CCDs were cut from the same silicon wafer and underwent similar processing, their sensitivities are continuous across the gap. The central doughnut-like structure is wavelength dependent. The pixels in the central region are less sensitive than surrounding pixels in the blue F435W flat, but they are more sensitive in the red F850LP flat.

There are a few types of artifacts present in WFC flat-field images. Dust motes are the shadows of dust particles located on the CCD windows. Dust motes consist of a characteristic dark ring approximately 30 pixels across. Flat-field correction mitigates their effects to <<1%. "Freckles" appear as small black dots a few pixels across. They are sparsely distributed in WFC images and stable over the history of the instrument. More information about freckles and dust motes can be found in ACS ISR 2001-11.

In May 2017, three new artifacts (dubbed "flecks") appeared in WFC calibration data. Two of the flecks are larger in size than the freckles, spanning 10–20 pixels. A careful analysis reveals that the flecks are particulates that have fallen onto the surface of the CCD, implying they originated inside the CCD housing. While this narrows down the potential sources of the particulates, the exact source could not be identified. For each fleck, pixels with less than 50% transmissivity have been listed in an updated bad pixel table (BPIXTAB) for use with data taken after May 5th, 2017. This information propagates to the data quality (DQ) extension of science data and allows the pixels affected by flecks to be identified and appropriately processed during image drizzling. For more details, please refer to ACS ISR 2018-03.

See ACS ISRs 2001-11, 2002-01, 2002-04, 2002-08, 2003-10, 2003-11, 2005-02, 2005-09, 2006-06, 2007-01, 2015-07, and 2020-01 for more information about the WFC flat fields.

Figure 4.4: WFC flat fields for selected broadband filters
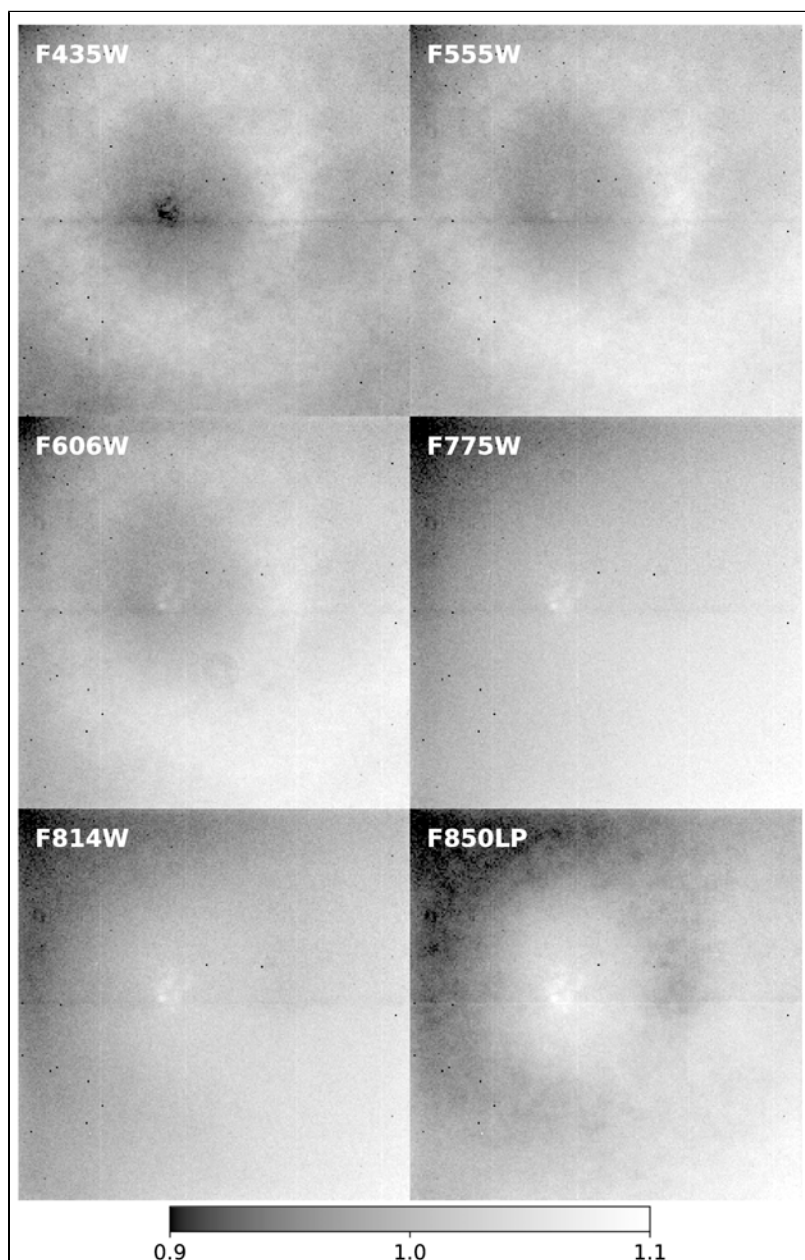
HRC

The HRC ground flats were refined using in-flight dithered observations of a rich star field designed to track low-frequency sensitivity variations. These L-flats revealed a corner-to-corner sensitivity gradient across the CCD of 6-12%, depending on wavelength. NUV flats were constructed from in-flight images of the bright Earth (see ACS ISR 2003-02) and include both the pixel-to-pixel and low-frequency structure of the detector response.

The HRC flat fields have a signal-to-noise of ~300 per pixel and support photometry to ~1% over the full HRC field of view. Figure 4.5 shows the corrected HRC ground flats derived for 6 broadband optical filters. The doughnut-like structure in the WFC flats is not seen in the HRC flats. For further discussion of HRC flat fields, see ACS ISRs 2001-11 and 2002-04.

Figure 4.5: HRC flat fields for selected broadband filters

4.3 CCD Operations and Limitations

> ✅ *Information regarding the HRC is provided for archival purposes only. Please check for updates regarding WFC on the ACS website.*
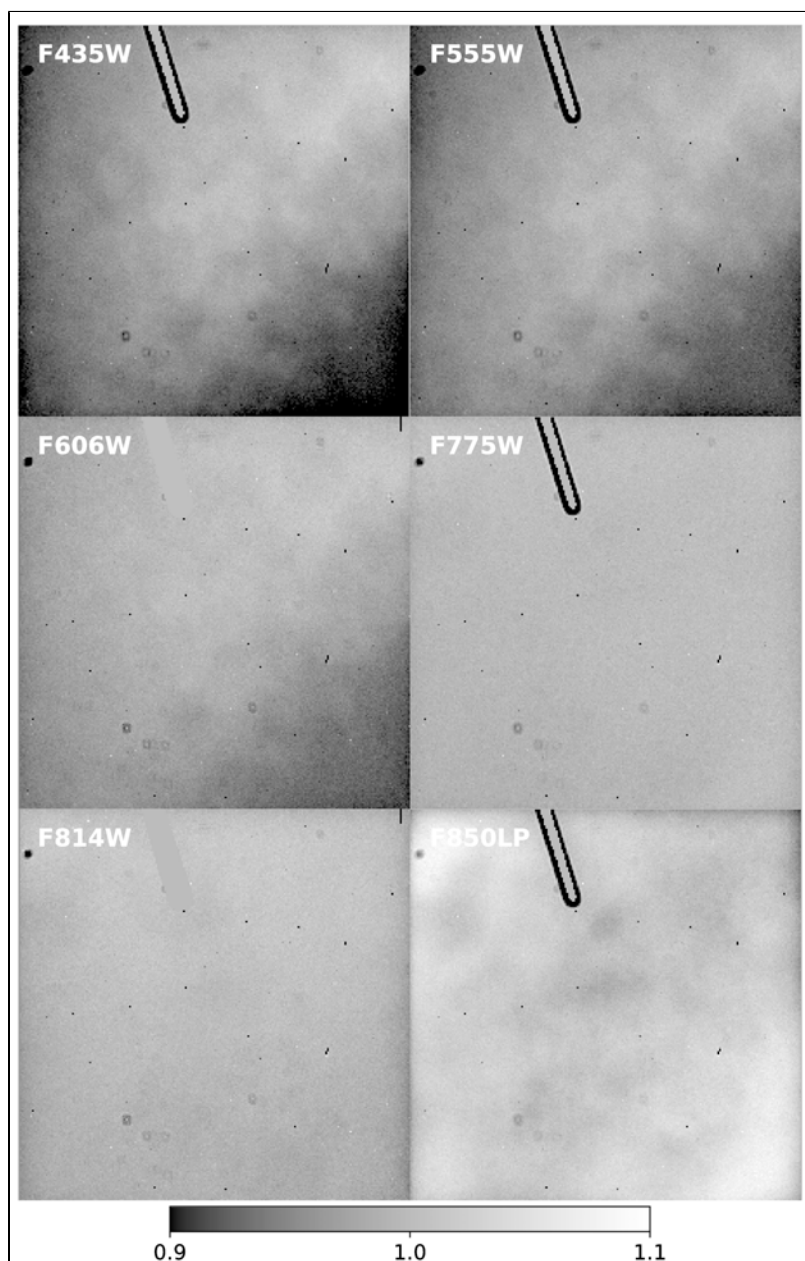
4.3.1 CCD Saturation and Full Well Thresholds

When CCDs are over-exposed, pixels will saturate and excess charge will flow into adjacent pixels along the column. This condition is known as "blooming" or "bleeding." For the WFC, we make a distinction between the saturation threshold and the full well depth based on a functional difference in the behavior of the detector at two different regimes of charge accumulation. We refer to the saturation threshold/level as the charge level beyond which the CCD pixels integrate further charge sub-linearly and begin to bloom. We refer to the full well depth as the charge level beyond which CCD pixels cannot accumulate any further significant amount of charge (i.e. ~100% blooming). The full well depth is always beyond the saturation level. Both of these thresholds span a range of values across the detector area.

The average value for the WFC saturation level is ~77,400 e⁻, and ranges between ~72,000 e⁻ to ~82,000 e⁻. The full well depth of the WFC CCD can reach ~95,000 e⁻ or more. For HRC, no distinction between saturation level and full well depth is made at the present time, and we report the average saturation level/full well depth to be 155,000 e⁻, but the pixel-to-pixel values vary by ~18% across the detector area. The values for both channels are also given in Table 3.1. See ACS ISR 2020-02 for details on the topics discussed in this section thus far.

Extreme overexposure does not cause any long-term damage to the CCDs, so there are no bright object limits for the ACS CCDs. When using GAIN = 2 for the WFC and GAIN = 4 for the HRC, the linearity of the detectors deviates by less than 1% up to the saturation levels. On-orbit tests using aperture photometry show that this linearity is maintained when summing over pixels that surround an area affected by charge bleeding, even when the central pixel is saturated by 10 times its full well depth (see ACS ISR 2004-01 and ACS ISR 2019-03 for details).

Note that there is another type of pixel saturation, often referred to as "A-to-D saturation." Since the 16-bit detector electronics can read out a maximum value of 65,535 DN, pixels that would have been read out with values in excess of this are simply read out at this maximum value. These A-to-D saturated pixels are not viable for science. For the WFC, this limitation is never reached when using GAIN = 2, which is the presently the only supported gain setting. A recent study (ACS ISR 2020-03) has found that post-SM4 A-to-D saturated pixels can actually have lower values than expected. The CALACS pipeline now flags all post-SM4 pixel values above 64,000 DN as A-to-D saturated.

4.3.2 CCD Shutter Effects on Exposure Times

The ACS camera has a very fast shutter; even the shortest exposure times are not significantly affected by the finite travel time of the shutter blades. On-orbit testing reported in ACS ISR 2003-03 verified that shutter shading corrections are not necessary to support 1% relative photometry for either the HRC or WFC. We note that the commanding overheads of WFC introduce an additional ~3.0 seconds of dark current integration time beyond the commanded exposure time. This additional dark-time is included in the dark-current subtraction stage of the CALACS pipeline (see the *ACS Data Handbook* for further details).

Four exposure times are known to have errors of up to 4.1%; e.g., the nominal 0.1 seconds HRC exposure was really 0.1041 seconds. These errant exposure times are accommodated by updates to the reference files used in image pipeline processing. No significant differences exist between exposure times controlled by the two shutters (A and B), with the possible exception of non-repeatability up to ~1% for WFC exposures in the 0.7 to 2.0 second range. The HRC provided excellent shutter time repeatability.

4.3.3 Read Noise

> ⊘ *Please check for updates on the ACS website.*

WFC

The read noise levels in the physical prescan and imaging regions of the four WFC amplifiers were measured for all gain settings during the orbital verification period following the installation of the CEB-R in SM4. The average WFC read noise is about 25% lower than before SM4 (ACS ISR 2011-04). This reduction is due to the use in the CEB-R of a dual-slope integrator (DSI) in the pixel signal processing chain instead of the clamp-and-sample method of pixel sampling used in the original CEB. The DSI method offers lower signal processing noise at the expense of a spatially variable bias level.

In Figure 4.6, the read noise of the four WFC amplifiers are plotted versus date. The read noise values are steady to 1% or better, except for five discrete events during the ACS lifetime. Two of these events were associated with ACS electronics changes: 1) a jump in the amplifier C noise after the 2006 failure of the Side 1 electronics, and 2) the overall drop in noise once the ACS was repaired during SM4 in 2009. The three other events, noise increases in amplifier A (June 2003) and amplifier D (January/February 2013 and July 2020), have been ascribed to radiation damage on the detector (ACS TIR 2013-02, ACS TIR 2020-01[1]). Fluctuating read noise levels stabilized after subsequent anneals (see Section 4.3.5).

Although amplifier D now has significantly elevated read noise compared with the other amplifiers, most WFC broad-band observations remain sky-limited rather than read-noise limited. Note also that the WFC pre-defined subarray apertures may now be specified for any amplifier, but we recommend the use of the lowest-noise amplifier B.

Prior to Cycle 24, data taken with the old subarray format experienced slightly increased read noise due to variations in the clocking rate of pixel readout of subarrays relative to full-frame images. The read noise increased with decreasing subarray size, and in the worst case was about 0.15 electrons higher in a 512 × 512 pixel subarray image than in a full-frame image. More information can be found in ACS ISR 2019-02. For subarrays taken in Cycle 24 and after, the method used to read out the detectors was updated, which removed this increased read noise (ACS ISR 2017-03).

Figure 4.6: History of ACS/WFC read noise
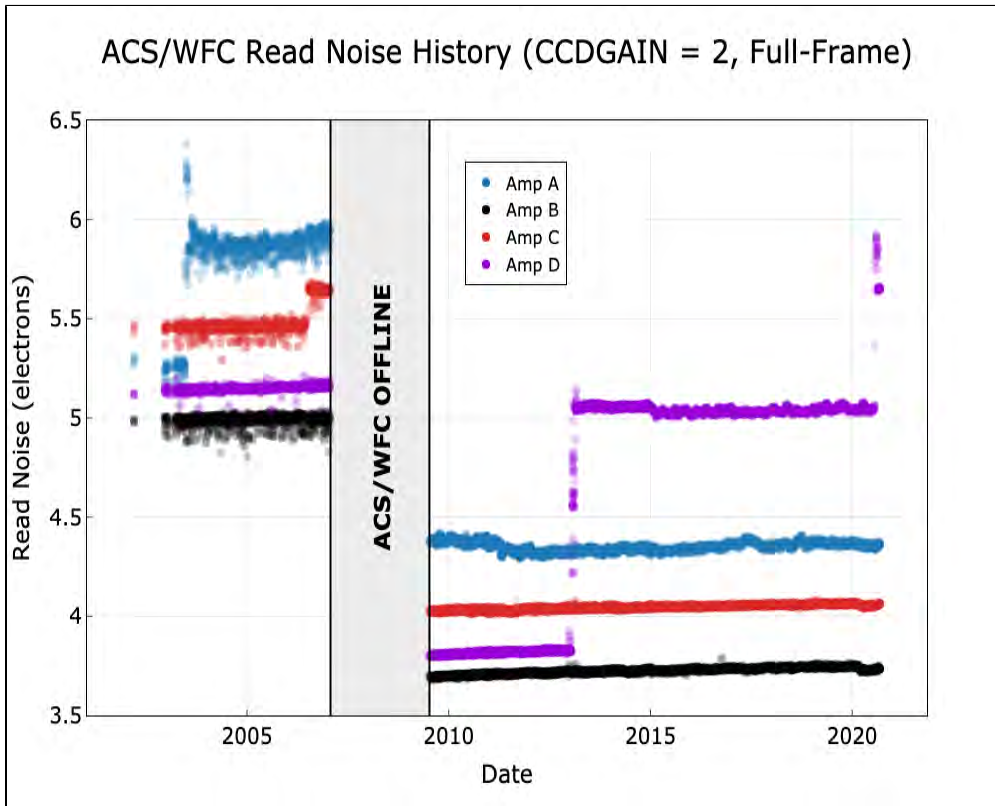
Read noise history of the four readout amplifiers of ACS/WFC. Amplifiers A and B read out WFC1, and amplifiers C and D read out WFC2 (see Figure 4.2 for schematic). These values are measured at the serial register using calibration bias frames taken regularly throughout the ACS lifetime. See text for discussion.

HRC

Prior to January 2007, the read noise of the HRC was monitored using only the default amplifier C and the default gain of 2 e⁻/DN. No variations were observed with time. The read noise measured in the physical prescan and image areas were consistent with the pre-flight values of 4.74 e⁻ (see Table 4.2 and Table 4.3).

4.3.4 Dark Current

> ✓ *Please check for updates on the ACS website.*

All ACS CCDs are buried channel devices which have a shallow n-type layer implanted below the surface to store and transfer the collected charge away from the traps associated with the Si-SiO$_2$ interface. Moreover, ACS CCDs are operated in Multi-Pinned Phase (MPP) mode so that the silicon surface is inverted and the surface dark current is suppressed. ACS CCDs therefore have very low dark current. The WFC CCDs are operated in MPP mode only during integration, so the total dark current figure for WFC includes a small component of surface dark current accumulated during the readout time.

Like all CCDs operated in a Low Earth Orbit (LEO) radiation environment, the ACS CCDs are subject to radiation damage by energetic particles trapped in the radiation belts. Ionization damage and displacement damage are two types of damage caused by protons in silicon. The MPP mode is very effective in mitigating the damage due to ionization such as the generation of surface dark current due to the creation of trapping states in the Si-SiO$_2$ interface. Although only a minor fraction of the total energy is lost by a proton via non-ionizing energy loss, the displacement damage can cause significant performance degradation in CCDs by decreasing the charge transfer efficiency (CTE), increasing the average dark current, and introducing pixels with very high dark current (hot pixels). Displacement damage to the silicon lattice occurs mostly due to the interaction between low energy protons and silicon atoms. The generation of phosphorous-vacancy centers introduces an extra level of energy between the conduction band and the valence band of the silicon. New energetic levels in the silicon bandgap have the direct effect of increasing the dark current as a result of carrier generation in the bulk depletion region of the pixel. As a consequence, the dark current of CCDs operated in a radiative environment is predicted to increase with time.

Ground testing of the WFC CCDs, radiated with a cumulative fluence equivalent to 2.5 and 5 years of on-orbit exposure, predicted a linear growth of ~1.5 e$^-$/pixel/hour/year. The dark current in ACS CCDs is monitored three days per week with the acquisition of four 1000-second dark frames (totaling 12 images per week and including post-flash as of January 2015). Dark frames are used to create reference files for the calibration of scientific images, and to track and catalog hot pixels as they evolve. The dark reference files are generated by combining one month of darks in order to remove cosmic rays and reduce the statistical noise. As expected, the dark current increases with time. From 2011 to 2020, the observed linear growth rates of dark current are 2.44 and 2.41 e$^-$/pixel/hour/year for WFC1 and WFC2 respectively. Prior to 2007, the observed linear growth rate of dark current was 2.1 e$^-$/pixel/hour/year for the HRC CCD.

At the beginning of the Side 2 operation in July 2006, the temperature set point of the WFC was lowered from −77 °C to −81 °C (documented in ACS TIR 2006-02[1]). Dark current and hot pixels depend strongly on the operating temperature. The reduction of the operating temperature of the WFC CCDs reduced the number of hot pixels by almost 50% (see Figure 4.8) and reduced the dark current in both WFC1 and WFC2. The dark rate shows a clear drop on July 4, 2006, when the temperature was changed. The new operating temperature brought the dark current of the WFC CCDs back to the level it was eighteen months after the launch.

All dark frames have been post-flashed since January 2015 (ACS ISR 2015-03). This has resulted in a slight increase in the noise of the final superdark images, but a more accurate representation of the dark current and hot/warm pixels. The higher background level provided by the flash alleviates the effects of CTE. As of August 2020, the dark current has been measured to be 40 to 50 e$^-$/pixel/hour among the four amplifiers.

Figure 4.7: Hot Pixel Growth Rate for HRC
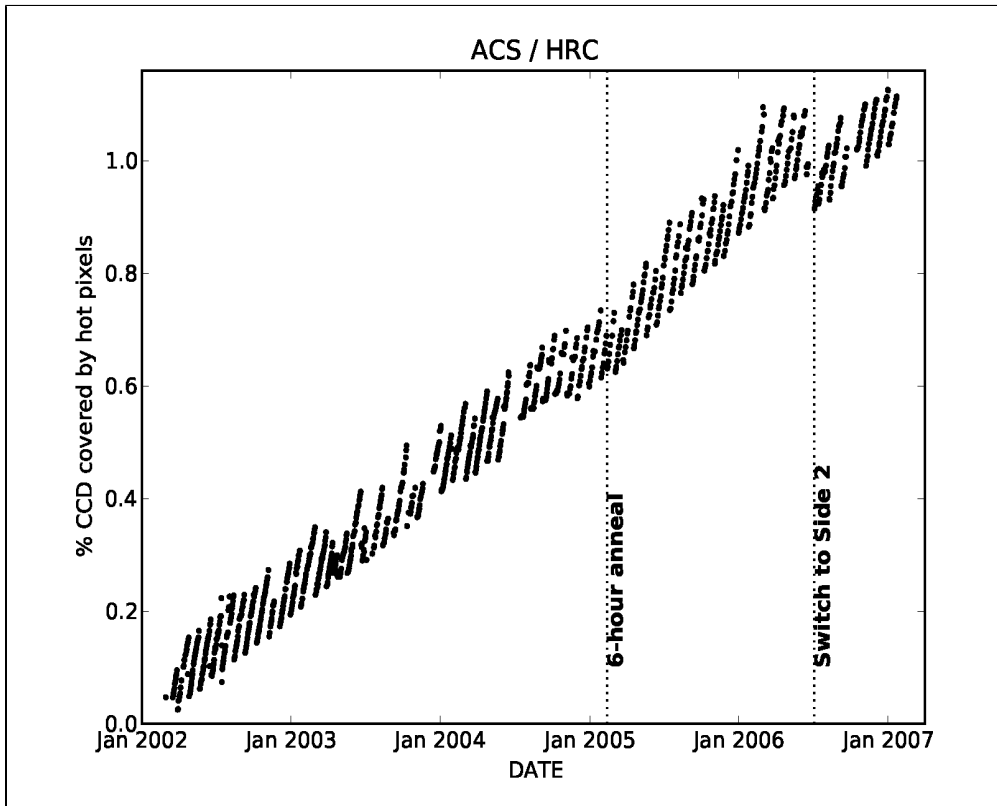
Hot pixel (DQ flag 16) growth rates in the HRC during its operational lifetime. The sawtooth pattern corresponds to ACS anneal cycles. The growth rate increased slightly when the anneal duration was switched from 12 to 6 hours. The slight drop in hot pixels coincided with the switch to Side 2 electronics.

Figure 4.8: Pixel Stability and Hot Pixel Growth in WFC.
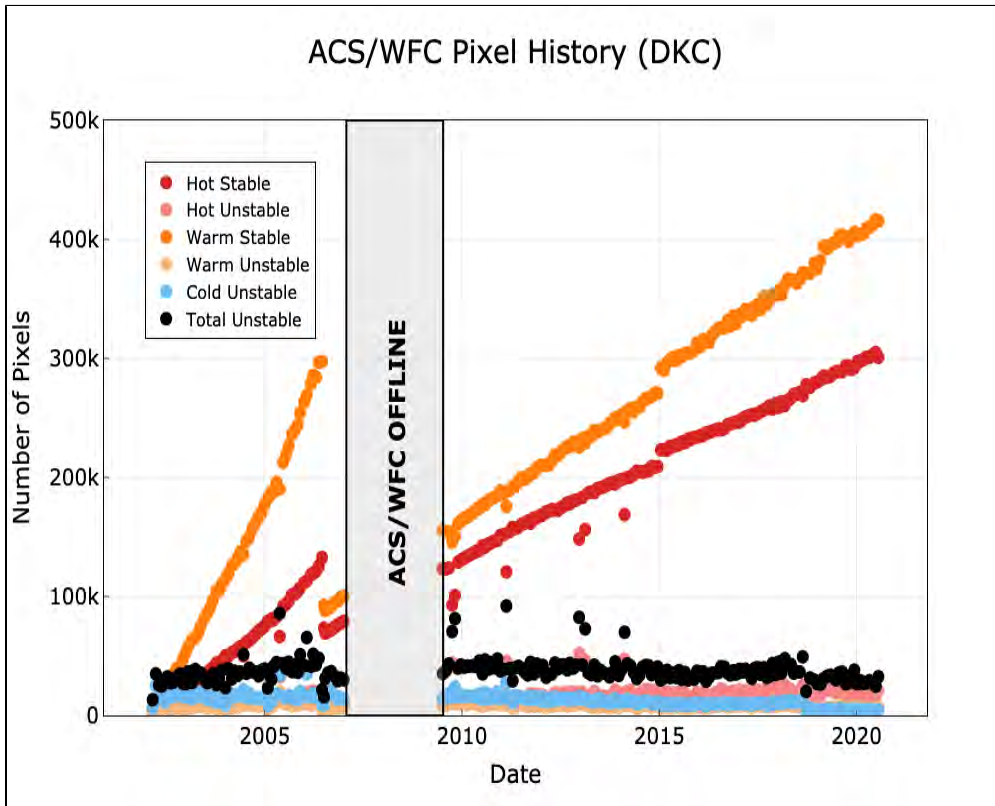
The populations of warm, hot, and unstable pixels in the WFC CCDs over their operational lifetime as measured from the monthly CTE-corrected superdarks. The sudden decrease in stable hot pixels in mid-2006 is attributed to the temperature change from -77 ºC to -81 ºC, which coincides with the switch to the Side 2 electronics. The small increase in stable hot pixels in early-2015 is the result of better CTE loss correction due to post-flashing dark images. The population of unstable pixels remains relatively steady over the history of ACS.

Figure 4.9: ACS/WFC Dark Current Histograms
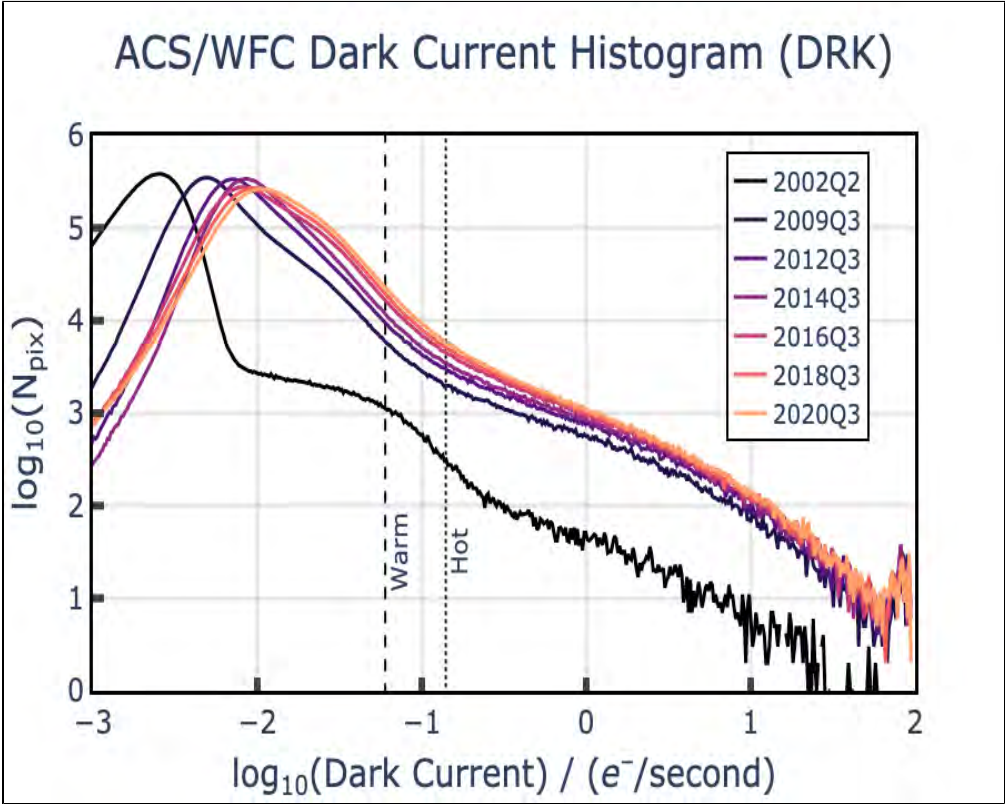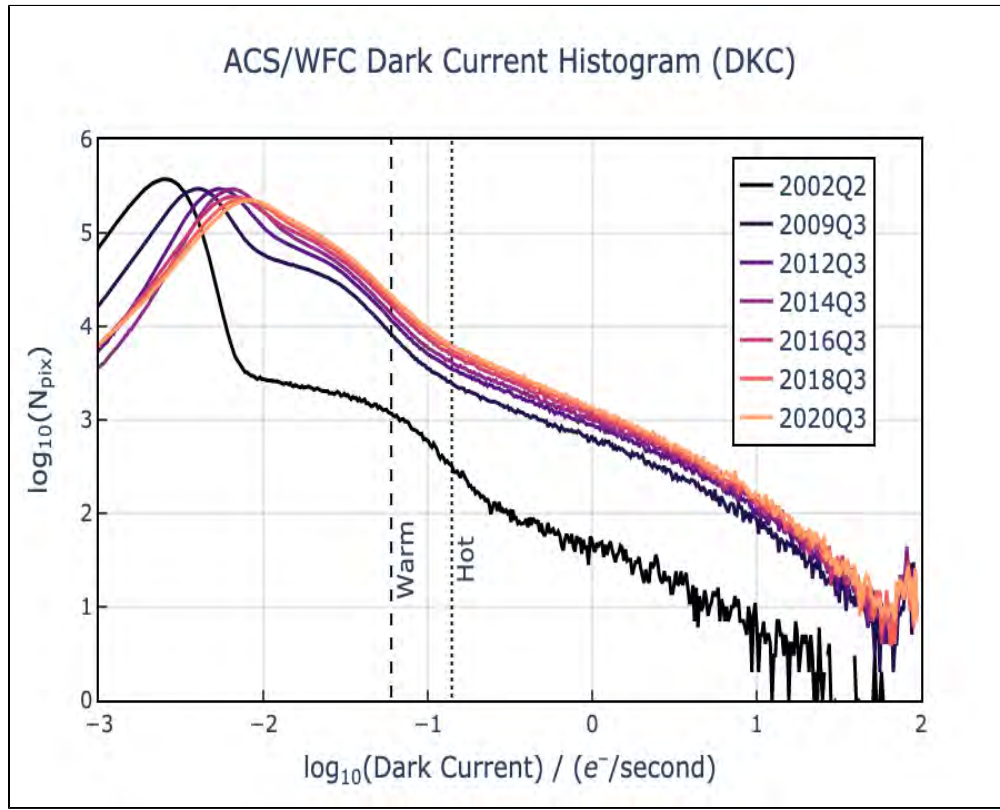
Distribution of dark current in WFC detector pixels over time as measured from normal (top) and CTE-corrected (bottom) superdark images. Over time, the distribution shifts to the right as the global dark current increases. The tail towards higher dark current values also increases in amplitude as the number of hot and warm pixels increases with time. The introduction of post-flash in the dark images in 2015 changed the shape of the distribution slightly, and allowed for a more accurate correction of CTE losses. While the shapes of the normal (top) and CTE-corrected (bottom) distributions are slightly different, the global dark current rates are similar.

4.3.5 Warm and hot pixels

> ✅ *Please check for updates on the ACS website.*

In the presence of a high electric field, the dark current of a single pixel can be greatly enhanced. Such pixels are called hot pixels. Although the increase in the mean dark current with proton irradiation is important, of greater consequence is the large increase in dark current nonuniformity.

We have chosen to classify the field-enhanced pixels into two categories: warm and hot pixels. The definition of "warm" and "hot" pixel is somewhat arbitrary, and there have been several changes to the definition of warm and hot pixel throughout the lifetime of ACS. The values associated with these flags over time are summarized in Table 4.5. In January 2015 we adjusted the ranges of hot and warm pixels as follows; a pixel above 0.14 e¯/pixel/second is considered a "hot" pixel. A pixel below the hot pixel range but above 0.06 e¯/pixel/second is considered a "warm" pixel. The new values were chosen by comparing the hot and warm pixel percentages found in the years following SM4 (ACS ISR 2015-03). For consistency, all archived WFC observations were updated in early 2018 to use the current warm and hot pixel definitions.

Warm and hot pixels accumulate as a function of time on orbit. Defects responsible for elevated dark rate are created continuously as a result of the ongoing displacement damage on orbit. The one-time reduction of the WFC operating temperature in 2006 dramatically reduced the overall dark current and hot pixel fraction but, by 2011, these values had degraded past their previous levels.

Table 4.4: Creation rate of new warm, hot, and unstable pixels (% of detector per year).

Pixel Type	WFC (−81 °C)
Warm Stable (0.06 - 0.14 e¯/pix/sec)	0.15
Hot Stable (>0.14 e¯/pix/sec)	0.1
Total Unstable	~0

Many hot pixels are transient. Like other CCDs on HST, the ACS WFC undergoes a monthly annealing process. The WFC CCDs and the thermal electric coolers are powered off, and heaters are powered on to warm the CCDs to ~19 °C. Although the annealing mechanism at such low temperatures is not yet understood, after this "thermal cycle" the population of hot pixels is slightly reduced (see Figure 4.7). The anneal rate depends on the dark current rate; very hot pixels are annealed more easily than warm pixels. For pixels classified as "hot" (those with dark rate > 0.14 e¯/pix/sec for WFC, and > 0.08 e¯/pix/sec for HRC) the anneal heals ~3% for WFC and ~14% for HRC.

Table 4.5: Hot and Warm Pixel Flags Over the History of ACS

Dates	Warm pixel flag (e¯/s)	Hot pixel flag (e¯/s)
Launch - Oct 8 2004	Not used	Static hot pixel list
Oct 8 2004 - Jan 2007 (Pre SM4)	0.02 - 0.08	≥0.08
May 2009 (Pre SM4) - Jan 15 2015	0.04 - 0.08	≥0.08
Jan 15 2015 - present	0.06 - 0.14[a]	≥0.14[a]

[a] In 2018, the ACS team re-calibrated all historical WFC observations to use the same warm and hot pixel thresholds of 0.06 and 0.14 e¯/s, respectively

Annealing has no effect on the normal pixels that are responsible for the increase in the mean dark current rate. Such behavior was also seen with STIS and WFC3 CCDs during ground radiation testing. Since the anneal cycles do not repair 100% of the hot pixels, there is a growing population of permanent hot pixels (see Figures 4.8, 4.9, and 4.10).

Figure 4.10: A subsection of WFC1 dark frames taken at different epochs showing the increasing population of hot pixels. From left to right: before launch, and 1, 2, 3, and 4 years on orbit.
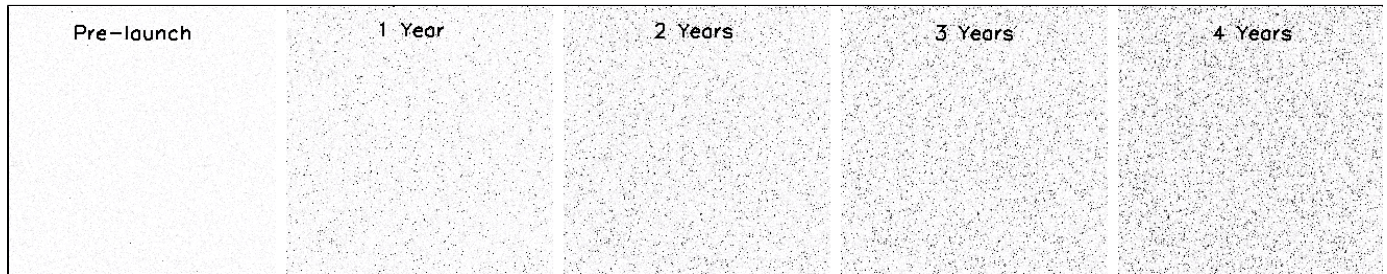
Stable warm and hot pixels are eliminated by the superdark subtraction. However, some pixels show a dark current that is not stable with time but switches between well defined levels. These fluctuations may have timescales of a few minutes and have the characteristics of random telegraph signal (RTS) noise. The dark current in field-enhanced hot pixels can be dependent on the signal level, so the noise is much higher than the normal shot noise. As a consequence, since the locations of warm and hot pixels are known from dark frames, they are flagged in the data quality array. Unstable pixels of any dark current level are also flagged in the data quality array. By default, only unstable pixels are discarded during image combination if multiple exposures are combined as part of a dither pattern (stable hot pixels are retained). In Figure 4.8, we show the prevalence of unstable pixels of various dark current levels over the lifetime of ACS/WFC (see ACS ISR 2017-05 for more information about pixel stability).

The standard CR-SPLIT approach allows rejection of cosmic rays, but hot pixels cannot be eliminated in post-observation processing without dithering between exposures.

> ✅ *Observers who previously used CR-SPLIT for their exposures are advised to use a dither pattern instead. Dithering by at least a few pixels allows the removal of cosmic rays, hot pixels, and other detector artifacts in post-observation processing.*

For example, a simple `ACS-WFC-DITHER-LINE` pattern has been developed that shifts the image by 2 pixels in X and 2 pixels in Y along the direction that minimizes the effects of scale variation across the detector. The specific parameter values for this pattern are given on the ACS Dither webpage.

Additional information can be found in the Phase II Proposal Instructions.

4.3.6 Sink Pixels

Sink pixels are certain pixels in a CCD detector that are anomalously low compared to the background, due to the presence of extra charge traps. These charge traps can trap electrons in the sink pixel itself and also trap electrons from pixels that are transferred through the sink pixel during the readout process, giving rise to a low-valued trail following the sink pixel. The length of the trail depends on the background level of the image, in that images with higher backgrounds exhibit shorter sink pixel trails. In addition, about 30% of the time, a charge excess is found in the pixel immediately downstream of the sink pixel, closer to the amplifier. About 0.3 to 0.5% of pixels in the WFC detector are considered sink pixels in a given anneal cycle. Depending on the background level of an image, in total, about 3% of pixels in an image are sink pixels or affected by sink pixels. These pixels are flagged with DQ flag 1024 in all WFC images observed after January 15, 2015. More details can be found in ACS ISR 2017-01.

4.3.7 Cosmic Rays

Studies have been made of the characteristics of cosmic ray impacts on the HRC and WFC. The fraction of pixels affected by cosmic rays varies from 1.5% to 3% during a 1000 second exposure for both cameras, similar to what was seen on WFPC2 and STIS. This number provides the basis for assessing the risk that the target(s) in any set of exposures will be compromised. The affected fraction is the same for the WFC and HRC despite their factor of two difference in pixel areas. This is because the census of affected pixels is dominated by charge diffusion, not direct impacts. Observers seeking rare or serendipitous objects, as well as transients, may require that every single WFC pixel is free from cosmic ray impacts in at least one exposure among a set of exposures. For the cosmic ray fractions of 1.5% to 3% in 1000 seconds, a single ~2400 second orbit must be broken into four exposures (500 to 600 seconds each) to reduce the number of pixels affected by CRs in every exposure to 1 or less. Users requiring lower read noise may prefer three exposures of ~800 seconds, in which case CR-rejection should still be very good for most purposes. Two long exposures (i.e., 1200 seconds) are not recommended because residual CR contamination would be unacceptably high in most cases. We recommend that users dither these exposures to remove hot pixels as well as cosmic rays (see Section 7.4).

The flux deposited on the CCD from an individual cosmic ray does not depend on the energy of the cosmic ray, but rather the distance it travels in the silicon substrate. An analysis of 13,311 WFC darks and 5,477 HRC darks demonstrates that the interaction of high energy cosmic rays with the silicon substrate has a very well-defined distribution (Miles et al. 2020, submitted to ApJ). The peak of the distribution occurs at ~1000 electrons and the distribution has a clear cut-off below ~500 electrons (see Figures 4.11 and 4.12).

Figure 4.11: Electron deposition by cosmic rays on WFC, normalized by the number of counts in the peak bin.
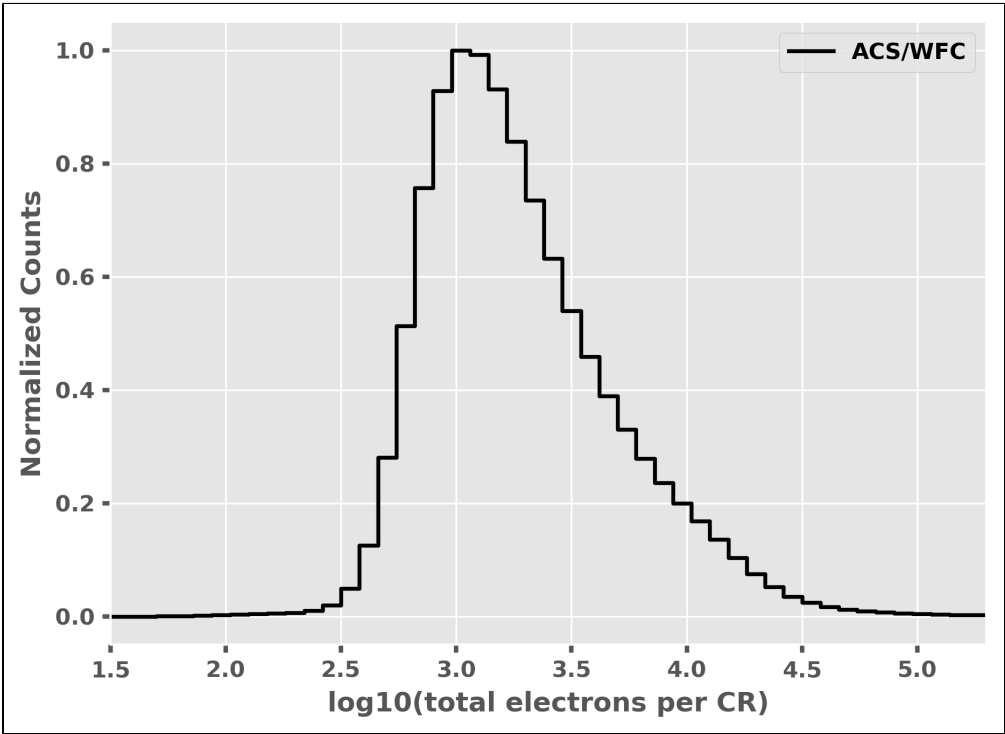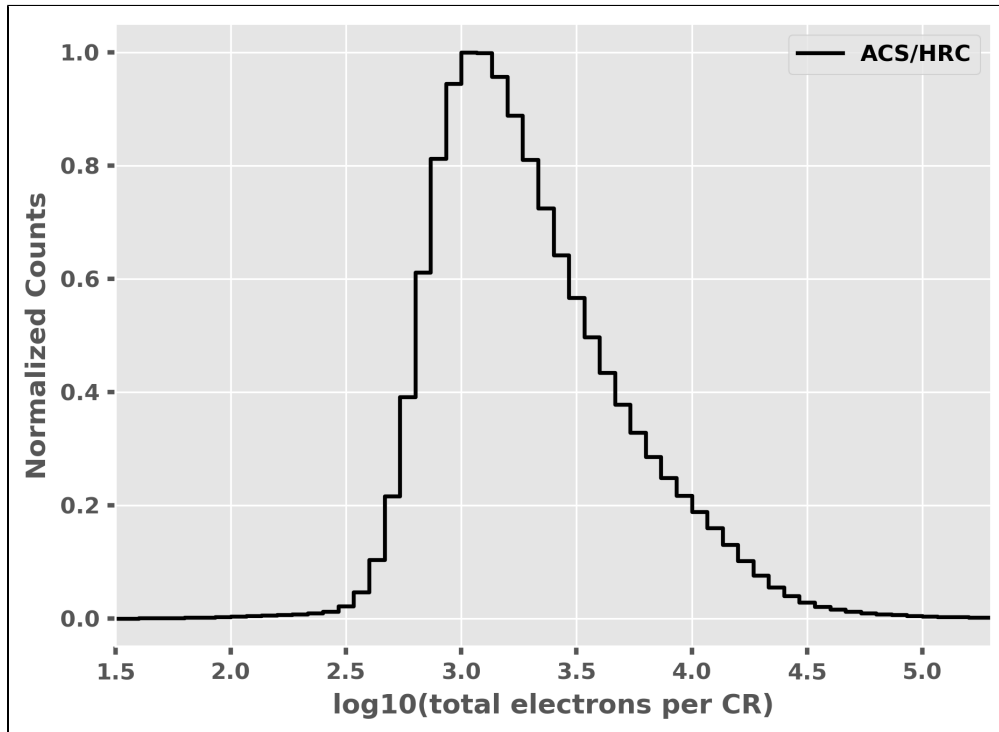
Figure 4.12: Electron deposition by cosmic rays on HRC, normalized by the number of counts in the peak bin.

The distribution of the number of pixels affected by a single cosmic ray is strongly peaked at 4 to 5 pixels. Although a few events encompass only one pixel, examination of these events indicates that some or maybe all of these sources are unstable pixels which can appear hot in one exposure (with no charge diffusion) and normal in the next. Such pixels are very rare but do exist. There is a long tail in the direction towards increasing numbers of attached pixels.

Distributions of sizes and anisotropies can be useful for distinguishing cosmic rays from astrophysical sources in a single image. The size distribution for both chips peaks near 0.4 pixels as a standard deviation (or 0.9 pixels as a FWHM). This is much narrower than the PSF and is thus a useful discriminant between unresolved sources and cosmic rays.

4.3.8 Charge Transfer Efficiency

> ⊘ *Please check for updates on the ACS website.*

Charge transfer efficiency (CTE) is a measure of how effectively the CCD moves charge between adjacent pixels during readout. A perfect CCD would be able to transfer 100% of the charge as it is shunted across the CCD and out through the serial register. In practice, small traps in the silicon lattice compromise this process by holding on to electrons, releasing them at a later time. Depending on the trap type, the release time ranges from a few microseconds to several seconds. For large charge packets (several thousands of electrons), losing a few electrons during readout is not a serious problem, but for smaller (~100e⁻ or less) signals, it can have a substantial effect.

The CTE numbers for the ACS CCDs at the time of installation are given in Table 4.6. While the numbers look impressive, reading out the WFC CCD requires 2048 parallel and 2048 serial transfers, which leads to almost 2% of the charge from a pixel in the corner opposite to the readout amplifier being lost during readout.

Table 4.6: Charge transfer efficiency measurements of the ACS CCDs prior to installation from Fe55 experiments (Sirianni et al. 2000, Proc. SPIE 4008)

CCD	Parallel	Serial
WFC1	0.999994	0.999999
WFC2	0.999995	0.999998
HRC	0.999997	0.999998

Like other CCD cameras aboard *HST*, ACS has suffered degraded CTE due to radiation damage since its installation in 2002. Since 2003, specific calibration programs aimed at characterizing the effects of the CTE on stellar photometry have been performed. Results from the internal CTE monitor program shows that CTE appears to decline linearly with time, and that CTE losses are stronger for lower signal levels (ACS ISR 2005-03, ACS ISR 2018-09). However, in order to derive an accurate correction formula for photometry, a number of observations at different epochs, sky backgrounds, and stellar fluxes have to be accumulated. The results of the observations taken through November 2011 are described in several ISRs (ACS ISR 2009-01, ACS ISR 2011-01, ACS ISR 2012-05) and are summarized here. For WFC, significant photometric losses are apparent for stars undergoing numerous parallel transfers (*y*-direction). As of 2015, the CTE loss was ~10% for a fiducial 100 e⁻ star at the center of the CCD with a typical background of 30e⁻. This loss can rise to >50% in worst cases (faint sources, low backgrounds, farthest from the CCD serial register), rendering faint sources undetectable and thus unrecoverable with current pixel-based CTE correction algorithms. The size of the photometric loss appears to have a strong power-law dependence on the stellar flux, as seen in other CCDs flown on *HST*.

The dependence on background is significant, and it is possible to increase the background by using the post-flash capability. This is unlikely to be useful for most observations, but may make a significant difference in observations with extremely low background (ACS ISRs 2014-01 and 2018-02). The use of post-flash is discussed in more detail in Section 9.6.6.

It may also be useful, in some specific cases, to choose the filter in order to obtain a higher background (e.g., F606W). CTE degradation also has an impact on astrometry (see ACS ISR 2007-04). Therefore, for astrometric programs of relatively bright objects, the use of post-flash may be considered. No losses are apparent for WFC due to serial transfers (*x*-direction). Further details on CTE corrections of very bright stars on subarrays can be found in the ACS ISR 2011-01. A study of the CTE evolution is presented in ACS ISR 2012-03.

The predicted photometric losses (due to imperfect CTE) in observations carried out with the ACS/WFC may be calculated with the formulae in the ACS ISR 2012-05. Here we consider three "typical" science applications:

1. A star of magnitude 22 in the VEGAMAG system observed with the F502N narrow band filter for an exposure time of 100 seconds has a sky background of 0.2 electrons. It is located 1000 parallel pixel transfers from the serial register, and therefore suffers a magnitude change of 0.51 mag.

2. A Type Ia supernova at z ~ 1.5 close to its peak brightness (~26.5 mag in VEGAMAG), observed with filter F775W for 600 seconds, results in a sky background of ~50 electrons. It is located 1000 parallel pixel transfers from the serial register, and therefore has a magnitude change of 0.138 mag.
3. A point source with a flux of 1 e⁻/second observed for 600 seconds with a filter that gives a sky background level of 30 electrons has a magnitude change of 0.142 mag when subject to 1000 parallel pixel transfers.

An online CTE correction calculator is available for users at the ACS website.

Anderson & Bedin 2010, PASP, 122, 1035 have developed an empirical approach based on the CTE-trailed profiles of warm and hot pixels to characterize the effects of CTE losses for the ACS/WFC. Their algorithm first develops a model that reproduces the observed trails and then inverts the model to convert the observed pixel values in an image into an estimate of the original pixel values.

An improved version of CALACS was released in 2012. Along with implementing the empirical CTE correction algorithm, that update also included corrections for the electronic artifacts introduced by the repair of the WFC during SM4, namely the bias shift effect (ACS ISR 2012-02), the bias striping effect (ACS ISR 2011-05), and the crosstalk effect (ACS ISR 2010-02). In addition to the standard data products (CRJ, FLT and DRZ files) there are three files (CRC, FLC and DRC) which contain the CTE-corrected data products. Users are now able to choose whether to use the standard or CTE-corrected products. CALACS applies the CTE correction to the raw images and requires CTE-corrected dark reference files. The ACS Team has produced the dark reference frames for the entire ACS archive (ACS TIR 2012-02 and 2018-01[1]).

The empirical CTE correction algorithm was updated again and included in CALACS in August 2017. It works very well for intermediate to high flux levels (>200 electrons) and is more effective at low flux levels (<100 electrons). The algorithm also includes a step for mitigating readnoise amplification, and employs a more accurate time and temperature dependence for CTE over the ACS lifetime (ACS ISR 2018-04). A tool that uses the CTE model to simulate ACS/WFC readout, called the forward model, has been made available to users as part of CALACS and acstools. A python notebook that provides guidelines for running the forward model is available at the ACS Analysis Tools page.

The results of the empirical CTE correction algorithm on stellar fields are found to be in agreement with the photometric correction formula of ACS ISR 2012-05. Please refer to the ACS website for the latest information.

4.3.9 UV Light and the HRC CCD

In the optical, each photon generates a single electron. However, shortward of ~3200 Å, there is a finite probability of creating more than one electron per UV photon (see Christensen, O., J. App. Phys. 47, 689, 1976). At room temperature, the theoretical quantum yield (i.e., the number of electrons generated for a photon of energy E > 3.5eV (λ~3500 Å)), is N_e = E(eV)/3.65. The HRC CCDs quantum efficiency curve has not been corrected for this effect. The interested reader may wish to see the *STIS Instrument Handbook* for details on the signal-to-noise treatment for the STIS CCDs.

[1]TIRs available upon request.

4.4 The SBC MAMA

4.4.1 MAMA Properties

The ACS MAMA detector is the STIS flight spare STF7, providing coverage from 1150 Å to 1700 Å. MAMA detectors are photon-counting devices which process events serially. The ACS MAMA only operates in the accumulate (ACCUM) mode, in which a time-integrated image is produced. Unlike the STIS MAMAs, ACS does not offer the high-resolution (2048 × 2048) mode or time-tagged data acquisition. Figure 4.13 illustrates the design of the MAMA, which has an opaque CsI photocathode deposited directly on the face of the curved microchannel plate (MCP). Target photons strike the photocathode, liberating single photoelectrons which pass into the MCP, where a pulse of ~4 × 10^5 e- is generated. The pulse is recorded by an anode array behind the photocathode and detected by the MAMA electronics which reject false pulses and determine the position of the photon event on the detector.

The field electrode, or *repeller wire*, repels electrons emitted from the microchannel plate back into the channels. This provides an increase in quantum efficiency of the detector at the price of an increase in the detector point spread function halo. The repeller wire voltage is always on for SBC observations.

The ACS MAMA has a broken anode which disables rows 600 to 605. There are three dark spots smaller than 50 µm at positions (334,977), (578,964), and (960,851), as well as two bright spots at (55,281) and (645,102) with fluctuating rates that are always less than 3 counts per second. The reference pixel has been moved to (512,400) to avoid these areas (see Table 7.10).
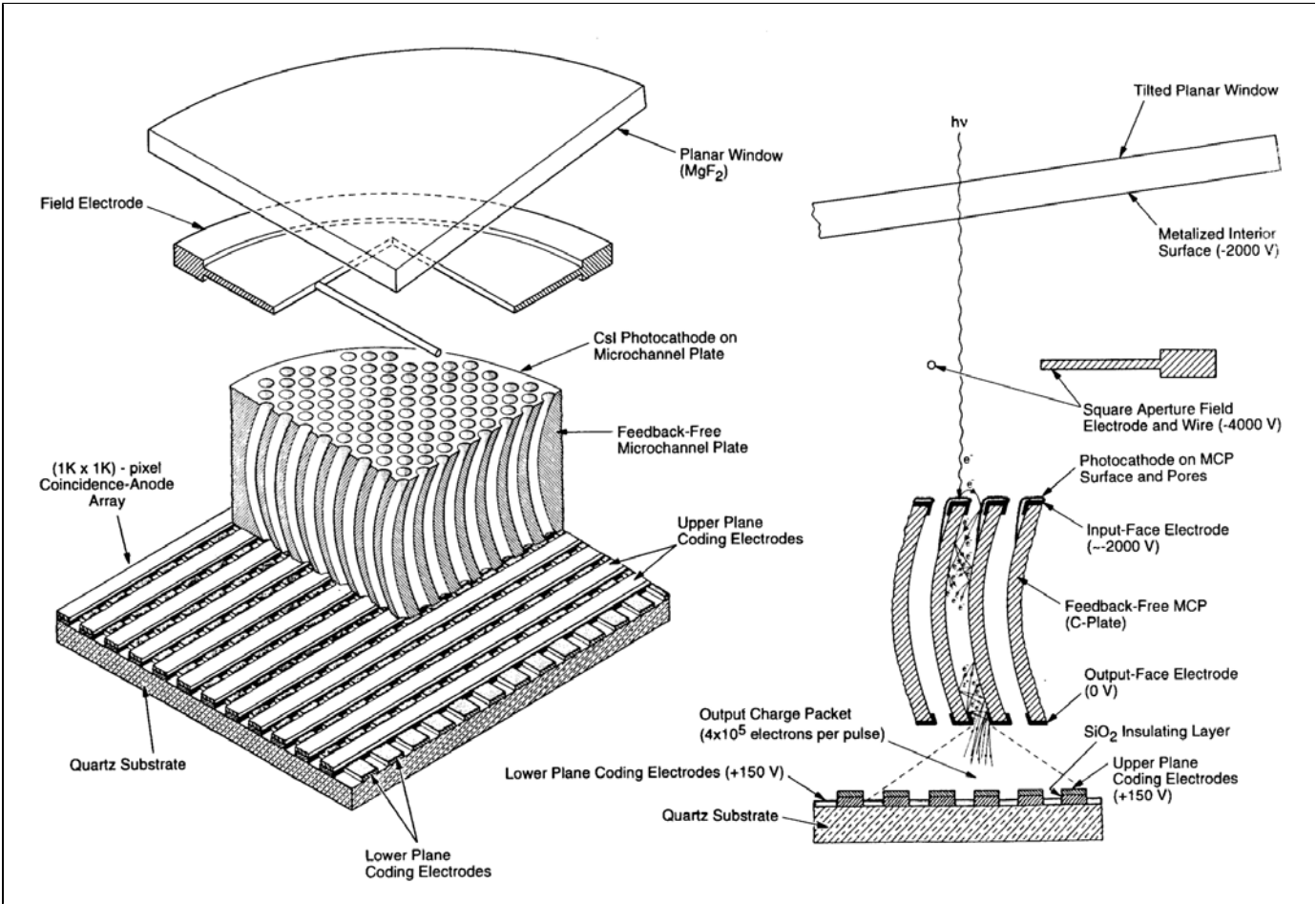
Figure 4.13: Design of the SBC MAMA.

Table 4.7: SBC detector performance characteristics.

Characteristic	SBC MAMA performance
Photocathode	CsI
Wavelength range	~1150 to 1700 Å
Pixel format	1024 × 1024 pixel
Pixel size	25 × 25 μm^2
Plate scale	~0.034 × 0.030 $arcsec^2$/pixel
Field of view	34.6 × 30.5 $arcsec^2$
Quantum efficiency	~35% @ 1216 Å
Dark count [a]	8.28×10^{-6} counts/s/pixel
Global count-rate linearity limit	200,000 counts/s
Local count-rate linearity limit	~22 counts/s/pixel
Visible light DQE	$< 1.2 \times 10^{-9}$ above 400 nm

[a] The dark current remains constant up to an instrument temperature ~25°C. Above that temperature, the dark current increases rapidly.

[b] Rate at which counting shows 1% deviation from linearity.

4.4.2 SBC Spectral Response

The total transmission curve for the SBC with the PR110L prism is shown in Figure 4.14. The peak photocathode response occurs at Lyman-α. Its spectral response is defined by the cutoff of the MgF_2 window at 1150 Å at short wavelengths, and by the relatively steep decline of the CsI photocathode at long wavelengths.

Observations of flux calibration stars and a G-type star using the SBC PR110L prism have revealed that the sensitivity of the MAMA detector to optical and near-UV light is apparently much larger than previously thought (ACS TIR 2008-02[1]).

Estimates of the real SBC throughput indicates that the detector efficiency is factors of approximately 50 and 1000 higher at wavelengths of 3000 Å and 4000 Å respectively compared to ground testing. For a solar type spectrum, this can mean that one-half or more of the counts detected are due to optical and near-UV photons, rather than from the expected FUV photons. The updated sensitivity curve has been incorporated both in the Exposure Time Calculator (ETC) and in the instrument throughput tables. There is also some evidence that this red leak changes as the SBC detector warms up, increasing by as much as 30% over the course of 5 orbits. It is not yet clear if this red leak has also been increasing secularly over time. STIS FUV MAMA data seem to show a similar, although perhaps somewhat smaller effect.

For dispersed PR110L and PR130L observations, it is straightforward to identify this extra red light; however, it clearly also affects SBC imaging observations done with the long pass filters. Until this effect is better understood and calibrated, extreme caution should be used when interpreting FUV imaging observations of red targets. Observers who need to measure FUV fluxes of red targets are strongly recommended to take interleaving observations with two different SBC long pass filters (e.g., F140LP and F165LP), so that the difference in the count rates can be used to isolate the true FUV flux. There is some recent evidence that the red leak is temperature dependent and cannot be accurately determined in the F165LP filter. For this reason it is recommended that this filter not be used for science. It should only be used in conjunction with other filters to subtract red photons from the measurements in other bandpasses.

Figure 4.14: Total transmission curve for ACS SBC plus the PR110L prism.
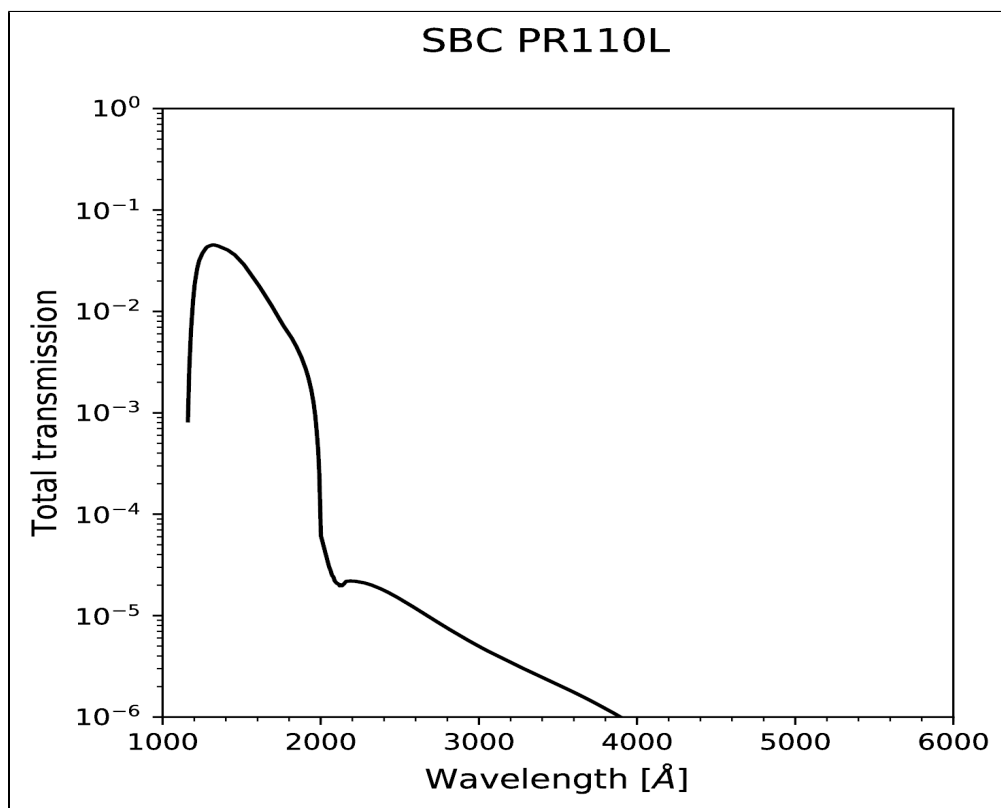
4.4.3 Optical Performance

The SBC exhibits low-level extended wings in the detector point-spread function (PSF) (ACS ISR 2016-05). Sample MAMA detector PSF profiles are shown in Figure 4.15.

Figure 4.15: MAMA point spread function. Solid lines are from observations, dashed lines are from Tiny Tim models.
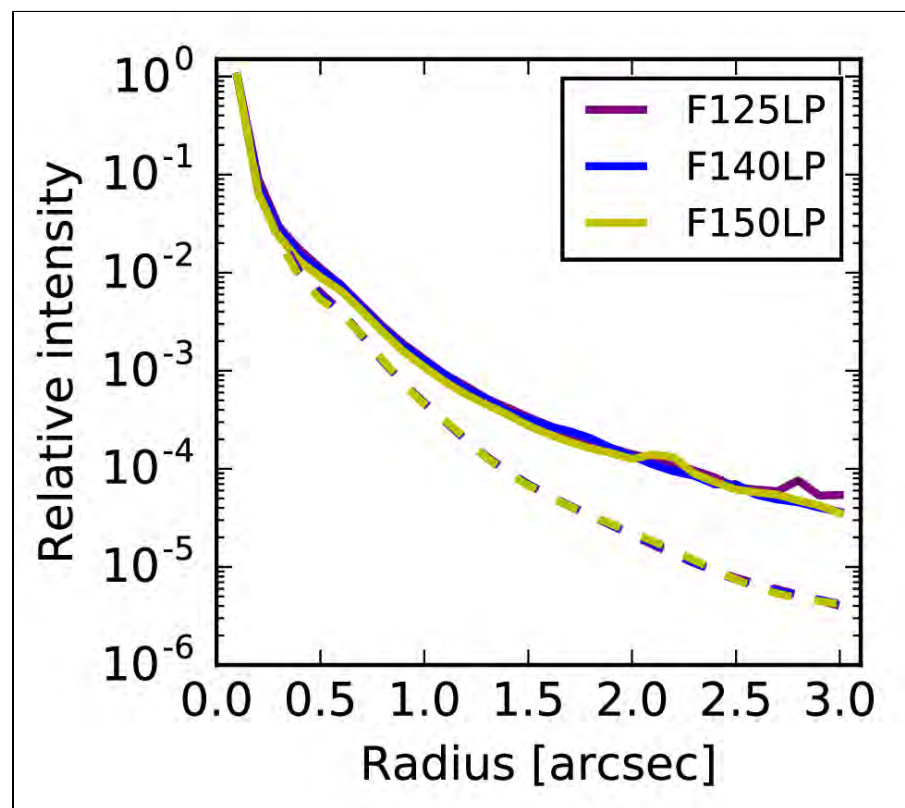
[1]Technical Instrument Reports (TIRs) available upon request.

4.5 SBC Operations and Limitations

4.5.1 SBC Scheduling Policies

The STIS MAMA control electronics are subject to resets due to cosmic-ray upsets. Therefore, STIS MAMAs are operated only during the contiguous orbits of each day that are free of the South Atlantic Anomaly (SAA). Even though the design of the ACS MAMA control electronics in the SBC was modified so that they would not be susceptible to cosmic-ray hits, the background count rate still exceeds the bright object limits for the SBC during SAA passage. Consequently, the SBC will only be scheduled for use during SAA-free orbits.

4.5.2 MAMA Overflow of the 16 Bit Buffer

The MAMA is a photon-counting detector: as each event is recorded, the buffer memory for the corresponding pixel is incremented by one integer. The buffer memory stores values as 16 bit integers; hence, the maximum number it can accommodate is 65,535 counts per pixel in a given ACCUM mode observation. When accumulated counts per pixel exceed this number, the values will wrap, i.e., the memory resets to 0. As an example, if you are counting at 25 counts/second /pixel, you will reach the MAMA "accumulation" limit in ~44 minutes.

The accumulated counts per pixel can be kept below this value by breaking individual exposures into multiple identical exposures, each of which is short enough that fewer than 65,535 counts are accumulated per pixel. There is no read noise for MAMA observations, so no penalty is paid in lost signal-to-noise ratio when exposures are split. There is only a small overhead for each MAMA exposure (see Section 8.2).

> ⚠️ *Keep the accumulated counts per SBC pixel below 65,535 by breaking single exposures into multiple exposures, as needed.*

4.5.3 MAMA Darks

MAMA detectors have intrinsically low dark currents. Ground test measurements of the ACS MAMA showed count rates in the range 10^{-5} to 10^{-4} counts/s/pixel as the temperature varied from 28°C to 35°C. The count rate increases by about 30% for one degree increase in temperature. A recent study of in-flight data investigated how the temperature impacts the dark rate when the detector is left on for a long period of time (ACS ISR 2017-04). The dark rate remains as stable as ever. It is 8.28×10^{-6} counts/s/pixel while the instrument is below ~25°C (Figure 4.16). Above that temperature, the central region of the detector begins to experience an increasingly higher dark rate (Figure 4.17). That being the case, dark frames cannot be subtracted from science observations like they are with CCDs. Unlike CCDs, MAMA dark images are not meant to capture hot and warm pixels. Instead, dark rate in MAMA detectors shows up as random background noise. For the purposes of scientific analysis, the dark rate can be subtracted along with the background, at least when the detector is still below ~25°C. Above that temperature, users should still be able to do a local subtraction, but should be aware of the pattern present in the dark rate. Alternatively, observers can use the SBC-LODARK aperture if they plan to use the SBC for visits longer than 2 orbits (see Section 7.7.6).

Figure 4.16: SBC Dark Rate and Operating Temperature.
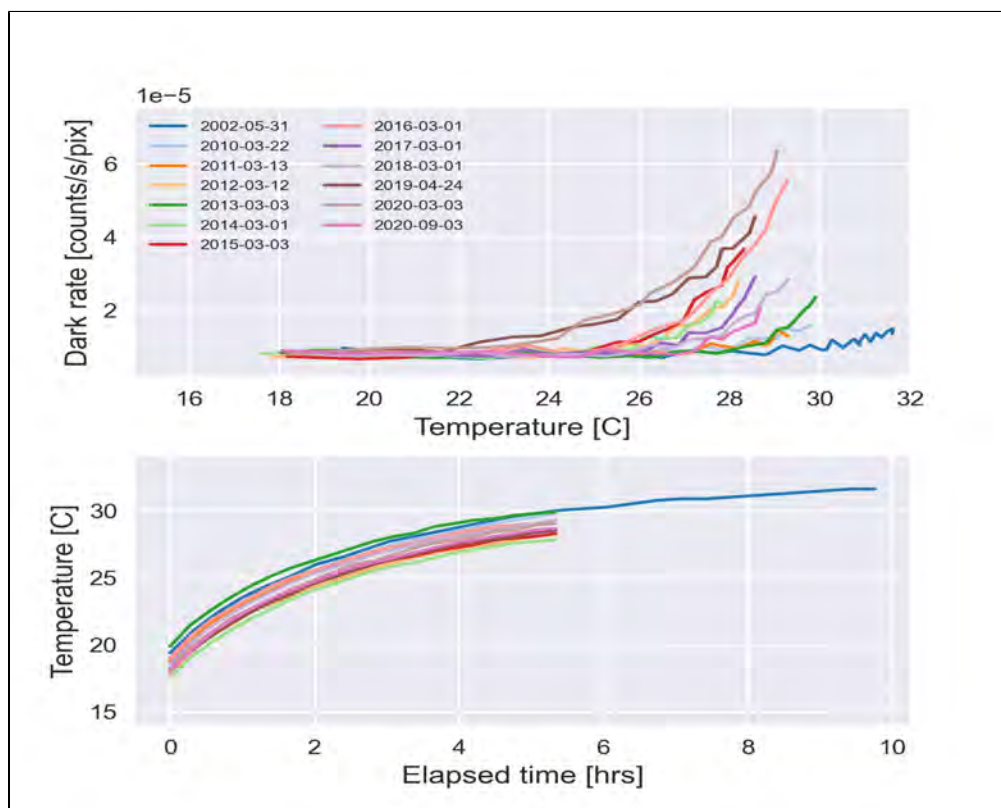
The top panel shows the dark rates vs. temperature. The bottom panel shows how the temperature changed from the time the instrument was turned on until the end of the observations. Dashed lines correspond to bad data not used in the analysis.

Figure 4.17: Dark Rate Image Comparison.
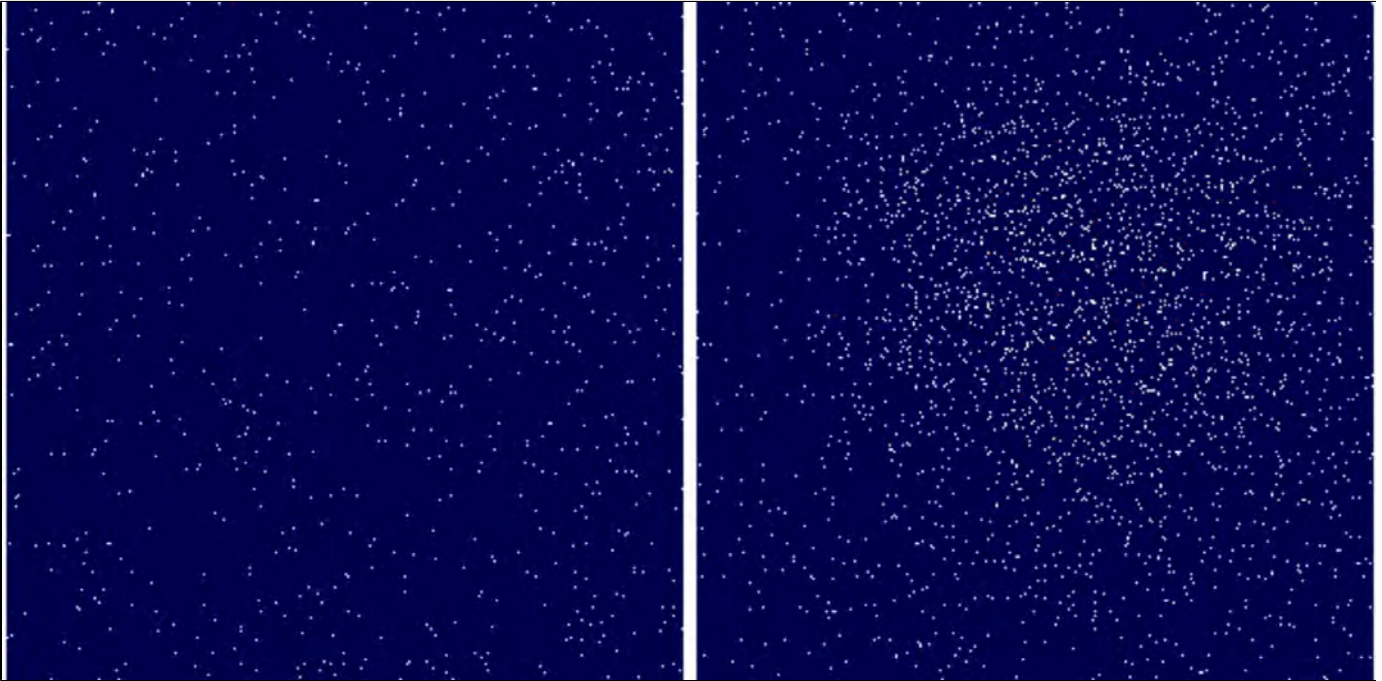
Left: Dark rate image taken immediately after the detector was turned on (from proposal ID 14513). Right: Dark rate image from the same program taken after the detector had been on for 5 hours. The increased dark rate visible to the top-right of the image drives the increased average of the entire detector, while the dark rate in the bottom-left corner remains constant throughout.

4.5.4 SBC Signal-To-Noise Ratio Limitations

MAMA detectors are capable of delivering signal-to-noise ratios of order 100:1 per resolution element (2 × 2 pixels) or even higher. On-orbit tests have demonstrated that such high S/N is possible with STIS (Kaiser et al., 1998, PASP, 110, 978; STIS ISR 1998-16). For targets observed at a fixed position on the detector, the signal-to-noise ratio is limited by systematic uncertainties in the small-scale spatial and spectral response of the detector. The MAMA flats show a fixed pattern that is a combination of several effects including beating between the MCP array and the anode pixel array, variations in the charge-cloud structure at the anode, and low-level capacitive cross-coupling between the fine anode elements. Intrinsic pixel-to-pixel variations are of order 4% but are stable to < 1%. Photometric accuracy can be improved by averaging over flat-field errors by dithering the observation (see Section 7.4).

4.5.5 SBC Flat field

Figure 4.18: SBC MAMA Pixel-to-Pixel Flat Field
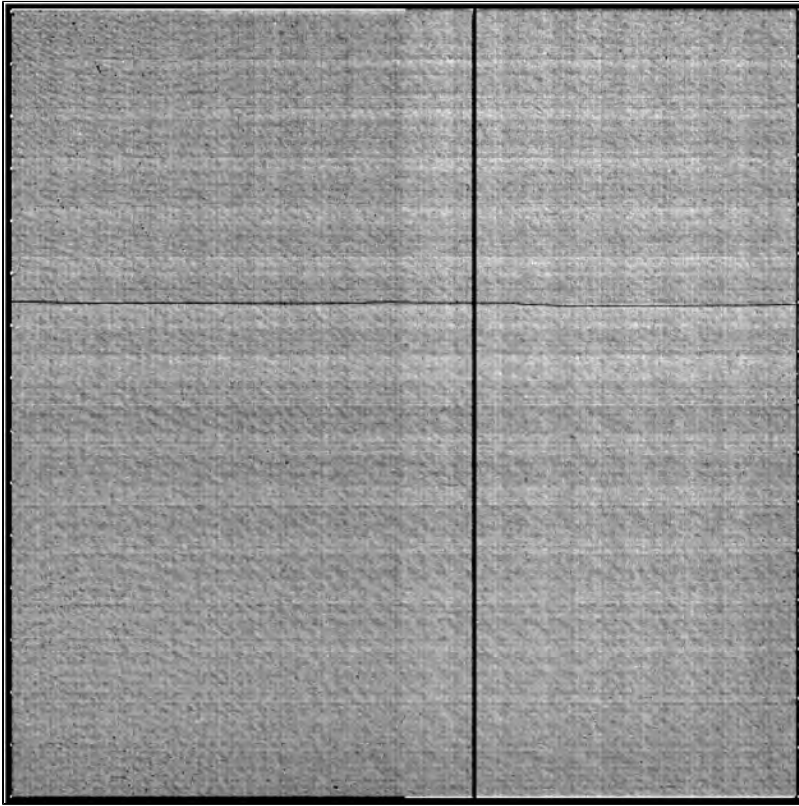
Wavelength independent P-Flat for the SBC MAMA (full frame shown).

The SBC requires two types of flat fields: the "pixel-to-pixel flats" (or P-flats), which take care of the high-frequency structures in the detector sensitivity, and the "low-order flats" (or L-flats), which handle the low-frequency components. Analysis using the on-board deuterium lamp shows that the P-flat has no wavelength dependence (ACS ISR 2005-04). More recent analysis showed that the high-frequency structure in the P-flat changed in 2007 (ACS ISR 2016-02), and therefore the file that is used in the construction of the LP-flat depends on the observation date. Images taken before Feb 20, 2007 use `p5p1513pj_pfl.fits`, and images taken after that date use `36h2201nj_pfl.fits`. The P-flat in Figure 4.18 shows the effect of the disabled broken anode for rows 600 to 605 and of the shadow of the repeller wire around column 577.

Figure 4.19: SBC MAMA LP Flat Field
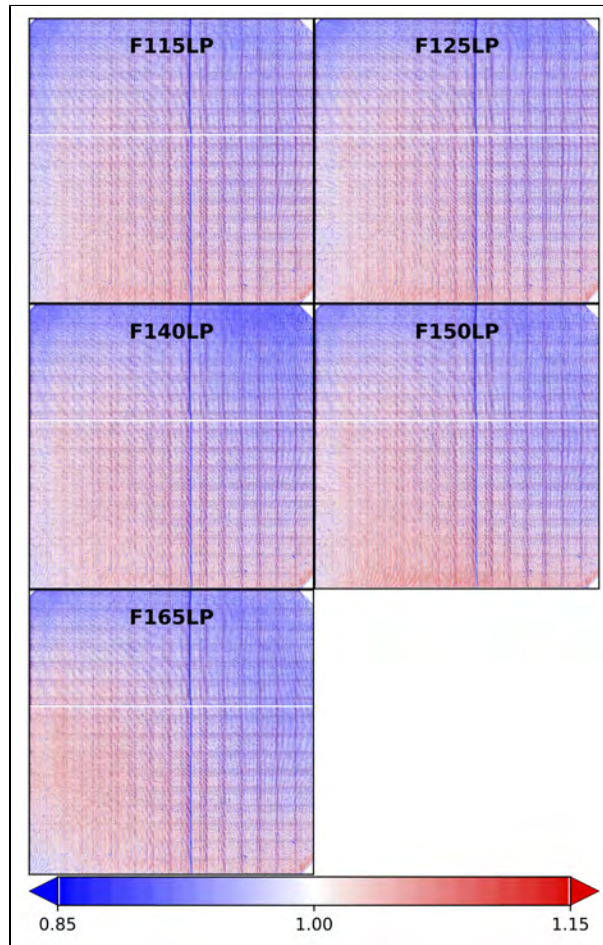
The LP-flats used for calibration of the SBC imaging modes. All images presented with the same stretch.
Low-frequency flat-field corrections for the SBC imaging modes have been derived using multiple exposures of the globular cluster NGC6681 (ACS ISR 2019-04). The low-frequency L-flats were derived by directly fitting 2D polynomial surfaces to the spatial sensitivity data. The resulting products are smoother than the previous versions, due to the different method of deriving the flats. The corrections in the flats are on the order of ±8%.

The L-flats are combined with the two sets of P-flats to make the final LP-flats. In June 2019, a set of ten LP-flats were delivered to the Calibration Reference Data System (CRDS) for use in the calibration pipeline. SBC images in MAST have been re-processed using these new LP-flats. Figure 4.19 shows five of the the imaging mode LP-flats used for new observations.

4.5.6 SBC Sensitivity

Figure 4.20: Sensitivity of five of the SBC imaging modes as a function of time
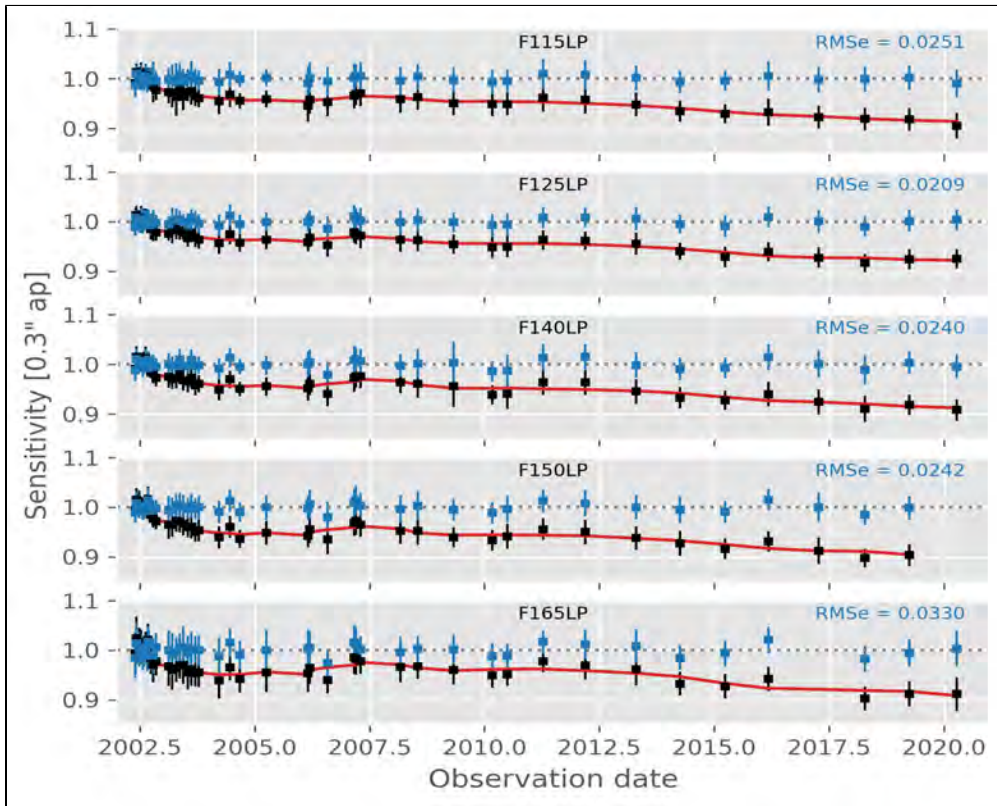
Sensitivity measurements for five SBC imaging modes. Black boxes are the mean and standard deviation of the sensitivity before time-dependent sensitivity (TDS) correction. The red line is the extracted TDS. Blue boxes are the sensitivity after applying TDS correction.

The sensitivity of MAMA detectors declines with time (ACS ISR 2019-04). The sensitivity of the SBC has declined by up to 9% since launch, with a rate of about 0.5% per year since 2007 (see Figure 4.20). This time-dependent sensitivity requires observation date-dependent zeropoints. The necessary files have been delivered to the calibration pipeline so that the `PHOTFLAM` header header keyword in SBC images is populated with the correct value.

The default behavior of pysynphot when performing simulations of imaging modes is to assume a sensitivity corresponding to the middle of the upcoming cycle. The ETC assumes the same date. Users should consult the ETC release notes to identify the exact date being used.

4.5.7 SBC Linearity

Global

The MAMA detector maintains linearity (i.e., photon impact rate is linearly proportional to detected count rate) at globally integrated count rates up to 200,000 counts/second. At global rates exceeding 285,000 counts/second, both the MAMA detector and processing software are unable to reliably count photons. For these reasons, and to protect the MAMA from over-illumination, observations yielding global count rates above 200,000 counts/second are not allowed (see Section 4.6).

Local

The MAMA pixels are linear to better than 1% up to ~22 counts/second/pixel. Linearity at higher count rates is image-dependent such that the linearity of one pixel depends on the photon rate affecting neighboring pixels. Consequently, it is impossible to reliably correct for local deviations from linearity in post-observation data processing. MAMA detectors are also subject to damage at high local count rates, so observations yielding local count rates above 50 counts/second /pixel are not allowed (see Section 4.6).

4.6 SBC Bright-Object Limits

STScI is responsible for ensuring that the MAMA detectors are not damaged by over-illumination. Consequently, procedures and rules have been developed to protect the MAMA. We ask all users to share this responsibility by reading and taking note of the information in this section, and designing observing programs that operate in the safe regime for these detectors. The safety of all proposed SBC targets and fields must be discussed in the Phase I proposal, so that their feasibility can be assessed by the TAC and STScI.

4.6.1 Overview

The SBC detector is subject to catastrophic damage at high global and local count rates, and cannot be used to observe sources that exceed the defined safety limits. The potential detector damage mechanisms include over-extraction of charge from the microchannel plates causing permanent reduction of response, ion feedback from the microchannel plates causing damage to the photocathode, and release of gas which can overpressure the tube. For more information, see ACS ISR 1998-03.

To safeguard the detector, checks of the global (over the whole detector) and local (per pixel) illumination rates are automatically performed in flight for all SBC exposures. The *global illumination rate* is monitored continuously; if the global rate approaches the level where the detector can be damaged, the high voltage on the detector is automatically turned off. This event can result in the loss of all observations scheduled to be taken with that detector for the remainder of the calendar (~1 week). The *peak local illumination rate* is measured over the SBC field at the start of each new exposure. If the local rate approaches the damage level, the SBC filter wheel will be used to block the light, since there is no "shutter." Also, all subsequent SBC exposures in the observation set will be lost until a new filter is requested.

> ⚠️ *Sources that would over-illuminate the SBC detector cannot be observed. It is the responsibility of the observer to avoid specifying observations that exceed the limits described below. Please refer to Section 7.2 for more information and address this issue in your Phase I proposal.*

4.6.2 Observational Limits

To ensure the safety of the SBC detector and the robustness of the observing timeline, we have established observational limits on the incident count rates. Observations which exceed the allowed limits will not be scheduled. The allowed limits are given in Table 7.3, which includes separate limits for nonvariable and irregularly-variable sources. The limits for irregularly-variable sources are a factor 2.5 more conservative than for sources with predictable fluxes. Predictable variables are treated as nonvariable for this purpose. Examples of sources whose variability is predictable are Cepheids or eclipsing binaries. Irregularly variable sources are, for instance, cataclysmic variables or AGN.

SBC observations of targets subject to large, unpredictable outbursts must be preceded by ground-based monitoring within the previous 24 hours, or by a WFC3/UVIS observation a couple of orbits in advance. In the latter case, the observation must be included in the Phase I orbit request. For further information about checking for SBC bright object limits while planning your observations, please refer to Section 7.2.

Chapter 5: Imaging

Chapter Contents

5.1 Imaging Overview

> ⚠️ *HRC has been unavailable since January 2007. Information regarding HRC is provided for archival purposes.*

ACS has been used to obtain images through a variety of optical and ultraviolet filters. The CCD filter wheels contain filters of two different sizes. Some filters (F435W, F475W, F502N, F550M, F555W, F606W, F625W, F658N, F660N, F775W, F814W, F850LP, and, G800L) are full-sized filters that can be used with both WFC and HRC. Others (F220W, F250W, F330W, F344N, F892N, POL0UV, POL60UV, POL120UV, POL0V, POL60V, POL120V, and PR200L) are smaller, giving a full un-vignetted field of view when used with the HRC, but a vignetted field of view of only 72 × 72 arcsec^2 when used with the WFC. Use of the small UV filters with WFC is not supported due to the unpredictable behavior of the silver coating shortward of 4000 Å.

For WFC and HRC imaging, the desired filter in one filter wheel is rotated into position and a CLEAR aperture in the other filter wheel is automatically selected, see Figures 3.2 and 3.3. (Users need not specify CLEAR in their *HST* proposals.) For SBC imaging, the single filter wheel is rotated to the desired position. Every third spot (#1, 4, 7, 10) in the SBC filter wheel is opaque, so the wheel must only be rotated to an adjacent slot to block the beam if a bright object limit violation occurs. Tables 5.1, 5.2, and 5.3 summarize the filters available for imaging with each channel. Figures 5.1 through 5.6 show the filter transmission curves. Figures 5.10 and 5.11 show the location of the filters in each filter wheel. Figure 5.7 shows the integrated system throughputs. Please visit the ACS System Throughputs webpage or refer to Chapter 10 for a full catalog of the ACS filter throughputs.

The ACS ramp filters are designed to allow narrow- or medium-band imaging centered at an arbitrary wavelength. Each ramp filter is divided into three segments, each of which can be used with the WFC while only the middle segment was used with the HRC. See Table 5.2 for the list of available ramp filters. More information is available in Section 7.3.1.

Filterless WFC or HRC is available, but unsupported, by specifying CLEAR as the filter name. Rough wavelengths and bandwidths for CLEAR imaging are listed in Table 5.1. CLEAR imaging yields significantly degraded WFC PSFs, but only slightly degraded HRC PSFs. See ACS ISR 2003-03 for more details about CLEAR imaging.

Table 5.1: ACS WFC/HRC filters in Filter Wheel #1.
(HRC information is provided for archival purposes only.)

Filter name	Central wavelength (Å)	Width (Å)	Description	Camera
CLEAR	6200	5200	Clear aperture	WFC/HRC
F555W	5346	1193	Johnson V	WFC/HRC
F775W	7764	1528	SDSS i	WFC/HRC
F625W	6318	1442	SDSS r	WFC/HRC
F550M	5580	547	Narrow V	WFC/HRC
F850LP	9445	1229	SDSS z	WFC/HRC
POL0UV	2000 to 6000	–	0° UV polarizer	HRC[/WFC] [a]
POL60UV	2000 to 6000	–	60° UV polarizer	HRC[/WFC] [a]
POL120UV	2000 to 6000	–	120° UV polarizer	HRC[/WFC] [a]
F892N	8917	154	Methane (2%)	HRC[/WFC] [a]
F606W	5907	2342	Broad V	WFC/HRC
F502N	5022	57	[OIII] (1%)	WFC/HRC
G800L	5800 to 11,000	–	Grism (R ~100)	WFC/HRC
F658N	6584	78	Hα (1%)	WFC/HRC
F475W	4760	1458	SDSS g	WFC/HRC

[a] [/WFC] indicates that polarizer filters, designed for the HRC field of view, induces vignetting when used with the WFC, producing a 72 × 72 arcsec^2 field of view.

Table 5.2: ACS WFC/HRC filters in Filter Wheel #2.
(Information regarding the HRC is provided for archival purposes only.).

Filter name	Central wavelength (Å)	Width (Å)	Description	Camera
CLEAR	6000	5200	Clear aperture	WFC/HRC
F660N	6602	40	[NII] (1%)	WFC/HRC
F814W	8333	2511	Broad I	WFC/HRC
FR388N	3710 to 4050	2%[1]	[OII] Ramp—middle segment	WFC/HRC
FR423N	4050 to 4420	2% [a]	[OII] Ramp—inner segment	WFC

FR462N	4420 to 4820	2% [a]	[OII] Ramp—outer segment	WFC
F435W	4297	1038	Johnson B	WFC/HRC
FR656N	6270 to 6850	2% [a]	Hα Ramp—middle segment	WFC/HRC
FR716N	6850 to 7470	2% [a]	Hα Ramp—inner segment	WFC
FR782N	7470 to 8160	2% [a]	Hα Ramp—outer segment	WFC
POL0V	4000 to 8000	–	0° Visible Polarizer	HRC[/WFC] [b]
F330W	3354	588	HRC U	HRC
POL60V	4000 to 8000	–	60° Visible Polarizer	HRC[/WFC] [b]
F250W	2696	549	Near-UV broadband	HRC
POL120V	4000 to 8000	–	120° Visible Polarizer	HRC[/WFC] [b]
PR200L	2000 to 4000	–	NUV Prism (R~100 @ 200 nm)	HRC
F344N	3434	60	Ne V (2%)	HRC
F220W	2228	485	Near-UV broadband	HRC
FR914M	7570 to 10,710	9% [a]	Broad Ramp—middle segment	WFC/HRC
FR853N	8160 to 8910	2% [a]	IR Ramp—inner segment	WFC
FR931N	8910 to 9720	2% [a]	IR Ramp—outer segment	WFC
FR459M	3810 to 5370	9% [a]	Broad Ramp—middle segment	WFC/HRC
FR647M	5370 to 7570	9% [a]	Broad Ramp—inner segment	WFC
FR1016N	9720 to 10,610	2% [a]	IR Ramp—outer segment	WFC
FR505N	4820 to 5270	2% [a]	[OIII] Ramp—middle segment	WFC/HRC
FR551N	5270 to 5750	2% [a]	[OIII] Ramp—inner segment	WFC
FR601N	5750 to 6270	2% [a]	[OIII] Ramp—outer segment	WFC

[a]The width of the ramp filters is a percentage relative to the central wavelength of the bandpass, Δλ/λ.

[b] [/WFC] indicates that polarizer filters, designed for the HRC field of view, induces vignetting when used with the WFC, producing a 72 × 72 arcsec^2 field of view.

Table 5.3: ACS SBC filter complement.

Filter name	Description
F115LP	MgF_2 (1150 Å longpass)
F125LP	$CavF_2$ (1250 Å longpass)
F140LP	BaF_2 (1400 Å longpass)
F150LP	Crystal quartz (1500 Å longpass)
F165LP	Fused Silica (1650 Å longpass)
F122M	Lyα (λ = 1200 Å, $\Delta\lambda$ = 60 Å)
PR110L	LiF Prism (R~100)
PR130L	CaF_2 Prism (R~100)

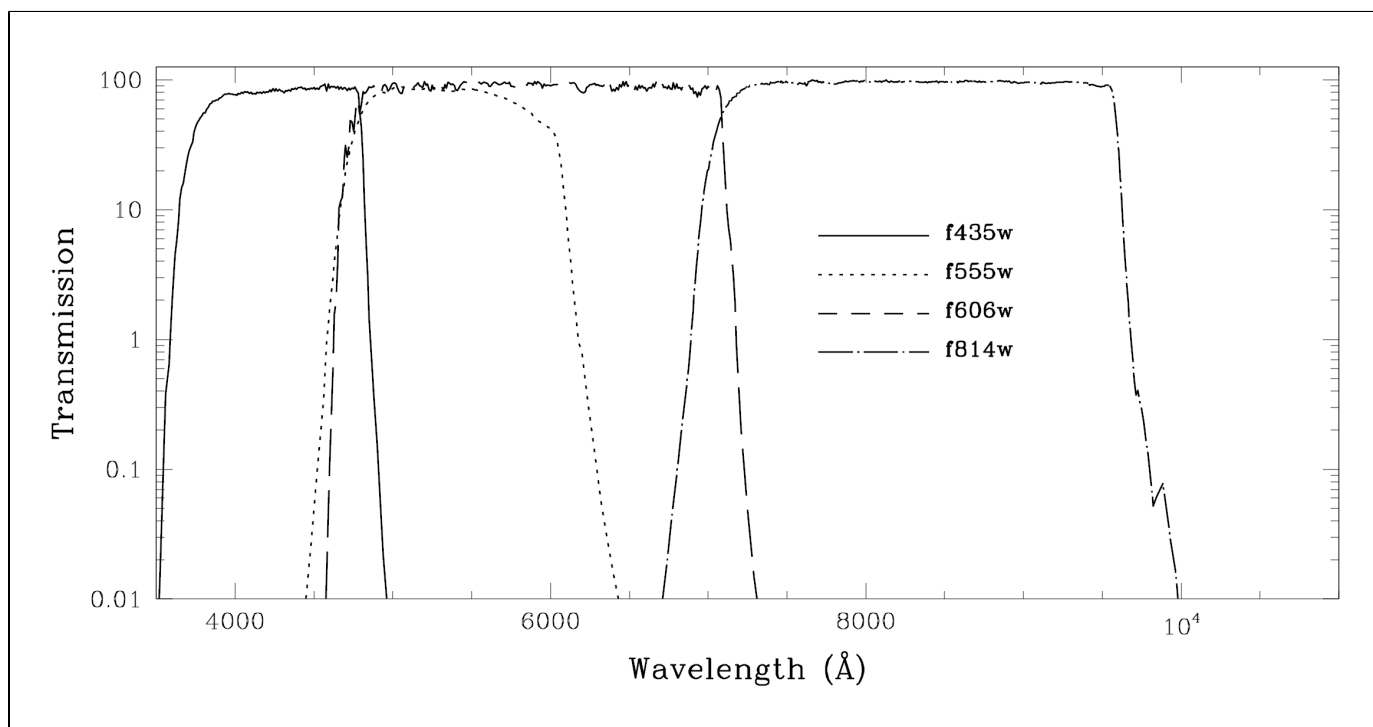**Figure 5.1: ACS broad-band filters.**

Figure 5.2: ACS SDSS filters.
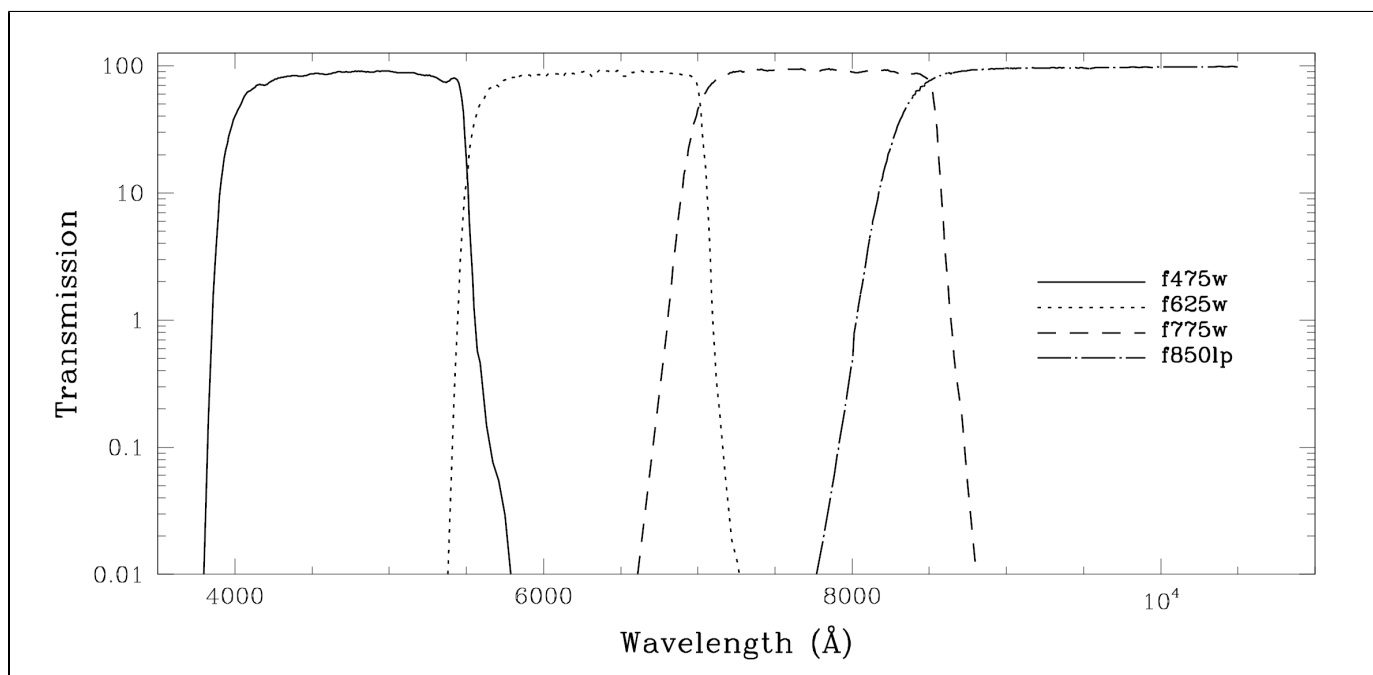
Figure 5.3: ACS UV and medium-band filters.
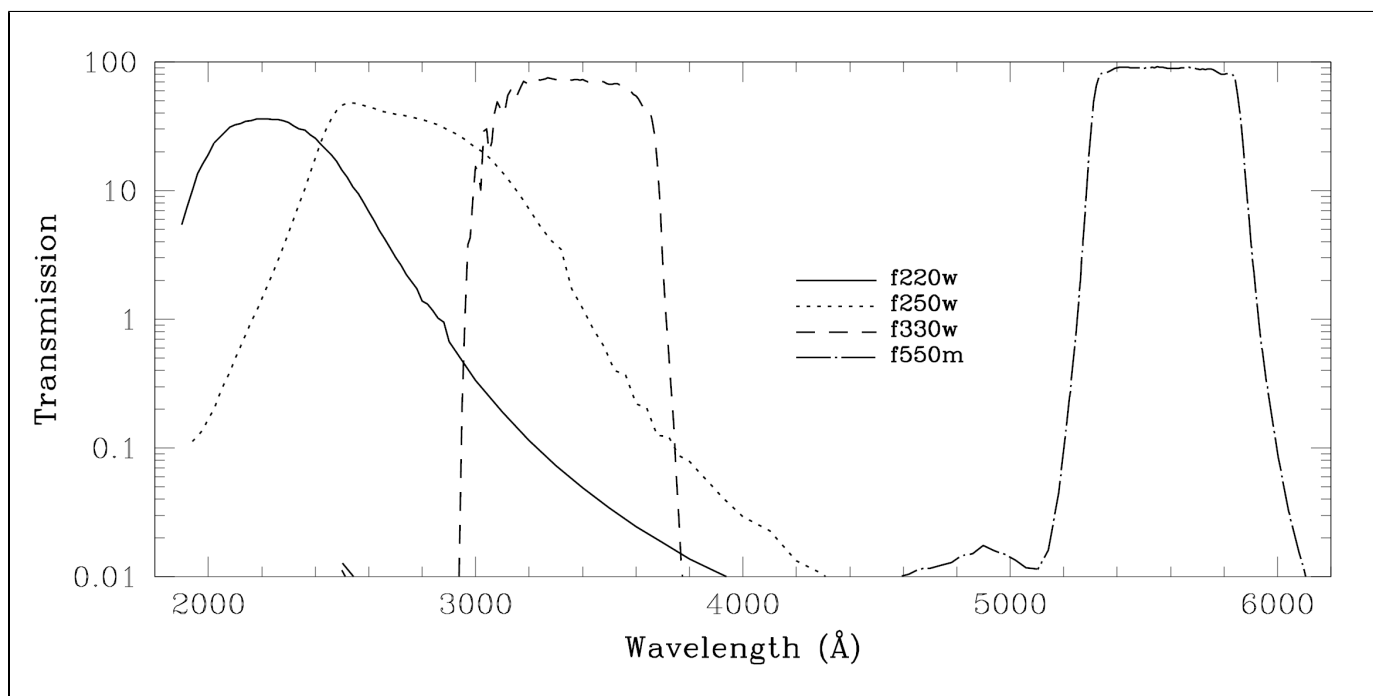
Figure 5.4: ACS narrow band filters.
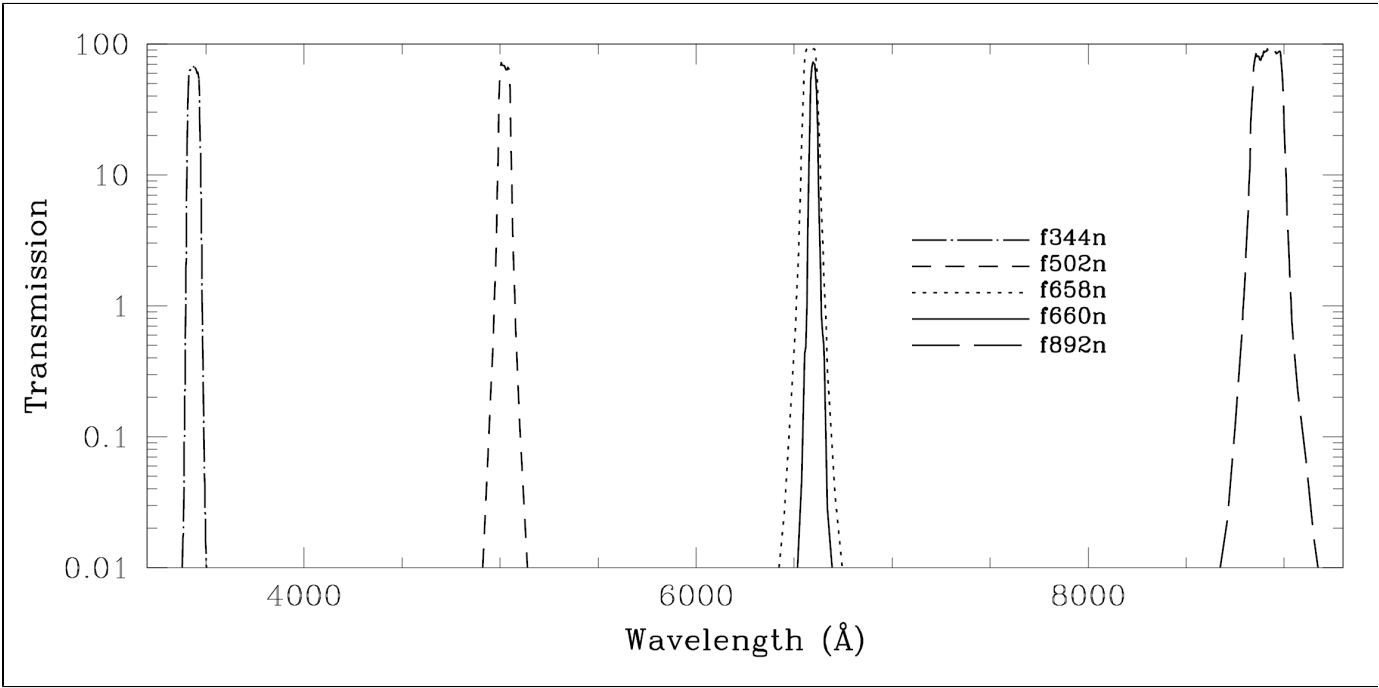
Figure 5.5: ACS SBC filters.
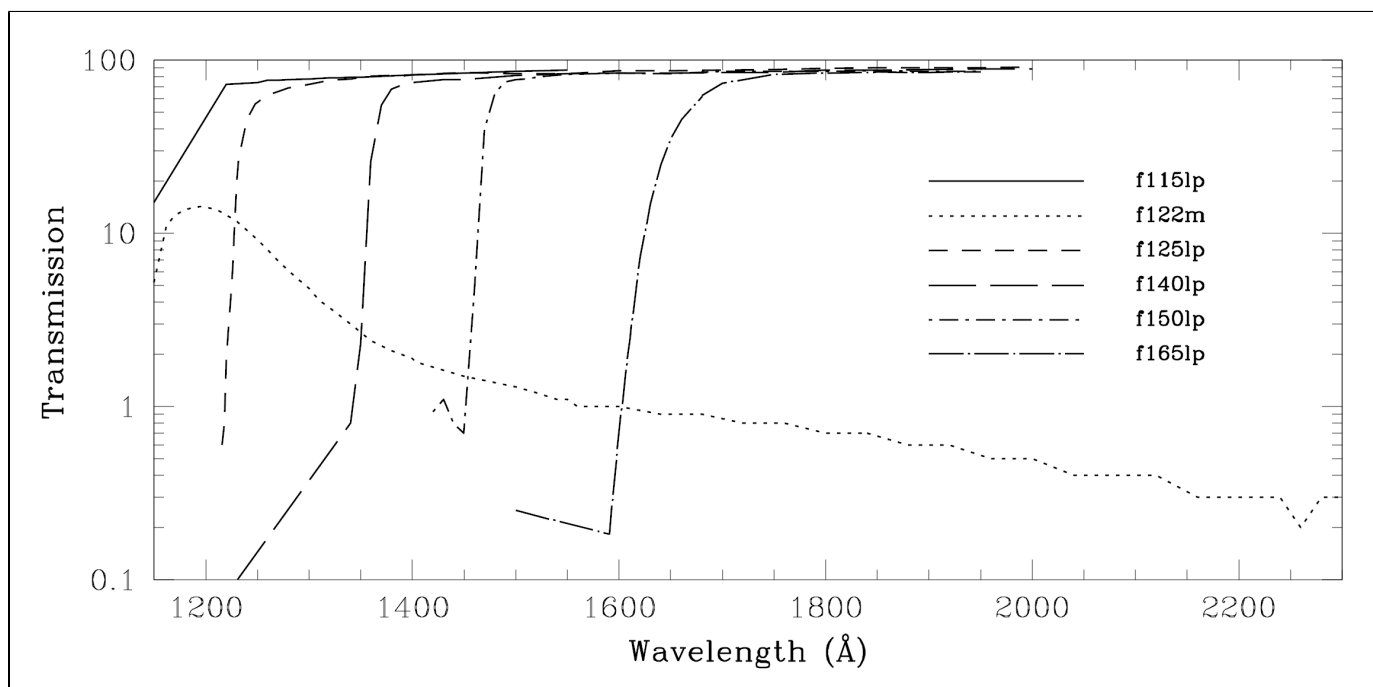
Figure 5.6: Comparison between the ACS and WFPC2 ramp filters.
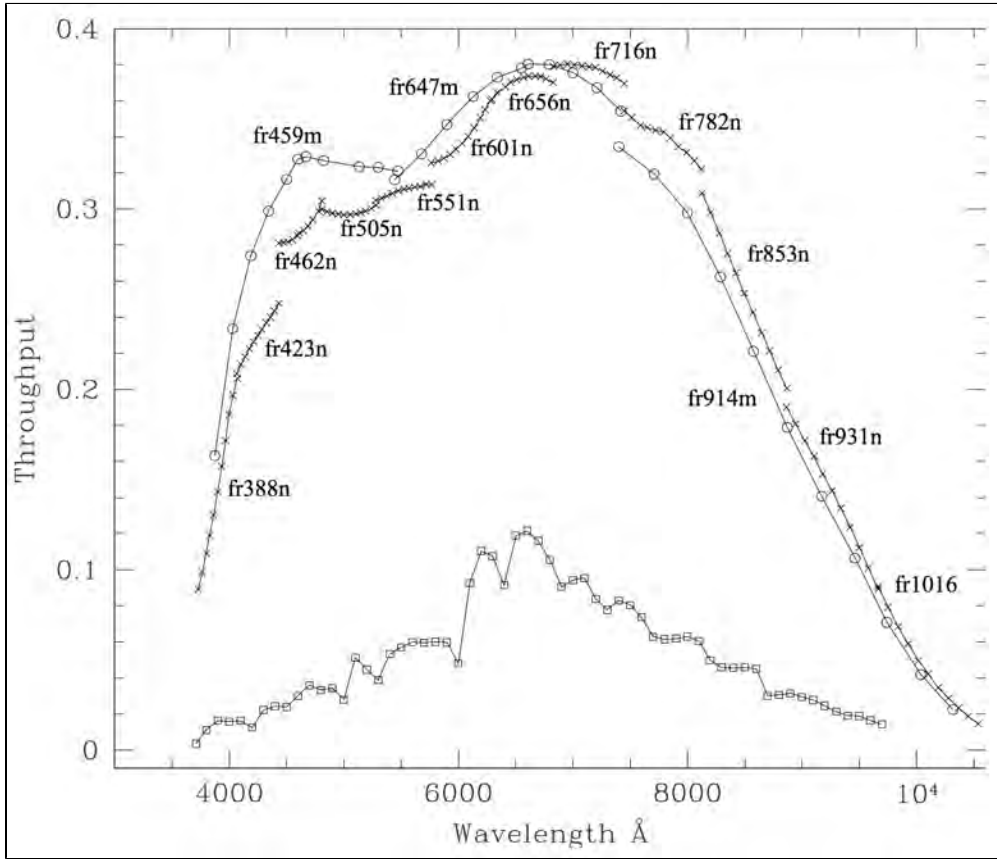
The crosses and open circles are the ACS narrow and medium band ramp filters. The open squares are the 4 WFPC2 ramp filters. For each of the ACS filters, the peak throughput for the central eleven wavelength points is plotted. For the WFPC2 filters, the peak throughput for every 100 Å within the field of view of any of the 4 chips and for a 0° filter rotation angle (as mapped in Figures 3.4 and 3.5 of the WFPC2 Instrument Handbook) is plotted.

5.2 Important Considerations for ACS Imaging

The following characteristics of ACS should be considered when planning ACS observations or archival research:

- The ACS/WFC filter set is more limited than that of WFC3/UVIS. In particular, WFC3/UVIS has an extensive set of ultraviolet, narrow-band, and Strömgren filters unavailable with ACS/WFC. On the other hand, ACS/WFC has polarizers and ramp filters unavailable with WFC3/UVIS.
- For sources subtending less than 5 arcsec, the `WFC1-CTE` aperture (10 arcsec from readout amplifier) will ensure minimal CTE losses.
- ACS ISR 2012-04 contains plots of likely minimum sky backgrounds as a function of exposure time. Observers should determine if their sky backgrounds are likely to be less than 20 electrons. If this is the case, they should consult ACS ISR 2014-01 and ACS ISR 2018-02 for details of the post-flash capability.
- SBC observations should generally be made with two different long pass filters (e.g., F140LP and F165LP), so that the difference in the count rates can be used to isolate the true FUV flux in the presence of filter red-leak contamination. In all cases, the F165LP filter should never be used alone for science since there is no way to account for the red leak. See Section 4.4.2.
- The ACS cameras are intended to be used with a single filter. Unfiltered or two-filter imaging yields significantly degraded PSFs (particularly for the WFC), so these modes are typically used only for polarization observations. The polarizers have zero optical thickness, so they can and should be used with another filter.
- The geometric distortion of the WFC is significant and causes the projected pixel area to vary by ±9% over the field of view. This distortion affects both the photometric and astrometric accuracy, and must be accounted for when the required accuracy is better than 10%. See Section 10.4.
- The cosmic ray fluxes of HRC and WFC are comparable to those of STIS and WFPC2, respectively, with more detail in Section 4.3.7. Typical observations should be dithered or CR-SPLIT for cosmic ray rejection. See Section 4.3.5 for more information about dithering strategies for removing cosmic rays and hot pixels.
- At wavelengths longer than ~8000 Å, internal scattering in the HRC CCD produced an extended PSF halo. Only a small number of observations were affected because WFC was mostly used at these wavelengths. The WFC CCDs were treated with a front-side metallization that eliminates the large angle, long wavelength halo problem for wavelengths less than 9000 Å. For observations of red targets with the F850LP refer to Section 9.3.2.
- The WFC and HRC share two filter wheels. Consequently, when the cameras were used simultaneously, only the filter for the primary camera was selectable.

- The ratios of in- and out-of-band transmission for HRC UV filters are similar to those of WFPC2, after accounting for differences in the detector's QE. The ACS F220W, F250W, and F330W filters have small red leaks, which are documented in ACS ISR 2007-03.

5.2.1 Optical Performance

Following the fine-alignment and focus activities of the SM3B Orbital Verification period, the optical qualities of all three ACS channels were judged to have met their design specifications. Measured encircled energy values for the WFC and HRC can be found in Bohlin 2016, AJ, 152, 60 and ACS ISR 2020-08. Those for the SBC can be found in ACS ISR 2016-05.

5.2.2 CCD Throughput Comparison

Figure 5.7 compares the wavelength-dependent throughputs of ACS/WFC and HRC with those of WFC3/UVIS, WFC3/IR, NICMOS/NIC3, and WFPC2.

5.2.3 Limiting Magnitudes

Table 5.4 contains the detection limits in Johnson-Cousins V magnitudes for unreddened O5V, A0V, and G2V stars, generated using the ETC. WFC and HRC values used the parameters CR-SPLIT=2, GAIN=2, and a 0.2 arcsecond circular aperture. For the SBC, a 0.5 arcsecond circular aperture was used. An average sky background was used in these examples. However, limiting magnitudes are sensitive to the background levels; for instance, the magnitude of an A0V in the WFC using the F606W filter changes by ±0.4 magnitudes at the background extremes. Figure 5.8 shows a comparison of the limiting magnitude for point sources achieved by the different cameras with a signal to noise of 5 in a 10 hour exposure. Figure 5.9 shows a comparison of the time needed for extended sources to attain ABMAG=26.

Figure 5.7: HST total system throughputs as a function of wavelength.
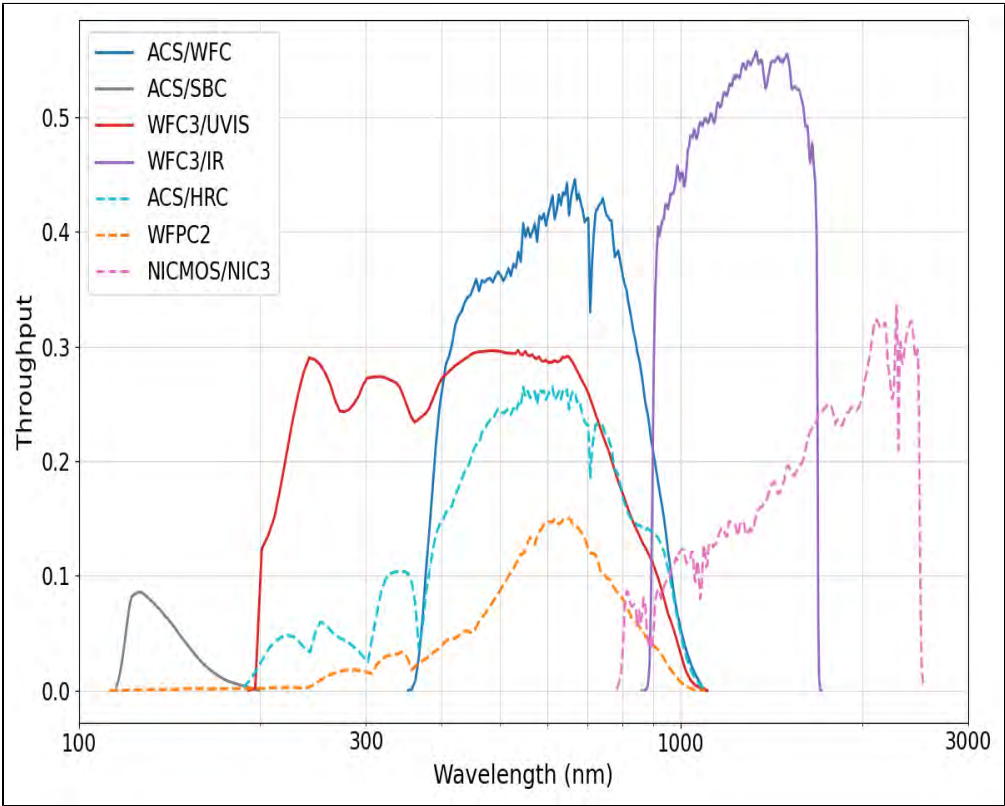
Figure 5.8: HST Limiting Magnitude for point sources in 10 hours, as a function of wavelength. Point source limiting magnitude achieved with a signal to noise of 5 in a 10 hour-long exposure with optimal extraction.
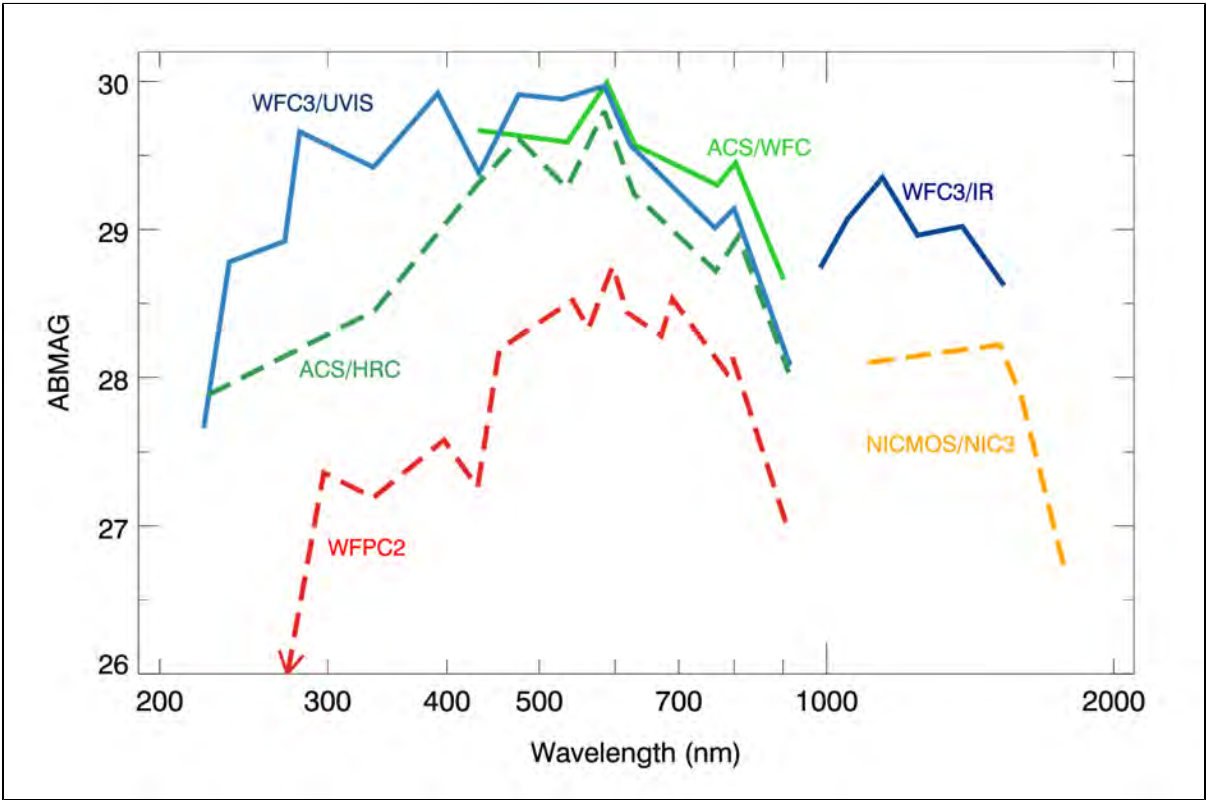
Figure 5.9: HST total integration time needed to attain ABMAG=26 for extended sources.
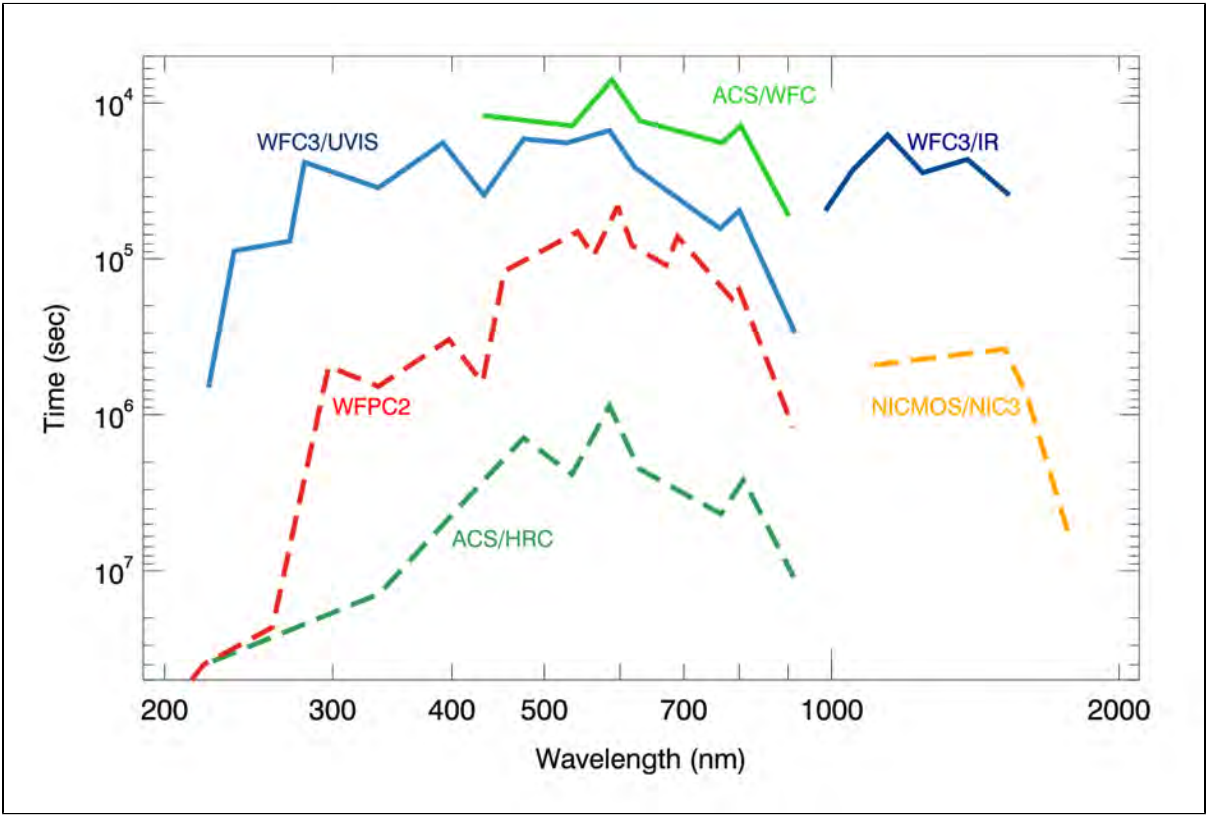
Table 5.4: V detection limits for ACS, HRC, and SBC direct imaging.

Camera	Filter	V limit (S/N = 5, exposure time = 1 hour)		
		O5V (Kurucz model)	A0V (Vega)	G2V (Sun)
WFC	F606W	27.7	27.8	28.0
WFC	F814W	26.6	27.0	27.7
HRC	F330W	26.8	24.7	24.1
HRC	F606W	27.3	27.3	27.5
SBC	F125LP	28.3	23.8	14.8

5.2.4 Signal-To-Noise Ratios

Chapter 10 contains plots of exposure time versus magnitude for a desired signal-to-noise ratio. These plots are useful for determining the exposure times needed for your scientific objectives. More accurate estimates require the use of the ACS ETC.

5.2.5 Saturation

Both CCD and SBC imaging observations are subject to saturation at high total accumulated counts per pixel. For the CCDs, this is due either to the depth of the full well or to the 16 bit data format. See Section 4.3.1, ACS ISR 2019-03, and ACS ISR 2020-02 for more information on WFC saturation. For the SBC, this is due to the 16 bit format of the buffer memory (see Section 4.3.1 and Section 4.5.2). There are also health and safety considerations for the MAMA detector. See Section 4.6 for a discussion of bright object limits.

5.2.6 Faint Horizontal Striping in WFC CCDs

Subsequent to the replacement of the ACS CCD Electronics Box during SM4, all WFC images show horizontal striping noise that is roughly constant across each row of readout in all four WFC amplifiers. This striping is the result of a 1/f noise on the bias reference voltage, and has an approximately Gaussian amplitude distribution with standard deviation of 0.9 electrons. The contribution of the stripes to the global read noise statistics is small, but the correlated nature of the noise may affect photometric precision for very faint sources and very low surface brightnesses.

During Cycle 17, an algorithm for removing the stripes from WFC science images was developed and tested. Because the WFC bias striping noise is so consistent among the four readout amplifiers, and because it also manifests within the WFC prescan regions, a prescan-based de-striping algorithm was incorporated into the ACS calibration pipeline CALACS. This de-striping algorithm, as well as its implementation in CALACS, are described in Section 3.4 of the *ACS Data Handbook*. This permits consistent striping-noise mitigation for all post-SM4 WFC full-frame images, including calibration images. However, the de-striping algorithm is NOT automatically applied to subarray images within CALACS.

Post-SM4 WFC images can also be fully calibrated with a tool called **acs_destripe_plus**, which is available as part of the **acstools** package in Astroconda. This tool includes a stand-alone version of the de-striping algorithm that fits the stripes across the full science array, rather than fitting the stripes solely in the prescan columns. Within **acs_destripe_plus**, the destriping algorithm is run between the basic calibration tasks of ACSCCD and, if desired, the pixel-based CTE correction of ACSCTE. Post-SM4 WFC subarray images can only be de-striped and CTE-corrected using **acs_destripe_plus**. More details on processing WFC subarrays can be found in Section 7.3.1, ACS ISR 2017-06, and the ACS Subarrays notebook on the ACS Analysis Tools webpage.

Please see the acstools website for details on running **acs_destripe_plus**, as well as the example given in Section 3.5 of the *ACS Data Handbook*. Further details regarding the WFC striping and its mitigation are provided in the ACS ISR 2011-05.

5.3 Wide Field Optical CCD Imaging

The Wide Field Channel of ACS was designed primarily for high throughput observations at visible wavelengths. The use of protected silver mirror coatings, the small number of reflections, and the use of a red sensitive CCD have provided the high throughput required for this camera at the expense of a 3700 Å blue cutoff. The WFC detectors are two butted 2K × 4K thinned, backside-illuminated, SITe CCDs with a red optimized coating and long-λ halo fix. The plate scale is 0.050 arcseconds per pixel, which provides a good compromise between adequately sampling the PSF and a wide field of view. The WFC PSF is critically (Nyquist) sampled at 11,600 Å and undersampled by a factor 3 at the blue end of the WFC sensitivity range (3700 Å). It is possible to achieve a final reconstructed FWHM of 0.100 to 0.140 arcseconds for well-dithered observations. However, dithering will not be able to recover the full resolution of the optical system because the WFC PSF FWHM is largely dependent on the blurring caused by CCD charge diffusion (ACS ISR 2003-06). See Section 7.4 for more discussion of how to use dithered observations to optimally sample the PSF.

The optical design of the camera introduces a two-component geometric distortion. The detectors themselves are at an angle with respect to the optical axis. This produces an 8% stretching of one pixel diagonal compared to the other. As a result, WFC pixels project on the sky as rhombuses rather than squares. These effects are purely geometrical and are routinely corrected in the ACS data reduction pipeline. The second component of geometric distortion is more complex. This distortion causes up to ±9% variation in effective pixel area and needs to be taken into account when doing accurate photometry or astrometry as the effective area of the detector pixels varies nonlinearly with field position. See Section 10.4 for a detailed discussion of the distortion in ACS.

5.3.1 Filter Set

Figure 5.10 shows the filter wheels used by the WFC.

WFPC2 and Johnson-Cousins filters

All of the most commonly used WFPC2 filters are included in the ACS filter set. In addition to a medium and a broad *V*-band filter (F550M and F606W), there is a complete Johnson-Cousins *BVI* set (F435W, F555W, F814W).

Sloan Digital Sky Survey filters

The Sloan Digital Sky Survey (SDSS) *griz* filter set (F475W, F625W, F775W, F850LP) is designed to provide high throughput for the wavelengths of interest and excellent rejection of out-of-band wavelengths. The filters were designed to provide wide, non-overlapping filter bands that cover the entire range of CCD sensitivity from blue to near-IR wavelengths.

Narrow Band filters

The Hα (F658N), [OIII] (F502N), and [NII] (F660N) narrow band filters are full-size, and can be used with both the WFC and HRC.

Ramp filters

ACS includes a complete set of ramp filters that provide full coverage of the WFC wavelength range at 2% and 9% bandwidth. Each ramp filter consists of three segments. The inner and outer filter segments can be used with the WFC only, while the middle segments could be used by both WFC and HRC. Unlike the WFPC2, where the desired wavelength is achieved by offsetting the telescope, the wavelength of ACS ramps is selected by rotating the filter while the target is positioned in one of the pre-defined apertures. The monochromatic field of view of the ramp filters is approximately 40 × 80 arcsec^2. Details of how to use the ramp filters are given in Section 7.3.

Figure 5.10: WFC and HRC filter wheels layout.

WFC/HRC Filter Wheel 1

WFC/HRC Filter Wheel 2
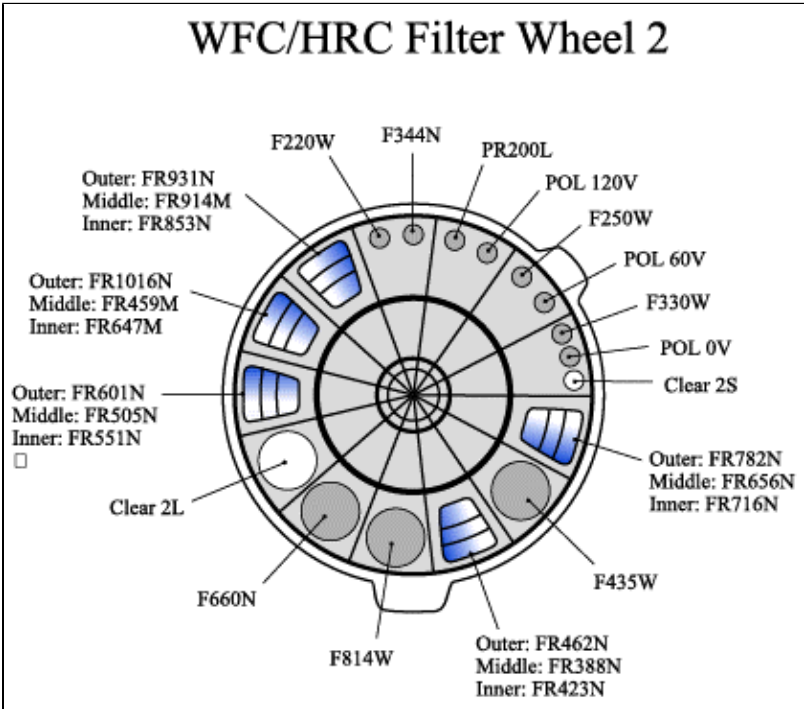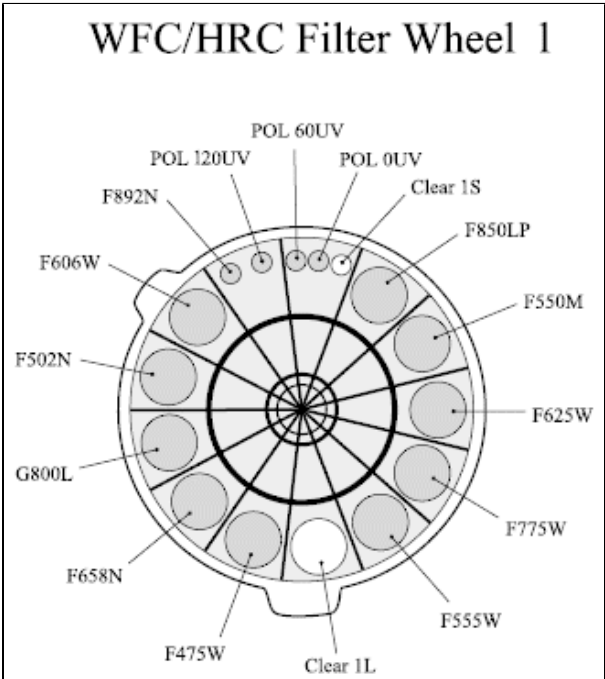
Polarizer filters

The WFC/HRC filter wheels contain polarizers with pass directions spaced by 60°, optimized for both the UV (POL0UV, POL60UV, and POL120UV) and the visible (POL0V, POL60V, and POL120V). All the polarizer filters are sized for the HRC field of view. They induce vignetting when used with the WFC, for which the FOV will be about 72 × 72 arcsec^2. More information on the use of the polarizers is given in Chapter 6.

Grism and Prism

The CCD channels also have a grism (G800L) for use with both WFC and HRC from 5500 Å to 11,000 Å, and a prism (PR200L) for use with the HRC from 1600 Å to 3500 Å. These are described in more detail in Chapter 6.

5.4 High-Resolution Optical and UV Imaging

> ⚠️ *Information regarding the HRC is provided for archival purposes only.*

Before its failure in January 2007, the High Resolution Channel of ACS was the primary camera for near-UV imaging. HRC provided high throughput at blue wavelengths and better PSF sampling than either the WFC or other CCD cameras on *HST*. HRC's pixel size critically sampled the PSF at 6300 Å and undersampled the PSF at the blue end of its sensitivity range (2000 Å) by a factor of 3.0. Well-dithered observations with the HRC led to a reconstructed PSF FWHM of 0.03 arcsec at ~4000 Å, increasing towards longer wavelengths. For these reasons, HRC was used mostly for UV and blue imaging. It was also used for red imaging when PSF sampling was important and in crowded stellar fields, such as the core of Galactic globular clusters. The photometric accuracy of the HRC was generally higher than that of the WFC. HRC also included a coronagraph that is discussed in Section 6.2. HRC's CCD scattered red light into a wide-angle halo (as does STIS's CCD). Production constraints prevented the remediation of this halo by front-side metallization, which was done for WFC's CCD. Although most of the HRC imaging occurred in the UV, users are cautioned to take into account the effect of the long wavelength halo when the HRC was used in combination with near-IR filters (see Section 5.6.5).

5.4.1 Filter Set

The HRC-specific filters were mostly UV and blue. The set included UV and visible polarizers (discussed in Section 6.1), a prism (PR200L, discussed in Section 6.3), three medium-broad UV filters (F330W, F250W, and F220W) and two narrow band filters (F344N and F892N). Use of the UV filters with the WFC is not supported because of the uncertainty of the WFC silver coating transmission below 4000 Å. All broad, medium and narrow band WFC filters could be used with the HRC whenever better PSF sampling was required. Generally, the throughput of WFC was higher than that of HRC where their sensitivities overlapped. Only some of the WFC ramp segments—the FR459M and FR914M broad ramps, and the FR505N [OIII], FR388N [OII], and FR656N (Hα) narrow ramps—could be used with the HRC because only the middle segment overlapped with the HRC FOV. Figure 5.10 shows the filter wheels used by the HRC instrument.

5.4.2 Multiple Electron Events

Unlike the WFPC2 CCD, the HRC CCD was directly sensitive to UV photons and was much more effective in detecting them. When a detector has non-negligible sensitivity over more than a factor of two in wavelength, however, it is possible for a UV photon to generate more than one electron and thus be counted more than once. This effect was noted during

ground testing of the HRC CCD and also has been noted for the STIS CCD. The effect is only important shortward of 3200 Å, reaching approximately 1.7 e⁻/photon at 2000 Å. Multiple counting of photons must be accounted for when estimating QE and the noise level of a UV observation because multiple photons distort the Poisson noise distribution of the electrons.

5.4.3 Red Leaks

When designing a UV filter, high suppression of out-of-band transmission, particularly at red wavelengths, must be balanced with overall in-band transmission. HRC's very high blue quantum efficiency made it possible to obtain red-leak suppression comparable to that of WFPC2 while using much higher transmission filters. Red leak calibration data was obtained in Cycle 14 and are described in ACS ISR 2007-03. Table 5.5 shows the ratio of in-band versus total flux for a few UV and blue filters in the now-defunct HRC, where the boundary between in-band and out-of-band flux is defined as the 1% transmission point. The same ratio is also listed for the equivalent WFPC2 filters. Correction factors for different stellar spectral types and non-stellar spectra are found in ACS ISR 2007-03. Red leaks were not a problem for F330W, F435W, and F475W. Red leaks were more important for F250W and F220W. In particular, accurate UV photometry of M stars requires correction for the F250W red leak and is essentially impossible in F220W. For F220W, red-leak correction is also necessary for G and K stars.

Table 5.5: In-band flux as a percentage of the total flux.

Stellar type	WFPC2 F218W	HRC F220W	WFPC2 F255W	HRC F250W	WFPC2 F300W	HRC F330W	WFPC2 F439W	HRC F435W	WFPC2 F450W	HRC F475W
O5 V	99.8	99.6	99.7	99.7	99.9	99.9	99.9	99.9	99.9	99.9
B1 V	99.7	99.6	99.6	99.7	99.9	99.9	99.9	99.9	99.9	99.9
A1 V	99.5	98.8	99.5	99.0	99.9	99.9	99.9	99.9	99.9	99.9
F0 V	98.7	97.0	98.5	98.3	99.4	99.9	99.9	99.9	99.9	99.9
G2 V	91.5	88.7	96.3	97.1	98.8	99.9	99.9	99.9	99.8	99.9
K0 V	91.4	60.6	96.2	95.2	98.7	99.9	99.9	99.9	99.8	99.9
M2 V	47.0	1.5	84.6	62.4	75.2	99.9	99.9	99.9	99.6	99.9

5.5 Ultraviolet Imaging with the SBC

The Solar Blind Channel is the ACS camera optimized for UV imaging. The SBC uses the same optical train as the HRC and is comparable in performance to the FUV MAMA of STIS. The use of the repeller wire increases the quantum efficiency of the detector by ~30%, but adds a halo to the PSF. Bright object limits are discussed in detail in Section 7.2.

5.5.1 Filter Set

Several filters are available for use with the SBC, including a Lyman α narrow band filter (F122M), a long pass quartz filter (F150LP), MgF$_2$ filter (F115LP), and a CaF$_2$ filter (F125LP). The SBC also includes two additional long pass filters (F140LP and F165LP) as well as prisms (discussed in Section 6.3). A list of filters is given in Table 5.3. Figure 5.11 shows the filter wheel used by SBC.

Figure 5.11: SBC Filter wheel layout
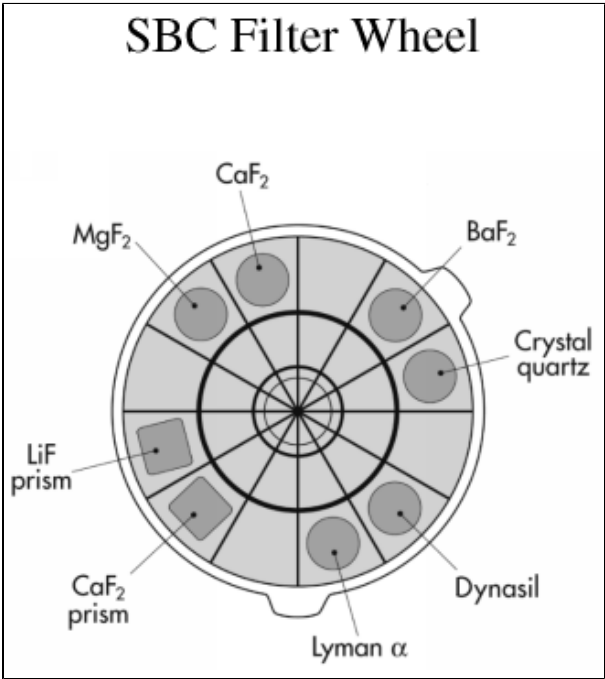
5.5.2 Red Leaks

The visible light rejection of the SBC is excellent, but users should be aware that stars of solar type or later will have a significant fraction of the detected flux coming from outside the nominal wavelength range of the detector. This is discussed in greater detail in Section 4.4.2, and more information is available in Table 5.6. The stellar spectra are from the Pickles catalog (Pickles A.J., 1998, PASP 110, 863).

Table 5.6: Visible-light rejection of the SBC F115LP imaging mode.

Stellar type	Percentage of all detected photons which have $\lambda < 1800$ Å	Percentage of all detected photons which have $\lambda < 3000$ Å
O5V	97.7	100
B1 V	98.7	100
A0 V	95.6	99.7
G0 V	29.0	40.5
K0 V	0.	5.4

5.5.3 SBC Imaging Filter Shifts

The SBC focal surface, like that of the HRC, is tilted significantly with respect to the chief ray. The MAMA detector is a STIS spare, and as such, its window is approximately parallel to the MCP surface and the whole detector must tilt to achieve good focus over the field. The window is therefore tilted, and to ameliorate the introduction of "lateral color", which would result in dispersion-induced degradation of the PSF, the filters are canted in the opposite direction to that of the window. The filter thickness is matched to the mean index of refraction over its bandpass to maintain focus. These result in unavoidable image location offsets between filters. In contrast, the WFC and HRC filters and windows are normal to the chief ray and the detector surfaces are tilted within their housings to match the focal surface tilt. In Table 5.7, we list the shifts for each SBC imaging filter with respect to the F115LP filter. No pointing compensations are made for these offsets.

Table 5.7: Shifts between SBC imaging filters.

Spectral Element	Offset (pixels) in the x direction	Offset (pixels) in the y direction
F115LP	0	0
F122M	0	0
F125LP	-5	15
F140LP	-7	21
F150LP	-3	11
F165LP	-4	12

5.6 ACS Point Spread Functions

The ACS point spread function (PSF) has been studied in ground test measurements, and by using on-orbit data and models generated by the Tiny Tim software developed by J. Krist and R. Hook. As with other *HST* instruments, the ACS point spread function is affected by both optical aberrations and geometric distortions. Point sources imaged with WFC and HRC experience blurring due to charge diffusion into adjacent pixels because of CCD subpixel variations, which reduces the limiting magnitudes that can be reached by WFC/HRC. The SBC PSF and the long-wavelength HRC PSF are also affected by a halo produced by the detectors themselves.

5.6.1 CCD Pixel Response Function

The sharpness of the CCD PSF is somewhat degraded by charge diffusion into adjacent pixels. The effect is usually described in terms of the pixel response function (PRF), which gives the distribution of flux from within the pixel into adjacent pixels. Charge diffusion results in ~0.5 magnitude loss in the WFC limiting magnitude at short wavelengths (the worst case). At longer wavelengths and at all wavelengths for the HRC the reduction in the limiting magnitude is ~0. 2 magnitudes or less. Due to variations in the CCD thickness, charge diffusion is not constant over the field of view. At different wavelengths, the CCD pixel response functions can be represented by the following kernels (for the center of the field):

$$K_{HRC} = \begin{bmatrix} 0.02 & 0.07 & 0.02 \\ 0.07 & 0.64 & 0.07 \\ 0.02 & 0.07 & 0.02 \end{bmatrix}, \ K_{WFC} = \begin{bmatrix} 0.04 & 0.11 & 0.04 \\ 0.11 & 0.40 & 0.11 \\ 0.04 & 0.11 & 0.04 \end{bmatrix}$$

(1)

at λ = 4000 Å,

$$K_{HRC} = \begin{bmatrix} 0.02 & 0.06 & 0.02 \\ 0.06 & 0.68 & 0.06 \\ 0.02 & 0.06 & 0.02 \end{bmatrix}, \ K_{WFC} = \begin{bmatrix} 0.03 & 0.10 & 0.03 \\ 0.10 & 0.48 & 0.10 \\ 0.03 & 0.10 & 0.03 \end{bmatrix}$$

(2)

at λ = 5500 Å, and

$$K_{HRC} = \begin{bmatrix} 0.02 & 0.04 & 0.02 \\ 0.04 & 0.76 & 0.04 \\ 0.02 & 0.04 & 0.02 \end{bmatrix}, \ K_{WFC} = \begin{bmatrix} 0.02 & 0.07 & 0.02 \\ 0.07 & 0.64 & 0.07 \\ 0.02 & 0.07 & 0.02 \end{bmatrix}$$

(3)

at λ = 8000 Å.

Due to optical and charge diffusion effects, the WFC and HRC PSFs vary across the detectors as explained in ACS ISR 2003-06.

5.6.2 Model PSFs

Table 5.8 and Table 5.9 give model PSFs for WFC and HRC in the central 5 × 5 pixel region in two filters. Numbers listed are the fraction of the total energy received in each pixel. The models have been generated using Tiny Tim, taking into account the *HST* optical aberrations and obscurations as well as the CCD pixel response function. Field-dependent geometrical distortions are included. The real PSF will also differ from the model because of the jitter in the *HST* pointing, HST focus variation (focus breathing), and other instrumental effects, some of which are briefly discussed below. The spatial PSF variations of the WFC and HRC detectors are fully described in ACS ISR 2004-15, ACS ISR 2006-01, and ACS ISR 2018-08.

Table 5.8: ACS Model PSFs in the central 5x5 pixel region (CCD).

WFC model PSF, filter F435W					WFC model PSF, filter F814W				
0.00	0.01	0.01	0.01	0.00	0.01	0.01	0.02	0.01	0.01
0.01	0.04	0.07	0.05	0.02	0.01	0.03	0.07	0.03	0.02
0.02	0.08	0.17	0.08	0.02	0.02	0.07	0.18	0.07	0.02
0.01	0.04	0.08	0.04	0.01	0.01	0.03	0.07	0.03	0.01
0.00	0.01	0.02	0.01	0.00	0.01	0.02	0.02	0.01	0.00
HRC model PSF, filter F435W					HRC model PSF, filter F814W				
0.01	0.01	0.01	0.01	0.01	0.00	0.01	0.02	0.01	0.00
0.02	0.03	0.06	0.03	0.01	0.01	0.04	0.05	0.04	0.01
0.01	0.06	0.16	0.06	0.01	0.02	0.05	0.08	0.05	0.02
0.01	0.03	0.07	0.03	0.01	0.01	0.04	0.05	0.04	0.01

| 0.01 | 0.02 | 0.01 | 0.01 | 0.01 | | 0.00 | 0.01 | 0.02 | 0.01 | 0.00 |

Table 5.9: ACS Model PSFs in central 5x5 pixel region (SBC).

SBC PSF at 120 nm						SBC PSF at 160 nm				
<0.01	0.01	0.01	0.01	<0.01		<0.01	<0.01	<0.01	<0.01	<0.01
0.01	0.02	0.03	0.02	0.01		<0.01	0.02	0.04	0.02	<0.01
0.01	0.03	0.15	0.03	0.01		<0.01	0.04	0.20	0.04	<0.01
0.01	0.02	0.03	0.02	0.01		<0.01	0.02	0.04	0.02	<0.01
<0.01	0.01	0.01	0.01	<0.01		<0.01	<0.01	<0.01	<0.01	<0.01

5.6.3 Encircled Energy

In general, the ACS/WFC encircled energy distribution has been found to be within the original instrument specifications. Figure 5.12 and Figure 5.13 show the ACS encircled energy curves derived from on-orbit images.

Due to telescope breathing over short time scales and focus drifts over long time scales, users are encouraged to measure the encircled energy directly from their science images, rather than depending on the tabulated values, where deviations at small radii may be significant. Further details on the encircled energy calibration can be found in Bohlin 2016, AJ, 152, 60, ACS ISR 2020-08, and ACS ISR 2016-05.

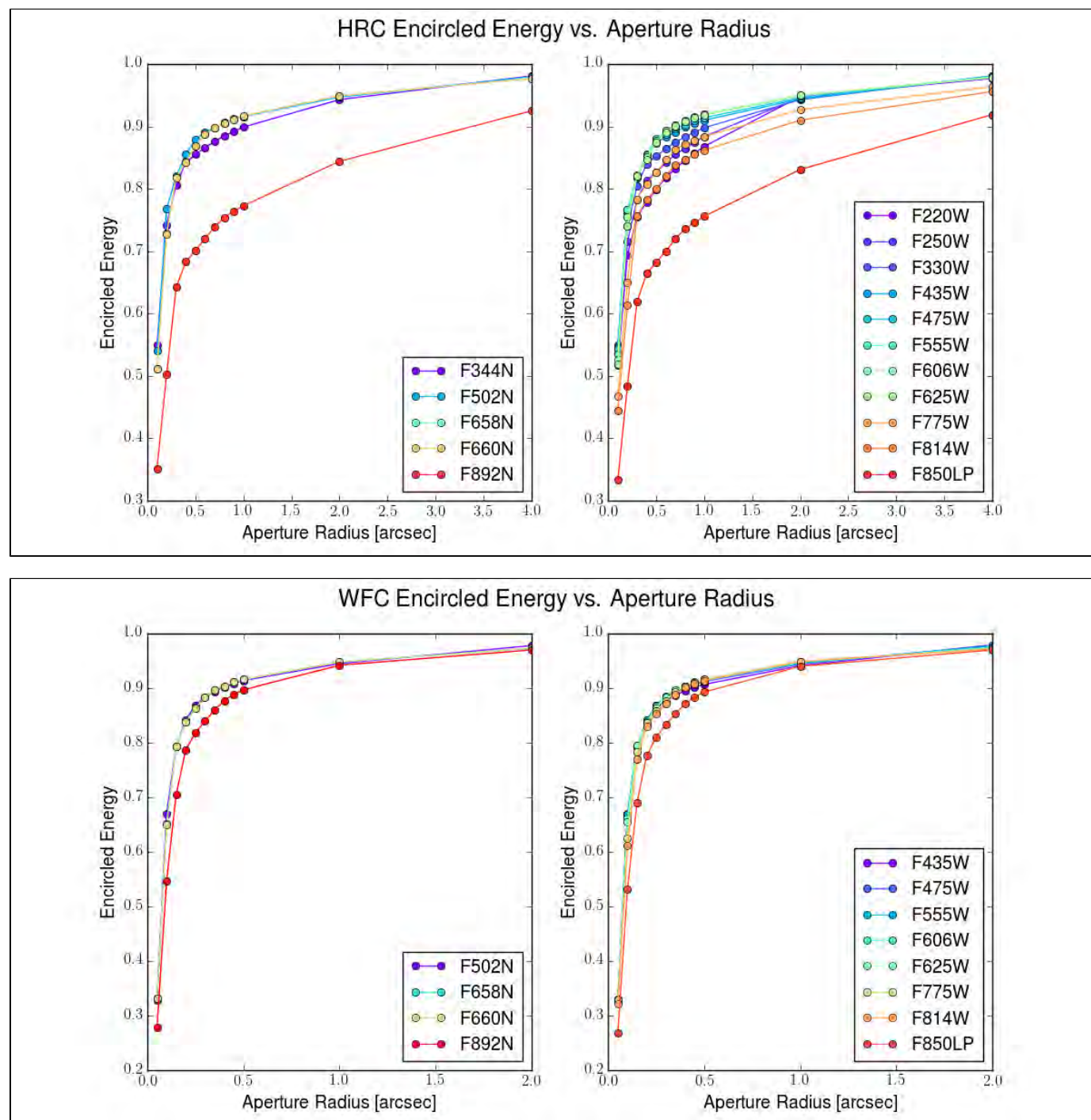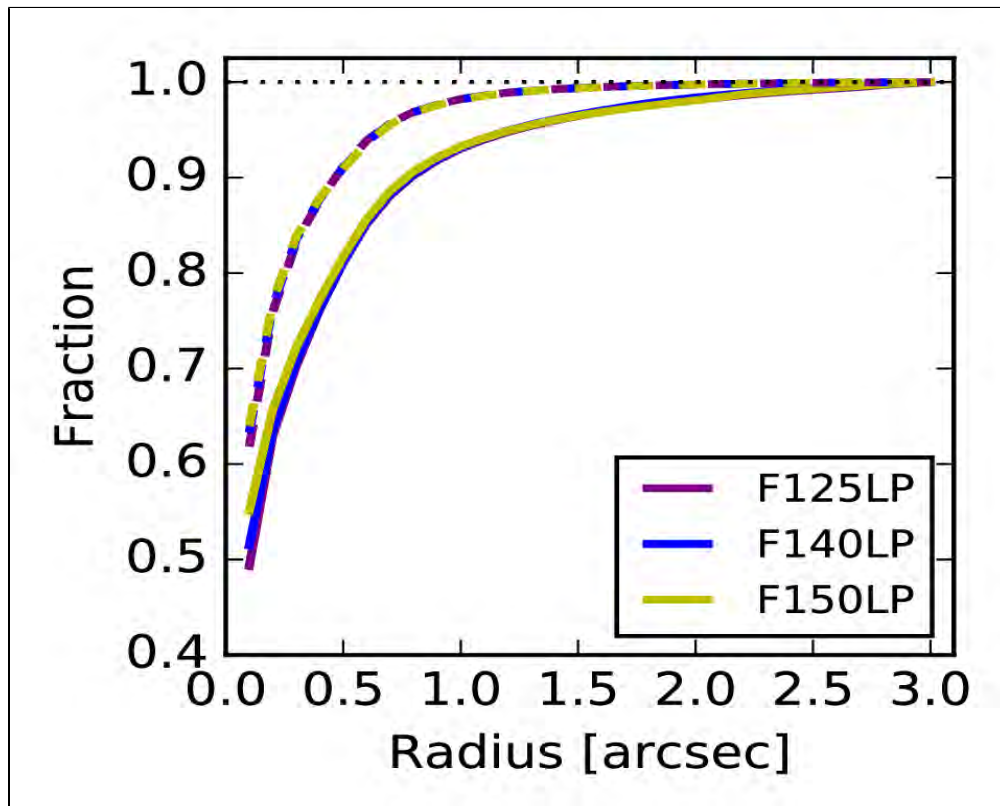**Figure 5.12: Encircled energy for the CCD channels.**

Figure 5.13: Encircled energy for the SBC. Solid lines correspond to observations, dashed lines correspond to Tiny Tim models.

5.6.4 Geometric Distortions

Geometric distortions produce a significant impact on the shape of the PSF in all three of the ACS channels, as can readily be seen in Figure 5.14 and Figure 5.15, which display WFC and HRC PSF images. The logarithm stretch enhances the spider diffraction patterns, which the distortion renders non-perpendicular, and the outer Airy rings, which appear elliptical. The distortion owes primarily to the tilt of the focal surface to the chief ray at the large OTA field angles of the ACS apertures. The linear, field-independent approximation for the WFC produces a difference in plate scale of about 8% between the two diagonals of the field and, in the HRC and SBC, about a 16.5% difference in scale between orthogonal directions rotated about 20° from the aperture edges. Field-dependent distortions, measured as actual vs. predicted distances from field center, amount to about 2% peak in the WFC and about 1% in the HRC and SBC.

The distortions render the pixels, as projected on the sky, trapezoidal in shape and their area varies over the field by about 19% and 3.5% in the WFC and HRC/SBC, respectively. These variations have significant ramifications concerning appropriate techniques for flat-fielding and photometric calibration, especially when complicated by resampling in order to combine dithered image sets. Related issues are the manner in which the halation effects of the HRC and SBC detectors are removed and the treatment of spectra from the prisms and grism, which are not subject to the same distortion effects.

More details concerning geometric distortions in ACS can be found in Section 10.4. Also see ACS ISR 2002-02, ACS ISR 2004-15, ACS ISR 2007-08, ACS ISR 2008-02, ACS ISR 2015-06, ACS ISR 2018-01, and ACS ISR 2020-09. An introduction to CALACS is available in the *ACS Data Handbook* and details for running CALACS can be found in the ACS Jupyter Notebooks on the Analysis Tools webpage. Information about *AstroDrizzle*, which applies corrections for geometric distortion, is available online at the *DrizzlePac* website.

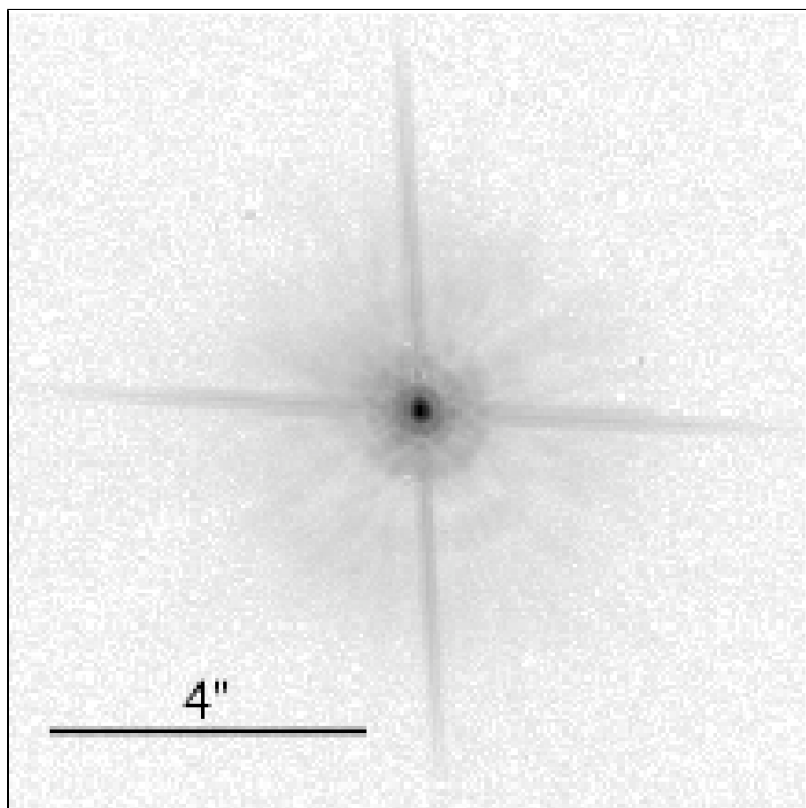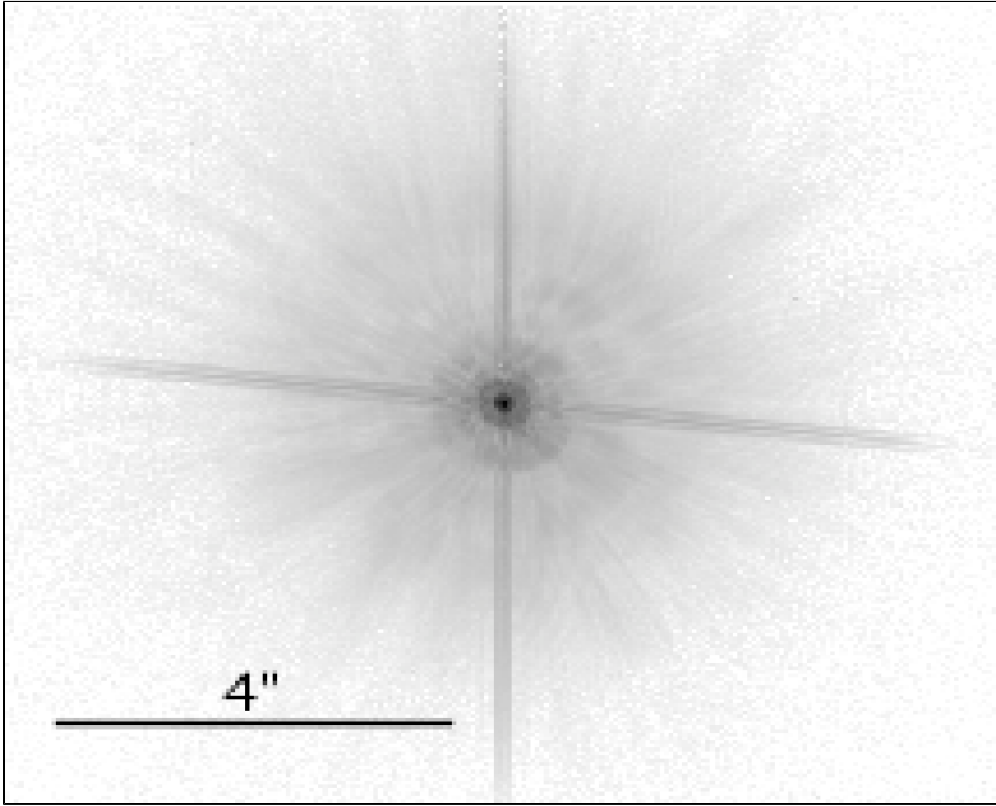**Figure 5.14: ACS WFC PSF - F625W.**

4"

Figure 5.15: ACS HRC PSF - F625W.

5.6.5 PSFs at Red Wavelengths and the UV

The CCDs used in the HRC and WFC suffer from a halo that is caused by very red photons passing through the device and being scattered back into the detector by the mounting substrate. This creates a large halo in HRC images beyond 7000 Å and WFC images past 9000 Å. At 8000 Å in the HRC, the halo contains about 10% of the light. At 10,000 Å, it contains about 30% and increases the surface brightness of the PSF wings by over an order of magnitude, overwhelming the PSF diffraction rings and spikes. A discussion of this may be found in Gilliland & Riess 2002. In the F850LP filter, in particular, extremely red stars show a progressive loss of flux in small to moderate sized apertures as a function of color. Additional information can be found in Sirianni et al. 2005, PASP, 117, 1049 and Bohlin 2016, AJ, 152, 60. These papers provide a detailed recipe to correct for this effect. This halo effect is only partially treated by the ETC. Observers can use pysynphot (see Section 9.3.2) to accurately calculate the photometry of red sources in the SDSS z-filter.

Long wavelength photons that pass through the CCD can also be scattered by the electrode structure on the back side of the device and will create two spikes that extend roughly parallel to the x-axis. These spikes are seen at wavelengths longer than 9500 Å in both the HRC and WFC (see Figure 5.16 and Figure 5.17).

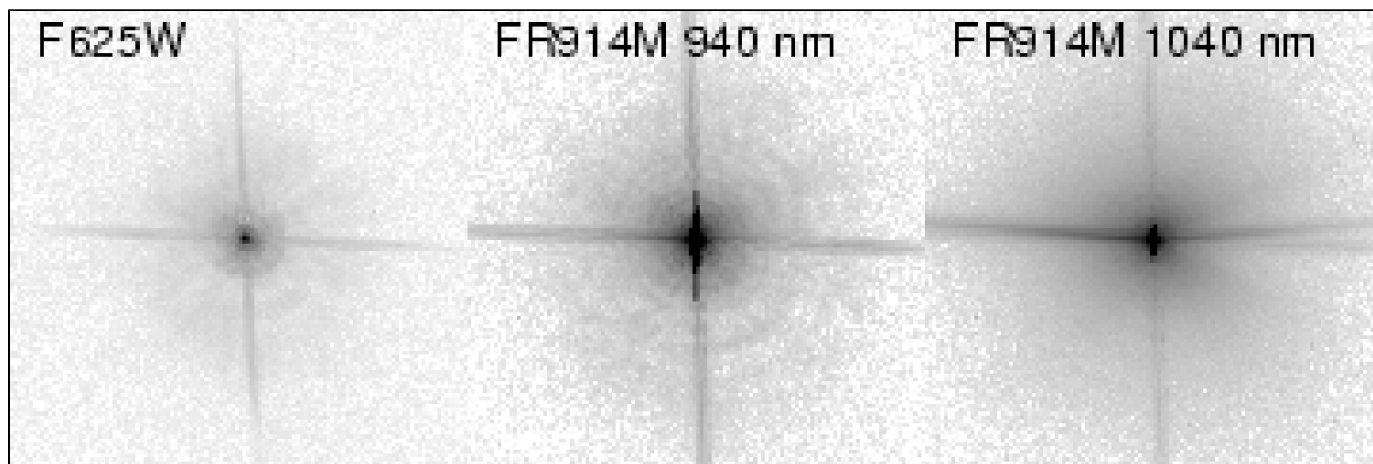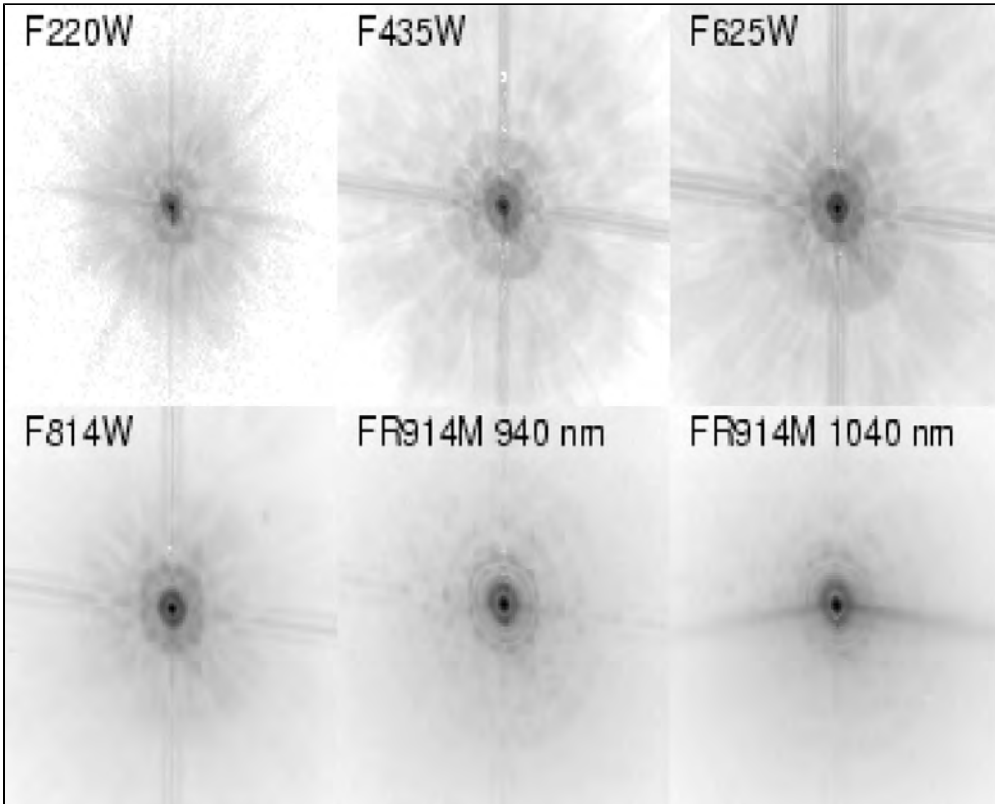Figure 5.16: ACS WFC PSFs (10 × 10 arcsec^2). FR914M images are saturated.

Figure 5.17: ACS HRC PSFs (3.25 × 3.25 arcsec^2).

In the UV, the core of the PSF becomes rather asymmetrical due to mid-frequency optical surface errors. In the SBC, a halo is created by charge migration at the microchannel plate surface. This effect, seen previously in STIS MAMA images, broadens the PSF core and redistributes a small portion of flux into a broad halo that can be approximated by a Gaussian with FWHM ~20 pixels. The peak flux for a point source centered on a pixel is reduced by 30 to 40% depending on wavelength.

The encircled energy curves presented in this handbook and incorporated into the ETC include all of the scattering effects discussed here.

5.6.6 Residual Aberrations

Residual aberration levels at the center of the field in each camera are 1/30 wave (HRC) and 1/20 wave (WFC) RMS at 5500 Å (excluding defocus). Coma and astigmatism are minimized at the field center of each camera. The ACS PSF varies far less over the field of view than those of WFPC2 and STIS. WFPC2 especially suffered from a variable obscuration pattern that significantly altered the PSF structure depending on field position. Lacking the additional obscurations present in WFPC2, ACS PSF variations are instead due to changes in aberrations, breathing, field distortion, and charge diffusion.

At the extreme corners of the WFC field, increased astigmatism slightly elongates the PSF core. The axis of elongation rotates by 90° if the system passes through focus due to breathing. This may affect ellipticity measurements of small galaxies with bright cores at the field edges. Focus variations in the WFC, which alter the amount of light in the peak, are

largely due to detector surface height irregularities and amount to the equivalent of 5 microns of breathing (1/18 wave RMS, ACS ISRs 2007-12 and 2008-03). The largest focus offset is along the gap between the two CCDs. Variations in the width of the PSF core are dominated by changes in CCD charge diffusion, which is dependent on the thickness of the detector (12 to 17 microns for the WFC). The PSF FWHM in F550M, for example, can vary by 20% (0.10 to 0.13 arcseconds) over the field. More information about the dependence of the WFC PSF on OTA temperature and breathing is provided in ACS ISR 2007-12 and ACS ISR 2008-03.

The PSFs in the HRC and SBC are reasonably constant over their fields. The HRC FWHM is 0.060 to 0.073 arcseconds in F550M. More details on ACS PSF field variations are provided in ACS ISR 2003-06. The Tiny Tim PSF simulator includes field dependent aberrations and charge diffusion and may be used to estimate the impact of these variations. For the WFC PSF, the effective PSFs created from empirical data and presented in both ACS ISR 2006-01 and ACS ISR 2018-08 also demonstrate field-dependent variability. ACS ISR 2017-03 provides a comparison between Tiny Tim PSFs and effective PSFs from ACS ISR 2006-01.

Chapter 6: Polarimetry, Coronagraphy, Prism and Grism Spectroscopy

Chapter Contents

6.1 Polarimetry

⚠ *HRC has been unavailable since January 2007. Information about the HRC is provided for archival purposes.*

6.1.1 Introduction

ACS offers two sets of polarizers, one optimized for near-UV/blue wavelengths (POLUV) and one optimized for visible/red wavelengths (POLV). Table 6.1 lists the filters that can be paired with the polarizers, as well as their availability (SUPPORTED, AVAILABLE but unsupported, or UNAVAILABLE). Note that the following filters are not able to be used with the polarizers: F850LP, F892N, and all of the Linear Ramp Filters. Rudimentary spectropolarimetry is possible by using the polarizers in conjunction with the dispersing elements. The large number of possible spectropolarimetric modes prevents automatic calibration of these modes by STScI, so observers must request additional orbits for their own spectropolarimetric calibrations. For normal polarimetric imaging, the location of the target remains fixed on the detector as successive images are obtained using a suitable filter and each of the constituent polarizers of the desired set. The varying intensities of the source in the successive images provide the basic polarimetric data for the source.

Table 6.1: Filters that can be used in conjunction with the ACS polarizers.

Polarizer set	Filters	Availability	Filter comments
POL0UV POL60UV POL120UV	F220W F250W F330W F435W [a] F660N [a] F814W	unavailable unavailable unavailable available available available	HRC NUV short HRC NUV long HRC U Johnson B Broad I
POL0V POL60V POL120V	F475W [a] F502N F550M F555W F606W [a]	supported available available available supported available available	SDSS g Johnson V SDSS r Hα

|		supported available	SDSS i
	F625W		
	F658N [a]		
	F775W [a]		
	G800L		

[a] These filters are part of ACS calibration programs 13964 and 14407 to calibrate the polarizer/filter combination to 1% or better

6.1.2 Performance of ACS Polarizers

At least three polarized images are required to determine the degree and position angle of polarization as well as the total intensity of the source. Each set of ACS polarizers comprise three polarizing filters with relative position angles 0°, 60°, and 120°. The polarizers are aplanatic optical elements coated with Polacoat 105UV (POLUV set) and HN32 polaroid (POLV set). The POLUV set is effective throughout the visible region; its useful range is approximately 2000 Å to 8500 Å. The POLV set is optimized for the visible region of the spectrum and is fully effective from 4500 Å to about 7500 Å.

The relative performance of the POLUV and POLV polarizers are shown in Figure 6.1. The POLV set provides superior perpendicular rejection in the 4500 Å to 7500 Å bandpass, while the POLUV set delivers lower overall rejection across a wider range from 2000 Å to 7500 Å. Performance degrades at wavelengths longer than about 7500 Å, but useful observations may still be obtained up to approximately 8500 Å. In such cases, imperfect rejection of orthogonally polarized light must be considered during data analysis.

Figure 6.1: Throughput and rejection of the ACS polarizers.
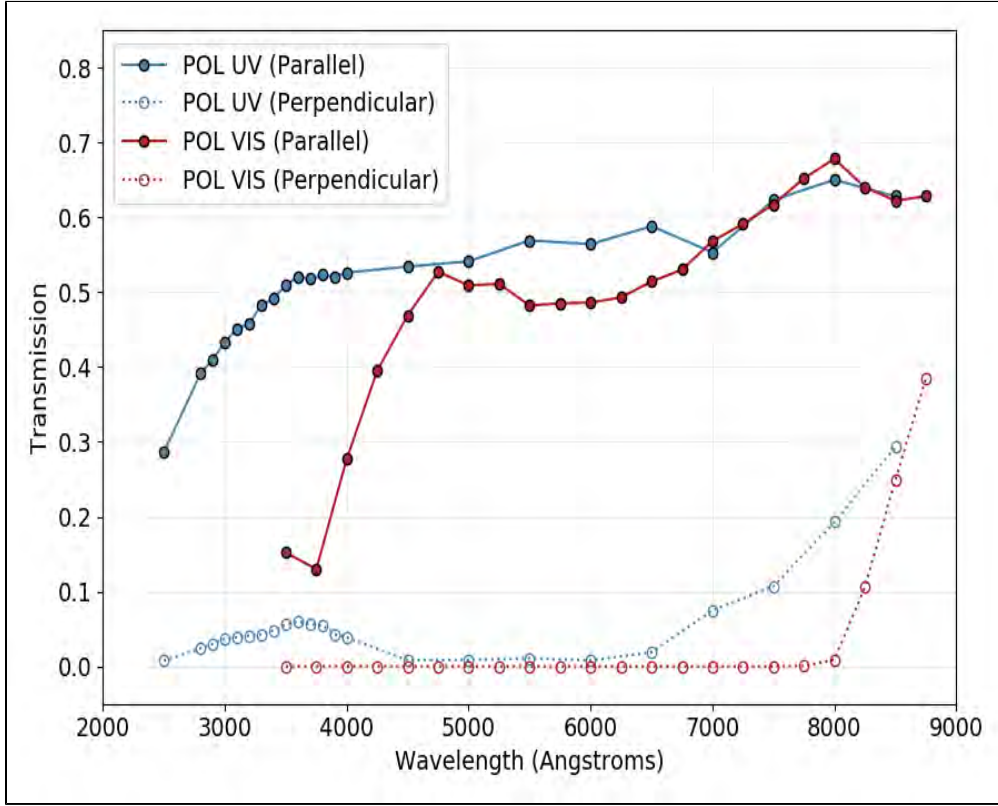
Parallel and perpendicular transmission as a function of wavelength for the POLUV and POLV polarizers.

The ACS polarizers are effectively perfect. Consequently, the Stokes parameters (I, Q, U) can be computed using simple arithmetic. Using *im1, im2*, and *im3* to represent the images taken through the polarizers POL0, POL60, and POL120 respectively, the Stokes parameters are:

(4)
$$Q = \frac{2}{3}(2im1 - im2 - im3)$$

(5)
$$U = \frac{2}{\sqrt{3}}(im2 - im3)$$

(6)
$$I = \frac{2}{3}(im1 + im2 + im3)$$

These parameters can be converted to the degree of polarization (P) and the polarization angle (θ) measured counterclockwise from the *x* axis as follows:

(7)
$$P = \frac{\sqrt{Q^2 + U^2}}{I}$$

$$(8) \qquad \theta = \frac{1}{2}\tan^{-1}(U/Q)$$

A more detailed analysis, including allowances for imperfections in the polarizers, is given by Sparks & Axon 1999, PASP, 111, 1298, who found that the important parameter in experiment design is the product of expected degree of polarization and signal-to-noise. For three perfect polarizers oriented at 60° relative position angles (as in ACS), the uncertainty in the degree of polarization P (which ranges from 0 for unpolarized light to 1 for fully polarized light) is approximately the inverse of the signal-to-noise per image. Specifically, Sparks & Axon found:

$$(9) \qquad \log\left(\frac{\sigma_P}{P}\right) = -0.102 - 0.9898\log\left(P\langle S/N\rangle_i\right)$$

where σ_P is the uncertainty in the degree of polarization, and <S/N>$_i$ is the signal-to-noise of the ith image. The uncertainty in the polarization angle, σ_θ, is given by:

$$(10) \qquad \log\sigma_\theta = 1.514 - 1.068\log\left(P\langle S/N\rangle_i\right)$$

This analysis pertains to ideal polarizers with no instrumental polarization. However, the ACS polarizers (especially the POLUV polarizers) allow significant leakage of cross-polarized light and the instrumental polarization of the WFC is ~2% (see ACS ISR 2004-09). The instrumental polarization of the HRC ranged from a minimum of 4% in the red to 14% in the far-UV. Other effects, such as phase retardance in the mirrors, may be significant as well. Please consult the STScI webpages for more detailed information, especially the *ACS Data Handbook* and *ACS ISRs*.

6.1.3 Implementation of ACS Polarizers

The ACS polarizers are easy to use. The observer selects a spectral element (filter or grism) and then takes successive images with the three polarizers of the VIS set (POL0V, POL60V, POL120V) or the UV set (POL0UV, POL60UV, POL120UV). Once the spectral element and polarizer set are specified, the scheduling system automatically generates the slews that place the target in the optimal region of the field of view.

Because the POLUV and POLV sets are housed on separate filter wheels, the number of spectral elements available to each set is restricted. The available elements are determined by the relative performance of the polarizers and the near-UV limitations of the WFC caused by its silver mirror coatings. The POLUV set is mounted on Filter Wheel 1 and may be crossed with any filter mounted on Filter Wheel 2. The POLV set is mounted on Filter Wheel 2 and may be crossed with the G800L grism or any of the other associated filters in Table 6.1. GOs must plan their own calibration observations for those filters listed as AVAILABLE in the table.

The polarizer sets were designed primarily for use with the HRC, where they offered a full unvignetted field of view (29 × 26 arcsec^2) with any allowed imaging, spectroscopic, and coronagraphic combinations. When used with the WFC, the polarizers provide a vignetted, rectangular field of view that fits inside the `WFC1B-2K` sub-array. Although this field of view is significantly smaller than the normal WFC field of view, it is approximately five times larger than that obtained with the HRC. To avoid the gap between the WFC CCDs and to optimize readout noise and CTE effects, the scheduling system will automatically slew the target to pixel (3096, 1024) on the WFC1 CCD whenever the `WFC` aperture and polarizer sets are selected. To reduce camera overhead times, a 2048 × 2048 subarray image centered on the target will be readout from WFC1 (Table 6.2).

Occasionally observers desire non-polarized images of targets at the same location on the detector as their polarized images. Doing so was straightforward with the HRC; one merely had to take an exposure without the polarizer in place. However, WFC polarimetry automatically invokes a large slew from the non-polarimetric imaging position. To obtain a non-polarized image at the same physical detector location as the polarized images, one must specify the `WFC1B-2K` aperture instead of the `WFC` aperture (Table 6.2).

Table 6.2: Examples of polarizer and non-polarizer exposures in a Phase II proposal. HRC apertures are no longer available but are shown for archival purposes.

Aperture	Filters	Comment
HRC	F606W, POL0V	1024 × 1024 image centered at usual HRC aperture.
HRC	F606W, POL60V	Same but with POL60V.
HRC	F606W, POL120V	Same but with POL120V.
HRC	F606W	Non-polarizer image centered at same detector location as polarizer exposure.
WFC	F606W, POL0V	Target automatically placed at WFC1 pixel (3096, 1024); 2048 × 2048 image.
WFC	F606W, POL60V	Same but with POL60V.
WFC	F606W, POL120V	Same but with POL120V.
WFC1B-2K	F606W	Non-polarizer image at same detector location. Target at WFC1 pixel (3096, 1024); 2048 × 2048 image.

6.1.4 Challenges and Limitations of ACS Polarimetry

The most accurate ACS polarimetry was obtained in the visible bands (i.e., F606W) with the HRC and POLV polarizers. This mode had the advantage of very high rejection of perpendicular polarization and known mirror coatings with readily modeled properties. Because the WFC mirror coatings are proprietary, models of their polarization properties (e.g., the phase retardance of the IM3 mirror) are unavailable. Consequently, calibrating WFC polarized images is much more difficult than calibrating the HRC images. The ACS Team has an ongoing campaign to photometrically calibrate WFC polarimetry with both sets of polarizers. Data has been obtained which should provide improved calibration for the following filters, in combination with the appropriate set of polarizers: F435W, F475W, F606W, and F775W. We encourage users to periodically check the ACS webpage and published ISRs for any updates.

UV polarimetry with ACS is challenging because the POLUV polarizers have relatively poor orthogonal rejection. In addition, while the instrumental polarization of the HRC was 4% to 7% in the visible, it rose to 8% to 9% in the UV and reached 14% at 2200 Å (see ACS ISR 2004-09). Far-UV polarimetry is especially challenging because the POLUV properties

are not well-characterized shortwards of 2800 Å, and they appear to change rapidly with wavelength. Moreover, the low UV transmission of the POLUV polarizers and the poor rejection in the far-red exacerbate the red leaks seen in the far-UV spectral filters.

The ACS team recently examined the impact of the pixel-based CTE correction algorithm on the ability to accurately measure polarization in ACS observations (ACS ISR in prep.). The study used simulated observations of point sources with different fractional polarizations, source brightnesses, and background levels. The study found that the pixel-based CTE corrected images induced ~0.1% additional polarization signal for 100% polarized sources farthest from the serial register, and that the induced signal decreases with decreasing polarization. Overall, this induced polarization effect is negligible compared to other sources of polarization uncertainty, therefore the net effect of CTE loss on ACS polarimetry is minimal.

The polarizers contribute a weak geometric distortion that rises to about 0.3 pixels near the edges of the HRC field of view. This distortion is caused by a weak positive lens in the polarizers that is needed to maintain proper focus when multiple filters are in the beam. The POLV polarizers also have a weak ripple structure intrinsic to their polaroid coatings. These ripples contribute an additional ±0.3 pixel distortion with a very complex structure (see ACS ISR 2004-10 and ACS ISR 2004-11). All these geometric effects are correctable with the AstroDrizzle software. However, astrometry will be less accurate with the polarizers because of residual errors and imperfect corrections.

Finally, the POL0V and POL60V filters contain bubbles which impact the PSF and flat fields. These bubbles are far out of focus and appear as large concentric bright and dark rings (400 pixels diameter in WFC, 370 pixels in HRC) and streaks in the flat fields. The worst case appeared in HRC POL60V images, where the amplitude of the artifacts reaches ±4% in the flats and the affected region was roughly centered at pixel (x, y) = (835, 430). Polarimetric combinations involving POL0V or the WFC are relatively minor, with typical amplitudes of ±1%. Observers requiring precision polarimetry should avoid these regions of the field of view. Although the polarizer flats attempt to correct these features (see ACS ISR 2005-10), the corrections are imperfect and dependent on the brightness and angular size of the target. The locations of these features and their effects can be discerned more accurately by examining the P-flats for the respective spectral filter crossed with the visual polarizers.

6.2 Coronagraphy

⚠ *HRC has been unavailable since January 2007. Information about the HRC is provided for archival purposes.*

The ACS High Resolution Channel had a user-selectable coronagraphic mode for imaging faint objects (e.g., circumstellar disks, substellar companions, quasar-host galaxies) near bright point sources (e.g., stars, quasars). The coronagraph suppressed the diffraction spikes and rings of the occulted source below the level of the scattered light, most of which was caused by surface errors in the *HST* optics. The coronagraph was added after ACS construction began, at which point it was impossible to insert it into the aberration-corrected beam. Instead, the system was deployed into the aberrated beam, which was subsequently corrected by the ACS optics. Although it was not as efficient as a corrected-beam coronagraph (especially for imaging close to the occulted source) the HRC coronagraph significantly improved the high-contrast imaging capabilities of *HST*.

6.2.1 Coronagraph Design

A schematic layout of the ACS coronagraph is shown in Figure 6.2. The aberrated beam from the telescope first encountered one of two occulting spots. The beam continued to the M1 mirror, which forms an image of the *HST* entrance pupil on the M2 mirror, which in turn corrects for the spherical aberration in the *HST* primary mirror. The coronagraph's Lyot stop was placed in front of M2. A fold mirror directed the beam onto the HRC's CCD detector. The field of view was 29×26 arcsec^2 with a mean scale of 0.026 arcseconds/pixel. Geometric distortion resulted in effectively non-square pixels. The coronagraph could be used with any filter over the entire HRC wavelength range of $\lambda = 2000$ Å to 10,000 Å.

The occulting spots were placed at the circle of least confusion of the converging aberrated beam. The balance of defocus and spherical aberration at this location allowed maximal occulted flux and minimal spot radius. Nevertheless, the angular extent of the aberrated PSF in the occulting plane necessitated larger spots than would have been used in an unaberrated beam (Figure 6.3).

Figure 6.2: Schematic layout of the ACS HRC coronagraph.
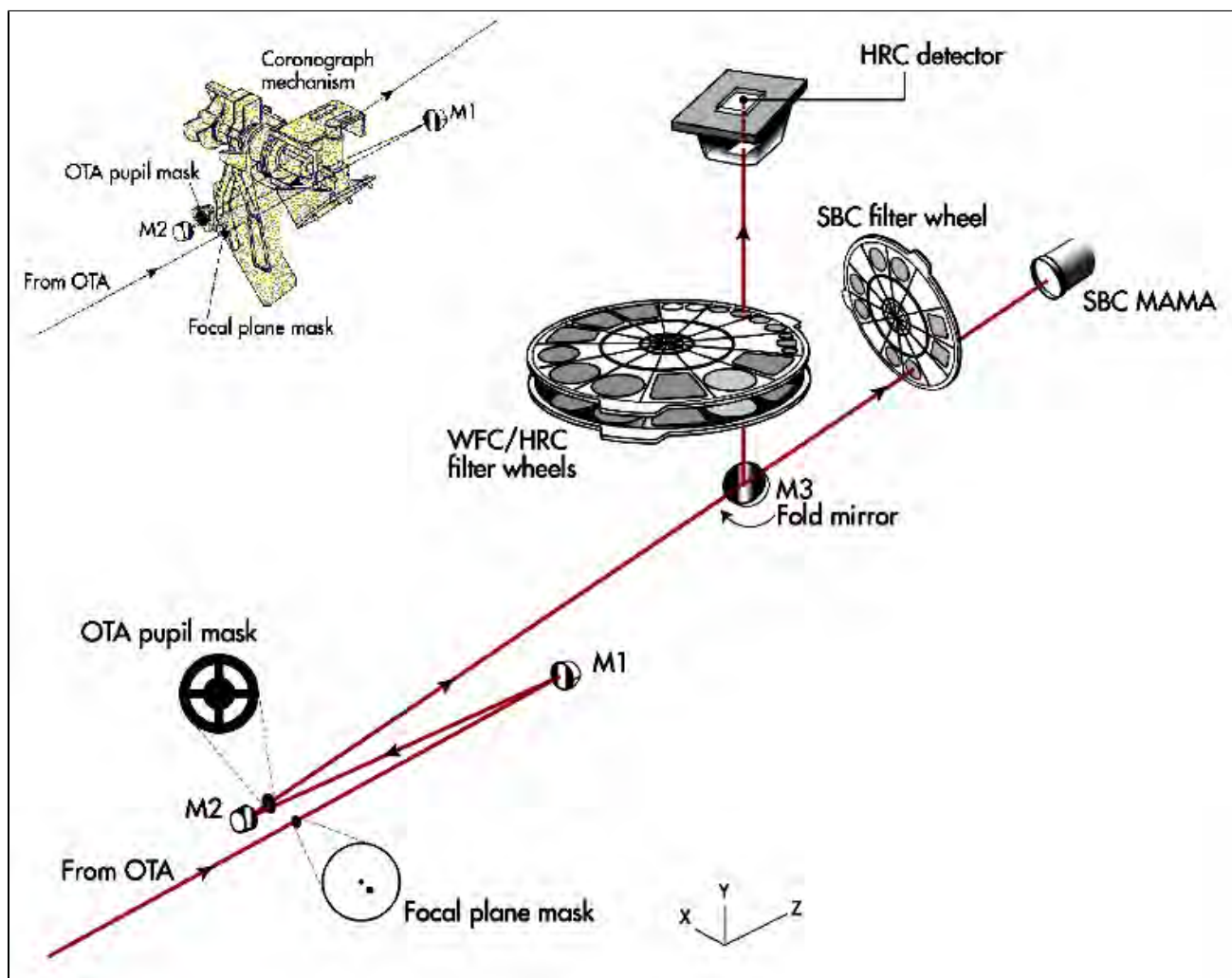
The upper left inset shows a schematic of the coronagraph mechanism that can be flipped in-and-out of the HRC optical path.

Figure 6.3: Simulated point spread functions at the plane of the occulting spots.
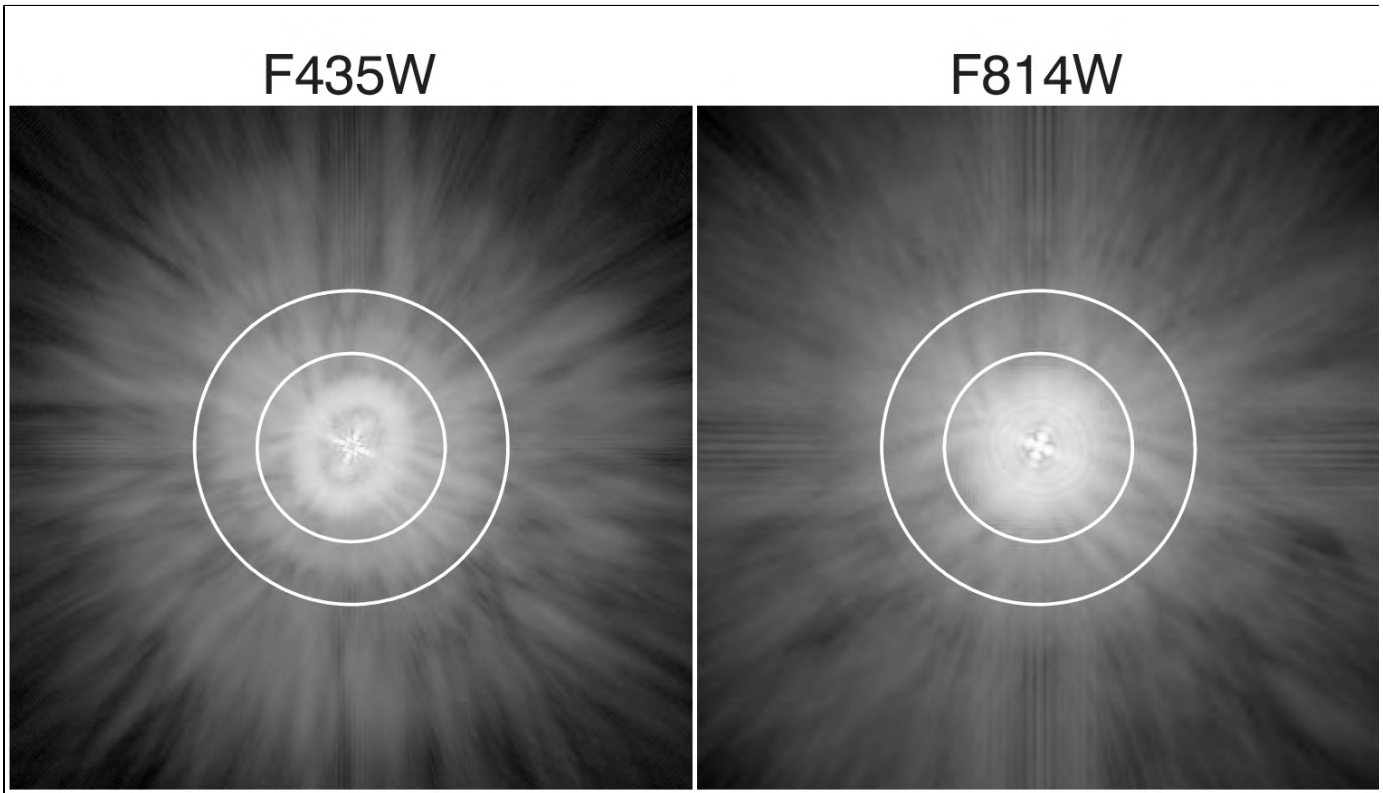
For filters F435W and F814W, shown with logarithmic intensity scaling. The elliptical, cross-shaped patterns in the cores are due to astigmatism at the off-axis ACS aperture. The astigmatism is corrected later by the ACS optics. The sizes of the two occulting spots (D = 1.8 arcseconds and 3.0 arcseconds) are indicated by the white circles.

The occulting spots were sharp-edged (unapodized) metallic coatings deposited on a glass substrate that reduced the throughput by 4.5%. The smaller spot was located at the center of the field and had a diameter of 1.8 arcseconds. Its aperture designation was `CORON-1.8`. The larger spot had a diameter of 3.0 arcseconds and was located near the edge of the field (Figure 6.4). Its aperture designation was `CORON-3.0`. The small spot was used for the most coronagraphic observations because it allowed imaging closer to the occulted source. The large spot was used for very deep imaging of bright targets with less saturation around the spot than would occur with the smaller spot. Its position near the edge of the field also allowed imaging of faint objects up to 20 arcseconds from the occulted source.

The Lyot stop was a thin metal mask that covered the diffracting edges in the *HST* OTA (i.e., the outer aperture, secondary mirror baffle, secondary mirror support vanes, and primary mirror support pads) at the reimaged pupil. The sizes of the Lyot stop and occulting spots were chosen to reduce the diffracted light below the level of the scattered light, which was unaltered by the coronagraph. The smaller aperture and larger central obscuration of the Lyot stop reduced the throughput by 48% and broadened the field PSF. The spots and Lyot stop were located on a panel attached to the ACS calibration door mechanism and could be flipped out of the beam when not in use. The inside surface of the calibration door could be illuminated by a lamp to provide flat field calibration images for direct imaging, but not coronagraphic imaging.

In addition to the two occulting spots, an occulting finger measuring 0.8 arcseconds × 5 arcseconds (designated `OCCULT-0.8`) was permanently located at the window of the CCD dewar. The finger was intended to allow unsaturated imaging

closer to stars than was possible with the occulting spots, but without suppression of diffracted light by the Lyot stop. It was originally aligned with the center of the large spot, but shifting of the spots during launch ultimately placed the finger near the edge of the large spot. Because the finger was located some distance from the focal plane, the field around its edges was significantly vignetted. This vignetting and the sensitivity of the occulted PSF to its position relative to the finger significantly reduced the efficacy of this observing mode.

Figure 6.4: Region of the Orion Nebula imaged with the coronagraph and filter F606W.
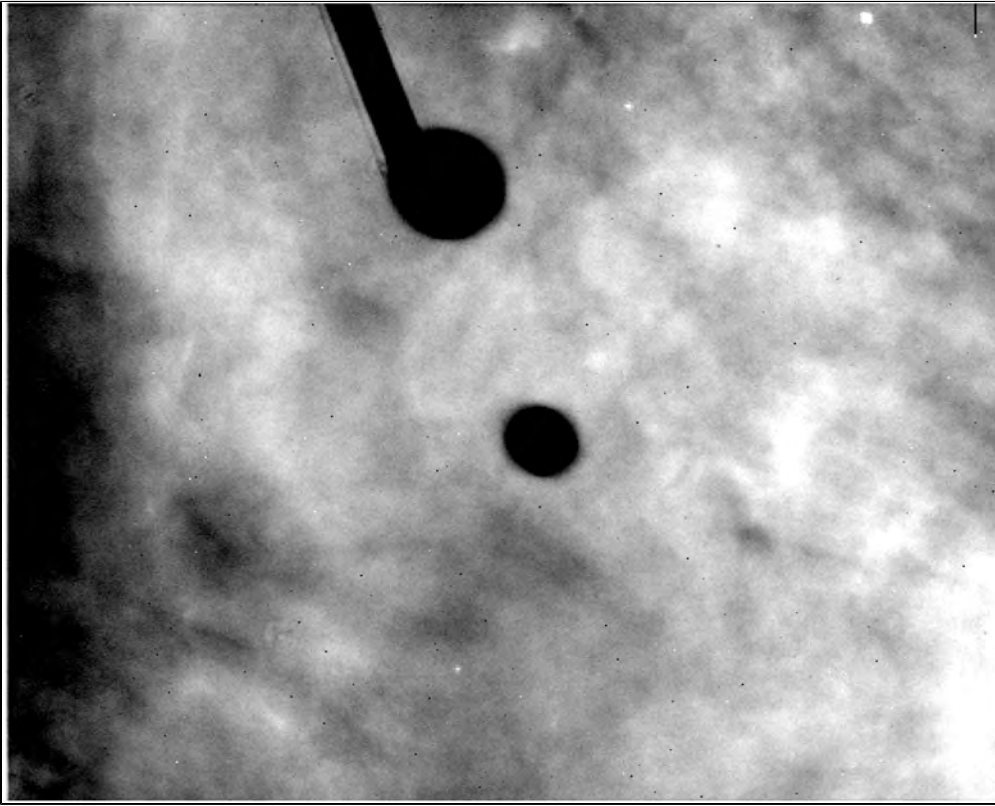
The silhouettes of the occulters can be seen against the background nebulosity. The 1.8 arcsecond spot is located at the center and the 3.0 arcsecond spot towards the top. The finger is aligned along one edge of the larger spot. This image has not been corrected for geometric distortion, so the spots appear elliptical.

6.2.2 Acquisition Procedure and Pointing Accuracy

A bright source had to be placed precisely behind the occulting spot to ensure the proper suppression of the diffracted light. The absolute pointing accuracy of *HST* is about 1 arcsecond, which is too crude to have ensured accurate positioning behind the spot. Consequently, an on-board acquisition procedure was used to provide better alignment. With the coronagraph deployed, acquisition images were taken using a 200 x 200 pixel^2 (5 × 5 arcsec^2) subarray at a region of the field near the small occulting spot. The observer specified a filter and exposure time that provided an unsaturated image of the bright source. Narrowband and crossed filters (e.g., F220W+F606W, F220W+F550M, and F220W+F502N) were most often used to obtain images that contained enough signal for a good centroid measurement. However, the photometric performance of the crossed filters was not well calibrated, so estimated count rates for these configurations from synthetic photometry or the ETC were accurate only within a factor of two.

Two identical acquisition images were taken, from which the on-board computer selected the minimum value for each pixel as a crude way of rejecting cosmic rays. The result was then smoothed with a 3 × 3 pixel^2 boxcar and the maximum pixel in the subarray was identified. The centroid of the unsmoothed image was then computed within a 5 × 5 pixel^2 box centered on this pixel. Based on this position, the telescope was slewed to place the source behind the occulting spot. The

combined acquisition and slew errors were approximately ±0.25 pixels (±6 milliarcseconds). While small, these errors required the use of subpixel registration techniques to subtract one coronagraphic PSF from another (Section 6.2.5). The position of the spots relative to the detector also varied over time. This movement further altered the PSF and caused subtraction residuals.

# 6.2.3 Vignetting and Flat Fields

ACS coronagraphic flat fields differ from standard flat fields because of the obscurations from the occulting spots and vignetting by the Lyot stop. The large angular size of the aberrated PSF caused vignetting beyond one arcsecond of the spot edge (Figure 6.4), but this could be corrected by dividing the image by the spot pattern (Figure 6.5). To facilitate this correction, separate flat fields were derived that contained just the spot patterns (spot flats) and the remaining static features (P-flats). For a full discussion see ACS ISR 2004-16.

The ACS data pipeline divides coronagraphic images obtained with filters F330W, F435W, F475W, F606W, and F814W using coronagraphic P-flats derived from either ground-based or on-orbit data. Coronagraphic images obtained with other filters are calibrated with non-coronagraphic flats, which may cause some small-scale errors around dust diffraction patterns. The pipeline then divides the images by the spot flat, using a table of time-dependent spot positions to determine the proper registration of the spot flat. Spot flats for the filters listed above are available for download from the *HST* Calibration Reference Data System webpage. For other filters, the available spot flat closest in wavelength should be used. The spot flat must be shifted by an amount listed in the coronagraphic spot table, *r3301467j_csp.fits*.

Because coronagraphic P-flats and spot flats exist only for the few filters listed above, observers are encouraged to use those filters. It is unlikely that coronagraphic flat fields for other filters will be available in the future.

Figure 6.5: Region of the Orion Nebula around the D = 1.8 arcseconds spot.
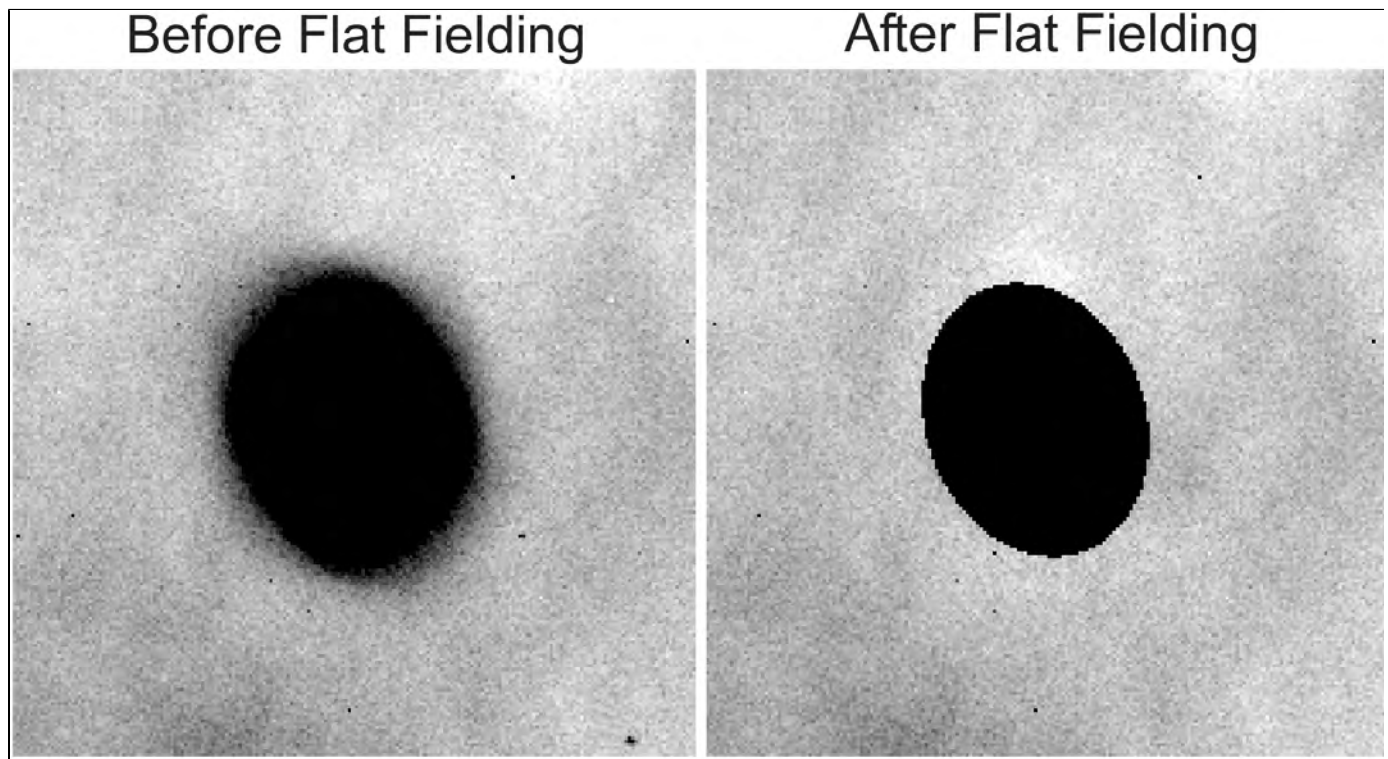
(Left) The spot edge appears blurred due to vignetting. The image has not been geometrically corrected. (Right) The same region after the image has been corrected by dividing by the flat field. The interior of the spot has been masked.

6.2.4 Coronagraphic Performance

Early in Cycle 11, HRC coronagraph performance verification images were taken of the V = 0 star Arcturus (Figure 6.6 and Figure 6.7). This star has an angular diameter of 25 milliarcseconds and was thus unresolved by the coronagraph. The images of the occulted star are atypical coronagraphic images because the occulting spots were placed in the aberrated beam. The interiors of the imaged spots are filled with a diminished and somewhat distorted image of the star that was caused by mirror M2's correction of unocculted aberrated light from the star. The image of the small spot is filled with light, while the image of the large one is relatively dark. Broad, ring-like structures surround the spots, extending their apparent radii by about 0.5 arcseconds. These rings are due to diffraction of the aberrated PSF by the occulting spots themselves. Consequently, the coronagraphic images of bright stars could saturate at the interior and edges of the spots within a short time. The brightest pixels within the small spot saturated in less than one second for a V = 0.0 star, while the pixels at edge of the large spot saturated in about 14 seconds.

The measured radial surface brightness profiles (Figure 6.8) show that the coronagraph was well aligned and operating as expected. The light diffracted by the *HST* obscurations was suppressed below the level of the scattered light—there are no prominent diffraction spikes, rings, or ghosts beyond the immediate proximity of the spots. At longer wavelengths ($\lambda > 6000$ Å) the diffraction spikes appear about as bright as the residual scattered light because the diffraction pattern is larger and not as well suppressed by the coronagraph. The spikes are more prominent in images with the large spot than the small one because the Lyot stop is not located exactly in the pupil plane but is slightly ahead of it. Consequently, the

beam can "walk" around the stop depending on the field angle of the object. Because the large spot is at the edge of the field, the beam is slightly shifted, allowing more diffracted light to pass around the edges of the stop.

The coronagraphic PSF is dominated by radial streaks that are caused primarily by scattering from zonal surface errors in the *HST* mirrors. This halo increases in brightness and decreases in size towards shorter wavelengths. One unexpected feature is a diagonal streak or "bar" seen in both direct and coronagraphic images. It is about 5 times brighter than the mean azimuthal surface brightness in the coronagraphic images. This structure was not seen in the ground test images and is likely due to scattering introduced by the *HST* optics. There appears to be a corresponding feature in STIS as well.

Figure 6.6: Geometrically corrected (29 arcseconds across) image of Arcturus observed in F814W behind the 1.8 arcseconds spot.
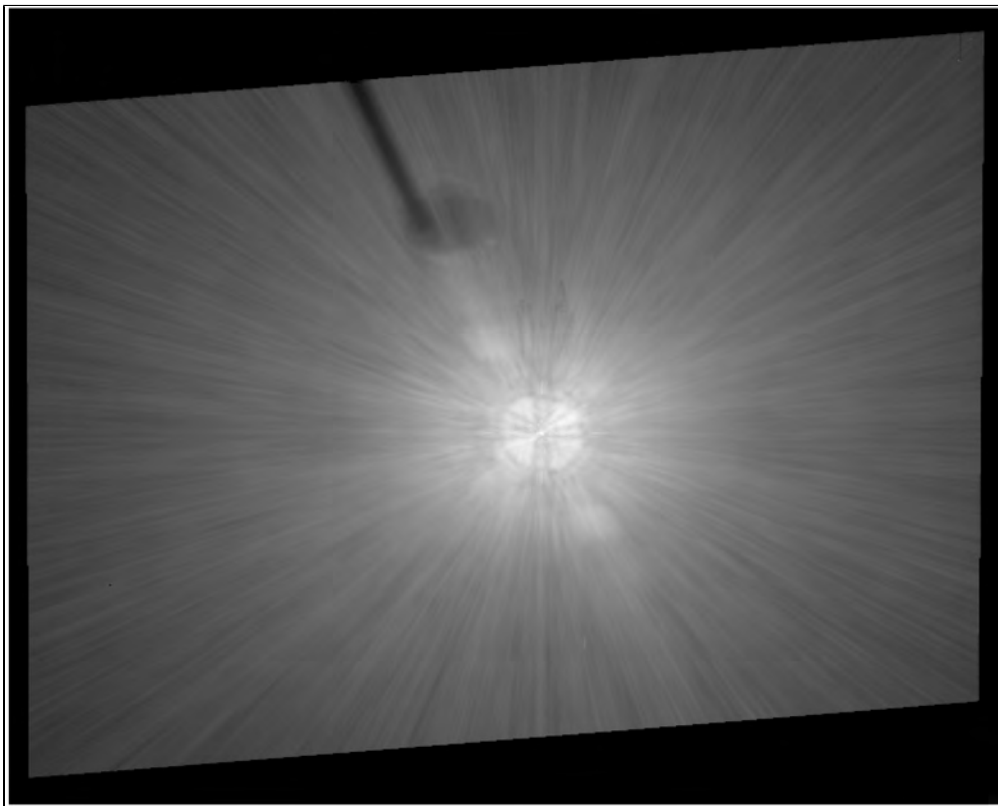
This is a composite of short, medium, and long (280 seconds) exposures. The "bar" can be seen extending from the upper left to lower right. The shadows of the occulting finger and large spot can be seen against the scattered light background. Logarithmic intensity scale.

**Figure 6.7: Regions around the occulting spots in different filters.**
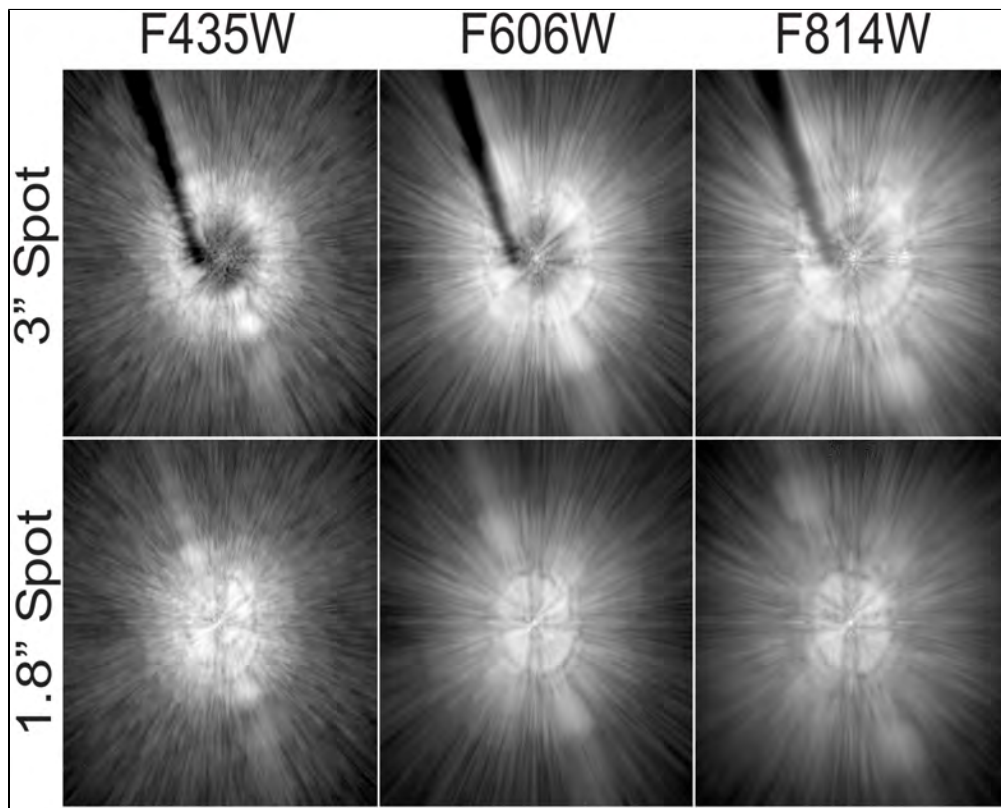
The occulting finger can be seen in the 3 arcseconds spot images. Logarithmic intensity scaled.

6.2.5 Subtraction of the coronagraphic PSF

Although the coronagraph suppressed the diffracted light from a bright star, the scattered light from the *HST* mirrors could still overwhelm faint, nearby sources. It is possible to subtract most of the remaining light using an image of another occulted star. PSF subtraction has been successfully used with images taken by other *HST* cameras, with and without a coronagraph. The quality of the subtraction depends critically on how well the target and reference PSFs match.

For any pair of target and reference PSF images, there is likely to be a difference of 5 to 20 milliarcseconds between the positions of the stars. The scattered light background is largely insensitive to small errors in star-to-spot alignment, so most of it can be subtracted if the images of the two stars are precisely registered and normalized. The numerous sharp, thin streaks that form the scattered light background allow registration errors as small as 0.03 pixels (0.75 milliarcseconds) to be visually detected. To achieve this level of accuracy, the reference PSF may be iteratively shifted and subtracted from the target PSF until an offset is found where the residual streaks are minimized. This method relies on the judgment of the observer, as any circumstellar material could unexpectedly bias a registration optimization algorithm. A higher-order sampling method, such as cubic convolution interpolation, should be used to shift the reference PSF by subpixel amounts. Simpler schemes such as bilinear interpolation degrade the fine PSF structure too much to provide good subtractions.

Figure 6.8: Surface brightness plots derived by computing the median value at each radius.
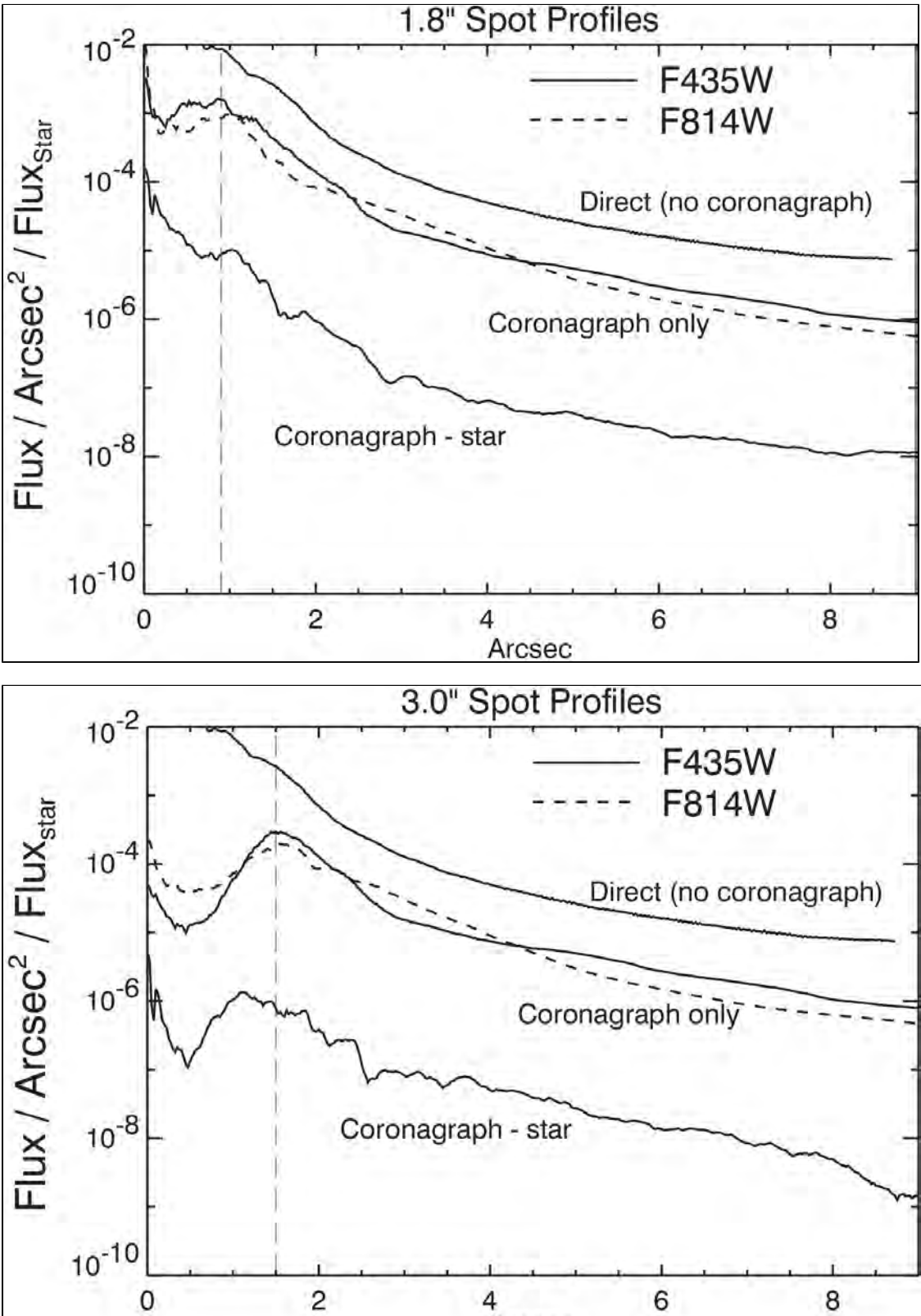
Arcsec

On the other hand, the shape and intensity of the diffraction rings near the spots' edges are very sensitive to the positions of the star-to-spot alignment. Differences between the diffraction rings of target and reference PSF images cannot be subtracted by simply adjusting the registration or normalization. These errors are especially frustrating because they increase the diameter of the central region where the data are unreliable. The only solution to this problem is to select target and reference PSF images that were obtained in adjacent orbits without retraction of the coronagraphic assembly.

Brightness normalization errors as small as 1% to 4% between the target and reference stars may also create significant subtraction residuals. However, derivation of the normalization factors from direct photometry is often not possible. Images of unocculted bright stars through medium or broadband filters were often saturated at the shortest exposure time (0.1 seconds). In such cases, accurate normalization may be obtained through synthetic photometry, a comparison of the relative numbers of saturated pixels in the images, and visual inspection of the PSF-subtracted image.

Color differences between the target and reference stars also affect the quality of the PSF subtraction. As wavelength increases, the speckles that make up the streaks in the coronagraphic PSF move away from the center while their intensity decreases (Figure 6.7). The diffraction rings near the spot edges also expand. These effects can be seen in images through wideband filters—a red star will appear to have a slightly larger PSF than a blue one. Thus, an M-type star should be subtracted using a similarly red star—an A-type star would cause significant subtraction residuals. Even the small color difference between A0 V and B8 V stars, for example, may be enough to introduce bothersome errors (Figure 6.9).

Changes in *HST*'s focus also altered the distribution of light in the coronagraphic PSF (Figure 6.10). Within an orbit, the separation between *HST*'s primary and secondary mirrors varies on average by 3 µm, which corresponds to a variation in the wavefront that results in 1/28 wavelengths of RMS focus difference at $\lambda = 5000$ Å (ACS ISR 2008-03). This effect, known as breathing, is caused by the occultation of the telescope's field of view by the warm Earth, which typically occurs during half of each 96-minute orbit. This heating by the warm Earth expands *HST*'s interior structure. After occultation the structure gradually shrinks. Changes relative to the sun (mostly anti-sun pointings) also cause contraction of the telescope, which gradually expands to "normal" size after a few orbits.

Figure 6.9: Predicted absolute mean subtraction residual levels for cases where the target and reference stars have mismatched colors.
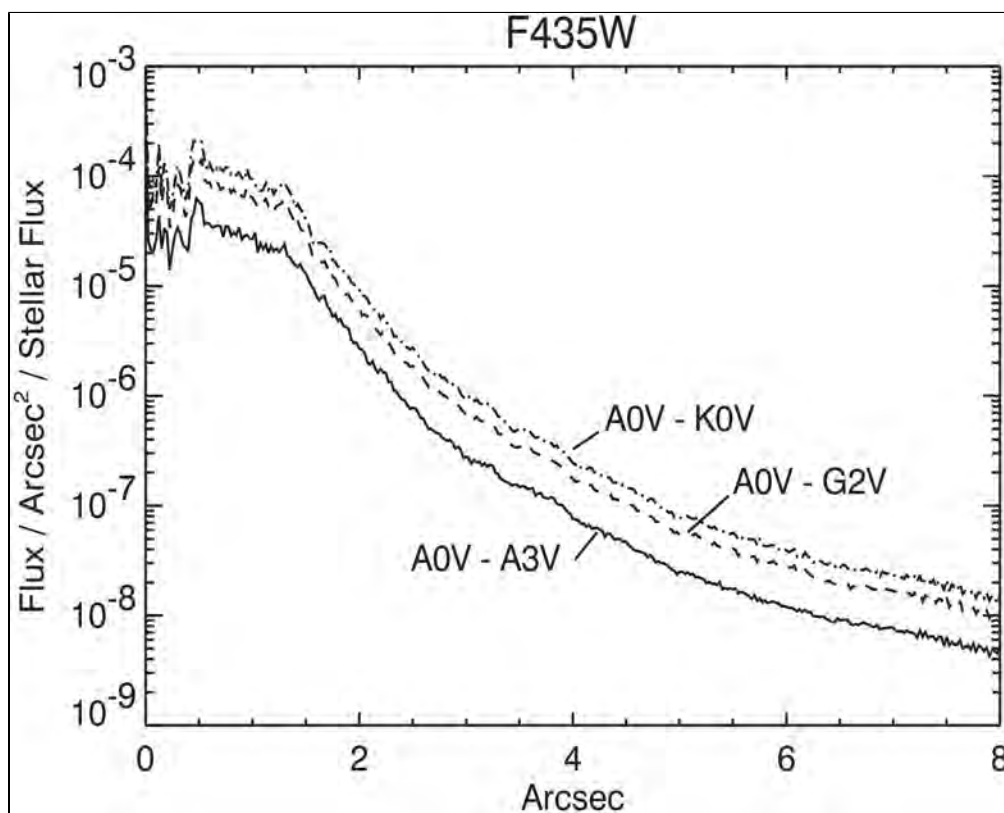
The brightness units are relative to the total flux of the target star.

Figure 6.10: Predicted absolute mean subtraction residual levels for cases where the target and reference stars are imaged at different breathing-induced focus positions.
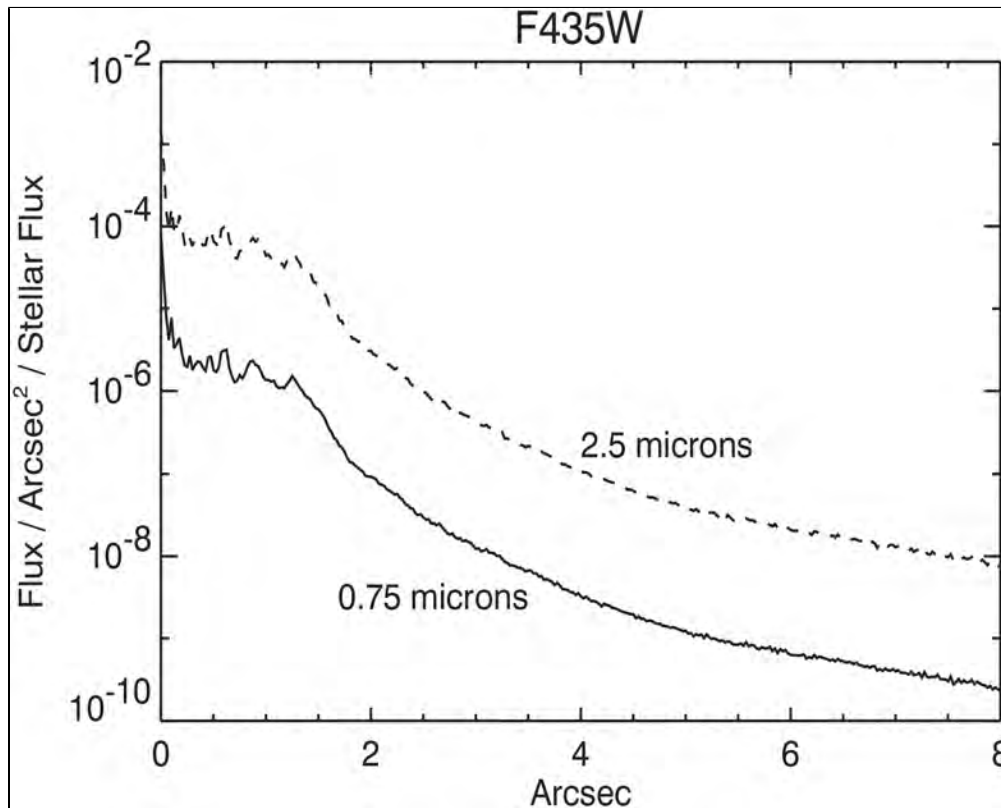

The offset (0.75 or 2.5 µm) from perfect focus (0 µm) is indicated with respect to the change in primary-secondary mirror separation. The typical breathing amplitude is 3 to 4 µm within an orbit. The brightness units are relative to the total flux of the target star.

In these cases, images of Arcturus were registered with and subtracted from similar images of the star taken a day later (Figure 6.8.) Combined with PSF subtraction, the coronagraph reduced the median background level by factors of 250 to 2500, depending on the radius and filter. Examples of PSF-subtracted images are shown in Figure 6.11 and Figure 6.12. The mean of the residuals is not zero; because of PSF mismatches, one image will typically be slightly brighter than the other over a portion of the field. The pixel-to-pixel residuals can be more than 10 times greater than the median level (Figure 6.13). Note that these profiles would be worse if there were color differences between the target and reference PSFs.

A frequently used method of avoiding the color and normalization problems involved the subtraction of images of the same target taken at two different field orientations. This technique, known as *roll subtraction*, was done either by requesting a roll of the telescope about the optical axis (up to 30°) between orbits, or by revisiting the target at a later date when the default orientation of the telescope was different. Roll subtraction only worked when the nearby or circumstellar object of interest was not azimuthally extended. It was the best technique for detecting point source companions or imaging strictly edge-on disks (e.g., Beta Pictoris). It could also be used to reduce the pixel-to-pixel variations in the subtraction residuals by rotating and co-adding the images taken at different orientations. (This worked for extended sources if another PSF star was used.) Ideally, the subtraction errors decreased as the square root of the number of orientations.

Figure 6.11: Residual errors from the subtraction of one image of Arcturus from another taken in a different visit (filter = F435W, D = 1.8 arcseconds spot).
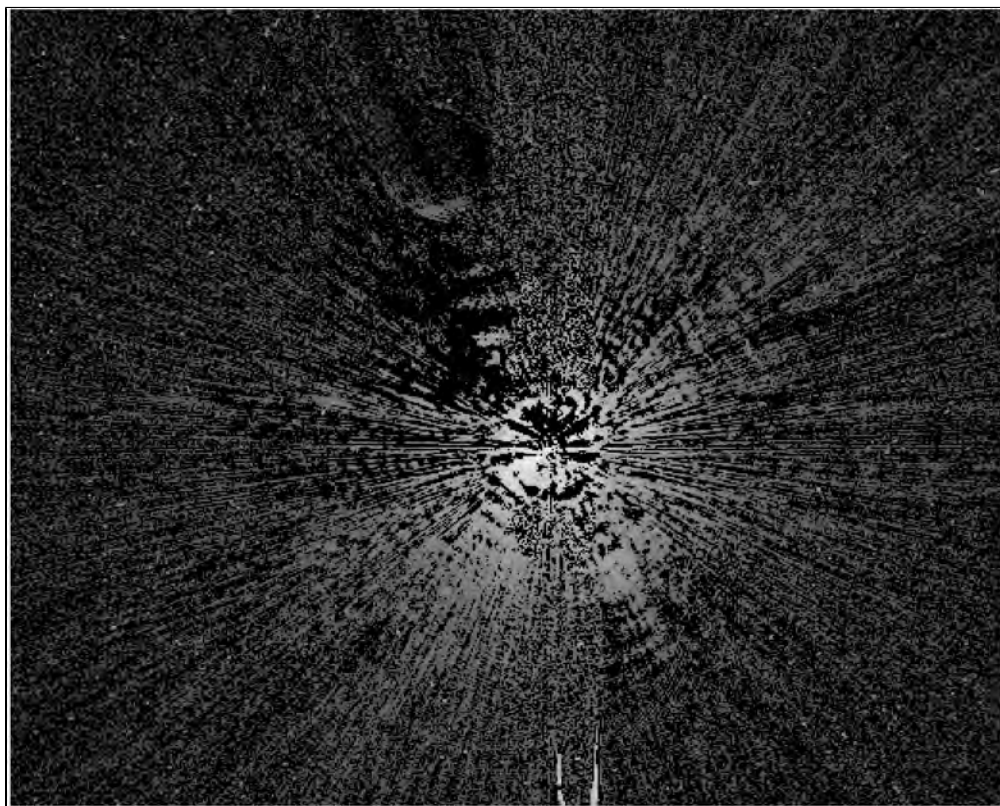
The image is 29 arcseconds across and has not been geometrically corrected. Logarithmic intensity scaled.

Figure 6.12: Subtraction of Arcturus from another image of itself taken during another visit using the large (D = 3.0 arcseconds) spot and F435W filter.
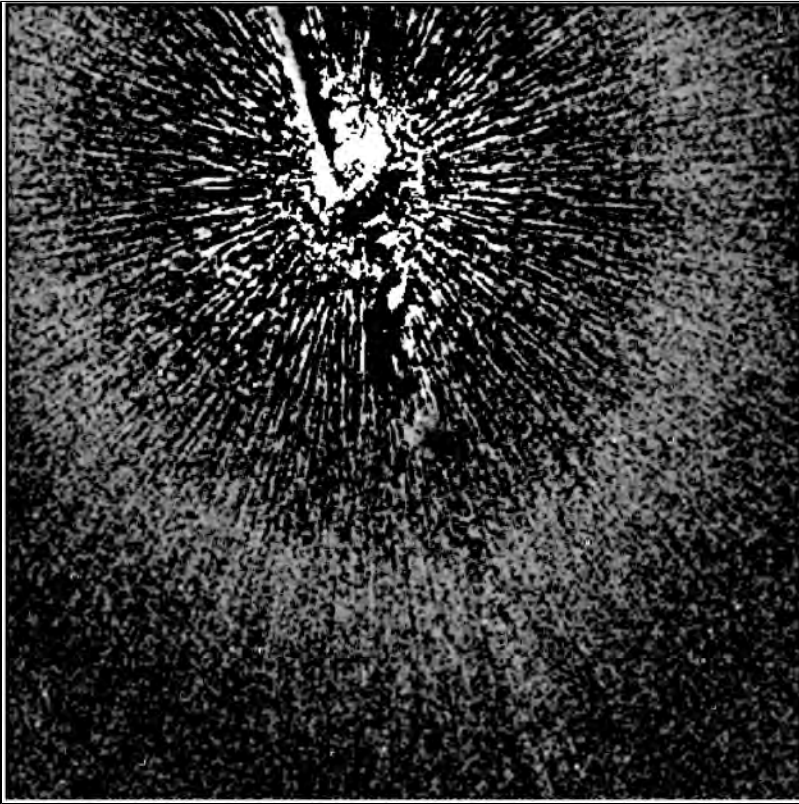
The image has been rebinned, smoothed, and stretched to reveal very low level residuals. The broad ring at about 13 arcseconds from the star is a residual from some unknown source—perhaps it represents a zonal redistribution of light due to focus differences (breathing) between the two images. The surface brightness of this ring is 20.5 magnitudes /arcsecond^2 fainter than the star. The diameter, brightness, and thickness of this ring may vary with breathing and filter. The image has not been geometrically corrected.

Figure 6.13: Plots of the azimuthal RMS subtraction residual levels at each radius for the large (3 arcseconds) spot.
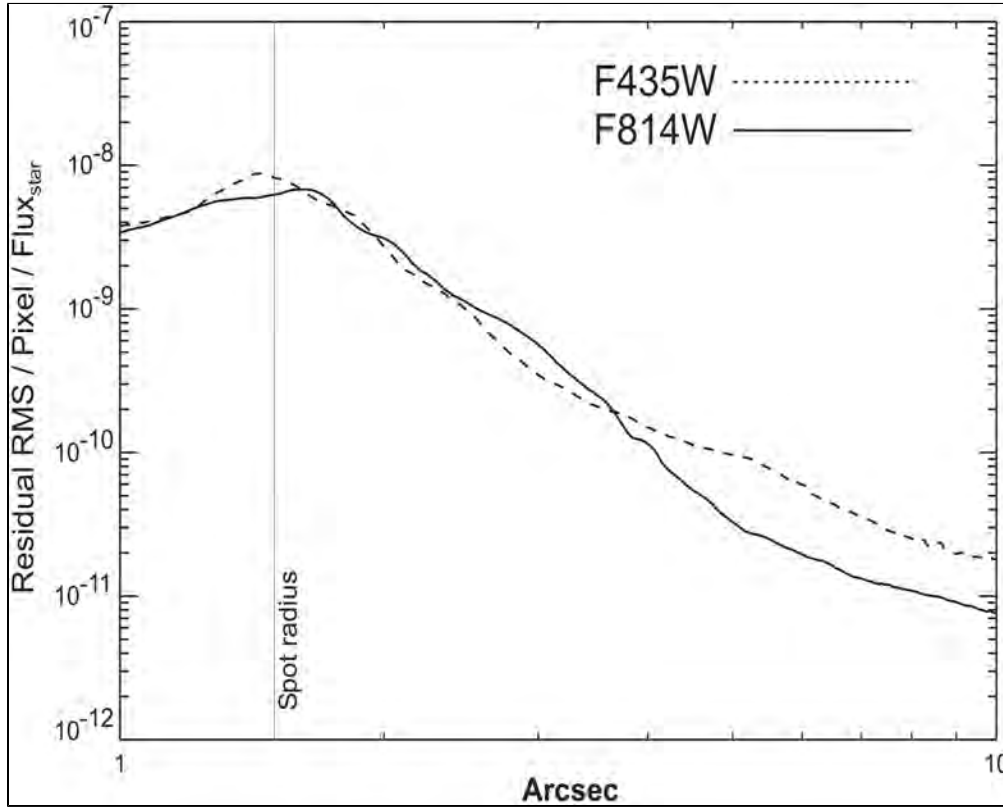

The flux units are counts per pixel relative to the total unocculted flux from the central source. These plots were derived from Arcturus-Arcturus subtractions, and represent the best results one is likely to achieve. The undistorted HRC scale assumed here is 25 milliarcseconds/pixel.

6.2.6 The Off-Spot PSF

Objects that were observed in the coronagraphic mode but not placed behind an occulting spot had PSFs that were defined by the Lyot stop. Because the Lyot stop effectively reduced the diameter of the telescope and introduced larger obscurations, this "off-spot" PSF was wider than normal, with more power in the wings and diffraction spikes (Figure 6.14). Together, the Lyot stop and occulting spot substrate reduced the throughput by 52.5%. In F814W, the "off-spot" PSF had a peak pixel containing 4.3% of the total (reduced) flux and a sharpness (including CCD charge diffusion effects) of 0.010. (Compare these to 7.7% and 0.026, respectively, for the normal HRC PSF.) In F435W, the peak was 11% and the sharpness is 0.025 (compared to 17% and 0.051 for the normal F435W PSF). Users needed to take the reduced throughput and sharpness into account when they determined the detection limits of HRC coronagraphic images. Tiny Tim may have been used to compute off-spot PSFs.

Figure 6.14: Image of Arcturus taken in coronagraphic mode with the star placed outside of the spot.
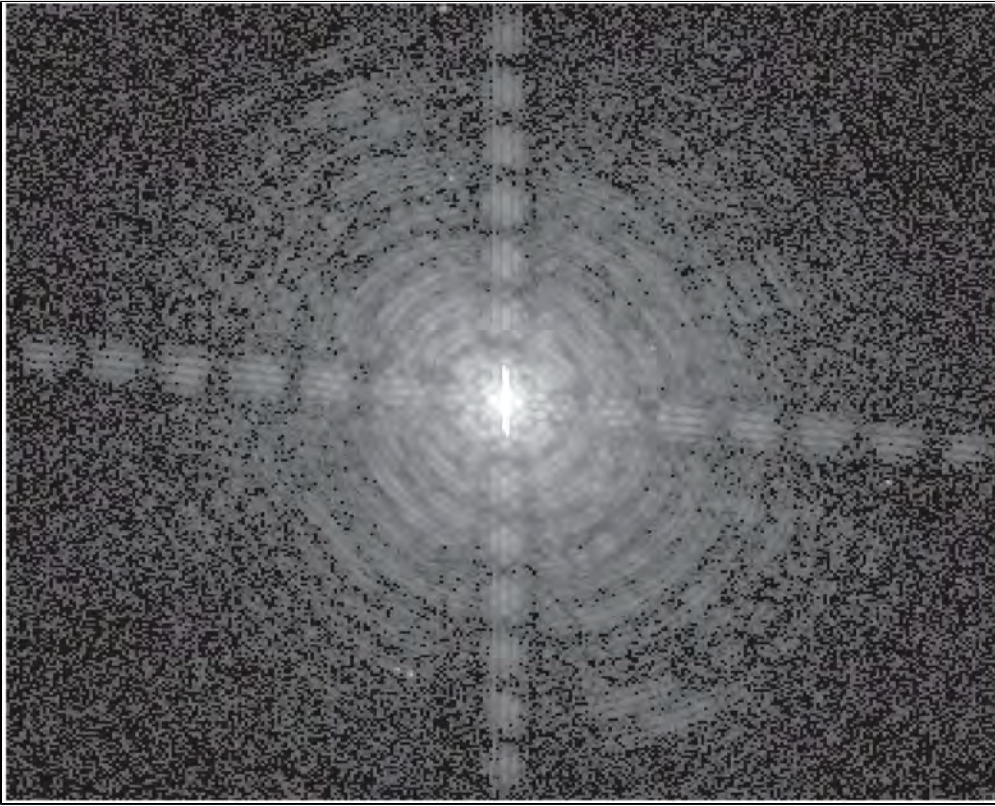
The coronagraphic field PSF has more pronounced diffraction features (rings and spikes) than the normal HRC PSF due to the effectively larger obscurations introduced by the Lyot stop. The central portion of this image is saturated. It was taken through a narrowband filter (F660N) and is not geometrically corrected.

6.2.7 Occulting Spot Motions

The positions of the occulting spots were measured at weekly intervals using Earth flats. These measurements showed that the spots moved over daily to weekly time scales in an unpredictable manner. The cause of this motion remains unknown. The spot positions typically varied by ~0.3 pixels (8 milliarcseconds) over one week, but they occasionally shifted by 1 to 5 pixels over 1 to 3 weeks. During a single orbit, however, the spots were stable to within ±0.1 pixel when continuously deployed and they recovered their positions within ±0.25 pixel when repeatedly stowed and deployed.

After on-board analysis of the acquisition images, a coronagraphic target was moved to the previously measured position of an occulting spot, which may have been several days old. The uncertainties in the day-to-day spot positions could cause star-to-spot registration errors that would affect coronagraphic performance. If the star was offset from the spot center by more than 3 pixels, then one side of the coronagraphic PSF would be brighter than expected and may have saturated earlier than predicted. A large offset also degraded the coronagraphic suppression of the diffraction pattern. Most importantly, slight changes in the spot positions could alter the coronagraphic PSFs of the target and reference stars enough to cause large PSF-subtraction residuals. Consequently, observers could not rely on reference PSFs obtained from other programs or at different times.

To reduce the impact of spot motion, observers usually obtained a reference PSF image in an orbit immediately before or after their science image. A single reference PSF could be used for two science targets if all three objects were observed in adjacent orbits and had similar colors.

6.3 Grism and Prism Spectroscopy

⚠️ *HRC has been unavailable since January 2007. Information about the HRC is provided for archival purposes.*

The ACS filter wheels include four dispersing elements for low resolution slitless spectroscopy over the field of view of the three ACS channels. One grism (G800L) provides low resolution spectra from 5500 Å to 10,500 Å for both the WFC and HRC. A prism (PR200L) in the HRC covered 1700 Å to beyond 3900 Å, although reliable wavelength and flux calibration was guaranteed only up to 3500 Å. For the SBC, a LiF prism (PR110L) covers the range 1150 Å to ~1800 Å, and a CaF_2 prism (PR130L) is useful from 1250 Å to ~1800 Å. The grism provides first order spectra with almost constant dispersion as a function of wavelength but with second order overlap beyond ~10,000 Å. The prisms have non-linear dispersion with maximum resolution at shorter wavelengths and much lower resolving power at longer wavelengths. Table 6.3 summarizes the essential features of the four ACS dispersers in the five supported modes.

Table 6.3: Optical parameters of ACS dispersers.

Disperser	Channel	Wavelength range (Å)	Resolving power	Å/pixel	Tilt [a](deg)
G800L	WFC	1st order: 5500 to 10500	100 @ 8000 Å	39.8 [b]	−2
G800L	WFC	2nd order: 5000 to 8500	200 @ 8000 Å	20.7 [b]	−2
G800L	HRC	1st order: 5500 to 10500	140 @ 8000 Å	23.9 [c]	−38
G800L	HRC	2nd order: 5500 to 8500	280 @ 8000 Å	12.0 [c]	−38
PR200L	HRC	1700 to 3900	59 @ 2500 Å	21.3	−1
PR110L	SBC	1150 to 1800	79 @ 1500 Å	9.5	0
PR130L	SBC	1250 to 1800	96 @ 1500 Å	7.8	0

[a] Tilt with respect to the positive X-axis of the data frame.

[b] The dispersion varies over the field by ±11%; the tabulated value refers to the field center.

[c] The dispersion varies over the field by ±2%; the tabulated value refers to the field center.

6.3.1 WFC G800L

The G800L grism provides two-pixel resolving power from 69 (at 5500 Å) to 131 (at 10,500 Å) for first order spectra over the whole accessible WFC field of 202 x 202 arcsec^2. Figure 6.15 shows the wavelength range and sensitivity for the zeroth, first, and second order WFC spectra. Figure 6.16 shows the same plot as a function of pixel range, where pixel 0 is the position of the direct image.

Figure 6.17 shows the full G800L spectrum of the white dwarf GD153 (V = 13.35 mag) obtained in one 60 second exposure. The first order is contaminated by the second order beyond ~10,000 Å. The total flux in the zeroth order is 2.5% of that in the first order, so locating the zeroth order is a less effective method of obtaining the wavelength zero point of weak spectra than using a matched pair of direct and grism images. The third and fourth orders contain about 1% of the flux in the first order, and the negative orders contain about 0.5% of that flux. When bright objects are observed, the signal in fainter orders may be mistaken for the spectra of fainter nearby objects. In crowded fields, many spectral orders from different objects may overlap.

Table 6.3 lists the linear dispersion for the first and second order spectra, but their dispersions are better described with second order fits (ACS ISR 2005-08). Because the grism is tilted with respect to the optical axis, the wavelength solutions are field-dependent. This dependence has been calibrated within 0.5 pixels over the whole field; the linear dispersion varies by ±11% from center to corner. The full extent of the spectrum of a bright source (orders –2, –1, 0, 1, 2, 3) is 1200 pixels (60 arcseconds). The higher spectral orders are not in focus, so their spectral resolutions are smaller than expected from their nominally higher dispersions.

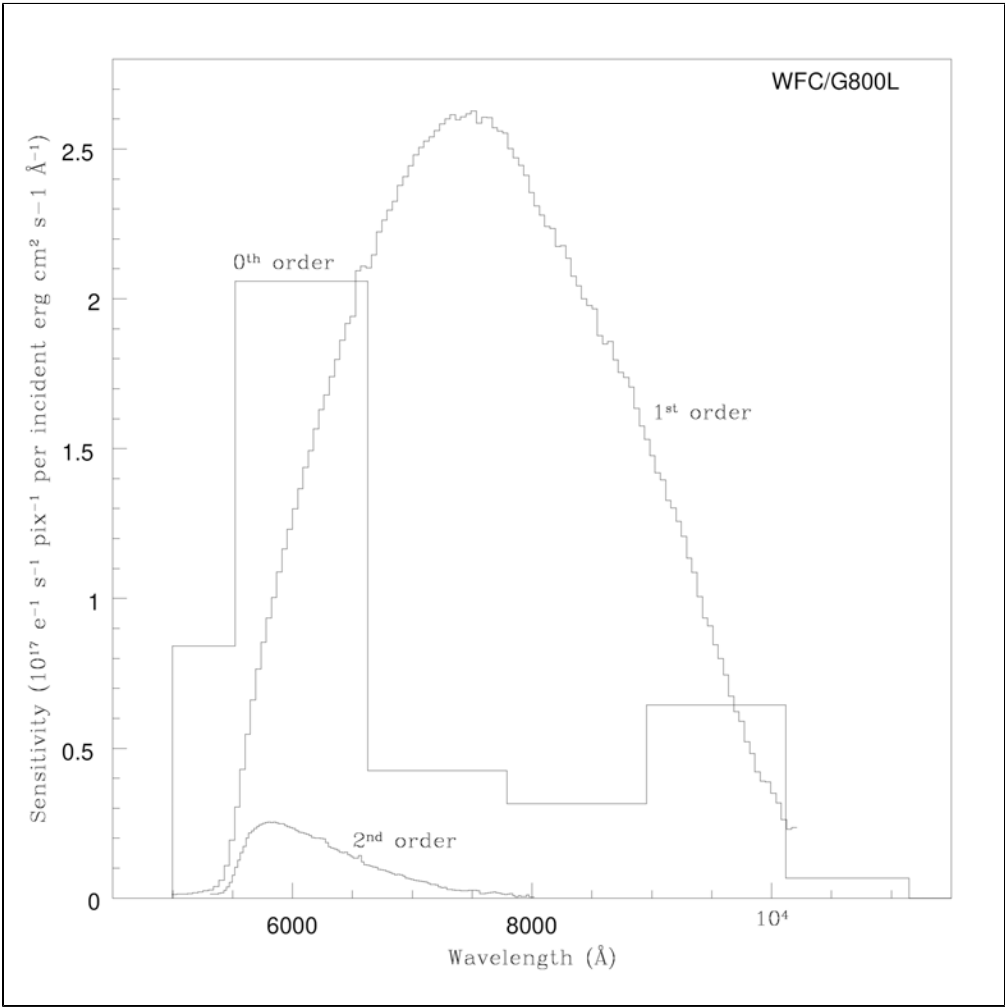**Figure 6.15: Sensitivity versus wavelength for WFC G800L.**

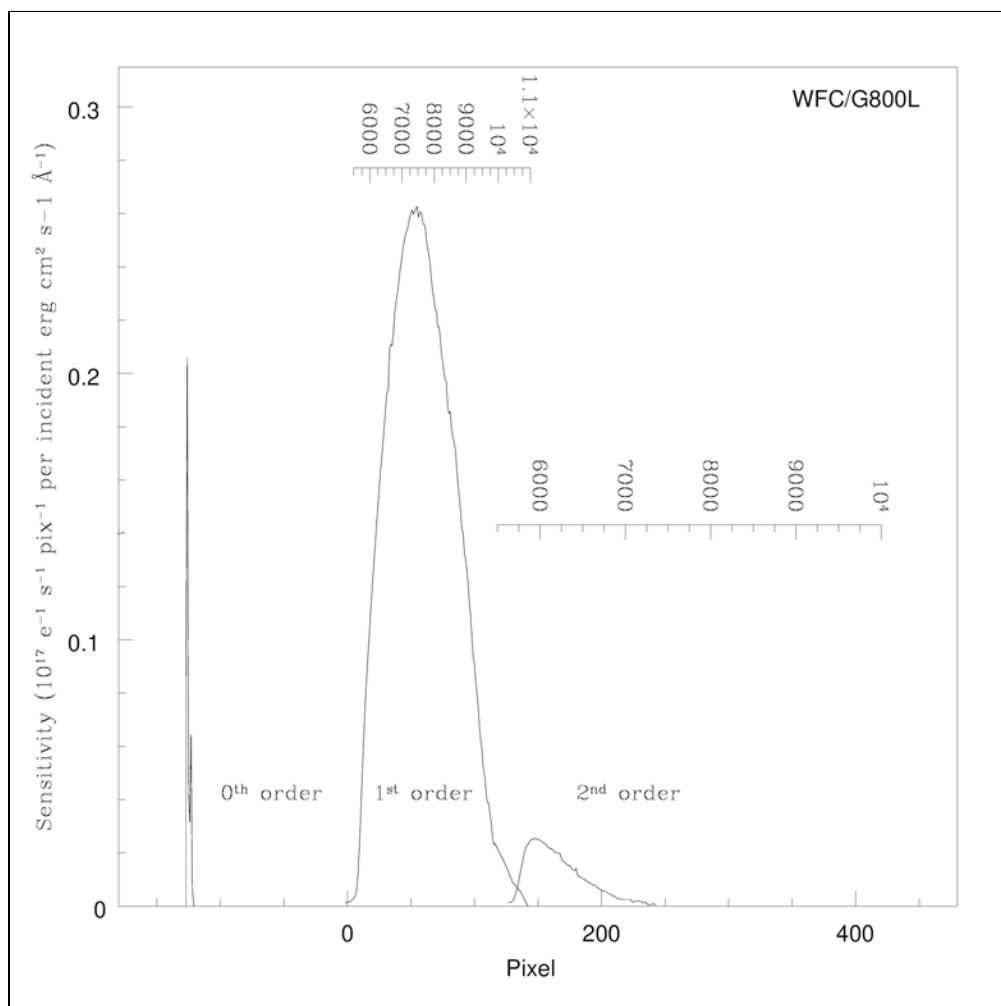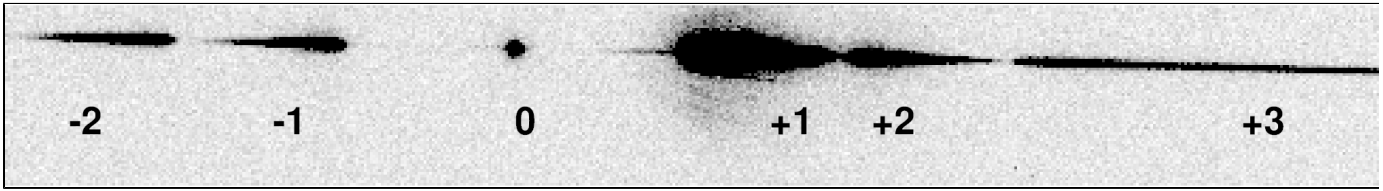**Figure 6.16: Sensitivity versus pixel position for WFC G800L.**

Figure 6.17: Fully dispersed spectrum for white dwarf GD153 with WFC/G800L.

The numbers indicate the different grism orders.

6.3.2 HRC G800L

G800L provided higher spatial resolution with the HRC than with the WFC, but the spectra were tilted at −38° with respect to the HRC's *X* axis. Figure 6.18 and Figure 6.19 show the ranges and sensitivities of the zeroth, first, and second orders as a function of wavelength and pixel, respectively. Figure 6.20 shows the spectrum of the standard star GD153. Orders −1 through +2 span about 70% of the 1024 detector columns, and the +2 order overlaps the +1 order beyond ~9500 Å. The dispersion varies by ±2% from the center to the corners of the detector. Because of the HRC's limited FOV, many G800L spectra were truncated by the edges of the detector or originated from objects located outside the corresponding direct image.

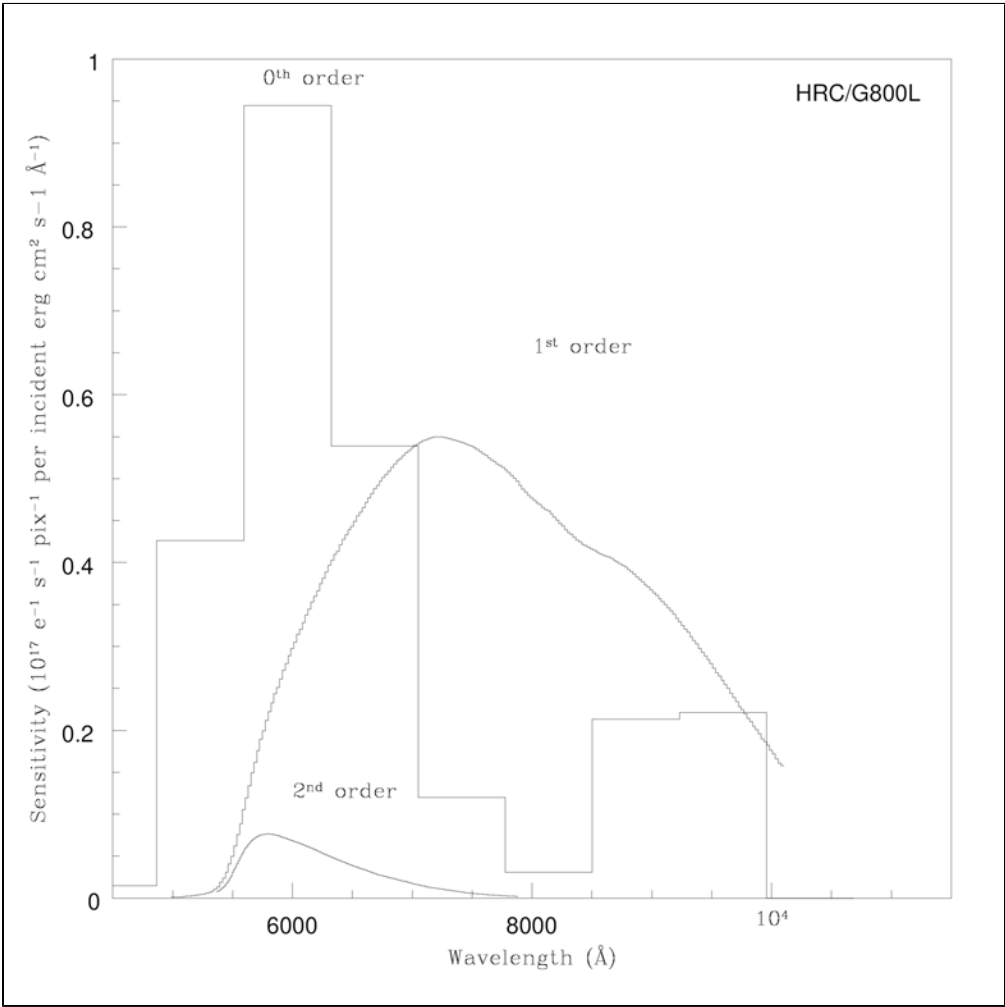**Figure 6.18: Sensitivity versus wavelength for HRC G800L.**

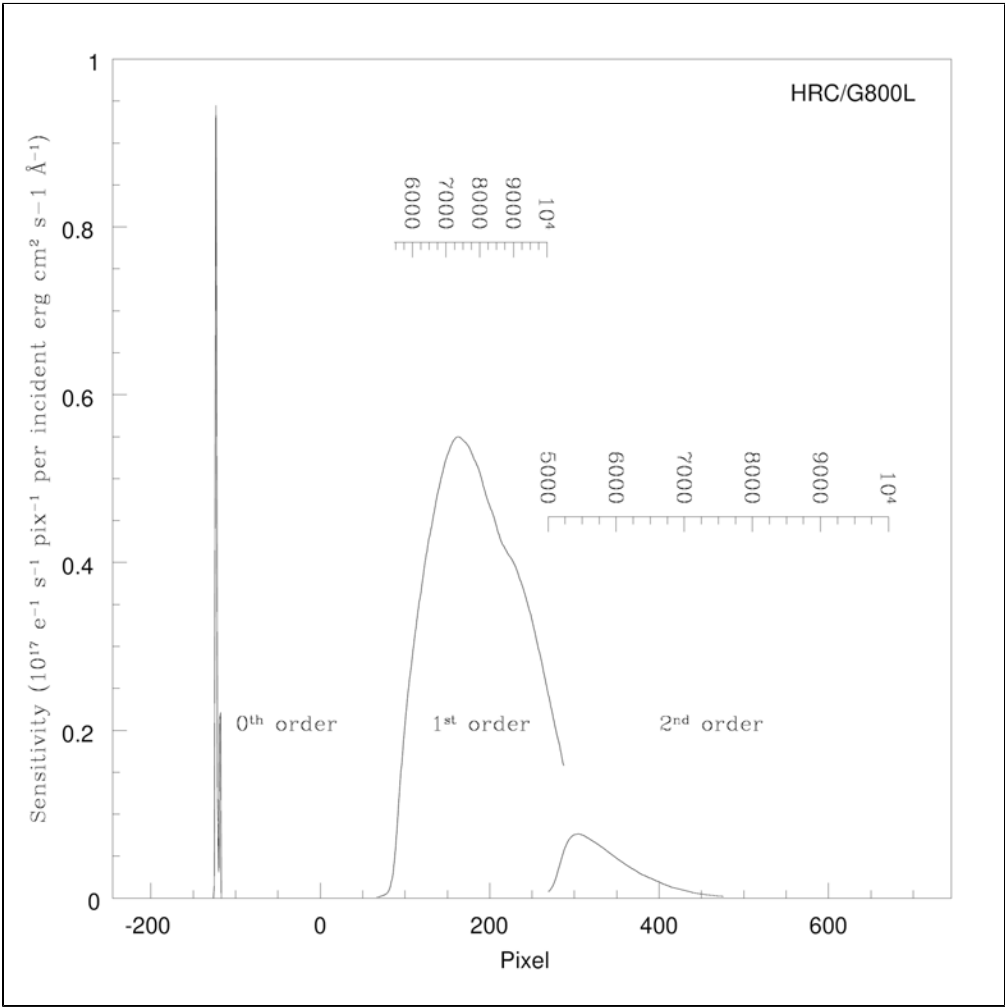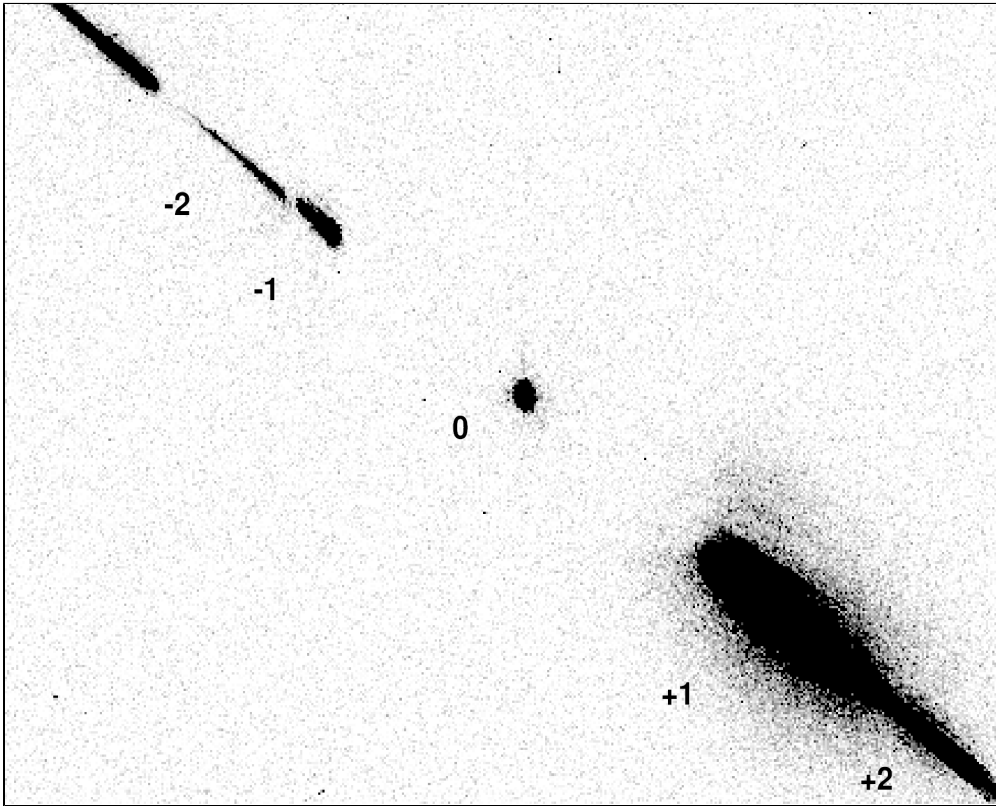**Figure 6.19: Sensitivity versus pixel position for HRC G800L.**

Figure 6.20: Fully dispersed spectrum of white dwarf GD153 with HRC/G800L.

The numbers indicate the different grism orders.

6.3.3 HRC PR200L

Figure 6.21 shows the sensitivity versus wavelength and the wavelength range of the HRC pixels for prism PR200L. The dispersion peaked at 5.3 Å/pix at 1800 Å, but dropped to 105 Å/pix at 3500 Å and then to 563 Å/pix at 5000 Å. Consequently, the spectrum piled up at longer wavelengths, where a range of 1500 Å was spanned by only 8 pixels. For bright objects, this effect could lead to saturation and blooming of the CCD, which could affect other spectra. The dispersion also varied by ±4% at 2000 Å between opposite corners of the detector. The tilt of the prism caused an offset of up to ~250 pixels between the CCD positions of the direct image and the PR200L spectrum of an object (Figure 6.21), and caused a similar amount of vignetting along the low-x side of the HRC image. Consequently, an additional prism aperture was defined with a reference point offset by 7.4 arcseconds from the geometric center of the CCD. The wavelength solution used by the aXe data reduction software (see Section 6.3.7) accounts for this aperture offset.

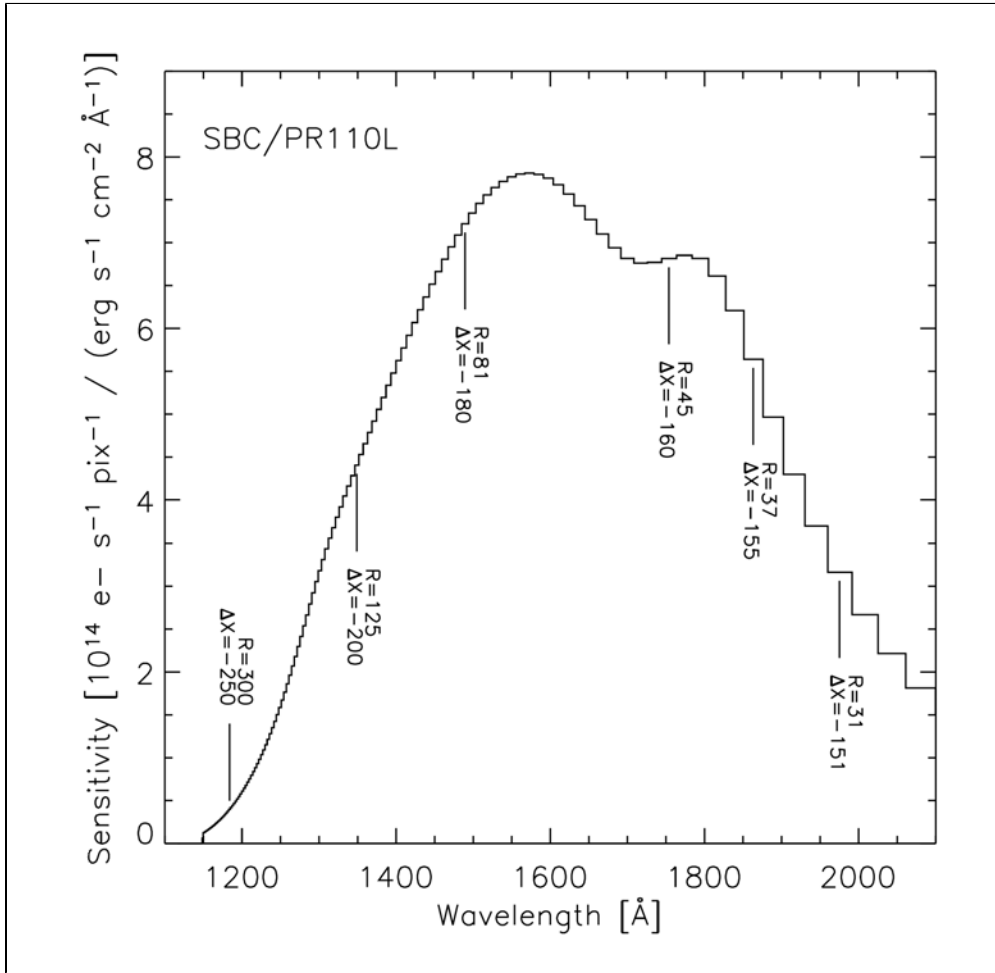**Figure 6.21: Sensitivity versus wavelength for HRC/PR200L.**
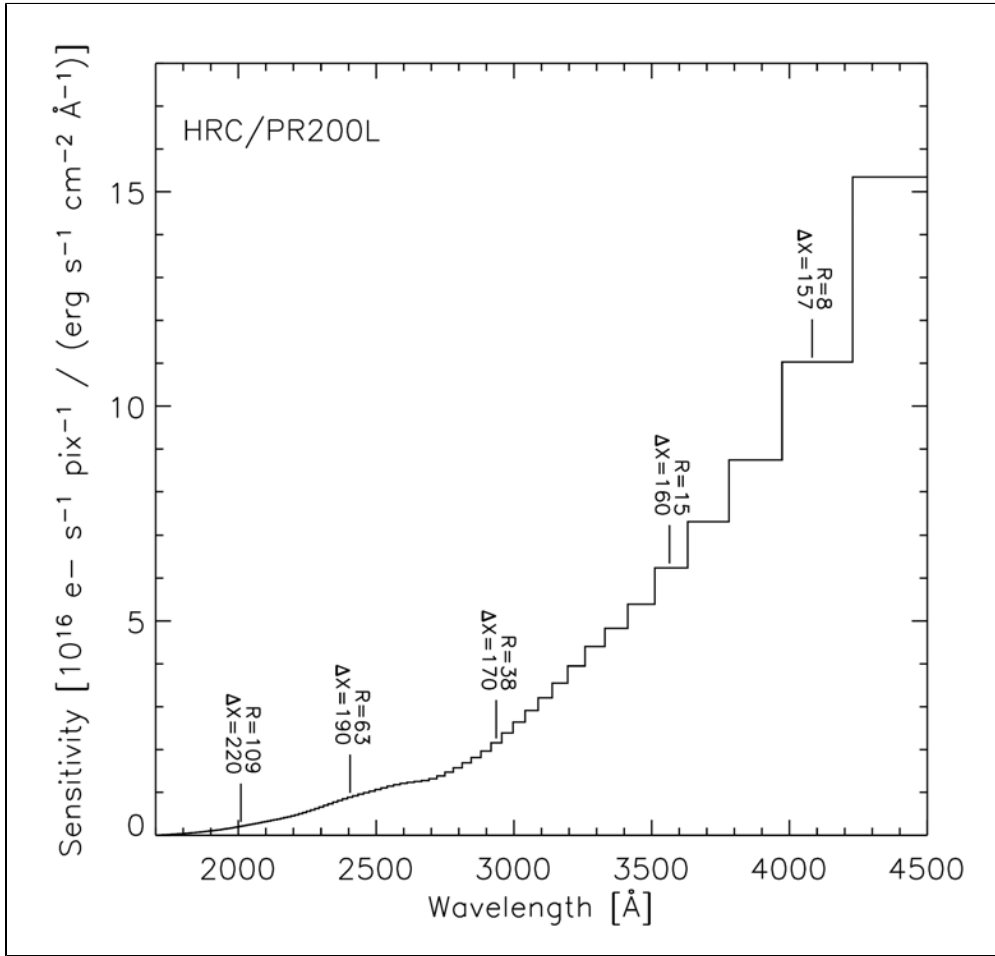
The numbers indicate the resolving power (R) and the offset from the direct image in pixels (Δx) as functions of wavelength.

6.3.4 SBC PR110L

Figure 6.22 shows the sensitivity with wavelength and the wavelength range of the pixels for PR110L. This prism is sensitive below 1200 Å and includes the geocoronal Lyman α line, so it is subject to large background signal. The dispersion is 2.6 Å/pix at Lyman α and decreases to 21.6 Å/pix at 1800 Å. The declining efficiency of the CsI MAMA detector beyond ~1800 Å occurs before the long wavelength pile-up, but observations of standard stars indicate that the throughput is ~1000 times higher at 4000 Å than indicated in Figure 4.14. Observations of stars redder than spectral type F experience significantly higher counts between 2000 Å and 6000 Å, with a peak count rate at ~3500 Å. For G stars, this peak can be ~3 times larger than the maximum UV count rate. This red leak and the geo-coronal Lyman α must not exceed the MAMA Bright Object Protection (BOP) limits (see Section 4.6). The prism's optical tilt causes an offset of up to ~250 pixels between the positions of the direct image and the PR110L spectrum of an object (Figure 6.22), and causes a similar amount of vignetting along the high-x side of the SBC image. Figure 6.23 demonstrates this offset with the summed direct image and PR110L image of the standard star WD1657+343. An appropriately offset aperture is

automatically implemented by the planning software for all PR110L observations. The wavelength solution used by aXe (Section 6.3.7) accounts for this aperture offset.

Figure 6.22: Sensitivity versus wavelength for SBC PR110L.

The numbers indicate the resolving power (R) and the offset from the direct image in pixels (Δx) as functions of wavelength. This plot was accurate as of launch of ACS. The SBC MAMA detector sensitivity has decreased by ~9% since launch (ACS ISR 2019-04).

Figure 6.23: Sum of direct (F122M) and PR110L prism exposure of the standard star WD1657+343.
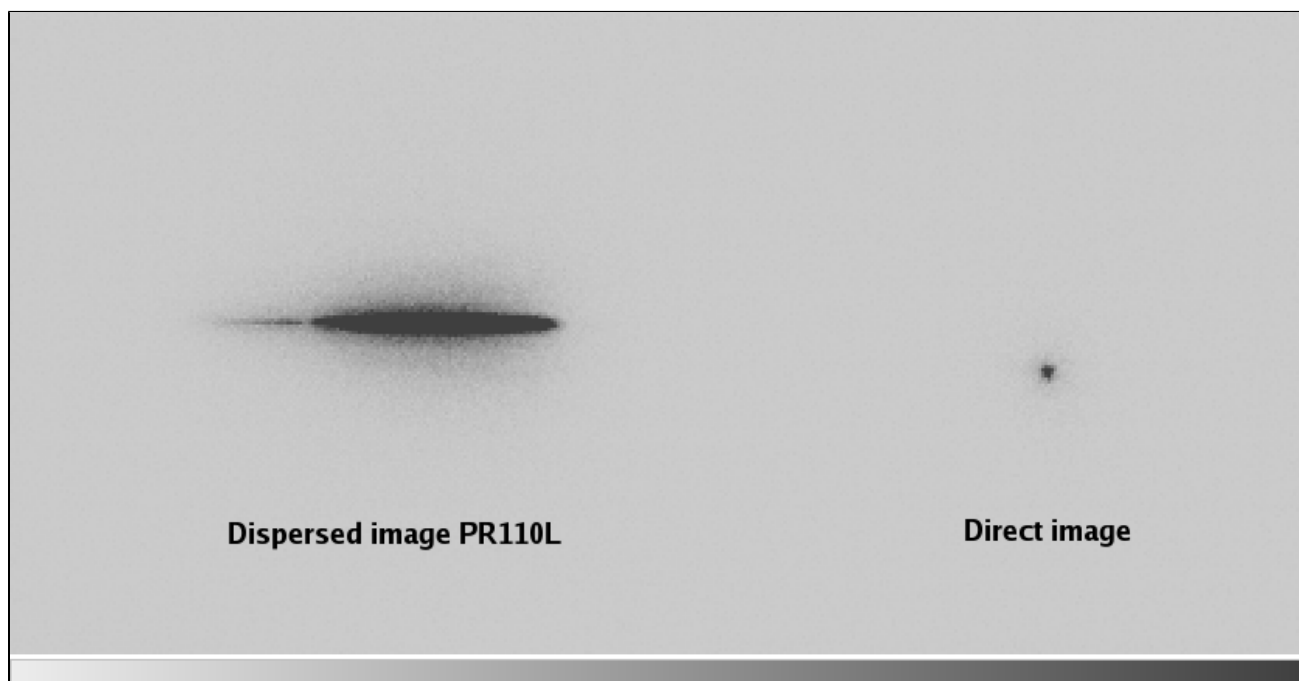
The direct image exposure was scaled prior to combination for representation purposes. The cutout shown covers 400 × 185 pixels, where the wavelength increases from left to right for the dispersed image.

6.3.5 SBC PR130L

The short wavelength cut-off of the PR130L prism at 1250 Å excludes the geo-coronal Lyman α, so PR130L is the preferred disperser for faint object detection between 1250 Å and 1800 Å. The dispersion varies from 1.65 Å/pixel at 1250 Å to 20.2 Å /pixel at 1800 Å. Figure 6.24 shows the sensitivity versus wavelength, along with the resolving power (R) and the offset from the direct image in pixels (Δx) as functions of wavelength. As for PR110L, Bright Object Protection must be considered when using this prism, even though the background count rate is lower (see Section 4.6). Just like the other prisms, the direct and dispersed images use different apertures with a small angle maneuver between them. This aperture offset is accounted for in the aXe software (Section 6.3.7).

Figure 6.24: Sensitivity versus wavelength for SBC/PR130L.
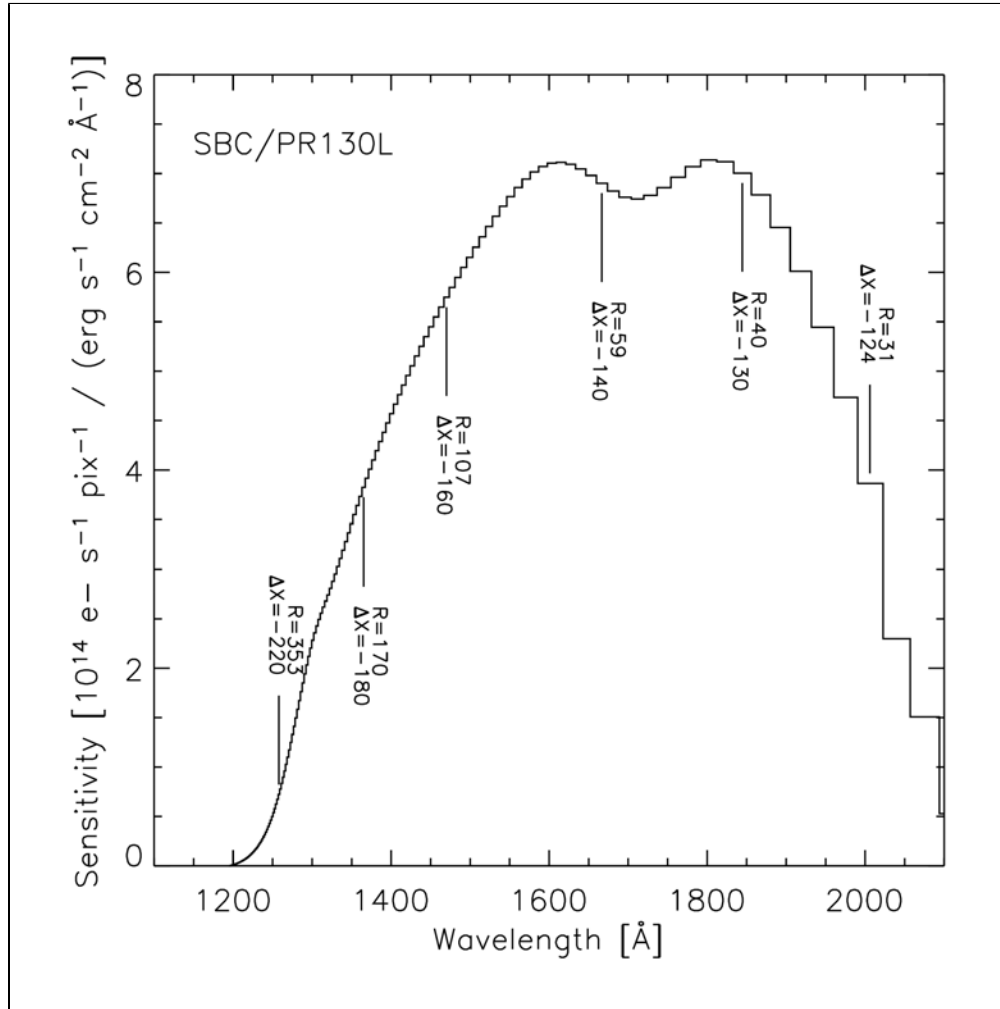
The numbers indicate the resolving power (R) and the offset from the direct image in pixels (Δx) as functions of wavelength. This plot was accurate as of launch of ACS. The SBC MAMA detector sensitivity has decreased by ~9% since launch (ACS ISR 2019-04).

6.3.6 Observation Strategy

The normal observing technique for all ACS spectroscopy is to obtain a direct image of the field followed by the dispersed grism/prism image. This technique allows the user to determine the wavelength zero points from the positions of the sources in the corresponding direct images. For WFC and HRC, the scheduling system automatically inserts a default direct image for each spectroscopic exposure, e.g., a 3 minute F606W exposure for G800L and a 6 minute F330W exposure for PR200L. The user may override the default image by setting the optional parameter AUTOIMAGE=NO. A direct image can then be manually defined with a different filter and/or exposure time or it can be eliminated entirely if the spectroscopic exposures are repeated or if no wavelength calibration is required. No default direct images are obtained for SBC prism exposures because of Bright Object Protection requirements (Section 7.2). The direct image must

always be specified manually and satisfy the BOP limits, which will be more stringent than for the dispersed image. Because of the offsets between the direct imaging and prism apertures, the SAME POS AS option will generally not have the desired effect for prism spectroscopy. Users who wish to specify offsets from the field center by means of the POS TARG option should do so by explicitly specifying the same POS TARG for the direct imaging and prism exposures.

Table 6.4 lists the V detection limits for the ACS grism/prism modes for unreddened O5V, A0V, and G2V stars generated by the ETC. These limits were computed for WFC and HRC using the parameters CR-SPLIT=2 and GAIN=2. An average sky background was used, but users should be aware that limiting magnitudes are sensitive to background levels, e.g., the limiting magnitude of an A0 V star in the WFC using the F606W filter changes by ±0.4 magnitudes at the background extremes.

Table 6.4: V detection limits for the ACS grism/prism modes.

Mode	V limit (S/N = 5, exposure time = 1 hour)			Reference wavelength (Å)
	O5V (Kurucz model)	A0V (Vega)	G2 V (Sun)	
WFC/G800L	24.2	24.4	24.9	7000
HRC/G800L	23.4	23.6	24.2	7000
HRC/PR200L	25.6	22.7	18.8	2500
SBC/PR110L	24.9	20.9	9.3	1500
SBC/PR130L	25.6	21.5	9.9	1500

Chapter 9 provides details of the calculations. Depending on the wavelength region, the background must also be taken into account in computing the signal to noise ratio. The background at each pixel consists of the sum of all the dispersed light in all the orders from the background source. For complex fields, the background consists of the dispersed spectrum of the unresolved sources; for crowded fields, overlap in the spectral direction and confusion in the direction perpendicular to the dispersion may limit the utility of the spectra.

The ETC supports all the available spectroscopic modes of the ACS and is available for more extensive calculations. The current version employs the on-orbit determinations of the dispersion solution and sensitivity where available.

For more detailed, two-dimensional simulations of ACS slitless spectra, an IRAF/PyRAF package called aXeSIM is available. aXeSIM generates slitless images and their associated direct images using object shapes and spectra given as input. In the most primitive form, aXeSIM uses Gaussians as object shapes and direct imaging magnitudes as "spectra," however, more realistic object shapes (e.g., a PSF from Tiny Tim) and high resolution spectra can be provided. aXeSIM is described in Kuemmel, Kuntschner & Walsh 2007, ST-ECF Newsletter 43, 8 and Kuemmel et al. 2009, PASP 121, 59.

> ✅ *Please refer to the ACS webpage and aXeSIM for the software and related information.*

6.3.7 Extraction and Calibration of Spectra

Because ACS spectroscopy is slitless, the point spread function of the target modulates the spectral resolution. For extended sources, the size of the target in the dispersion direction limits the achievable resolution (ACS ISR 2001-02). The dispersions of the grism and prisms are well characterized, but the zeroth order of grism spectra are generally too weak to reliably set the wavelength zero point. For typical spacecraft jitter, wavelength zero points to ±0.4 pixels should be routinely achievable using a direct image taken just before or after the grism or prism image. The jitter information can be used to obtain more accurate coordinates for the center of the FOV. These coordinates allow one to determine better relative offsets between the direct and the spectroscopic images. The red wavelength range of each pixel in G800L images is small enough that fringing can modulate the spectra. The peak-to-peak fringe amplitude was about 30% at 9500 Å for the HRC, and it is about 25% for the WFC. Models of the fringing in the WFC and HRC are described in ACS ISR 2003-12. In practice, the fringing is significantly reduced by the smoothing effects of the PSF and intrinsic object size in the dispersion direction. ACS ISR 2008-01 shows that the errors due to fringing are less than 0.1% for continuum sources and can therefore be neglected. For narrow emission lines, however, fringing can cause line flux variations of 12% and more. For realistic scenarios like Wolf Rayet emission lines, variations of ~4% are seen.

The STSCI pipeline does not provide an extracted spectral count rate vs. wavelength, but the software package aXe is available to extract, wavelength calibrate, and flux calibrate ACS grism and prism spectra. Full details are presented by Kuemmel et al. 2009, PASP 121, 59.

ACS grism extraction for 47,919 sources were performed by ST-ECF and are available via the Hubble Legacy Archive. Information about these extractions is available at the HLA ACS/WFC grism data release web page.

Chapter 7: Observing Techniques

Chapter Contents

7.1 Designing an ACS Observing Proposal

In this section, we describe the sequence of steps you should follow when designing your ACS observing proposal. The sequence is an iterative one, as trade-offs are made between signal-to-noise ratio and the limitations of the instrument itself. The basic sequence of steps in defining an ACS observation are:

- Identify science requirements and select the basic ACS configuration to support those requirements.
- Estimate exposure time to achieve the required signal-to-noise ratio, using the Exposure Time Calculator (ETC).
- Identify any additional target acquisition and calibration exposures needed.
- Calculate the total number of orbits required, taking into account the overheads.

> ⚠️ It is essential that observers proposing to use the SBC read and abide by the procedures and rules described in Section 4.6 and 7.2 to ensure the safety of the MAMA detectors.

Figure 7.1: Defining an ACS observation.
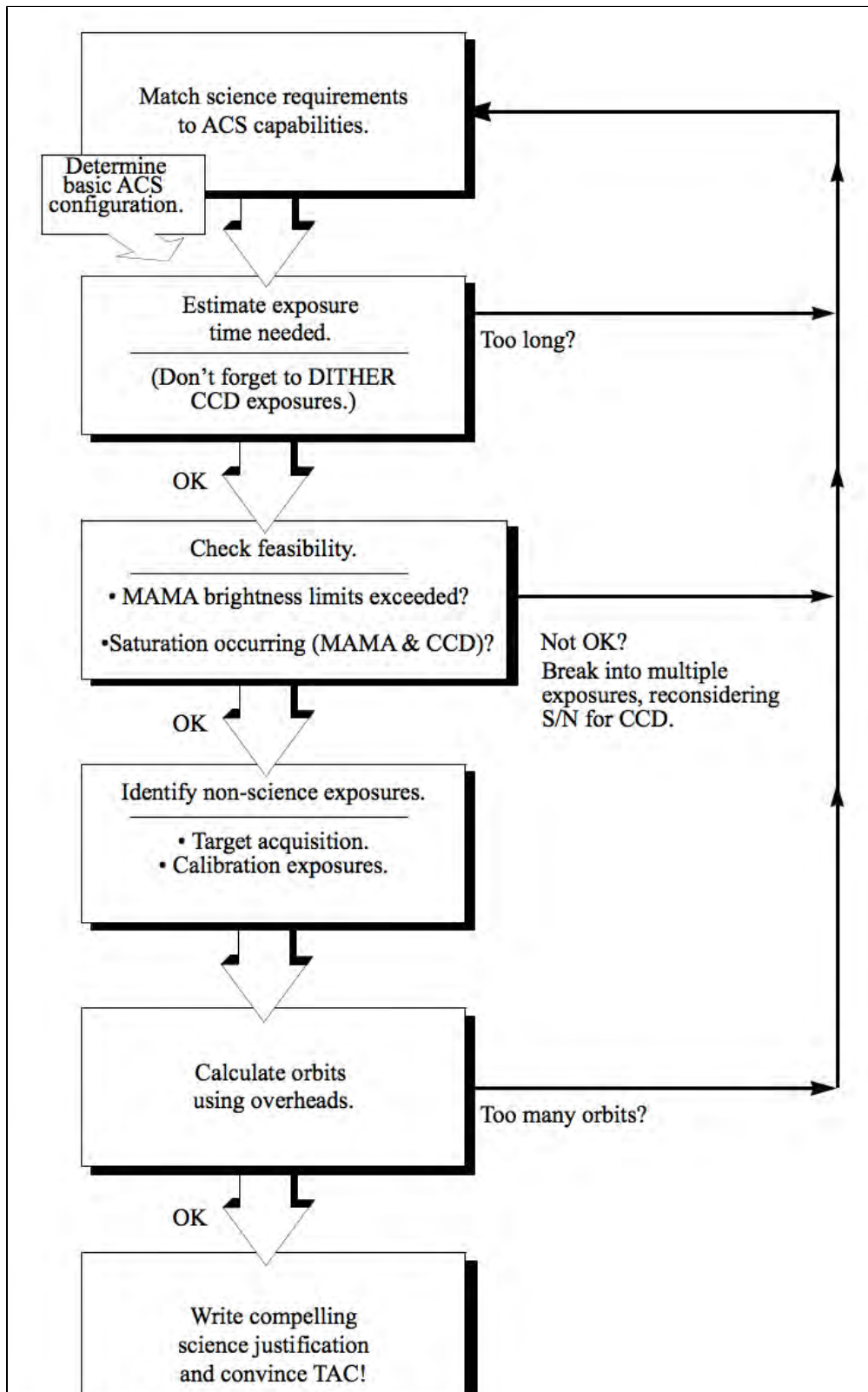
7.1.1 Identify Science Requirements and Define ACS Configuration

First, you must identify the science goals you wish to achieve with ACS. Basic decisions you must make are:

- Nature of target
- Filter selection

Trade-offs involving only ACS modes are described in Table 7.1. A discussion of trade-offs between different instruments can be found in Section 2.2.

Table 7.1: Science decision guide.

Decision	Choices	Trade-offs
Field of view	Camera Filter selection	WFC: 202 × 202 arcsec^2 SBC: 35 × 31 arcsec^2
Spectral response	Camera Filter selection	WFC: 3700–11,000 Å SBC: 1150–1700 Å
Spatial resolution	Camera	WFC: ~0.05 arcsecond/pixel SBC: ~0.032 arcsecond/pixel
Filter selection	Camera	WFC: broad, medium & narrow band, ramps SBC: broad band
Spectroscopy	Camera Spatial resolution Field of view Wavelength range	Grism (`G800L`): WFC Prism (`PR110L`, `PR130L`): SBC
Polarimetry	Filters	UV polarizers combine with Wheel 2 filters VIS polarizers combine with Wheel 1 filters

Imaging

For imaging observations, the basic configuration consists of detector, operating mode (MODE=ACCUM), and filter. Chapter 5 presents detailed information about each ACS imaging mode.

Special Uses

We refer you to Chapter 6 if you are interested in slitless spectroscopy or polarimetry.

7.1.2 Available but Unsupported Modes

> ✅ *Please check for updates on the ACS website.*

STScI provides full calibration and user support for most of ACS's operational modes. However, there are some "available but unsupported" modes accessible to observers in consultation with an ACS Instrument Scientist. These unsupported modes include particular apertures, limited interest optional parameters, some GAIN options, and filterless (CLEAR) operation. If your science cannot be obtained using fully supported modes, or would be much better with use of these special cases, then you may consider using an unsupported mode.

Unsupported modes should only be used if the technical requirements and scientific justifications are particularly compelling. The following caveats apply:

- STScI does not provide calibration reference files for available-but-unsupported modes. It is the observer's responsibility to obtain any needed calibrations.
- Requests to repeat failed observations taken with unsupported modes will not be honored if the failure is related to use of this mode.
- User support from STScI will be more limited.

Phase I proposals that include unsupported ACS modes must include the following:

- Explanation of why supported modes don't suffice.
- A request for any observing time needed for calibration purposes.
- Justification for added risk of use in terms of scientific payback.
- Demonstration that the observers are able to analyze such data.

During the Phase II proposal submission process, use of unsupported modes requires formal approval from the ACS Team at STScI. To request an unsupported mode, send a brief e-mail to your Program Coordinator (PC) that addresses the above four points. The PC will relay the request to the contact scientist or relevant ACS instrument scientist, who will then decide whether the use will be allowed. This procedure ensures that any potential technical problems have been taken into account. Note also that archival research may be hindered by use of these modes. Requests for unsupported modes that do not adequately address the above four points or that will result in only marginal improvements in the quality of the data obtained may be denied, even if the request was included in your approved Phase I proposal.

The current list of available-but-unsupported items are:

- Targets: `BIAS`
- Optional parameters: `SIZEAXIS1, SIZEAXIS2, CENTERAXIS1, CENTERAXIS2, COMPRESSION, AMP, FLASHEXP, WFC: GAIN=0.5, 1.0, 1.4`
- Spectral elements: `CLEAR` (WFC)
- ACQ mode: optional parameter `GAIN`
- POLUV modes in conjunction with filters: F435W, F660N, F814W

- POLV modes in conjunction with filters: F502N, F550M, F555W, F625W, F658N

7.1.3 Determine Exposure Time and Check Feasibility

Once you have selected your basic ACS configuration, the next steps are:

- Estimate the exposure time needed to achieve your required signal-to-noise ratio, given your source brightness. (You can use the ETC for this; see also Chapter 9 and the plots in Chapter 10).
- For observations using the CCD detectors, ensure that you do not exceed the pixel full well.
- For observations using the MAMA detector, ensure that your observations do not exceed brightness (count rate) limits.
- For observations using the MAMA detector, ensure that for pixels of interest, your observations do not exceed the limit of 65,535 accumulated counts per pixel per exposure imposed by the ACS 16 bit buffer.

To determine your exposure-time requirements, consult Chapter 9 where an explanation of how to calculate a signal-to-noise ratio and a description of the sky backgrounds are provided. To assess whether you are close to the brightness, signal-to-noise, and dynamic-range limitations of the detectors, refer to Chapter 4.

If you find that the exposure time needed to meet your signal-to-noise requirements is too large, or that you are constrained by the detector's brightness or dynamic-range limitations, you must adjust your basic ACS configuration. Table 7.2 summarizes the available options and actions for iteratively selecting an ACS configuration that is suited to your science and is technically feasible.

Table 7.2: Science feasibility guide.

Action	Outcome	Recourse
Estimate exposure time.	If too long, re-evaluate instrument configuration.	Consider another filter.
Check full-well limit for CCD observations.	If full well exceeded and you wish to avoid saturation, reduce time per exposure.	Divide total exposure time into multiple, short exposures.[a]
Check bright object limits for MAMA observations.	If source is too bright, re-evaluate instrument configuration.	Consider another filter or change detectors and wavelength regime.
Check 65,535 counts/pixel limit for MAMA observations.	If limit exceeded, reduce time per exposure.	Divide total exposure time into multiple, short exposures.

[a]Splitting CCD exposures affects the exposure time needed to achieve a given signal-to-noise ratio because of the read noise.

7.1.4 Identify Need for Additional Exposures

Having identified a sequence of science exposures, you need to determine what additional exposures you may require to achieve your scientific goals. Specifically, if the success of your science program requires calibration to a higher level of precision than is provided by STScI calibration data, and if you are able to justify your ability to reach this level of calibration accuracy yourself, you will need to include the necessary calibration exposures in your program, including the orbits required for calibration in your total orbit request.

7.1.5 Data Volume Constraints

ACS data taken at the highest possible rate for more than a few orbits or in the Continuous Viewing Zone (CVZ) may accumulate data faster than they can be transmitted to the ground. High data volume proposals will be reviewed and, on some occasions, users may be requested to break the proposal into different visits. Consider using subarrays, or take other steps to reduce data volume.

7.1.6 Determine Total Orbit Request

In this step, you place all of your exposures (science and non-science alike) into orbits, including tabulated overheads, and determine the total number of orbits required. Refer to Chapter 8 when performing this step. If you are observing a small target and find your total time request is significantly affected by data transfer overheads (which will be the case *only* if you are taking many separate exposures under 337 seconds with the WFC), you can consider the use of CCD subarrays to lessen the data volume. Subarrays are described in Section 7.3.1 and Section 8.2.1.

If you are unhappy with the total number of orbits required, you can adjust your instrument configuration, lessen your acquisition requirements, or change your target signal-to-noise or wavelength requirements, until you find a combination that allows you to achieve your science goals. If you are happy with the total number of orbits required, you are done!

7.1.7 Charge Transfer Efficiency

All CCDs operated in a radiative environment are subject to a significant degradation in charge transfer efficiency (CTE). The degradation is due to radiation damage of the silicon, inducing the creation of traps that impede an efficient clocking of the charge on the CCD.

Special CTE-monitoring programs show that CTE degradation proceeds largely linearly with time. For the current Cycle, a star with 100 total electrons, a sky background of 10 electrons, and a placement at row 1024 (center) in one of the WFC chips would experience a loss of about 28% for aperture photometry within a 3-pixel radius. A target placed at the WFC aperture reference point, near the maximum number of parallel shifts during readout, would have approximately twice the loss. Expected absolute errors after calibration of science data, at these low-loss levels, is expected to be of order 10% the relative loss. See ACS ISR 2012-05 for more details.

When observing a single target that is significantly smaller than the detector footprint, it is possible to place it near an amplifier to reduce the impact of imperfect CTE. This is easy to accomplish by judicious choice of aperture and target position, or by utilizing POS TARG commands. However, be aware that large POS TARGs are not advisable because they change the fractional pixel shifts of dither patterns due to the geometric distortion of ACS. An alternative means to achieve the placement of a target near the amplifier is by using some of the subarray apertures. For example, `WFC1B-512`

, `WFC1B-1K`, and `WFC1B-2K` place the target near the B amplifier (target will have 256, 512, and 1024 parallel transfers). The aperture `WFC1-CTE` is available to mitigate CTE loss and includes the entire chip 1 4096 × 2048 pixel area. However, the reference position is in the upper right corner of chip 1, 200 pixels from both the top and right edges. Therefore, `WFC1-CTE` is not appropriate for highly extended targets.

The ACS Team has developed a post-observation correction for CTE losses based upon the Anderson & Bedin 2010, PASP, 122, 1035 methodology. This empirical algorithm first develops a model to reproduce the observed CTE trails, then inverts the model to convert observed pixel values in any image to an estimate of the original pixel values, undoing the effects of the degraded CTE.

The original version of the algorithm, implemented in CALACS, worked very well for intermediate to high flux levels (>200 electrons). Improvements to the algorithm, which was most recently updated in 2017, have made corrections more effective at low flux levels (<100 electrons), employed more accurate time- and temperature-dependent corrections for CTE over ACS's lifetime, and do a better job of mitigating readnoise amplification. More details on this subject can be found in ACS ISR 2011-01, ACS ISR 2012-03, ACS ISR 2012-05 and ACS ISR 2018-04. Check the ACS website and the *ACS Data Handbook* for further details.

7.1.8 Image Anomalies

ACS was designed with a requirement that no single stray light feature can contain more than 0.1% of the detected energy in the object producing it. This goal has generally been met, but during the extensive ground and SMOV test programs a few exceptions have been identified (Hartig et al. 2003, Proc. SPIE 4854; HLA ISR 2008-01) such as the WFC elliptical haloes and the F660N ghosts. SBC observations of bright objects sometimes show optical ghosts due to reflection between the back and front sides of the filter. The mean energy of the ghost is about 0.82% of the energy of the primary target (ACS ISR 2007-05).

A tool has been developed to predict and characterize scattered light anomalies due to bright stars near the field of view of an ACS/WFC observation. For more detail, see the ACS anomalies webpage, the *ACS Data Handbook*, and ACS ISR 2016-06.

While some of these anomalies exceed the specified intensity, some judicious planning of your science observations is recommended to help alleviate their effect on your data, especially if bright sources are expected in the field of view. For instance, the impact of diffraction spikes (which for ACS lie along x and y axes) and of CCD blooming (which occurs along the y direction) due to saturation of a bright star(s), can be reduced by choosing an ORIENT that prevents the source of interest from being connected to the bright star along either of these axes. Alternatively, a suitable ORIENT could move the bright star(s) off the field of view altogether. Similarly, the impact of WFC elliptical haloes can be minimized by avoiding the placement of a bright star in the quadrant associated with amplifier D.

Subsequent to the replacement of the ACS CCD Electronics Box during SM4, all WFC images exhibit a horizontal striping that is constant across the full row (for both amplifiers) of each chip. This striping is the result of $1/f$ noise on the bias reference voltage and has a standard deviation of 0.9 e–. The contribution of the stripes to the global readnoise statistics is small, but the correlated nature of the noise can affect photometric precision for very faint sources and very low surface brightnesses. Please see Section 5.2.6 for additional details and mitigation strategy. Destriping is now part of the CALACS pipeline. Further information can be found in ACS ISR 2011-05.

Artifacts present in WFC flat field and post-flashed dark images, including dust motes, "freckles", and "flecks", are discussed in Section 4.2.7.

7.2 SBC Bright Object Protection

7.2.1 Bright Object Violation: SBC Exposures

High global and local count rates can cause catastrophic damage to the SBC detector. Therefore, targets should be checked to verify that their fluxes do not exceed the defined SBC safety limits. As a first step, you can check your source V magnitude and peak flux against the bright object screening magnitudes in Table 7.4 for your chosen observing configuration (ACS ISR 2019-10). In many cases, your source properties will be much fainter than these limits, and you need not worry further.

However, the magnitudes in this table are hard screening limits that correspond to the count rate limits in Table 7.3 and the output of the ETC. In earlier editions of this Handbook, these magnitudes were made fainter by arbitrary 1 or 2 magnitude pads, depending on the spectral type range, but these have now been removed. If your target is near these limits (within 2 magnitudes or a factor of 6.3 of the flux limits), then you need to carefully consider whether your source will be observable in the chosen configuration. Remember that the limits in these tables assume zero extinction. Thus, you will want to correct the limits appropriately for your source reddening due to interstellar dust.

Table 7.3: Absolute SBC count rate screening limits for nonvariable and variable objects.

Target	Limit type	Screening limit[a]
Nonvariable	Global	200,000 counts/second
Nonvariable	Local	50 counts/second/pixel [b]
Irregularly variable [c]	Global	80,000 counts/second
Irregularly variable [c]	Local	20 counts/second/pixel

[a] The limits for irregularly variable sources are a factor 2.5 more conservative than for sources with predictable fluxes. Predictable variables are treated as nonvariable for this purpose. Examples of sources for which variability is predictable are Cepheids or eclipsing binaries. Irregularly variable sources are, for instance, cataclysmic variables or AGN.
[b] While this is the health limit, the detector becomes non-linear at ~22 counts/second/pixel.
[c] Applies to the brightest state of the target.

You can use the information presented in Section 9.2 to calculate peak and global count rates. You can also use the ETC to

calculate the expected count rate from your source. The ETC has a host of template stellar spectra. If you have a spectrum of your source (e.g., from IUE, FOS, GHRS, or STIS) you can also use it directly in the calculator. As implied by the footnotes to Table 7.4, the model spectra in the ETC cannot be used for bright object checking at the solar spectral type and later; the UV spectra of such stars are dominated by emission lines and continua not reproduced by the models. For these types, more realistic theoretical or observational input spectra (e.g., from the IUE or HST archives) must be used (ACS ISR 2019-10). The calculator will evaluate the global and per pixel count rates, and will warn you if your exposure exceeds the absolute bright object limits.

7.2.2 Policy and Observers' Responsibility in Phase I and Phase II

> ⚠ *It is the responsibility of the observer to ensure that observations do not exceed the bright object count rate limits stated in Table 7.3. Please address this issue in your Phase I proposal.*

It is your responsibility to ensure that you have checked your planned observations against the brightness limits prior to proposing for Phase I. To conduct this check, use the bright object tool (BOT) in APT. The APT training page contains detailed instructions on running the BOT. If your proposal is accepted and we (or you) subsequently determine in Phase II that your source violates the absolute limits, then you will either have to change the configuration or target, if allowed, or lose the granted observing time. We request that you address the safety of your SBC targets by means of the ACS ETC, and if needed, consult with an ACS Instrument Scientist via the Help Desk. For SBC target-of-opportunity proposals, please include in your Phase I proposal an explanation of how you will ensure that your target can be safely observed.

In Phase II, proposers of SBC observations are required to check their targets and fields in detail for excessively bright sources by the Phase II deadline. The relevant policies and procedures are described in more detail in the Phase II Proposal Instructions.

The BOT conducts detailed field checking prior to SBC program implementation. It is based on automated analysis of the fields by means of data from the second Guide Star Catalogue (GSC2) and displays of the Digital Sky Survey (DSS). GSC2 provides two magnitudes (photographic J and F), hence one color, for most fields down to about 22nd magnitude. Combined with conservative spectral-type vs. color relationships, this color supports determinations of safety or otherwise for individual objects. In the best cases, these procedures allow expeditious safety clearing, but in some cases the GSC2 is inadequate because of crowding or absence of one of the filters, for instance. Then supplementary information must be provided by the proposers to support the bright object protection (BOP) process. The target should always be checked directly in the ETC with the more detailed information generally available for it, rather than relying on its field report data.

Subsequently, automated GALEX screening has been added as a selectable option in the BOT. GALEX All-sky Imaging Survey (AIS) sources are screened as unreddened O5 stars and reported as either safe or unsafe. This is a powerful tool because it is based directly on UV fluxes; e.g., previously unknown hot companions to late-type stars will be revealed.

The target should still be checked by entering the appropriate GALEX magnitude into the ETC. Unsafe objects require further investigation; the GALEX fluxes are upper limits in crowded regions because of the relatively low spatial resolution, or the source may clear with more specific parameter information.

Table 7.4: Bright limit V-band magnitudes for observations with the SBC filters and prisms (no reddening) (ACS ISR 2019-10).

Spectral Type[a]	F122M	F115LP	F125LP	F140LP	F150LP	F165LP	PR110L	PR130L
O5V	16.3	19.5	19.4	18.7	18.1	16.7	19.0	19.0
B1V	15.5	18.8	18.6	17.9	17.4	16.0	18.2	18.2
B3V	14.6	18.0	17.9	17.3	16.8	15.5	17.5	17.5
B5V	13.6	17.2	17.2	16.7	16.2	14.8	16.8	16.8
B8V	12.3	16.3	16.2	15.8	15.3	14.1	15.8	15.9
A1V	9.4	14.1	14.0	13.9	13.7	12.8	13.7	13.8
A5V	6.8	12.1	12.1	12.0	12.0	11.8	11.9	11.9
F0V	4.9	10.3	10.3	10.3	10.3	10.2	10.1	10.1
F2V	4.3	9.8	9.7	9.7	9.7	9.6	9.5	9.5
78 UMa, F2V[b]	--	10.2	10.1	10.0	9.9	9.8	9.9	9.8
F5V	2.5	8.2	8.1	8.1	8.1	8.0	7.8	7.8
Iota Peg, F5V[b]	--	8.6	8.5	8.4	8.3	8.1	8.1	8.1
F8V	1.0	7.1	7.1	7.0	7.0	7.0	6.3	6.3
Beta Vir, F9V[b]	--	7.3	7.2	7.1	7.0	6.8	6.6	6.6
Beta Hyi, G0V[b]	--	6.9	6.7	6.6	6.5	6.2	5.9	5.9
Sun, G2V	2.5	6.4	6.2	6.2	6.2	6.0	5.2	5.1
Tau Ceti, G8V[b]	--	6.2	6.1	6.0	5.9	5.7	5.1	5.0
Epsilon Eri, K2V[b]	--	6.2	5.9	5.7	5.6	5.2	5.2	5.1
Alpha Bootes, K2III [b]	--	4.5	4.5	4.3	4.2	4.0	3.0	3.0
Alpha Ceti, M2III[b]	--	4.6	4.6	4.1	3.9	3.5	3.7	3.8
Binary[c]	14.6	17.8	17.6	17.0	16.4	15.0	17.2	17.2

a O5V through F8V values, not including named individual stars, are based on Castelli & Kurucz models.

b The magnitudes listed for these stars are generated from combining IUE data and model spectra for the stellar types and renormalizing the combined spectrum (using pysynphot) to the magnitude that corresponds to 50 counts/sec in the

brightest pixel. The F122M magnitudes are not listed because the Ly-α line in the IUE spectra may be contaminated by Earth's geocoronal emission. The F115LP filter also contains the Ly-α line in its passband, and therefore the F115LP magnitudes for these stars are more uncertain than in the other filters.

[c] System made of a late-type star with an O5 companion contributing 20% to the total light in the V band. In the UV, the O5 component dominates and sets the same magnitude limit for companion types A to M.

STScI will check all targets and fields before any SBC observations are cleared. However, it is STScI's policy that GOs must provide screened, safe targets for SBC programs, and supplementary data as needed to verify target and field safety. The APT/BOT, including an Aladin interface, makes the BOP procedures accessible for GO use. Extensive help files and training movies are available on the HST Training Materials webpage.

All SBC proposers must conduct BOP reviews of their targets and fields in conjunction with their Phase II preparations. With this information, they will become aware of any problems earlier, such as the need for supplementary data, which may otherwise entail lengthy implementation delays following the Phase II deadline. (An exception is moving target fields, which must be cleared after the scheduling windows have been established.) To assist with these procedures, a Contact Scientist (CS) who is an SBC/BOP specialist will be assigned to each SBC program to interact with the GO during the Phase II preparations and through program execution.

To briefly summarize the BOP process, a field of 70 arcseconds in diameter must be cleared for a single default SBC pointing with an unconstrained orientation. The APT/BOT automatically reports on all GSC2 stars or GALEX sources within that field. If any displacements from the default pointing (e.g., POS TARGs, patterns, or mosaics) are specified, the field to be cleared increases commensurately. POS TARG vectors and the enlarged, rotated field circles are conveniently displayed in APT/Aladin. No unsafe or unknown star may lie within 5 arcseconds of the detector edge at any orientation. Conversely, POS TARGs and orientation restrictions may be introduced to avoid bright objects in the fields. In case a single guide star implementation becomes necessary, the field to be cleared increases to 140 arcseconds in diameter, but usually that will not become known until scheduling is attempted after the Phase II deadline.

By the Phase II deadline, a SBC GO must send their CS ETC calculations for each discrete target and reports on any unsafe or unknown stars from APT/BOT for each field, either showing that the observations are safe or documenting any unresolved issues. In the latter case, including inadequacy of BOT/GSC2 to clear the observations, other photometric or spectroscopic data sources must be sought by the GO to clear the fields. Many of these are available directly through the APT/Aladin interface (although automatic BOP calculations are available only with GSC2 and GALEX), including the Mikulski Archive for Space Telescopes (MAST), which contains IUE and GALEX data in addition to *HST* data. An existing UV spectrum of the target or class may be imported directly into the ETC. IUE data must be low resolution and large aperture for BOP. None of the provided models are adequate for stars later than the Sun because they lack chromospheric emission lines; actual UV data must be used for them. As shown in Table 7.4, some F stars also do not match expectations from the models, and therefore, checking actual UV data for those stars is highly recommended as well (ACS ISR 2019-10). In worst cases, new ground-based data or *HST* CCD UV exposures may be required to clear the fields for BOP. In general, the latter must be covered by the existing Phase I time allocation.

If a given star has only a V magnitude, it must be treated as an unreddened O5 star. If one color is available, it may be processed as a reddened O5 (which will always have a lower UV flux than an unreddened star of the same color). If two colors are available, then the actual spectral type and reddening can be estimated separately. The APT/BOT now automatically clears stars with only a single GSC2 magnitude, if they are safe on the unreddened O5 assumption. Any other "unknowns" must be cleared explicitly.

In some cases, the 2MASS JHK might be the only photometry available for an otherwise "unknown" star. It is possible to estimate V and E(B–V) from those data on the assumption of a reddened O5 star, and thus determine its count rates in the ETC. Martins & Plez 2006, A&A, 457, 637 derive $(J–H)_0 = −0.11$ for all O stars and $(V–J)_0 = −0.67$, $(V–H)_0 = −0.79$ for early O types. The K band should be avoided for BOP because of various instrumental and astrophysical complications. In Bessell & Brett 1988, PASP, 100, 1134, Appendix B gives relationships between NIR reddenings and E(B–V). These data determine the necessary parameters. Note that the ETC also supports direct entry of observed J and H magnitudes with E(B–V).

It is not expected that all such issues will be resolved by the Phase II deadline, but they should at least be identified and have planned resolutions by then. Another possible resolution is a change to a less sensitive SBC configuration. Any SBC targets or fields that cannot be demonstrated to be safe to a reasonable level of certainty as judged by the CS will not be observed. It is possible that equivalent alternative targets can be approved upon request in that case, but any observations that trigger the onboard safety mechanisms will not be replaced.

A related issue is SBC pointing specification changes after the targets and fields have been cleared by the STScI BOP review. Any such changes must be approved by the ACS Team on the basis of a specific scientific justification and a new BOP review by the GO, which may be submitted via the CS if absolutely necessary. However, in general such requests should be avoided by ensuring that submitted SBC specifications are final, to prevent a need for multiple BOP reviews.

GOs planning SBC observations of unpredictably variable targets, such as cataclysmic variables, are reminded of the special BOP procedures in effect for them, which are detailed in ACS ISR 2006-04.

Policy on Observations Which Fail Because they Exceed Bright-Object Limits

If your source passes screening, but causes the automatic flight checking to shutter your exposures or shut down the detector voltage causing the loss of your observing time, *then that lost time will not be returned to you*. It is the observer's responsibility to ensure that observations do not exceed the bright-object limits.

7.2.3 Bright-Object Protection for Solar System Observations

Observations of planets with the SBC require particularly careful planning due to very stringent overlight limits. In principle, Table 7.3 and Table 7.4 can be used to determine if a particular observation of a solar-system target exceeds the safety limit. In practice, the simplest and most straightforward method of checking the bright object limits for a particular observation is to use the ETC. With a user-supplied input spectrum, or assumptions about the spectral energy distribution of the target, the ETC will determine whether a specified observation violates any bright object limits.

Generally speaking, for small (< ~0.5 to 1 arcseconds) solar system objects, the local count rate limit is the more restrictive constraint, while for large objects (> ~1 to 2 arcseconds), the global limit is more restrictive.

As a first approximation, small solar system targets can be regarded as point sources with a solar (G2 V) spectrum, and if the V magnitude is known, Table 7.3 and Table 7.4 can be used to estimate whether an observation with a particular SBC

prism or filter is near the bright-object limits. V magnitudes for the most common solar system targets (all planets and satellites, and the principal minor planets) can be found in the Astronomical Almanac. This approximation should provide a conservative estimate, particularly for the local limit, because it is equivalent to assuming that all of the flux from the target falls on a single pixel, which is an overestimate, and because the albedos of solar system objects in the UV are almost always significantly less than their values in the visible part of the spectrum. A very conservative estimate of the global count rate can be obtained by estimating the peak (local) count rate assuming all the flux falls on one pixel, and then multiplying by the number of pixels subtended by the target. If these simple estimates produce numbers near the bright object limits, more sophisticated estimates may be required to provide assurance that the object is not too bright to observe in a particular configuration.

For large solar system targets, checking of the bright object limits is most conveniently done by converting the integrated V magnitude (V_0, which can be found in the Astronomical Almanac) to V magnitude/arcsec^2 as follows:

(11)
$$V/(\mathrm{arcsec}^2) = V_0 - 2.5 \log{(1/\mathrm{area})}$$

where area is the area of the target in arcsec^2. The surface brightness and the diameter of the target in arcseconds can then be input into the ETC (choose the solar template spectrum for the spectral energy distribution) to test whether the bright object limits are satisfied.

7.2.4 Prime and Parallel Observing with the SBC

STScI will perform screening of all SBC exposures prior to scheduling. Targets not established as safe for the configuration in which they are being observed will not be scheduled. Observations that pass screening but are lost in orbit due to a bright object violation will not be rescheduled. Observers are responsible for ensuring that their observations do not violate the SBC count rate limits.

To ensure that STScI can adequately screen observations, special constraints are imposed on parallel observing with the SBC (see Section 7.9 for details on parallel observations). In particular:

- No pure or coordinated parallels are allowed using the SBC
- SNAPSHOT observations with the SBC are not allowed

Table 7.5: Bright object protection policy for SBC observations.

Type of observing	Policy
Prime	Allowed if target passes screening
Snapshots	Not allowed
Coordinated parallel	Not allowed
Pure parallel	Not allowed

Targets that are one magnitude or more fainter than the magnitude limits in the screening tables generally automatically pass screening. For a target that is within one magnitude of the screening limits, observers must provide a calibrated

spectrum of the source at the intended observing wavelength. If such a spectrum is not available, the prospective GO must request an orbit in Phase I for a pre-qualification exposure, during which the target spectrum must be determined by observation in an allowed configuration.

Please note that if you are proposing SBC target-of-opportunity observations, we ask you to provide an explanation in your Phase I proposal of how you will ensure that your target can be safely observed.

7.3 Operating Modes

> ⚠️ *HRC has been unavailable since January 2007.*

ACS supports two types of operating modes:

- ACCUM for each of the cameras. This is the standard data taking mode used by observers.
- ACQ (acquisition). This was the mode used to acquire a target for coronagraphic observations. ACQ was only available with the HRC.

7.3.1 WFC ACCUM Mode

In this mode, the WFC CCD accumulates signal during the exposure in response to photons. The charge is read out at the end of the exposure and translated by the A-to-D converter into a 16 bit data number (DN), ranging from 0 to 65,535. The number of electrons per DN can be specified by the user as the GAIN value. The full well of the WFC CCD is about 85,000 electrons and consequently, all GAIN values larger than 1 will allow the observer to count up to the full well capacity. For GAIN=1, only 75% of full well capacity is reached when the DN value saturates at 65,535. The readout noise of the WFC CCD is about 4 electrons RMS and thus is critically sampled at GAIN=2. WFC can make use of a user-transparent, lossless, on-board compression algorithm, the benefits of which will be discussed in the context of parallel observations. The algorithm is more effective with higher GAIN values (i.e., when the noise is undersampled). Note that only GAIN=2 is supported by STScI.

Several supported apertures (see Table 7.7) are accessible to WFC users. `WFC1-FIX` and `WFC2-FIX` select the geometric centers of the two WFC camera chips. `WFCENTER` corresponds to the geometric center of the combined WFC field, and is useful for facilitating mosaics and obtaining observations at multiple orientations. Due to maximal CTE loss, `WFCENTER` is not recommended for a single compact target. `WFC`, `WFC1`, and `WFC2` are located near the field of view center and the centers of chips 1 and 2, respectively (see Figure 7.3). Their locations were chosen to be free of detector blemishes and hot pixels, and they are the preferred apertures for typical observations. See Section 7.7 for more details about ACS apertures, including subarray apertures.

Usually each CCD is read from two amplifiers to minimize charge transfer efficiency (CTE) losses and readout time. As a result, the two 2K by 2K halves of a single chip will have slightly different readout noise. The WFC chips have both a physical prescan and a virtual overscan that can be used to estimate the bias level and the readout noise on each single image. The present flight software does not allow reading an ACS frame directly into the *HST* onboard recorder. Images must first be stored in the internal buffer. When more than one WFC full-frame image is obtained during an orbit, a buffer dump must occur during the visibility period so as to create space in the buffer for a new WFC image.

> ⚠️

> *If each WFC full-frame exposure is longer than approximately 337 seconds, buffer dumps can occur during the integration of the following image with no impact on observing efficiency.*

Conversely, short full-frame integrations with the WFC during the same orbit will cause buffer dumps to be interleaved with observations and will negatively affect the observing efficiency. See Chapter 8 for more details about ACS overheads.

WFC CCD Subarrays

It is possible to read out only a portion of a detector with subarrays, which have a smaller size than the full frame. Subarrays are used to reduce data volume, to store more frames in the internal buffer (thus avoiding the efficiency loss due to buffer dumps), or to read only the relevant portion of the detector when imaging with ramp filters, polarizers, or HRC filters (which produce a vignetted field of view on WFC). The supported WFC subarray modes were made available to users in October 2016, at the beginning of Cycle 24. As noted in Section 2.1, the post-SM4 WFC electronics have the property that differences in CCD readout timing can result in a significant difference in bias structure. This was observed between WFC full-frame and subarray images prior to the update in October 2016. It is also the case that the profile of CTE trailing varies markedly with different CCD readout timings, particularly in the dwell time between parallel shifts. Lastly, subarray modes in place before October 2016 were reading out all 4096 columns of the CCD and retaining only a small portion of them. Because of this, some subarray readout overheads were actually larger than the full-frame readout overhead. The subarray update in October 2016 revised the *HST* flight software so that all WFC subarray modes have exactly the same readout timing as the full-frame readout.

There are three geometry choices at each amplifier corner, resulting in twelve supported subarray modes, listed in Table 7.8. The readout areas are rectangles with 2048 columns (plus 24 columns of physical prescan) and either 512, 1024, or 2048 rows. The full 2048 columns are retained for all subarrays, so that the scene-dependent bias shift (ACS ISR 2012-02) can also be corrected exactly as with full-frame readout. Situating the subarrays at the amplifier corner mitigates the impact of the degraded CTE on source photometry, astrometry, and morphology. At the time of writing, the WFC amplifier with the lowest readout noise is amplifier B. Therefore, subarrays that use amplifier B are recommended over other amplifiers whenever possible. The reference pixel and extent of the subarrays are listed in Table 7.8. Calibration frames will be provided for supported subarrays only. Users who propose non-supported subarrays must request their own subarray bias images, which will typically be scheduled during the Earth-occultation portion of their *HST* visits. More information about pre-defined subarray apertures can be found in Section 7.7.

The bias-striping effect (ACS ISR 2011-05) is present in all post-SM4 subarrays. If de-striping is desired, it must be performed by the user with **acs_destripe_plus** (see Section 5.2.6). If pixel-based CTE correction is desired, de-striping beforehand (if appropriate) is highly recommended. Table 7.6 contains guidance for de-striping and CTE-correcting subarrays based on their observation dates.

Table 7.6: WFC subarray modes and processing considerations.

Subarray Mode	Pre- or Post-SM4 electronics?	Is bias striping present?	Can CTE-correction be performed?
Before Oct 2016 (Cycle 23 and before)	Pre-SM4, Before July 2009	No	Yes, only 2k × 2k subarrays [a]
		Yes	Yes, only 2k × 2k subarrays [b]

	Post-SM4, After July 2009		
After Oct 2016 (Cycle 24 and after)	Post-SM4, After July 2009	Yes	Yes, all subarrays [b]

[a] Perform processing with CALACS with CTE correction enabled.

[b] Perform processing with **acs_destripe_plus** with CTE correction enabled.

Ramp Filters

 In practice, the observer specifies a ramp filter and a central wavelength and the the filter wheel is automatically rotated to place the central wavelength at the reference point of the relevant aperture. The different ramp apertures and their reference points on the WFC CCDs are shown in Table 7.7 and Figure 7.4.

Unlike WFPC2, ACS ramp filter observations at different wavelengths are obtained at the same location on the CCD, thus simplifying data processing. To select the desired wavelength, the ramp filter is automatically rotated to move the central wavelength specified by the observer over the reference point of the relevant aperture. Observations with different ramp filters do not generally occur at the same pointing. The precise location where a given observation will be performed can be found from Table 7.7, which lists the reference points for the apertures corresponding to the inner IRAMP, middle MRAMP, and outer ORAMP filter segments for each ramp filter. The inner segment corresponds to the WFC1 CCD, while the outer segment corresponds to the WFC2 CCD. The middle segment can be used with either of the WFC CCDs, but only the WFC1 aperture is supported.

For any ramp filter observation, three ramp filters will end up in the FOV even though the target is properly positioned for only the requested one. Table 5.1 and Table 5.2 can be used to determine if the remaining two ramp filter segments are useful for serendipitous observations. The user can request either full-frame readout or the 2K subarray readout containing only the primary ramp filter's illumination region.

7.3.2 SBC ACCUM Mode

The SBC ACCUM mode accumulates photons into a 1024 by 1024 pixel array, with 16 bits per pixel. The data are sent to the onboard recorder via the internal ACS memory buffer at the end of the exposure. ACCUM is the only mode available for SBC observations; the Time Tag mode of the STIS MAMAs is not available on ACS. The minimum SBC exposure time is 0.1 second and the maximum is 1.0 hour. The minimum time between SBC exposures is 40 seconds.

The maximum number the memory buffer can accommodate is 65,535 counts per pixel in a given observation. When accumulated counts per pixel exceed this number, the values will wrap, i.e., the memory resets to 0. The accumulated counts per pixel can be kept below this value by breaking individual exposures into multiple identical exposures, each of which is short enough that fewer than 65,535 counts are accumulated per pixel. Note that the SBC, like the STIS MAMAs, has no readout noise. As a consequence there is no scientific driver for longer exposure times apart from the small overhead between successive images, described in Section 8.2.

Up to 16 SBC images can be stored in the internal buffer. SBC images can also share the buffer with a single, compressed WFC image.

7.4 Patterns and Dithering

A number of dither patterns are available for ACS that automatically shift the target pointing between exposures. The size of the shifts depends on the purpose of dithering between exposures. It is useful to distinguish between *mosaicing* and *dithering*. Mosaicing is done with the aim of increasing the area covered by a particular set of exposures, while providing a seamless joining of contiguous frames. Dithering is done for a variety of reasons, such as:

- Better removal of detector blemishes
- Straightforward removal of hot pixels
- Improving the PSF sampling
- Improving the photometric accuracy by averaging over flat fielding errors
- Obtaining a contiguous field of view for the WFC (filling in the interchip gap)

Patterns have been defined that easily implement mosaicing and dithering. These patterns allow exposures to be automatically associated in CALACS pipeline processing with the following restrictions: only exposures obtained within a single visit and exposures whose cumulative offset is under the ~100 arcsecond guide star limitation can be associated. The latter condition includes the dither patterns for all three cameras, the SBC mosaic patterns, the 2-point `ACS-WFC-MOSAIC-LINE` pattern, and all patterns designed with POS TARGs. These are described in detail on the ACS Dither webpage.

The plate scale for the WFC varies across the FOV by about ±5% due to distortion, so a one pixel dither near the center will be 0.95 or 1.05 pixels near the corners. For this reason, dither patterns should strike a balance between being large enough to reject detector artifacts, and being as compact as possible to maintain the integrity of the pattern over the entire field of view. Large displacements will have varying sub-pixel properties across the image.

In addition to the plate-scale variation associated with the significant ACS geometric distortion, there can also be a temporal variation of the overall image alignment. Some CR-SPLIT images taken during SMOV (SM3B) testing, in which the two components were separated by the scheduling system across orbital occultations (about a one hour gap), showed registration differences of about 0.5 pixel corner-to-corner. Thus, to combine multiple images to create oversampled images at the resolution ACS is capable of providing, the user may need to allow for the general problem of combining distorted, misregistered images. A number of tools are available to help users align and combine dithered data. For information on how best to reduce dithered ACS data we recommend users check the *DrizzlePac* website.

7.5 A Road Map for Optimizing Observations

Dithering and CR-SPLITing more than the minimum recommended values tends to yield higher quality images with fewer residual detector defects, hot pixels, or CR signatures in the final combined image. Dithering is recommended over CR-SPLITs since it allows the removal of both detector artifacts (hot pixels, bad columns, etc.) and cosmic rays. Unfortunately, splitting a given exposure time into several exposures reduces its signal-to-noise when the sub-exposures are readnoise limited.

Broadband and grism WFC exposures longer than about 300 seconds are usually background limited (backgrounds >20e⁻), while medium- and narrow-band images are readnoise limited for all practical exposure times. Thus, the optimal number of sub-exposures is a result of a trade-off between completeness of the unstable hot pixel elimination, CR-rejection, final image quality, and optimal S/N. A schematic flow chart of this trade-off is given in Figure 7.2. The main steps in this, possibly iterative, process are the following:

1. Determine the exposure time required to achieve the desired S/N.
2. Determine the maximum number of acceptable residual CRs in the final combined image. This number depends critically on the scientific objective. For example, for a survey of distant galaxies or a globular cluster color magnitude diagram, a few residual CRs will not compromise the scientific output of the observations. In contrast, for a search for an optical counterpart of a radio- or gamma ray-selected object, even one residual CR would not be acceptable over the region of interest. In this latter case, since we expect about ~4% to 7% of the pixels to be affected by CR hits during a one-orbit exposure on the WFC, the requirement that no pixel in the final drizzle stack be affected by CR hits would force one to use at least 4 sub-exposures. For an experiment in which the number of allowed false alarms is zero (e.g., a search for cosmological supernovae), observers may wish to further increase the number of sub-exposures.
3. Note that even a few thousand residual CR hits cover but a tiny fraction of the 16 megapixel area of the full-frame WFC. In general, the number of pixels affected by coincident CR hits for a given total exposure time and number of sub-exposures N will be:

(12)
$$\left(0.05 \times \frac{\text{Exposure Time}}{2400\text{s} \times N} \right)^{N} \times 4096^{2}$$

4. Determine whether dithering is required. CR-SPLITs do not mitigate unstable hot pixels, sink pixels, or other detector defects. If such features would critically affect the science, then dithering is required to remove them. Hot pixels currently cover nearly 2% of the WFC CCDs though <10% of them are unstable (see Section 4.3.5). For some imaging programs, the spatial resolution provided by the WFC and the presence of some detector defects and hot pixels in the final image are acceptable. For such observations, dithering would not be required and one would simply split the exposure time for CR correction. For observations where several orbits worth of data are obtained with each filter, the best strategy is to observe using a sub-pixel dither pattern *without* obtaining multiple images at each position. Due to the increase of detector defects of the WFC CCDs with age, we only recommend the use of CR-SPLITs over dithering when it is absolutely essential that the sub-exposures place the source of interest at exactly the same location on the detector.

5. Once the required number of individual exposures has been established on the basis of CR rejection and dithering requirements, the observer will need to verify whether the resulting readout noise affects the achieved S/N.

Figure 7.2: Schematic flowchart of the CR-SPLIT vs. dithering vs. S/N trade-off
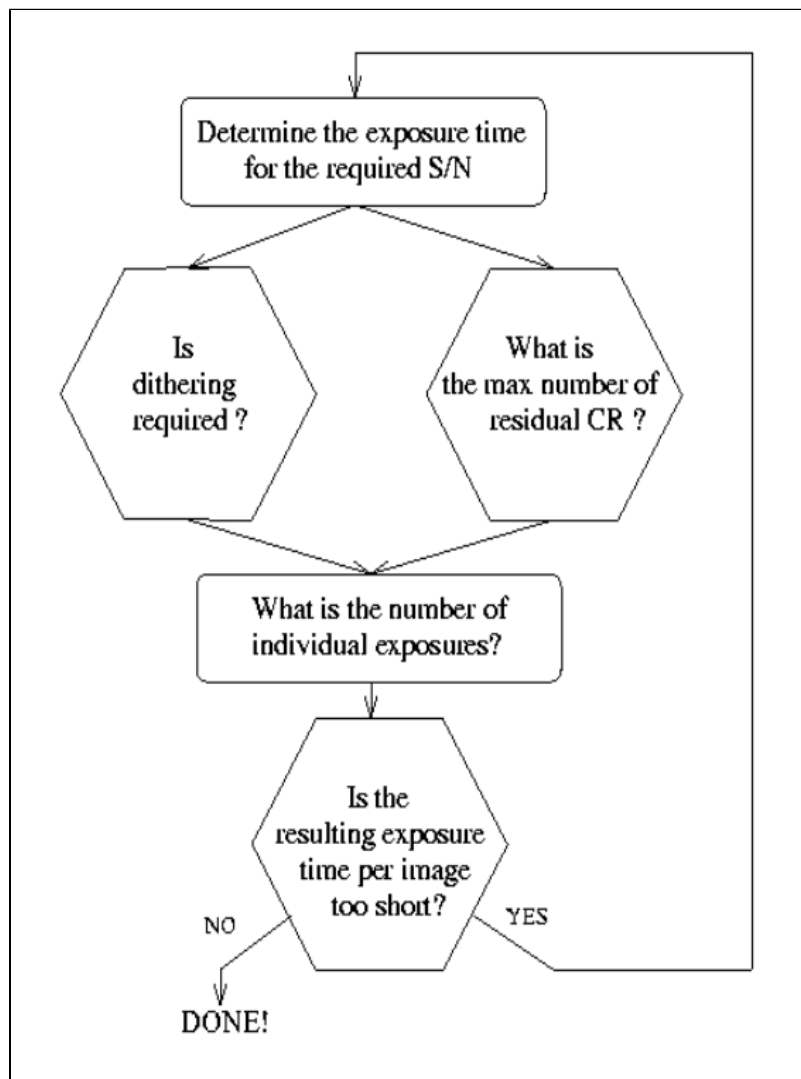
7.6 CCD Gain Selection

> ✅ *Please check for updates on the ACS website.*

As quantified in Table 4.1, the WFC CCDs have selectable gain values of 0.5, 1.0, 1.4, and 2.0 electrons per digital number. Various factors should influence the gain selected in Phase II for your science program: level of support and calibrations provided, influence of associated readout noise on data quality, dynamic range on the bright end, and data compressibility for WFC in limited applications.

Only GAIN=2.0 is fully supported for the WFC. Calibration support will not be provided for the GAIN=0.5, 1.0, and 1.4 settings; users proposing their use should provide special justification and discussion of calibrations to be used. Please note that post-SM4 WFC images appear to have substantial (>10^{-3} fractional) amplifier crosstalk when the ADC saturates.

GAIN=2.0 completely samples the full well depth of nearly 85,000 e⁻. Furthermore, charge is conserved even beyond filling the full well depth; for point sources at GAIN=2.0 it is possible to obtain valid aperture photometry several magnitudes beyond saturation by summing over all pixels affected by the bleeding due to saturation (see Section 4.3.1). GAIN=2.0 provides critical sampling of the readout noise, supporting robust background sky-level determination even at low values.

7.7 ACS Apertures

7.7.1 WFC Apertures

The active image area of each WFC detector is 4096 × 2048 pixel^2. The mean plate scale is 0.05 arcseconds/pixel, and the combined detectors cover an approximately square area of 202 arcseconds on a side. In establishing reference pixel positions, we have to consider the physical prescans, which extend 24 pixels beyond the edges in the horizontal direction. Each CCD must therefore be regarded as a 4144 × 2048 pixel^2 area. The gap between the two CCDs is equivalent to 50 pixels. In Figure 7.3, the letters A, B, C, and D show the corner locations of the four readout amplifiers.

We define apertures named `WFC1` and `WFC2`, which represent the two CCDs, with their reference points near the geometric center of each chip. The positions have been moved about 50 pixels from the center line to avoid a discontinuity at the amplifier readout boundary. However, we keep two other apertures named `WFC1-FIX` and `WFC2-FIX` at the original central locations (2072,1024). For extended sources, choosing new positions may not be of any advantage and it may be more effective to use these fixed positions.

The aperture `WFC` encompasses both detectors, and has its reference point near the overall center but about 10 arcseconds away from the inter-CCD gap. This reference point is (2124, 200) on the WFC1 CCD. Again, this point has been moved away from the center line, but the reference point for `WFC-FIX` remains at (2073, 200). Selection of `WFC1`, `WFC2`, or `WFC` only changes the pixel where the target will be positioned. In all three cases, data is normally delivered in a file containing two science image extensions, one for each detector. See the *ACS Data Handbook* for details of the ACS data format. Reading out a subarray, which consists of part of only one of the CCDs, is done only if requested.

Figure 7.3: WFC aperture definitions.
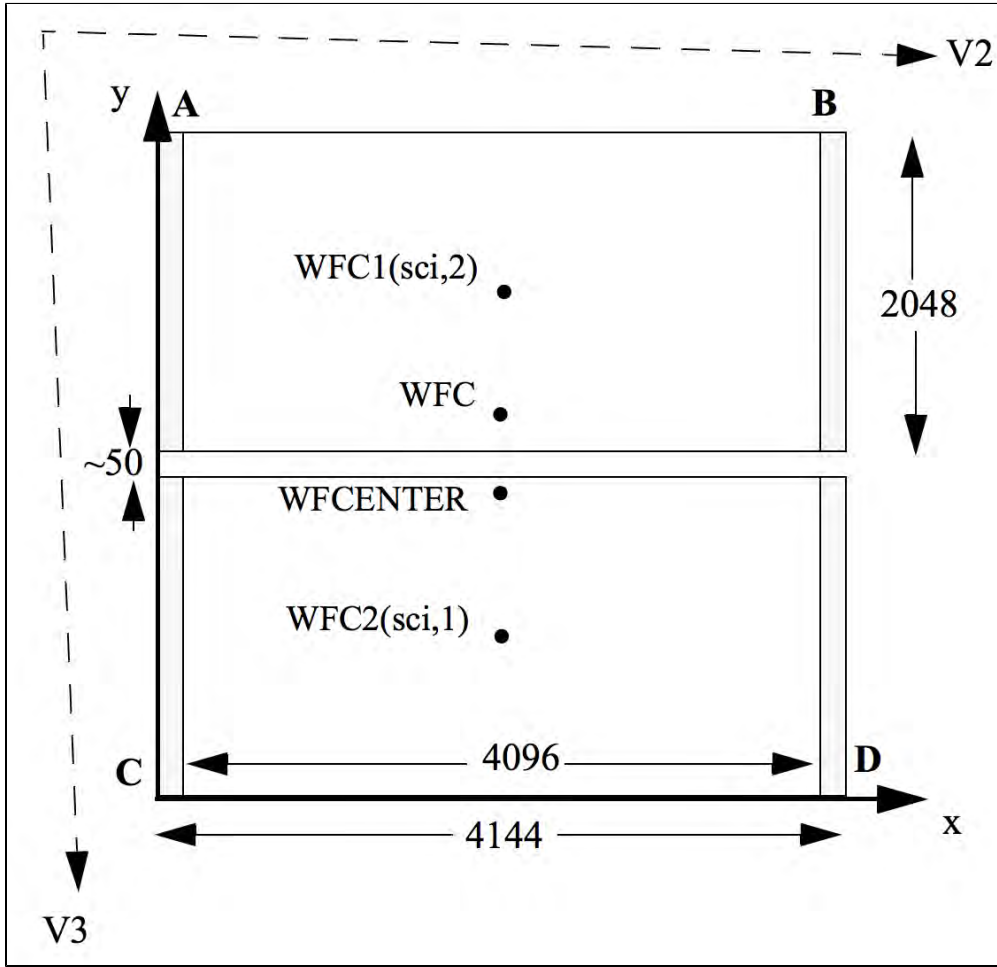
WFCENTER is similar to WFC, but is placed at the center of the combined WFC full field. The center is defined as the average of the four corners in the distortion-corrected space. Because of the scale variation, this does not appear at the center in pixel space, but rather is on WFC2 about 20 pixels from the edge. Selection of WFCENTER can be of use in obtaining observations with maximum overlap at unique orientations and for mosaics.

For sets of observations that take place over a substantial part of a year, the telescope roll limitations will require measurements to be taken over most of the angular range. On sky, the WFC aperture is roughly square, and it is natural to design observations in steps of 90° to consistently cover the same area. There will be some region at the edges not covered at all four orientations. However, a square area of side 194.8 arcseconds centered on WFCENTER, and with edges parallel to the V2 and V3 axes, is overlapped at all four positions. In designing a mosaic that combines observations at 90° steps, a translation of about 190 arcseconds between pointings would provide continuous coverage.

Figure 7.4: Schematic WFC apertures and ramp filters.
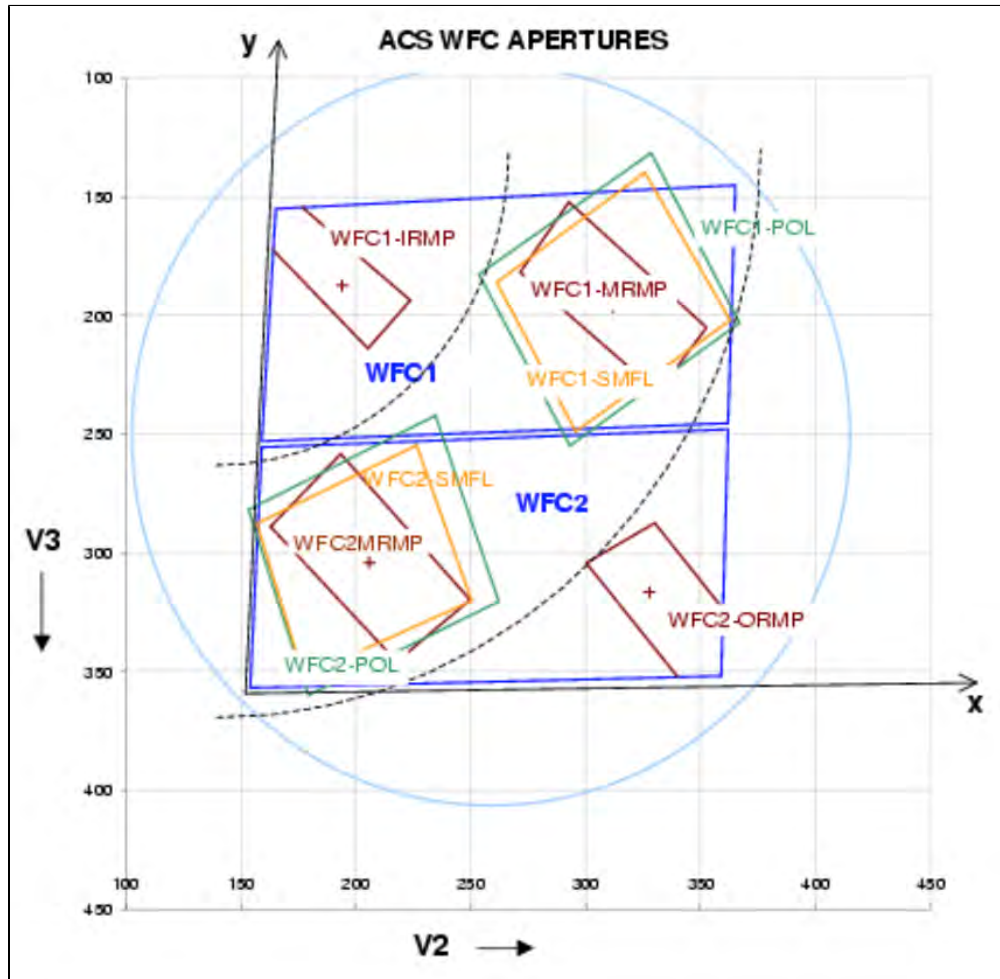
Shown are the approximate active areas defined by the filters. The actual readout areas are the quadrants for the polarizers and small (HRC) filters, and either the quadrant or the full chip for the ramp filters.

7.7.2 Ramp-Filter Apertures

WFC Ramp-Filter Apertures

There are five ramp filters. Each ramp filter consists of three segments (inner, middle, outer) that can be rotated across the WFC field of view as indicated in Figure 7.4. The IRAMP filters can only be placed on WFC1 in a location that will define the aperture `WFC1-IRAMP` and the ORAMP filters only on WFC2 creating the aperture `WFC2-ORAMP`. The MRAMP filters can lie on WFC1 or WFC2 with corresponding apertures `WFC1-MRAMP` and `WFC2-MRAMP`. The approximate aperture locations are indicated in Figure 7.4, while actual data obtained during ground calibrations are overlaid on an image of a ramp filter in Figure 7.5. Operationally, a fixed reference point will be defined for each detector and filter combination. Then the ramp filter will be rotated to place the required wavelength at the reference position.

The reference positions for all defined apertures are given in Table 7.7 in pixels, and in the telescope (V2, V3) reference frame where values are measured in arc seconds. The values given here are based on in-flight calibration results. The x and y axis angles are measured in degrees from the V3 axis towards the V2 axis. This is in the same sense as measuring from North to East on the sky. The "extent" of the ramp filter apertures given in Table 7.7 are the FWHM of the monochromatic patches (visible in Figure 7.4) measured from a small sample of ground calibration data. To use a ramp filter in a Phase II program, specify the filter name, the central wavelength, and the aperture. The scheduling software will then automatically rotate the filter to the appropriate wavelength and point at the reference point of the aperture chosen.

The aperture chosen may either be the full CCD or just the quadrant on which the ramp filter lies. This second choice was new as of Cycle 15, and requires that the aperture be specified. The apertures matching each filter are given in Table 7.7. Those with names ending in Q are the quadrants. It will normally be preferable to choose the quadrant aperture to save data volume and buffer dumping time. All apertures may be used with non-ramp filters. A target may be put at the same position using a ramp and a non-ramp filter. Please see the footnotes to Table 7.7 for a complete list of available but unsupported apertures.

HRC Ramp Filter Apertures

> ⚠️ *HRC has been unavailable since January 2007.*

Only the middle segments of the five ramp filters could be used with the HRC. They are FR914M, FR459M, FR505N, FR388N and FR656N. All five middle segments could be used with any of the HRC apertures listed in Table 7.8 (see Table 7.9 for the aperture reference positions). There were no special ramp apertures with the HRC because when a ramp filter is used with the HRC it covered the entire HRC CCD. This region was defined by the HRC aperture in Table 7.9. To use the `HRC-512` or `HRC-SUB1.8` subarray apertures with a ramp filter, POS TARGs had to be used to align the aperture correctly.

As with the WFC, the fixed reference point of the ramp aperture was defined operationally depending on the detector, aperture, and filter combination. Please refer to Section 7.3.1, Section 5.3.1, and ACS ISR 2002-01 for further information.

Figure 7.5: Monochromatic patches in ground calibration data showing actual aperture sizes through ramp filters (superimposed on photo of ramp filters).

7.7.3 The Small Filter Apertures

When a filter designed for the HRC is used with the WFC, it only covers a small area on either WFC1 or WFC2. The projected filter position can be placed on either chip by selection of the filter wheel setting. Figure 7.4 shows how the filter projection may be placed so as to avoid the borders of the CCDs. When a WFC observation is proposed using a HRC filter, spacecraft commanding software automatically uses internal built-in apertures designed for these observing scenarios, called `WFC1-SMFL` and `WFC2-SMFL`. Reference positions at or near the center of these apertures are defined so that a target may be placed in the region covered by the chosen filter. Note that `WFC2-SMFL` is available but not supported.

The axis angles given in Table 7.7 do not refer to the edges of the apertures as drawn, but rather to the orientation of the x and y axes at the WFC reference pixel. These angles vary slightly with position due to geometric distortion.

For the polarizers and F892N used with WFC, the default is to readout a subarray. The subarray is a rectangular area with sides parallel to the detector edges which encompasses the indicated filtered areas. For ramp filters, the default is to read out the entire WFC detector, unless a polarizer is used with the ramp filter, in which case a subarray is readout. Users cannot override the small filter subarrays.

Table 7.7: WFC aperture parameters.

APT Aperture Name	Readout area	Extent [a] (arcsec)	Reference pixel	Reference V2,V3 (arcsec)	x-axis angle (degrees from V3 through V2)	y-axis angle (degrees from V3 through V2)
WFC	4096 × 4096	202 × 202	(2124,200) on WFC1	(262.41,238.91)	92.163	177.552
WFC-FIX	4096 × 4096	202 × 202	(2072,200)	(259.84,239.01)	92.178	177.532
WFCENTER	4096 × 4096	202 × 202	(2114.1,2029.9) on WFC2	(261.53,252.30)	92.056	177.527
WFC1	4096 × 4096	202 × 202	(2124,1024)	(264.21,198.55)	92.459	177.352
WFC1-FIX	4096 × 4096	202 × 202	(2072,1024)	(261.65,198.66)	92.476	177.329
WFC2	4096 × 4096	202 × 202	(2124,1024)	(259.97,302.48)	91.700	177.780
WFC2-FIX	4096 × 4096	202 × 202	(2072,1024)	(257.37,302.56)	91.710	177.765
WFC1-IRAMP	4096 × 4096	25 × 65	(680,1325)	(194.82,187.43)	93.125	176.619
WFC1-MRAMP	4096 × 4096	35 × 80	(3096,1024)	(312.46,196.61)	92.152	177.776
WFC2-MRAMP	4096 × 4096	40 × 80	(1048,1024)	(206.82,304.16)	91.941	177.464
WFC2-ORAMP	4096 × 4096	35 × 65	(3494,708)	(328.52,316.63)	91.363	178.237
WFC1-SMFL [b]	2048 × 2048	70 × 80	(3096,1024)	(312.46,196.61)	92.152	177.776
WFC2-SMFL [b], [c]	2048 × 2048	70 × 80	(1048,1024)	(206.82,304.16)	91.941	177.464
WFC1-POL0UV [d]	2048 × 2048	90 × 80	(3096,1024)	(312.46,196.61)	92.142	177.761
WFC1-POL0V [d]	2048 × 2048	90 × 80	(3096,1024)	(312.46,196.61)	92.156	177.783
		90 × 80	(1048,1024)	(206.82,304.16)	91.925	177.444

WFC2-POL0UV [c], [d]	2048 × 2048				
WFC2-POL0V [c], [d]	2048 × 2048	90 × 80	(1048,1024)	(206.82,304.16)	91.925	177.454
WFC1A-2K	2048 × 2048	101 × 101	(1048,1024)	(211.69,200.98)	92.845	176.890
WFC1B-2K	2048 × 2048	101 × 101	(3096,1024)	(312.46,196.61)	92.152	177.776
WFC1A-1K	2048 × 1024	101 × 50	(1048,1536)	(213.07,176.39)	93.059	176.708
WFC1B-1K	2048 × 1024	101 × 50	(3096,1536)	(313.45,171.72)	92.303	177.670
WFC1A-512	2048 × 512	101 × 25	(1048,1792)	(213.78,164.20)	93.167	176.612
WFC1B-512	2048 × 512	101 × 25	(3096,1792)	(313.96,159.38)	92.380	177.614
WFC2C-2K	2048 × 2048	101 × 101	(1048,1024)	(206.82,304.16)	91.941	177.464
WFC2D-2K	2048 × 2048	101 × 101	(3096,1024)	(308.82,301.11)	91.518	178.068
WFC2C-1K	2048 × 1024	101 × 50	(1048,512)	(205.72,329.82)	91.722	177.625
WFC2D-1K	2048 × 1024	101 × 50	(3096,512)	(307.96,327.09)	91.368	178.161
WFC2C-512	2048 × 512	101 × 25	(1048,256)	(205.19,343.72)	91.612	177.705
WFC2D-512	2048 × 512	101 × 25	(3096,256)	(307.55,340.14)	91.293	178.207
WFC1-512 [c]	512 × 512	25 × 25	(3864,1792)	(352.33,157.88)	92.106	177.969
WFC1-1K [c]	1024 × 1024	50 × 50	(3608,1536)	(339.04,170.73)	92.130	177.903
WFC1-2K [c]	2048 × 2046	101 × 101	(3096,1024)	(312.46,196.61)	92.152	177.776
WFC2-2K [c]	2048 × 2046	101 × 101	(1048,1024)	(206.82,304.16)	91.941	177.464
WFC1-IRAMPQ	2048 × 2046	25 × 65	(680,1325)	(194.82,187.43)	93.125	176.619

WFC1-MRAMPQ	2048 × 2046	35 × 80	(3096,1024)	(312.46,196.61)	92.152	177.776
WFC2-MRAMPQ [c]	2048 × 2046	40 × 80	(1048,1024)	(206,304)	91.9	177.5
WFC2-ORAMPQ	2048 × 2046	35 × 65	(3494,708)	(328.52,316.63)	91.363	178.237
WFC1-CTE	4096 × 4096	202 × 202	(3920,1848)	(354.24,155.08)	92.099	178.984

a Extent (arcsec) is the smaller of actual pixel domain readout and the area actively exposed to sky. For RAMP associated apertures the leading dimension is size yielding coverage at the specified wavelength.

b Apertures are automatically created by commanding software when an HRC filter is used in WFC observations. (Apertures are not listed in the APT aperture pull-down menu.)

c These are available but unsupported modes.

d Apertures are automatically created by commanding software when a polarizer filter is used. Same parameters apply for POL60 and POL120 in V and UV. (Apertures are not listed in the APT aperture pull-down menu.)

Table 7.8: Ramp filter apertures.

Detector	Filter	Ramp Segment	Full-frame apertures	Quadrant or subarray aperture
WFC	FR423N FR716N FR853N FR5551N FR647M	Inner	WFC1-IRAMP	WFC1-IRAMPQ
WFC	FR388N FR656N FR459M FR505N FR914M	Middle	WFC1-MRAMP	WFC1-MRAMPQ
WFC	FR462N FR782N FR931N FR1016N FR601N	Outer	WFC2-ORAMP	WFC2-ORAMPQ
HRC	FR914M FR459M	Middle	HRC HRC-FIX	HRC-CORON1.8 HRC-CORON3.0

FR505N			HRC-OCCULT08	
FR388N			HRC-ACQ	
FR656N			HRC-SUB1.8	

7.7.4 Polarizer Apertures

Apertures have been provided for use with the polarizer sets similar to the `SMFL` apertures. These apertures are selected automatically when a polarizing spectral element is used, and a single WFC chip quadrant readout is obtained. The aperture parameters given in Table 7.7 are valid for all three polarizing filters in each polarizer set, UV or visible, to the stated significant figures.

7.7.5 HRC Apertures

> ⚠️ *Information regarding the HRC is provided for archival purposes only.*

The HRC had an area of 1062 × 1024 pixel^2 including 19 physical overscan pixels at each end in the x direction. The active area was 1024 × 1024 pixel^2. The mean scales along the x and y directions was 0.028 and 0.025 arcseconds/pixel, thus providing a field of view of about 29 × 26 arcsec^2 in extent. The anisotropy and variation of scales is discussed in Section 10.4. The reference point for the aperture labelled `HRC-FIX`, and initially for `HRC`, was at the geometric center, (531, 512). As with the WFC apertures, there may be reason to move the `HRC` reference point later.

Figure 7.6: HRC coronagraphic finger and spots (left), coronagraphic finger always in data (right)
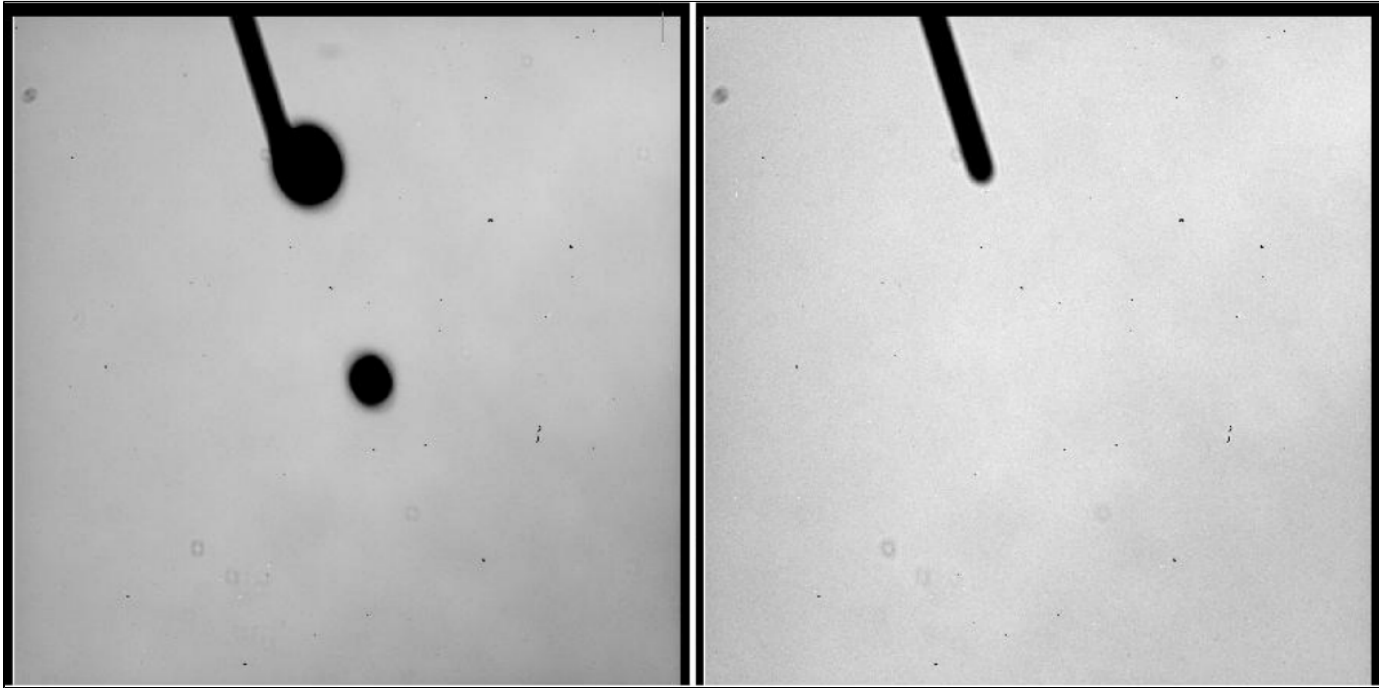
The HRC was equipped with two coronagraphic spots, nominally 1.8 and 3.0 arcseconds in diameter, and a coronagraphic finger, 0.8 arcseconds in width. Apertures `HRC-CORON1.8`, `HRC-CORON3.0`, and `HRC-OCCULT0.8` were defined to correspond to these features. The coronagraphic spots were only in the optical train, and thus in the data, if `HRC-CORON1.8` or `HRC-CORON3.0` was specified. Their locations are shown in Figure 7.6 (left panel). In addition, we defined a target acquisition aperture, `HRC-ACQ`, designed for acquiring targets that were subsequently automatically placed behind a coronagraphic spot or the occultation finger. The positions of the coronagraphic spots had been found to fluctuate. Observations needed to incorporate a `USE OFFSET` Special Requirement to allow current values to be inserted at the time of the observation.

A substantial region masked out by the occulting finger was present in the HRC data (Figure 7.6, right panel). The occulting finger was not retractable. However, as with any other detector feature or artifact, the "lost" data could be recovered by combining exposures which were suitably shifted with respect to each other. A dither pattern, ACS-HRC-DITHER-LINE had been defined for this purpose and spanned the area flagged for the HRC occulting finger (~1.6 arcseconds or ~56 pixels wide), with an extra ~0.3 arcseconds or ~10 pixels of overlap.

Table 7.9: HRC aperture parameters.

APT Aperture Name	Active area	Extent (arcsec)	Reference pixel	Reference V2,V3 (arcsec)	x-axis angle	y-axis angle
HRC	1024 × 1024	29 × 26	(531,512)	(206,472)	−84.1	0.1
HRC-FIX	1024 × 1024	29 × 26	(531,512)	(206,472)	−84.1	0.1
HRC-CORON1.8	200 × 200	6 × 5	(564,466) [a]	(205,471) [a]	−84.1	0.1

HRC-CORON3.0	200 × 200	6 × 5	(467,794) [a]	(208,479) [a]	–84.2	0.1
HRC-OCCULT0.8	200 × 200	6 × 5	(443,791)	(209,477)	–84.2	0.2
HRC-ACQ	200 × 200	6 × 5	(735,575)	(200,474)	–84.1	0.0
HRC-512	512 × 512	15 × 13	(276,256)	(214,465)	–84.1	0.2
HRC-SUB1.8	512 × 512	15 × 13	(570,468)	(205,471)	–84.1	0.1
HRC-PRISM [b]	744 × 1024	21 × 26	(671,512)	(214,471)	–84.2	0.2

a These values fluctuate and will be updated at the time of the observation.
b HRC-PRISM is automatically created by commanding software when spectral element PR200L and aperture HRC are selected in APT.

Use of the prism PR200L required specifying aperture HRC, but resulted in a reference point of (671, 512) to optimally center the target coordinates within the somewhat vignetted prism field of view. Although the HRC direct imaging and PR200L prism apertures had the same name in APT, they were actually distinct, and HST executed a small angle maneuver between observations of a given target with them, to compensate for the positional deflection by the prism. One consequence is that the Special Requirement SAME POS AS could not be used among mixed direct and prism exposures.

7.7.6 SBC Apertures

The SBC aperture is 1024 pixels square. There are no overscan pixels to consider. The x and y scales are 0.034 and 0.030 arcseconds/pixel leading to a coverage on the sky of 35 × 31 arcsec^2. The reference point has been moved to (512, 400) to place targets further from a bad anode that disables several rows of the detector near y = 600. As with the CCDs we maintain an SBC-FIX aperture that will always have position (512, 512). MAMA detectors slowly lose efficiency with each exposure, therefore the SBC reference point may be shifted again if the chosen position exhibits significant loss of efficiency. The new aperture SBC-LODARK was enabled in October 2018. Near the reference pixel (175, 185) of this aperture, the dark rate of the detector remains at nominal level even at high temperatures. This aperture is therefore recommended when a visit will be longer than ~2 orbits and the target is small enough that it will not be affected by the elevated dark rates in the rest of the detector. See ACS ISR 2018-07 for further details.

The (512, 512) reference point falls near to the same position in (V2, V3) as the HRC, namely (205, 470), and the x and y axis angles are –85.4° and –0.9°. Use of either prism PR110L or PR130L requires use of aperture SBC and results in a reference point of (425, 400) to optimally center the target coordinates with respect to vignetting on the right side of the field and to avoid a set of bad rows from 599 to 605.

Although the SBC direct imaging and prism apertures have the same name in APT, they are actually distinct, and *HST* executes a small angle maneuver between observations of a given target with them, to compensate for the positional deflection by the prisms. One consequence is that the Special Requirement SAME POS AS cannot be used among mixed direct and prism exposures. Figure 7.7 shows a direct and prism observation of the same field. The prism now is vignetted on the positive x side. The reference points and the small angle maneuver place the same target near the reference point of each view.

Table 7.10: SBC aperture parameters

APT Aperture Name	Active area	Extent (arcsec)	Reference pixel	Reference V2,V3 (arcsec)	*x*-axis angle	*y*-axis angle
SBC	1024 × 1024	34 × 31	(512, 400)	(205, 467)	−84.6	−0.1
SBC-FIX	1024 × 1024	34 × 31	(512, 512)	(205, 470)	−84.6	−0.1
SBC-PRISM [a]	1024 × 1024	28 × 31	(425, 400)	(203, 467)	−84.6	−0.1
SBC-LODARK	1024 × 1024	24 × 31	(175, 185)	(217, 459)	-84.7	0.4

[a] `SBC-PRISM` is automatically created by commanding software when spectral elements PR110L and PR130L, and aperture `SBC`, are selected in APT.

Figure 7.7: Direct and prism observations of NGC6681.
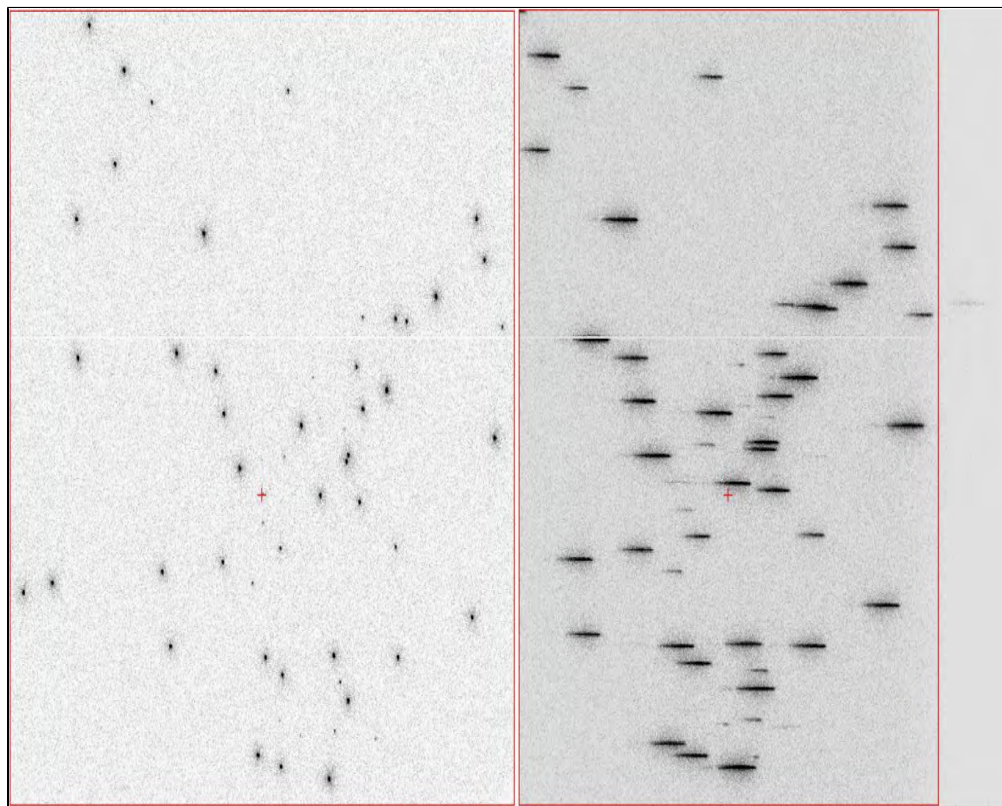
Direct and prism observations of NGC 6681. The reference point is defined to be at the center of each aperture in the x direction but below the center in the y direction to avoid the bad rows.

7.8 Specifying Orientation on the Sky

Determining the orientation of an image requires knowledge of the telescope roll and the angle of the aperture relative to the *HST* coordinate frame. A target may need to be oriented in a preferred direction on a detector, particularly when spectroscopy is to be performed.

To specify an ORIENT in a Phase II, use the ORIENT selection in APT. Keep in mind that this parameter is just the Position Angle (PA) of the *HST* U3 axis, which is the inverse of V3, as seen Figure 3.1 and Figure 7.9 in this Handbook and the *Phase II Proposal Instructions*. APT provides a convenient interactive display of the aperture and orientations in your field. The ORIENT parameter is related to the following discussion of ACS geometry.

All *HST* aperture positions and orientations are defined within an orthogonal Euler angle coordinate system that is labeled V1, V2, and V3, in which V1 is nominally along the telescope roll axis, which is the same as the optical axis. The location of all apertures are therefore defined in the (V2, V3) plane. For more information about *HST* instrument aperture locations and axes in the *HST* FOV, please visit the Observatory Support webpage section on apertures.

The V3 position angle (PA_V3 in Figure 7.8) is defined as the angle of the projection of the V3 axis on the sky, measured from North to East with the aperture denoting the origin. This is almost identical to the telescope roll angle. There is a small difference between roll angles measured at the V1 axis and those measured at the aperture, as the (V2, V3) system is spherical (see ACS TIR 2014-02[1] for more detailed explanation). Due to the fact that ACS is far from the optical axis, this 3-dimensional correction can amount to several tenths of a degree depending on the target declination. In the (V2, V3) coordinate system, as shown in Figure 7.8, aperture orientations are defined by the angles their x and y axes make with the V3 axis, *ßx* and *ßy*, measured in an anticlockwise direction (the value of *ßx* as illustrated in Figure 7.8 would be considered negative). Hence, the angles these axes make with North are found by adding the axis angles to the position angle.

Figure 7.8: Aperture and image feature orientation.
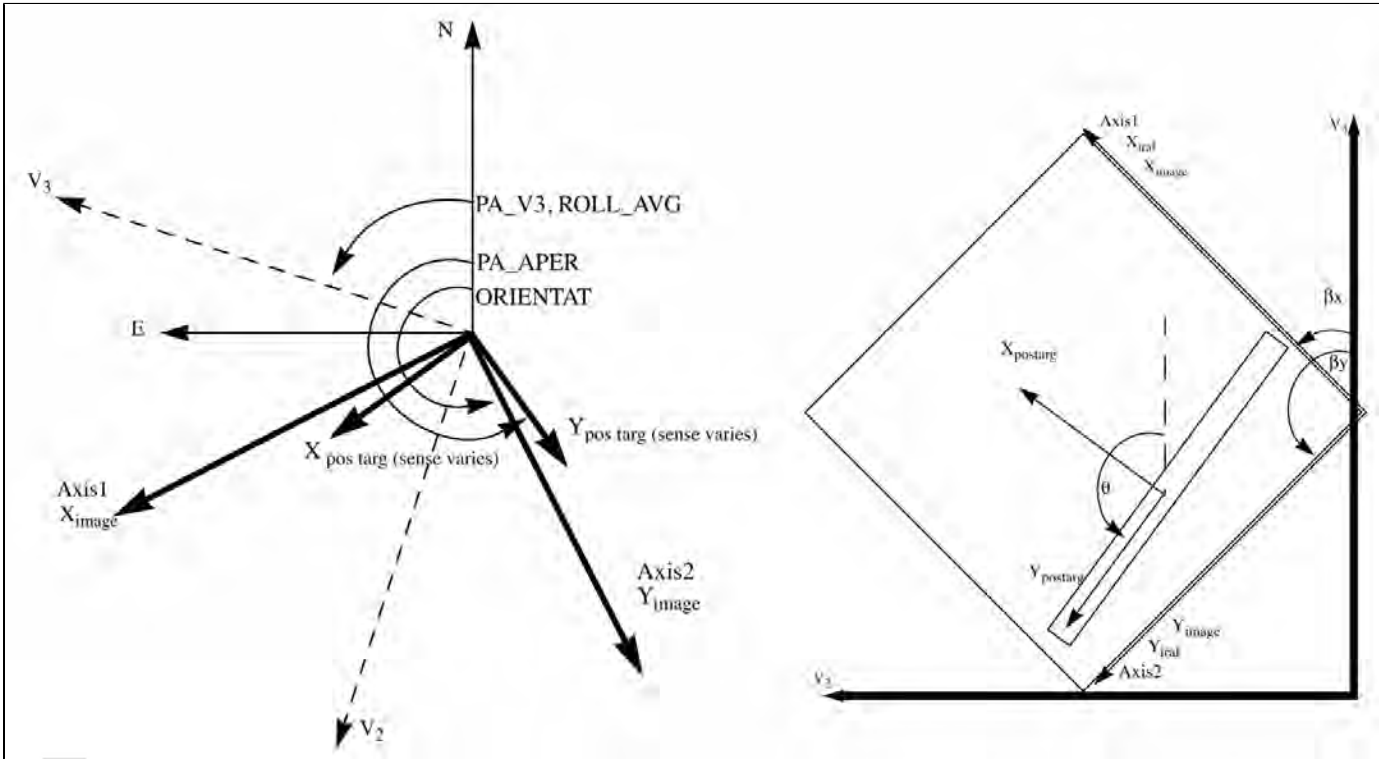
The figure accurately describes ORIENTAT and PA_APER. All of the orientations are taken from HST FOV.

The science image header supplies the value of `ORIENTAT`, the angle the detector y axis makes with North, which is equal to $p + ßy$, where p is the angle from North relative to V3 and $ßy$ is the angle of the y axis of the detector relative to V3. Another angle keyword supplied is `PA_APER`, which is the angle the aperture y axis makes with North. Both angles are defined at the aperture so using them does not involve the displacement difference. Normally, the aperture and detector y axes are parallel, and so `PA_APER = ORIENTAT`. Several STIS slit apertures were not aligned parallel to the detector axes, so this distinction was meaningful, but ACS has no slit apertures so this difference will probably not arise in almost all science cases. In any case, we recommend using `PA_APER` in Phase II's (see Section 7.8.1).

Beyond establishing the direction of the aperture axes, it will often be necessary to know the orientation of a feature, such as the plane of a galaxy, within an image. Conversely, we need to know what direction within an image corresponds to North. To this end we define a feature angle a within the aperture as measured on the science image, anti-clockwise from the y axis so that it is in the same sense as the previously defined angles. For an orthogonal set of aperture axes, the direction of this feature would be PA_APER + a, and the image direction of North would be the value of a which makes this angle zero, namely `PA_APER`, still measured in an anti-clockwise direction from the y axis.

Figure 7.9: ACS apertures in the V2/V3 reference frame.
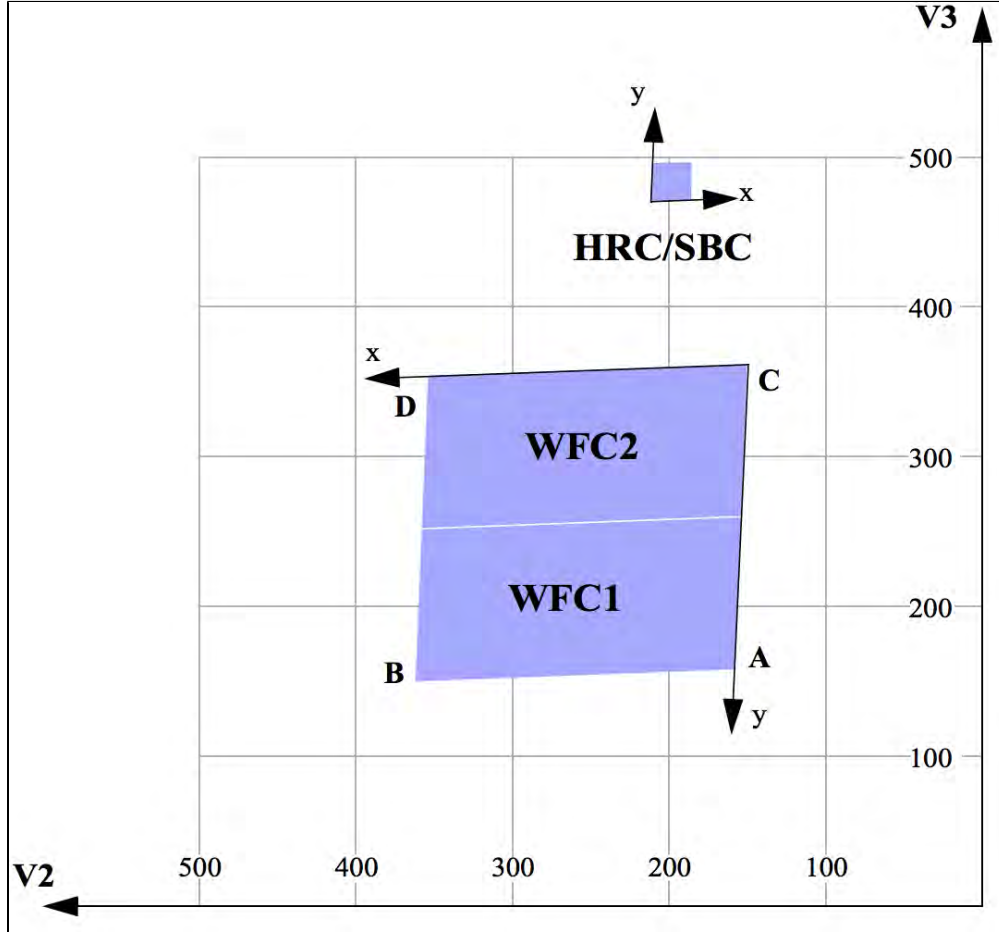
The readout amplifiers (A,B,C,D) are indicated on the figure. The WFC data products from the calibration pipeline will be oriented so that WFC1 (chip 1, which uses amplifiers A and B) is on top. The HRC data products will also be oriented such that amps A and B are on top, but they will be inverted from WFC images with respect to the sky.

The x and y axes projected on the sky are not necessarily orthogonal. For all instruments prior to the ACS, the departure from orthogonality has been negligible, but for the ACS the angle between the axes is about 85°. Figure 7.9 realistically represents the alignment of the ACS apertures and shows that the apertures are not square on the (V2, V3) system or on the sky. The x and y axes indicated are those that will be used for the science images. The (V2, V3) coordinates can be calculated from the x y coordinates according to

(13)
$$V2 = V2_0 + s_x \sin \beta_x x + s_y \sin \beta_y y$$

(14)
$$V3 = V3_0 + s_x \cos \beta_x x + s_y \cos \beta_y y$$

where s_x and s_y are scales in arcseconds per pixel along the image x and y axes. V2 and V3 are the coordinates of the aperture origin, but they do not enter into the angle calculations as they are fixed in the system. Figure 7.9 shows that a

rotation from x to y is in the opposite sense to a rotation from V2 to V3. This will be the arrangement for ACS apertures. This is significant in defining the sense of the rotation angles. For a direction specified by displacements Δ_x and Δ_y in the image, the angle α is arctan($-\Delta_x/\Delta_y$).

Because of the oblique coordinates, the angle α_s on the sky will not be equal to α. To calculate the sky angle, it is convenient to define another set of orthogonal axes (x_s, y_s), similar to the (V2, V3) but rotated so that y_s lies along y, and x_s is approximately in the x direction. Let $\omega = \beta_y - \beta_x$ be the angle between the projected detector axes and let their origins be coincident, for simplicity. Then the transformation is:

(15)
$$x_s = s_x \sin \omega x$$

(16)
$$y_s = s_x \cos \omega x + s_y y$$

By comparing differentials and defining α_s as arctan($-\Delta x_s/\Delta y_s$) we find:

$$\tan \alpha_s = \frac{s_x \sin \omega \sin \alpha}{s_y \cos \alpha - s_x \cos \omega \sin \alpha}$$
(17)

The equation as written will place the angle in the proper quadrant if the Fortran `atan2` function, the IDL `atan` function, or the Python `atan2` function is used. To get the true angle East of North, for a feature seen at angle α in the image, calculate α_s, and add to `PA_APER`.

The inverse relation is

$$\tan \alpha = \frac{s_y \sin \alpha_s}{s_x \sin(\alpha_s + \omega)}.$$
(18)

To find the value of α corresponding to North, we need the value of α_s such that `PA_APER` + α_s = 0. This guarantees that the reference frame is correctly oriented. To do this, substitute `PA_APER` for α_s in the equation to get the angle α in the image that corresponds to North. The values of the pixel scales and axis angles for all instruments are maintained in the *DrizzlePac Handbook*.

For the ACS apertures, the values in Table 7.11 have been derived from results of operating the ACS in the Refractive Aberrated Simulator. These should not be considered as true calibrations but they indicate some aperture features, such as the non-orthogonality of the aperture axes, and the x and y scale differences for HRC and SBC.

Table 7.11: Plate scales and axis angles for the 3 ACS channels.

Aperture	s_x	s_y	β_y	β_x	β_y–β_x
WFC1	0.049313	0.048651	92.46	177.35	–84.89
WFC2	0.049895	0.050328	91.7	177.78	–86.08
HRC	0.028431	0.024843	–84.12	0.08	–84.2

SBC	0.033658	0.030009	−84.56	−0.05	−84.51

7.8.1 Determining Orientation for Phase II

A particular orientation is specified in an *HST* Phase II proposal using yet another coordinate system: (U2, U3). In this system, the U2 and U3 axes are opposite to V2 and V3, so, for example, U3 = −V3. The angle `ORIENT`, used in a Phase II proposal to specify a particular *HST* orientation, is the position angle of U3 measured from North towards East. This means the direction of the V3 axis with respect to North is `PA_APER` − β_y and so

(19)
$$\texttt{ORIENT} = \texttt{PA\_APER} - \beta_y \pm 180°$$

This orientation can be checked by using APT, specifying the orientation, and then viewing in Aladin.

[1]TIRs available upon request.

7.9 Parallel Observations

Parallel observing allows *HST* to operate several other instruments while the prime instrument is executing its observations. While the primary instrument observes a fixed target at user-specified coordinates, the parallel instrument observes at coordinates 5 to 10 arcminutes away, depending on the parallel instrument. The *HST* field of view following SM4 (Figure 3.1) shows the general locations of the instrument apertures adjacent to one another on the sky. Accurate relative positions for all instruments can be found on the HST Observatory Apertures webpage.

The recommended method of determining the field of view for any instrument is to use APT. A Digital Sky Survey (or user supplied) image of the primary target area is displayed with an *HST* field of view overlay. Any desired coordinate and ORIENT combination for the primary target will then display the possible pointings of any instrument operated in parallel. If the primary exposure is to be executed at a specific (absolute) orientation, APT will display the exact field of view for any instrument executed in parallel. If the primary exposure is to be executed at a random (nominal) orient or range of orient values, APT allows the *HST* field of view to be rotated interactively about the primary pointing. APT can be a valuable resource for parallel observing programs, especially those designed for, or restricted to, specific pointings for the parallel FOV.

Certain operating limits are in place to restrict use of configurations, modes, parameters, elements, and requirements allowed for each instrument while used in parallel. Details on these limits are documented in the *HST Proposal Opportunities and Science Policies* pages. General information on ACS-specific parallel operations are documented in the following sections for each of the types of ACS parallel observing: coordinated and pure.

ACS Coordinated Parallels

Coordinated parallel observations are specified in the same Phase II observing program as the primary observations via the prime and parallel group containers in APT. Only a single ACS channel can be used for a coordinated parallel observation, with, and only with, another instrument. Coordinated parallels cannot be used to operate the WFC and SBC simultaneously. ACS exposures cannot be used as both the prime and parallel exposures within the same parallel container.

In order to protect the ACS SBC detector from inadvertent over-illumination, the ACS/SBC configuration is no longer supported as a coordinated parallel.

Users frequently wish to employ ACS and WFC3 in parallel. Because users also generally want to dither their observations, exposures of these two cameras are generally taken synchronously. However, both ACS and WFC3 images must first be loaded into and then transferred from the camera buffers to the solid state data recorders (SSDRs). The ACS buffer can hold only one full frame image, while the WFC3 buffer can hold two full frame optical images and two or more NIR images, depending on the number of NIR readouts per image. However, images from these cameras cannot be transferred to the SSDRs simultaneously, and each transfer takes about 350 seconds. It is possible to take three or more images per orbit in each of the two cameras.

ACS Pure Parallels

In ACS pure-parallel observations, an observation is taken with ACS on an essentially random area of the sky while another instrument is making prime observations. No SBC pure parallels will be allowed due to bright object concerns.

Unlike the previous two types of parallel programs, pure parallels contain only parallel visits. Use of the GO/PAR proposal category will make any visit in the program a pure parallel.

The ACS default (archival) pure parallel program continued to execute for the community until midway through Cycle 13 when all of them were discontinued to prolong the lifetime of transmitters on *HST*. This non-proprietary data came from programs 9575, 9584, and 9701.

Archival pure parallel programs can be queried through MAST using their Program ID. Observers can request ACS pure parallels; however, there are many constraints that can render pure parallels unselectable in any given orbit. Pure parallels will always be given lower priority than primaries, and are thus scheduled only on a non-interference basis. Users should consult the *HST Proposal Opportunities and Science Policies* pages for more information about pure parallel opportunities with ACS.

7.10 Pointing Stability for Moving Targets

Observations of Solar System targets are subject to some special limitations on the achievable pointing stability during a visit. These limitations apply to both two-gyro and three-gyro operations.

For moving targets, the *HST* ground system assumes that the position of the target as seen from the center of the Earth can be approximated as a linear function of time. This is done using rates of motion calculated from the object's ephemeris for a time near the start of each orbit. If the target's geocentric ephemeris departs significantly from this linear approximation over the course of an orbit, this can lead to small but noticeable pointing offsets. If you think this may adversely affect your science, please consult with your Program Coordinator about possible strategies for ameliorating this effect.

The correction for the variable parallax to a Solar System object due to *HST*'s orbit around the Earth is calculated on-orbit using the best ephemeris for *HST*'s orbit that was available at the time the detailed weekly schedule was created. However, the real position of *HST* along its orbit often differs by up to 1 to 2 seconds (7 to 15 kilometers) from the predicted ephemeris position. This leads to small errors in the phasing of the calculated parallax correction. For example, when observing a Solar System object at a distance of 0.5 AU from the Earth, this can cause typical pointing offsets over the course of an orbit of order 20 to 40 milliarcseconds. As these offsets depend on unpredictable changes in *HST*'s orbit, such drifts are unavoidable when observing near-Earth objects.

Chapter 8: Overheads and Orbit-Time Determination

Chapter Contents

8.1 Overview

After you establish a set of scientific exposures, as well as any additional target acquisition or calibration exposures required for your program, you are ready to determine the total number of orbits to request. Generally, this straightforward exercise involves compiling the overheads for individual exposures, packing exposure plus overhead time into individual orbits, and tallying up the results to determine the total number of orbits needed. It may be an iterative process as you refine your exposures to better use the orbit visibility times.

The *Call for Proposals* includes instructions that provide information on the Observatory policies and practices with respect to orbit time requests. The *HST Primer* provides specific advice on orbit determination. Both can be found on the *HST Proposal Opportunities and Science Policies* web page. In this Chapter, we provide a summary of the ACS specific overheads, and give several examples that illustrate how to calculate your orbit requirements for a Phase I Proposal.

8.2 ACS Exposure Overheads

✅ *Please check for updates on the ACS website.*

Exposure overheads are summarized in Table 8.1 and Table 8.2. All numbers given are approximate; they do not make detailed differentiations between overheads for different ACS modes and configurations. These overhead times are to be used (in conjunction with the actual exposure times and the instructions in the *HST Primer* on the *HST Proposal Opportunities and Science Policies* web page) to estimate the total number of orbits for your proposal, but they may not be exact. Please use the APT scheduling software to obtain the best estimates of overhead times for your Phase I proposal. After your *HST* proposal is accepted, you will be asked to submit a Phase II proposal to support scheduling of your approved observations. At that time you will be presented with actual, up-to-date overheads by the APT scheduling software. *Allowing sufficient time for overhead in your Phase I proposal is important; additional time to cover unplanned overhead will not be granted later.*

The following list presents important points for each type of overhead:

Generic (Observatory Level) Overheads

- The first time you acquire an object, you must include overhead for the guide star acquisition (6.5 minutes).
- In subsequent contiguous orbits you must include the overhead for the guide star *reacquisition* (6.5 minutes); if you are observing in the Continuous Viewing Zone (see the Call for Proposals on the Proposal Opportunities webpage), no guide star reacquisitions are required.
- Allocate time for each deliberate movement of the telescope; e.g., if you are performing a target acquisition exposure on a nearby star and then offsetting to your target, or if you are taking a series of exposures in which you move the target on the detector, you must allow time for the moves: 20 to 60 seconds, depending on the size of the slew, (see Tables 8.1 and 8.2).

Table 8.1: Science Exposure Overheads: General.

Action	Overhead
Generic (Observatory Level)	
Guide star acquisition	Initial acquisition overhead = 6.5 minutes. Reacquisitions on subsequent orbits = 6.5 minutes per orbit.
Spacecraft moves	For offsets less than 1.5 arcminutes and more than 10 arcseconds = 1 minute. For offsets between 10 arcseconds and 1 arcseconds = 0.5 minutes. For offsets less than 1 arcseconds in size = 20 seconds.

Table 8.2: ACS Science Exposure Overhead Times (Minutes).

Exposure type	WFC	SBC
Mode: ACCUM		
Single exposure or the first exposure in a series of identical exposures.	4.0	1.4
Subsequent identical exposures in series (within an orbit).	2.5	0.6
Additional overhead for each serial buffer dump (whenever an ACS exposure will exceed buffer storage capacity, and is too short for a parallel buffer dump).	5.8	5.8
Using FLASH	4 sec + 1 sec/14e⁻	N/A
Predefined imaging exposure for grism spectroscopy.	7	N/A

> ⚠ *Target acquisitions were used for the HRC coronographic finger and spot. HRC has been unavailable since January 2007. Information about the HRC is provided for archival purposes.*

Onboard Target Acquisition Overheads

- Onboard target acquisitions are needed to place the target under one of the coronagraphic spots or coronographic finger.
- An onboard target acquisition is done once for a series of observations in contiguous orbits (i.e., once per visit).
- The drift rate induced by the observatory is less than 10 milliarcseconds per hour. Thermal drifts internal to ACS are even smaller.

Scientific Exposures Overheads

- The overhead times are dominated by the time required to move the filter wheel, the CCD readout time, and any necessary serial buffer dumps. Again, it should be stressed that in Phase II, the overheads will frequently be lower, but it is important to plan the Phase I using the conservative overheads given in Table 8.2 to ensure adequate time for the proposal's scientific goals.

Spectroscopy Overheads

- Each CCD spectroscopic observation is preceded by an imaging exposure used for calibration, with exposure times of 3 and 6 minutes, respectively, for grism and prism observations. SBC prism exposures are not preceded by an automatic calibration exposure. Technically, this is an individual single exposure requiring all regular science

exposure overheads. For the observer, however, it represents an additional overhead in the observation time budget, so it has been included in the table of instrument overhead times for science exposures. However, if the observing program is already taking an appropriate broadband image, the automatic imaging and associated overheads preceding the spectroscopic grism or prism observations can be avoided by invoking the Optional Parameter `AUTOIMAGE = NO` during the Phase II preparations. More details can be found in the [Phase II Proposal Instructions](#).

Note that exposures with identical observing modes are automatically generated if the observer specifies:

- Phase II proposal optional parameter CR-SPLIT with a value greater than or equal to 2. (The default value is CR-SPLIT = 0. Single exposures are allowed, but are typically strongly discouraged. A CR-SPLIT value ranging from 2 through 8 may be specified if `Number_of_Iterations` = 1. However, it is recommended that such individual exposures be dithered rather than CR-SPLIT if possible, since dithering allows the observer to mitigate the effects of cosmic rays, unstable hot pixels, and chip defects, and can allow for the recovery of higher resolution than the native pixel scale of the camera.)
- Phase II exposure log sheet field `Number_of_Iterations` is greater than or equal to 2 (where CR-SPLIT must be set to "NO.")
- Phase II special requirement `PATTERN` is used to execute a dither pattern. In this instance, overheads will also include slew overheads.

The overhead time for serial buffer dumps arises, in certain cases, from the overheads associated with the onboard data management and switching over the cameras. The onboard buffer memory has the capacity equivalent to a single full-frame WFC image. If a commanded WFC image cannot fit into the available buffer space upon readout, the buffer must first be dumped. This process requires 349 seconds for an entirely filled buffer, or correspondingly less for a partially filled buffer.

Buffer dump overheads

- If a commanded exposure time is longer than about 340 seconds, for an exposure which cannot fit in the remaining buffer storage, an entirely filled buffer can be dumped during that exposure, and no overhead is imposed. However, if the next exposure time is shorter than about 340 seconds, then the dump may be required to occur between the two exposures, depending on the fraction of the buffer.
- Sequences of many short SBC exposures can also lead to serial dumps when the buffer becomes full. In this case the buffer dump time becomes an overhead to be included into the orbit time budget. This overhead can severely constrain the number of short exposures that can be squeezed into an orbit. Subarrays can be used to lower the data volume for some applications.

The APT scheduling software has an "Orbit Planner" module that shows the buffer-dump periods in relation to the exposure sequence. The prior discussions regarding parallel versus serial buffer-dumping only applies when no other *HST* instrument is taking data at the same time as ACS. Please consult the APT Orbit Planner for buffer dump management when using two instruments simultaneously.

8.2.1 Subarrays

The minimum exposure time for WFC is 0.5 seconds and for HRC was 0.1 seconds. The minimum time between successive identical full frame exposures is ~135 seconds for WFC and was 45 seconds for HRC. These times can be reduced to ~36 seconds using WFC subarray readout modes.

At the end of each exposure, data are read out into ACS's internal buffer memory where they are stored until they are dumped into *HST*'s solid state data recorder. The ACS internal buffer memory holds 34 MB or the equivalent of 1 full WFC frame, or 16 SBC frames. Thus, after observing a full WFC frame, the internal buffer memory must be dumped before the next exposure can be taken. The dump of a completely filled buffer takes 349 seconds and may not occur while ACS is being actively commanded. Of this time, about 340 seconds is spent dumping the image. Correspondingly, less time is required to dump the buffer in parallel, if the buffer is less than full when needing to be dumped to store the next exposure. The buffer dump cannot be executed in parallel with the next exposure if the latter is shorter than about 340 seconds. If the next exposure is less than about 340 seconds, the buffer dump will create an extra 5.8 minutes of overhead.

If your science program is such that a smaller FOV can be used, then one way of reducing the frequency of buffer dumps (and their associated overheads) is to use WFC subarrays. During subarray readouts, only one amplifier is used, and with potentially reduced number of rows from the full 2048. Many more subarray frames can be stored before requiring a buffer dump: four 2K-frames; eight 1K-frames; or sixteen 512-frames. Subarrays with fewer than 2048 rows also benefit from reduced overhead due to smaller readout times.

8.3 Orbit Use Determination Examples

The easiest way to learn to compute total orbit time requests is to work through a few examples. Below we provide five different examples:

- Example in Section 8.3.1 is a simple WFC image in one filter, using dithers.
- Example in Section 8.3.2 is a two-orbit multi-filter WFC observation using dithering.
- Example in Section 8.3.3 is a one-orbit WFC grism spectroscopic observation.
- Example in Section 8.3.4 is a two-orbit SBC observation.

These examples represent fairly typical uses of ACS.

8.3.1 Sample Orbit Calculation 1

Consider a target to be imaged with WFC in a given filter in one orbit. Using the ETC, we find that we need 2400 seconds of exposure time to reach the desired level of signal-to-noise ratio. Given that the observation is split into a series of two dithers, we map the overheads and the science exposure times onto the orbit as follows:

Table 8.3: Orbit Calculation for Example 1

Action	Time (Minutes)	Explanation
Orbit 1		
Initial guide star acquisition	6.5	Needed at start of observation of a new target
WFC overhead for the first exposure	4.0	Includes filter change, camera set-up, and readout
Spacecraft slew	0.5	
First science exposure	20.0	
WFC overhead for the subsequent science exposure in the series	2.5	Includes readout
The next science exposure in the series	20.0	

Total time for science exposures	40.0	
Total used time in the orbit	53.5	

Thus, the two WFC exposures totaling 2400 seconds make full use of the typically available time in one orbit. The exposure times can be adjusted if the actual target visibility time differs from the derived total used time.

8.3.2 Sample Orbit Calculation 2

This example illustrates the orbit calculation for a WFC observation with the ACS box pattern, which implements imaging at four offset pointings. The goal of the observation is to obtain a dithered image of a field in such a way that would allow us to bridge the 50 pixel interchip gap between the WFC CCDs in the combined image. Given the WFC plate scale 0.05 arcseconds/pixel, this requires that the offsets in the dithering pattern are larger than 2.5 arcseconds. Each offset will then take 0.5 minutes to move the spacecraft from one pointing in the pattern to another. We have determined that the exposure time necessary to reach the desired signal-to-noise ratio is 80 minutes. The orbit calculation will involve a series of 8 exposures (two exposures at each of the four pointings in the dithering pattern) split across two orbits. Slew time below is only applicable for slews <10 arc seconds. For longer slews overhead time may increase. If the exposure time of each image is less than 337 seconds, extra time for the buffer dump will be needed:

Table 8.4: Orbit Calculation for Example 2

Action	Time (Minutes)	Explanation
Orbit 1		
Initial guide star acquisition	6.5	Needed at start of observation of a new target
WFC overhead for the first exposures	4.0	Includes camera set-up, and readout
WFC overhead for the second exposures	3.0	Includes filter change, and readout
Spacecraft slew	0.5	
WFC overhead for the third and fourth exposures	2 × 3.0 = 6.0	Includes filter change and readout
Four science exposures	4 × 8.0 = 32.0	
Total used time in the orbit	52.0	
Orbit 2		
Guide star re-acquisition	6.5	Needed at start of observation
WFC overhead for the first and second exposures	2 × 3.0 = 6.0	Includes camera set-up and readout
Spacecraft slew	0.5	
WFC overhead for the third and fourth exposures	2 × 3.0 = 6.0	Includes filter change and readout

Four science exposures	4 × 8.0 = 32.0	
Total used time in the orbit	51.0	

8.3.3 Sample Orbit Calculation 3

This example illustrates the orbit calculation for a simple 30 minute WFC grism spectroscopic observation broken with a series of two dithered exposures.

Table 8.5: Orbit calculation for example 3.

Action	Time (Minutes)	Explanation
Orbit 1		
Initial guide star acquisition	6.5	Needed at start of observation of a new target
Predefined imaging exposure for grism spectroscopy	7.0	Needed to co-locate the targets and their spectra in the FOV
WFC overhead for the first science exposure in the series	4.0	Includes filter change, camera set-up, and readout
Spacecraft slew	0.5	
WFC overhead for the subsequent science exposure in the series	2.5	Includes readout
Two science exposures	2 × 15.0 = 30.0	
Total science exposure time	30.0	
Total used time in the orbit	50.5	

Unlike similar imaging exposures, here we have to take into account an additional imaging exposure before the sequence of spectroscopic exposures, which takes 10 minutes off the available orbit time.

8.3.4 Sample Orbit Calculation 4

This example deals with the orbit calculation for an observation of a relatively faint extended object using the SBC. The target has to be observed using two filters, F150LP and F165LP. The ETC shows that the required S/N for the observations are achieved in 3200 seconds and 2000 seconds for the F150LP and the F165LP filters, respectively. There is no readout noise associated with SBC exposures; therefore, the observations can be split into four equally long dither pointings. Since the average visibility time for the target is ~55 minutes, the images can be taken in two orbits, as shown in Table 8.6 . The standard ACS-SBC-DITHER-BOX pattern, which allows for the rejection of most artifacts, is suitable for these observations. Here are the details of the orbit calculation:

Table 8.6: Orbit calculation for example 4.

Action	Time (Minutes)	Explanation
Orbit 1		
Initial guide star acquisition	6.5	Needed at start of observation of a new target
SBC overhead for the first exposure	1.4	Includes filter change and camera setup
SBC overhead for each of the following three exposures	3 × 1.0	Includes filter change (3 × 0.4 minutes)
Spacecraft slew	0.3	Slew performed between the second and third exposures in this orbit
Exposures with filter F150LP	2 × 13.3 = 26.6	Exposures at the first two pointings of the dither pattern
Exposures with filter F165LP	2 × 8.3 = 16.6	Exposures at the first two pointings of the dither pattern
Total time used in the orbit	54.4	
Orbit 2		
Guide star re-acquisition	6.5	Needed at start of new orbit to observe the same target
SBC overhead for each of the following three exposures	4 × 1.0	Includes filter change (4 × 0.4 minutes)
Spacecraft slew	0.3	Slew performed between the second and third exposures in this orbit
Exposures with filter F150LP	2 × 13.3 = 26.6	Exposures at the first two pointings of the dither pattern
Exposures with filter F165LP	2 × 8.3 = 16.6	Exposures at the first two pointings of the dither pattern

Total time used in the orbit	54.0	

The total time is slightly shorter in the second orbit because of the shorter time required for SBC overheads. There is also ~1 min of visibility available in the first orbit that can be used for the observations. However, we recommend dithered observations in each filter using the same exposure time for each pointing.

Chapter 9: Exposure-Time Calculations

Chapter Contents

9.1 Overview

In this chapter, we explain how to use sensitivities and throughputs to determine the expected count rate from your source, and how to calculate exposure times to achieve a given signal-to-noise ratio taking all background contributions into account. At the end of this chapter, you will find examples to guide you through specific cases. In this chapter, for CCD observations, **one electron is equivalent to one count, unless stated otherwise**.

9.1.1 The ACS Exposure Time Calculator

The ACS ETC is available to help with proposal preparation. It can calculate count rates for given source and background parameters, signal-to-noise ratios for a given exposure time, or count rates and exposure time for a given signal-to-noise ratio for imaging, spectroscopic, and coronagraphic observations. A variety of apertures are now available, both circular and square, allowing the user to either select a radius in arcseconds or a size in pixels. The current default apertures for all three channels enclose 80% of the PSF flux. Square and circular apertures are available between 0.1 and 2.0 arcseconds. For extended sources, the S/N calculation is based on counts summed over one resolution element of 2×2 pixel^2, as the source size is assumed to be larger than the ACS resolution. A calibrated spectrum of your source can be provided directly to the ETC. The ETC also determines peak per-pixel count rates and total count rates to aid in feasibility assessment. Warnings appear if the source exceeds the local or global brightness limits for SBC observations (see Section 7.2). For the CCDs, a warning will appear if the background of the observation is below the recommended limit of 20 electrons. A higher background mitigates CTE losses. An ETC user's guide is available for execution and interpretation of results, and further questions can be directed to the HST Help Desk. Alternatively, users can use **pysynphot** in AstroConda to calculate count rates and the wavelength distribution of detected counts.

9.2 Determining Count Rates from Sensitivities

In this Chapter, specific formulae appropriate for imaging and spectroscopic modes are provided to calculate the expected count rates and the signal-to-noise ratio from the flux distribution of a source. The formulae are given in terms of sensitivities, but we also provide transformation equations between the throughput, QT, and sensitivity, S, for imaging and spectroscopic modes.

Throughputs are presented in graphical form as a function of wavelength for the prisms and for the imaging modes in Chapter 10. Given your source characteristics and the sensitivity of the ACS configuration, calculating the expected count rate over a given number of pixels is straightforward, since the ACS PSF is well characterized. The additional required information is the encircled energy fraction, ε_f, in the peak pixel, the plate scale, and the dispersions of the grisms and prisms. This information is summarized in Table 9.1 and Table 9.2 for observations after the temperature decrease in July 2006. For updates please see the ACS webpage.

Table 9.1: Useful quantities for the ACS WFC, at −81°C (since July 2006).

Filter	Pivot λ(Å)	$\int Q_\lambda T_\lambda$ dλ/λ	$\int S_\lambda$ dλ	ABMAG Zero point	Encircled Energy (0.2 arcsec)	Flux in Central Pixels	Background sky rate (per pixel)
F435W	4329.9	0.0733	3.13 E+18	25.65	0.84	0.22	0.0309
F475W	4747.0	0.1053	5.40 E+18	26.04	0.84	0.21	0.0569
F502N	5023.0	0.0033	1.88 E+17	22.27	0.84	0.21	0.0020
F550M	5581.5	0.0350	2.48 E+18	24.84	0.84	0.22	0.0268
F555W	5361.0	0.0769	5.03 E+18	25.70	0.84	0.21	0.0541
F606W	5921.9	0.1584	1.27 E+19	26.48	0.84	0.22	0.1291
F625W	6311.8	0.0917		25.89	0.84	0.22	0.0834

Filter	Pivot λ (Å)	$\int Q_\lambda T_\lambda\, d\lambda /\lambda$	$\int S_\lambda\, d\lambda$	ABMAG Zero point	Encircled Energy (0.4 arcsec)	Flux in Central Pixel	Background sky rate (per pixel)
			8.32 E+18				
F658N	6584.0	0.0051	4.99 E+17	22.74	0.84	0.22	0.0047
F660N	6599.4	0.0019	1.91 E+17	21.70	0.84	0.22	0.0018
F775W	7693.5	0.0737	9.93 E+18	25.65	0.84	0.21	0.0789
F814W	8045.5	0.0953	1.41 E+19	25.93	0.83	0.19	0.1039
F850LP	9031.5	0.0350	6.51 E+18	24.85	0.78	0.15	0.0401
F892N	8914.8	0.0036	6.60 E+17	22.39	0.78	0.15	0.0042
G800L	7471.4	0.1589	2.02 E+19	26.49	–	–	–
CLEAR	6278.5	0.3792	3.40 E+19	27.43	0.84	0.22	0.2954

Table 9.2: Useful quantities for the ACS SBC.

Filter	Pivot λ (Å)	$\int Q_\lambda T_\lambda\, d\lambda /\lambda$	$\int S_\lambda\, d\lambda$	ABMAG Zero point	Encircled Energy (0.4 arcsec)	Flux in Central Pixel	Background sky rate (per pixel)
F115LP	1392.9	0.0206	9.12 E+16	24.27	0.76	0.11	0.0721
F122M	1267.1	0.0012	4.52 E+15	21.22	0.76	0.09	0.0111
F125LP	1426.5	0.0168	7.78 E+16	24.05	0.76	0.11	0.0065
F140LP	1519.3	0.0088	4.60 E+16	23.34	0.76	0.13	4.94E-05
F150LP	1605.7	0.0047	2.78 E+16	22.68	0.77	0.14	3.51E-07
F165LP	1758.1	0.0012	8.13 E+15	21.14	0.77	0.16	3.31E-07

| PR110L | 1416.8 | 0.0181 | 8.29 E+16 | 24.13 | – | – | – |
| PR130L | 1427.6 | 0.0179 | 8.33 E+16 | 24.12 | – | – | – |

In each Table, the following quantities are listed:

- The pivot wavelength, a source-independent measure of the characteristic wavelength of the bandpass, defined such that it is the same if the input spectrum is in units of F_λ or F_v. $Q(\lambda)$ is the instrument sensitivity and $T(\lambda)$ is the filter transmission.

$$\lambda_p = \sqrt{\frac{\int Q(\lambda)T(\lambda)d\lambda}{\int Q(\lambda)T(\lambda)((d\lambda)/\lambda)}}$$

(20)

- The integral $\int Q_\lambda T_\lambda d\lambda/\lambda$, used to determine the count rate when given the astronomical magnitude of the source.
- The sensitivity integral, defined as the count rate that would be observed from a constant F_λ source with flux 1 erg /cm^2/second/Å.
- The ABmag zero point, defined as the AB magnitude of a source with a constant F_v that gives 1 count/second with the specified configuration.
- The encircled energy, defined as the fraction of PSF flux enclosed in the specified aperture, which is 0.2 arcsecond radius for the WFC and 0.4 arcsecond radius for the SBC.
- The fraction of PSF flux in the central pixel, useful for determining the peak count rate to check for overflow or bright object protection possibilities.
- The sky background count rate, which is the count rate that would be measured with average zodiacal background, and average earthshine. It does not include the contribution from the detectors, tabulated separately in Table 3.1.

Here, we describe how to determine two quantities:

1. The counts/second, C, from your source over some selected area of N_{pix} pixels, where a signal of an electron on a CCD is equivalent to one count.
2. The peak counts/second/pixel, P_{cr}, from your source, which is useful for avoiding saturated CCD exposures, and for assuring that SBC observations do not exceed the bright-object limits.

We consider the cases of point sources and diffuse sources separately in each of the imaging and spectroscopy sections following.

9.2.1 Imaging

Point Source

For a point source, the count rate, C, can be expressed as the integral over the bandpass of the filter:

$$C = A \int F_\lambda \frac{\lambda}{hc} Q_\lambda T_\lambda \varepsilon_f \, d\lambda = \int F_\lambda S_\lambda \varepsilon_f \, d\lambda$$

(21)

where:

- A is the area of the unobstructed 2.4 meter telescope (i.e., 45,239 cm^2).
- F_λ is the flux from the astronomical source in erg/second/cm^2/Å.
- h is Planck's constant.
- c is the speed of light.
- The factor λ/hc converts units of ergs to photons.
- $Q_\lambda T_\lambda$ is the system fractional throughput, i.e., the probability of detecting a count per incident photon, including losses due to obstructions of the full 2.4 meter OTA aperture. It is specified this way to separate out the instrument sensitivity Q_λ and the filter transmission T_λ.
- ε_f is the fraction of the point source energy encircled within N_{pix} pixels.
- S_λ is the total imaging point source sensitivity with units of counts/second/Å per incident erg/second/cm^2/Å.

The peak counts/second/pixel from the point source, is given by:

$$C_{\text{peak}} = \int F_\lambda S_\lambda \varepsilon_f(1) d\lambda$$

(22)

where:

- F_λ and S_λ are as above.
- $\varepsilon_f(1)$ is the fraction of energy encircled within the peak pixel.

Again, the integral is over the bandpass.

If the flux from your source can be approximated by a flat continuum (F_λ = constant) and ε_f is roughly constant over the bandpass, then:

$$C = F_\lambda \varepsilon_f \int S_\lambda d\lambda$$

(23)

We can now define an equivalent bandpass of the filter (B_λ) such that:

$$\int S_\lambda d\lambda = S_{\text{peak}} B_\lambda$$

(24)

where:

- S_{peak} is the peak sensitivity.
- B_λ is the effective bandpass of the filter.

The count rate from the source can now be written as:

(25)
$$C = F_\lambda \varepsilon_f S_{\text{peak}} B_\lambda$$

In Tables 9.1 and 9.2, we give the value of:

(26)
$$\int S_\lambda d\lambda$$

for each of the filters.

Alternatively, we can write the equation in terms of V magnitudes:

(27)
$$C = 2.5 \times 10^{11} \varepsilon_f \left(\int QT d\lambda/\lambda \right) \times 10^{-0.4(V+AB_V)}$$

where V is the visual magnitude of the source, the quantity under the integral sign is the mean sensitivity of the detector+filter combination, and is tabulated in Tables 9.1 and 9.2, and AB_V is the filter-dependent correction for the deviation of the source spectrum from a constant F_v spectrum. This latter quantity is tabulated for several different astronomical spectra in Table 10.1 to Table 10.3 in Chapter 10.

Diffuse Source

For a diffuse source, the count rate, C, per pixel, due to the astronomical source can be expressed as:

(28)
$$C = \int I_\lambda S_\lambda m_x m_y d\lambda$$

where:

- I_λ is the surface brightness of the astronomical source, in erg/second/cm^2/Å/arcseconds^2.
- S_λ as above.
- m_x and m_y are the plate scales along orthogonal axes.

Emission Line Source

For a source where the flux is dominated by a single emission line, the count rate can be calculated from the equation:

(29)
$$C = 2.23 \times 10^{12} (QT)_\lambda F(\lambda) \lambda$$

where C is the observed count rate in counts/second, $(QT)_\lambda$ is the system throughput at the wavelength of the emission line, $F(\lambda)$ is the emission line flux in units of erg/cm^2/second, and λ is the wavelength of the emission line in Angstroms. $(QT)_\lambda$ can be determined by inspection of the plots in Chapter 10. See Section 9.6.4 for an example of emission-line imaging using ACS.

9.2.2 Spectroscopy

Point Source

For a point source spectrum with a **continuum flux distribution**, the count rate, C, is per pixel in the dispersion direction, and is integrated over a fixed extraction height N_{spix} in the spatial direction perpendicular to the dispersion:

(30)
$$C = F_\lambda S'_\lambda \varepsilon'_{N_{\text{spix}}} = F_\lambda A \frac{\lambda}{hc} T_\lambda \varepsilon'_{N_{\text{spix}}} d$$

where:

- S'_λ is the total point source sensitivity in units of counts/second per incident erg/second/cm^2/Å; and $S'_\lambda = S_\lambda d$.
- d is the dispersion in Å/pixel.
- $\varepsilon'_{N_{\text{spix}}}$ is the fraction of the point source energy within N_{spix} in the spatial direction.
- the other quantities are defined above.

For an **unresolved emission line** at $\lambda = L$ with a flux of F_L in erg/second/cm^2 the total counts recorded over the N_{spix} extraction height is:

(31)
$$C = F_\lambda S'_\lambda / d$$

These counts will be distributed over pixels in the wavelength direction according to the instrumental line spread function.

In contrast to the case of imaging sensitivity S_λ, the spectroscopic point source sensitivity calibration $(S'_\lambda \times \varepsilon'_{N_{\text{spix}}})$ for a default extraction height of N_{spix} is measured directly from observations of stellar flux standards after insertion of ACS into HST. Therefore, the accuracy in laboratory determinations of T_λ for the ACS prisms and grisms is NOT crucial to the final accuracy of their sensitivity calibrations.

The peak counts/second/pixel from the point source, is given by:

(32)
$$P_{\text{cr}} = \varepsilon'_F(1) F_\lambda S'_\lambda$$

where:

- $\varepsilon'_f(1)$ is the fraction of energy contained within the peak pixel.
- the other quantities are as above.

9.3 Computing Exposure Times

To derive the exposure time to achieve a given signal-to-noise ratio, or to derive the signal to noise ratio in a given exposure time, there are five principal ingredients:

- Expected counts, C, from your source over some area.
- The area (in pixels) over which those counts are received, N_{pix}.
- Sky background, B_{sky}, in counts/pixel/second.
- The detector background, B_{det}, or dark rate in units of counts/second/pixel.
- The readnoise, R, in counts of the CCD.
- Section 9.4 provides the information for determining the sky-plus-detector background.

9.3.1 Calculating Exposure Times for a Given Signal-to-Noise

The signal-to-noise ratio, Σ, is given by:

$$\Sigma = \frac{Ct}{\sqrt{Ct + N_{pix}(B_{pix} + B_{det})t + N_{pix}N_{read}R^2}}$$

(33)

where:

- C is the signal from the astronomical source in counts/second, or electrons/second from the CCD. The actual output signal from a CCD is C/G where G is the gain. You must remember to multiply by G to compute photon events in the raw CCD images.
- G is the gain in units of electrons per count. It is always 1 for the SBC and 0.5, 1, 1.4, or 2 for the WFC after SM4, depending on GAIN. For archival purposes, gains prior to SM4 for WFC and HRC were ~1, 2, 4, or 8.
- N_{pix} is the total number of detector pixels integrated over to achieve C.
- B_{sky} is the sky background in counts/second/pixel.
- B_{det} is the detector dark current in counts/second/pixel.
- R is the readnoise in electrons; it is equal to zero electrons for SBC observations. See Table 4.1 for WFC after SM4. For archival purposes, see Table 4.2 and Table 4.3 for WFC and HRC prior to SM4.
- N_{read} is the number of CCD readouts.
- t is the integration time in seconds.

This equation assumes the optimistic (and often realistic) condition that the background level under the object is sufficiently well known (and subtracted) to not significantly contribute; in crowded fields this may not be true.

Observers using the CCD normally take sufficiently long integrations that the CCD readnoise is not important. This condition is met when:

(34)
$$Ct + N_{\text{pix}}(B_{\text{sky}} + B_{\text{det}})t > 2N_{\text{pix}}N_{\text{read}}R^2$$

For the CCD in the regime where readnoise is not important and for all SBC observations, the integration time to reach a signal-to-noise ratio Σ, is given by:

(35)
$$t = \frac{\Sigma^2[C + N_{\text{pix}}(B_{\text{sky}} + B_{\text{det}})]}{C^2}$$

If your source count rate is much brighter than the sky plus detector backgrounds, then this expression reduces further to:

(36)
$$t = \frac{\Sigma^2}{C}$$

i.e., the usual result for Poisson statistics of $\Sigma = \sqrt{\text{total counts}}$.

More generally, the required integration time to reach a signal-to-noise ratio Σ is given by:

(37)
$$t = \frac{\Sigma^2[C + N_{\text{pix}}(B_{\text{sky}} + B_{\text{det}})] + \sqrt{\Sigma^4[C + N_{\text{pix}}(B_{\text{sky}} + B_{\text{det}})]^2 + 4\Sigma^2 C^2[N_{\text{pix}}N_{\text{read}}R^2]}}{2C^2}$$

9.3.2 Exposure Time Estimates for Red Targets in F850LP

At wavelengths greater than 7500 Å (HRC) and about 9000 Å (WFC), ACS CCD observations are affected by a red halo due to light scattered off the CCD substrate. An increasing fraction of the light as a function of wavelength is scattered from the center of the PSF into the wings. This problem particularly affects the very broad z-band F850LP filter, for which the encircled energy mostly depends on the underlying spectral energy distribution. The encircled energy fraction is calculated at the effective wavelength which takes into account the source spectral distribution. This fraction is then multiplied by the source counts. (The effective wavelength is the weighted average of the system throughput AND source flux distribution integrated over wavelength). However, this does not account for the variation in enclosed energy with wavelength.

As a consequence, in order to obtain correct estimated count rates for red targets, observers are advised to use the pysynphot package available in AstroConda.

To quantify this new pysynphot capability, we compare the ETC results with pysynphot for a set of different spectral energy distributions and the observation mode WFC/F850LP. In Table 9.3, the spectral type is listed in the first column.

The fraction of light with respect to the total integrated to infinity is listed in the other two columns, for the ETC and pysynphot calculations respectively. These values are derived for a 0.2 arcsecond radius aperture for the ETC calculations and pysynphot.

Table 9.3: Encircled energy comparison for WFC/F850LP.

Spectral type	ETC	pysynphot
O	0.76	0.74
M	0.74	0.72
L	0.70	0.69
T	0.65	0.64

The ETC results are off by 3% (O star), 2% (M star), 2% (L star), and 1% (T star). If this small effect is relevant to particular observations, then the pysynphot software package can be used. Further information about filter F850LP can be found in Sirianni, M. et al. 2005, PASP, 117, 1049, Bohlin 2016, AJ, 152, 60, and ACS ISR 2020-08.

9.4 Detector and Sky Backgrounds

When calculating expected signal-to-noise ratios or exposure times, the background from the sky and the background from the detector must be taken into account.

> ⚠️ *Sky background determination is crucial for a successful observation, especially with the increasing CTE losses found in the ACS/WFC. We encourage observers to simulate the sky background for their proposed observations using the ACS ETC and to compare those values with actual on-orbit sky levels observed during Cycle 18 using the results from ACS ISR 2012-04.*

9.4.1 Detector Backgrounds

See Table 3.1 for read noise and dark current characteristics of the detectors, including variations by amplifier and GAIN for the CCDs.

9.4.2 Sky Background

The sources of sky background which will affect ACS observations include:

- Earth shine (ES).
- Zodiacal light (ZL).
- Geocoronal emission (GC).

The background in counts/second/pixel for **imaging observations** can be computed as:

(38)
$$B_{\text{sky}} = \int I_\lambda S_\lambda m_x m_y d\lambda$$

where:

- I_λ is the surface brightness of the sky background, in erg/second/cm^2/Å/arcseconds^2.
- S_λ is the point source sensitivity for the imaging mode.
- m_x and m_y are the plate scales along orthogonal axes.

The image of the sky through a disperser is not uniform, since some wavelengths fall off the detector for regions of sky near the edge of the field of view (FOV). Since the ACS grism spectra are of order 200 pixels long, the regions of lower sky will be strips at the long and short wavelength edges of the FOV. The maximum width of the strips from where the signal

starts to decline to the edge, where the signal is down by roughly 2×, is about half the total length of a spectrum of a point source, i.e., roughly 100 pixels in the case of a sky background with a **continuum** of wavelengths. In the case of the HRC, the sky for the dispersed mode will not have the low background strips, since the FOV is not masked to the detector size. These small strips of lower sky background in the SBC and the WFC are ignored in the following formulae. Furthermore in the SBC and the WFC, since the spectra do not lie along the direction of the anamorphic distortion, the plate scales of m_x and m_y above must be replaced by the plate scales m_s and m_λ in the orthogonal spatial and dispersion directions, respectively. Interior to the strips, a point on the detector sees a region of sky over the full wavelength coverage of the disperser. Thus, for **spectroscopic observations**:

$$B_{\text{sky}}^\lambda = \int I_\lambda S'_\lambda m_s m_\lambda \, d\lambda$$

(39)

For a **monochromatic** sky emission line at λ = L like Lyman-α, which will dominate the background through the LiF prism:

$$B_{\text{sky}}^L = I_L S'_\lambda m_s m_\lambda / d$$

(40)

where

- I_L is the monochromatic intensity of a line at wavelength L in erg/second/cm^2/ arcseconds^2.

The total sky background is:

$$B_{\text{sky}} = B_{\text{sky}}^\lambda + B_{\text{sky}}^L$$

(41)

Figure 9.1 and Table 9.6 show "high" sky background intensity as a function of wavelength, identifying the separate components which contribute to the background. The "None" and "Average" values of the Earthshine contribution in the ETC correspond, respectively, to 0 and 50% of the "High" values in Figure 9.1 and Table 9.6.

"Extremely high" Earthshine corresponds to twice the "High" value. For the zodiacal sky background, the values in Figure 9.1 and Table 9.6 and the ETCs correspond to the high value of m_v = 22.1 from Table 9.4, while the "low" and "average" zodiacal light is scaled to m_v = 23.3 and 22.7, respectively.

Figure 9.1: High sky background intensity as a function of wavelength.
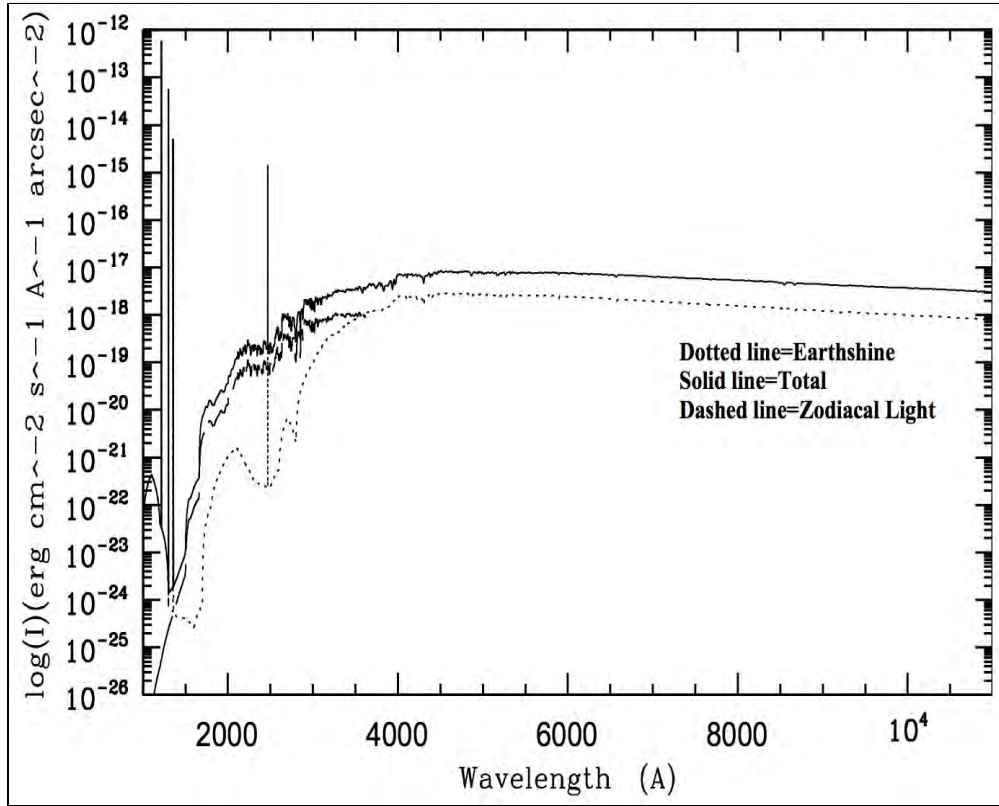
The zodiacal contribution (ZL) is at ecliptic latitude and longitude of 30° and 180°, respectively, and corresponds to m_v = 22.1 per square arcseconds. The Earthshine (ES) is for a target which is 38° from the limb of the sunlit Earth. Use Figure 9.2 to estimate background contributions at other angles. The daytime geocoronal line intensities are in erg/cm^2/second /arcseconds^2 (see Table 9.5).

Background Variations and LOW-SKY

In the ultraviolet, the background contains bright airglow lines, which vary from day to night and as a function of *HST* orbital position. The airglow lines may be the dominant sky contributions in the UV both for imaging-mode and spectroscopic observations. Away from the airglow lines, at wavelengths shortward of ~3000 Å, the background is dominated by zodiacal light, where the small area of sky that corresponds to a pixel of the high resolution *HST* instrumentation usually produces a signal that is much lower than the intrinsic detector background. The contribution of zodiacal light does not vary dramatically with time, and varies by only a factor of about three throughout most of the sky. Table 9.4 gives the variation of the zodiacal background as a function of ecliptic latitude and longitude. For a target near ecliptic coordinates of (50,0) or (–50,0), the zodiacal light is relatively bright at m_v = 20.9, i.e., about 9 times the faintest values of m_v = 23.3. Deep imaging applications must carefully consider expected sky values!

On the other hand, Earthshine varies strongly depending on the angle between the target and the bright Earth limb. The variation of the Earthshine as a function of limb angle from the sunlit Earth is shown in Figure 9.2. This figure also shows the contribution of the Moon, which is typically much smaller than the zodiacal contribution, for which the upper and

lower limits are shown. For reference, the limb angle is approximately 24° when the *HST* is aligned toward its orbit pole (i.e., the center of the CVZ), this limb angle corresponds to "Extremely High" Earthshine. The Earthshine contribution shown in Figure 9.1 and Table 9.6 corresponds to a limb angle of 30°, High Earthshine.

For observations taken longward of 3500 Å, the Earthshine dominates the background at small (<22°) limb angles. In fact, the background increases exponentially for limb angles <22°. The background near the bright limb can also vary by a factor of ~2 on timescales as short as two minutes, which suggests that the background from Earthshine also depends upon the reflectivity of the terrain over which *HST* passes during the course of an exposure. Details of the sky background as it affects ACS, as well as STIS, are discussed in STIS ISR 1998-21. The impact of Earthshine on ACS observations is discussed in ACS ISR 2003-05.

Figure 9.2: Background contributions in V magnitude per arcseconds[2].
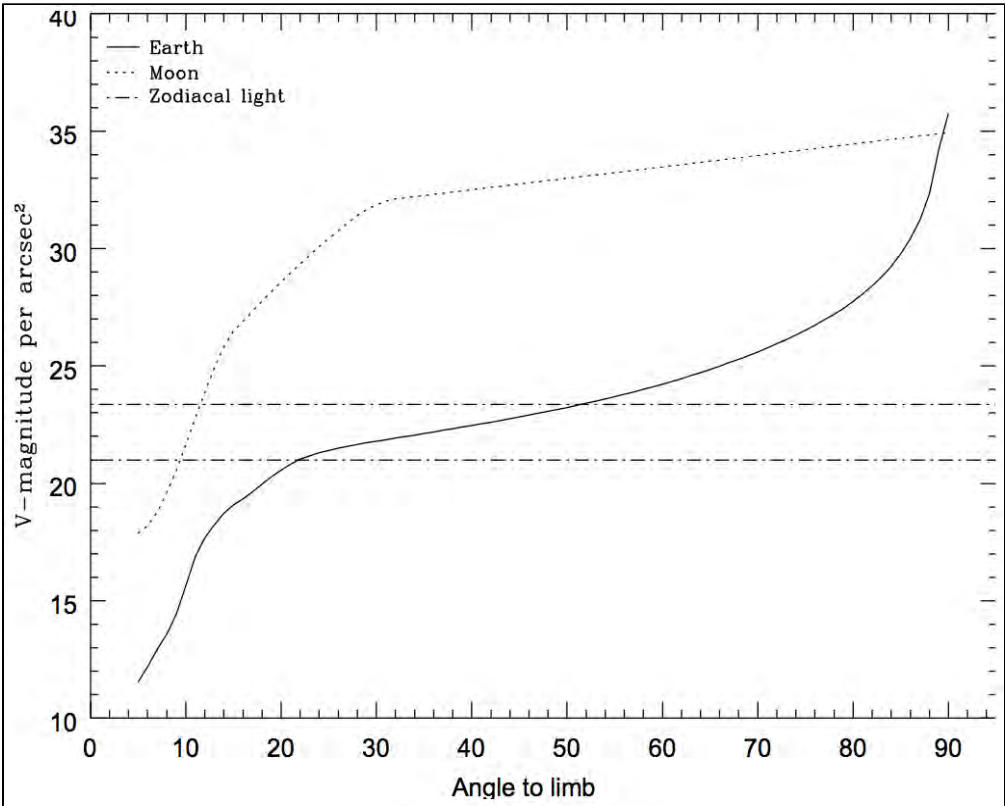
Background due to the zodiacal light, Moon, and the sunlit Earth, as a function of angle between the target and the limb of the Earth or Moon. The two zodiacal light lines show the extremes of possible values.

Table 9.4: Approximate zodiacal sky background as a function of ecliptic latitude and ecliptic longitude. (In V magnitudes per square arcseconds.)

Ecliptic longitude (degrees)	Ecliptic latitude (degrees)			
	0	30	60	90
180	22.1	22.7	23.2	23.3
145	22.4	22.9	23.3	23.3
110	22.3	22.9	23.3	23.3
50	20.9	22.2	22.9	23.3

Observations of the faintest objects may need the special requirement LOW-SKY in the Phase II observing program. LOW-SKY observations are scheduled during the part of the year when the zodiacal background light is no more than 30% greater than the minimum possible zodiacal light for the given sky position. LOW-SKY in the Phase II scheduling also

invokes the restriction that exposures will be taken only at angles greater than 40° from the bright Earth limb to minimize Earthshine and the UV airglow lines. The `LOW-SKY` special requirement limits the times at which targets within 60° of the ecliptic plane will schedule, and limits visibility to about 48 minutes per orbit. The use of `LOW-SKY` must be requested and justified in the Phase I Proposal.

The ETC provides the user with the flexibility to separately adjust both the zodiacal (Low, Average, High) and Earthshine (None, Average, High, Extremely High) sky background components in order to determine if planning for use of `LOW-SKY` is advisable for a given program. However, the absolute sky levels that can be specified in the ETC may not be achievable for a given target; e.g., as shown in Table 9.4, the zodiacal background minimum for an ecliptic target is m_v = 22.4, which is still brighter than both the low and average options with the ETC. By contrast, a target near the ecliptic pole would always have a zodiacal = Low background in the ETC. The user is cautioned to carefully consider sky levels as the backgrounds obtained in *HST* observations can cover significant ranges.

Geocoronal Emission and Shadow

Background due to geocoronal emission originates mainly from hydrogen and oxygen atoms in the exosphere of the Earth. The emission is concentrated in the four lines listed in Table 9.5. The brightest line is Lyman-α at 1216 Å. The strength of the Lyman-α line varies between about 2 and ~30 kilo-Rayleighs (i.e., between 6.1×10^{-14} and 6.1×10^{-13} erg /second/cm^2/arcseconds^2 where 1 Rayleigh = 10^6 photons/second/cm per 4π steradian) depending on the position of *HST* with respect to the day-night terminator and the position of the target relative to the Earth limb. The next strongest line is the OI line at 1304 Å, which rarely exceeds 10% of Lyman-α. The typical strength of the OI 1304 Å line is about 1 kilo-Rayleighs (which corresponds to about 2.85×10^{-14} erg/second/cm^2/arcseconds^2) on the daylight side and about 75 times fainter on the night side of the *HST* orbit. OI 1356 Å and OI 2471 Å lines may appear in observations on the daylight side of the orbit, but these lines are ~10 times weaker than the OI 1304 Å line. The width of the lines also vary with temperature, the line widths given in Table 9.5 are representative values assuming a temperature of 2000 °K.

Except for the brightest objects (e.g., planets), a filter or prism mode which does not transmit at Lyman-α should be employed. To minimize geocoronal emission the special requirement `SHADOW` can be requested. Exposures using this special requirement are limited to roughly 25 minutes per orbit, exclusive of the guide-star acquisition (or reacquisition), and can be scheduled only during a small percentage of the year. `SHADOW` reduces the contribution from the geocoronal emission lines by roughly a factor of ten while the continuum Earthshine is set to zero. `SHADOW` requirements must be included and justified in your Phase I proposal (see the *Call for Proposals*).

Table 9.5: Geocoronal emission lines.

Wavelength (Å)	ID	Line width (Å)	Intensity			
			Day		Night	
			kilo-Rayleighs	erg/s/cm^2/arcsec^2	kilo-Rayleighs	erg/s/cm^2/arcsec^2
1216	Ly-α	0.04	~20	6.1×10^{-13}	2	6.1×10^{-14}
1304	OI	0.013	~2	5.7×10^{-14}	0.013	3.8×10^{-16}

| 1356 | OI | 0.013 | ~0.2 | $\sim 5 \times 10^{-15}$ | ~0.001 | $\sim 3 \times 10^{-17}$ |
| 2471 | OI | 0.023 | <0.2 | $<3 \times 10^{-15}$ | <0.001 | $<1.5 \times 10^{-17}$ |

9.5 Extinction Correction

Extinction can dramatically reduce the counts expected from your source, particularly in the ultraviolet. Figure 9.3 shows the average $A_V/E(B-V)$ values for our galaxy, taken from Seaton 1979, MNRAS, 187, 73. Large variations about the average are observed (Witt, Bohlin, & Stecher 1984, ApJ, 279, 698).

Extinction curves have a strong metallicity dependence, particularly in the UV wavelengths. Sample extinction curves can be seen in Koornneef & Code 1981, ApJ, 247, 860 (LMC); Bouchet et al. 1985, A&A, 149, 330 (SMC); and Calzetti, Kinney, & Storchi-Bergmann 1994, ApJ, 429, 582, and references therein. At lower metallicities, the 2200 Å bump which is so prominent in the Galactic extinction curve disappears; and $A_V/E(B-V)$ may increase monotonically at UV wavelengths.

Figure 9.3: Extinction versus wavelength.
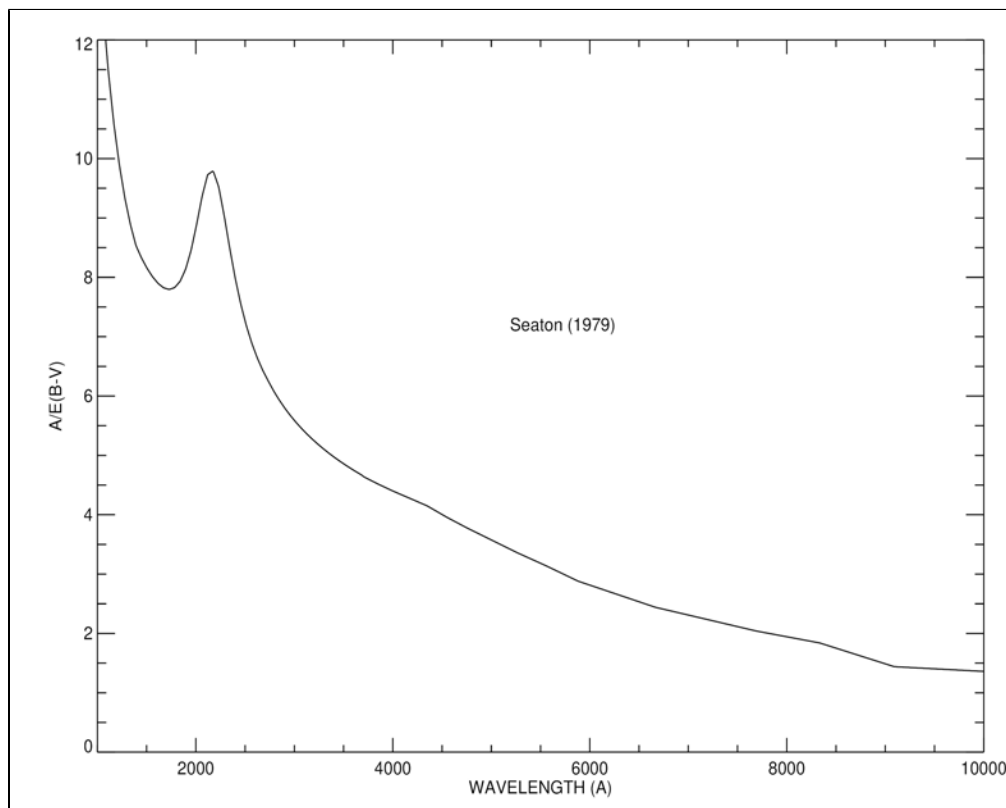
The mean UV interstellar extinction curve of the Milky Way as a function of wavelength. The curve features a prominent bump at 2200 Å, which has been shown to disappear at lower metallicities.

9.6 Exposure-Time Examples

In the following you will find a set of examples for the three different channels and for different types of sources. The examples were chosen in order to present typical objects for ACS and also to present interesting cases that may arise with the use of ACS.

> ⚠ *Actual ETC calculation results may differ slightly from these published values due to recent improvements in the ETC tables.*

9.6.1 Example 1: WFC Imaging a Faint Point Source

What is the exposure time needed to obtain a signal-to-noise of 10 for a point source of spectral type F2V, normalized to V = 26.5, when using the WFC, F555W filter? Assume a GAIN of 1, a box size of 11 × 11 pixel^2, and average sky values.

The ETC gives a total exposure time of 4866 seconds to obtain this S/N in a single exposure. Since such an exposure would be riddled with cosmic rays and essentially useless, it is necessary to specify how many exposures to split the observation into. ACS WFC observations generally should be split if the exposure time is larger than about 11 minutes, but for multi-orbit observations, splitting into 2 exposures per orbit is generally sufficient.

For a typical object visibility of 53 minutes, after applying the requisite overheads (see Chapter 8), there is time for two 1200 second exposures per orbit. The required exposure time can thus be reached in 4 exposures, but re-running the ETC using `CR-SPLIT` = 4 raises the required exposure time to 5339 seconds (because of the extra noise introduced by the four extra readouts). To achieve the required exposure time would require `CR-SPLIT` = 5, or three orbits.

Using the pencil and paper method, Table 9.1 gives $\int QTd\lambda/\lambda = 0.0769$, and the AB$_V$ correction term can be retrieved from Table 10.1 as 0.02. According to Figure 5.12, a circular aperture of radius 0.3 arcseconds (which has an area of 116 pixels, close to the 121 pixel box specified) encloses about 88% of the light from a star.

The count rate is given by Equation 8 in Section 9.2.1:

$$C = (2.5 \times 10^{11}) \times 0.0769 \times 0.88 \times 10^{-0.4(26.5+0.02)} = 0.417 \text{ counts/second,}$$

which agrees with the ETC-returned value of 0.435.

The exposure time can then be found by using Equation 3 in Section 9.3.1, which gives t = 4958 seconds, which is close to the ETC-derived value of 4866 seconds (CR-SPLIT = 1). We have inserted the background rate from Table 9.1 (B_{sky} = 0.0541) and Table 3.1 (B_{det} = 0.0137), and assumed that the noise on the background is much greater than the readout noise.

Note that this can be greatly shortened by specifying a smaller analysis box (for example, 5 × 5) and using LOW-SKY. Dropping the aperture size to 5 × 5, which still encloses 80% of the light, requires 1214 seconds at average sky. Including both the smaller 5 × 5 box and LOW-SKY (Zodiacal = LOW, Earthshine = AVERAGE), using the ETC gives the required exposure time as only 1314 seconds with CR-SPLIT = 1, or 1452 seconds with CR-SPLIT = 2. The LOW-SKY visibility per orbit is 47 minutes, which allows a total on-target exposure time of 2000 seconds in one orbit with CR-SPLIT = 2.

9.6.2 Example 2: SBC Objective Prism Spectrum of a UV Star

What is the peak count rate using the PR110L prism in the SBC for the *HST* standard star HS2027+0651 (V = 16.9) that was used for the STIS prism calibration? This spectrum is not in the ETC list, therefore we quote below the flux which can be found by dearchiving the STIS spectrum.

The sensitivity peaks in the 1500 Å to 1600 Å region. To find the count rate at 1537 Å, inspection of Figure 6.22 gives the sensitivity of 7.7×10^{14} counts/second/(erg/cm^2/s/Å). Multiplying by the stellar flux of 5.3587×10^{-14} gives 41.3 counts /second, summed in the cross dispersion direction. For the fraction of light in the central pixel ε = 0.31, the brightest pixel at 1437.6 Å is 12.9 counts/second/pixel, well below the bright object limit.

The SBC has no readout noise, and the dark current rate is negligible, while the main sky contribution for PR110L is from Lyman-α. For daytime Lyman-α intensity of 20kR = 6.1×10^{-13} ergs/cm^2/second/arcseconds^2, S' = 1.81×10^{14}, and d, the dispersion in Å/pixel, is 2.58. Therefore, the background count rate is given by Equation 3 in Section 9.4.2:

$$B_{sky}^{L} = (6.1 \times 10^{-13}) \times (1.81 \times 10^{14}) \times 0.032^2/2.58 = 0.044 \text{ counts/sec/pix.}$$

This value varies somewhat over the field, as the plate scale varies from the nominal 0.032 arcseconds/pixel. For faint source spectroscopy, it is better to use PR130L, which is on a CaF$_2$ substrate to block Ly-α.

9.6.3 Example 3: WFC VIS Polarimetry of the Jet of M87

What signal-to-noise ratio is reached in three one orbit exposures (~2400 seconds each) for M87, when using the WFC, F555W for one orbit each in the three VIS polarizers? Gain is 2, box size is 5 × 5 pixel^2, CR-SPLIT = 2, and average sky.

If the M87 jet region has μ_V = 17 magnitudes/arcseconds^2, using the ETC with a flat continuum spectral distribution and an exposure time of 2400 seconds (CR-SPLIT = 2), gives S/N = 321 for an observation with each VIS polarizer filter (which is an average of the polarizer at the 3 available position angles 0°, 60°, and 120°). If the polarization P is 20%, then $P \times S$ /N = 64.2, so using Equation 6 in Section 6.1.2, σ_P/P = 0.013, or σ_P = 2.6×10^{-3}, which is the error on the fractional polarization. The error on the position angle, σ_θ, is 0.4° using Equation 7 in Section 6.1.2.

9.6.4 Example 4: SBC imaging of Jupiter's Aurora at Lyman-alpha

What signal-to-noise ratio is reached in a one orbit exposure (2000 seconds) observing Jupiter's aurora in Ly-α using the SBC and F122M filter?

Equation 10 in Section 9.2.1 can be used to calculate the expected count rate. The aurora is variable, up to ~100kR. The value of *(QT)* for the SBC+F122M filter at 1216 Å is 0.0126, from inspection of Figure 10.104 and checking the throughput of the bandpass with pysynphot. For a surface brightness of 40kR = 1.22 x 10^{-12} erg/cm^2/second/arcseconds^2 (see Section 9.4.2 for conversion), the total counts per pixel are

$$Ct = (2.23 \times 10^{12}) \times 0.0126 \times (1.22 \times 10^{-12}) \times 1216 \times 0.032^2 \times 2000 = 85.56 \text{ counts/pix}.$$

The background contributions are the detector dark of 8.28 x 10^{-6} counts/pixel/second (which can be ignored in this case) and a sky background which is dominated by geocoronal Lyman-α. Using the same formula listed in Example 9.6.2, Equation 3 in Section 9.4.2, we compute the geocoronal background from Lyman-α in the F122M bandpass. During the daytime, the geocoronal background count rate is 0.022 counts/second/pix, while at night the value drops to one tenth of this, or 0.0022 counts/second/pix. After 2000 seconds of integration, the Lyman-α background is 43.7 counts/pix and 4.37 counts/pix for day and night, respectively.

Finally, we calculate the signal-to-noise ratio Σ for a 2 × 2 pixel^2 resolution element. In the daytime,

$$\Sigma = \frac{CtN_{\text{pix}}}{\sqrt{(Ct + Bt)N_{\text{pix}}}} = \frac{85.56 \times 4}{\sqrt{(85.56 + 43.7) \times 4}} = 15.05,$$

and at night,

$$\Sigma = \frac{88.1 \times 4}{\sqrt{(88.1 + 4.37) \times 4}} = 18.04.$$

9.6.5 Example 5: Coronagraphic imaging of the Beta-Pictoris Disk

In this example, using the now inoperative HRC, we shall consider the case where we are trying to determine the S/N achieved on the Beta Pictoris disk, assuming a disk surface brightness of 16 magnitudes/arcseconds^2 in the R band at a distance of 6 arcseconds from the central star with a V magnitude of 3.9, for an exposure time of 1000 seconds with an F435W filter. Assume that the star and disk have an A5V-type spectrum. Using the ETC and considering the case for the 3.0 arcseconds occulting mask:

- Disk count rate = 4.98 e⁻/second for a 2 × 2 pixel^2 aperture (including 47.5% throughput of coronagraph).
- Sky count rate = 0.010 e⁻/second/pixel.
- Detector dark rate = 0.012 e⁻/second/pixel.

- In 1000 seconds, this gives 4,980 e$^-$/(2 × 2 pixel^2) aperture in the disk region.
- Central star count rate = 3.63 × 10^8 e$^-$/second in a 101 × 101 pixel^2 aperture (101 × 101 pixel^2 aperture used to estimate total integrated flux).
- At a distance 6 arcseconds from the central star, the fraction of flux per square arcsecond in the PSF wings is 2.6 × 10^{-6}. B$_{PSF}$ = (3.63 × 10^8) × (2.6 × 10^{-6}) = 943.8 e$^-$ per square arcsecond. The counts collected in 4 pixels are 4 × 0.027^2 × 943.8 = 2.752.
- The S/N in a 2 × 2 pixel^2 box is then $\Sigma = \frac{4980}{\sqrt{4980+2.8}} = 70.5$.

9.6.6 Example 6: WFC Imaging: Post-Flash to Mitigate Low Sky

WFC images with low background (below ~30 e$^-$/pixel of sky plus dark current) suffer increasingly severe CTE losses far from the serial registers. In some cases, it may be advantageous to post-flash such images to improve recovered signal-to-noise. In the following ETC example, we incorporate post-flash to boost the background for a single 90-second exposure with filter F850LP and "average" levels for earthshine, zodiacal light, and airglow.

We configure the ETC to calculate the S/N ratio obtained in 90 seconds with WFC using the F850LP filter (with `CR-SPLIT` = 1). The ETC also reports the background level as usual. For this example, the flux of the target is irrelevant. Adopting a photometry region of 1 × 1 pixel^2 for simplicity, and otherwise using default settings, the ETC results page includes a low-background warning (currently triggered below 20e$^-$ per pixel of sky plus dark current) near the top of the report. In this example, the expected background level is only 4.37e$^-$/pixel (3.55e$^-$ from the sky and 0.83e$^-$ from dark current).

Depending on science goals, supplementing this background with post-flash may be a viable solution. For the current example, adding a post-flash of 25e$^-$ on the ETC front page results in the low-background warning no longer triggering, as well as a reduction of the reported S/N because of the increased background. However this extra post-flash would considerably boost the recovered signal for sources far from the serial register, resulting in a net gain in S/N for such sources. The ETC is not currently capable of estimating WFC CTE-induced signal losses. The ACS Team has provided such a calculator, suitable for point-source photometry, at the ACS CTE Calculator website.

The above example should be treated with caution, however, for the following reasons:

- There is nothing ideal about a WFC background of 25–30 e$^-$/pixel. In general, a higher background reduces CTE losses at the cost of added noise, and the optimal post-flash level will depend upon source position and intensity.
- The lowest ETC settings for earthshine, airglow, and zodiacal light may occasionally overestimate actual WFC background levels, based upon recent comparisons with Cycle 18 observations (ACS ISR 2012-04). Users especially concerned with CTE should err on the side of lower-than-predicted background when determining how much post-flash to add.
- As shown in Figure 9.4, the WFC post-flash illumination declines by 50% with radius from the detector center, with approximately azimuthal symmetry. When the post-flash is the dominant source of background, both the noise properties and the degree of CTE mitigation across the image will therefore be highly nonuniform. The non-uniformity is such that the post-flash signal is highest where CTE losses have the most effect, i.e., far from the amplifier in the parallel transfer direction. As a consequence, mitigation of CTE losses will be best for the sources

that need it the most. However, the nonuniform noise of the post-flash background will require a careful treatment during subsequent analyses.

- For users desiring to use the post-flash capabilities, it is recommended to read Section 5 of ACS ISR 2018-02. The APT assumes a single value of 14 e⁻/sec to compute the flash duration required to achieve a specified signal (e.g., for a 20e⁻ post-flash, t = 20e⁻/(14 e⁻/sec) = 1.4 seconds). Due to the nonuniform post-flash signal, this flash rate could be an overestimation of the true post-flash signal. The aforementioned ISR provides a convenient method for computing the necessary scaling factor to ensure the desired number of electrons are deposited at the location of your source.

ACS ISR 2018-02 and ACS ISR 2014-01 provide detailed guidance for the appropriate use cases of post-flash.

Figure 9.4: Post-flash reference file for ACS/WFC.
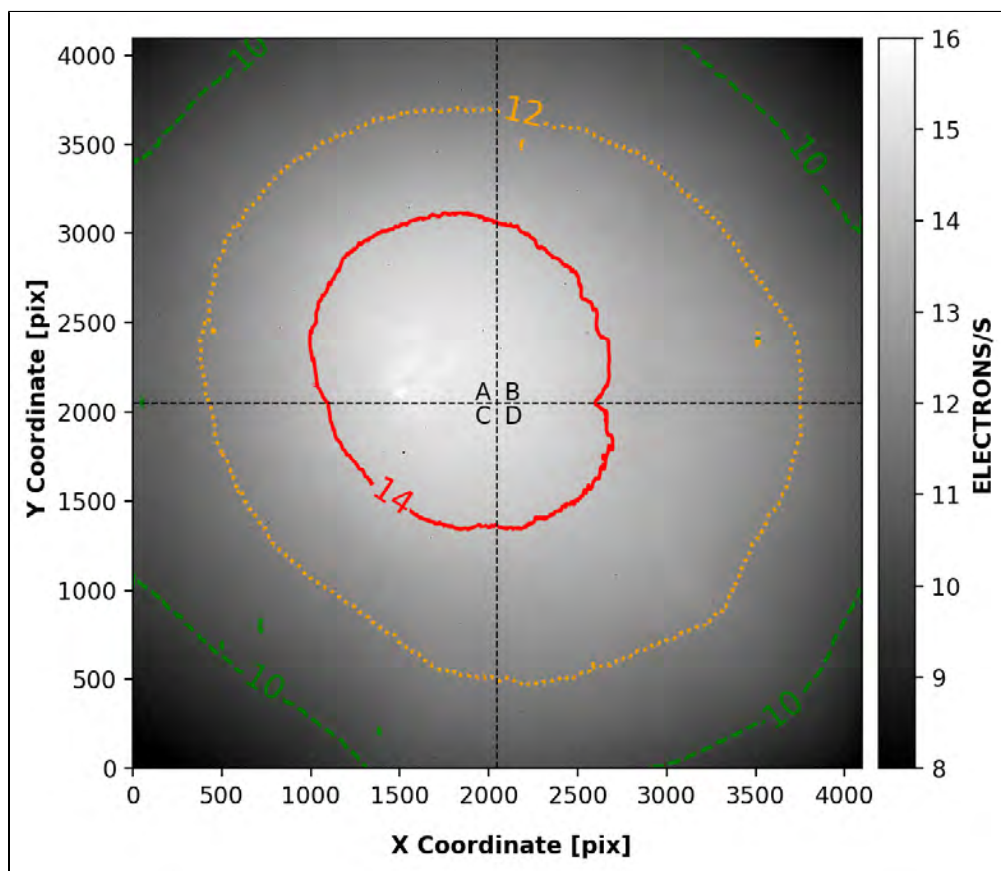
The creation of a post-flash reference image free of dark current artifacts is described in ACS ISR 2018-02. Contours at 10, 12, and 14 e⁻/sec highlight the non-uniformity of the LED illumination pattern.

9.7 Tabular Sky Backgrounds

We provide Table 9.6 of the "high" sky background numbers as plotted in Figure 9.1. See the text and the caption in Figure 9.1 for more details. These high sky values are defined as the earthshine at 38° from the limb and the high zodiacal light of $m_V = 22.1$ magnitude/arcseconds^2.

Table 9.6: High sky backgrounds.

Wavelength	Earthshine	Zodiacal light	Total background
Å	erg/sec/cm^2/Å/arcsec^2	erg/sec/cm^2/Å/arcsec^2	erg/sec/cm^2/Å/arcsec^2
1000.	2.41E-23	1.26E-28	2.41E-23
1100.	4.38E-22	1.02E-26	4.38E-22
1200.	4.01E-23	1.05E-25	4.02E-23
1400.	4.29E-25	2.50E-24	2.93E-24
1500.	4.16E-25	9.12E-24	9.54E-24
1600.	2.55E-25	2.30E-22	2.30E-22
1700.	7.89E-23	7.06E-21	7.14E-21
1800.	9.33E-23	1.50E-20	1.51E-20
1900.	4.39E-22	2.20E-20	2.24E-20
2000.	1.01E-21	3.49E-20	3.59E-20
2100.	1.60E-21	1.21E-19	1.23E-19
2200.	7.49E-22	2.16E-19	2.17E-19
2300.	3.32E-22	1.75E-19	1.75E-19
2400.	2.50E-22	1.79E-19	1.79E-19
2500.	2.39E-22	2.47E-19	2.47E-19
2600.	5.62E-22	2.93E-19	2.94E-19
2700.	6.77E-21	9.95E-19	1.00E-18
2800.	2.03E-21	2.82E-19	2.91E-19
2900.	4.32E-20	2.04E-18	2.08E-18

3000.	9.34E-20	1.20E-18	1.29E-18
3100.	2.07E-19	1.46E-18	1.67E-18
3200.	3.60E-19	2.25E-18	2.61E-18
3400.	6.40E-19	2.81E-18	3.45E-18
3500.	8.20E-19	2.73E-18	3.55E-18
3600.	1.06E-18	2.68E-18	3.74E-18
3700.	1.22E-18	3.25E-18	4.47E-18
3800.	1.23E-18	3.05E-18	4.28E-18
3900.	1.52E-18	3.27E-18	4.79E-18
4000.	2.38E-18	4.54E-18	6.92E-18
4250.	2.33E-18	4.48E-18	6.81E-18
4500.	2.78E-18	5.32E-18	8.10E-18
5000.	2.55E-18	4.92E-18	7.47E-18
5250.	2.69E-18	5.28E-18	7.97E-18
5500.	2.56E-18	5.20E-18	7.76E-18
5750.	2.56E-18	5.33E-18	7.89E-18
6000.	2.40E-18	5.11E-18	7.51E-18
6250	2.27E-18	4.94E-18	7.21E-18
6500.	2.20E-18	4.88E-18	7.08E-18
6750.	2.07E-18	4.69E-18	6.76E-18
7000.	1.90E-18	4.40E-18	6.30E-18
7250.	1.85E-18	4.34E-18	6.19E-18
7500.	1.73E-18	4.13E-18	5.86E-18
7750.	1.63E-18	3.95E-18	5.58E-18
8000.	1.57E-18	3.85E-18	5.42E-18
8250.	1.48E-18	3.68E-18	5.16E-18
8500.	1.37E-18	3.46E-18	4.83E-18
8750.	1.31E-18	3.36E-18	4.67E-18

Chapter 10: Imaging Reference Material

Chapter Contents

10.1 Introduction

This chapter provides reference material to help you select your filter and detector configuration and determine your observing plan (e.g., total required exposure time, and number of exposures). For the most part, this chapter is organized by *filter* and *detector*. For each imaging mode, the following are provided:

- Plots of integrated system throughput as a function of wavelength.
- Plots of the time needed to achieve a desired signal-to-noise ratio vs. magnitude for all filters for a point source and a one square arcsecond extended source.
- Tables of color corrections AB_V to go from Johnson V magnitude to AB magnitude, and for SBC, to go from GALEX NUV and FUV to AB magnitude.

> ⊙ *The Tables and Figures that are provided in this Chapter may differ slightly from the current results obtained using synthetic photometry software. Such differences are due to the fact that the component throughput tables are updated as needed to reflect the latest calibration results. Please contact the HST Help Desk if you have any questions regarding this subject.*

10.2 Using the Information in this Chapter

10.2.1 Sensitivity Units and Conversions

This chapter contains plots of throughputs for each imaging mode in Section 10.3.1. Section 9.2 explains how to use these throughputs to calculate expected count rates from your source.

The first figure for each imaging mode gives the integrated system throughput, which is the combination of the efficiencies of the detector and of the optical elements in the light path. The throughputs in this handbook are based in part on ground test data, although at the time of writing the handbook, the overall detector efficiency curve and most filter throughputs have been adjusted based on in-flight data. The total system unitless quantum efficiency, i.e., throughput, at any wavelength is defined as the probability that a monochromatic photon incident on the primary mirror produces a detected photo-electron. For the CCD, "counts" is the number of electrons detected. For the MAMA, "counts" is the number of valid photo-electron events processed by the detector electronics after passing through the various pulse-shape and anti-coincidence filters. In both cases, the detected counts obey Poisson statistics. The throughput includes all reflections and transmissions in the optical train (e.g., due to the *HST* secondary).

To recalculate the throughput with the most recent CCD QE tables in pysynphot, you can create total system throughput tables (instrument plus OTA) using the **pysynphot.ObsBandpass** class.

A bandpass object is created by providing any valid `obsmode` command string as an argument to **pysynphot.ObsBandpass**. For example, to evaluate the throughput of the F475W filter and the WFC detector, chip 1, you would use the command:

```
>>import pysynphot
>>bp_F475W = pysynphot.ObsBandpass("acs, wfc1, f475w")
```

The resulting throughput table is stored as an attribute of the `bp_F475W` bandpass object, it is accessed by the command:

```
>>throughput_table = bp_F475W.throughput
```

The ramp filters are not included in this chapter because the passband will change depending on the chosen central wavelength. The width of the passband and available range of central wavelengths for each ramp segment are listed in Table 5.2. The passbands for ramp filters can also be obtained using **pysynphot.**

10.2.2 Signal-to-Noise

For each imaging mode, plots are provided to estimate the signal-to-noise ratio (S/N) for a representative source, see Section 10.3.1. The first figure shows S/N for point sources (GAIN=1). The second figure shows S/N for uniform extended sources of area 1 arcsecond^2.

The different line styles in the S/N figures delineate regions where different sources of noise dominate. A particular source of noise (read noise for example) is presumed to dominate if it contributes more than half the total noise in the observations.

The point- and extended-source S/N figures are shown for average and low sky levels. For point sources, an aperture size of 5 × 5 pixel^2 is used for the WFC, 9 × 9 pixel^2 for HRC, and 15 × 15 pixel^2 for the SBC S/N evaluation. For extended sources, a 1 arcsecond^2 aperture is used. For the CCD, the readnoise is computed assuming a number of readouts `NREAD` = integer (t/1000 seconds), where t is the exposure time, with a minimum `NREAD` = 2. That is, each exposure has a minimum `CR-SPLIT` = 2. Different line styles in the figures are used to indicate which source of noise dominates.

To the left of the vertical line in the SBC S/N plots, the count rate from the source exceeds the 50 counts/second/pixel local count rate limit. This is computed from the model PSF, which gives 14% to 22% of the flux in the central pixel.

In situations requiring more detailed calculations (non-stellar spectra, extended sources, other sky background levels, unknown target V magnitude, etc.), the ACS ETC should be used.

Follow these steps to use the signal-to-noise plots:

1. Determine the AB magnitude of your source at the wavelength of interest. There are several ways to do this.
   - Examine Table 10.1, 10.2, or 10.3 and find AB$_V$ for the desired spectral type and filter. Sum the V magnitude of the target and AB$_V$ derived from the table.
   - Alternatively, compute ABMAG (= V + AB$_V$) from the source flux, using the relation

   (42)
   $$\mathrm{ABMAG} = -2.5 \log f_\nu - 48.60$$

   or

   (43)
   $$\mathrm{ABMAG} = -2.5 \log f_\lambda - 5 \log \lambda - 2.406$$

   where λ is pivot wavelength.
2. Find the appropriate plot for the filter in question, and locate V + AB$_V$ on the horizontal axis. Then read off the signal-to-noise ratio for the desired exposure time, or vice-versa.

The "x" characters at the top of each plot indicate the onset of saturation, in the case of the CCD. For the MAMA detector, the "x" shows where the total number of counts exceeds the 16 bit buffer size of 65,535.

Note that the plots show the S/N as a function of source magnitude for exposure times as short as 0.1 seconds, although the minimum exposure time for the WFC CCD channel is 0.5 seconds.

10.2.3 Point Spread Functions

All information about the PSFs are based on the modeled encircled energy data presented in Section 5.6.

10.3 Throughputs and Correction Tables

10.3.1 Filter Throughputs and Sensitivities

- WFC F435W
- WFC F475W
- WFC F502N
- WFC F550M
- WFC F555W
- WFC F606W
- WFC F625W
- WFC F658N
- WFC F660N
- WFC F775W
- WFC F814W
- WFC F850LP
- WFC G800L
- WFC CLEAR
- HRC F220W
- HRC F250W
- HRC F330W
- HRC F344N
- HRC F435W
- HRC F475W
- HRC F502N
- HRC F550M
- HRC F555W
- HRC F606W
- HRC F625W
- HRC F658N
- HRC F660N
- HRC F775W
- HRC F814W
- HRC F850LP
- HRC F892N
- HRC G800L
- HRC PR200L
- HRC CLEAR

- [SBC F115LP](#)
- [SBC F122M](#)
- [SBC F125LP](#)
- [SBC F140LP](#)
- [SBC F150LP](#)
- [SBC F165LP](#)
- [SBC PR110L](#)
- [SBC PR130L](#)

10.3.2 Color Correction Tables

Table 10.1: Color corrections AB_V to go from Johnson V magnitude to AB magnitude for the WFC ([ACS ISR 2019-10](#)).

Spectrum[a]	F435W	F475W	F502N	F550M	F555W	F606W	F625W
Avg Sky	0.61	0.34	0.21	-0.04	0.05	-0.11	-0.23
Low Sky	0.60	0.33	0.20	-0.04	0.05	-0.10	-0.22
O5V	-0.43	-0.28	-0.15	0.07	-0.03	0.13	0.29
B0V	-0.39	-0.25	-0.13	0.06	-0.03	0.13	0.28
A0V	-0.10	-0.09	-0.07	0.03	0.00	0.09	0.17
A5V	0.03	-0.01	-0.03	0.02	0.01	0.07	0.11
F2V	0.25	0.12	0.06	-0.01	0.02	0.01	-0.02
G2V	0.59	0.31	0.17	-0.04	0.04	-0.07	-0.16
K0V	0.76	0.40	0.23	-0.06	0.05	-0.12	-0.24
M0V	1.17	0.69	0.87	-0.18	0.11	-0.32	-0.56
M6V	1.19	0.71	0.98	-0.19	0.13	-0.35	-0.60
O6I	-0.42	-0.27	-0.15	0.07	-0.03	0.13	0.28
B0I	-0.35	-0.22	-0.12	0.05	-0.03	0.12	0.25
G0III	0.58	0.30	0.17	-0.03	0.04	-0.07	-0.16
K0III	1.05	0.54	0.31	-0.07	0.06	-0.16	-0.32
M0III	1.50	0.82	0.79	-0.16	0.11	-0.33	-0.58
Elliptical	0.82	0.44	0.26	-0.05	0.06	-0.18	-0.34
Sa	0.76	0.43	0.28	-0.06	0.07	-0.15	-0.30
Sbc	0.58	0.34	0.18	-0.04	0.05	-0.13	-0.26

Scd	0.48	0.26	0.03	-0.02	0.04	-0.10	-0.20
Starburst E(B–V) = 0.51–0.60	0.42	0.25	-0.01	-0.01	0.04	-0.24	-0.41
Starburst E(B–V) < 0.1	0.23	0.06	-1.02	0.11	-0.03	-0.11	-0.14
Sun	0.57	0.30	0.17	-0.04	0.04	-0.07	-0.17
Vega	-0.10	-0.09	-0.08	0.03	0.00	0.09	0.17

Table 10.1 (continued)

Spectrum[a]	F658N	F660N	F775W	F814W	F850LP	F892N	G800L	CLEAR
Avg Sky	-0.25	-0.28	-0.40	-0.42	-0.48	-0.48	-0.36	-0.06
Low Sky	-0.24	-0.26	-0.38	-0.40	-0.44	-0.45	-0.33	-0.05
O5V	0.40	0.39	0.68	0.76	1.01	0.98	0.56	0.06
B0V	0.41	0.39	0.66	0.74	0.98	0.96	0.55	0.08
A0V	0.38	0.30	0.40	0.44	0.54	0.51	0.33	0.16
A5V	0.31	0.22	0.27	0.30	0.39	0.37	0.23	0.15
F2V	0.08	0.02	0.02	0.04	0.09	0.08	0.02	0.10
G2V	-0.17	-0.20	-0.26	-0.27	-0.28	-0.29	-0.23	0.02
K0V	-0.28	-0.30	-0.40	-0.42	-0.46	-0.47	-0.36	-0.04
M0V	-0.82	-0.83	-1.33	-1.45	-1.72	-1.66	-1.19	-0.63
M6V	-0.93	-0.94	-1.57	-1.72	-2.04	-1.95	-1.41	-0.81
O6I	0.39	0.38	0.67	0.74	0.99	0.97	0.55	0.06
B0I	0.36	0.35	0.61	0.68	0.91	0.89	0.51	0.08
G0III	-0.16	-0.19	-0.25	-0.25	-0.27	-0.28	-0.22	0.02
K0III	-0.39	-0.40	-0.55	-0.58	-0.67	-0.70	-0.50	-0.10
M0III	-0.81	-0.82	-1.28	-1.39	-1.65	-1.63	-1.15	-0.58
Elliptical	-0.45	-0.46	-0.69	-0.75	-0.90	-0.91	-0.61	-0.21
Sa	-0.45	-0.42	-0.57	-0.62	-0.76	-0.78	-0.52	-0.15
Sbc	-0.34	-0.34	-0.55	-0.60	-0.75	-0.72	-0.49	-0.15
Scd	-0.26	-0.27	-0.38	-0.40	-0.45	-0.43	-0.33	-0.07

Spectrum								
Starburst E(B–V) = 0.51–0.60	-1.50	-0.99	-0.50	-0.52	-0.60	-0.59	-0.50	-0.20
Starburst E(B–V) < 0.1	-1.20	-0.36	-0.14	-0.17	-0.25	-0.20	-0.17	-0.04
Sun	-0.17	-0.20	-0.27	-0.27	-0.28	-0.29	-0.24	0.01
Vega	0.38	0.29	0.39	0.43	0.53	0.50	0.32	0.15

[a]Castelli & Kurucz models are used for the stellar spectra.

Table 10.2: Color corrections AB_V to go from Johnson V magnitude to AB magnitude for the HRC (ACS ISR 2019-10).

Spectrum[a]	F220W	F250W	F330W	F344N	F435W	F475W	F502N	F550M	F555W	F606W
Avg Sky	2.19	1.42	2.01	1.89	0.63	0.32	0.21	-0.04	0.05	-0.10
Low Sky	5.46	3.73	2.09	1.97	0.62	0.31	0.20	-0.04	0.05	-0.09
O5V	-1.46	-1.20	-0.83	-0.79	-0.43	-0.27	-0.15	0.07	-0.03	0.12
B0V	-1.23	-1.00	-0.67	-0.64	-0.39	-0.24	-0.13	0.06	-0.03	0.12
A0V	1.77	1.55	1.15	1.11	-0.09	-0.09	-0.07	0.03	0.00	0.09
A5V	2.44	2.05	1.40	1.36	0.05	-0.01	-0.03	0.02	0.01	0.06
F2V	3.38	2.49	1.46	1.40	0.26	0.12	0.06	-0.01	0.02	0.01
G2V	5.56	3.46	1.87	1.83	0.61	0.29	0.17	-0.04	0.04	-0.07
K0V	6.88	4.23	2.33	2.35	0.79	0.38	0.23	-0.06	0.05	-0.11
M0V	8.24	6.96	3.81	3.79	1.19	0.66	0.87	-0.17	0.12	-0.29
M6V	8.05	6.88	3.74	3.69	1.21	0.68	0.98	-0.19	0.13	-0.32
O6I	-1.41	-1.16	-0.81	-0.77	-0.42	-0.26	-0.15	0.07	-0.03	0.12
B0I	-1.05	-0.89	-0.64	-0.61	-0.36	-0.22	-0.12	0.05	-0.03	0.11
G0III	5.77	3.67	2.04	1.95	0.60	0.29	0.17	-0.03	0.04	-0.06
K0III	8.24	5.60	3.22	3.14	1.08	0.51	0.31	-0.07	0.07	-0.15
M0III	8.43	8.10	5.11	5.12	1.53	0.78	0.79	-0.16	0.12	-0.31
Elliptical	5.22	3.83	2.33	2.25	0.84	0.42	0.26	-0.05	0.06	-0.17

Sa	4.58	3.68	2.38	2.31	0.79	0.41	0.28	-0.06	0.07	-0.13
Sbc	2.99	2.64	1.88	1.78	0.60	0.32	0.18	-0.04	0.05	-0.12
Scd	2.09	1.89	1.44	1.39	0.49	0.25	0.03	-0.02	0.04	-0.09
Starburst E(B–V) = 0.51–0.60	1.53	1.35	1.05	1.09	0.43	0.24	-0.01	0.00	0.04	-0.22
Starburst E(B–V) < 0.1	1.10	0.97	0.79	0.80	0.24	0.05	-1.02	0.11	-0.03	-0.10
Sun	5.67	3.55	1.84	1.73	0.59	0.29	0.17	-0.04	0.05	-0.07
Vega	1.68	1.49	1.18	1.15	-0.08	-0.09	-0.08	0.03	0.00	0.09

Table 10.2 (continued)

Spectrum[a]	F625W	F658N	F660N	F775W	F814W	F850LP	F892N	G800L	PR200L	CLEAR
Avg Sky	-0.22	-0.25	-0.28	-0.40	-0.43	-0.48	-0.48	-0.35	0.19	0.26
Low Sky	-0.21	-0.24	-0.26	-0.38	-0.40	-0.45	-0.45	-0.33	0.23	0.31
O5V	0.29	0.40	0.38	0.67	0.77	1.03	0.98	0.56	-0.41	-0.53
B0V	0.27	0.41	0.39	0.66	0.75	1.00	0.96	0.55	-0.30	-0.40
A0V	0.17	0.38	0.30	0.40	0.44	0.54	0.51	0.33	0.34	0.40
A5V	0.11	0.31	0.22	0.27	0.31	0.39	0.37	0.23	0.37	0.44
F2V	-0.02	0.08	0.02	0.02	0.04	0.09	0.08	0.02	0.34	0.41
G2V	-0.16	-0.17	-0.20	-0.26	-0.27	-0.28	-0.29	-0.23	0.28	0.36
K0V	-0.24	-0.28	-0.30	-0.40	-0.42	-0.46	-0.47	-0.35	0.24	0.32
M0V	-0.55	-0.82	-0.83	-1.32	-1.47	-1.74	-1.66	-1.19	-0.33	-0.24
M6V	-0.58	-0.93	-0.94	-1.55	-1.74	-2.07	-1.94	-1.42	-0.51	-0.43
O6I	0.28	0.38	0.38	0.66	0.76	1.01	0.97	0.55	-0.39	-0.51
B0I	0.25	0.36	0.35	0.61	0.70	0.93	0.89	0.51	-0.24	-0.32
G0III	-0.15	-0.16	-0.19	-0.25	-0.26	-0.27	-0.28	-0.22	0.29	0.37
K0III	-0.32	-0.39	-0.40	-0.55	-0.59	-0.68	-0.70	-0.50	0.18	0.27
M0III	-0.57	-0.81	-0.82	-1.26	-1.41	-1.68	-1.63	-1.16	-0.28	-0.20
Elliptical	-0.33	-0.45	-0.46	-0.68	-0.76	-0.91	-0.91	-0.62	0.07	0.15

Spectrum									
Sa	-0.29	-0.45	-0.42	-0.56	-0.63	-0.78	-0.78	-0.52	0.13	0.21
Sbc	-0.25	-0.34	-0.34	-0.54	-0.61	-0.77	-0.72	-0.49	0.11	0.18
Scd	-0.20	-0.26	-0.27	-0.38	-0.40	-0.45	-0.43	-0.33	0.16	0.23
Starburst E(B–V) = 0.51–0.60	-0.41	-1.50	-1.00	-0.50	-0.53	-0.61	-0.59	-0.50	0.02	0.08
Starburst E(B–V) < 0.1	-0.13	-1.20	-0.36	-0.14	-0.18	-0.27	-0.20	-0.18	0.12	0.17
Sun	-0.17	-0.17	-0.20	-0.27	-0.27	-0.28	-0.29	-0.23	0.28	0.36
Vega	0.17	0.38	0.29	0.39	0.43	0.53	0.49	0.32	0.34	0.40

[a]Castelli & Kurucz models are used for the stellar spectra.

Table 10.3: Color corrections AB_V to go from Johnson V magnitude to AB magnitude for the SBC (ACS ISR 2019-10).

Spectrum [a]	F115LP	F122M	F125LP	F140LP	F150LP	F165LP	PR110l	PR130L
Avg Sky	-2.67	-3.69	-0.29	4.31	9.03	7.56	-2.12	-0.26
Low Sky	-1.20	-2.29	4.02	8.51	10.34	8.90	-0.59	4.04
O5V	-1.95	-2.00	-1.95	-1.87	-1.81	-1.74	-1.94	-1.94
B0V	-1.55	-1.55	-1.56	-1.48	-1.42	-1.41	-1.54	-1.56
A0V	3.33	4.70	3.13	2.70	2.40	2.05	3.11	3.07
A5V	5.97	8.22	5.78	5.14	4.47	3.23	5.59	5.58
F2V	8.37	10.81	8.17	7.53	6.85	5.42	7.94	7.93
G2V[b]	12.19	16.36	11.98	11.33	10.67	9.20	11.56	11.56
K0V[b]	12.91	18.58	12.70	12.05	11.39	9.91	12.26	12.26
M0V[b]	14.07	25.89	13.86	13.21	12.55	11.07	13.40	13.40
M6V[b]	14.04	28.31	13.83	13.17	12.52	11.04	13.37	13.37
O6I	-1.82	-1.86	-1.81	-1.75	-1.70	-1.66	-1.81	-1.81
B0I	-1.09	-1.05	-1.11	-1.07	-1.06	-1.10	-1.09	-1.11
	12.32	16.51	12.11	11.46	10.80	9.33	11.69	11.69

G0III[b]								
K0III[b]	13.74	23.50	13.53	12.87	12.22	10.74	13.07	13.07
M0III[b]	14.63	30.34	14.42	13.77	13.11	11.63	13.97	13.97
Elliptical	6.66	6.80	6.62	6.54	6.48	6.33	6.62	6.60
Sa	5.73	5.88	5.69	5.59	5.43	5.22	5.68	5.67
Sbc	4.22	4.57	4.14	3.93	3.74	3.45	4.13	4.11
Scd	2.90	3.14	2.84	2.68	2.54	2.33	2.83	2.82
Starburst E(B–V) = 0.51–0.60	2.35	2.52	2.31	2.18	2.09	1.89	2.30	2.29
Starburst E(B–V) < 0.1	1.50	1.60	1.47	1.40	1.35	1.30	1.47	1.46
Sun	11.51	11.78	11.62	11.02	10.38	9.00	11.17	11.28
Vega	2.76	4.02	2.56	2.17	2.00	1.87	2.57	2.52

a Castelli & Kurucz models are used for the stellar spectra.

b Stars of stellar type G and later may have chromospheric activity leading to UV emission lines not reproduced by the models, which may affect the color corrections listed here.

Table 10.4: Color corrections to go from GALEX NUV AB magnitude to AB magnitude for the SBC (ACS ISR 2019-10).

Spectrum[a]	F115LP	F122M	F125LP	F140LP	F150LP	F165LP	PR110l	PR130L
Avg Sky	-4.64	-5.66	-2.26	2.34	7.06	5.59	-4.09	-2.24
Low Sky	-6.42	-7.51	-1.20	3.29	5.13	3.68	-5.81	-1.18
O5V	-0.51	-0.56	-0.51	-0.43	-0.37	-0.30	-0.50	-0.50
B0V	-0.35	-0.35	-0.36	-0.27	-0.21	-0.20	-0.34	-0.35
A0V	1.58	2.95	1.38	0.94	0.64	0.30	1.36	1.31
A5V	3.55	5.79	3.36	2.72	2.05	0.81	3.17	3.16
F2V	5.05	7.49	4.85	4.20	3.53	2.10	4.61	4.61
G2V[b]	6.99	11.16	6.78	6.13	5.47	4.00	6.37	6.37
K0V[b]	6.53	12.19	6.32	5.66	5.01	3.53	5.87	5.87

Spectrum								
M0V[b]	2.85	14.67	2.64	1.98	1.33	-0.15	2.18	2.18
M6V[b]	2.67	16.95	2.46	1.80	1.15	-0.33	2.00	2.00
O6I	-0.43	-0.47	-0.43	-0.36	-0.31	-0.27	-0.42	-0.42
B0I	-0.07	-0.02	-0.09	-0.04	-0.03	-0.07	-0.07	-0.08
G0III[b]	6.86	11.05	6.65	6.00	5.34	3.87	6.24	6.24
K0III[b]	5.14	14.90	4.93	4.28	3.62	2.14	4.48	4.48
M0III[b]	1.42	17.12	1.21	0.55	-0.10	-1.59	0.75	0.75
Elliptical	1.56	1.70	1.52	1.44	1.38	1.23	1.52	1.51
Sa	1.21	1.36	1.17	1.07	0.91	0.70	1.16	1.15
Sbc	1.26	1.61	1.18	0.97	0.78	0.49	1.17	1.15
Scd	0.82	1.07	0.76	0.61	0.47	0.26	0.76	0.74
Starburst E(B–V) = 0.51–0.60	0.81	0.98	0.77	0.65	0.55	0.36	0.76	0.75
Starburst E(B–V) < 0.1	0.40	0.50	0.37	0.30	0.25	0.20	0.37	0.36
Sun	6.15	6.43	6.27	5.67	5.03	3.64	5.81	5.92
Vega	1.10	2.36	0.90	0.51	0.34	0.21	0.91	0.86

a Castelli & Kurucz models are used for the stellar spectra.

b Stars of stellar type G and later may have chromospheric activity leading to UV emission lines not reproduced by the models, which may affect the color corrections listed here.

Table 10.5: Color corrections to go from GALEX FUV AB magnitude to AB magnitude for the SBC (ACS ISR 2019-10).

Spectrum[a]	F115LP	F122M	F125LP	F140LP	F150LP	F165LP	PR110l	PR130L
Avg Sky	-14.68	-15.70	-12.30	-7.70	-2.98	-4.45	-14.13	-12.27
Low Sky	-13.43	-14.52	-8.21	-3.72	-1.88	-3.33	-12.81	-8.19
O5V	-0.10	-0.15	-0.09	-0.01	0.05	0.11	-0.08	-0.08
B0V	-0.09	-0.09	-0.10	-0.01	0.05	0.06	-0.08	-0.09
A0V	0.72	2.09	0.52	0.09	-0.21	-0.56	0.50	0.46

A5V	0.75	2.99	0.56	-0.08	-0.76	-1.99	0.37	0.36
F2V	0.20	2.65	0.00	-0.64	-1.31	-2.75	-0.23	-0.24
G2V[b]	-2.03	2.16	-2.24	-2.89	-3.55	-5.02	-2.66	-2.66
K0V[b]	-3.59	2.08	-3.80	-4.45	-5.11	-6.59	-4.24	-4.24
M0V[b]	-10.07	1.75	-10.28	-10.93	-11.59	-13.07	-10.73	-10.73
M6V[b]	-12.63	1.63	-12.84	-13.49	-14.15	-15.63	-13.29	-13.29
O6I	-0.11	-0.15	-0.10	-0.02	0.06	0.13	-0.09	-0.10
B0I	-0.10	-0.10	-0.12	-0.01	0.06	0.03	-0.09	-0.11
G0III[b]	-2.05	2.14	-2.26	-2.92	-3.57	-5.05	-2.68	-2.68
K0III[b]	-7.19	1.57	-7.40	-8.05	-8.71	-10.19	-7.86	-7.86
M0III[b]	-12.32	1.36	-12.53	-13.18	-13.84	-15.32	-12.98	-12.98
Elliptical	0.11	0.26	0.07	-0.01	-0.07	-0.22	0.07	0.06
Sa	0.19	0.35	0.15	0.05	-0.11	-0.32	0.15	0.13
Sbc	0.33	0.67	0.25	0.03	-0.15	-0.44	0.24	0.22
Scd	0.25	0.49	0.19	0.03	-0.11	-0.32	0.18	0.17
Starburst E(B–V) = 0.51–0.60	0.20	0.37	0.16	0.04	-0.06	-0.25	0.15	0.14
Starburst E(B–V) < 0.1	0.13	0.23	0.10	0.03	-0.03	-0.08	0.10	0.09
Sun	-0.94	-0.66	-0.83	-1.43	-2.06	-3.45	-1.28	-1.17
Vega	0.65	1.90	0.45	0.06	-0.11	-0.25	0.46	0.40

[a] Castelli & Kurucz models are used for the stellar spectra.

[b] Stars of stellar type G and later may have chromospheric activity leading to UV emission lines not reproduced by the models, which may affect the color corrections listed here.

WFC F435W

Description

Johnson B filter.

Figure 10.1: Integrated system throughput for WFC/F435W.
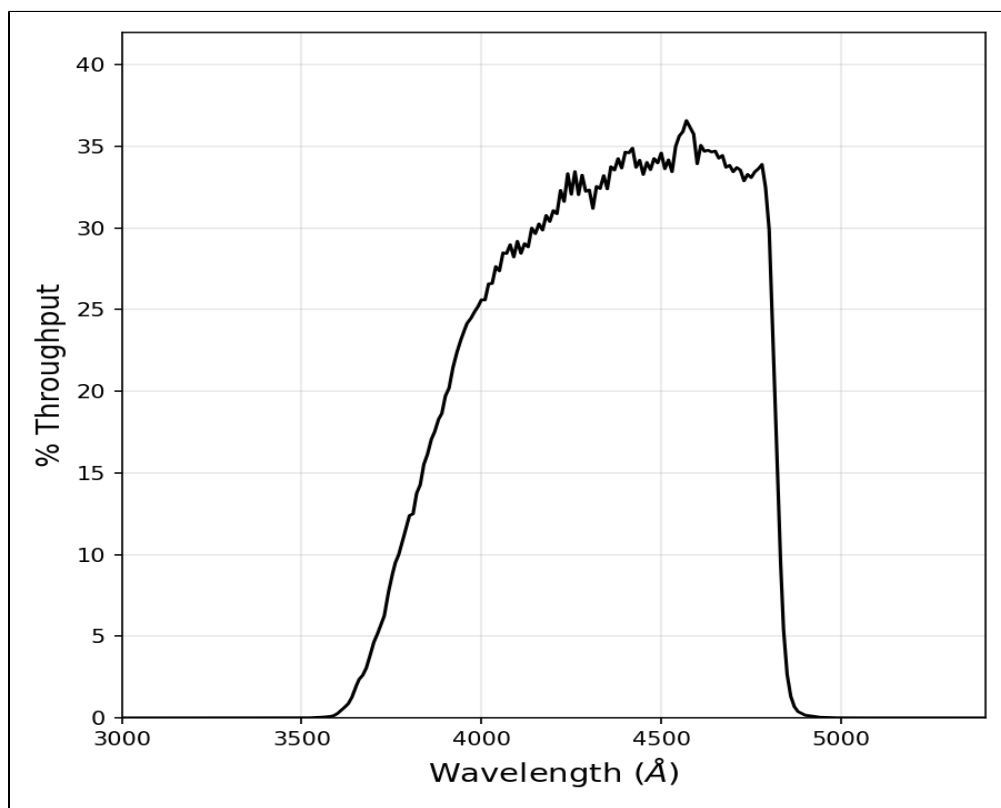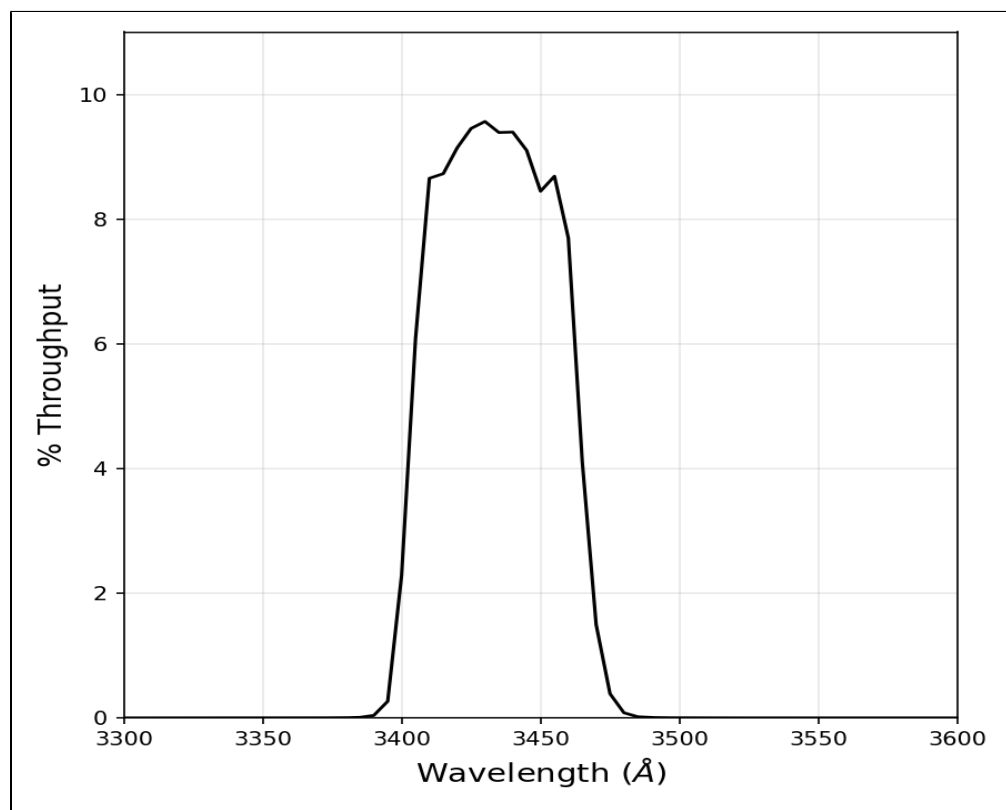
Figure 10.2: Point source S/N vs. V+ABv for the WFC/F435W filter. Top curves are for low sky; bottom curves are for average sky.
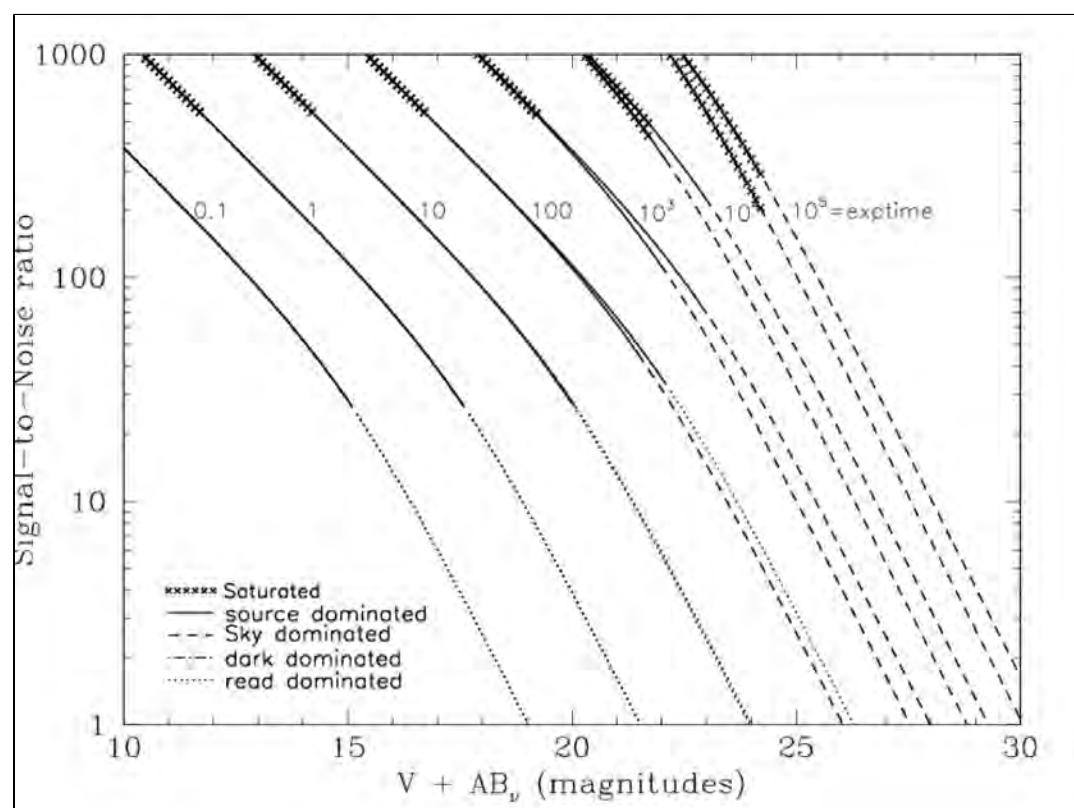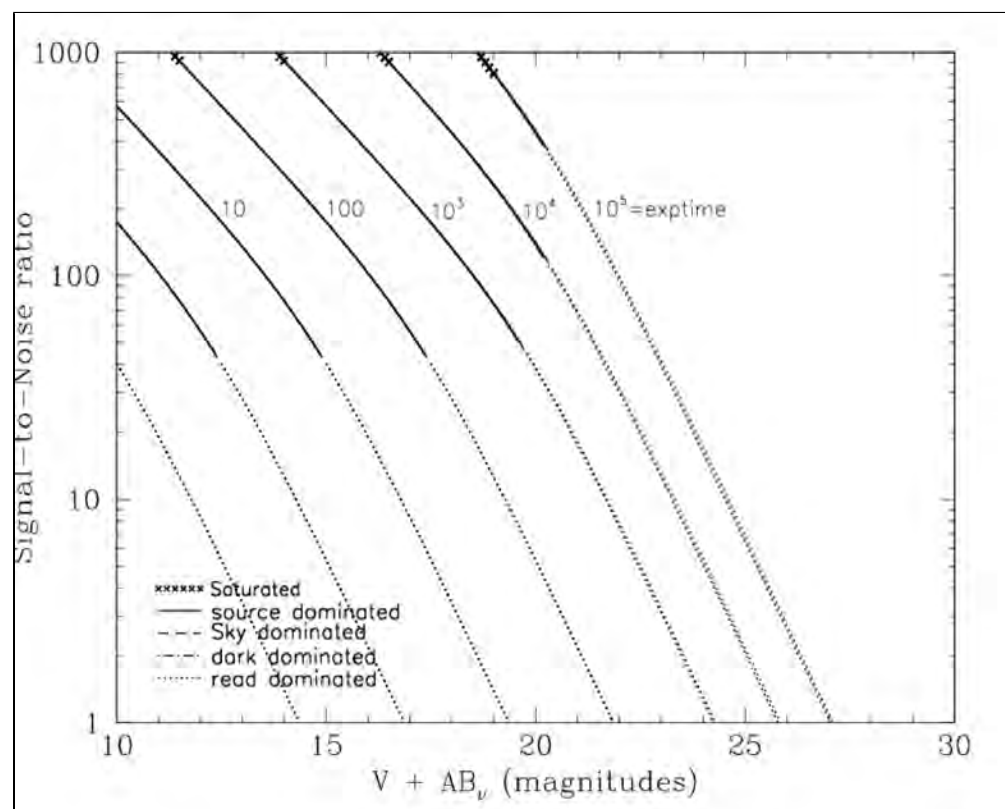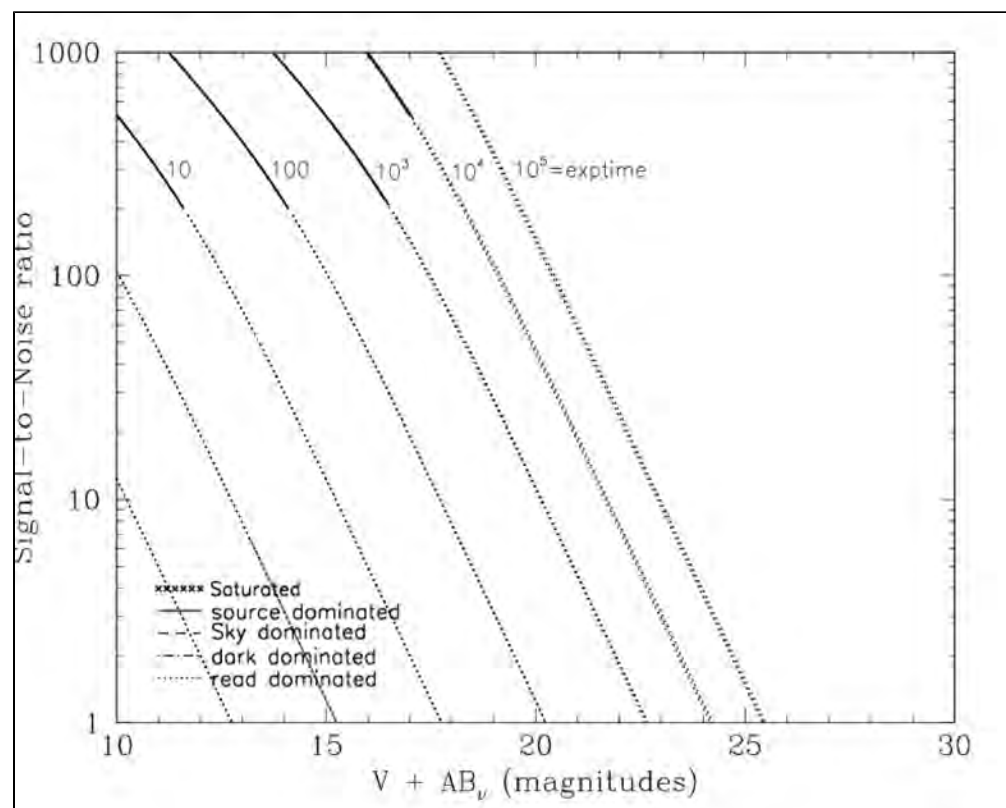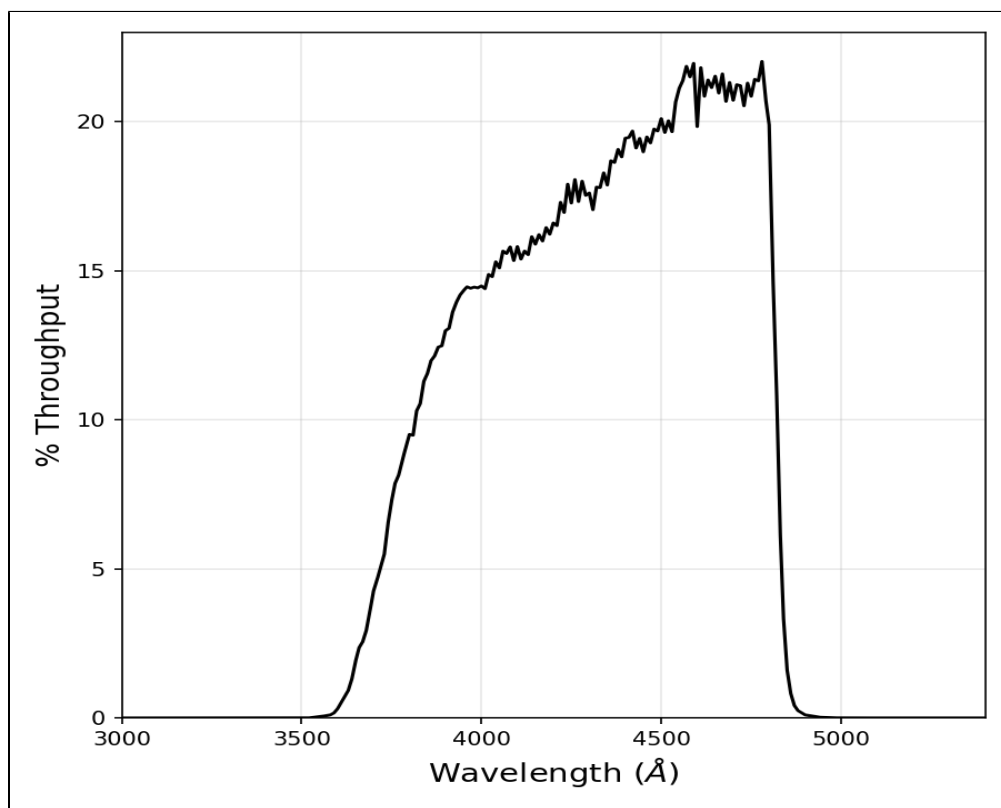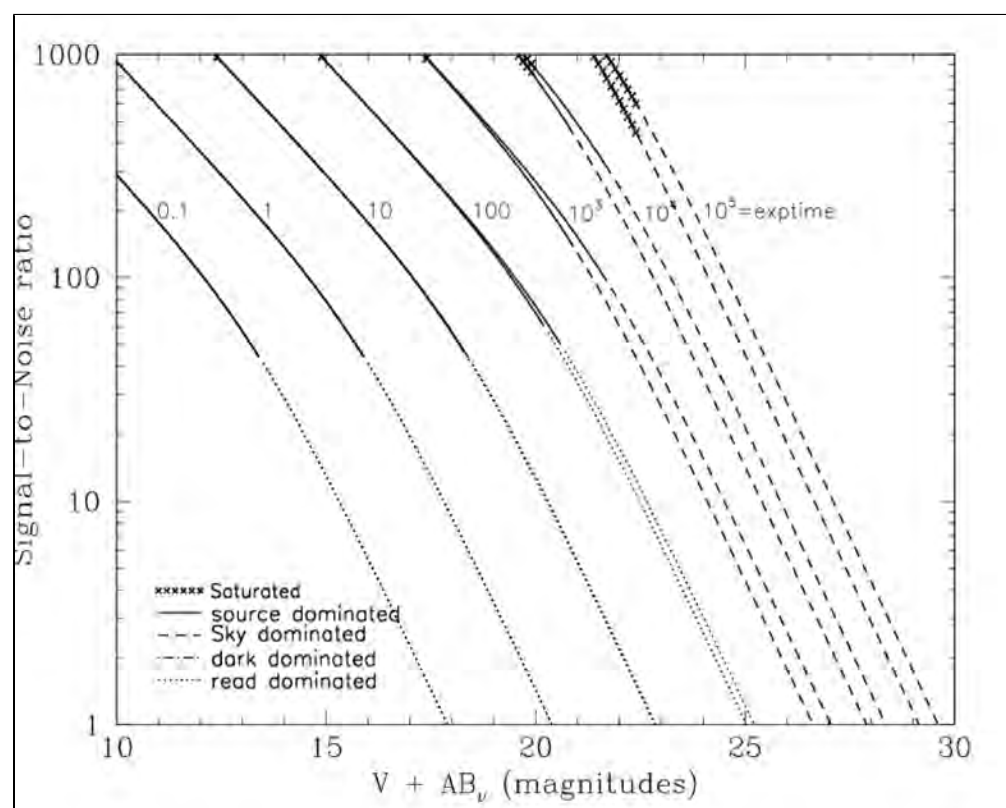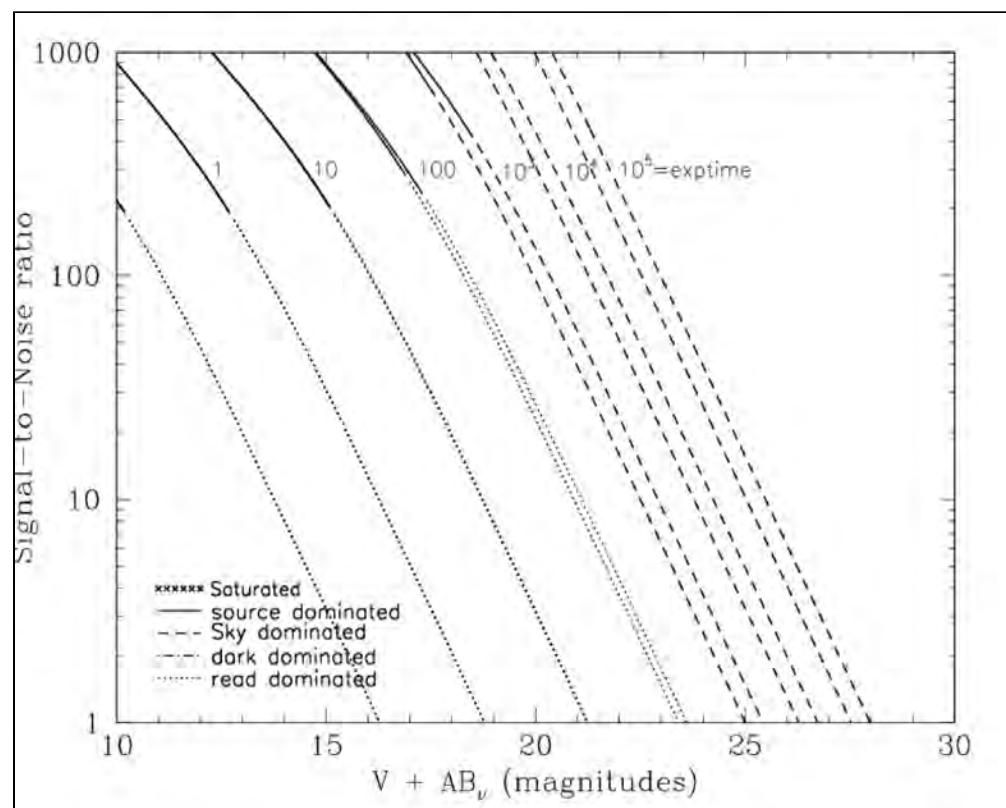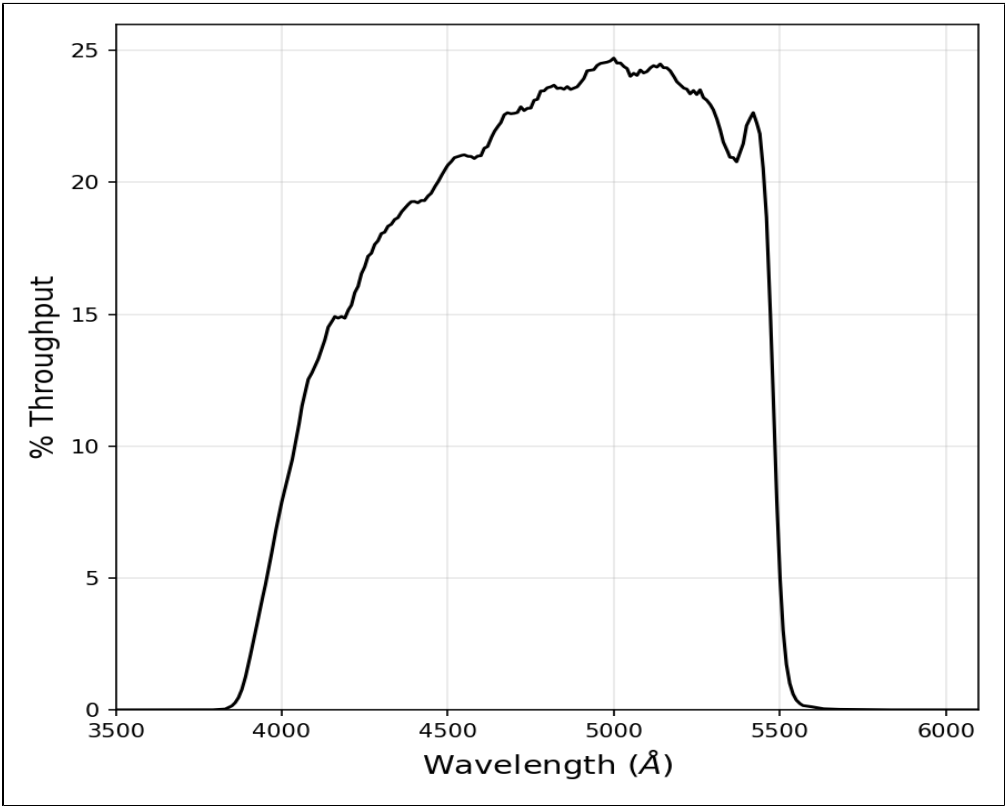
Figure 10.3: Extended source S/N vs. V+ABv for the WFC/F435W filter. Top curves are for low sky and bottom curves are for average sky for a 1 arcsec^2 area.
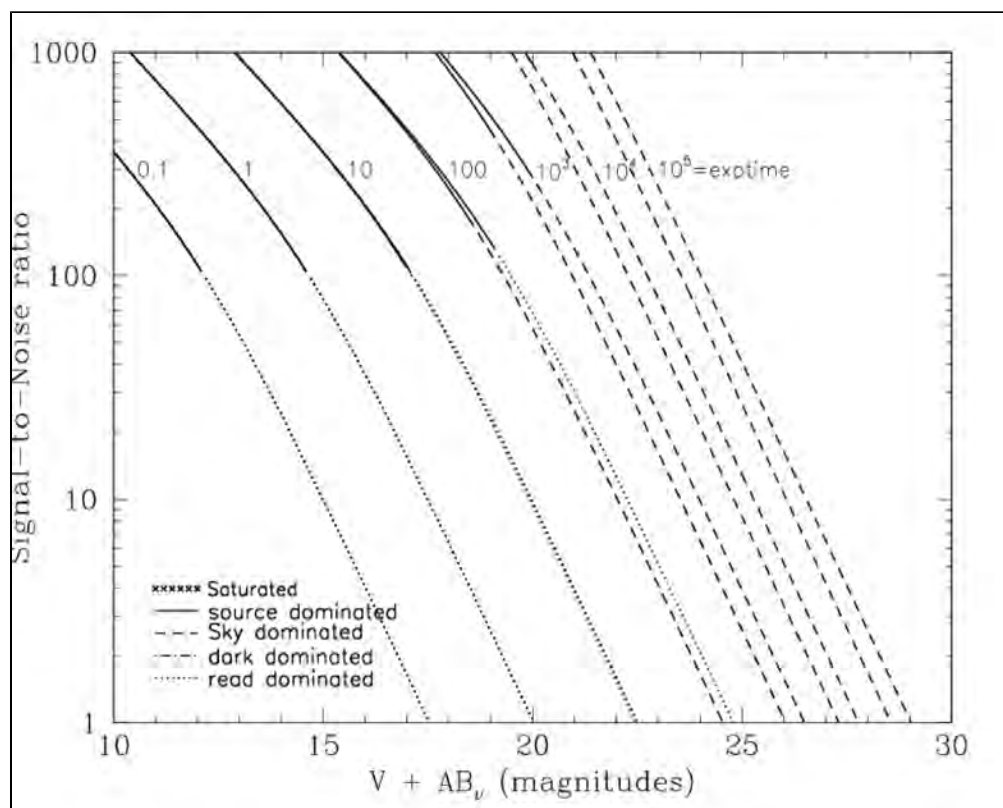
WFC F475W

Description

Sloan Digital Sky Survey g filter.

Figure 10.4: Integrated system throughput for WFC/F475W.
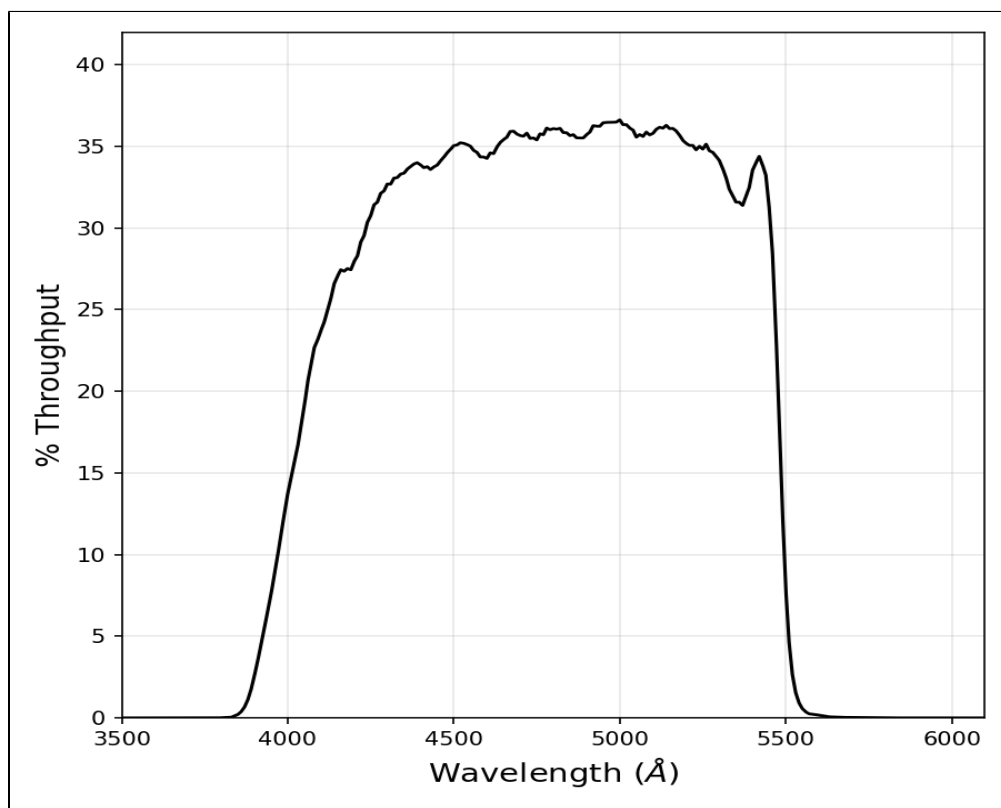
Figure 10.5: Point source S/N vs. V+ABv for the WFC/F475W filter. Top curves are for low sky; bottom curves are for average sky.
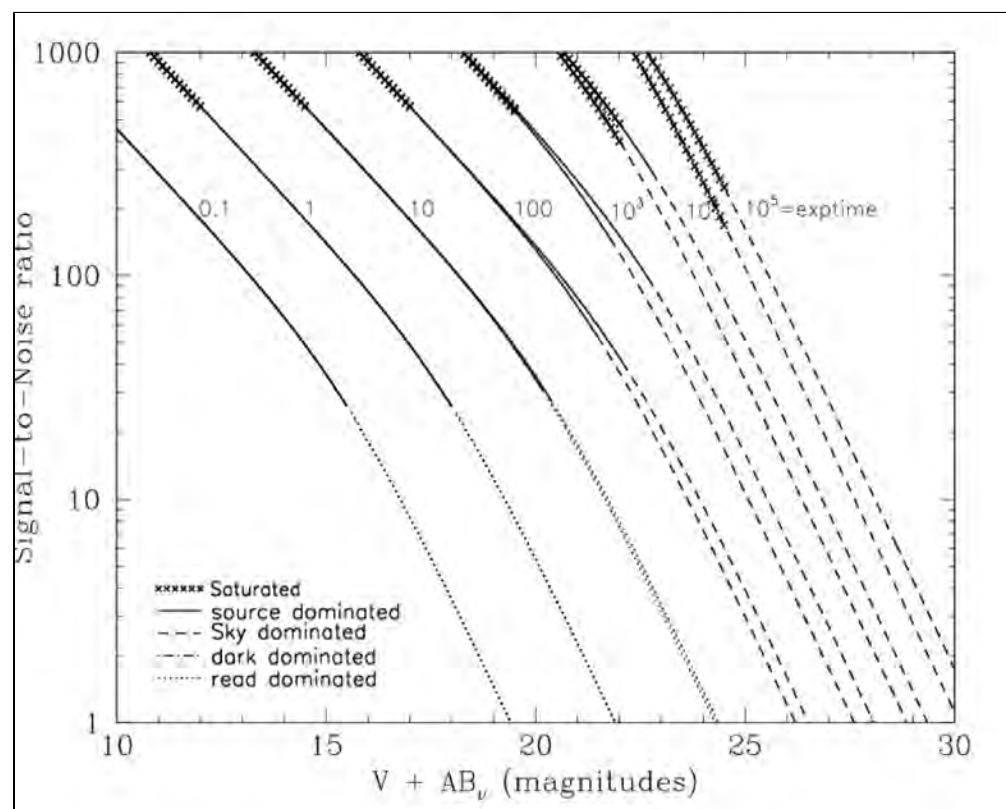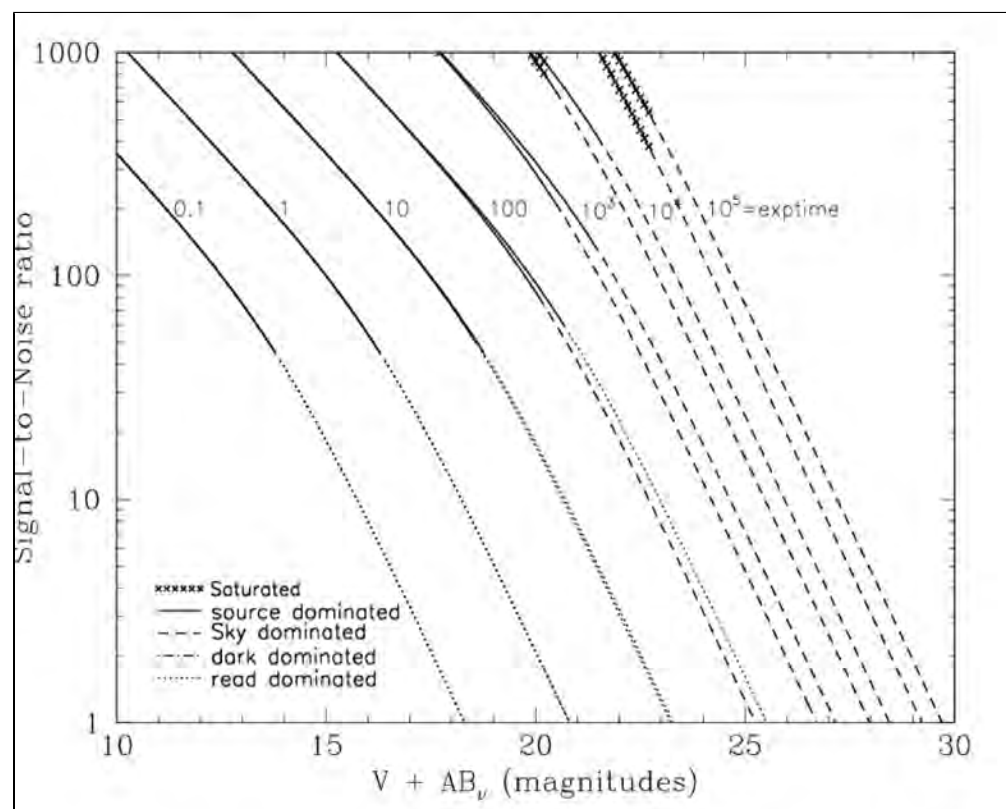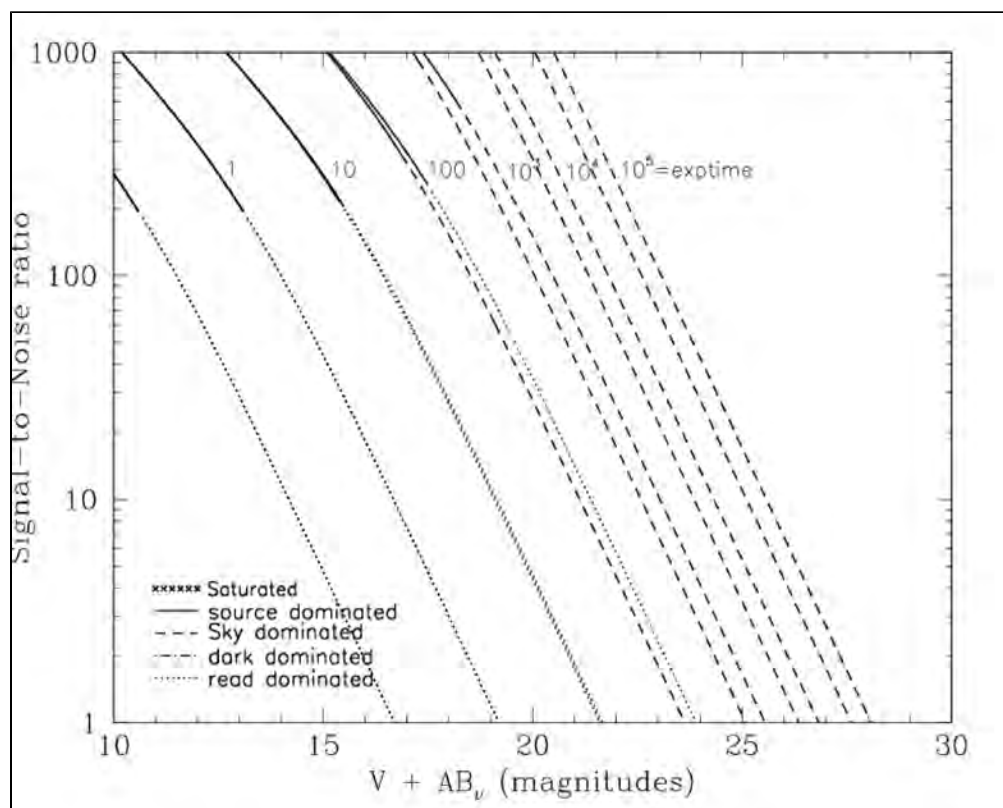
Figure 10.6: Extended source S/N vs. V+ABv for the WFC/F475W filter. Top curves are for low sky and bottom curves are for average sky for a 1 arcsec^2 area.
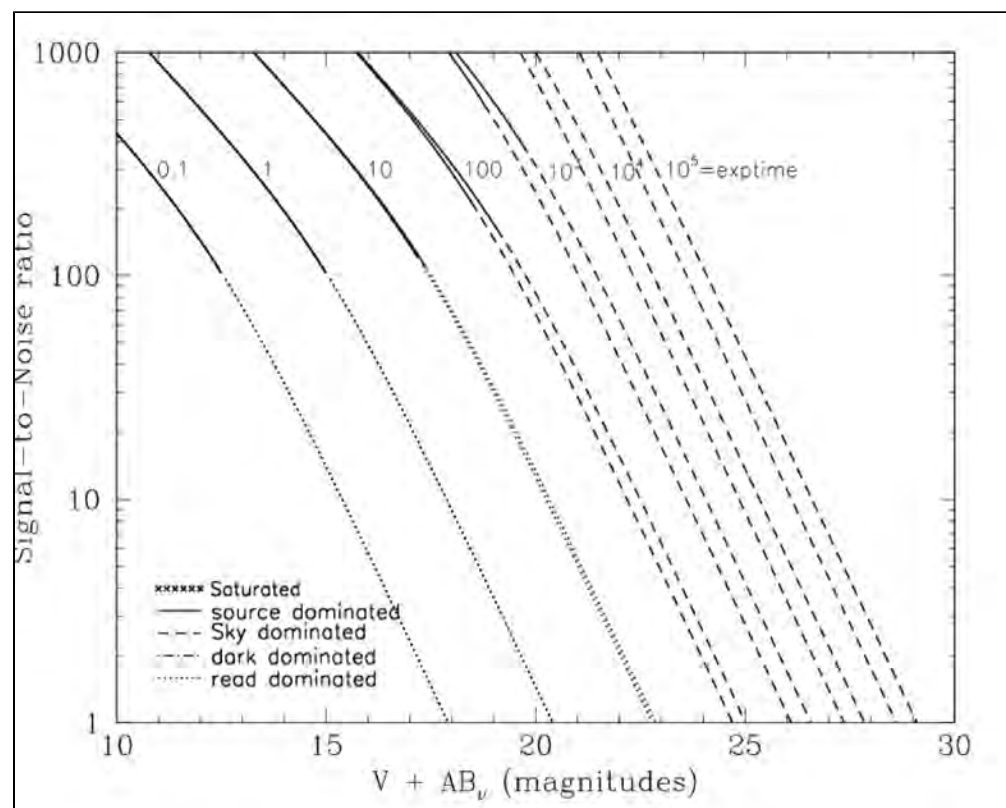
WFC F502N

Description

O$_{III}$ filter.

Figure 10.7: Integrated system throughput for WFC/F502N.
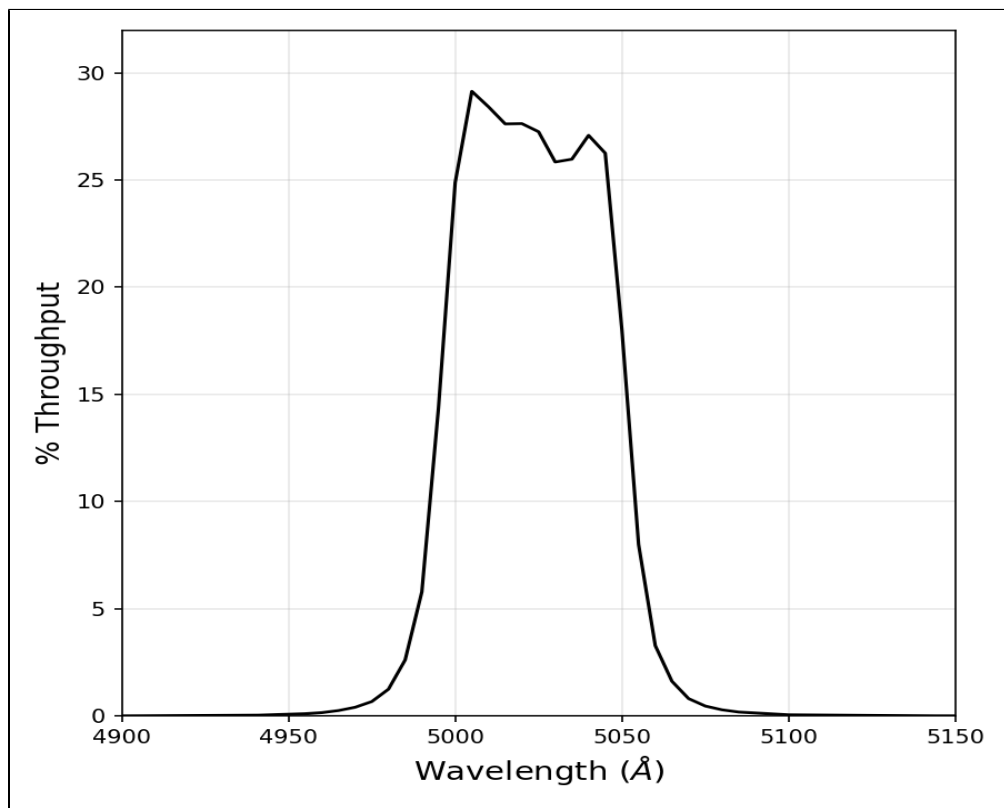
Figure 10.8: Point source S/N vs. V+ABν for the WFC/F502N filter. Top curves are for low sky; bottom curves are for average sky.
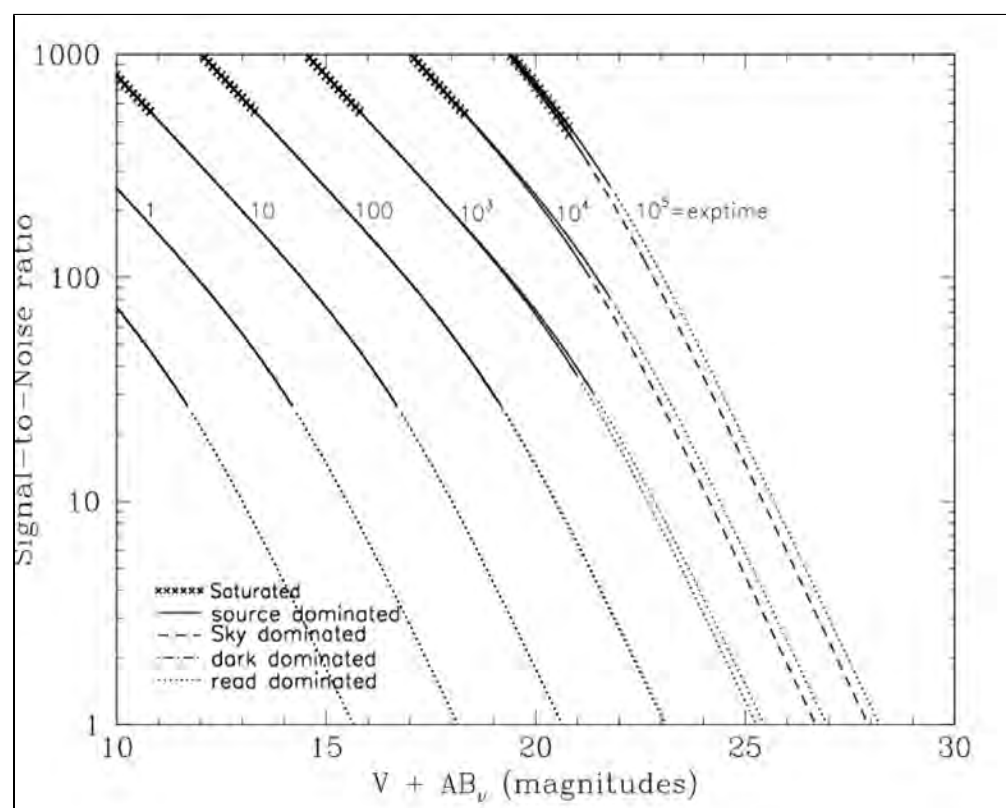
Figure 10.9: Extended source S/N vs. V+ABv for the WFC/F502N filter. Top curves are for low sky and bottom curves are for average sky for a 1 arcsec^2 area.
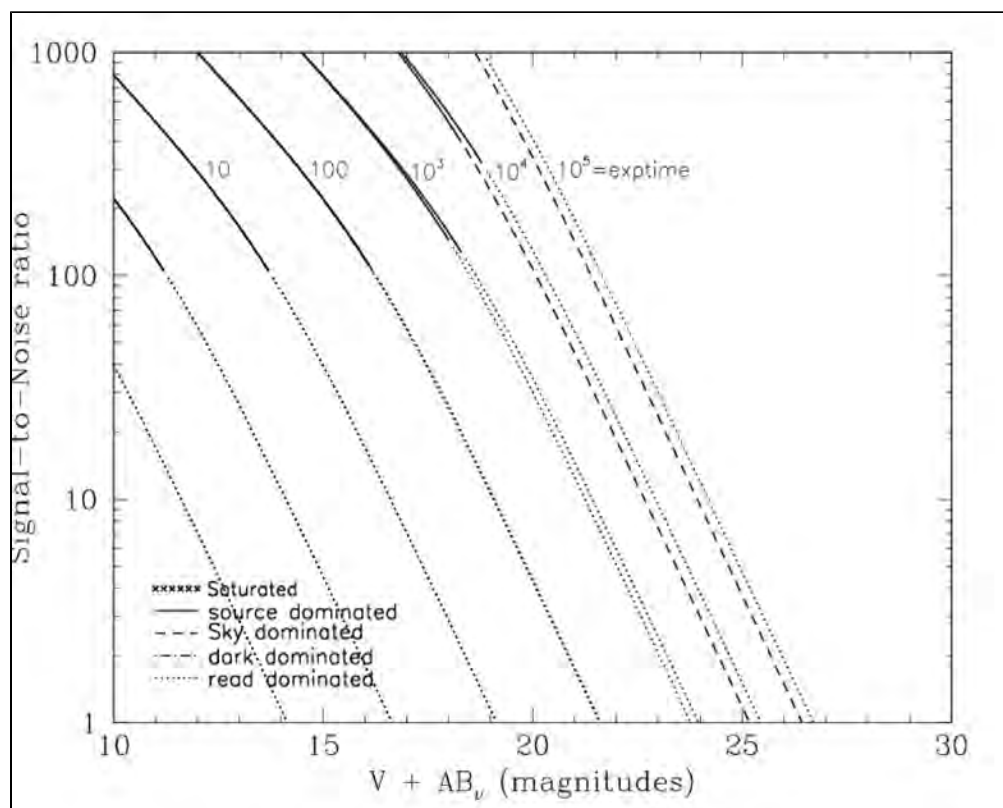
WFC F550M

Description

Narrow V filter.

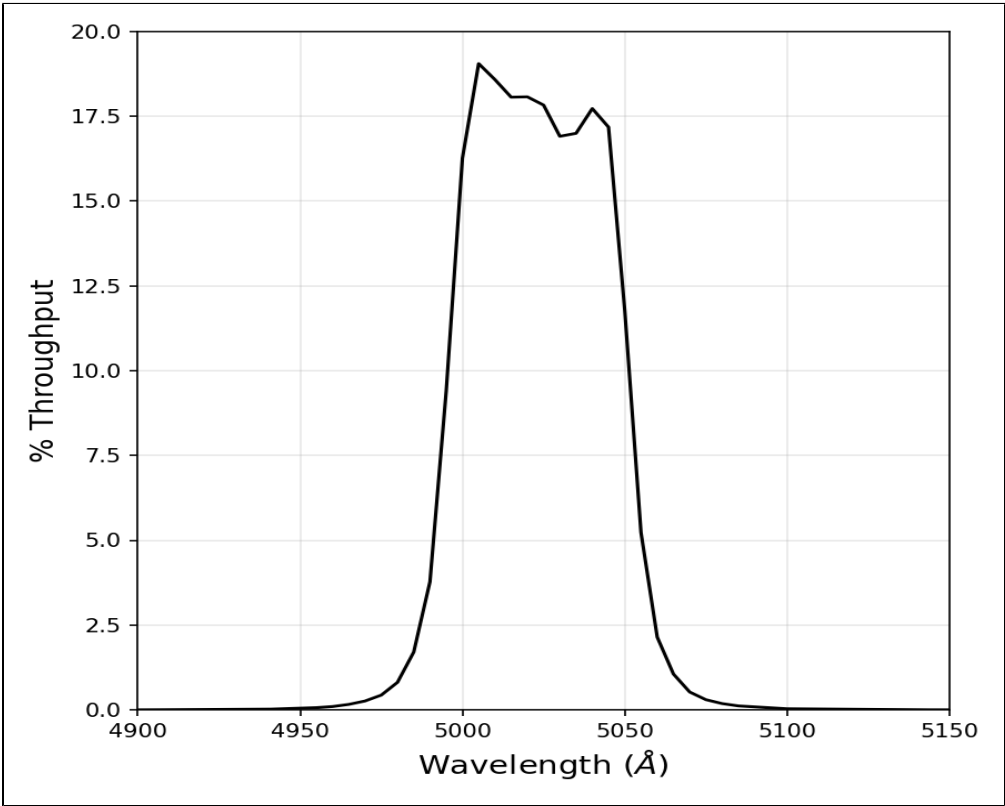**Figure 10.10:** Integrated system throughput for WFC/F550M.
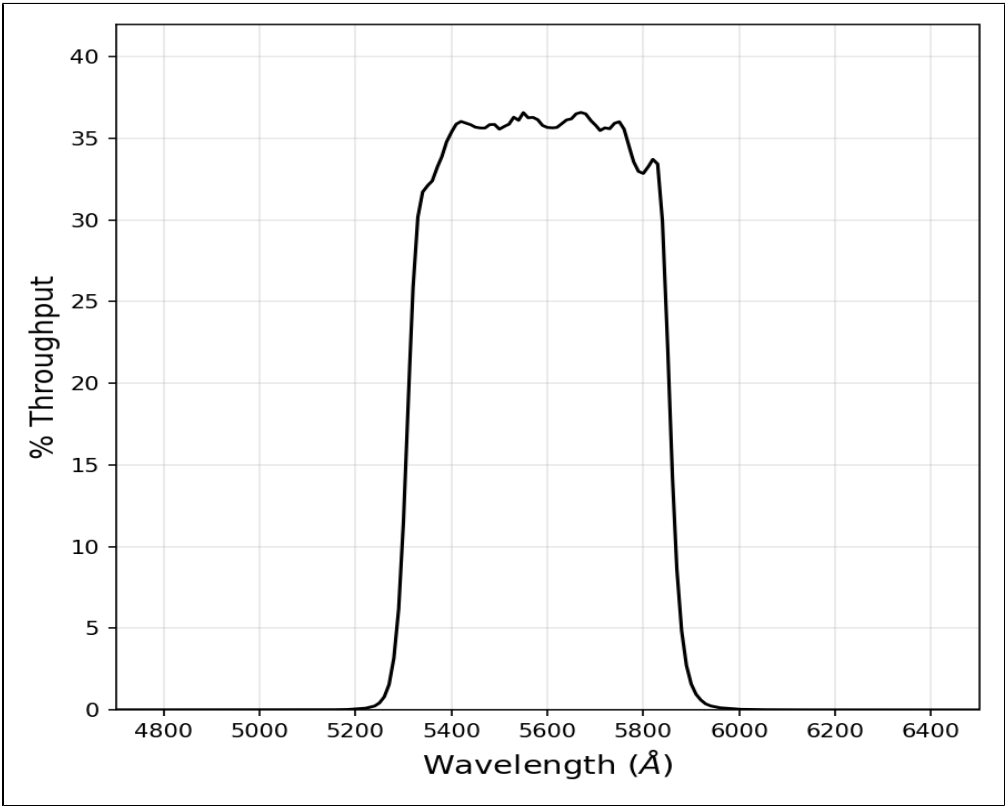
Figure 10.11: Point source S/N vs. V+ABν for the WFC/F550M filter. Top curves are for low sky; bottom curves are for average sky.
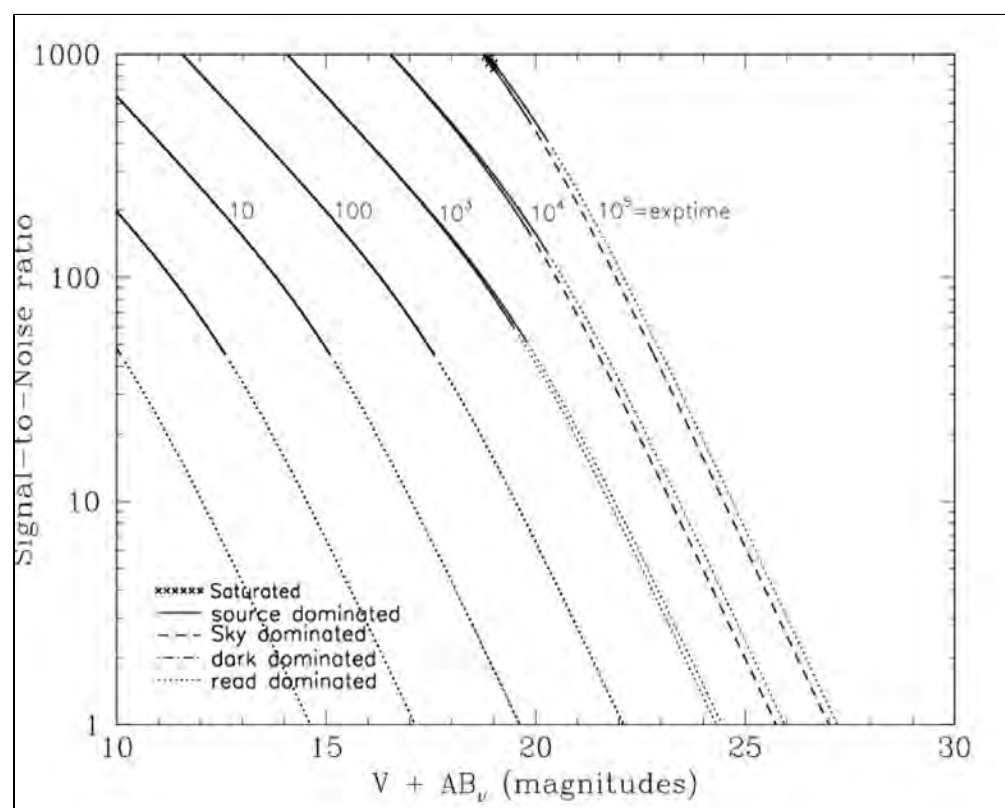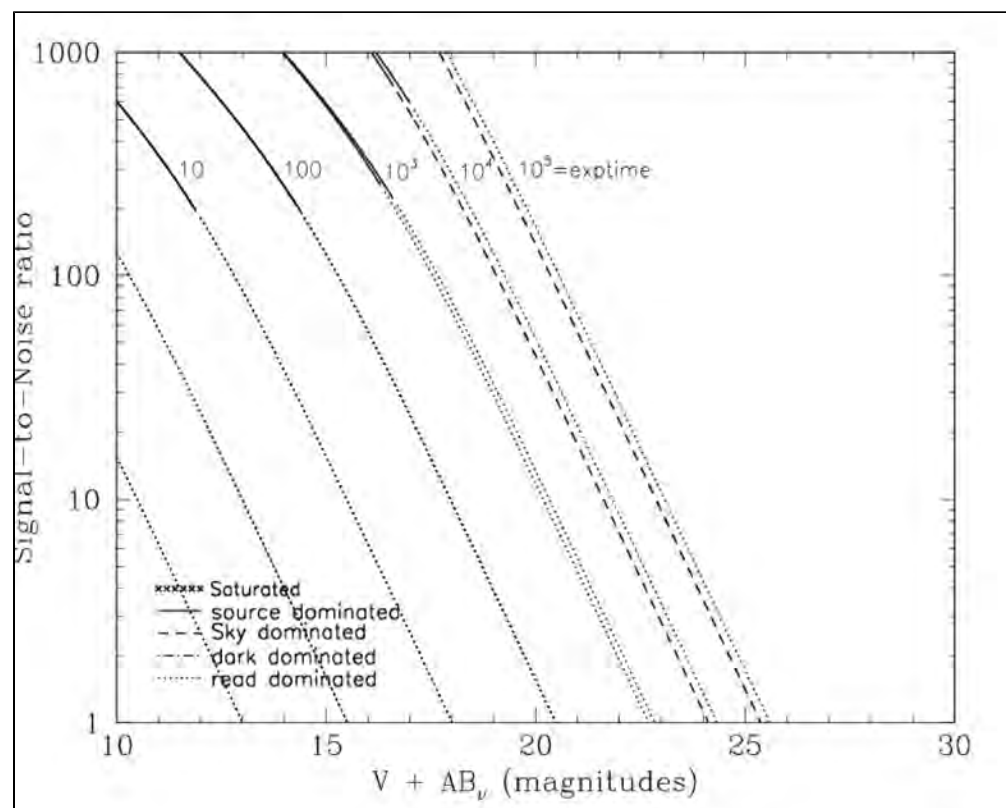
Figure 10.12: Extended source S/N vs. V+ABv for the WFC/F550M filter. Top curves are for low sky and bottom curves are for average sky for a 1 arcsec² area.
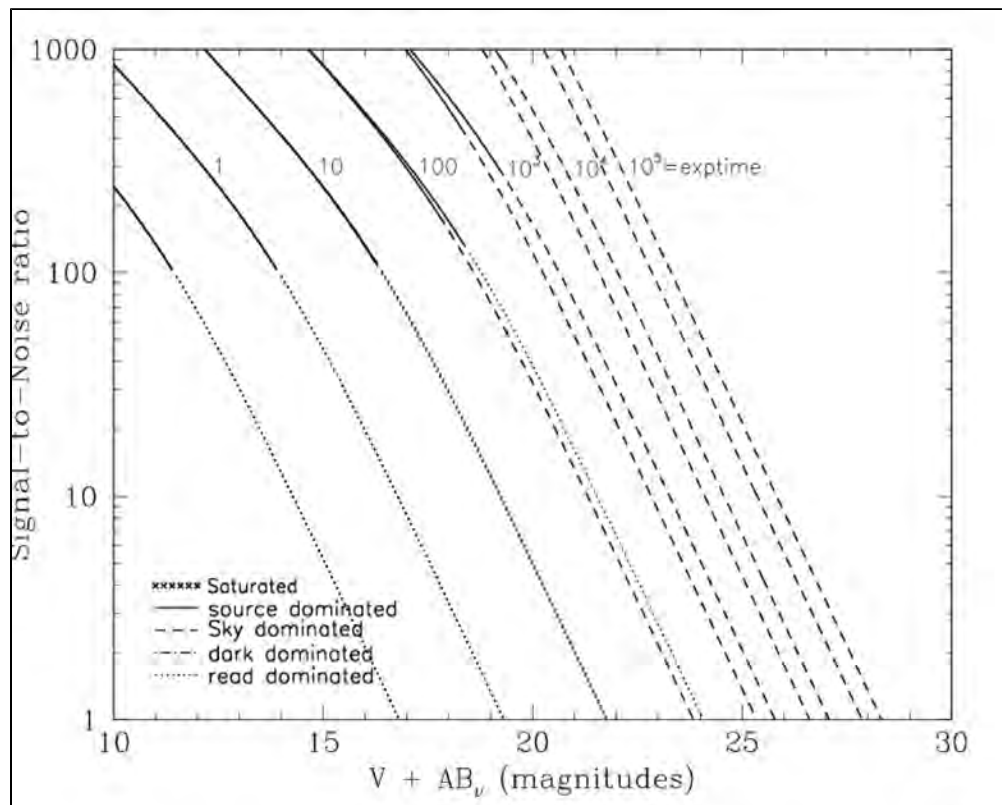
WFC F555W

Description

Johnson V filter.

Figure 10.13: Integrated system throughput for WFC/F555W.
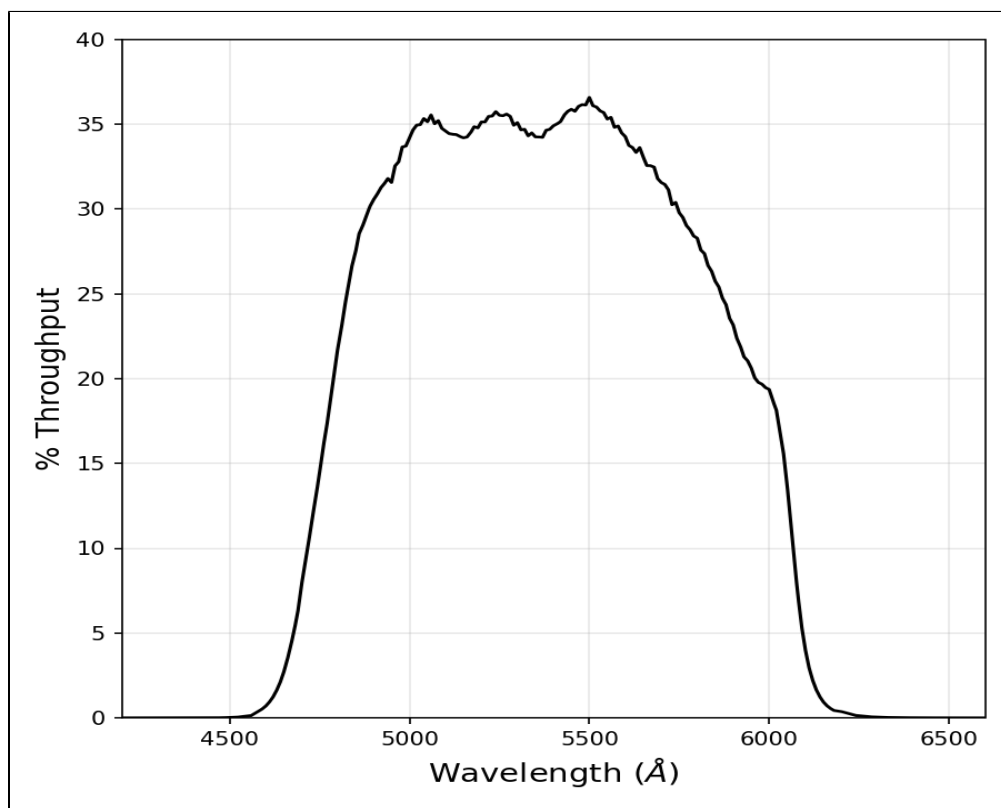
Figure 10.14: Point source S/N vs. V+ABν for the WFC/F555W filter. Top curves are for low sky; bottom curves are for average sky.

Figure 10.15: Extended source S/N vs. V+ABv for the WFC/F555W filter. Top curves are for low sky and bottom curves are for average sky for a 1 arcsec² area.
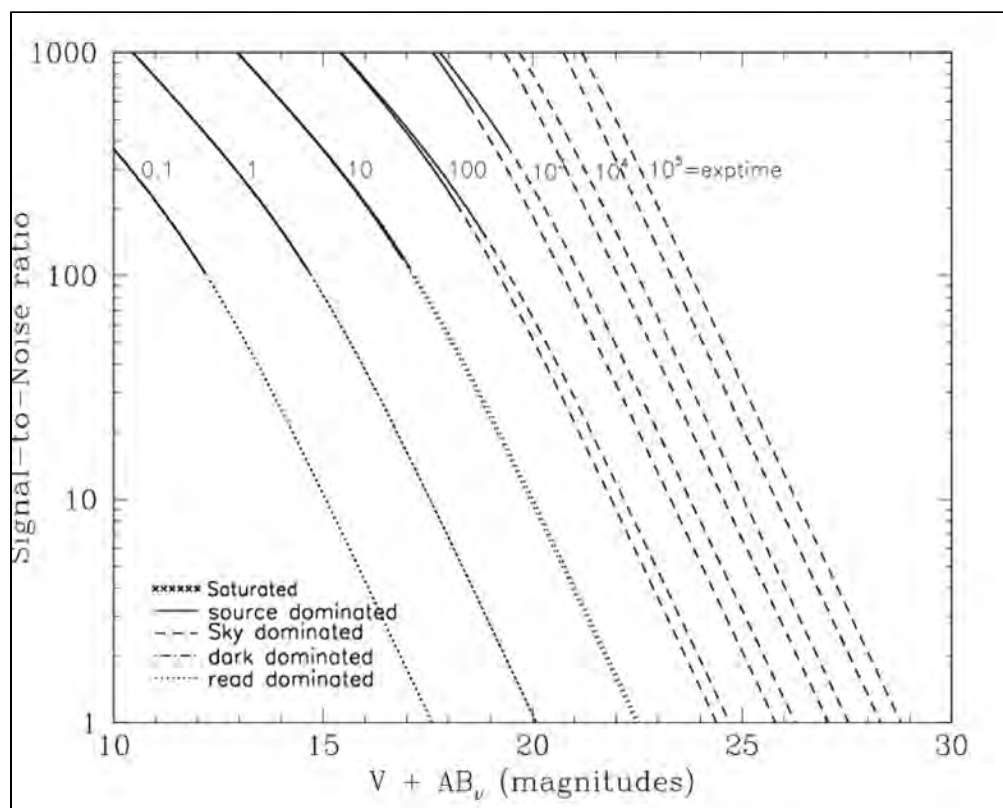
WFC F606W

Description

Broad V filter.

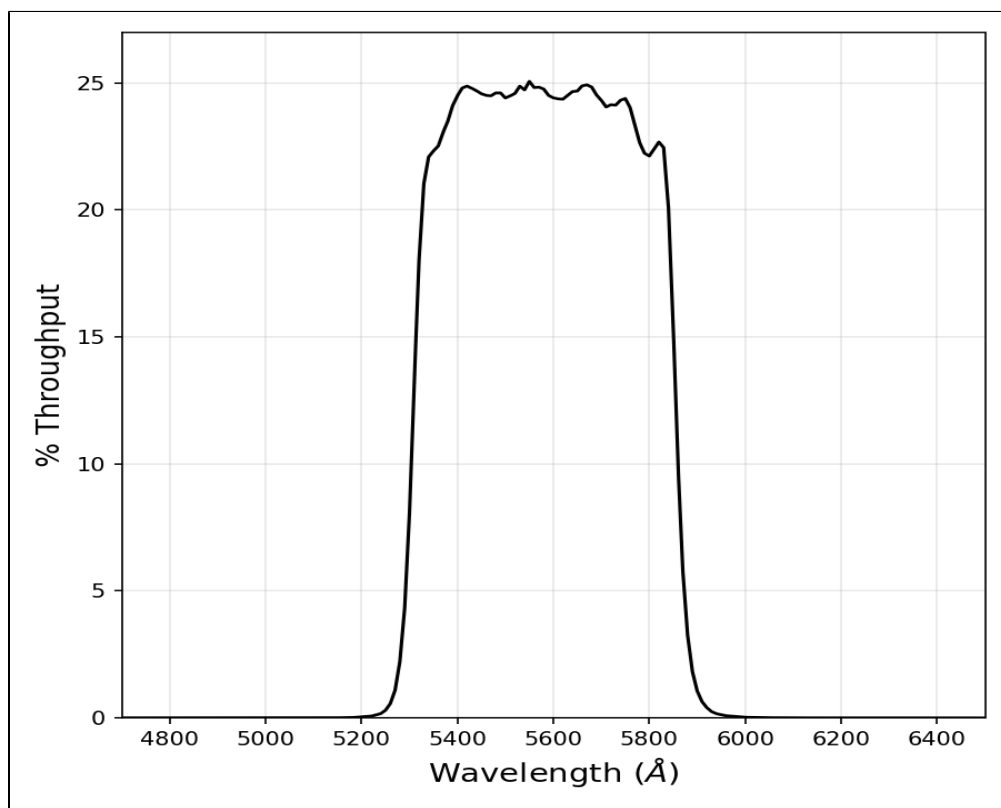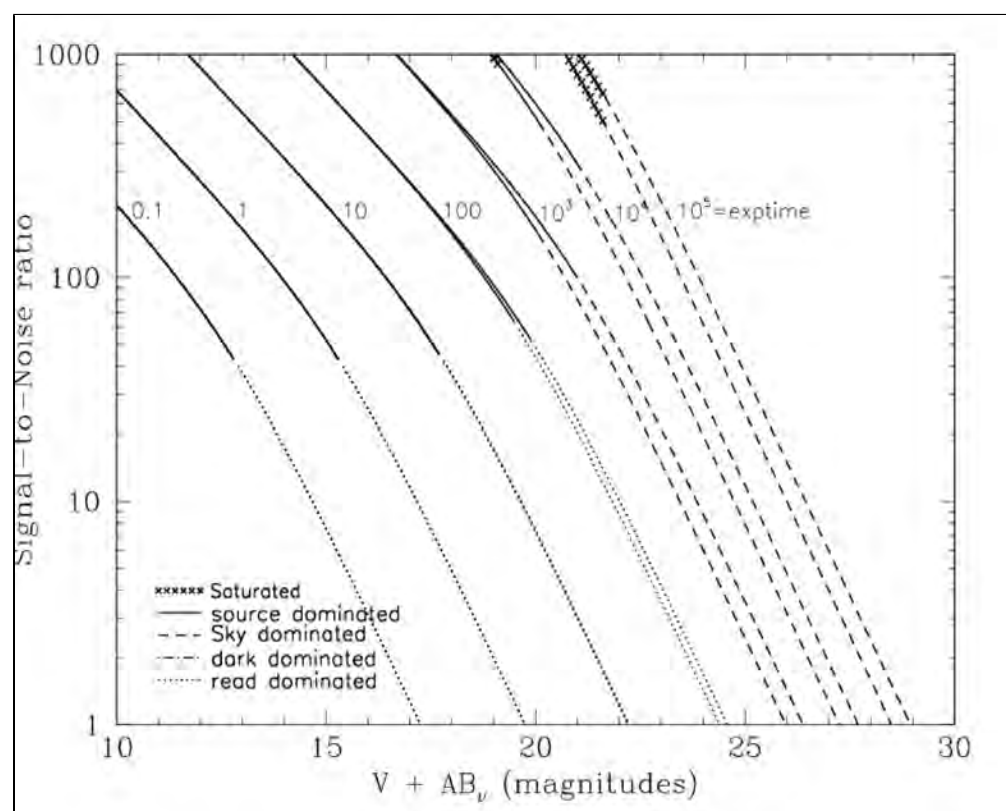**Figure 10.16:** Integrated system throughput for WFC/F606W.
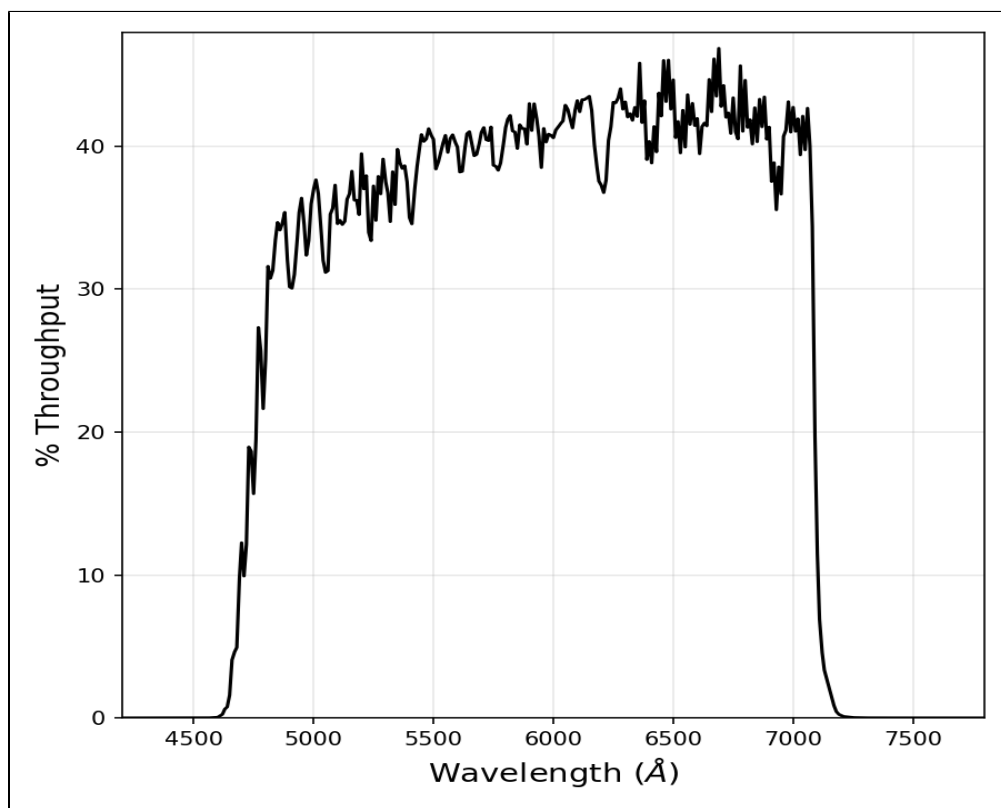
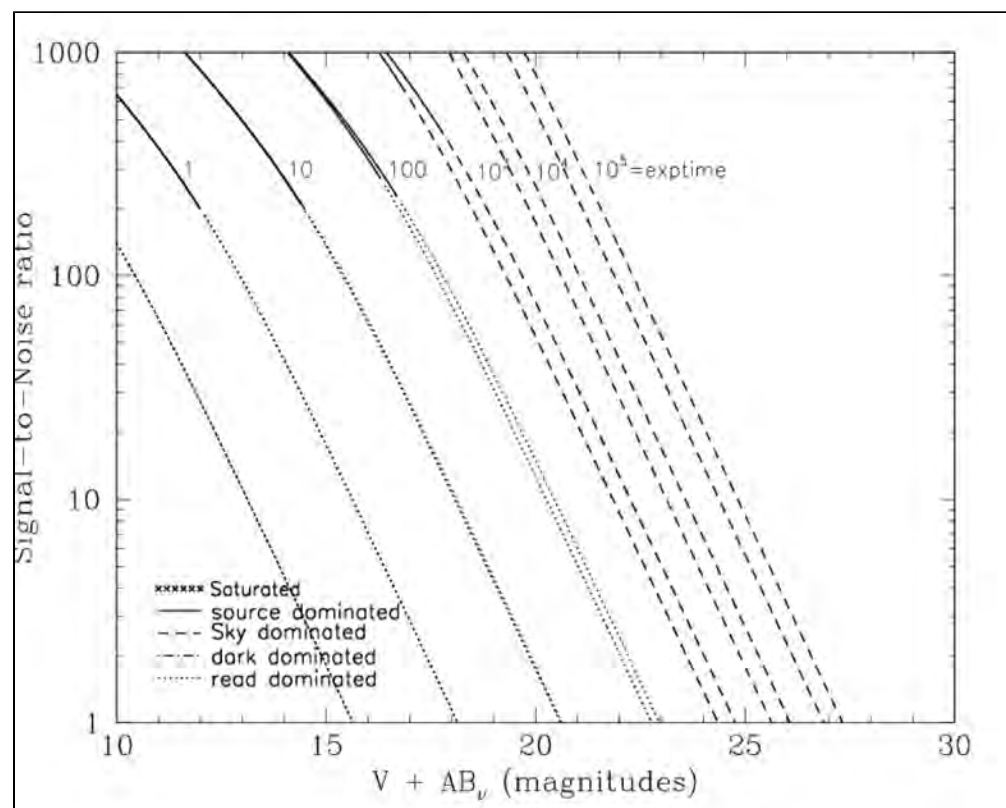Figure 10.17: Point source S/N vs. V+ABv for the WFC/F606W filter. Top curves are for low sky; bottom curves are for average sky.
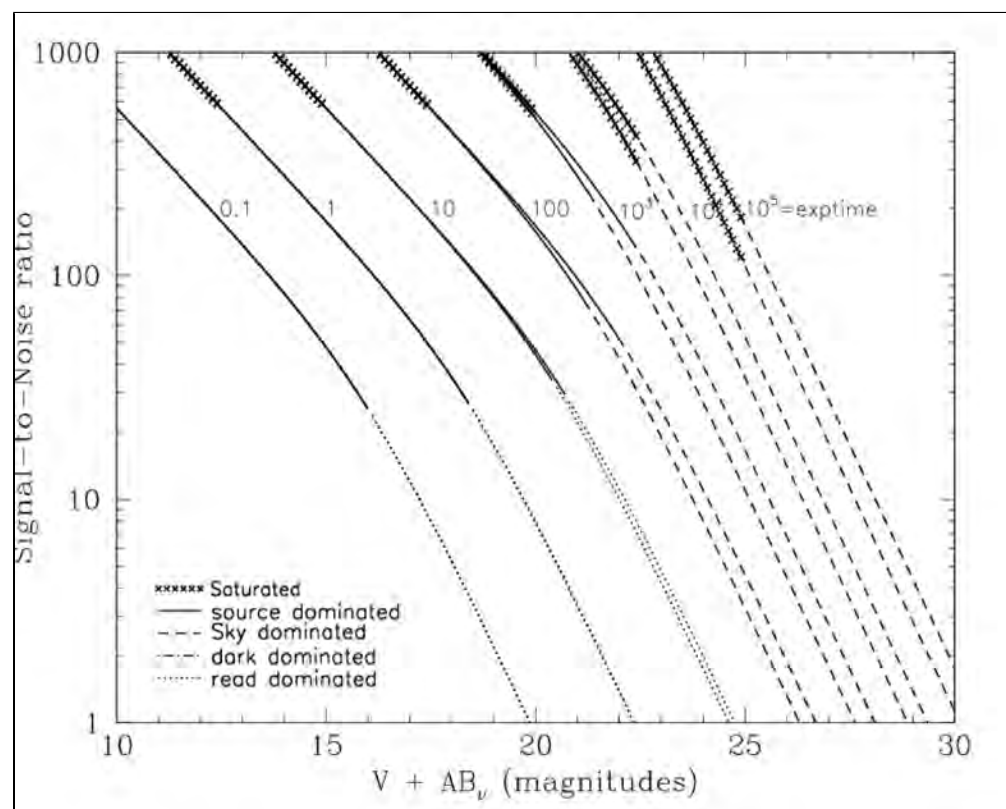
Figure 10.18: Extended source S/N vs. V+ABv for the WFC/F606W. Top curves are for low sky and bottom curves are for average sky for a 1 arcsec^2 area.
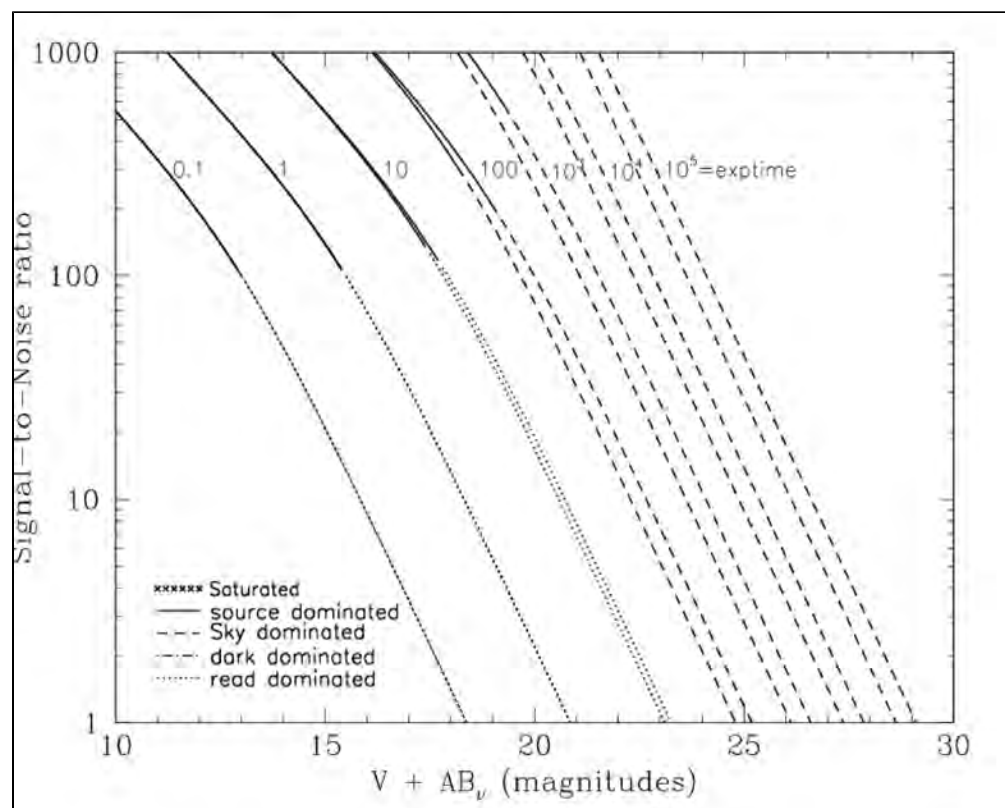
WFC F625W

Description

Sloan Digital Sky Survey r filter.

Figure 10.19: Integrated system throughput for WFC/F625W.
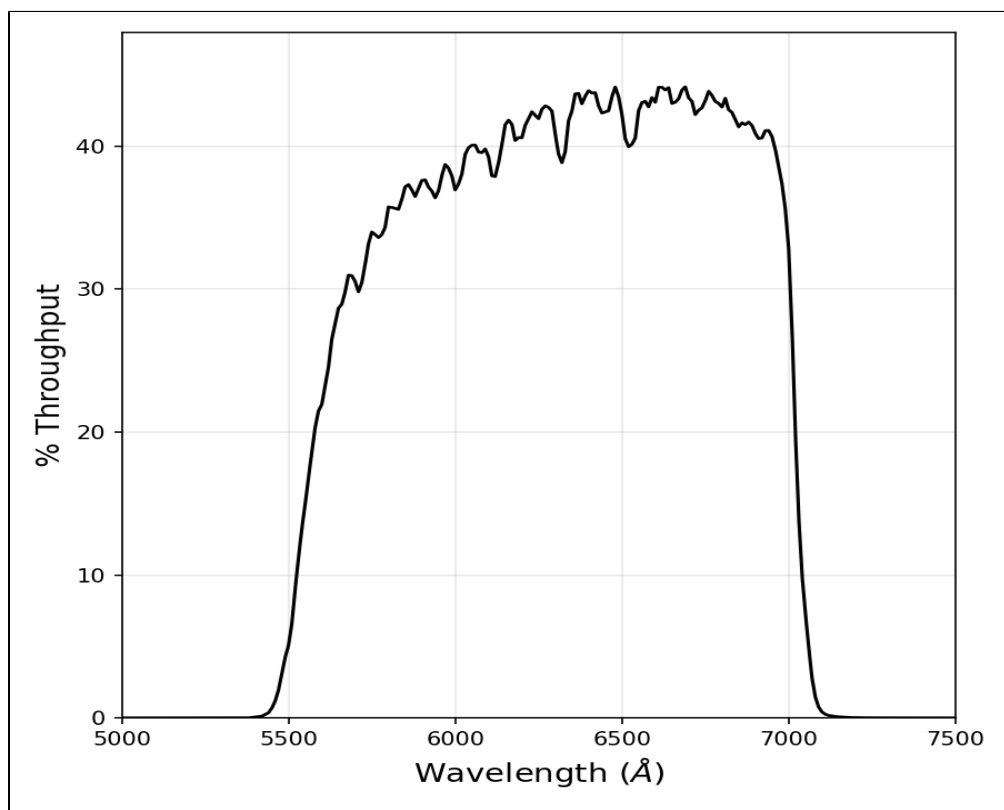
Figure 10.20: Point source S/N vs. V+ABν for the WFC/F625W filter. Top curves are for low sky; bottom curves are for average sky.
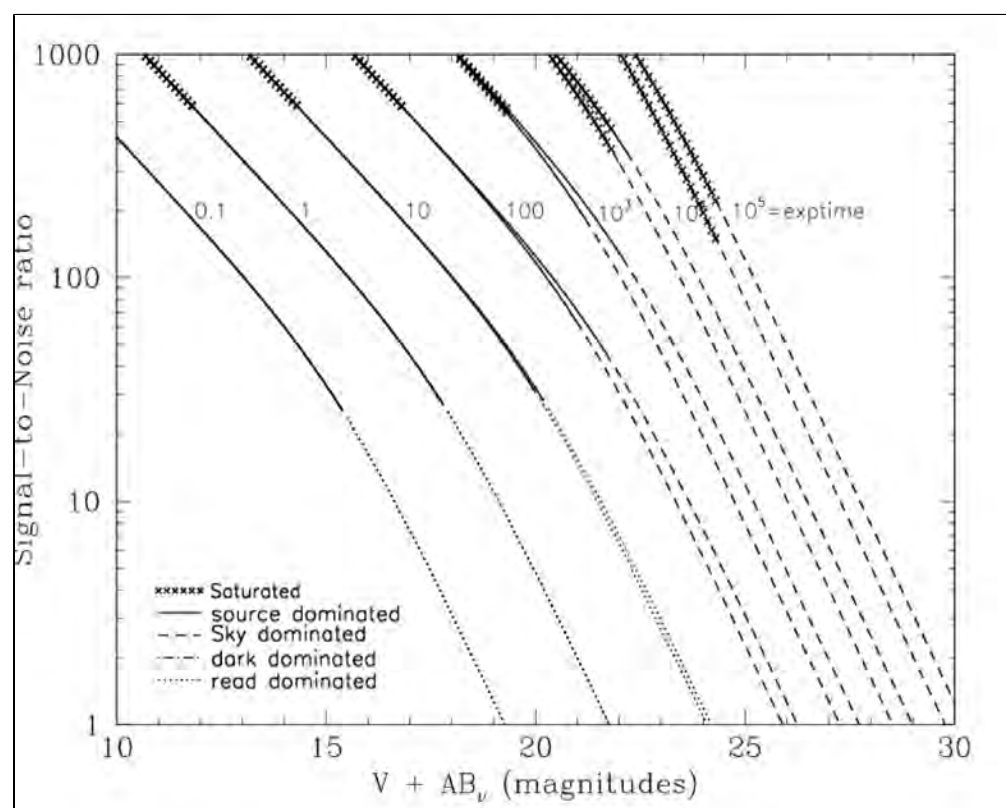
Figure 10.21: Extended source S/N vs. V+ABv for the WFC/F625W filter. Top curves are for low sky and bottom curves are for average sky for a 1 arcsec^2 area.
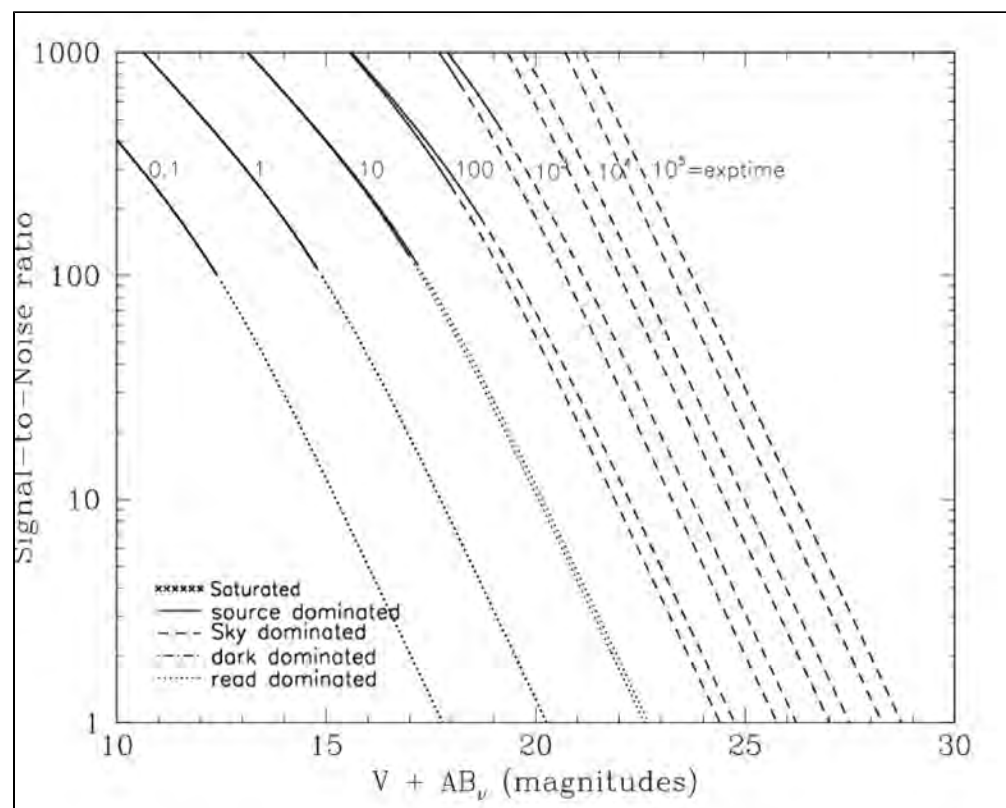
WFC F658N

Description

Hα filter.

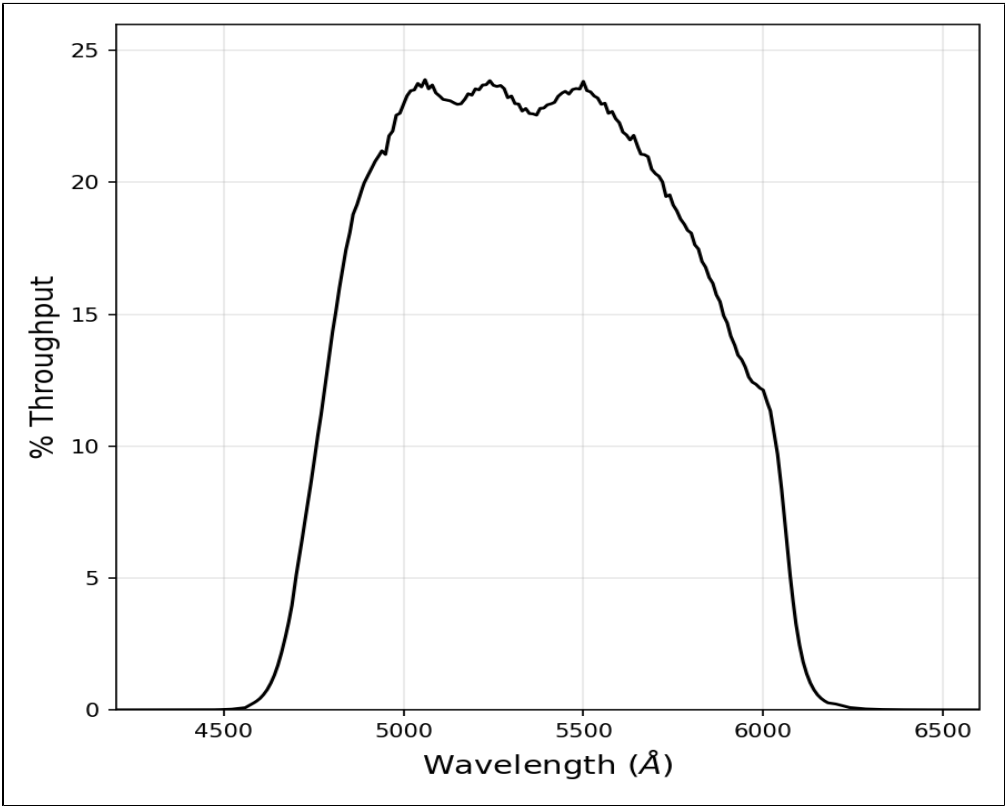**Figure 10.22: Integrated system throughput for WFC/F658N.**
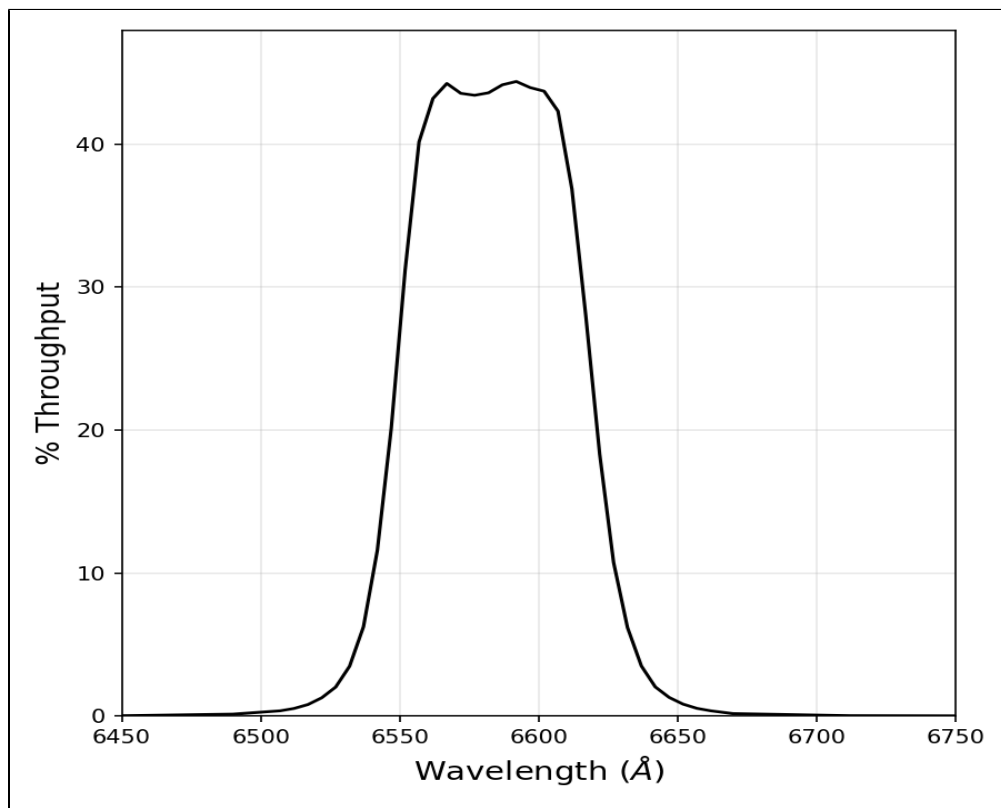
Figure 10.23: Point source S/N vs. V+ABν for the WFC/F658N filter. Top curves are for low sky; bottom curves are for average sky.
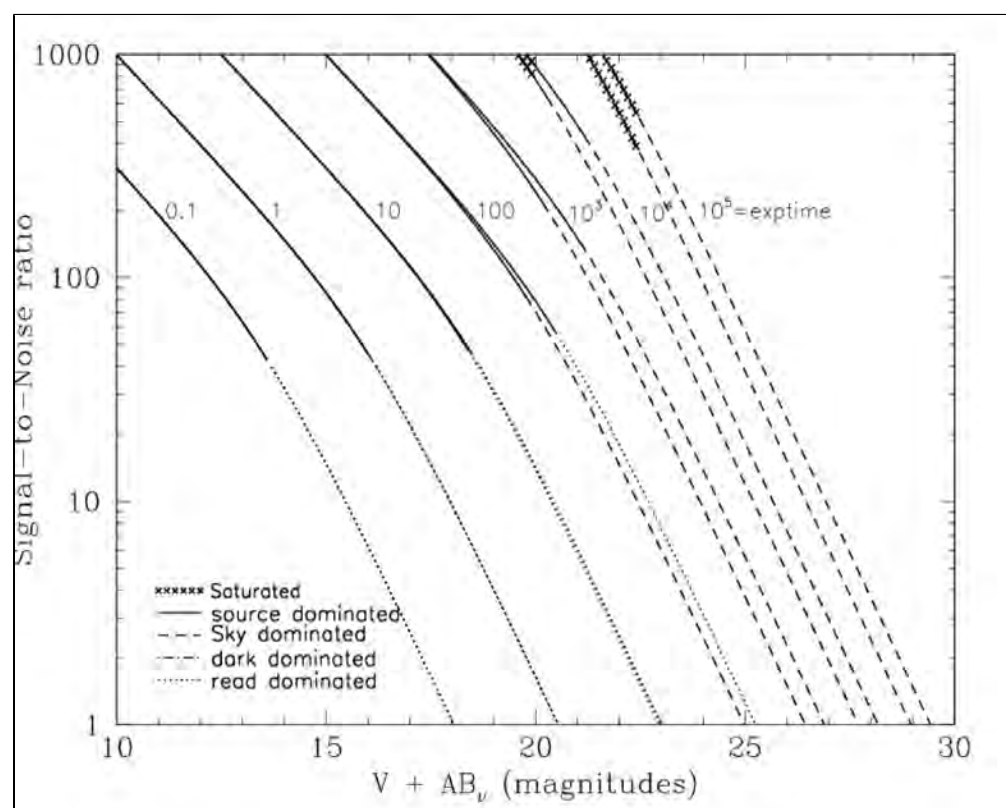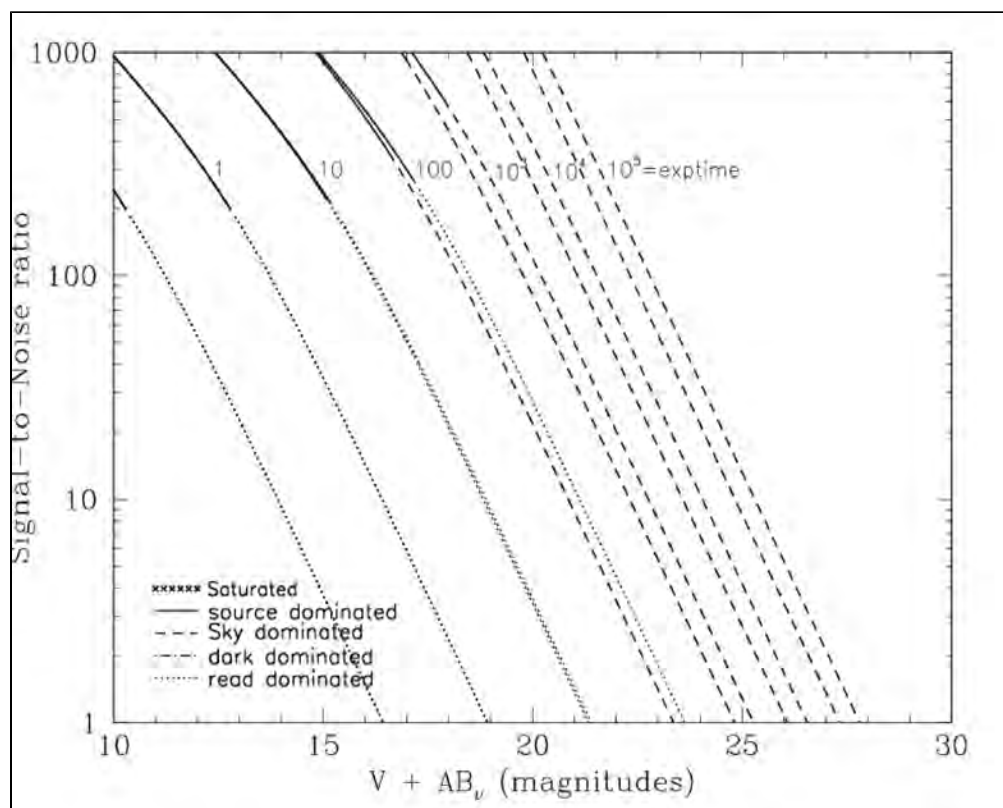
Figure 10.24: Extended source S/N vs. V+ABv for the WFC/F658N filter. Top curves are for low sky and bottom curves are for average sky for 1 arcsec^2 area.
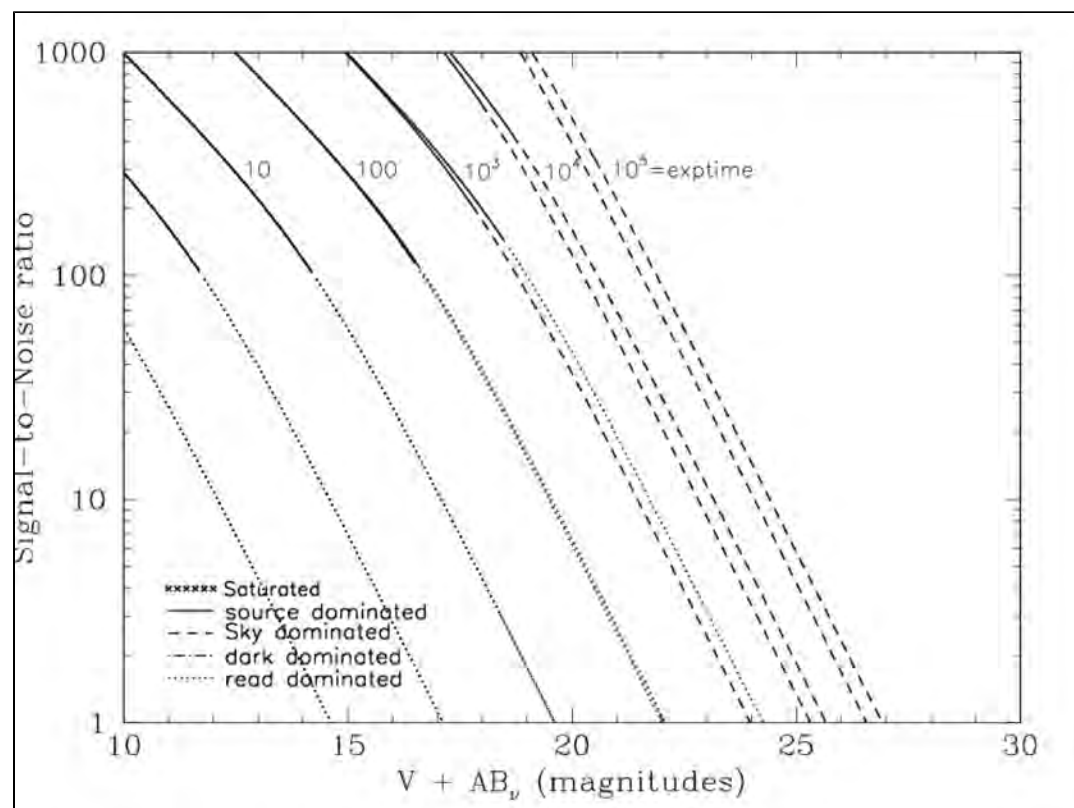
WFC F660N

Description

NII filter.

Figure 10.25: Integrated system throughput for WFC/F660N.
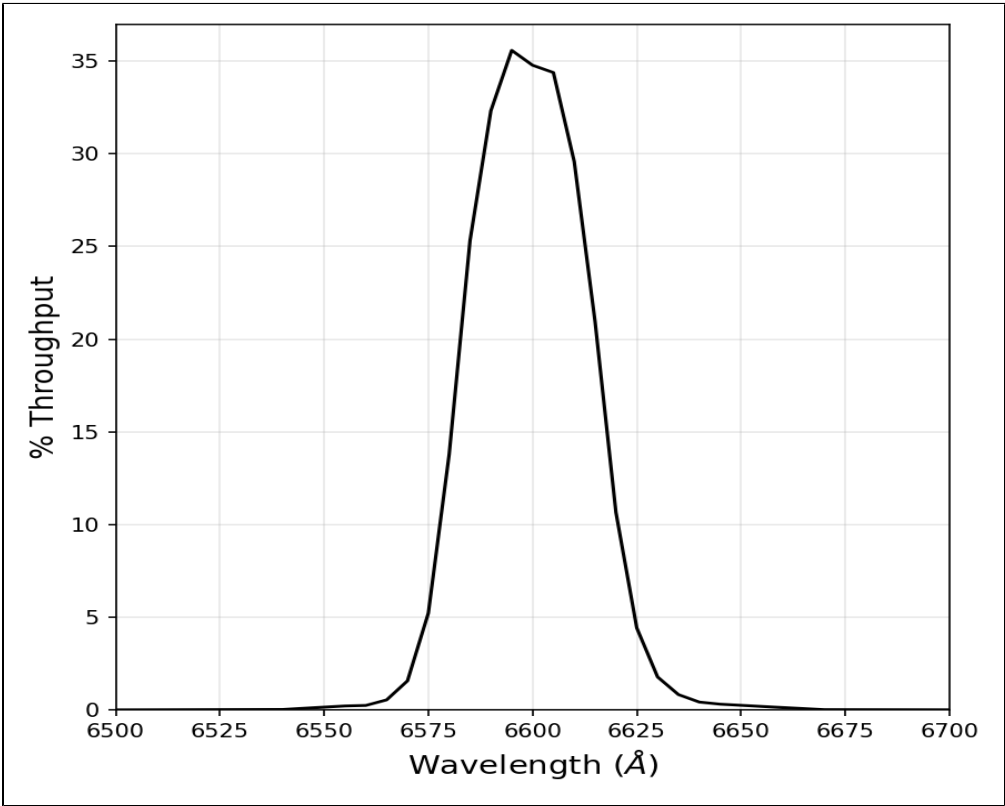
Figure 10.26: Point source S/N vs. V+ABv for the WFC/F660N filter. Top curves are for low sky; bottom curves are for average sky.
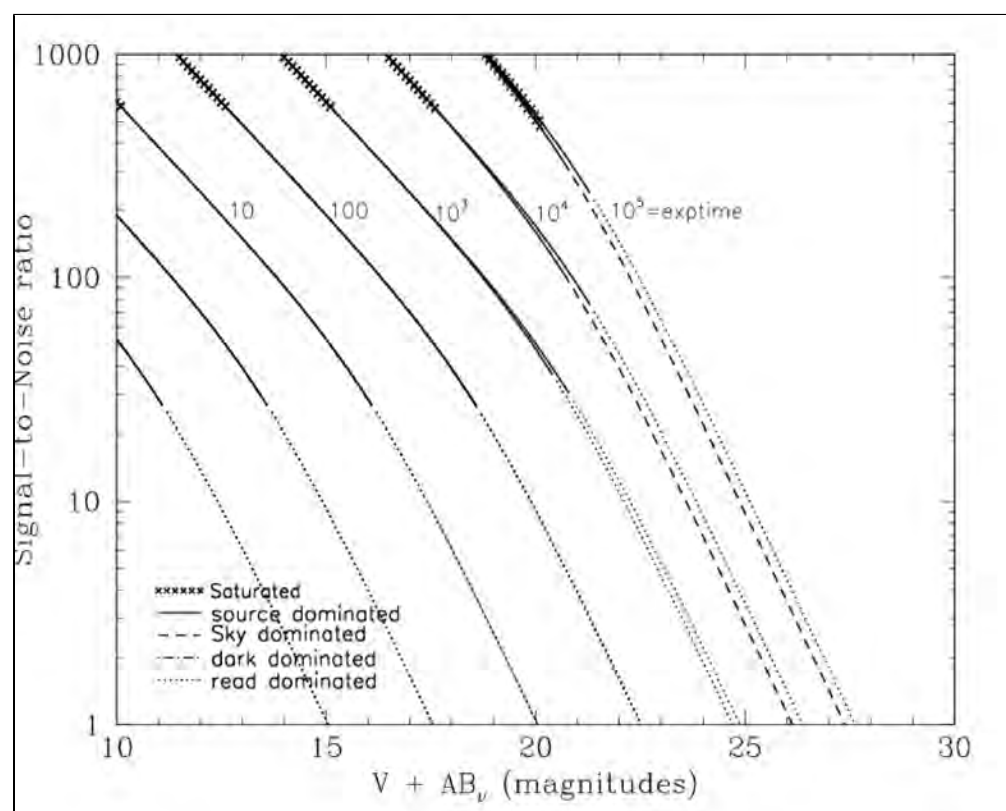
Figure 10.27: Extended source S/N vs. V+ABν for the WFC/F660N filter. Top curves are for low sky and bottom curves are for average sky for a 1 arcsec^2 area.
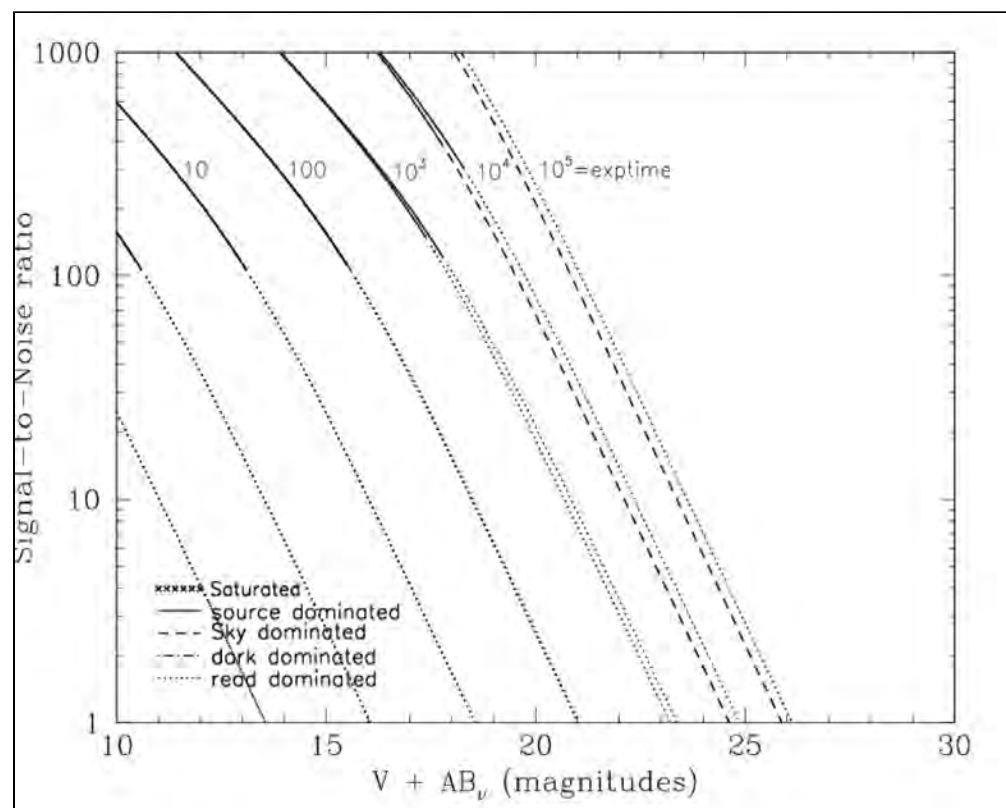
WFC F775W

Description

Sloan Digital Sky Survey i filter

Figure 10.28: Integrated system throughput for WFC/F775W.
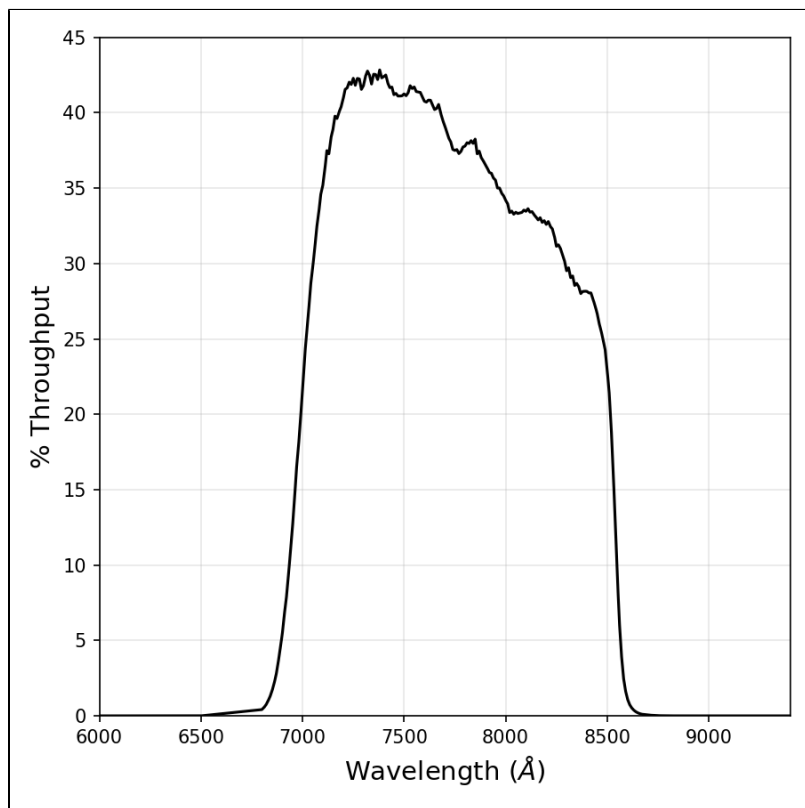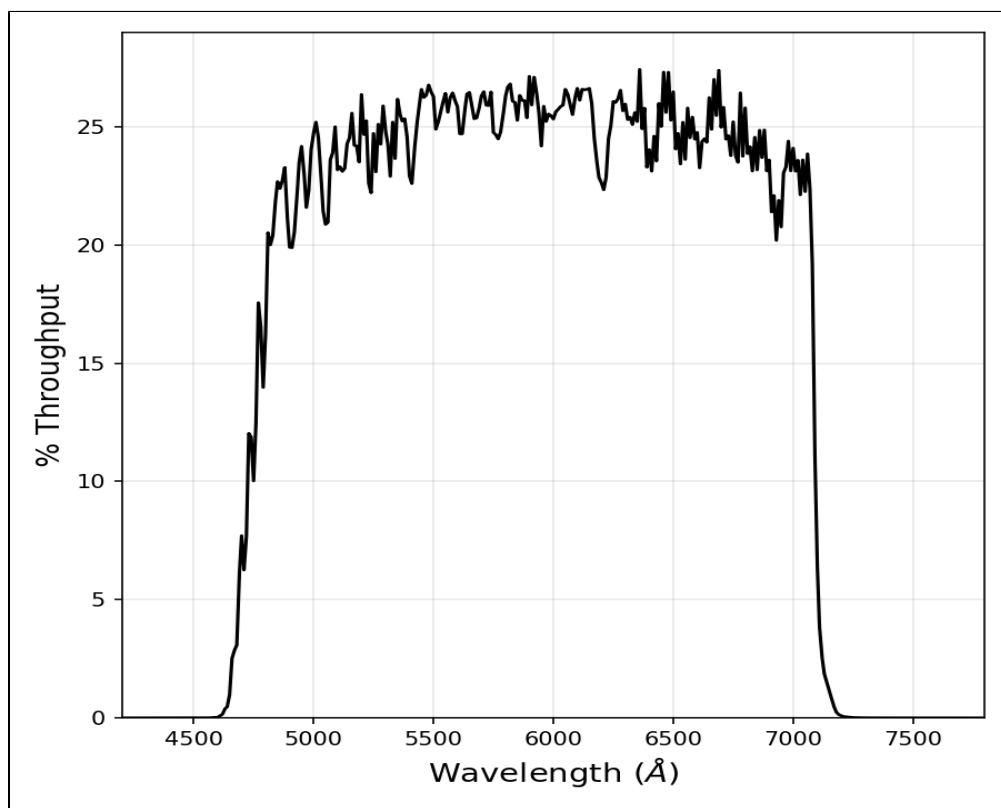
Figure 10.29: Point source S/N vs. V+ABν for the WFC/F775W filter. Top curves are for low sky; bottom curves are for average sky.
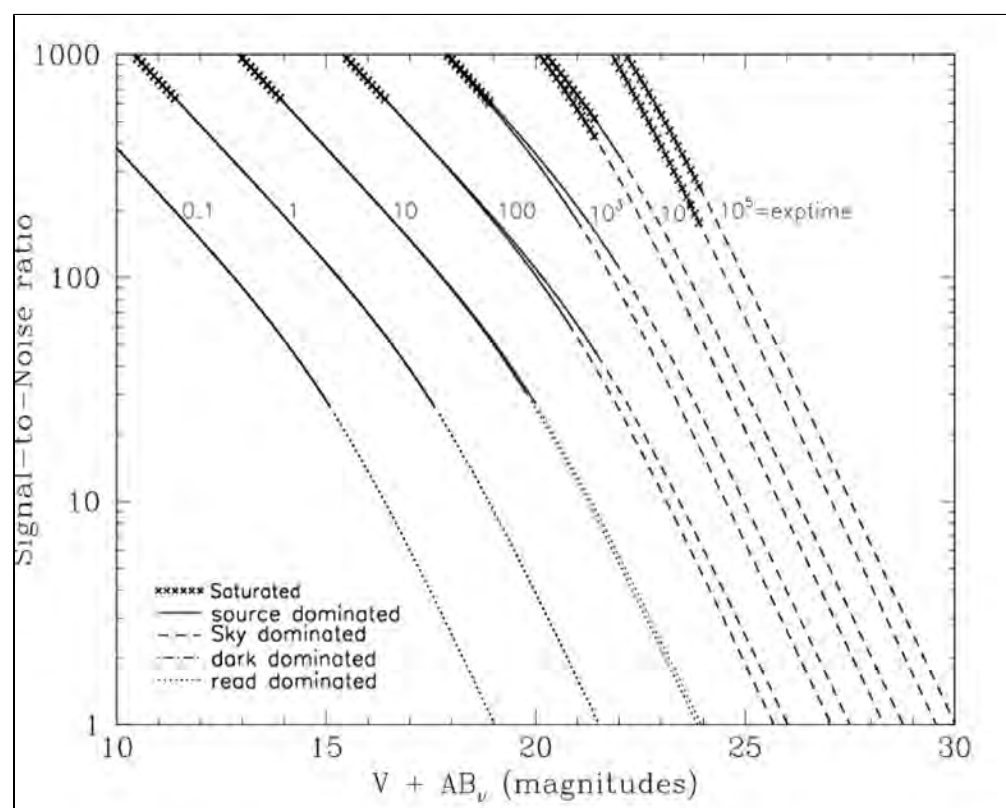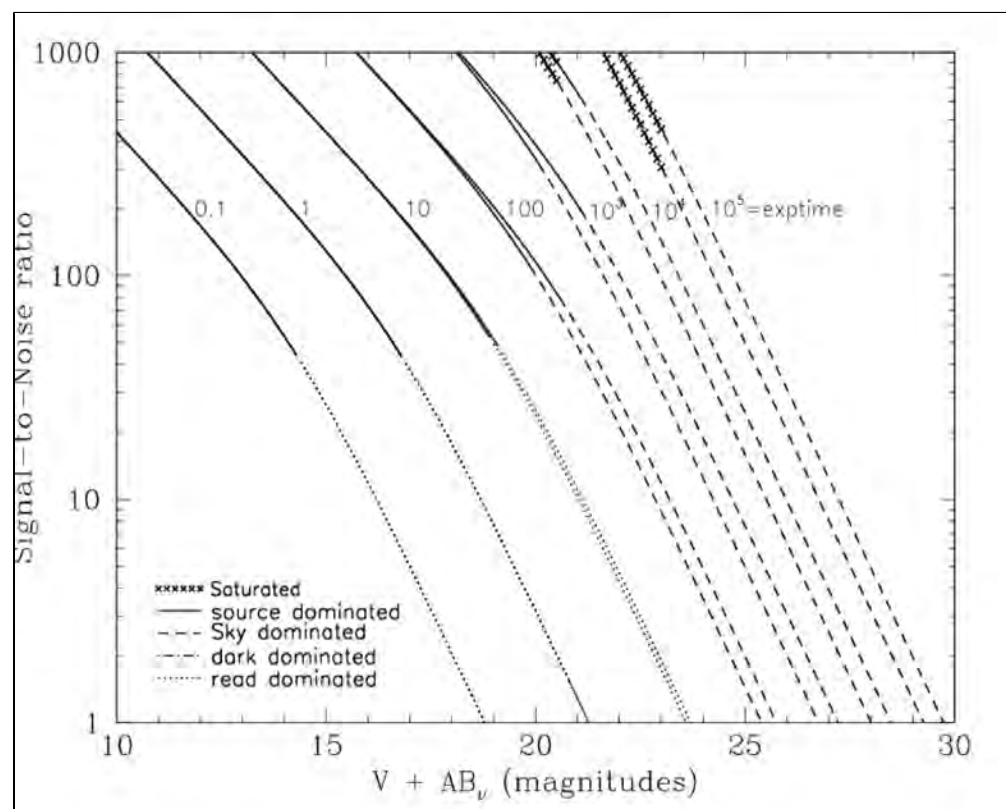
Figure 10.30: Extended source S/N vs. V+ABv for the WFC/F775W filter. Top curves are for low sky and bottom curves are for average sky for a 1 arcsec^2 area.
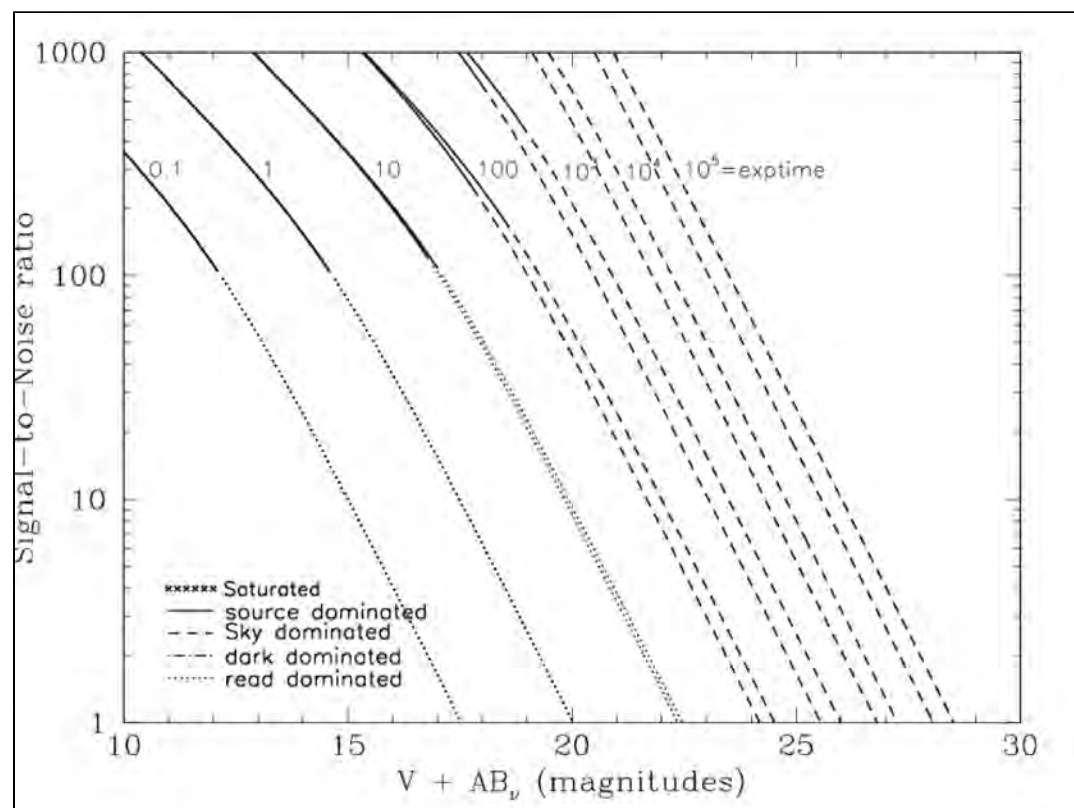
WFC F814W

Description

Broad I filter.

Figure 10.31: Integrated system throughput for WFC/F814W.
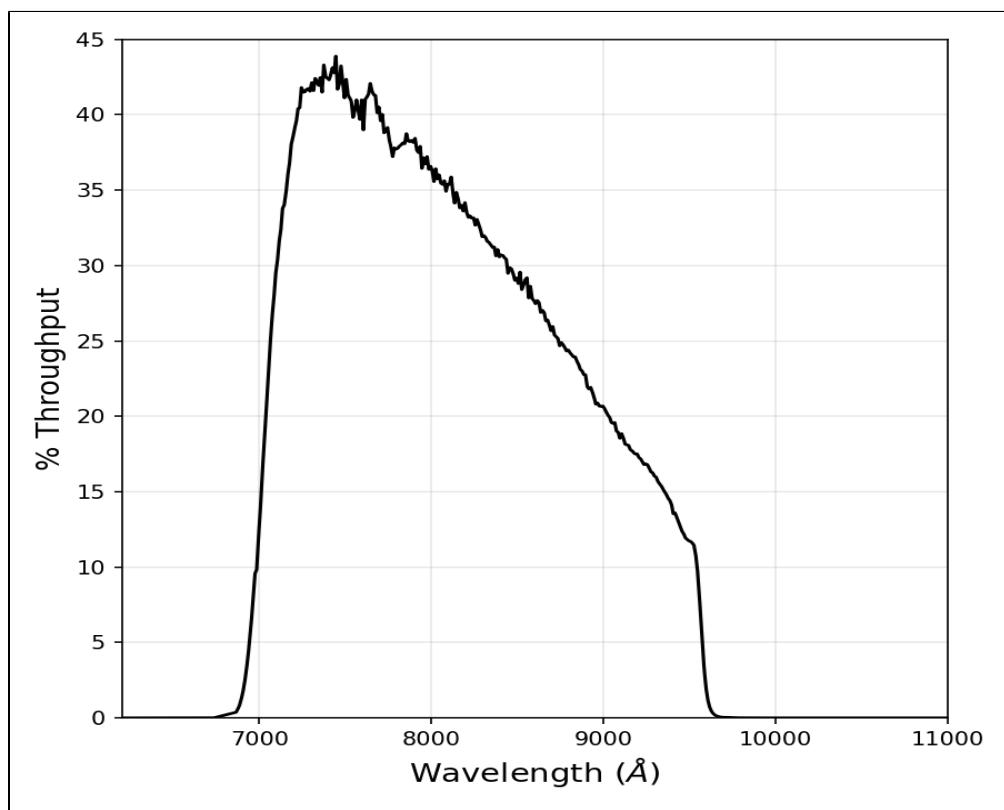
Figure 10.32: Point source S/N vs. V+ABν for the WFC/F814W filter. Top curves are for low sky; bottom curves are for average sky.
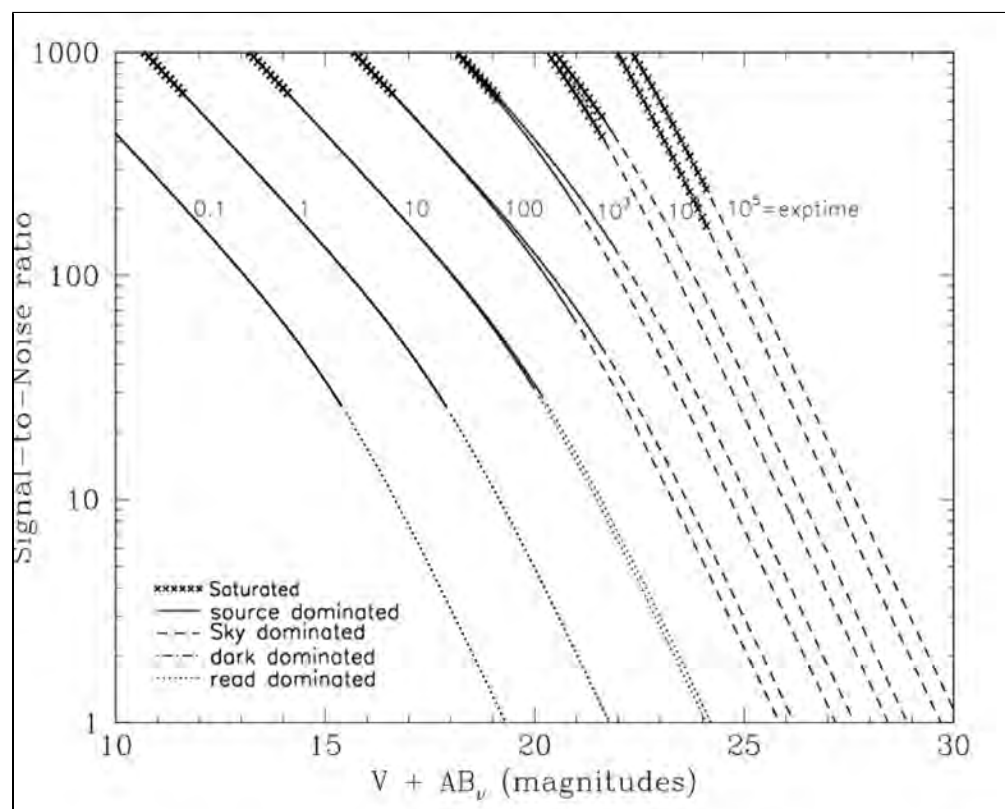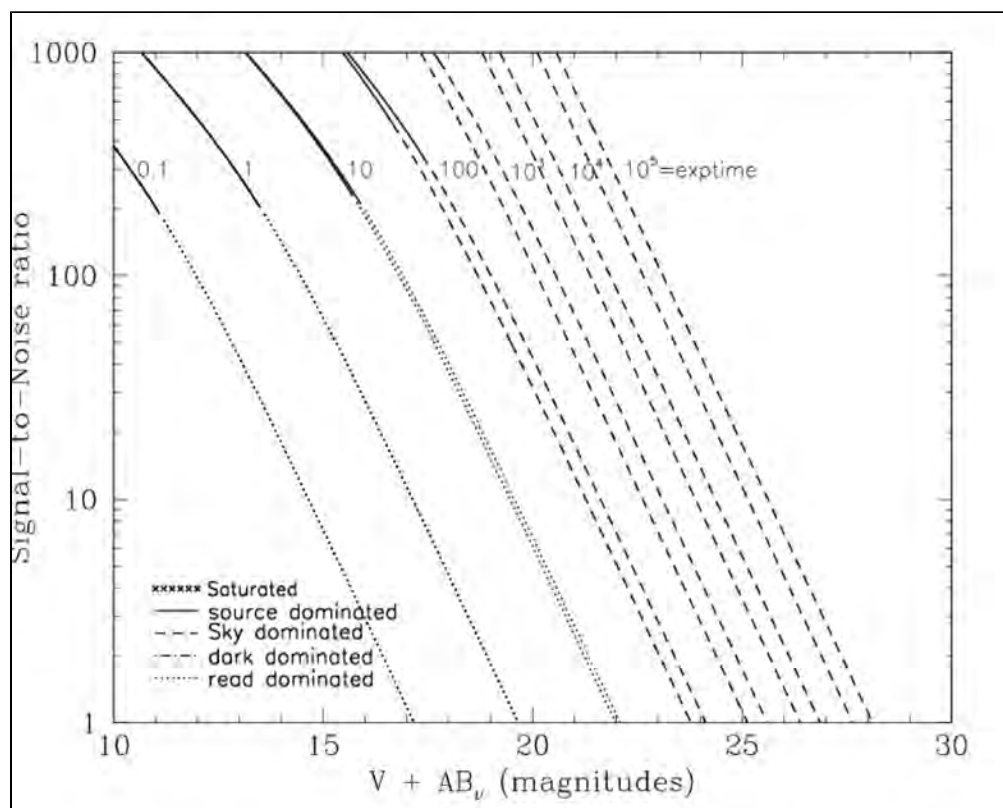
Figure 10.33: Extended source S/N vs. V+ABν for the WFC/F814W filter. Top curves are for low sky and bottom curves are for average sky for a 1 arcsec^2 area.
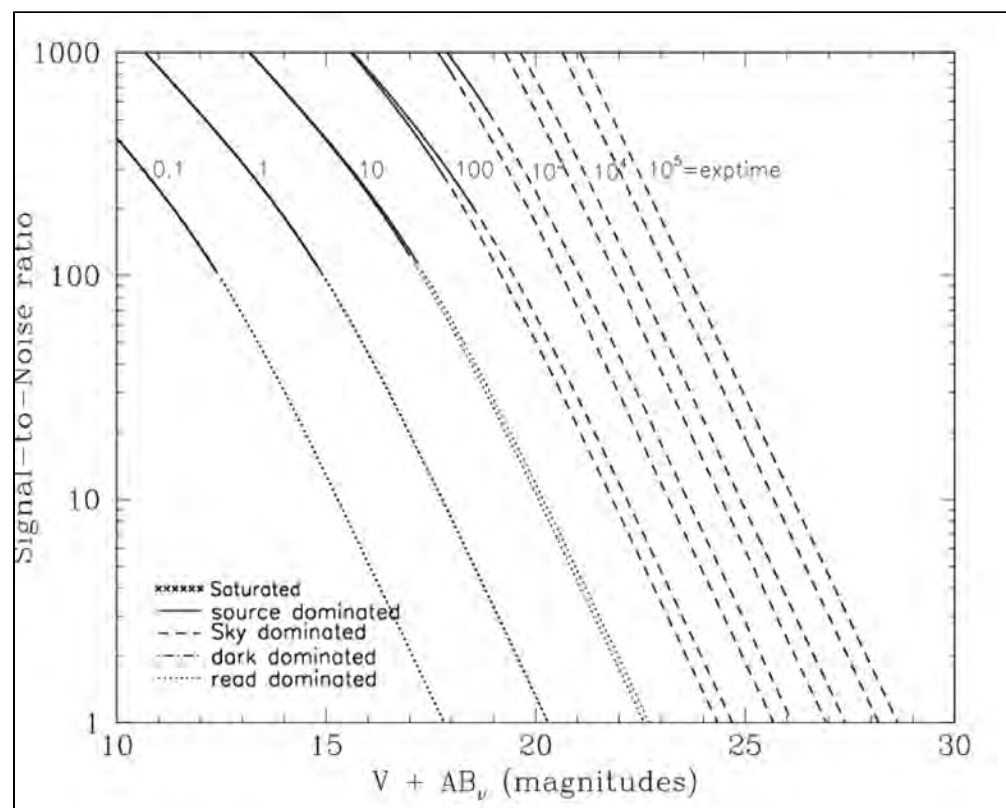
WFC F850LP

Description

Sloan Digital Sky Survey z filter.

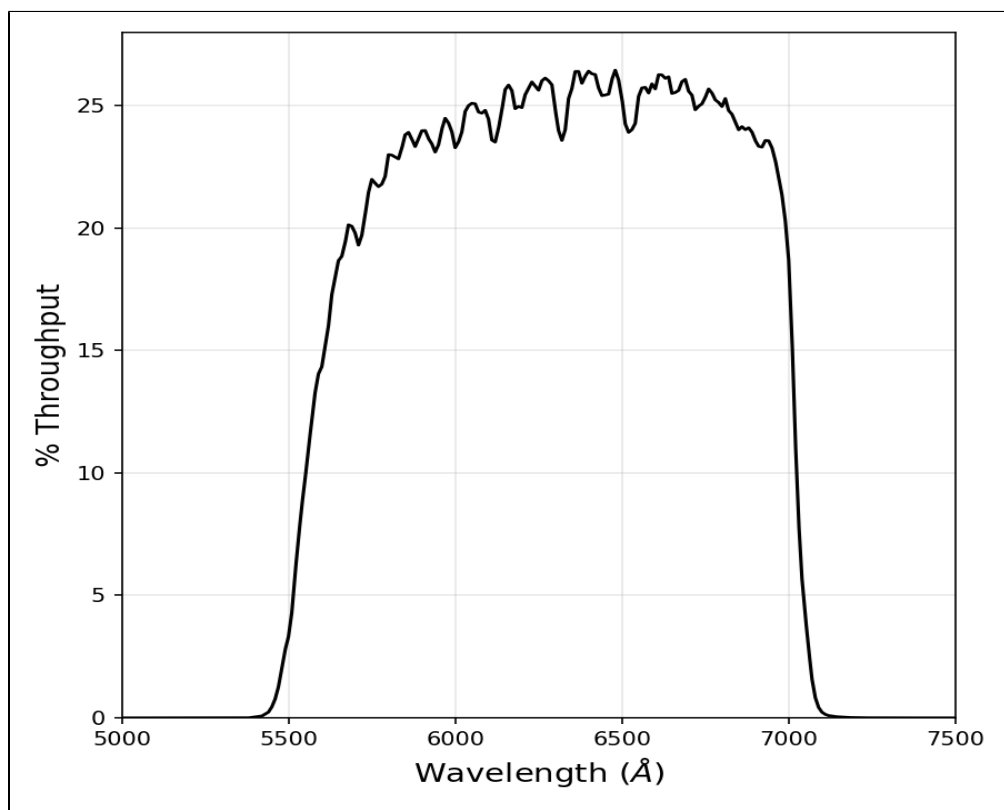**Figure 10.34: Integrated system throughput for WFC/F850LP.**
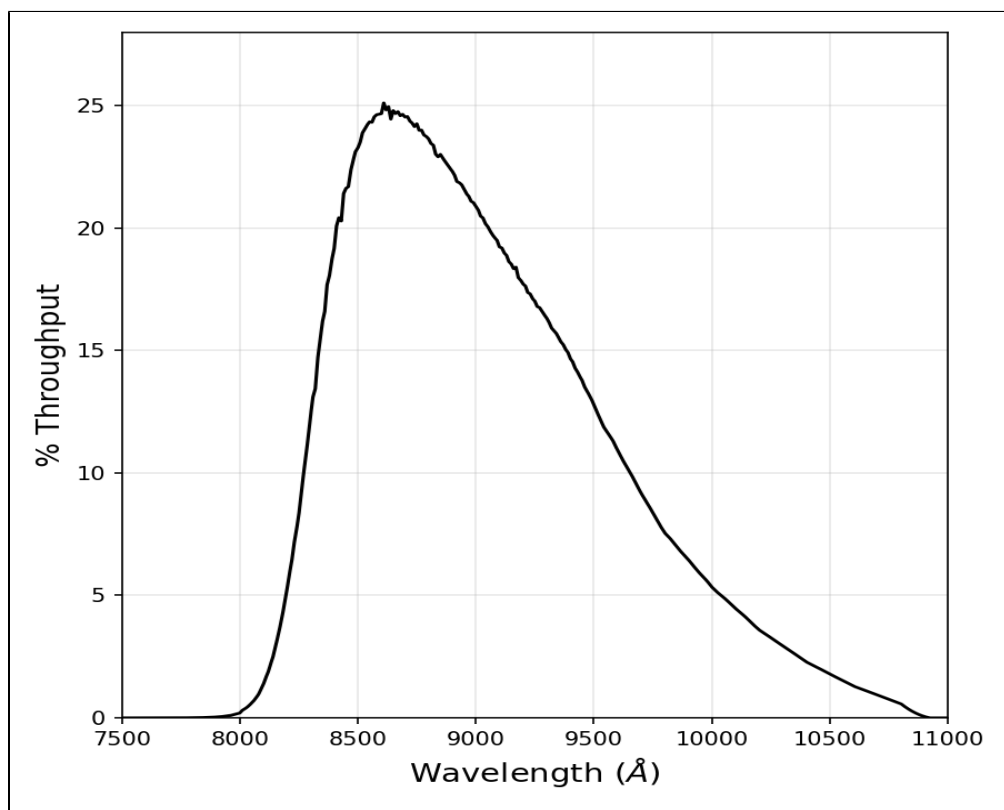
Figure 10.35: Point source S/N vs. V+ABv for the WFC/F850LP filter. Top curves are for low sky; bottom curves are for average sky.
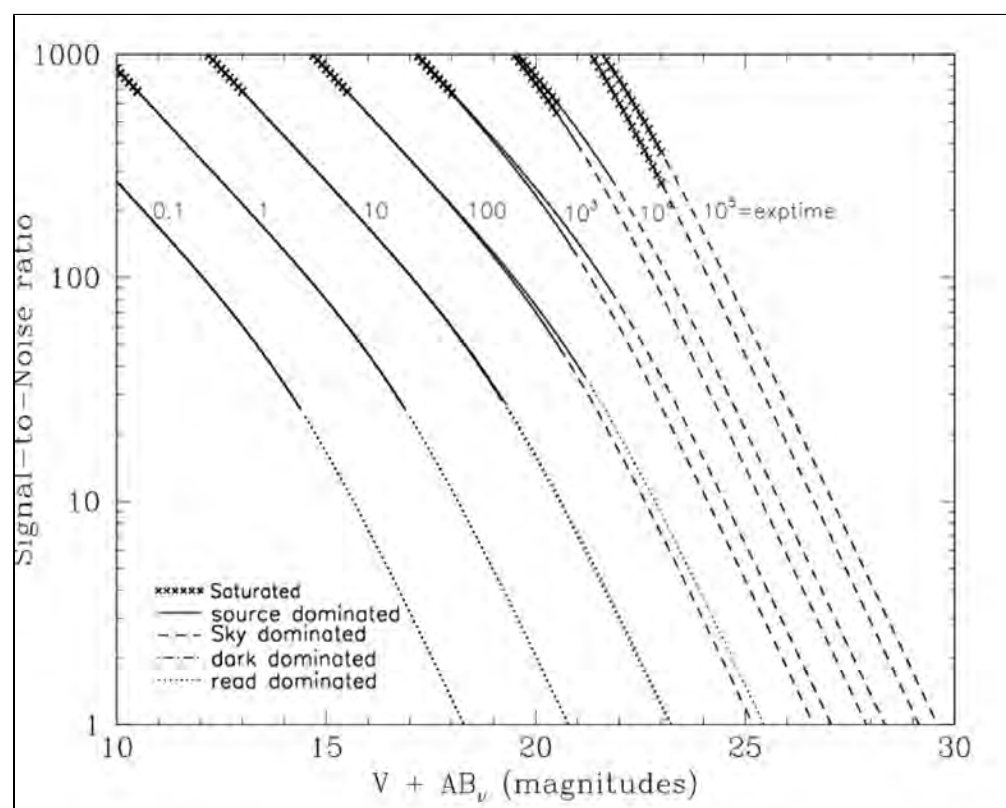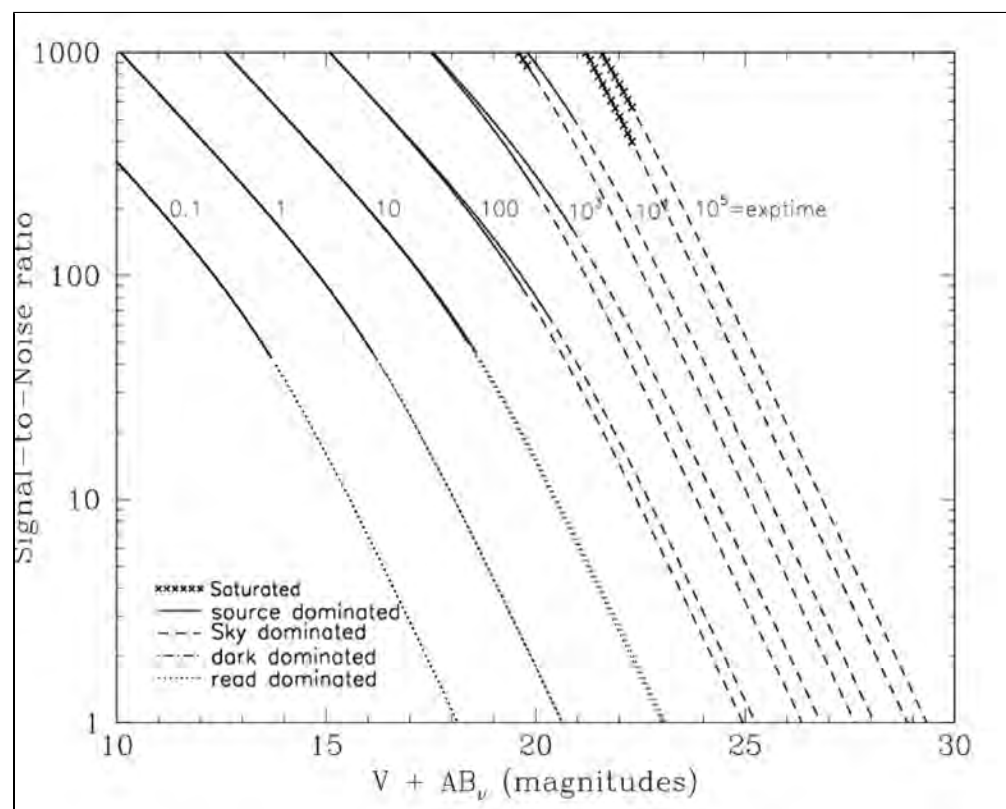
Figure 10.36: Extended source S/N vs. V+ABv for the WFC/F850LP filter. Top curves are for low sky and bottom curves are for average sky for a 1 arcsec^2 area.
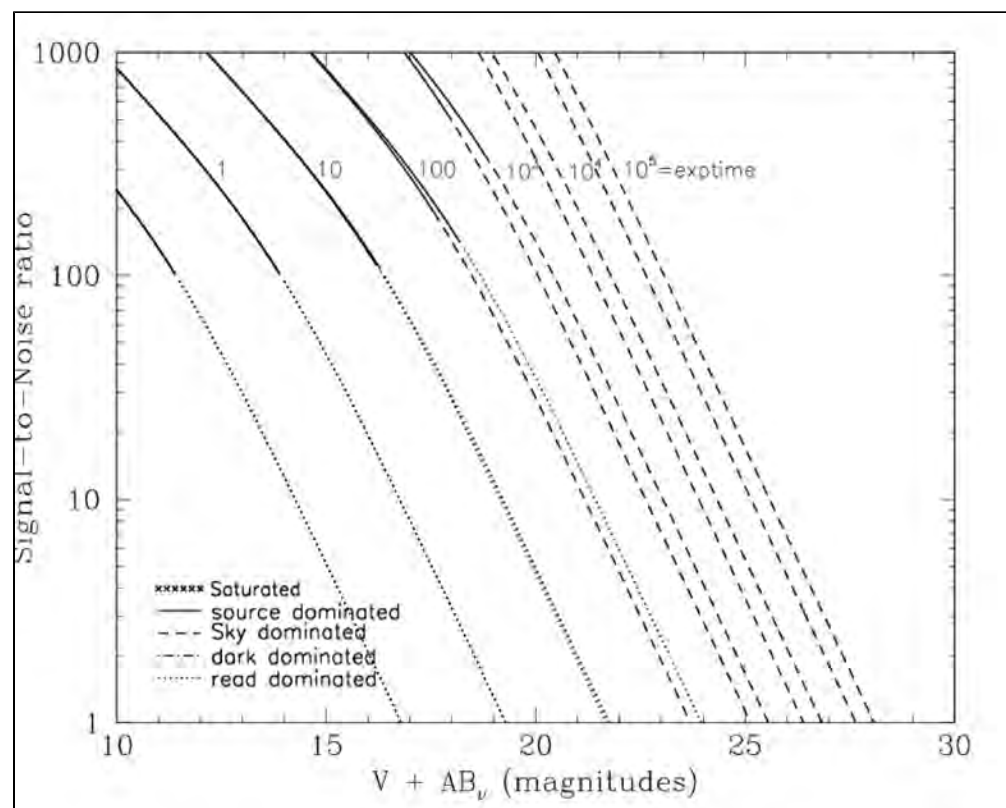
WFC G800L

Description

Grism.

Figure 10.37: Integrated system throughput for WFC/G800L.
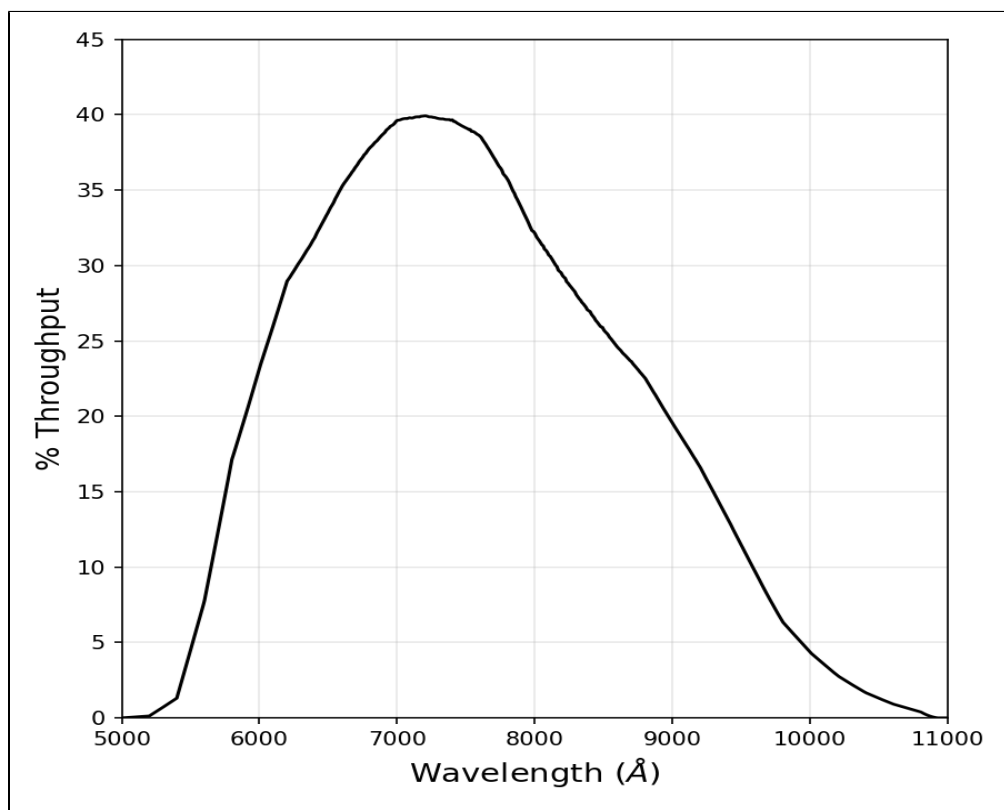
Figure 10.38: Point source S/N vs. V+ABv for the WFC/G800L filter. Top curves are for low sky; bottom curves are for average sky.
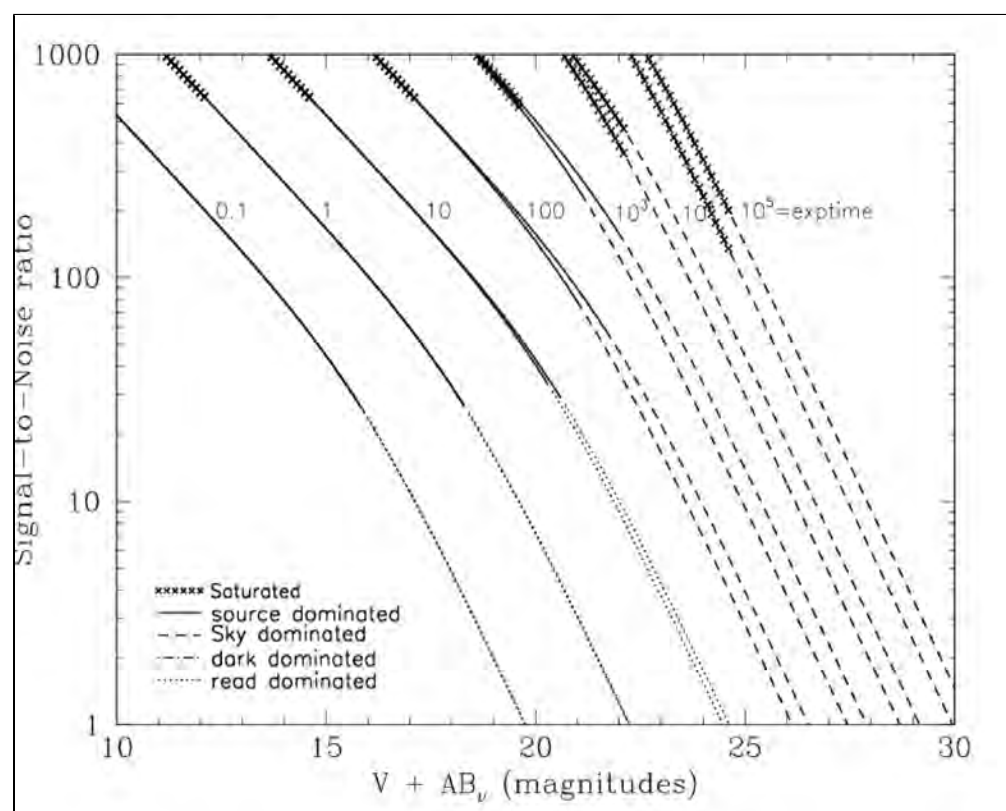
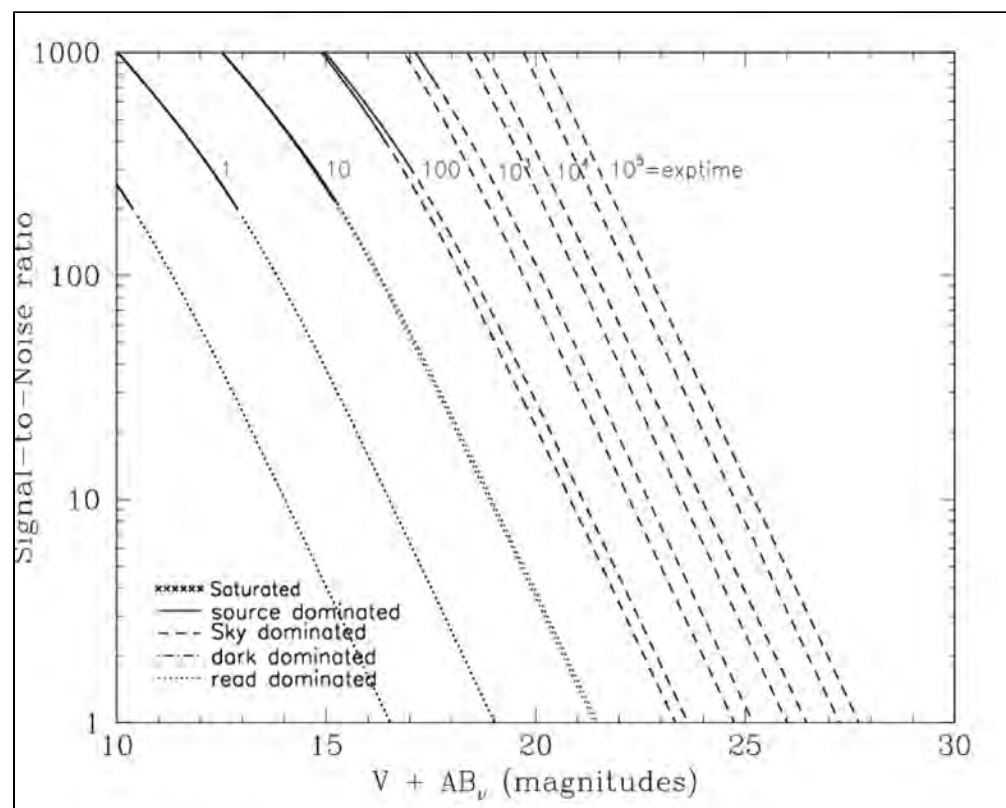Figure 10.39: Extended source S/N vs. V+ABv for the WFC/G800L filter. Top curves are for low sky and bottom curves are for average sky for a 1 arcsec^2 area.
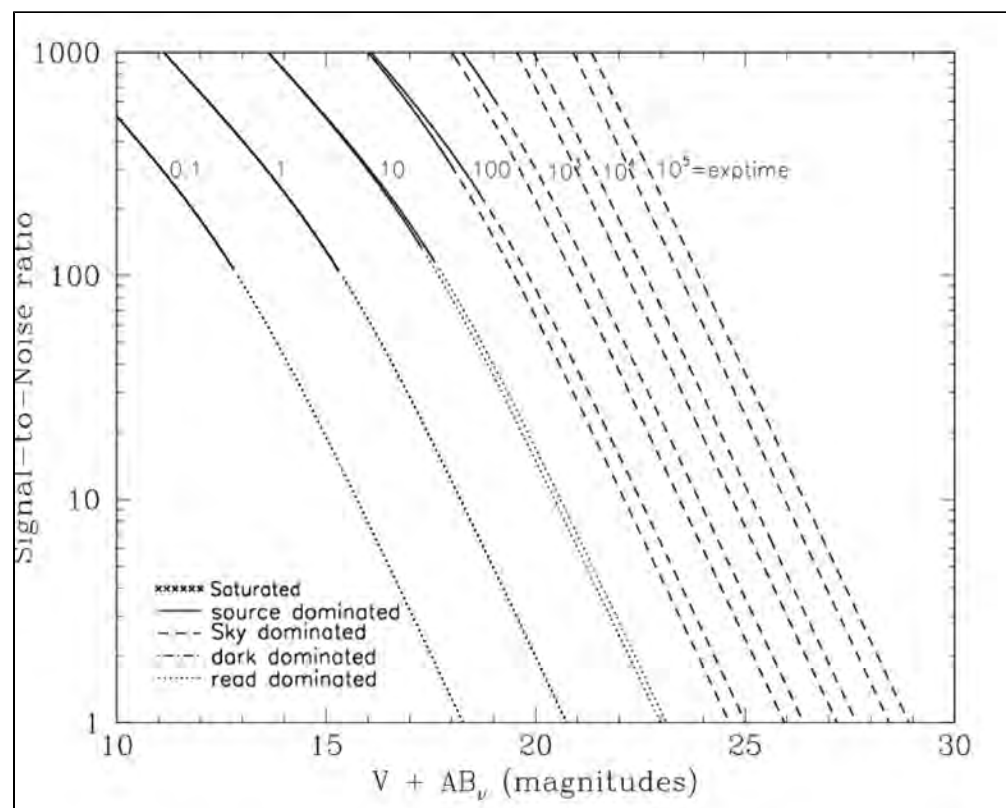
WFC CLEAR

Description

Clear filter.

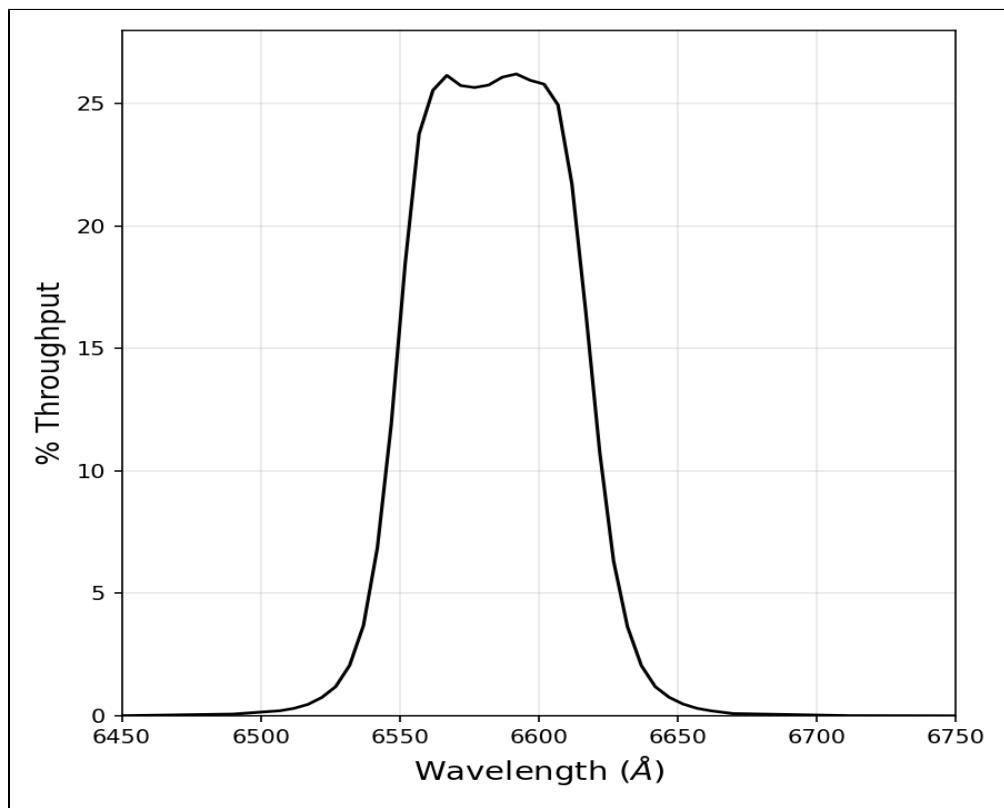**Figure 10.40:** Integrated system throughput for WFC/Clear.
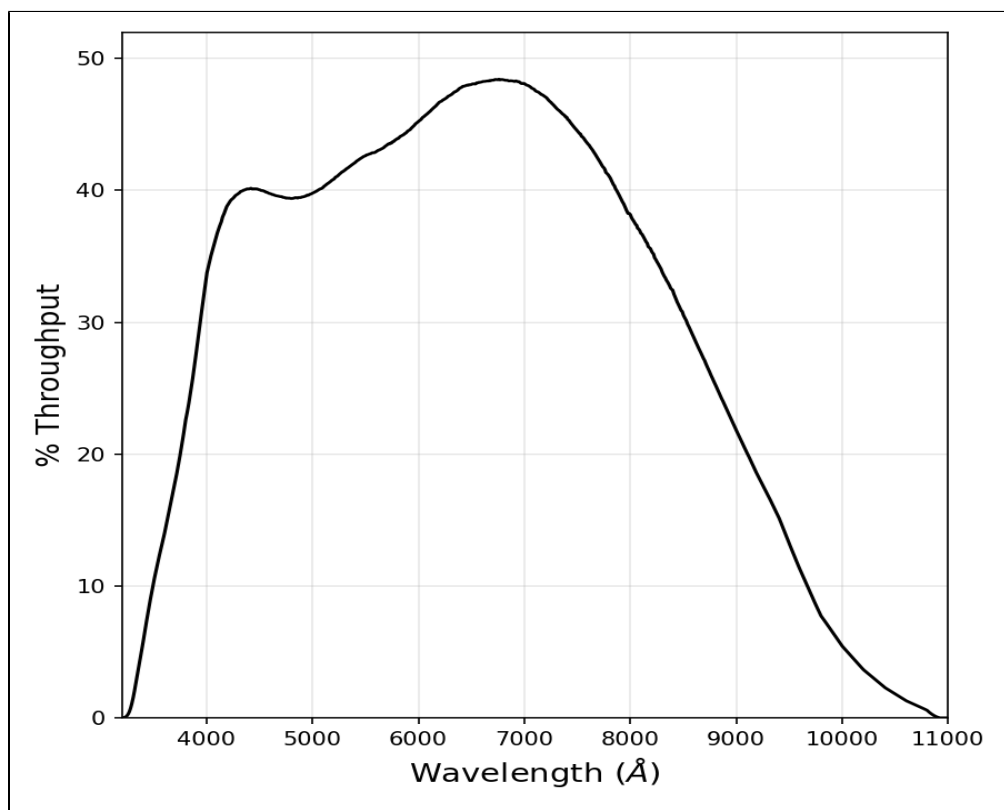
Figure 10.41: Point source S/N vs. V+ABv for the WFC/Clear filter. Top curves are for low sky; bottom curves are for average sky.
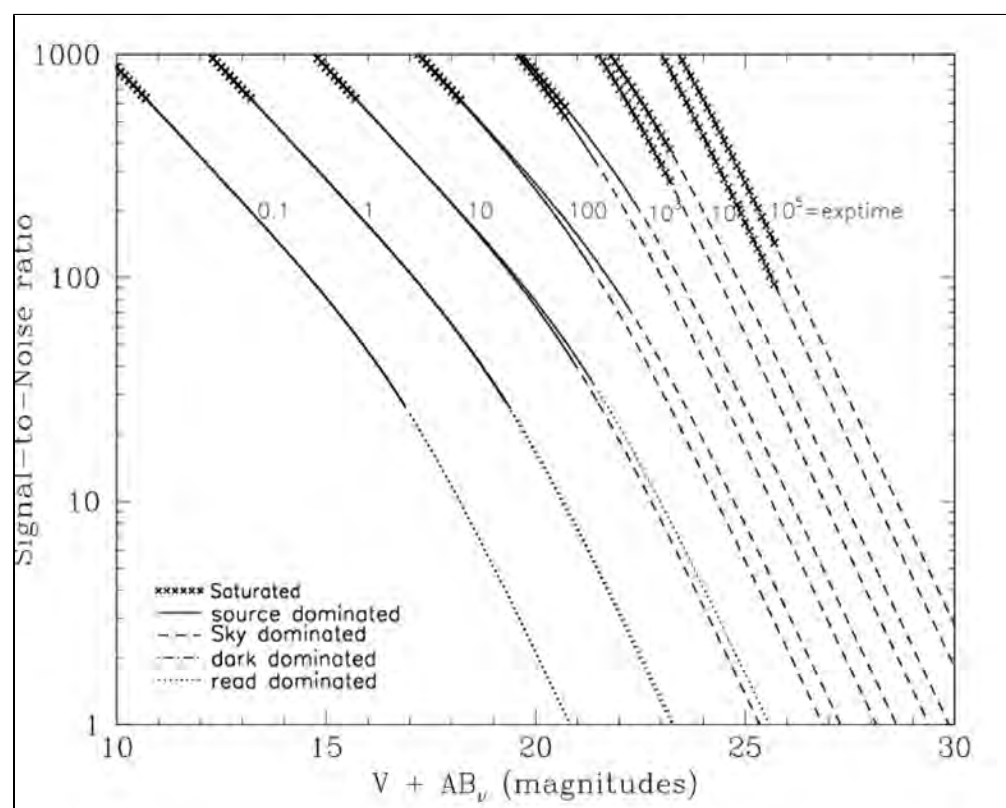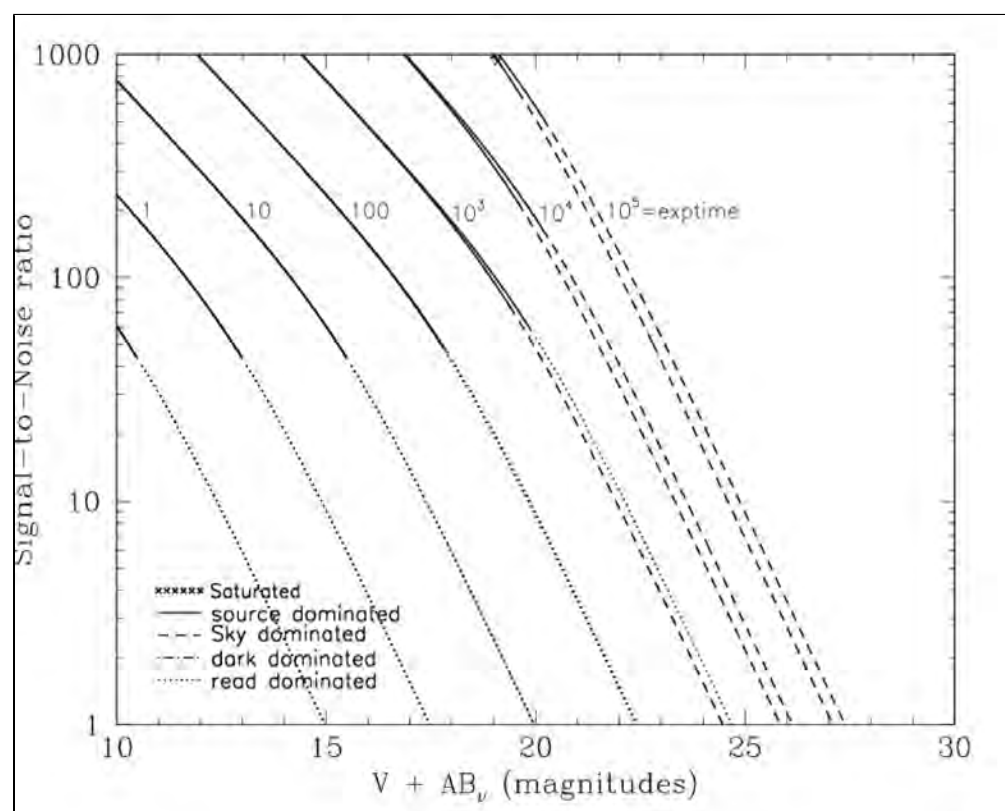
Figure 10.42: Extended source S/N vs. V+ABv for the WFC/Clear filter. Top curves are for low sky and bottom curves are for average sky for a 1 arcsec^2 area.
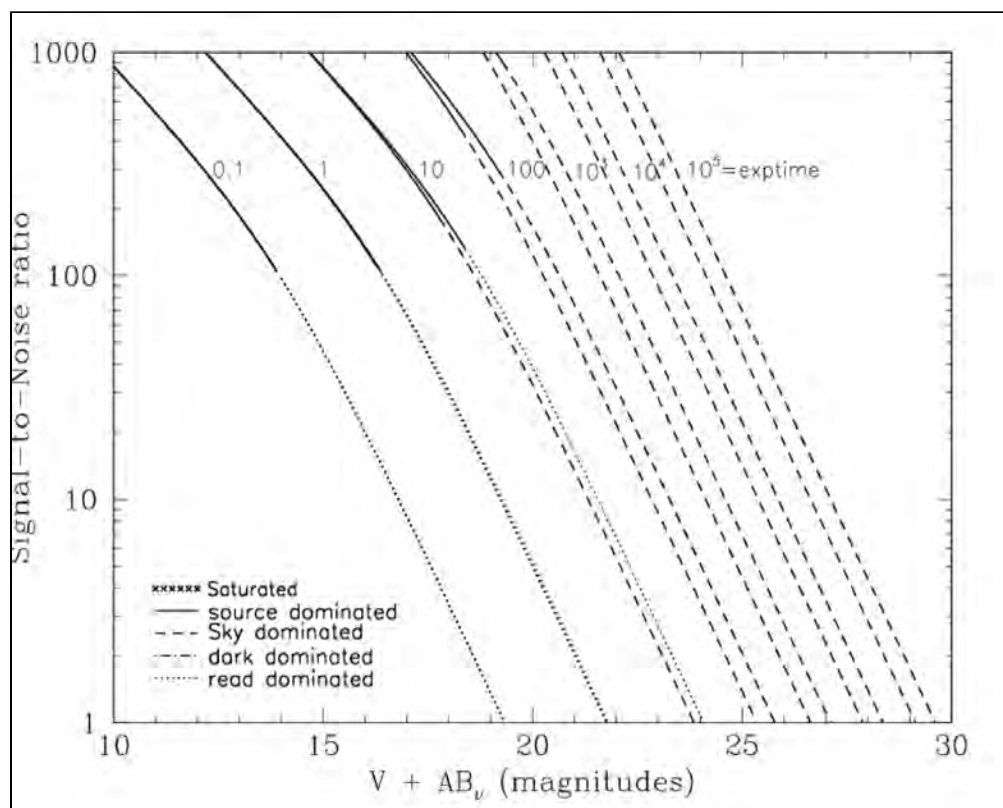
HRC F220W

Description

Near-UV filter.

Figure 10.43: Integrated system throughput for HRC/F220W.
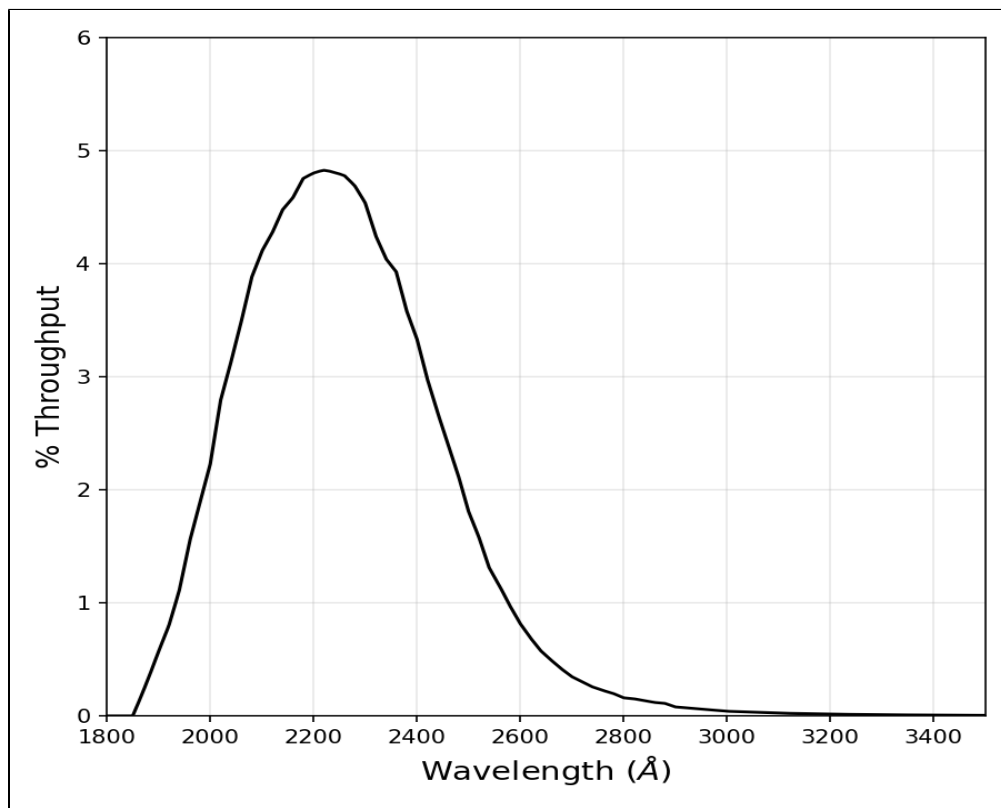
Figure 10.44: Point source S/N vs. V+ABν for the HRC/F220W filter. Top curves are for low sky; bottom curves are for average sky.
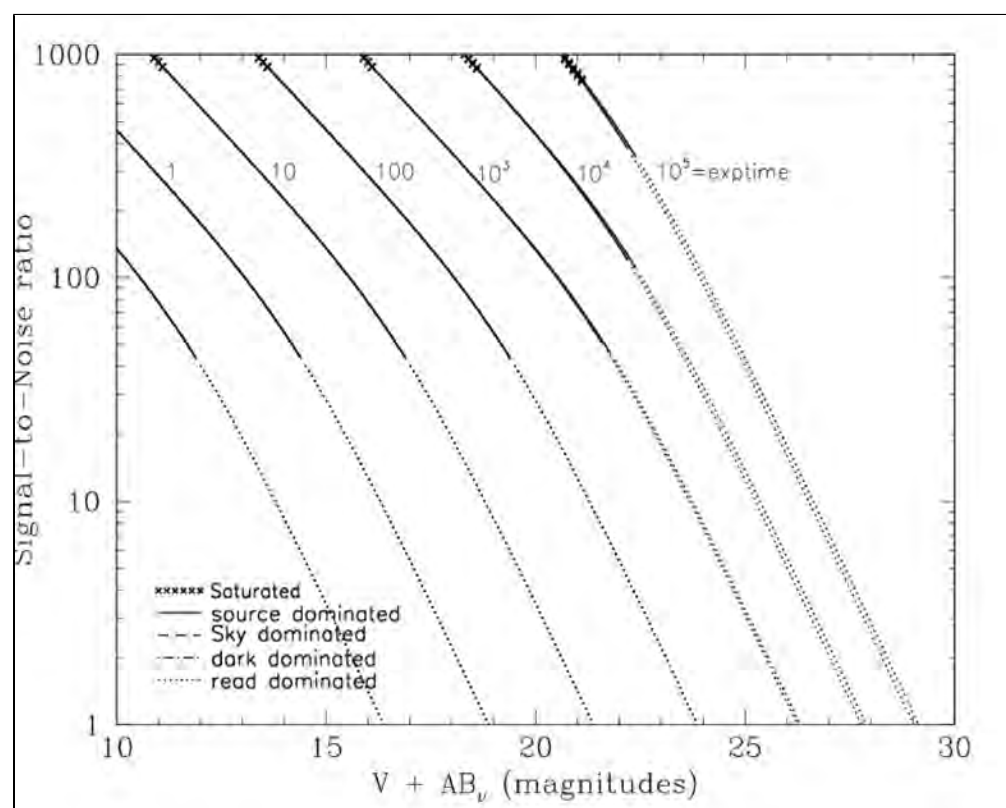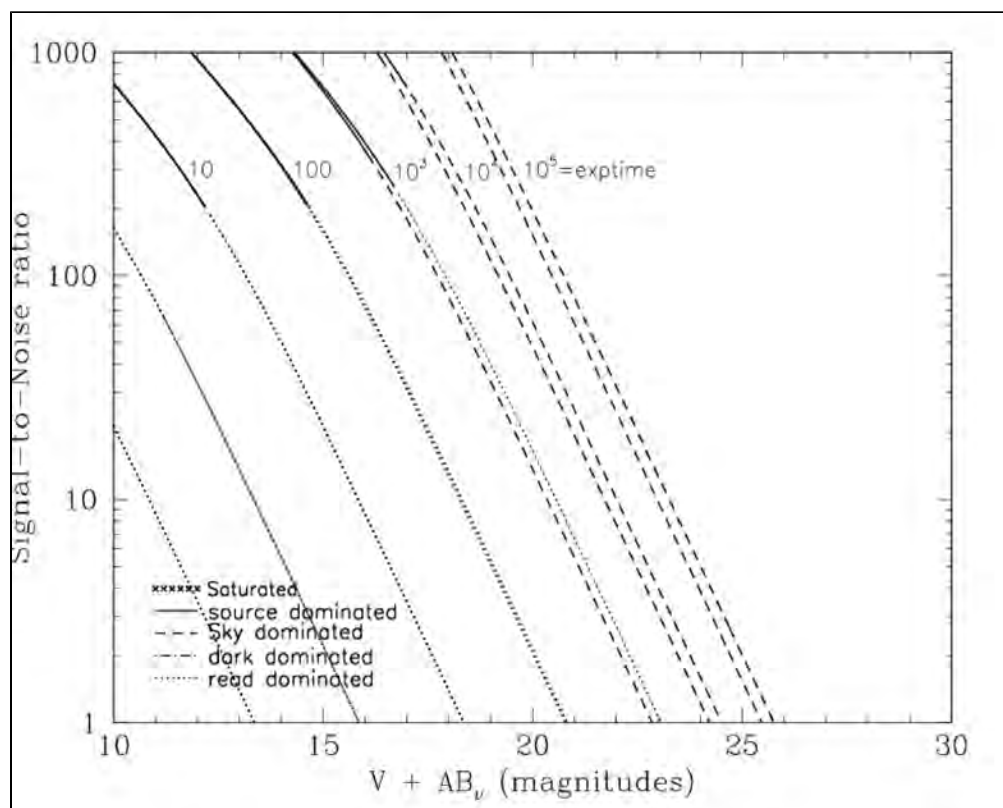
Figure 10.45: Extended source S/N vs. V+ABv for the HRC/F220W filter. Top curves are for low sky and bottom curves are for average sky for a 1 arcsec^2 area.
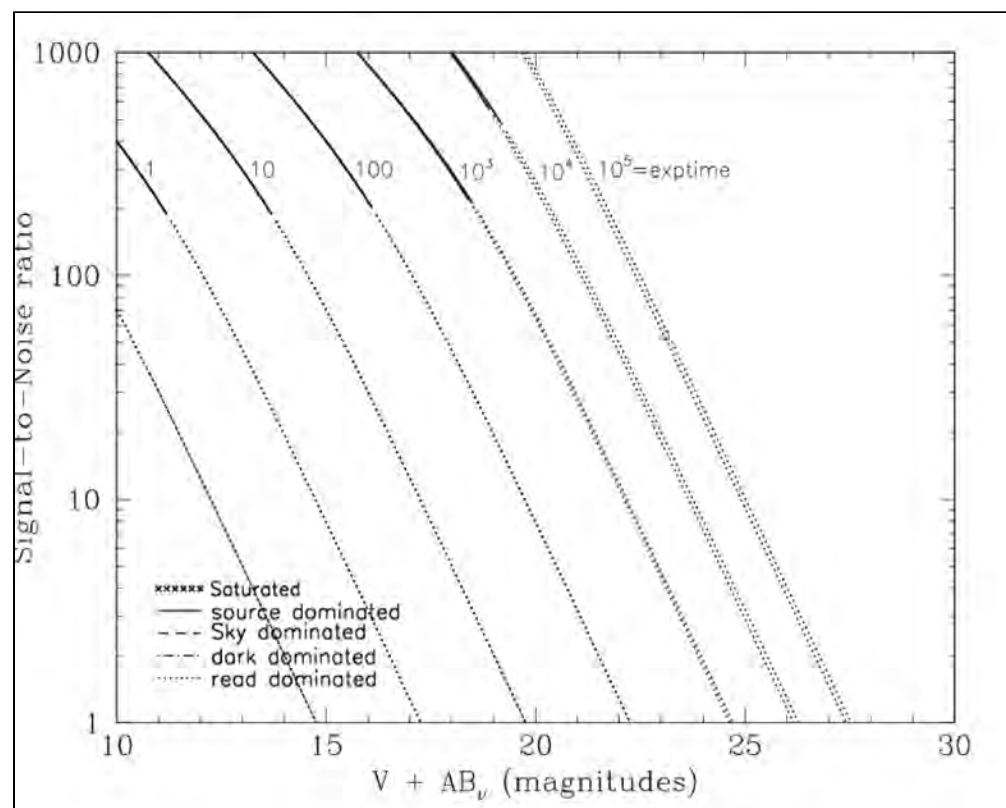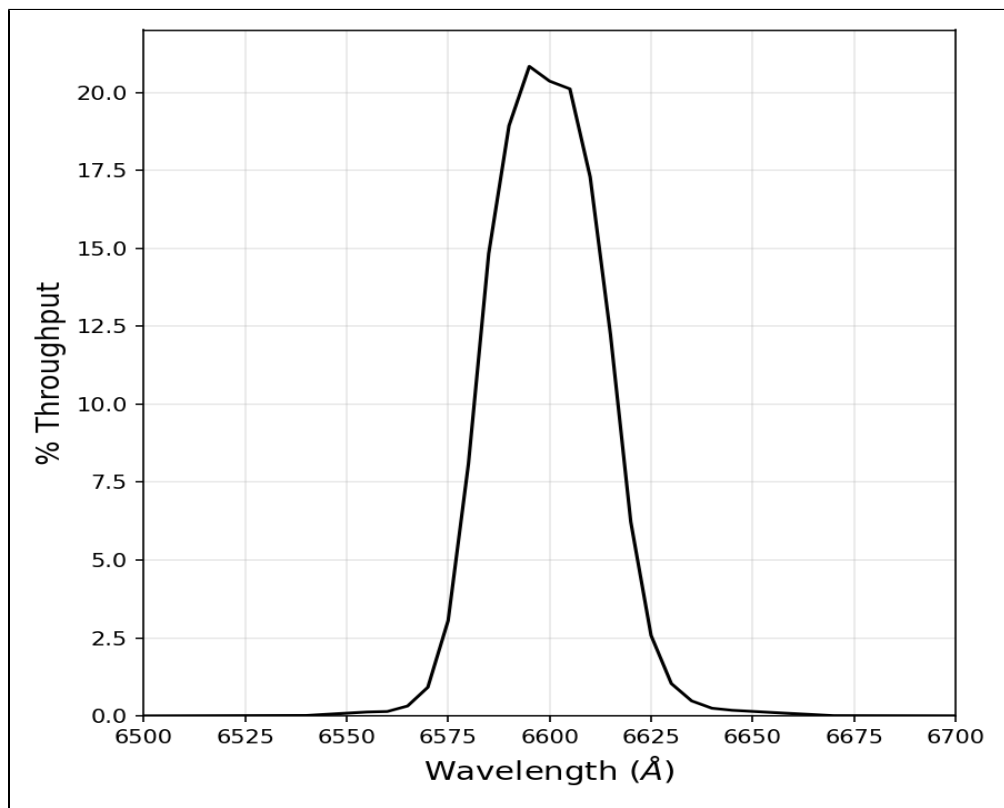
HRC F250W

Description

Near-UV filter.
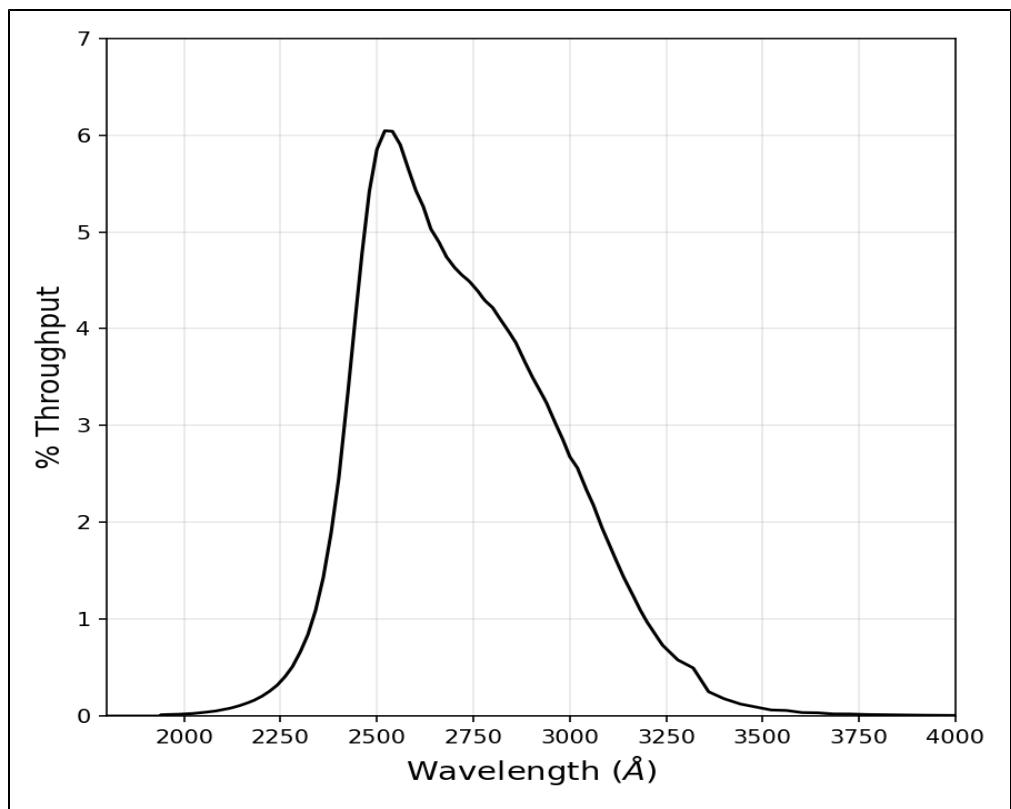
Figure 10.47: Point Source S/N vs. V+ABν for the HRC/F250W filter. Top curves are for low sky; bottom curves are for average sky.
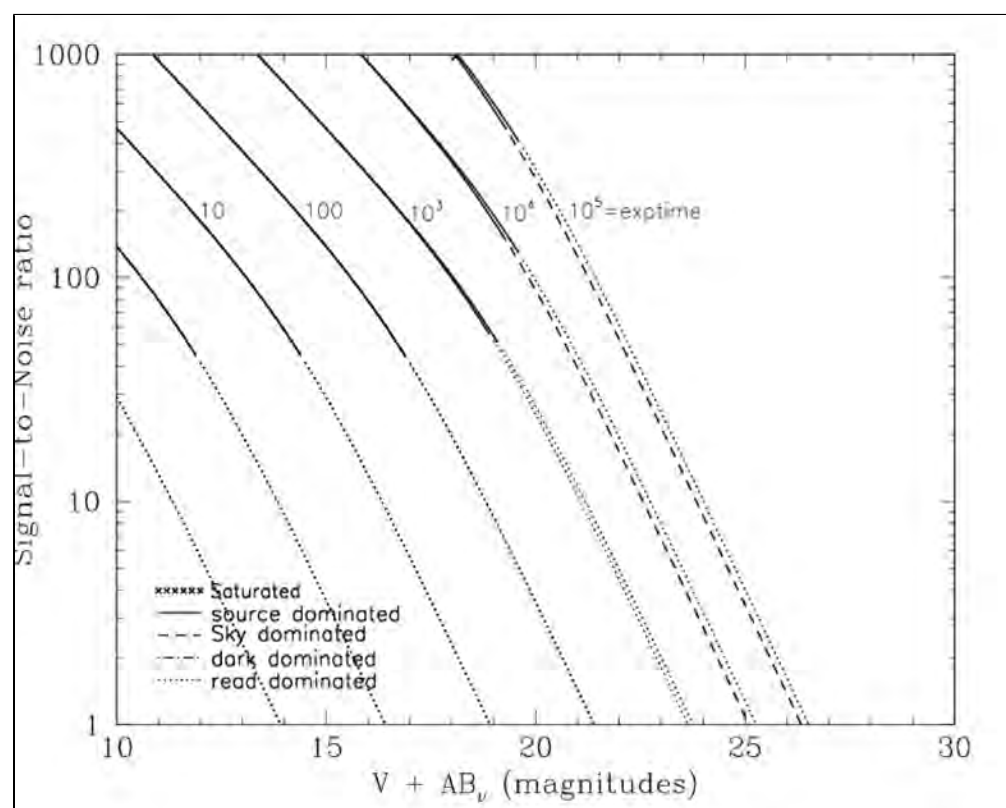
Figure 10.48: Extended Source S/N vs. V+ABv for the HRC/F250W filter. Top curves are for low sky and bottom curves are for average sky for a 1 arcsec² area.
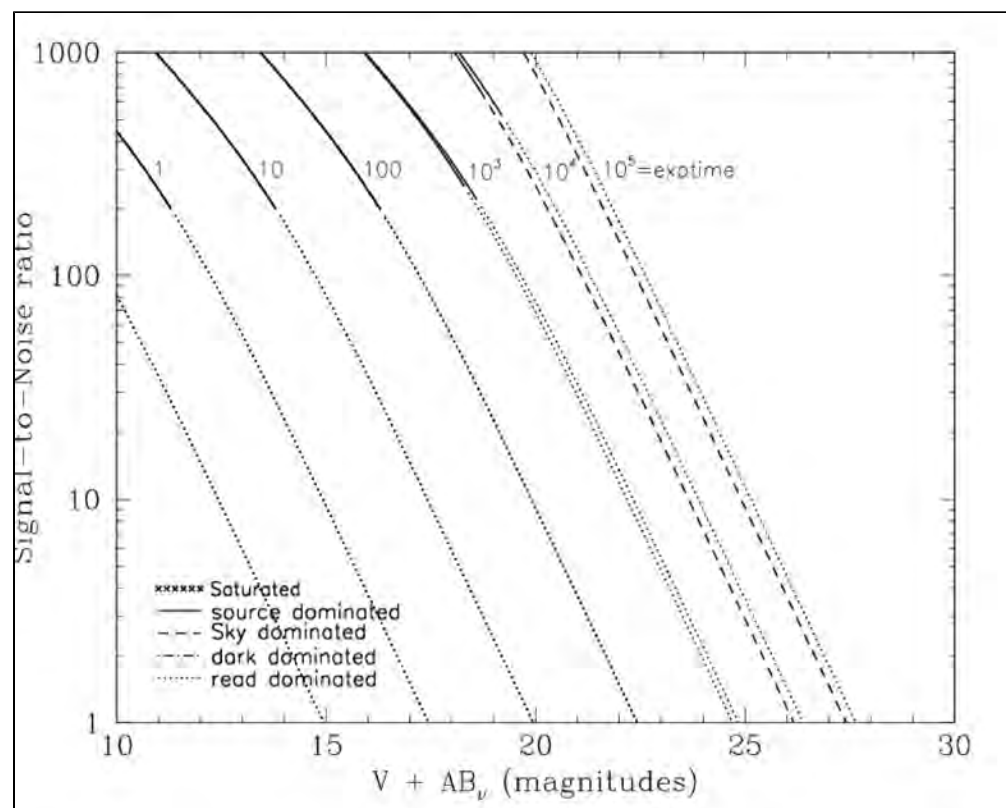
HRC F330W

Description

HRC u filter.

Figure 10.49: Integrated system throughput for HRC/F330W.
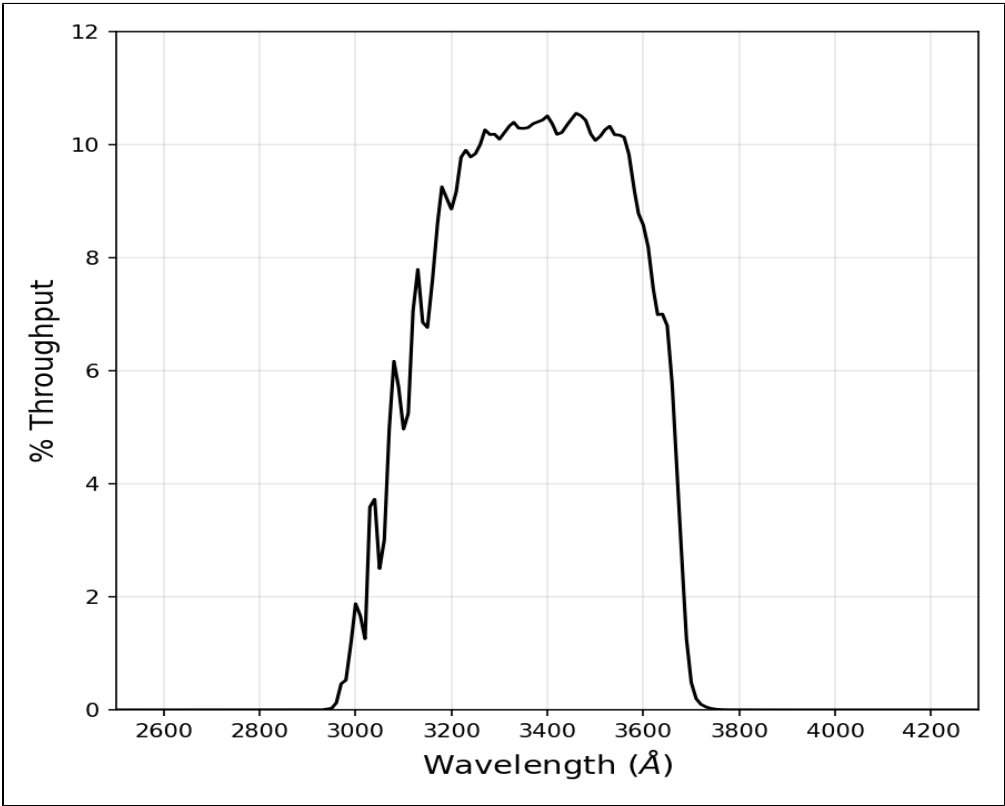
Figure 10.50: Point source S/N vs. V+ABv for the HRC/F330W filter. Top curves are for low sky; bottom curves are for average sky.
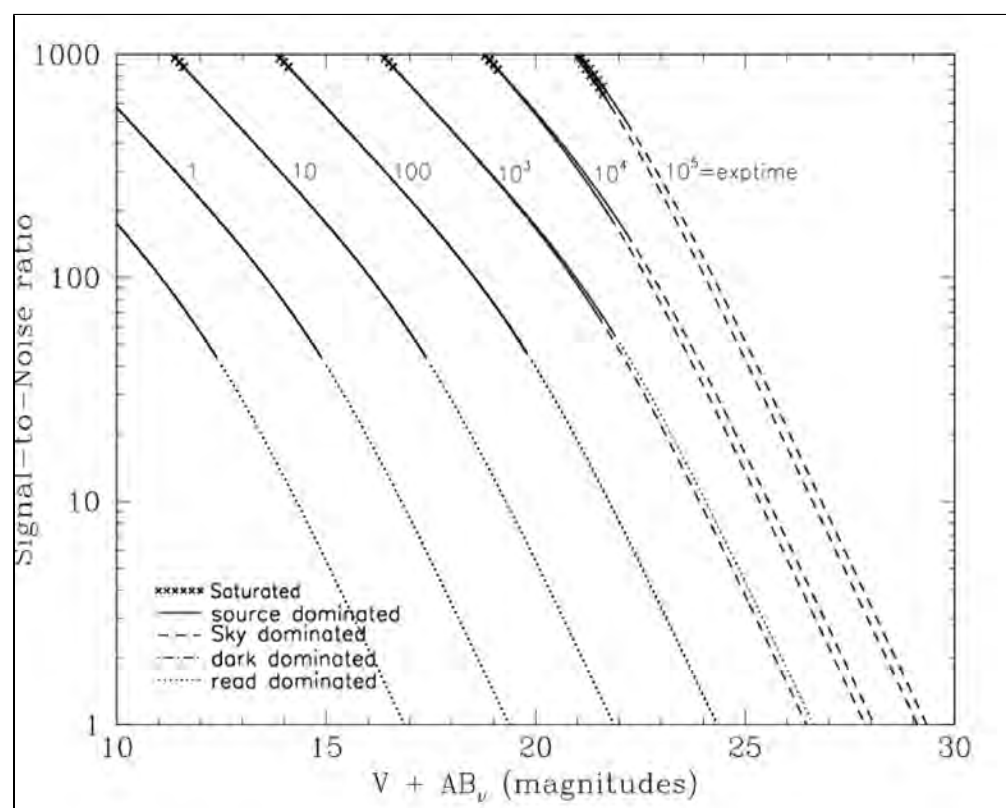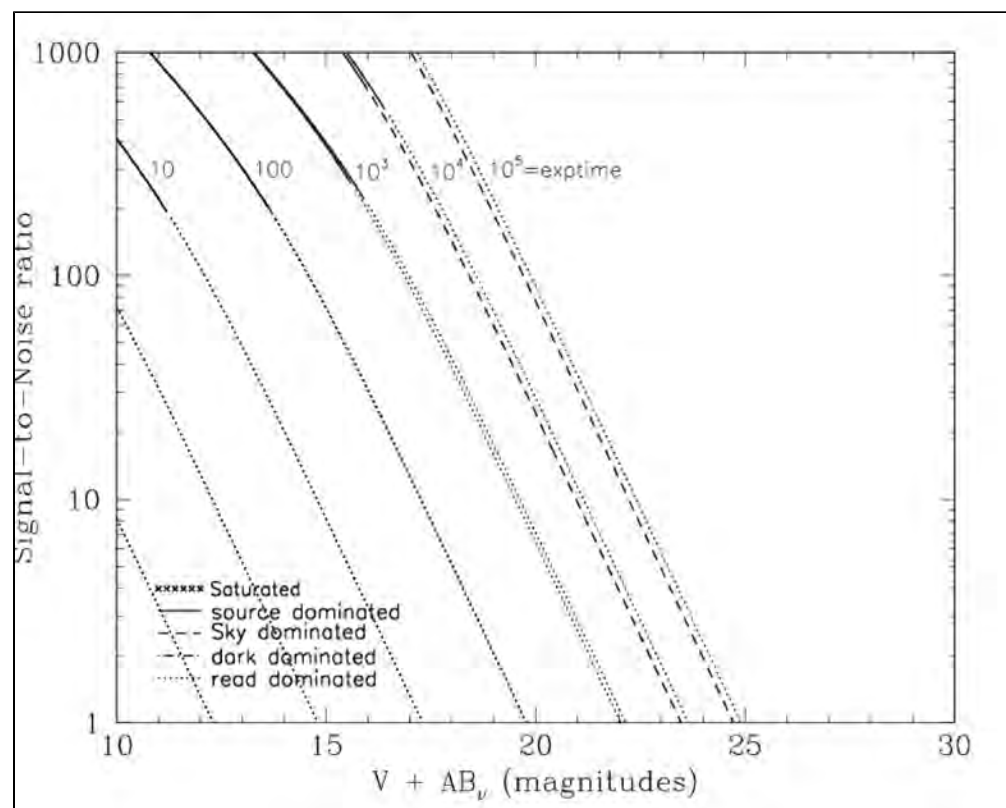
Figure 10.51: Extended source S/N vs. V+ABν for the HRC/F330W filter. Top curves are for low sky and bottom curves are for average sky for a 1 arcsec² area.
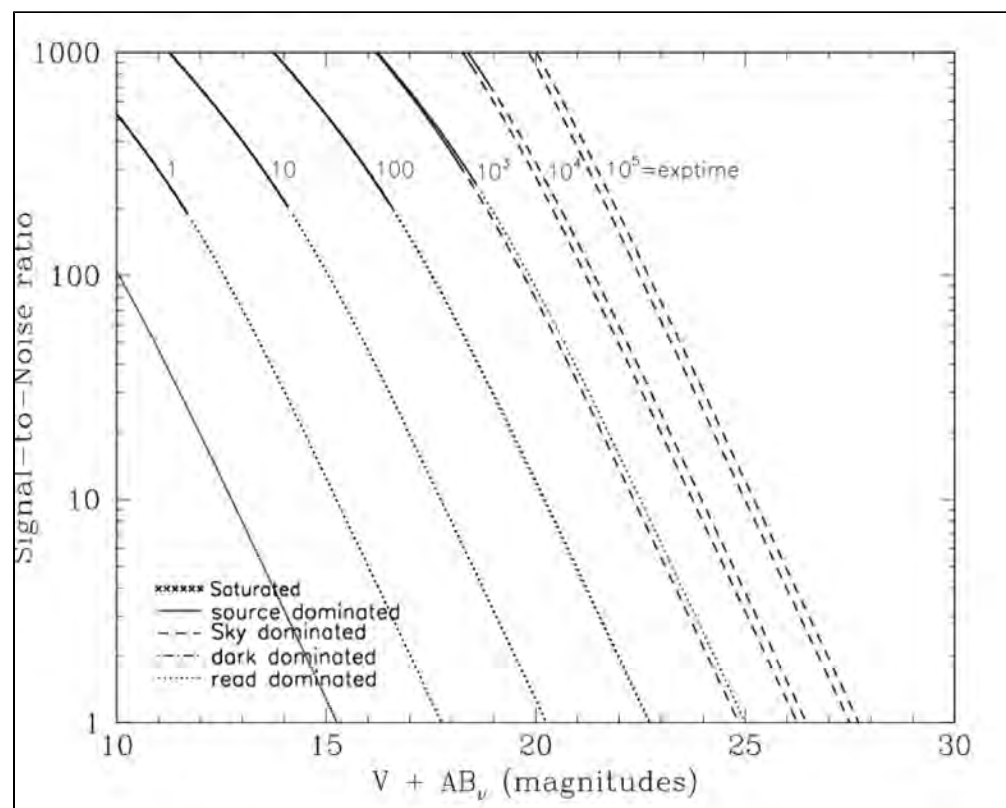
HRC F344N

Description

NeV filter.

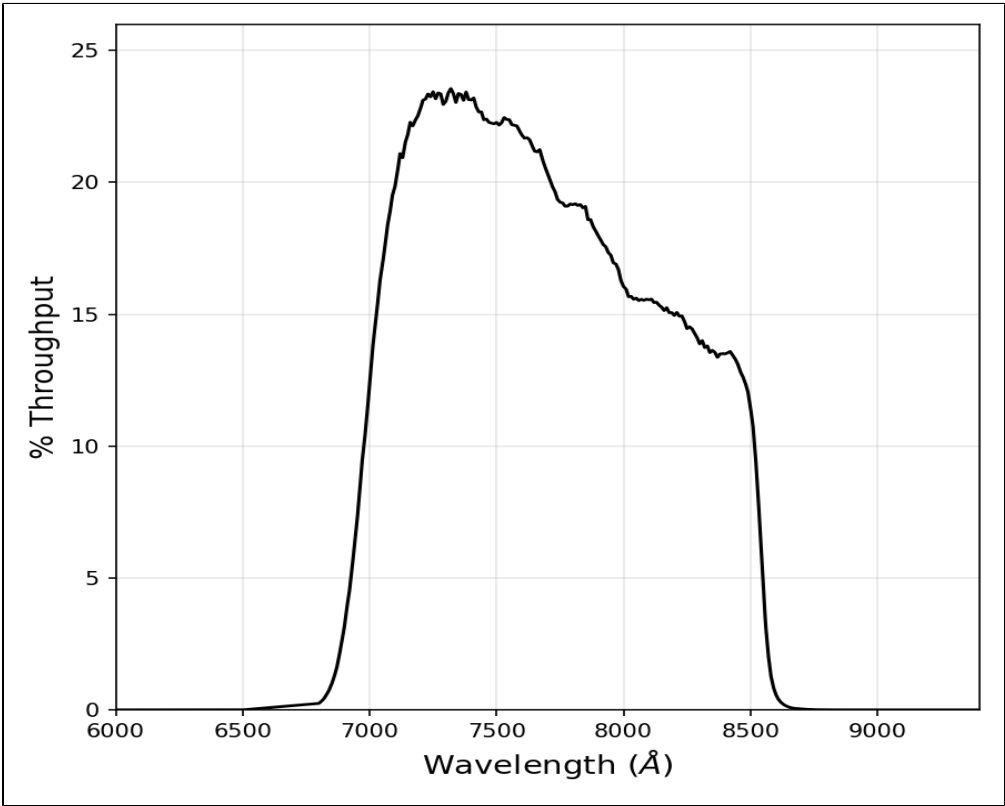**Figure 10.52:** Integrated system throughput for HRC/F344N.

Figure 10.53: Point source S/N vs. V+ABv for the HRC/F344N filter. Top curves are for low sky; bottom curves are for average sky.

Figure 10.54: Extended source S/N vs. V+ABv for the HRC/F344N filter. Top curves are for low sky and bottom curves are for average sky for a 1 arcsec^2 area.

HRC F435W

Description

Johnson B filter.

Figure 10.55: Integrated system throughput for HRC/F435W.

Figure 10.56: Point source S/N vs. V+ABν for the HRC/F435W filter. Top curves are for low sky; bottom curves are for average sky.
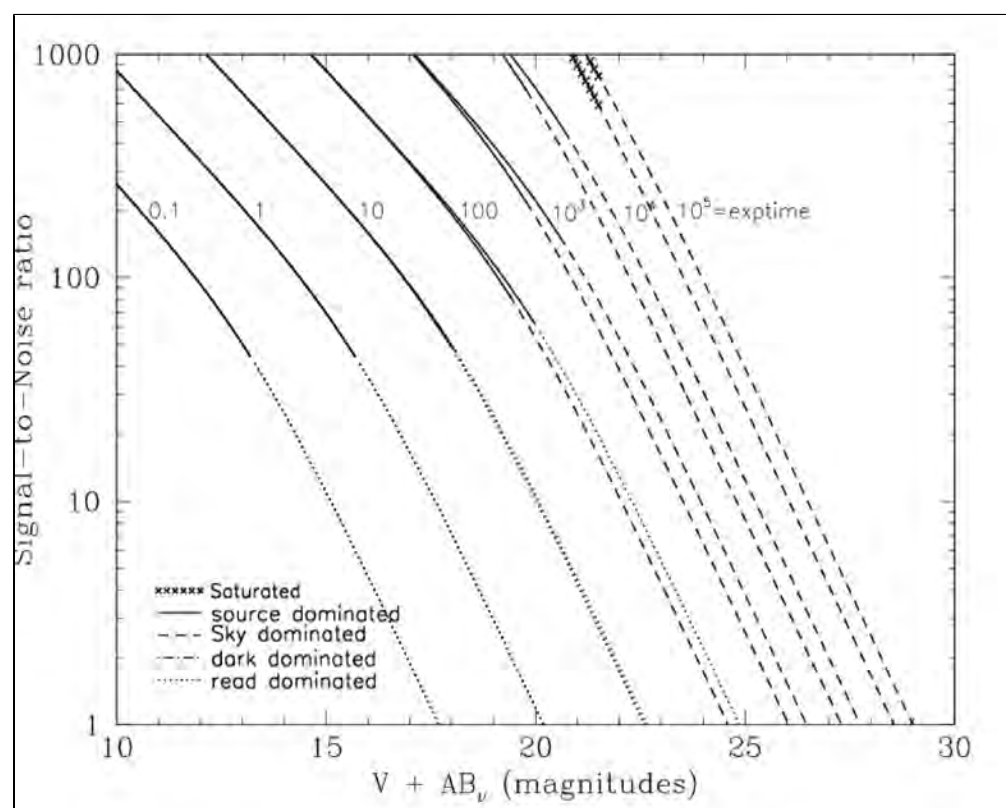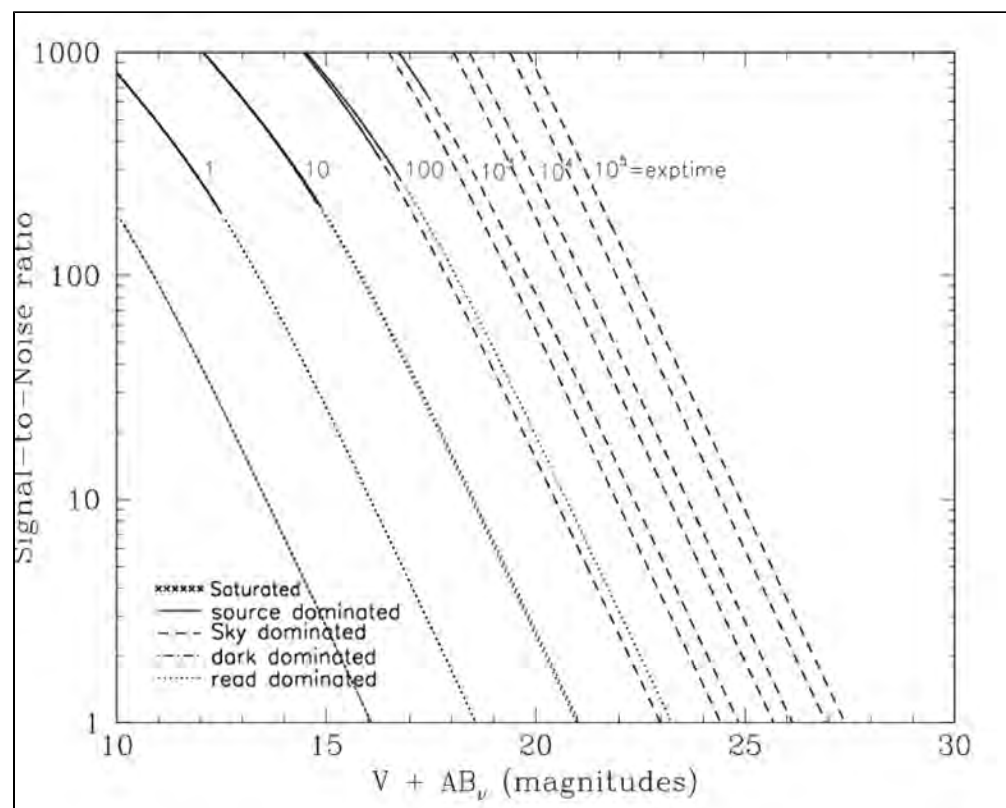
Figure 10.57: Extended source S/N vs. V+ABv for the HRC/F435W filter. Top curves are for low sky and bottom curves are for average sky for a 1 arcsec^2 area.

HRC F475W

Description

Sloan Digital Sky Survey g filter.

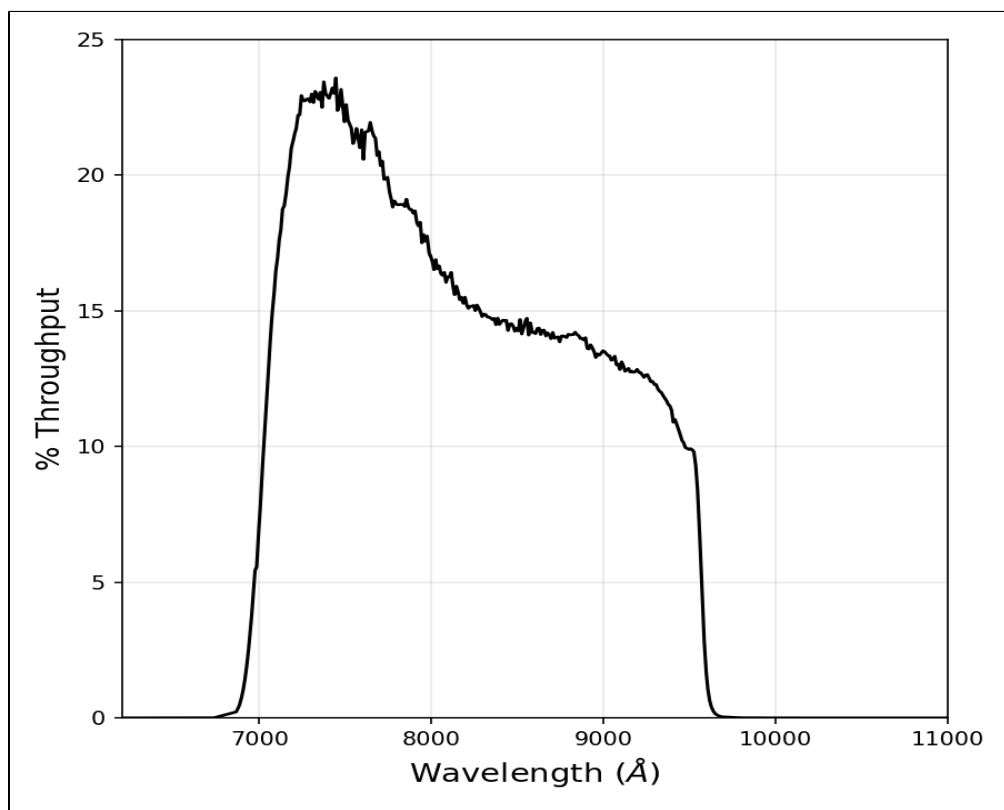**Figure 10.58:** Integrated system throughput for HRC/F475W.

Figure 10.59: Point source S/N vs. V+ABv for the HRC/F475W filter. Top curves are for low sky; bottom curves are for average sky.

Figure 10.60: Extended source S/N vs. V+ABν for the HRC/F475W filter. Top curves are for low sky and bottom curves are for average sky for a 1 arcsec^2 area.

HRC F502N

Description

OIII filter.

Figure 10.61: Integrated system throughput for HRC/F502N.

Figure 10.62: Point source S/N vs. V+ABv for the HRC/F502N filter. Top curves are for low sky; bottom curves are for average sky.
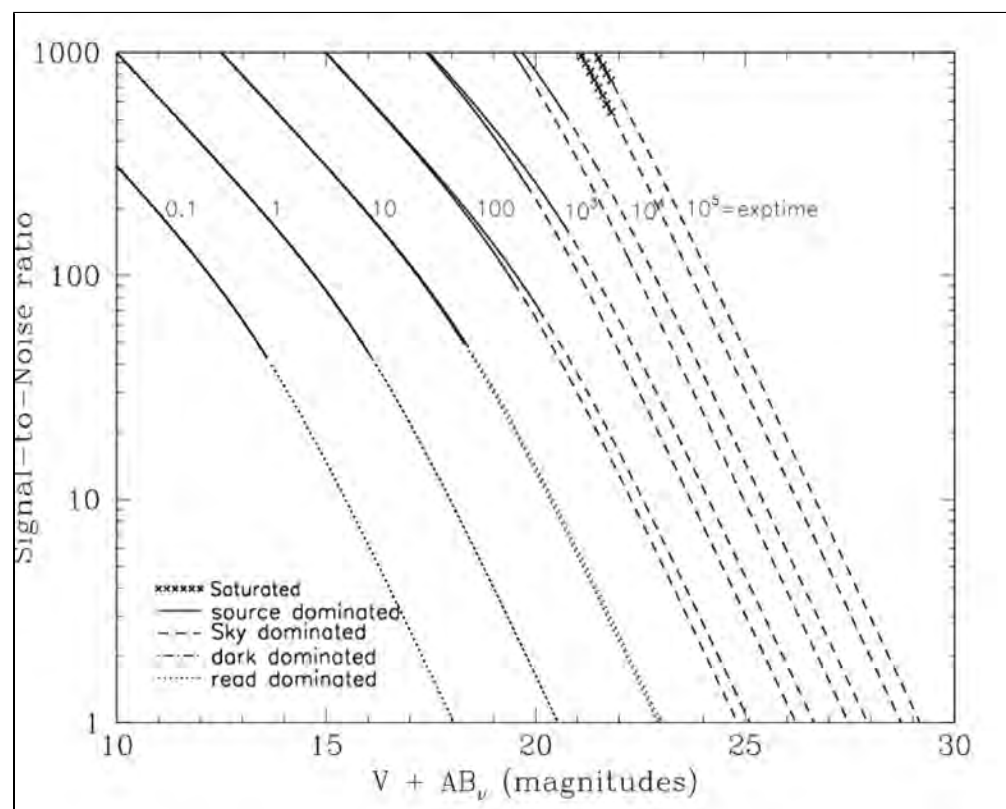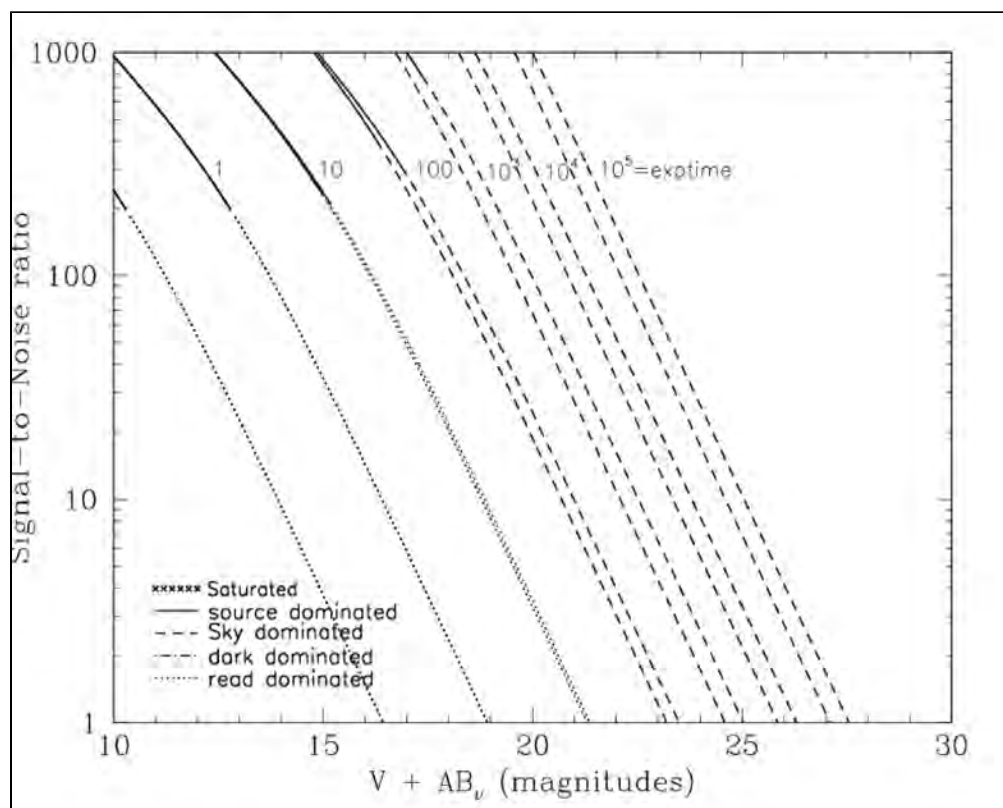
Figure 10.63: Extended source S/N vs. V+ABv for the HRC/F502N filter. Top curves are for low sky and bottom curves are for average sky for a 1 arcsec^2 area.

HRC F550M

Description

Narrow V filter.

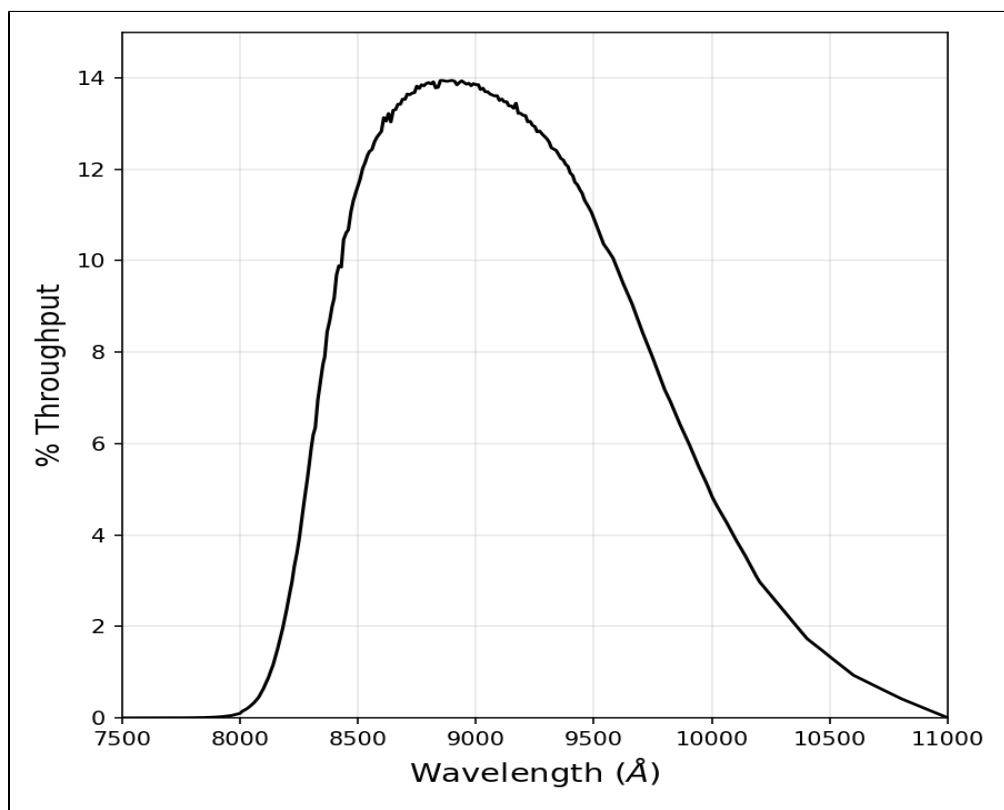**Figure 10.64:** Integrated system throughput for HRC/F550M.

Figure 10.65: Point source S/N vs. V+ABv for the HRC/F550M filter. Top curves are for low sky; bottom curves are for average sky.

Figure 10.66: Extended source S/N vs. V+ABv for the HRC/F550M filter. Top curves are for low sky and bottom curves are for average sky for a 1 arcsec^2 area.

HRC F555W

Description

Johnson V filter.

Figure 10.67: Integrated system throughput for HRC/F555W.

Figure 10.68: Point source S/N vs. V+ABv for the HRC/F555W filter. Top curves are for low sky; bottom curves are for average sky.
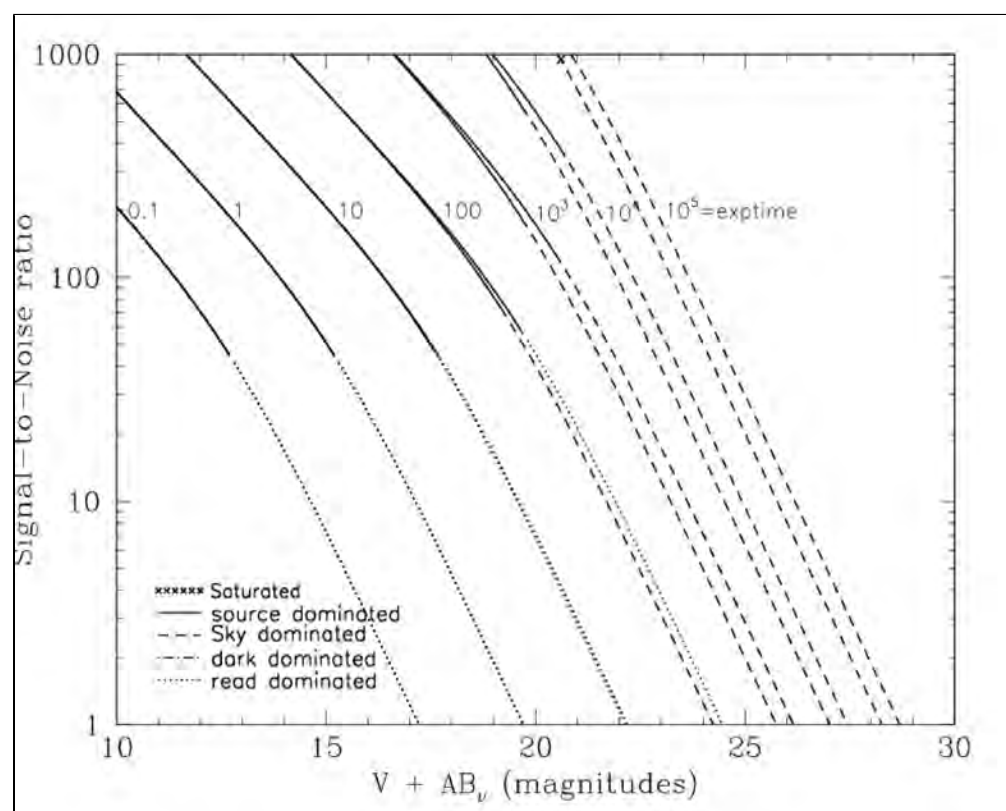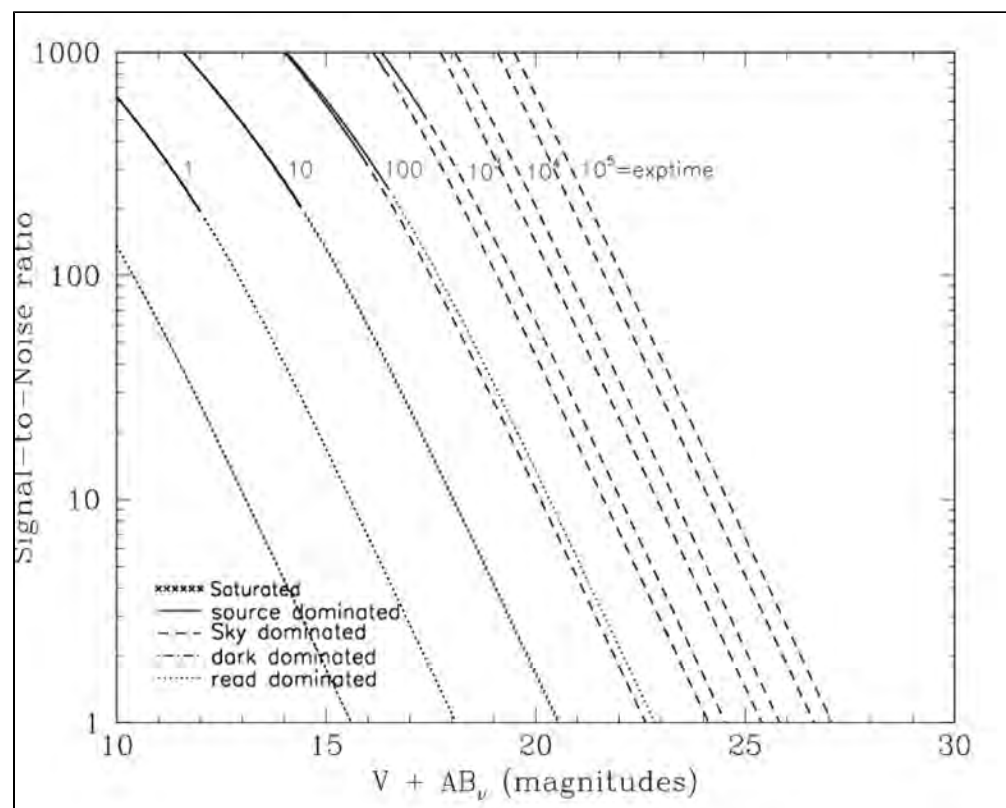
Figure 10.69: Extended source S/N vs. V+ABν for the HRC/F555W filter. Top curves are for low sky and bottom curves are for average sky for a 1 arcsec^2 area.

HRC F606W

Description

Broad V filter.

Figure 10.70: Integrated system throughput for HRC/F606W.
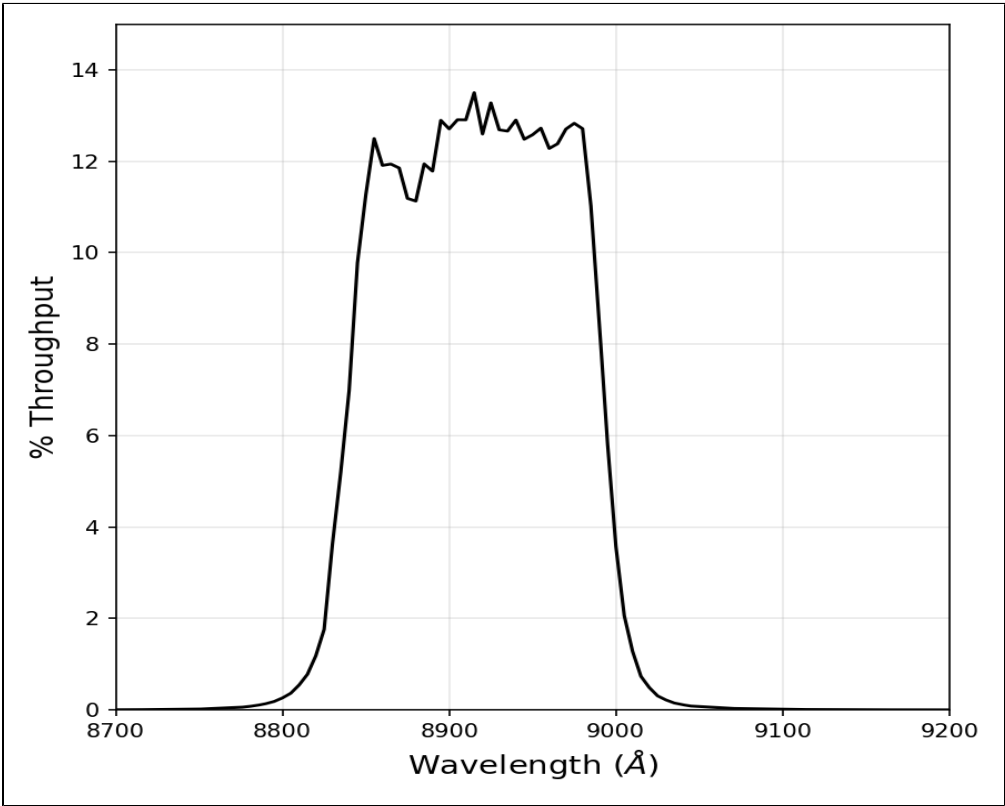
Figure 10.71: Point source S/N vs. V+ABν for the HRC/F606W filter. Top curves are for low sky; bottom curves are for average sky.

Figure 10.72: Extended source S/N vs. V+ABv for the HRC/F606W filter. Top curves are for low sky and bottom curves are for average sky for a 1 arcsec^2 area.

HRC F625W

Description

Sloan Digital Sky Survey r filter.

Figure 10.73: Integrated system throughput for HRC/F625W.

Figure 10.74: Point source S/N vs. V+ABν for the HRC/F625W filter. Top curves are for low sky; bottom curves are for average sky.
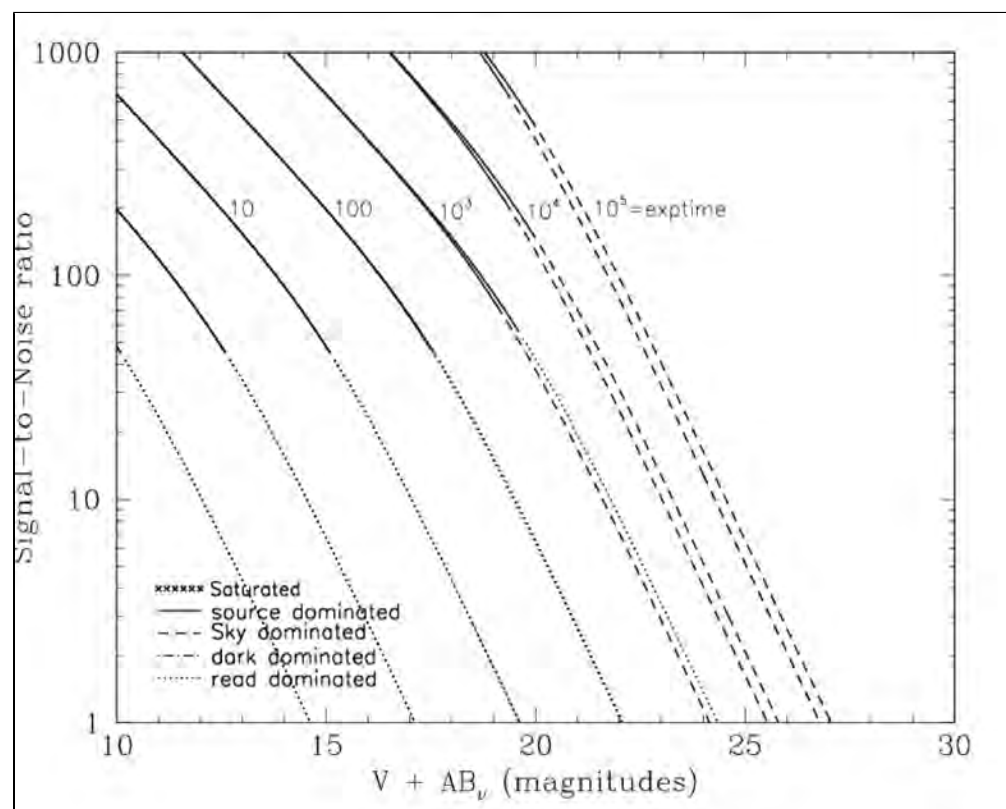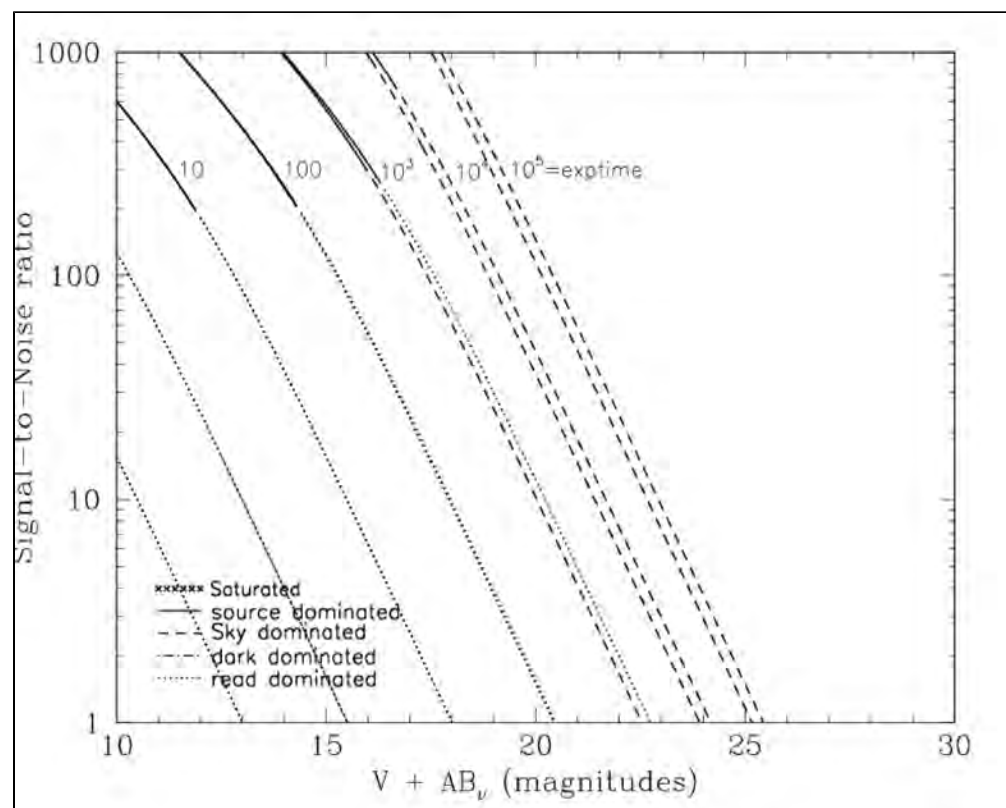
Figure 10.75: Extended source S/N vs. V+ABv for the HRC/F625W filter. Top curves are for low sky and bottom curves are for average sky for a 1 arcsec^2 area.

HRC F658N

Description

Hα filter.

Figure 10.76: Integrated system throughput for HRC/F658N.
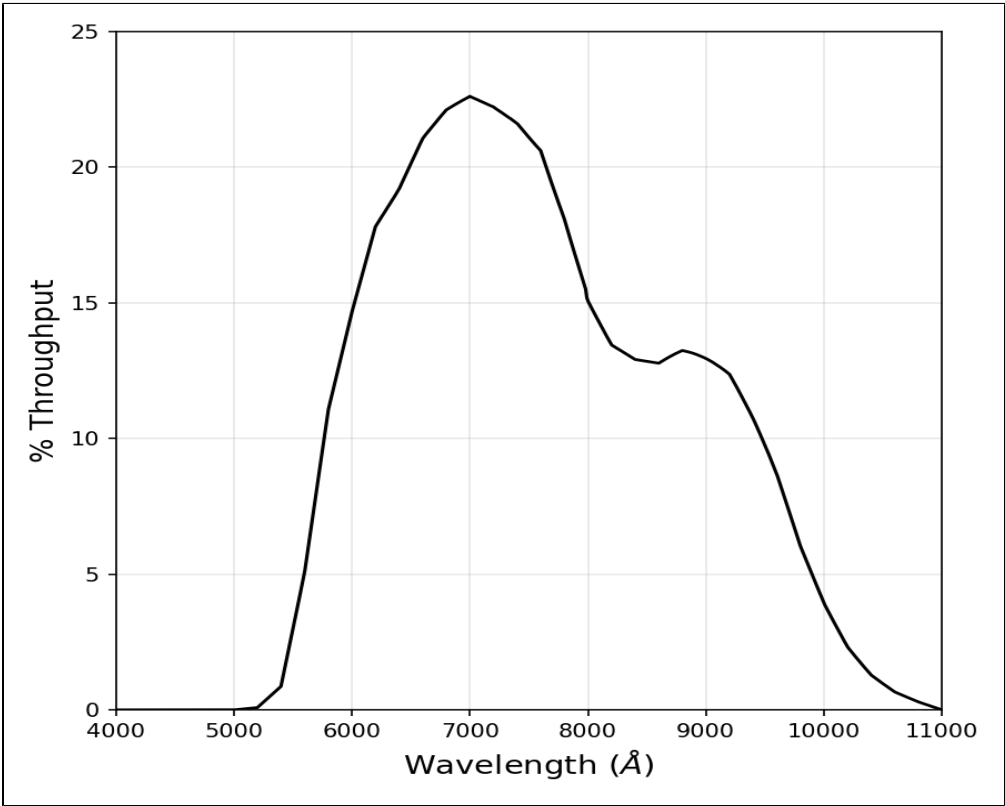
Figure 10.77: Point source S/N vs. V+ABv for the HRC/F658N filter. Top curves are for low sky; bottom curves are for average sky.

Figure 10.78: Extended source S/N vs. V+ABv for the HRC/F658N filter. Top curves are for low sky and bottom curves are for average sky for a 1 arcsec² area.

HRC F660N

Description

NII filter.

Figure 10.79: Integrated system throughput for HRC/F660N.

Figure 10.80: Point source S/N vs. V+ABν for the HRC/F660N filter. Top curves are for low sky; bottom curves are for average sky.
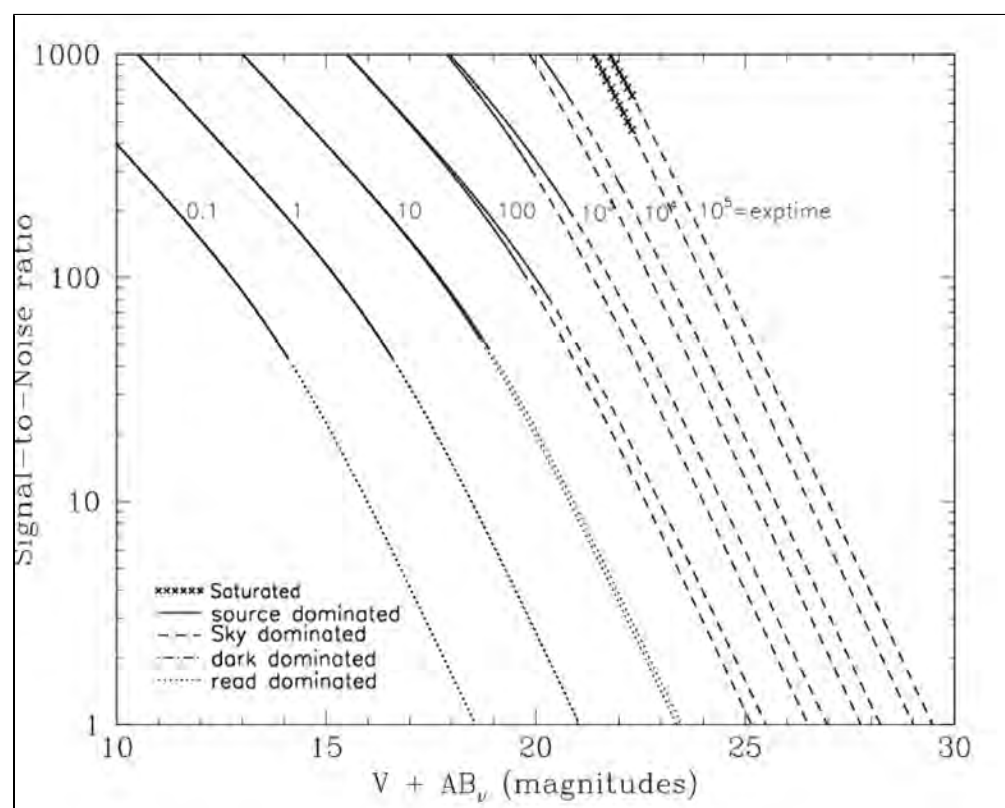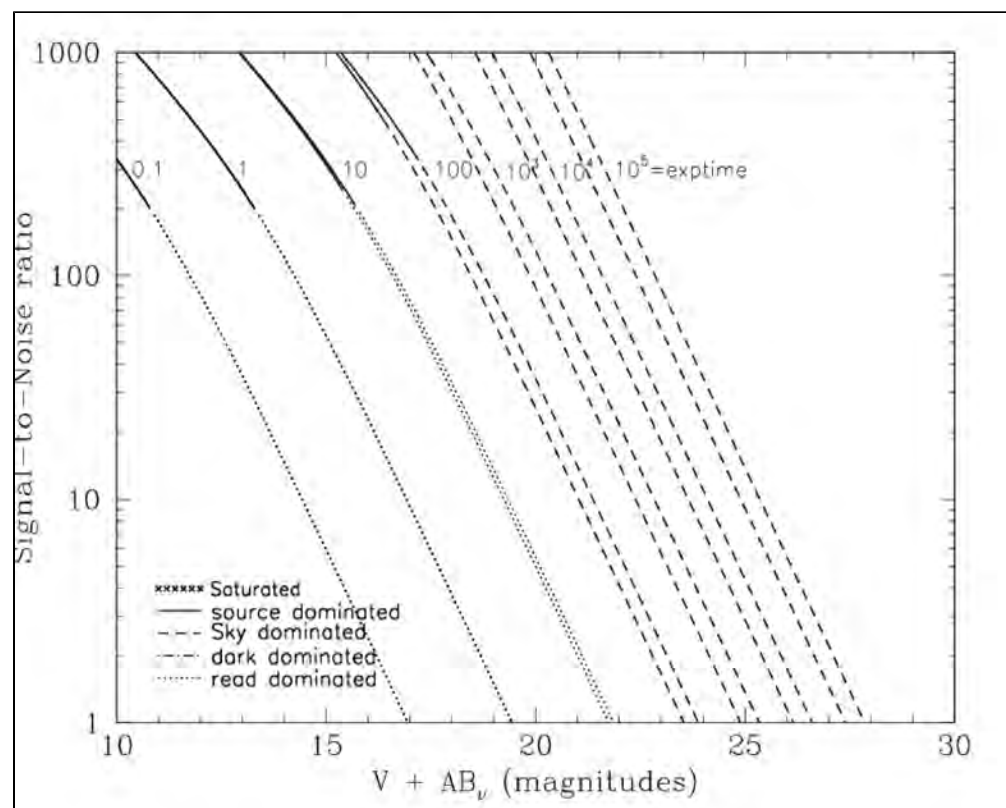
Figure 10.81: Extended source S/N vs. V+ABv for the HRC/F660N filter. Top curves are for low sky and bottom curves are for average sky for a 1 arcsec^2 area.

HRC F775W

Description

Sloan Digital Sky Survey i filter.

Figure 10.82: Integrated system throughput for HRC/F775W.

Figure 10.83: Point source S/N vs. V+ABv for the HRC/F775W filter. Top curves are for low sky; bottom curves are for average sky.

Figure 10.84: Extended source S/N vs. V+ABv for the HRC/F775W filter. Top curves are for low sky and bottom curves are for average sky for a 1 arcsec^2 area.

HRC F814W

Description

Broad I filter.

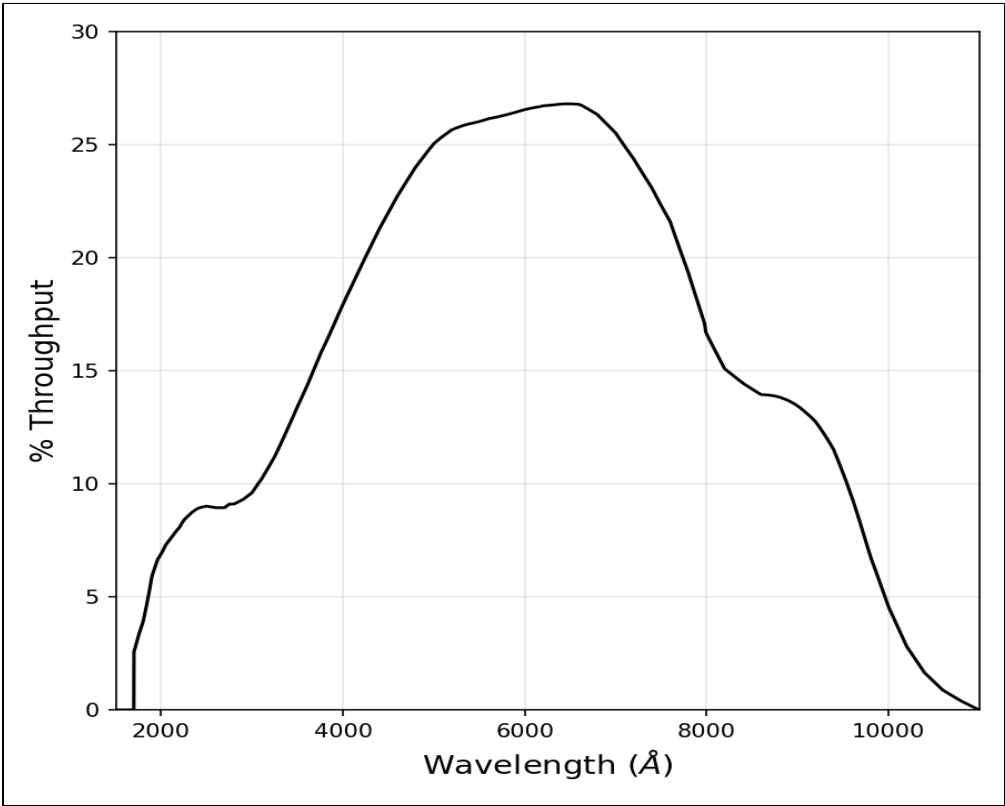**Figure 10.85: Integrated system throughput for HRC/F814W.**

Figure 10.86: Point source S/N vs. V+ABν for the HRC/F814W filter. Top curves are for low sky; bottom curves are for average sky.
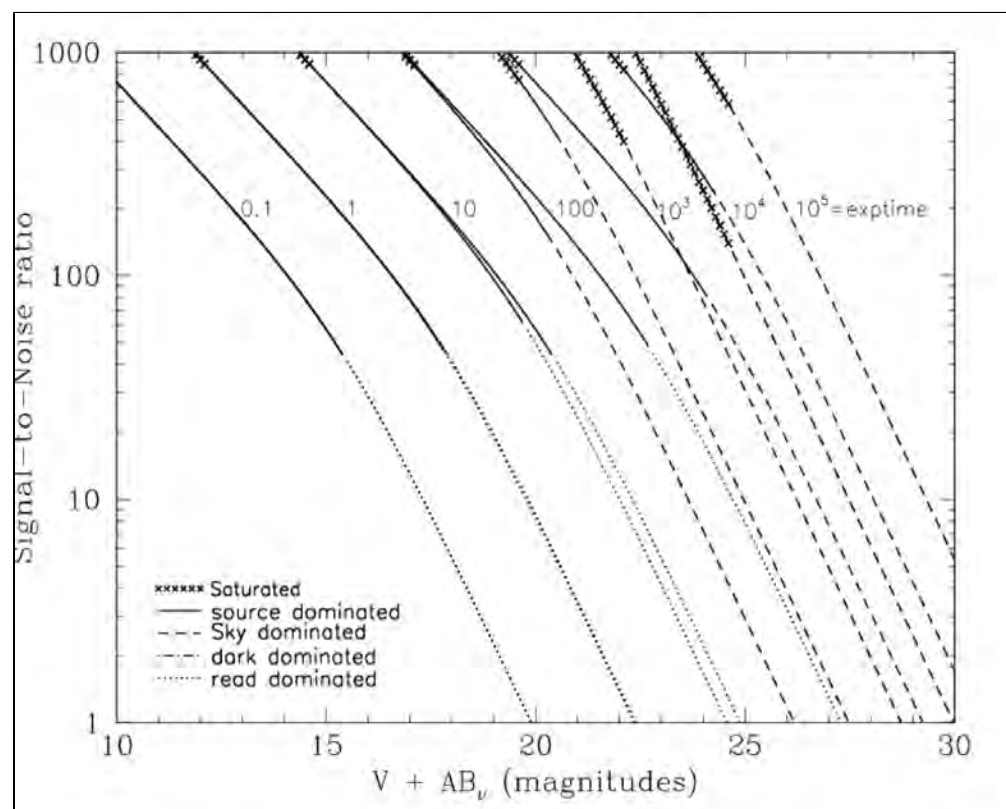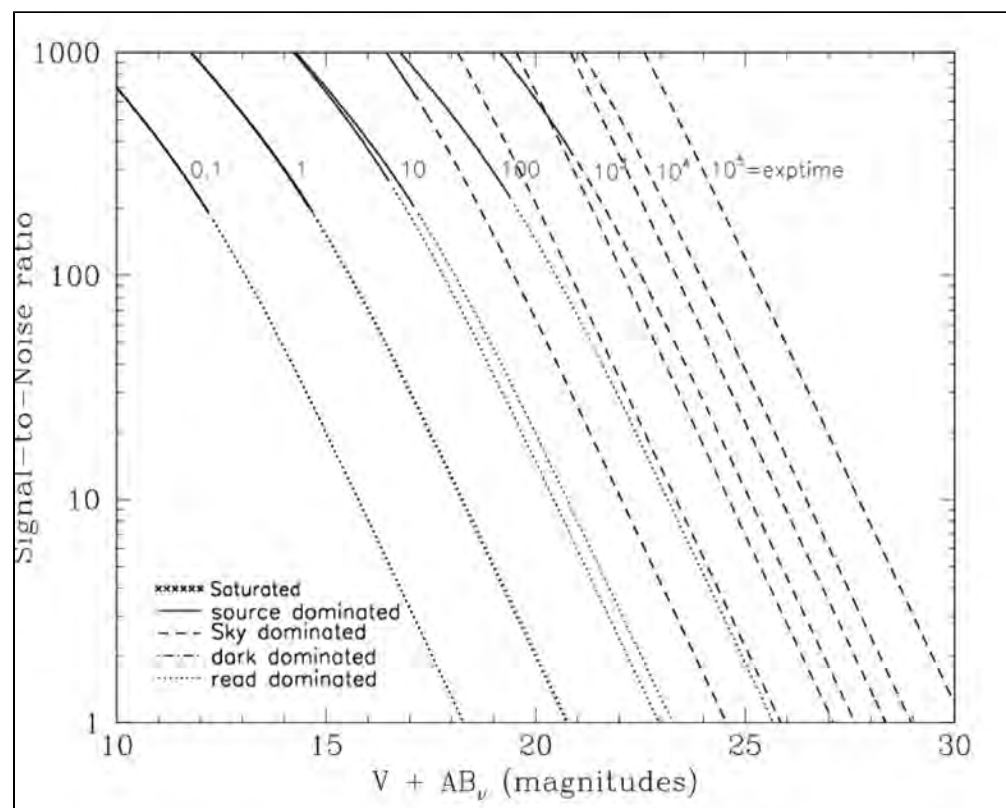
Figure 10.87: Extended source S/N vs. V+ABv for the HRC/F814W filter. Top curves are for low sky and bottom curves are for average sky for a 1 arcsec^2 area.

HRC F850LP

Description

Sloan Digital Sky Survey z filter.

Figure 10.88: Integrated system throughput for HRC/F850LP.

Figure 10.89: Point source S/N vs. V+ABv for the HRC/F850LP filter. Top curves are for low sky; bottom curves are for average sky.

Figure 10.90: Extended source S/N vs. V+ABv for the HRC/F850LP filter. Top curves are for low sky and bottom curves are for average sky for a 1 arcsec^2 area.

HRC F892N

Description

Methane filter.

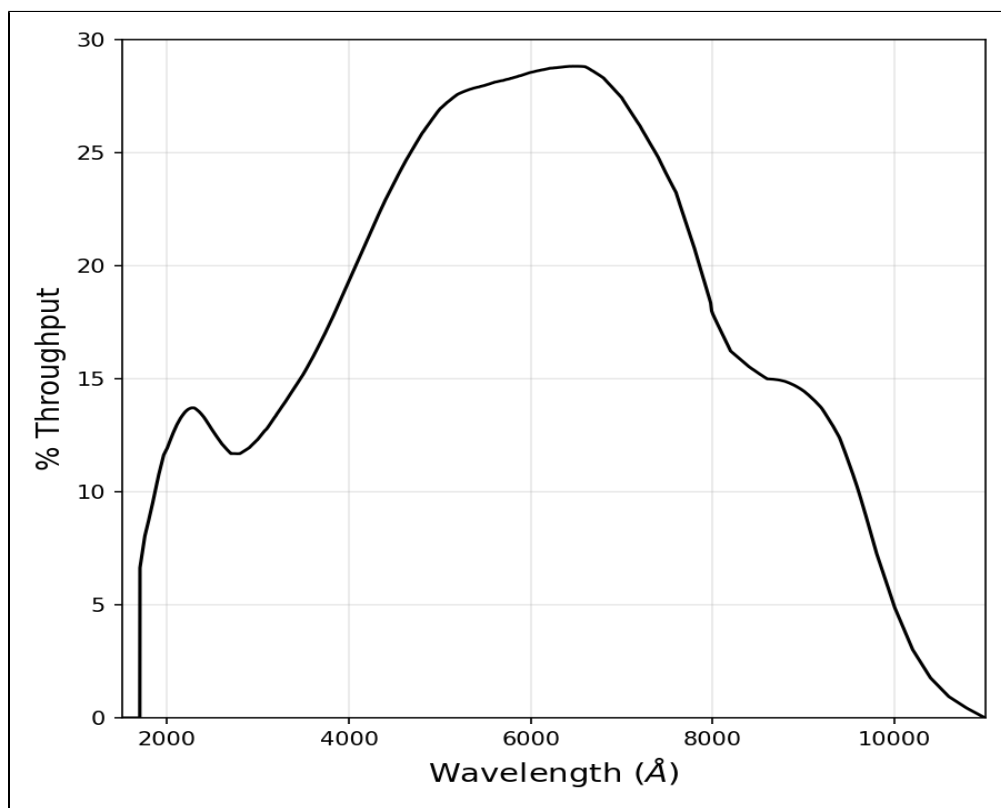**Figure 10.91: Integrated system throughput for HRC/F892N.**

Figure 10.92: Point source S/N vs. V+ABv for the HRC/F892N filter. Top curves are for low sky; bottom curves are for average sky.
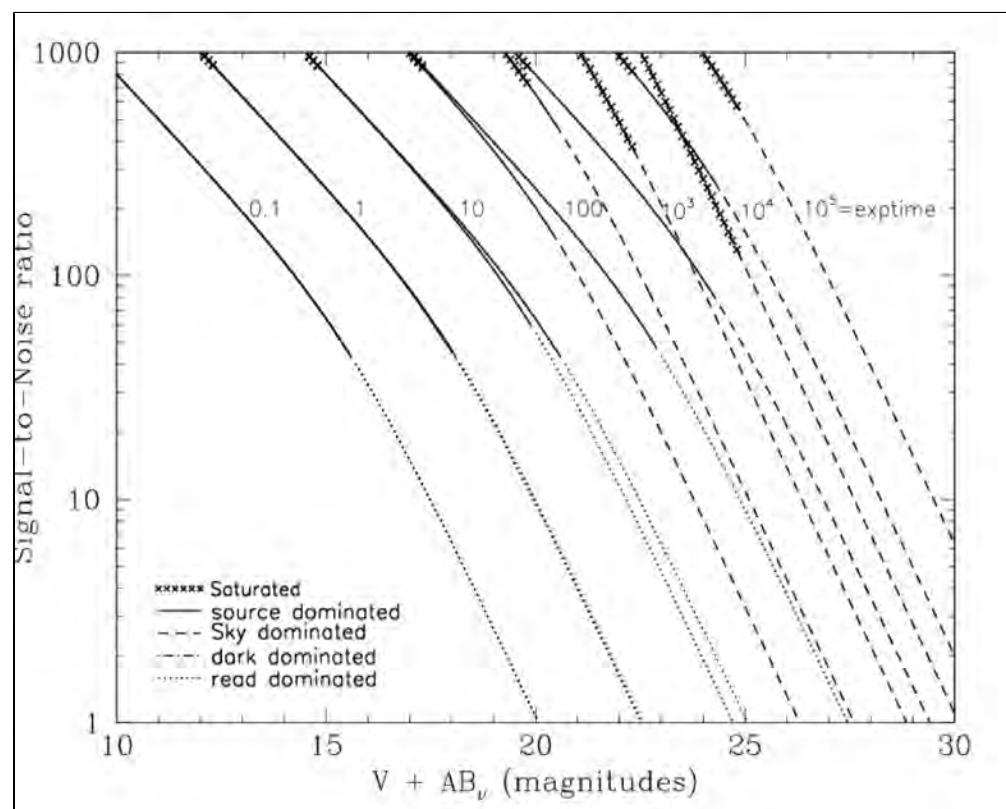
Figure 10.93: Extended source S/N vs. V+ABv for the HRC/F892N filter. Top curves are for low sky and bottom curves are for average sky for a 1 arcsec^2 area.

HRC G800L

Description

Grism.

Figure 10.94: Integrated system throughput for HRC/G800L.

Figure 10.95: Point source S/N vs. V+ABν for the HRC/G800L filter. Top curves are for low sky; bottom curves are for average sky.

Figure 10.96: Extended source S/N vs. V+ABv for the HRC/G800L filter. Top curves are for low sky and bottom curves are for average sky for a 1 arcsec^2 area.

HRC PR200L

Description

HRC Prism.

Figure 10.97: Integrated system throughput for HRC/PR200L.

Figure 10.98: Point source S/N vs. V+ABν for the HRC/PR200L filter. Top curves are for low sky; bottom curves are for average sky.

Figure 10.99: Extended source S/N vs. V+ABv for the HRC/PR200L filter. Top curves are for low sky and bottom curves are for average sky for a 1 arcsec^2 area.

HRC CLEAR

Description

HRC Clear Filter.

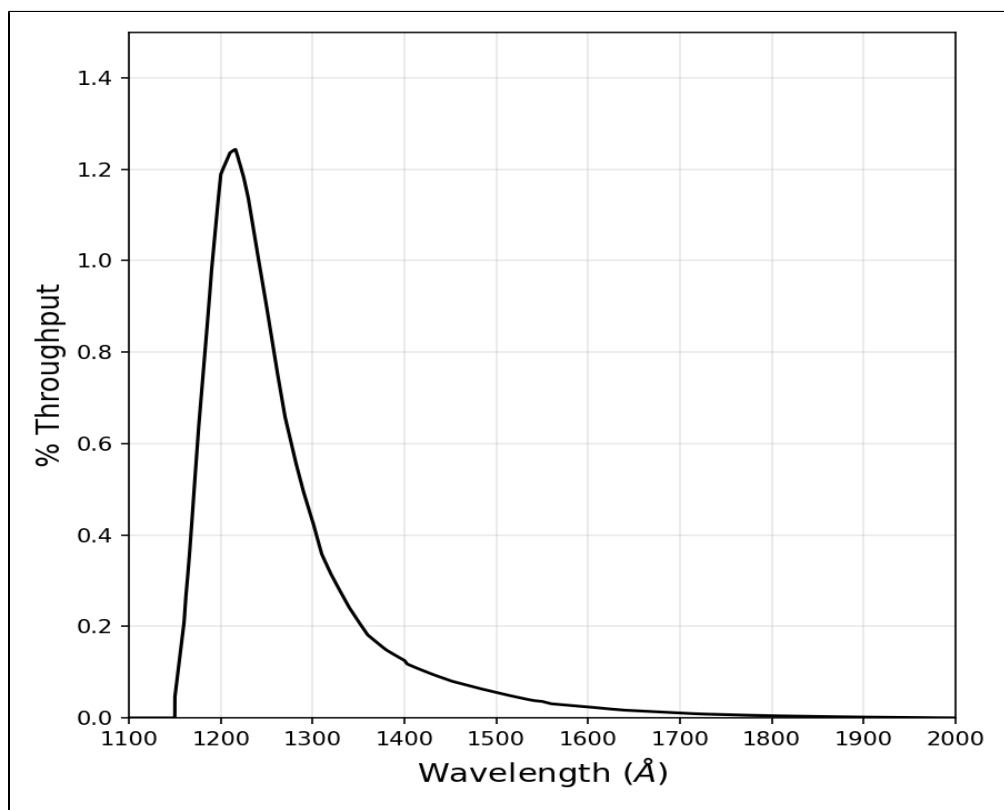**Figure 10.100: Integrated system throughput for HRC/Clear.**

Figure 10.101: Point source S/N vs. V+ABν for the HRC/Clear filter. Top curves are for low sky; bottom curves are for average sky.

Figure 10.102: Extended source S/N vs. V+ABv for the HRC/Clear filter. Top curves are for low sky and bottom curves are for average sky for a 1 arcsec^2 area.
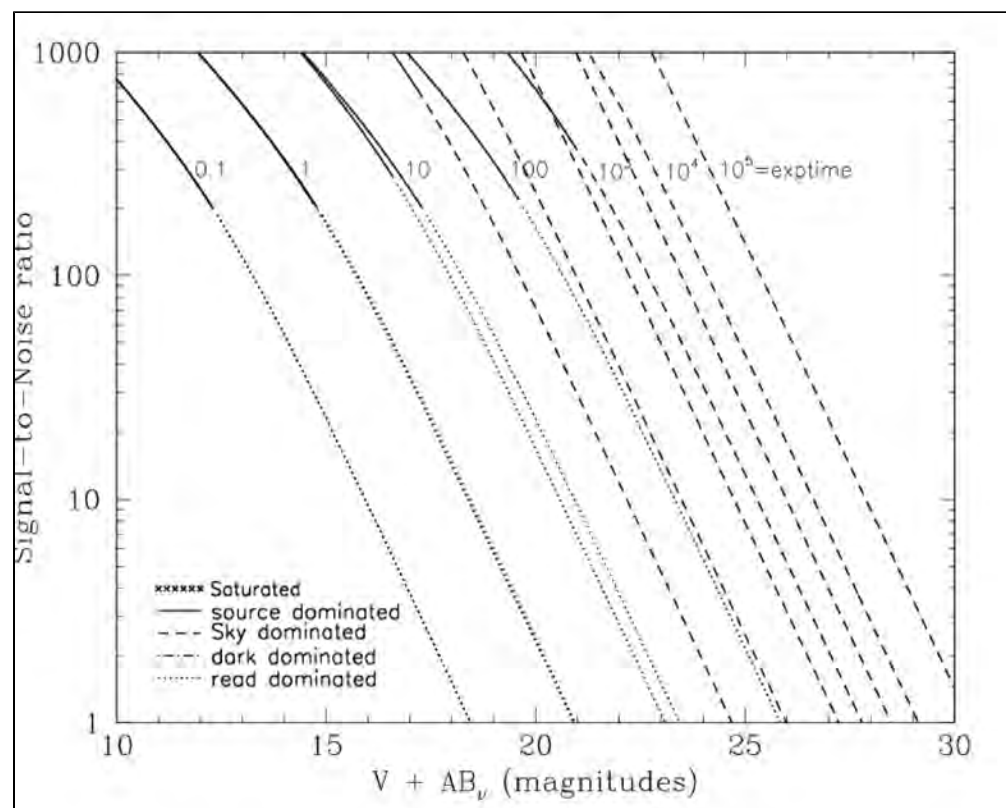
SBC F115LP

Description

MgF$_2$ filter.

Figure 10.103: Integrated system throughput for SBC/F115LP.
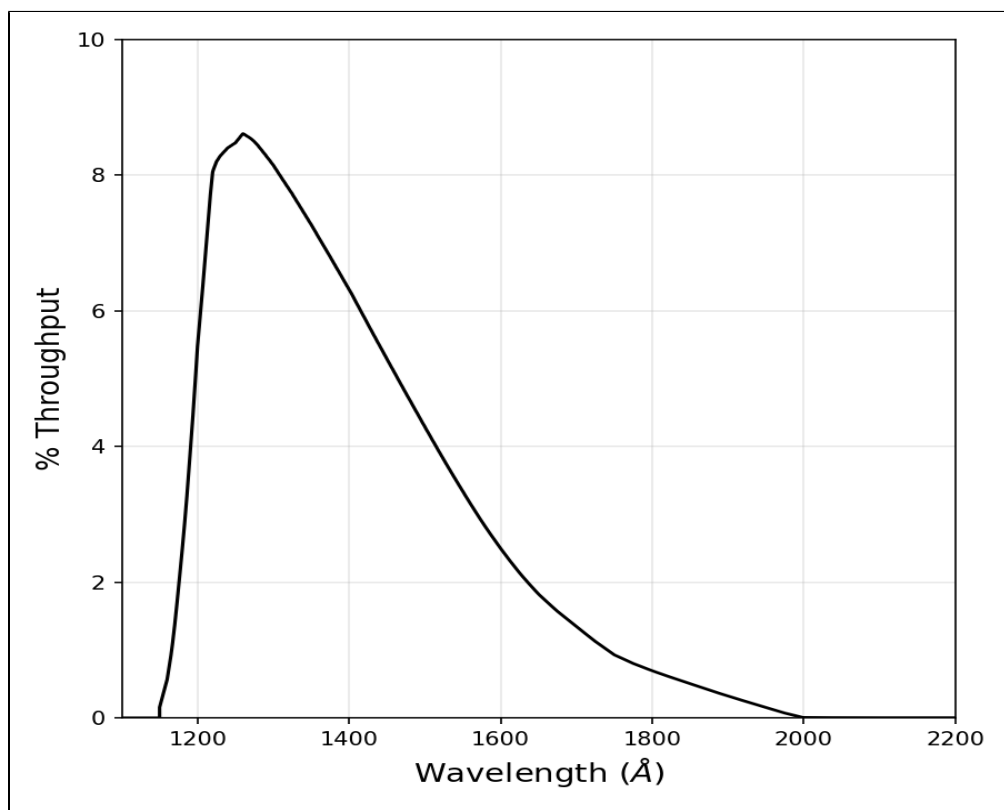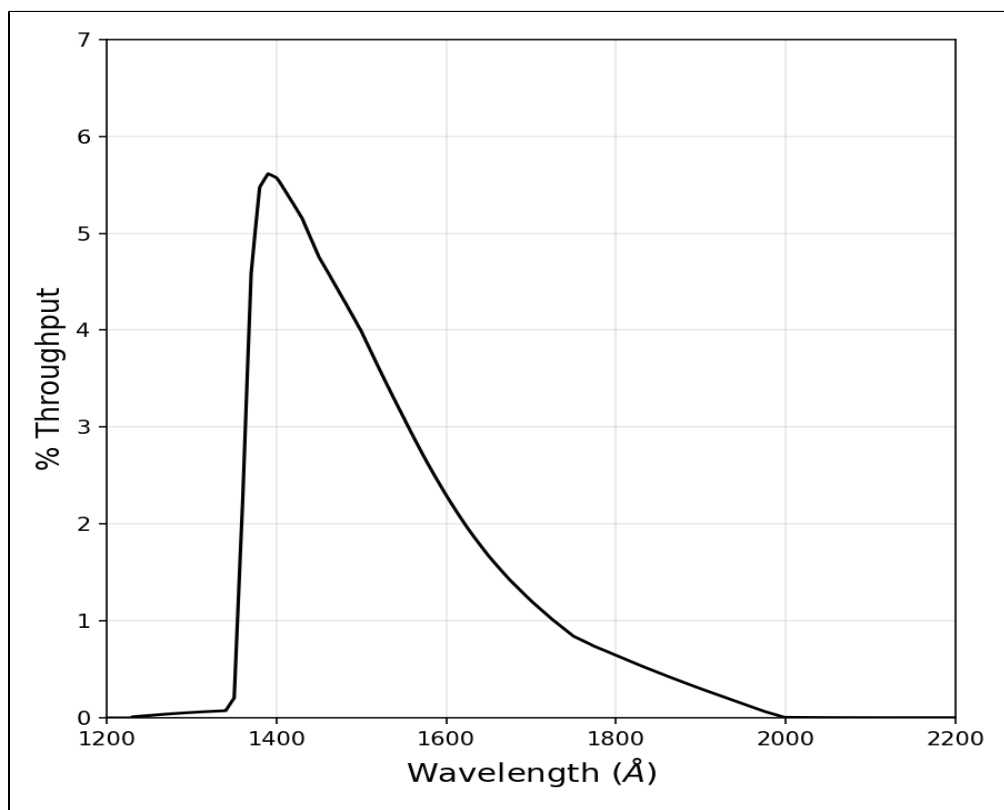

Please use the ACS ETC to estimate the required exposure time for the desired signal-to-noise of your sources.

SBC F122M

Description

Lyman α filter.

Figure 10.104: Integrated system throughput for SBC/F122M.

Please use the ACS ETC to estimate the required exposure time for the desired signal-to-noise of your sources.

SBC F125LP

Description

CaF$_2$ filter.

Figure 10.105: Integrated system throughput for SBC/F125LP.
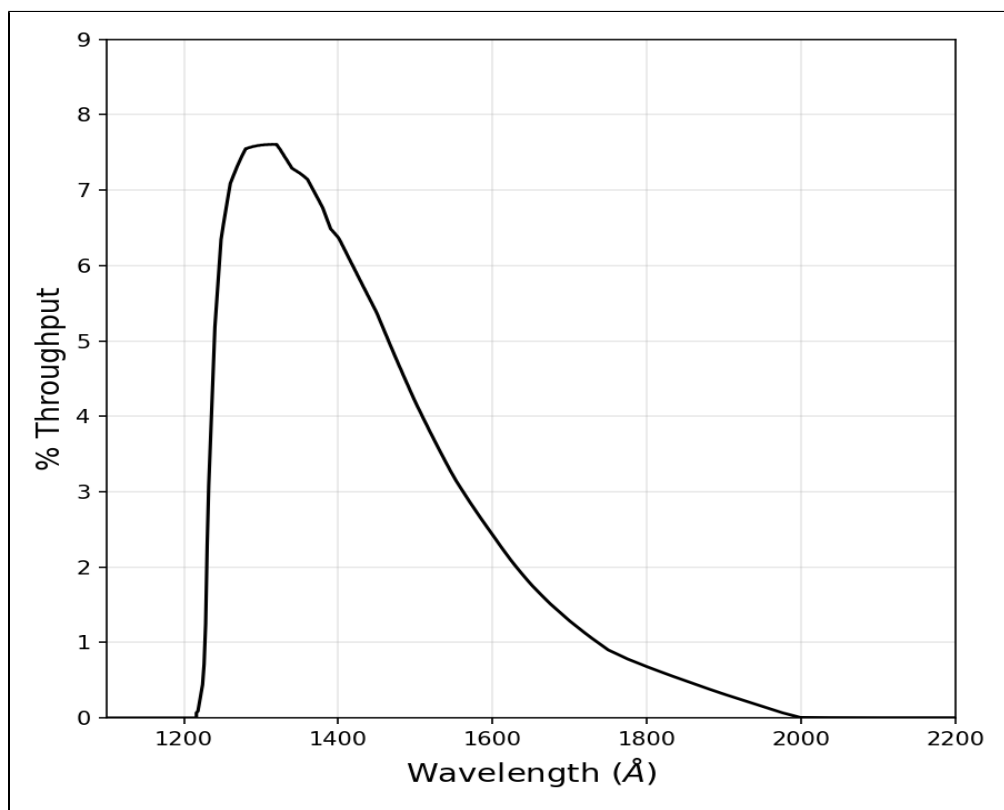
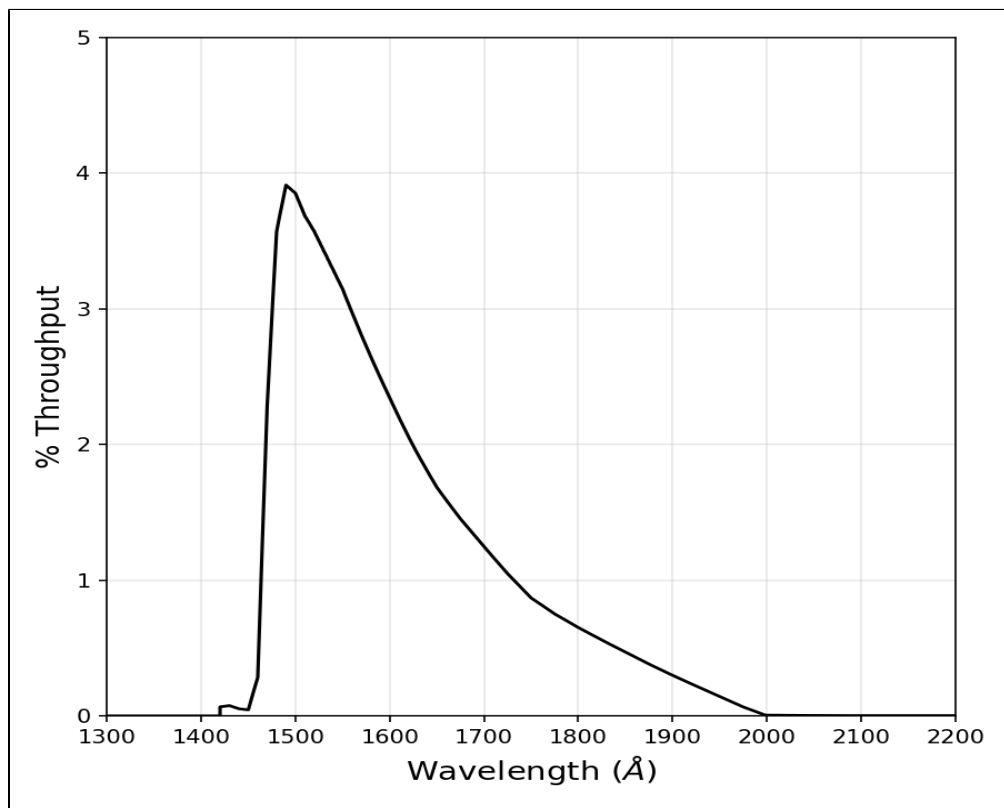Please use the ACS ETC to estimate the required exposure time for the desired signal-to-noise of your sources.

SBC F140LP

Description

BaF$_2$ filter.

Figure 10.106: Integrated system throughput for SBC/F140LP.

Please use the ACS ETC to estimate the required exposure time for the desired signal-to-noise of your sources.

SBC F150LP

Description

Crystal Quartz filter.

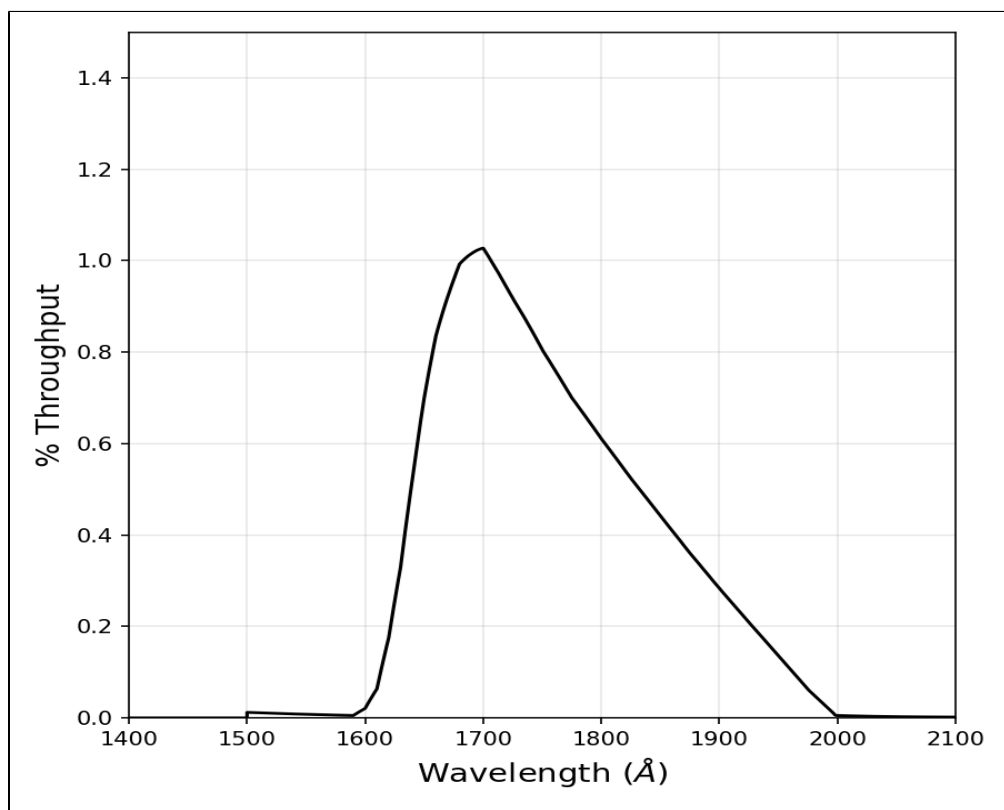**Figure 10.107: Integrated system throughput for SBC/F150LP.**

Please use the ACS ETC to estimate the required exposure time for the desired signal-to-noise of your sources.

SBC F165LP

Description

Dynasil filter.

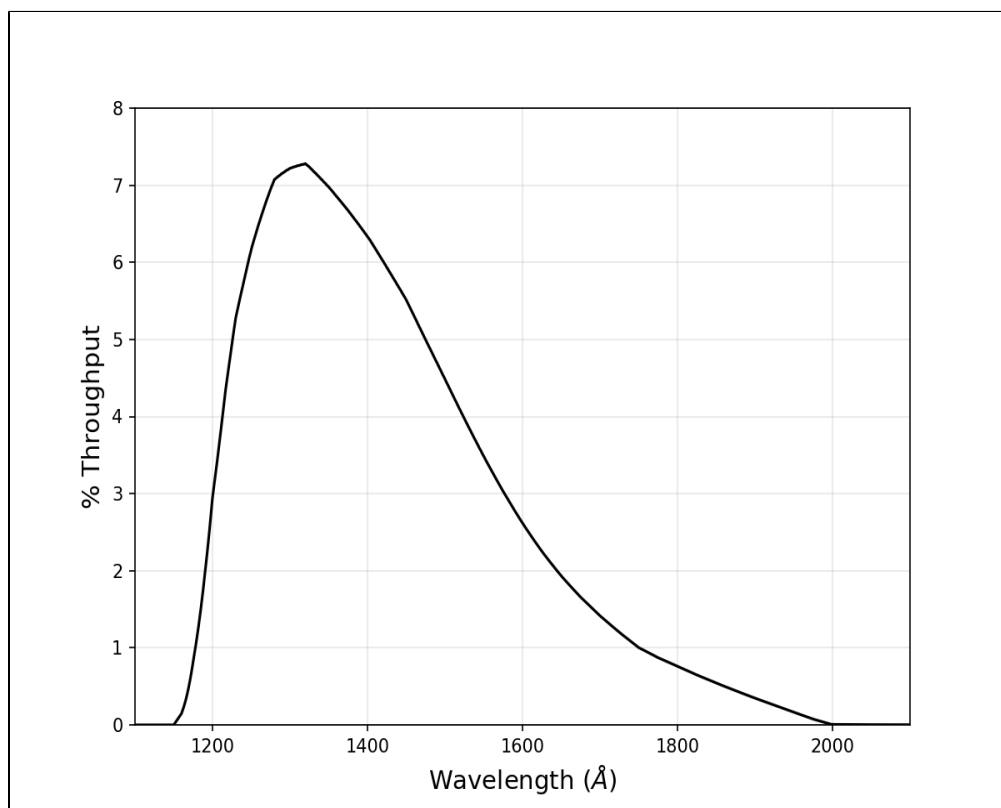**Figure 10.108: Integrated system throughput for SBC/F165LP.**

Please use the ACS ETC to estimate the required exposure time for the desired signal-to-noise of your sources.

SBC PR110L

Description

LiF$_2$ Prism.

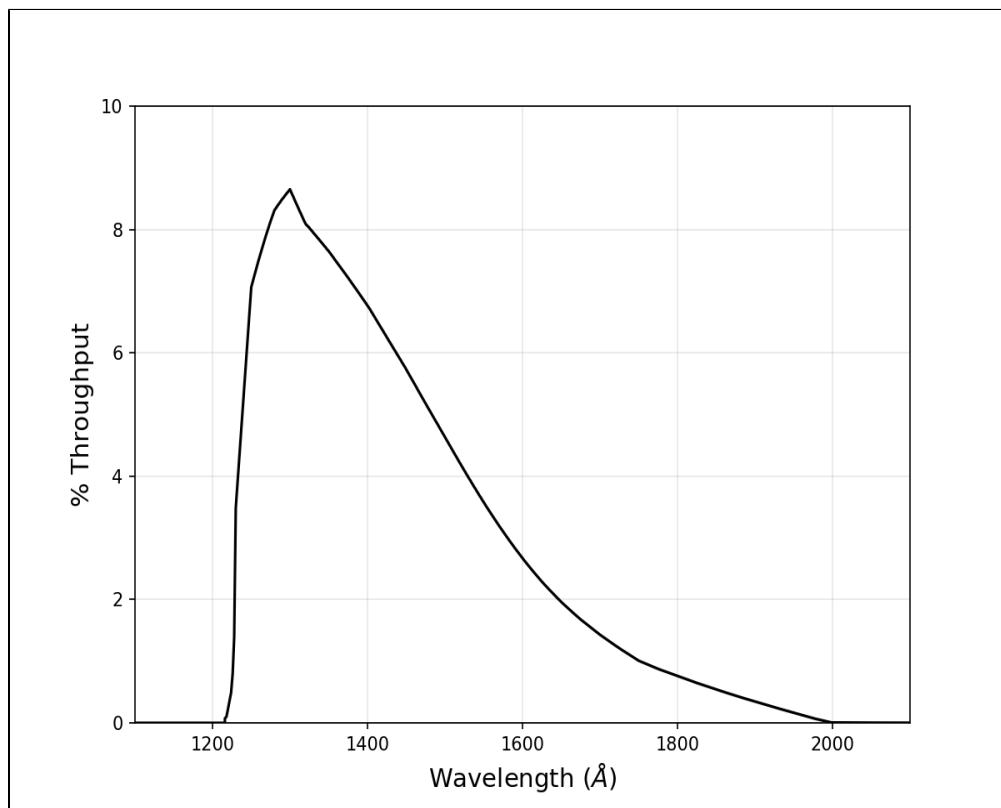**Figure 10.109: Integrated system throughput for SBC/PR110LP.**

Please use the ACS ETC to estimate the required exposure time for the desired signal-to-noise of your sources.

SBC PR130L

Description

CaF_2 Prism.

Figure 10.110: Integrated system throughput for SBC/PR130LP.

Please use the ACS ETC to estimate the required exposure time for the desired signal-to-noise of your sources.

10.4 Geometric Distortion in ACS

The ACS detectors exhibit more distortion than previous *HST* instruments. The principal reason is that the optics have been designed with a minimum number of components, consistent with correcting for the spherical aberration induced by the Optical Telescope Assembly (OTA), without introducing coma. The result is a high throughput, but with focal surfaces far from normal to the principal rays. The WFC detector is tilted at 22° giving an elongation of 8% while the HRC and SBC have a 25° tilt leading to an elongation of 12%. In each case, the scales in arcseconds per pixel are smaller along the radial direction of the OTA field of view than along the tangential direction.

The orientations of the ACS detector edges are approximately 2.1° and 2.7° offset from the V2 and V3 coordinate axes of the telescope. Consequently, the eigenaxes of the scale transformation are along the diagonals for WFC, and the apertures and pixels appear non-rectangular in the sky projection. For the HRC and SBC, the situation is even more irregular because the aperture diagonals do not lie along a radius of the *HST* field of view. Figure 7.9 shows the ACS apertures in the telescope's (V2, V3) reference frame. For a telescope roll angle of zero, this would correspond to an on-sky view with the V3 axis aligned with North and the V2 with East.

There is not only a strong geometric distortion of ACS detectors, but a significant variation of the scale across each detector. For the WFC, the scale changes by approximately 10% from corner to corner. For the HRC and SBC, this variation is only about 1% as they cover much smaller fields of view. The Science Instrument Aperture File (SIAF) provides the most accurate values of the scale for all instruments on board *HST*. The area on the sky covered by a WFC pixel varies by about 18% from corner to corner, corrections for which must be made in photometry of extended objects. This variation of scale creates a problematic effect in combining ACS images by the fact that an integral pixel shift near the center of the detector will translate into a non-integral displacement for pixels near the edges. Therefore, image alignment and combining require an accurate geometric distortion model.

The HRC geometric distortion calibration is fully described in ACS ISR 2004-15. The SBC geometric distortion is described in ACS ISR 2008-02. The WFC geometric distortion is described in ACS ISR 2015-06. The geometric distortion model is expressed by high-order polynomials for each of the ACS detectors in the form of reference files called as Instrument Distortion Coefficients Tables (IDCTAB) in the FITS format. On the top of the geometric distortion described by the polynomial equations, there are additional filter-dependent components of the distortion that are presented by a 2-D array and are applied to each row/columns of the WFC or HRC images. This filter-dependent component of the distortion is applied via a calibration file called NPOLFILE. In the case of the WFC, there is an additional component of the distortion called pixel-grid irregularities. These are caused by irregularities in the manufacturing process and are also presented by 2-D array to correct each row/column on WFC images. This correction is applied via the FITS formatted D2IMFILE. All distortion reference files are installed in the ACS data pipeline and used with the Drizzlepac software distributed by STScI.

10.4.1 WFC

The rhombus shape of the WFC is evident in Figure 7.9. The angle between the X and Y axes is 84.9° for WFC1 and 86.1° for WFC2. The geometric distortion map for WFC1 and WFC2 is illustrated in Figure 10.111. A vector diagram shows the contribution of the non-linear part of a quadratic fit only. At the center of chip WFC1, the scale in the X direction is 0.0493 arcsecond/pixel, and 0.0486 arcsecond/pixel in the Y direction. In the case of WFC2, the scale is 0.0498 arcsecond /pixel in the X direction, and 0.0503 arcsecond/pixel in the Y direction. Between the corner of WFC nearest to the V1 axis and the diagonally opposite corner, the scale increases by 10%. Therefore, WFC1 forms a slightly distorted rectangle 201 × 100 arcsecond^2 in size, while WFC2 is 203 × 103 arcsecond^2. There is a 2.5 arcsecond gap between the two chips. Additionally, the SIAF, orientation, and exact location of the ACS/WFC in the HST V2-V3 coordinate system were calibrated with respect to Gaia DR2 using observations of the open cluster M35 (TEL ISR 2019). See the SIAF website for more details.

ACS ISR 2007-08 shows that the linear terms of the WFC geometric distortion are changing over time and distortion-corrected positions are noticeable after almost 20 years on orbit, reaching about 25 milliarseconds from the original 2002-based distortion solution (ACS ISR 2015-06, ASC-ISR-2020-09). The X-scale and Y-skew changed after SM4, but the reason for the change is not yet understood. The time-dependent distortion has been calibrated for pre- and post-SM4 (ACS ISR 2015-06) and its parameters are implemented via the IDCTAB, which is used by both the ACS data pipeline and the Drizzlepac software. Geometric distortion reference files including the IDCTAB were updated (ACS ISR 2020-09) to reflect a new geometric distortion solution derived with respect to the Gaia DR2 catalog.
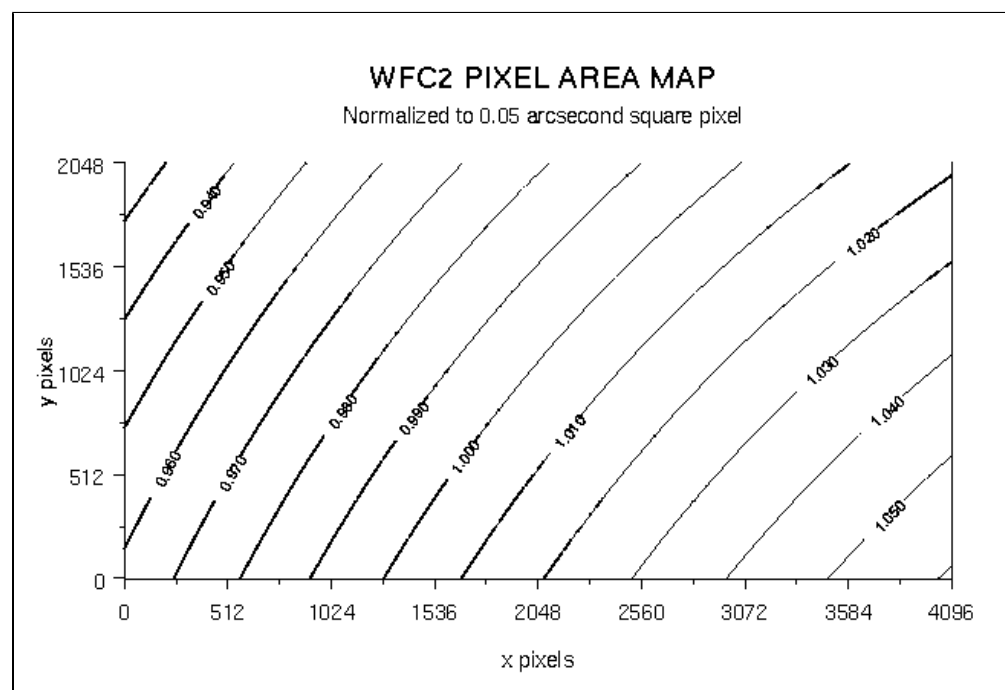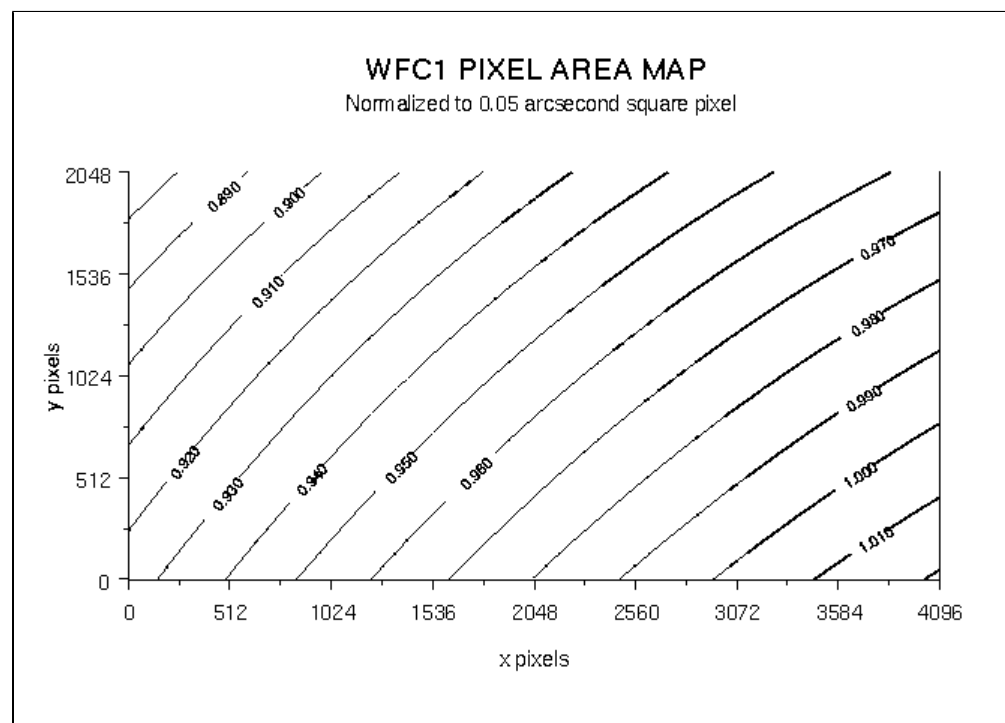
Geometric distortion affects not only the astrometry, but also the photometry, since it induces an apparent variation in surface brightness across the field of view. In order to preserve the photometric accuracy of non-drizzled images, an additional correction to the photometry is required via multiplication of the ACS/WFC flat-fielded images by the pixel area map. The effective area of each pixel is shown in Figure 10.112 as a contour plot. The range of area goes from 0.89 to 1.08 times the central value.

Figure 10.111: The geometric distortion map for the ACS/WFC, which shows only the non-linear component to the solution.
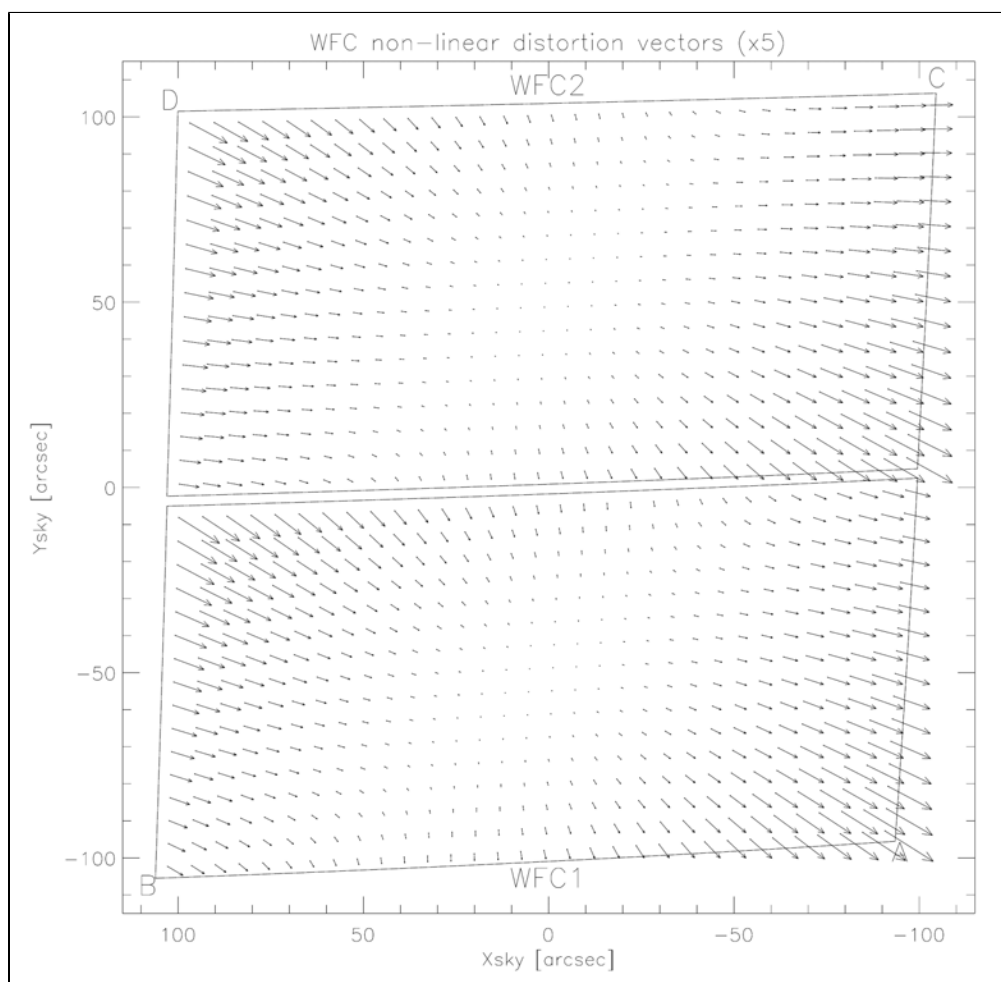
This figure is rotated 180° with respect to the pipeline calibration products, where WFC2 is the lower half of the detector.

Figure 10.112: The map of the effective pixel areas of the ACS/WFC chips.

WFC1 PIXEL AREA MAP
Normalized to 0.05 arcsecond square pixel

WFC2 PIXEL AREA MAP
Normalized to 0.05 arcsecond square pixel

10.4.2 HRC

The High Resolution Channel has its edges aligned approximately along the V2 and V3 axes. In this case, the center of the aperture lies on a line passing through the V2-V3 origin and making an angle of 22° with the V3 axis. The diagonal of the aperture does not correspond to a radius of the *HST* field of view, so the distortion has no particular symmetry with respect to the detector axes. The focal plane of HRC is also 25° away from the plane normal to the light path, hence the scales along the axes differ by 14%. The full field of view of the HRC is less than 30 arcseconds, therefore the scale variation over the field is much less than for the WFC, about 1%. At the center, the X and Y scales are 0.0284 and 0.0248 arcsecond/pixel respectively. The average scales across the middle of the detector are 0.02842 and 0.02485 arcsecond /pixel, making the X and Y widths 29.1 and 25.4 arcseconds. The slightly non-square projected aperture shape is evident in Figure 7.8. The angle between the X and Y axes on the sky is 84.2°. The geometric distortion map for HRC is given in Figure 10.113, where the residuals from the non-linearity are scaled by a factor of 10, with residuals as large as 0.14 arcseconds or 4.9 pixels.

As in the case for the WFC, geometric distortion affects not only the astrometry but also the photometry, and a correction for the pixel area is required in order to restore the proper total counts of the target. The effective area of each pixel is shown as a contour plot in Figure 10.114. The maximum deviation from the central value is about 3%. Because the pixel area map is normalized to square pixels of 0.025 arcsecond on a side rather than an area equal to that of the central HRC pixel, the pixel area map ranges from about 1.1 to 1.15.

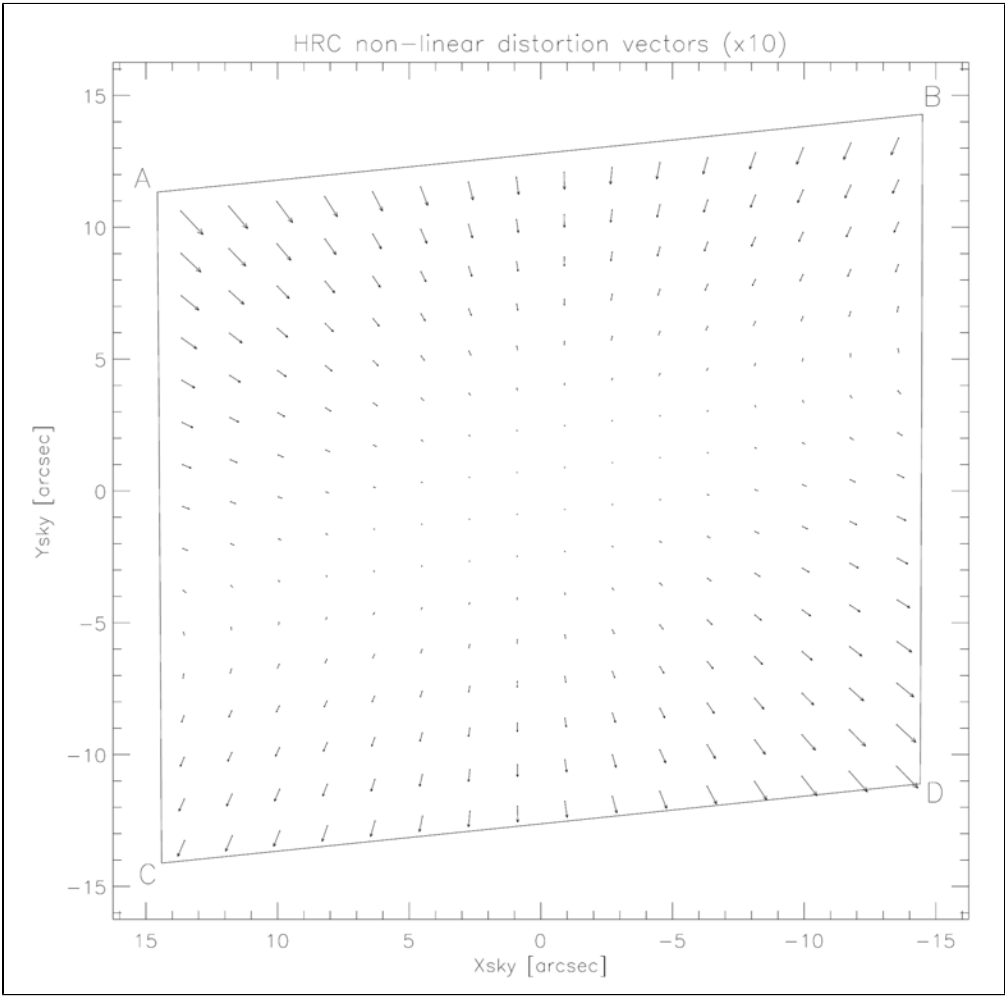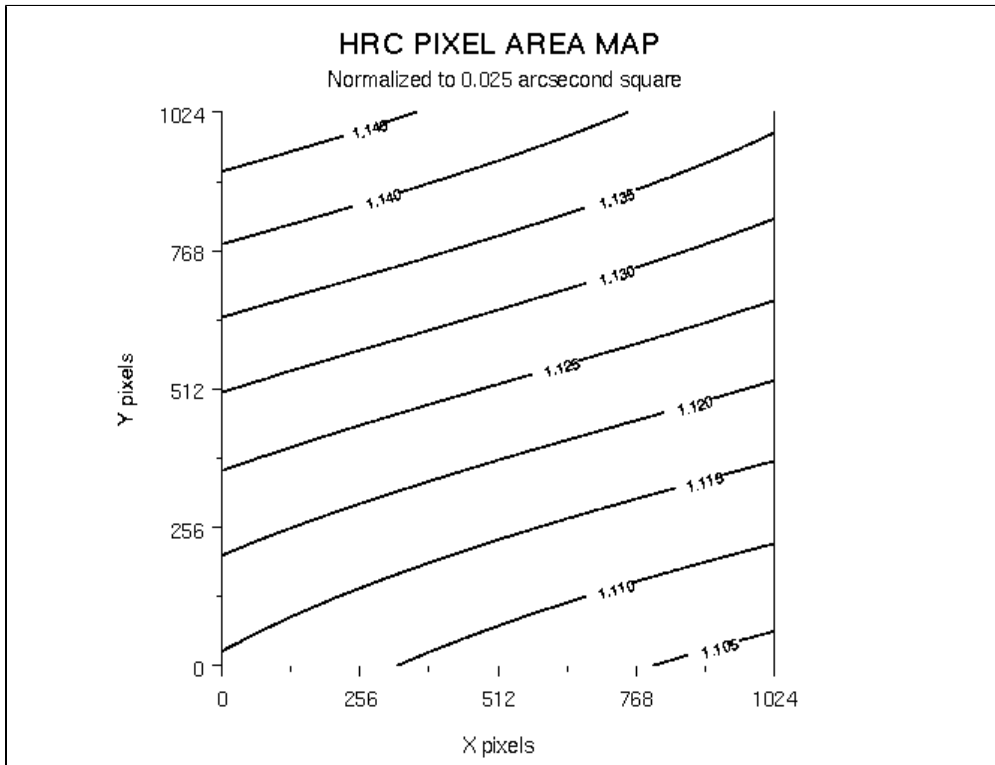**Figure 10.113: The geometric distortion map for the HRC.**

Figure 10.114: The map of the effective pixel areas of the HRC.

10.4.3 SBC

The Solar Blind Channel contains the MAMA detector, which is centered close to the HRC position in the (V2, V3) plane and has a slightly larger field of view, about ~35 × 31 arcsec^2. The scales and distortions have been directly measured. The maximum distortion displacement is about 2 pixels or 0.06 arcseconds. Figure 10.115 shows the distortion map for the SBC detector.

The HRC and SBC both have much smaller fields of view than the WFC. For the SBC, the X direction scale is 0.0338 arcsecond/pixel and the Y direction scale is 0.0301 arcsecond/pixel. Similar to the HRC, the SBC exhibits a 13% difference between X and Y scales with a variation across the aperture of a little over 2%. As with the other cameras, geometric distortion affects photometry by a variation in pixel size across the SBC.

The map of the effective pixel areas of the SBC is shown in Figure 10.116. Because the pixel area map is normalized to square pixels which are 0.025 arcseconds on a side rather than an area equal to that of the central SBC pixel, the pixel area map ranges from about 1.58 to 1.65. (Meurer et al. 2002). The maximum deviation from the central value is about 5% (ACS ISR 2007-09 and ACS ISR 2008-02).

Figure 10.115: The geometric distortion map for the ACS/SBC.
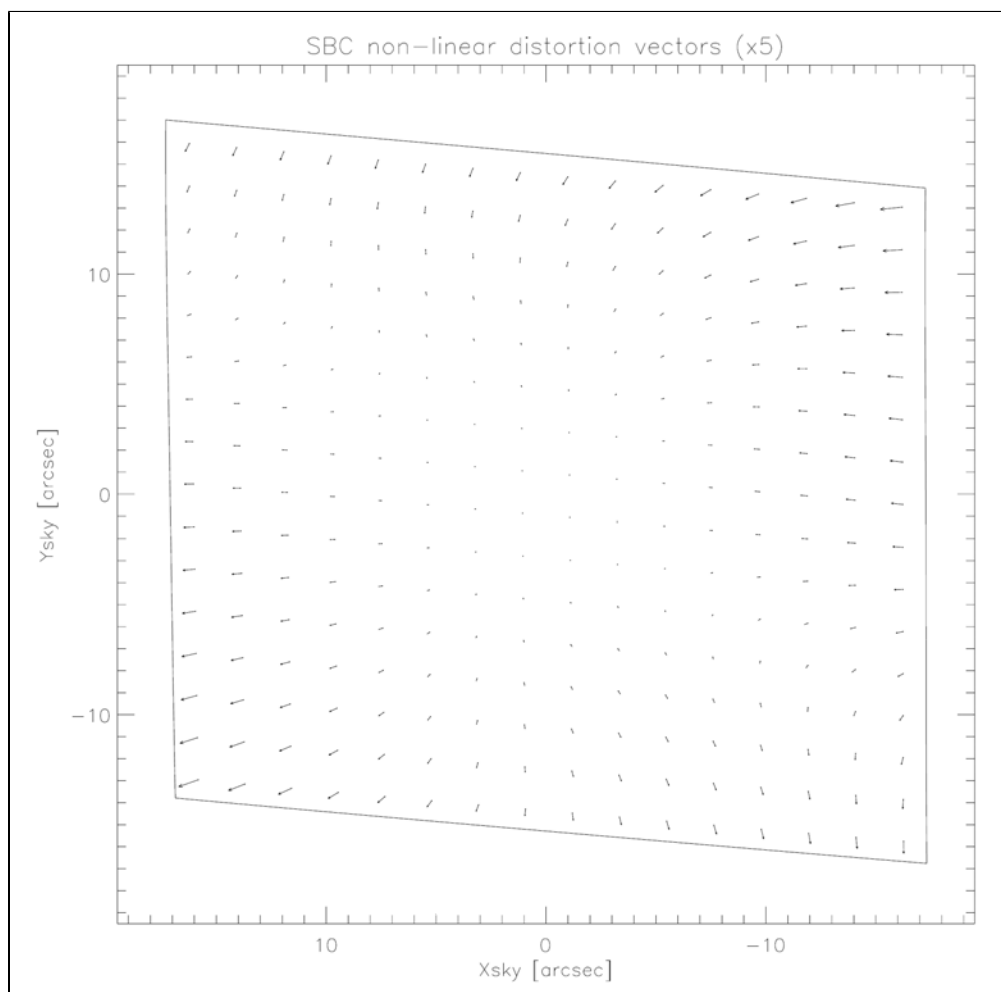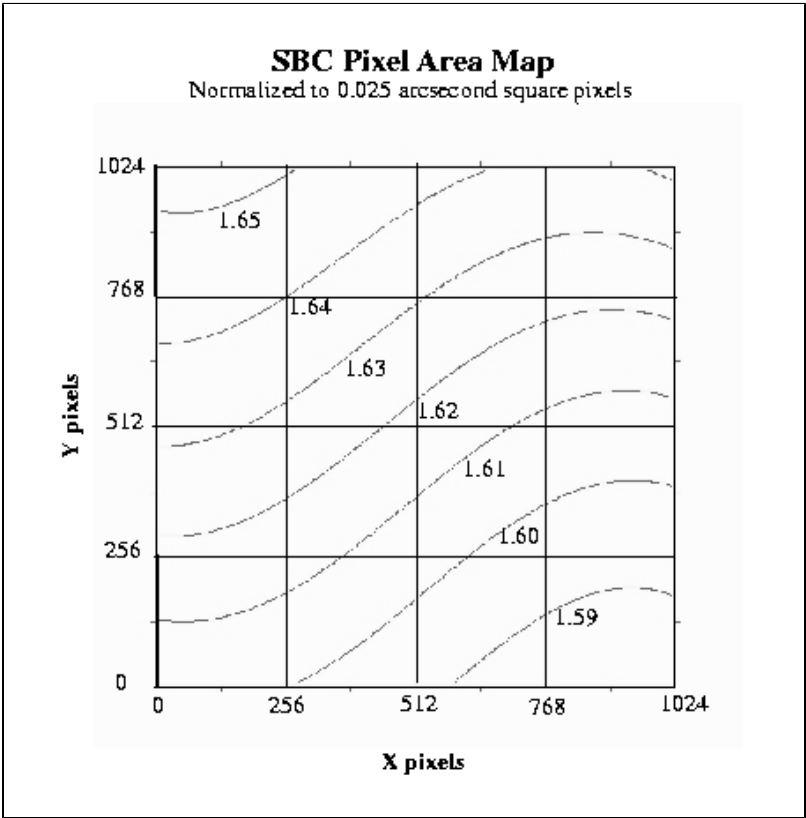
Figure 10.116: The map of the effective pixel areas of the ACS/SBC. The areas are normalized to 0.025 arcsecond square pixels.

Glossary

The following terms and acronyms are used in this Handbook.

2MASS: Two Micron All Sky Survey

A&A: Astronomy & Astrophysics journal.

ABMAG: $-2.5 \log (F\nu) - 48.60$ where $F\nu$ is the flux from the source in erg cm^{-2} sec^{-1} Hz^{-1}.

AB$_\nu$: Correction to ABMAG to account for the fact that the source spectrum is not constant in $F\nu$ (ABMAG=V+AB$_\nu$).

ACS: Advanced Camera for Surveys.

ACS-R: Repaired ACS from SM4.

ADC: Analog to digital converter.

AJ: The Astronomical Journal

Aladin: Interactive sky atlas (http://aladin.u-strasbg.fr).

ApJ: The Astrophysical Journal

APT: Astronomer's Proposal Tool.

ASIC: Application-Specific Integrated Circuit in CEB-R.

AstroConda: Software package and management system that provides the tools and utilities required to process and analyze HST data.

aXe: Spectroscopic Data Extraction Software.

BOP: Bright Object Protection.

BOT: Bright Object Tools for SBC proposing.

CALACS: ACS calibration pipeline software.

CCD: Charge Coupled Device. Solid-state, light detecting device.

CDS: Correlated Double Sampling mode in CEB-R (dual-slope integration or clamp-and-sample).

CEB: CCD Electronics Box.

CEB-R: New CCD Electronics Box installed during SM4.

CMD: Color Magnitude Diagram.

CR: Cosmic ray.

CR-SPLIT: Division of a CCD exposure into shorter exposures to be used for cosmic ray rejection.

CS: Contact Scientist for a HST proposal.

CTE: Charge transfer efficiency.

CVZ: Continuous viewing zone.

DN: Data number.

DQ: Data Quality

DSI: Dual-Slope Integrator.

DSS: Digital Sky Survey.

ETC: Exposure Time Calculator. ETCs are Web-based tools which can be accessed through the ACS webpages.

FGS: Fine Guidance Sensors.

FOS: Faint Object Spectrograph.

FOV: Field of view.

FUV: Far ultraviolet (~912 to 2000 Å).

FWHM: Full width at half maximum.

GALEX: Galaxy Evolution Explorer.

GHRS: Goddard High-Resolution Spectrograph.

GO: General Observer.

GSC: Guide Star Catalog.

GSC2: Guide Star Catalog II.

Help Desk: System for getting help on HST-related topics are http://hsthelp.stsci.edu/ and help@stsci.edu.

HRC: High Resolution Channel.

HST: Hubble Space Telescope.

IDT: Investigation Definition Team.

IR: Infrared.

IRAF: Image Reduction and Analysis System. The environment in which -STSDAS operates.

ISR: Instrument Science Report

IUE: International Ultraviolet Explorer Satellite

K: Degree Kelvin.

LED: Light-emitting diode

L-flats: Low Frequency Variations Flats.

LMC: Large Magellanic Cloud.

LVPS-R: replacement Low Voltage Power Supply.

MAMA: Multi-Anode Microchannel Array.

MAST: Mikulski Archive for STScI Telescopes.

MCP: Microchannel Plate.

MNRAS: Monthly Notices of the Royal Astronomical Society

MPP: Multi Pinned Phased, a CCD mode that reduces dark current rate.

NICMOS: Near-Infrared Camera and Multi-Object Spectrograph.

NIR: Near infrared.

NUV: Near ultraviolet (~2000 to 4000 Å).

OTA: Optical Telescope Assembly.

PASP: Publications of the Astronomical Society of the Pacific.

PC: Program Coordinator.

Phase I proposal: A proposal for observing time on HST.

Phase II program: An approved HST program; includes precise detail of how program is to be executed.

P-flats: pixel-to-pixel high-frequency flats.

POS TARG: POSition TARGet is used to move the sky in the FOV of the camera.

PRF: Pixel Response Function.

Proc. SPIE: Proceedings of the SPIE, an international professional society for optics and photonics technology.

PSF: Point-spread function.

PyRAF: version of IRAF implemented in the Python language.

pysynphot: Python package for synthetic photometry.

QE: Quantum Efficiency.

QEH: Quantum Efficiency Hysteresis.

Quadrant: Section of detector that is read out by an amplifier. For WFC, there are 4 amplifiers, two for each detector, so each amplifier reads one 2048 x 2048 pixel quadrant.

reference file: data file containing ACS parameters or calibration information which is used by the calibration pipeline.

rms: Root mean square.

RQE: Responsive Quantum Efficiency.

SAA: South Atlantic anomaly.

SBC: Solar-Blind Channel.

SDSS: Sloan Digital Sky Survey.

SIDECAR: System Image, Digitizing, Enhancing, Controlling, And Retrieving.

SITe: Scientific Image Technologies; company that designed the ACS CCDs.

SM3B: Servicing Mission 3b to HST in March 2002.

SM4: Servicing Mission 4 to HST in May 2009.

SMOV: Servicing Mission Observatory Verification.

S/N: signal-to-noise ratio.

SNAPSHOT: Short exposures taken during unused blocks of telescope time.

SSDR: Solid state data recorders.

ST-ECF: Space Telescope European Coordinating Facility.

STIS: Space Telescope Imaging Spectrograph.

STScI: Space Telescope Science Institute.

TAC: Telescope Allocation Committee.

TEC: Thermal Electric Coolers.

Tiny Tim: PSF simulation software developed by John Krist & Richard Hook.

TIR: Technical Instrument Report.

UV: Ultraviolet.

UVIS: Ultraviolet and Visual (CCD channel of WFC3).

VEGAMAG: A magnitude system in which Vega has an apparent magnitude of 0 at all wavelengths

WFC: Wide-Field Channel.

WFC3: Wide Field Camera 3, new instrument installed during SM4.

WFPC2: Wide Field Planetary Camera-2. Replacement for WF/PC installed during first servicing mission of December 1993.